

Summer 8-29-2014

Mechanistic Studies of Salt Effects on Bimolecular Electron-Transfer Reactions of Pentaamine Ruthenium Pyridyl Complexes Studied by ^{19}F NMR Line-Broadening and T2 Spin-Echo Techniques

Nicholas J. Magarian
njmagarian@gmail.com

Follow this and additional works at: <https://repository.usfca.edu/thes>

 Part of the [Inorganic Chemistry Commons](#), and the [Physical Chemistry Commons](#)

Recommended Citation

Magarian, Nicholas J., "Mechanistic Studies of Salt Effects on Bimolecular Electron-Transfer Reactions of Pentaamine Ruthenium Pyridyl Complexes Studied by ^{19}F NMR Line-Broadening and T2 Spin-Echo Techniques" (2014). *Master's Theses*. 101.
<https://repository.usfca.edu/thes/101>

This Thesis is brought to you for free and open access by the Theses, Dissertations, Capstones and Projects at USF Scholarship: a digital repository @ Gleeson Library | Geschke Center. It has been accepted for inclusion in Master's Theses by an authorized administrator of USF Scholarship: a digital repository @ Gleeson Library | Geschke Center. For more information, please contact repository@usfca.edu.

**Mechanistic Studies of Salt Effects on Bimolecular Electron-Transfer
Reactions of Pentaamine Ruthenium Pyridyl Complexes Studied by
 ^{19}F NMR Line-Broadening and T_2 Spin-Echo Techniques**

A Thesis Presented to the Faculty
of the Department of Chemistry
at the University of San Francisco
in partial fulfillment of the requirements for the Degree of
Master of Science in Chemistry

Written by

Nicholas Magarian
Bachelor of Science in Chemistry
California Polytechnic State University, San Luis Obispo, California

8/29/2014

**Mechanistic Studies of Salt Effects on Bimolecular Electron-Transfer
Reactions of Pentaamine Ruthenium Pyridyl Complexes Studied by
¹⁹F NMR Line-Broadening and T₂ Spin-Echo Techniques**

Thesis Written By Nicholas Magarian

This thesis is written under the guidance of the Faculty Advisory Committee, and
approved by all its members, has been accepted in partial fulfillment of the
requirements for the degree of

**Master of Science
in Chemistry
at
The University of San Francisco**

Thesis Committee

Jeff Curtis, Ph. D.
Research Advisor

Tami Spector, Ph. D.
Professor

William Melaugh, Ph. D.
Professor

Marcelo Camperi, Ph. D.
Dean, College of Arts and Sciences

Acknowledgements

I would first like to acknowledge my advisor Dr. Jeff Curtis for his patience, support, and guidance, as well as for providing me with skills I will carry with me throughout my career. I would like to give a special thanks to Dr. William Melaugh and Dr. Tami Spector for their advice and time in reviewing my work. I would also like to thank the technical support staff: Jeff Oda, Andy Huang, Chad Schwietert, and Angela Qin for all their assistance throughout my time at USF. I would also like to thank the program assistant, Deidre Shymanski, as well as the USF chemistry department staff. Finally, to my family and friends, thank all of you for listening and supporting me throughout the years, without you I never would have made it through.

Table of Contents

Chapter 1 - An Overview of Electron-Transfer Reactions

1.1	Introduction.....	1
1.2	Complementary Aspects Between Thermal and Optical ET	2
1.2.1	Thermal ET	2
1.2.2	Optical ET.....	5
1.3	The Outer-Sphere Mechanistic Pathway for Activated ET	7
1.4	The Reorganizational Energy Barrier, λ , Associated with ET.....	11
1.4.1	The “inner-sphere” reorganizational energy, λ_{in}	13
1.4.2	The “outer-sphere” (solvent) reorganizational energy, λ_{out}	14
1.5	Potential Energy Surfaces	16
1.5.1	The harmonic oscillator approximation	16
1.5.2	Potential energy surfaces in the “zero-order” diabatic limit.....	21
1.5.3	Potential energy surfaces to first-order (adiabatic ET).....	24
1.5.4	The ET rate expression	25
1.6	Quantum Super-Exchange Theory of H_{AB} Modulation	31
1.7	Debye-Hückel Theory and the Effects of Ionic Strength on Activity Coefficients.....	34
1.8	Association Constants.....	45

Chapter 2 - Kinetic Studies of Salt Effects and Concentration Effects of Reactants on Self-Exchange Reactions Monitored by ^{19}F NMR Spectroscopy

2.1	Introduction.....	61
2.1.1	Known effects of added simple salts on ET rates	65
2.1.2	Known effects of added dicarboxylate salts on the rate of ET	70
2.1.3	Known effects of added hexacyano complexes ($\text{K}_4\text{M}(\text{CN})_6$, where $\text{M} = \text{Fe}^{\text{II}}, \text{Ru}^{\text{II}}, \text{Os}^{\text{II}}$) on the rate of ET	75
2.2	Determination of Kinetic Rate Constants from NMR Line-Broadening and T_2	79
2.3	The T_2 Spin-Echo Experiment	90
2.4	Synthesis and Purification of Reactants and Salts	98
2.4.1	Preparation of ruthenium(III)chloropentaaminedichloride, $[(\text{NH}_3)_5\text{Ru}^{\text{III}}\text{Cl}]\text{Cl}_2$	98
2.4.2	Recrystallization of ruthenium(III)chloropentaaminedichloride, $[(\text{NH}_3)_5\text{Ru}^{\text{III}}\text{Cl}]\text{Cl}_2$	99
2.4.3	Preparation of Zn/Hg amalgum	99
2.4.4	Preparation of ruthenium(II)L-pentaamminehexafluorophosphate, $[(\text{NH}_3)_5\text{Ru}^{\text{II}}\text{-L}](\text{PF}_6)_2$, where $\text{L} = \text{tfpm}$	100
2.4.5	Acetone/Ether purification pentaammineruthenium(II)-L- hexafluorophosphate, $[(\text{NH}_3)_5\text{Ru}^{\text{II}}\text{-L}](\text{PF}_6)_2$ where $\text{L} = \text{tfpm}$	101
2.4.6	Preparation of pentaammineruthenium(II)-L-chloride, $[(\text{NH}_3)_5\text{Ru}^{\text{II}}\text{-L}]\text{Cl}_2$ where $\text{L} = \text{tfmp}$	101

2.4.7	Preparation of pentaammineruthenium(III)-L-chloride, $[(\text{NH}_3)_5\text{Ru}^{\text{III}}\text{-L}]\text{Cl}_3$, where L = tfmp	102
2.4.8	Preparation of disodium dicarboxylate salts, $\text{Na}_2\text{-X}$, where X = muc, tere, 1,4-dcch, adip	103
2.4.9	Preparation of potassium ruthenocyanide, $\text{K}_4\text{Ru}^{\text{II}}(\text{CN})_6$	103
2.4.10	Preparation of potassium osminocyanide, $\text{K}_4\text{Os}^{\text{II}}(\text{CN})_6$	104
2.4.11	Recrystallization of potassium ferrocyanide, $\text{K}_4\text{Fe}^{\text{II}}(\text{CN})_6$	104
2.4.12	Recrystallization of potassium hexacyano complexes, $\text{K}_4\text{M}(\text{CN})_6$, where M = Ru^{II} , Os^{II}	105
2.5	Solution Preparation	106
2.5.1	Solution preparation of reactant solutions for NMR ET self-exchange measurements	106
2.5.2	Solution preparation for added-salt NMR kinetic measurements	107
2.6	NMR Instrument Set-Up and Experiment Execution	108
2.6.1	Setting up the ^{19}F NMR experiment	108
2.6.2	NMR pulse calibration	109
2.6.3	Setting up the ^{19}F spin-lattice (longitudinal) relaxation, T_1 , experiment	114
2.6.4	Setting up the ^{19}F T_2 spin-echo experiment	120
2.6.5	NMR probe/sample temperature calibration	124
2.7	Experimental Methodology used in Measuring Kinetic Salt Effects	132
2.8	Sample Degassing	133
2.8.1	Degassing with argon	134

2.8.2	Degassing by vacuum	134
2.8.3	Saturation with oxygen	136
2.9	Methods for Assessing the Effects of Degassing on the ^{19}F T_2 Spin-Echo ET Kinetic Measured with added Sodium Muconate	136
2.10	NMR Temperature Dependent Kinetic Experiments	138
2.10.1	Line-broadening measurements	138
2.10.2	^{19}F T_2 spin-echo measurements	139
2.11	Validation of the ^{19}F T_2 Spin-Echo Experiment	140
2.12	Reactant Concentration Effects on the Rate of ET (Self-Salting)	146
2.13	Kinetic Salt Effects at Various (Constant) Reactant Concentrations	151
2.14	Sodium Muconate Effects on the Rate of ET as Established by NMR	173
2.15	Effect of Added Group VIII Metal Hexacyano Salts on the Rate of ET	185
2.16	Temperature Dependent Kinetic Studies	195
2.16.1	Reactant concentration effects on activation parameters	198
2.16.2	The effects of added salts on activation parameters	211
2.16.3	Effects of added Group VIIIb hexacyano salts on reaction (2-2) activation parameters	231
2.17	Kinetic Modeling	243
2.17.1	Application of our model to self-salting data	254
2.17.2	Salt-specific kinetic modeling at 0.10 <u>mM</u> reactants	259
2.17.3	Salt-specific kinetic modeling at 0.50 <u>mM</u> reactants	281
2.17.4	Salt-specific kinetic modeling at 1.00 <u>mM</u> reactants	296
2.17.5	Salt-specific kinetic modeling at 5.00 <u>mM</u> reactants	307

2.17.6	Kinetic modeling of added hexacyano's at 0.10 mM reactants	321
2.17.7	Kinetic modeling of added hexacyano's at 5.00 mM reactants	326
2.18	Discussion	332
2.19	Conclusions	347
Appendix A	354

List of Figures

Chapter 1 - An Overview of Electron-Transfer Reactions

Figure 1.1	Optical and thermal ET mechanisms.....	3
Figure 1.2	Harmonic oscillator and associated wavefunctions.....	18
Figure 1.3	Potential energy surfaces showing non-adiabatic ET.....	22
Figure 1.4	Potential energy surfaces showing adiabatic ET.....	25
Figure 1.5	Surfaces and vibrational levels relevant to the three types of tunneling processes in the quantum non-adiabatic ET model	30
Figure 1.6	The “electron-transfer” and “hole-transfer” quantum super-exchange mechanisms.....	34
Figure 1.7	The collective charge-dipole behavior which results in the bulk observable D_s allowing for the medium to be treated as a “polarizable isotropic continuum”	38
Figure 1.8	The first and second hydration spheres around the reactant ions forming the Debye-Hückel ion-atmosphere.....	39
Figure 1.9	A simple cubic “lattice” model which can be used to calculate the effective center-center interreactant distance.....	49
Figure 1.10	A representation of the interpenetrating crystal lattice structures	51
Figure 1.11	The change in the interreactant distance in solution as a function of reactant concentration for reaction (1-27)	55

Chapter 2 - Kinetic Studies of Salt Effects and Concentration Effects of Reactants on Self-Exchange Reactions Monitored by ^{19}F NMR Spectroscopy

Figure 2.1	A schematic of reaction (2-1), the “ <i>pseudo</i> -self-exchange” reaction between $[(\text{NH}_3)_5\text{Ru}^{\text{II}}3\text{-Fpy}]^{2+}$ and $[(\text{NH}_3)_5\text{Ru}^{\text{III}}\text{py}]^{3+}$	61
Figure 2.2	A schematic of reaction (2-2), the “true” (zero-driving force) ET self-exchange reaction between $[(\text{NH}_3)_5\text{Ru}^{\text{II}}\text{tfmp}]^{2+}$ and $[(\text{NH}_3)_5\text{Ru}^{\text{III}}\text{tfmp}]^{3+}$	62
Figure 2.3	Effect of the halide salts on the rate of reaction (2-1) measured by stopped-flow at an equimolar reactants concentration of 0.10 mM.....	67
Figure 2.4	Effect of the halide salts on the rate of reaction (2-2) measured by NMR line-broadening at an equimolar reactants concentration of 5.00 mM.....	69
Figure 2.5	Effect of the dicarboxylate salts on the rate of reaction (2-1) measured by stopped-flow at an equimolar reactants concentration of 0.10 mM.....	72
Figure 2.6	Effect of the dicarboxylate salts on the rate of reaction (2-2) measured by NMR line-broadening at an equimolar reactants concentration of 5.00 mM.....	74
Figure 2.7	Effect of the hexacyano salts on the rate of reaction (2-1) measured by stopped-flow at an equimolar reactants concentration of 0.10 mM.....	77

Figure 2.8	Effect of the hexacyano salts on the rate of reaction (2-2) measured by NMR line-broadening at an equimolar reactants concentration of 5.00 mM.....	78
Figure 2.9	A schematic illustration of how NMR peak resonances arise.....	81
Figure 2.10	An illustration of how NMR line-shapes depend on exchange rate processes as the magnitudes of τ and T_2 are varied	87
Figure 2.11	The CPMG T_2 spin-echo pulse sequence diagram.....	94
Figure 2.12	The rotating frame depiction the net of magnetization vector and Isochromat behaviors during execution of the T_2 spin-echo pulse sequence.....	95
Figure 2.13	An illustration of a pw90 determination <i>via</i> peak intensity vs. angular rotation plot out past pw360	111
Figure 2.14	A coarse pw90 calibration curve for the complex $[(\text{NH}_3)_5\text{Ru}^{\text{II}}\text{tfmp}]\text{Cl}_2$ in D_2O at a concentration of 5.00 mM using the ^{19}F nucleus.....	113
Figure 2.15	A screenshot of the “Channels” sub-tab showing the correct parameters for the ^{19}F T_1 inversion-recovery determination	115
Figure 2.16	A screenshot of the “Acquisition” sub-tab showing the correct parameters for the ^{19}F T_1 inversion-recovery determination	116
Figure 2.17	A screenshot of the “Array Parameter” window for the ^{19}F T_1 inversion-recovery experiment on the $[(\text{NH}_3)_5\text{Ru}^{\text{II}}\text{tfmp}]\text{Cl}_2$ complex in D_2O at a concentration of 5.00 mM.....	117

Figure 2.18	The ^{19}F T_1 inversion-recovery pulse sequence displaying parameters associated with the $[(\text{NH}_3)_5\text{Ru}^{\text{II}}\text{tfmp}]\text{Cl}_2$ complex in D_2O at a concentration of 5.00 mM.....	118
Figure 2.19	An example of the ^{19}F T_1 inversion-recovery curve corresponding to the spin-lattice relaxation of the $[(\text{NH}_3)_5\text{Ru}^{\text{II}}\text{tfmp}]\text{Cl}_2$ complex in D_2O at a concentration of 5.00 mM.....	120
Figure 2.20	The ^{19}F T_2 spin-echo pulse sequence displaying the parameters associated with the $[(\text{NH}_3)_5\text{Ru}^{\text{II}}\text{tfmp}]\text{Cl}_2$ complex in D_2O at a concentration of 5.00 mM.....	123
Figure 2.21	An example of The ^{19}F T_2 spin-echo decay curve of the $[(\text{NH}_3)_5\text{Ru}^{\text{II}}\text{tfmp}]\text{Cl}_2$ complex in D_2O at a concentration of 5.00 mM.....	124
Figure 2.22	The ^1H NMR spectrum of the standard 100% methanol sample displaying the chemical shift difference between the two peaks, $\Delta\delta$, arising from the -OH and -CH ₃ functional groups of the methanol.....	125
Figure 2.23	The temperature calibration curve obtained over the range of 263.15 K (-10°C) to 328.15 K (55°C) using the standard 100% methanol sample	128
Figure 2.24	The instrument readout temperature error as the increment $(T_{\text{Sample}} - T_{\text{Readout}})$ over the temperature range 263.15 K (-10°C) to 328.15 K (55°C).....	130

Figure 2.25	The measured $\log k_{\text{ex}}$ vs. GP behavior found for reaction (2-2) as measured by the T_2 spin-echo method and NMR line-broadening data as well as for reaction (2-1) measured previously by stopped-flow	148
Figure 2.26	The effect of added KF, NaCl, and KBr on the measured k_{ex} for reaction (2-2) at a reactants a concentration of 0.10 mM	155
Figure 2.27	The effect of added Na ₂ muc, Na ₂ adip, Na ₂ tere, Na ₂ (1,4-dcch), KF, and KBr on the k_{ex} for reaction (2-2) at a reactants concentration of 0.10 mM.....	156
Figure 2.28	The effect of added KF, NaCl, and KBr on the measured k_{ex} for reaction (2-2) at a reactants a concentration of 0.50 mM	162
Figure 2.29	The effect of added Na ₂ muc, Na ₂ adip, KF, and KBr on the k_{ex} for reaction (2-2) at a reactants concentration of 0.50 mM	163
Figure 2.30	The effect of added KF, NaCl, KBr, and Na ₂ muc on the measured k_{ex} for reaction (2-2) at a reactants a concentration of 1.00 mM.....	166
Figure 2.31	The effect of added KF, NaCl, and KBr on the measured k_{ex} for reaction (2-2) at a reactants a concentration of 5.00 mM	169
Figure 2.32	The effect of added Na ₂ muc, Na ₂ adip, KF, and KBr on the k_{ex} for reaction (2-2) at a reactants concentration of 5.00 mM	170
Figure 2.33	The effect of added Na ₂ muc on the rate of ET for reaction (2-1) as measured by stopped-flow ⁶ compared to the effect on the rate of reaction (2-2) found using the T_2 spin-echo NMR method at the equimolar reactants concentrations of 0.10 mM.....	175

Figure 2.34	The effect of sodium muconate on the rate of ET for reaction (2-2) as measured by T_2 at a reactants concentrations of 0.10 mM in D_2O and H_2O	178
Figure 2.35	Degassing and O_2 -saturation effects on the rate of reaction (2-2) in D_2O at a reactants concentration of 0.10 mM using raw $\log k_{ex}$ values for the effects of air-saturation, vacuum degassing, Ar degassing, and O_2 saturation.....	181
Figure 2.36	Degassing and O_2 -saturation effects on the rate of reaction (2-2) in D_2O at a reactants concentration of 0.10 mM using $\log k_{ex}$ values normalized to the average $\log k_{ex}$ starting value for effects of air-saturation, vacuum degassing, Ar degassing, and O_2 saturation.....	182
Figure 2.37	The temporal decay of the measured $\log k_{ex}$ over a period of 25 minutes for reaction (2-2) at a reactants concentration of 5.00 mM with the addition of $K_4Fe^{II}(CN)_6$ at 0.01 mM.....	188
Figure 2.38	The stability of the measured $\log k_{ex}$ over a period of 25 minutes for reaction (2-2) at a reactants concentration of 5.00 mM with the addition of $K_4Fe^{II}(CN)_6$ at 0.39 mM.....	189
Figure 2.39	The effect of added $K_4Fe^{II}(CN)_6$, $K_4Os^{II}(CN)_6$, and $K_4Ru^{II}(CN)_6$ on k_{ex} for reaction (2-2) at a reactants concentration of 5.00 mM along with previous results obtained by Qin	191

Figure 2.40	The effect of added $\text{K}_4\text{Fe}^{\text{II}}(\text{CN})_6$, $\text{K}_4\text{Os}^{\text{II}}(\text{CN})_6$, and $\text{K}_4\text{Ru}^{\text{II}}(\text{CN})_6$ on k_{ex} for reaction (2-2) at a reactants concentration of 0.10 mM along with previous results obtained <i>via</i> stopped-flow (reaction 2-1) by Mehmood	194
Figure 2.41	Eyring plots of the data in Tables 2.21 and 2.22 at equimolar reactants concentrations of 0.10 mM, 0.50 mM, 3.00 mM, 5.00 mM, 5.30 mM, 5.50 mM, 6.50 mM, and 8.00 mM	204
Figure 2.42	The approximately linear relationship between ΔH^\ddagger vs. GP (reactant concentrations ranging from 0.10 mM to 8.00 mM) for reaction (2-2) as taken from Table 2.24.....	207
Figure 2.43	The approximately linear relationship between ΔS^\ddagger vs. GP (reactant concentrations ranging from 0.10 mM to 8.00 mM) for reaction (2-2) as taken from Table 2.24.....	208
Figure 2.44	ΔH^\ddagger vs. ΔS^\ddagger for reaction (2-2) at reactant concentrations ranging from 0.10 mM to 8.00 mM showing evidence for enthalpy-entropy compensation	210
Figure 2.45	Temperature dependent normalized rate data for reaction (2-2) at 0.10 mM reactants with no added salt, added KF (1.80 mM), KBr (1.80 mM), Na_2muc (0.60 mM), and Na_2adip (0.60 mM)	214
Figure 2.46	Temperature dependent rate data for reactions (2-1) and (2-2) observed <i>via</i> stopped-flow and T_2 spin-echo, respectively, at 0.10 mM reactants with added KF (1.80 mM), Na_2muc (0.60 mM), and Na_2adip (0.60 mM).....	216

Figure 2.47	Enthalpy-Entropy compensation at a 0.10 mM reactants in the presence of KF, KBr, Na ₂ Muc, and Na ₂ Adip (non-forcing conditions, GP = 0.0494) for reaction (2-2) studied by NMR compared with the entire halide series and dicarboxylate salts for reaction (2-1) studied by stopped-flow	220
Figure 2.48	Temperature dependent normalized rate data for reaction (2-2) at 0.10 mM reactants with no added salt (GP=0.0291), added KF (6.00 mM), and KBr (6.00 mM) such that the total solution GP was 0.0767 (“forcing conditions”).....	223
Figure 2.49	Enthalpy-Entropy compensation at 0.10 mM reactants in the presence of KF and KBr (forcing conditions, [X ⁻] = 0.006 M) for reaction (2-2) studied by NMR compared with kinetic data for the entire halide series obtained in studies of reaction (2-1) by stopped-flow	228
Figure 2.50	Enthalpy-Entropy compensation at 0.10 mM reactants in the presence of the halides and dicarboxylate salts for reaction (2-2) studied by NMR (red circles) compared with kinetic data for the entire halide series and dicarboxylate salts obtained in studies of reaction (2-1) by stopped-flow ⁶ (blue circles) at both non-forcing conditions (GP = 0.0494) and forcing conditions (GP = 0.0767).....	229

Figure 2.51	Temperature dependent line-broadening data for reaction (2-2) obtained at 5.00 <u>mM</u> reactants with no added salt (GP = 0.171), and 3.9×10^{-4} <u>M</u> added $\text{K}_4\text{Fe}^{\text{II}}(\text{CN})_6$, $\text{K}_4\text{Ru}^{\text{II}}(\text{CN})_6$, and $\text{K}_4\text{Os}^{\text{II}}(\text{CN})_6$ such that the total solution GP = 0.181 compared with previous data obtained by Qin.....	234
Figure 2.52	Enthalpy-Entropy compensation at 5.00 <u>mM</u> reactants in the presence of the hexacyano salts (at 3.9×10^{-4} <u>M</u>) for reaction (2-2) compared with previous data obtained by Qin	238
Figure 2.53	Temperature dependent rate data for reaction (2-2) at 0.10 <u>mM</u> reactants with no added salt (black squares, GP = 0.0291), added $\text{K}_4\text{Ru}^{\text{II}}(\text{CN})_6$ (8×10^{-6} <u>M</u> , green circles), and $\text{K}_4\text{Os}^{\text{II}}(\text{CN})_6$ (8×10^{-6} <u>M</u> , yellow circles) making a total solution GP = 0.0295.....	241
Figure 2.54	Showing experimental derived $\log k_{\text{ex}}$ values vs. GP compared with calculated values of $\log k_{\text{ex}}$ theoretically predicted by both the Debye-Hückle-Bronsted equation (1-38) and equation (2-36)	255
Figure 2.55	Experimental data and kinetic modeling results for the self-salting curve (reactants concentration 0.10 <u>mM</u> – 5.00 <u>mM</u>).....	258
Figure 2.56	Experimental data and kinetic modeling results at 0.10 <u>mM</u> reactants with added KF (presumed crystallographic F^- radius of 1.50 Å). Also shown are Sista and Mehmood's stopped flow data for added NaF and KF	266

Figure 2.57	Experimental data and kinetic modeling results at 0.10 mM reactants with added KF now using the hydrated F^- radius of 3.89 Å. Also shown are Sista and Mehmood's stopped flow data for added NaF and KF.....	267
Figure 2.58	Experimental data and kinetic modeling results at 0.10 mM reactants with added NaCl using the crystallographic Cl^- radius for of 1.90 Å compared with previous stopped-flow data for added KCl.....	268
Figure 2.59	Experimental data and kinetic modeling results at 0.10 mM reactants with added NaCl now using the hydrated Cl^- radius of 4.41 Å compared with previous stopped-flow data for added KCl.....	269
Figure 2.60	Experimental data and kinetic modeling results at 0.10 mM reactants with KBr using the crystallographic Br^- radius of 2.61 Å compared with previous stopped-flow data	270
Figure 2.61	Experimental data and kinetic modeling results at 0.10 mM reactants with added KBr now using the hydrated Br^- radius of 4.08 Å compared with previous stopped-flow data	271
Figure 2.62	Experimental data and kinetic modeling results at 0.10 mM reactants with added Na_2muc using the crystallographic muc^{2-} radius of 3.86 Å.....	272

Figure 2.63	Experimental data and kinetic modeling results at 0.10 mM reactants with added Na ₂ adip using the crystallographic adip ²⁻ radius of 3.97 Å compared with previous stopped-flow data	273
Figure 2.64	Experimental data and kinetic modeling results at 0.10 mM reactants with added Na ₂ tere using the crystallographic tere ²⁻ radius of 4.13 Å compared with previous stopped-flow data	274
Figure 2.65	Experimental data and kinetic modeling results at 0.10 mM reactants with added Na ₂ (1,4-dcch) using the crystallographic dcch ²⁻ radius of 4.11 Å compared with previous stopped-flow data	275
Figure 2.66	Experimental data and kinetic modeling results at 0.50 mM reactants with added KF using the crystallographic F ⁻ radius of 1.50 Å	287
Figure 2.67	Experimental data and kinetic modeling results at 0.50 mM reactants with added KF now using the hydrated F ⁻ radius of 3.89 Å	288
Figure 2.68	Experimental data and kinetic modeling results at 0.50 mM reactants with added NaCl using the crystallographic Cl ⁻ radius of 1.90 Å	289
Figure 2.69	Experimental data and kinetic modeling results at 0.50 mM reactants with added NaCl now using the hydrated Cl ⁻ radius of 4.41 Å	290

Figure 2.70	Experimental data and kinetic modeling results at 0.50 mM reactants with added KBr using the crystallographic Br ⁻ radius of 2.61 Å	291
Figure 2.71	Experimental data and kinetic modeling results at 0.50 mM reactants with added KBr now using the hydrated Br ⁻ radius of 4.08 Å	292
Figure 2.72	Experimental data and kinetic modeling results at 0.50 mM reactants with added Na ₂ muc using the crystallographic muc ²⁻ radius of 3.86 Å.....	293
Figure 2.73	Experimental data and kinetic modeling results at 0.50 mM reactants with added Na ₂ adip using the crystallographic adip ²⁻ radius of 3.97 Å.....	294
Figure 2.74	Experimental data and kinetic modeling results at 1.00 mM reactants with added KF using the crystallographic F ⁻ radius of 1.50 Å.....	300
Figure 2.75	Experimental data and kinetic modeling results at 1.00 mM reactants with added KF now using the hydrated F ⁻ radius 3.89 Å.....	301
Figure 2.76	Experimental data and kinetic modeling results at 1.00 mM reactants with added NaCl using the crystallographic Cl ⁻ radius of 1.90 Å	302

Figure 2.77	Experimental data and kinetic modeling results at 1.00 mM reactants with added NaCl now using the hydrated Cl^- radius of 4.41 Å	303
Figure 2.78	Experimental data and kinetic modeling results at 1.00 mM reactants with added KBr using the crystallographic Br^- radius of 2.61 Å	304
Figure 2.79	Experimental data and kinetic modeling results at 1.00 mM reactants with added KBr now using the hydrated Br^- radius of 4.08 Å	305
Figure 2.80	Experimental data and kinetic modeling results at 1.00 mM reactants with added Na_2muc using the crystallographic muc^{2-} radius of 3.86 Å.....	306
Figure 2.81	Experimental data and kinetic modeling results at 5.00 mM reactants with added KF now using the crystallographic F^- radius of 1.5 Å	312
Figure 2.82	Experimental data and kinetic modeling results at 5.00 mM reactants with added KF now using the hydrated F^- radius of 3.89 Å	313
Figure 2.83	Experimental data and kinetic modeling results at 5.00 mM reactants with added NaCl using the crystallographic Cl^- radius of 1.90 Å	314

Figure 2.84	Experimental data and kinetic modeling results at 5.00 mM reactants with added NaCl now using the hydrated Cl^- radius of 4.41 Å	315
Figure 2.85	Experimental data and kinetic modeling results at 5.00 mM reactants with added KBr using the crystallographic Br^- radius of 2.61 Å	316
Figure 2.86	Experimental data and kinetic modeling results at 5.00 mM reactants with added KBr now using the hydrated Br^- radius of 4.08 Å	317
Figure 2.87	Experimental data and kinetic modeling results at 5.00 mM reactants with added Na_2muc using the crystallographic muc^{2-} radius of 3.86 Å.....	318
Figure 2.88	Experimental data and kinetic modeling results at 5.00 mM reactants with added Na_2adip using the crystallographic adip^{2-} of 3.97 Å	319
Figure 2.89	Experimental data and kinetic modeling results at 0.10 mM reactants with added $\text{K}_4\text{Fe}(\text{CN})_6$ using the crystallographic $\text{Fe}(\text{CN})_6^{4-}$ radius of 4.24 Å.....	323
Figure 2.90	Experimental data and kinetic modeling results at 0.10 mM reactants with added $\text{K}_4\text{Os}(\text{CN})_6$ using the crystallographic $\text{Os}(\text{CN})_6^{4-}$ radius of 4.35 Å	324

Figure 2.91	Experimental data and kinetic modeling results at 0.10 <u>mM</u> reactants With added $\text{K}_4\text{Ru}(\text{CN})_6$ using crystallographic $\text{Ru}(\text{CN})_6^{4-}$ radius of 4.38 Å	325
Figure 2.92	Experimental data and kinetic modeling results at 5.00 <u>mM</u> reactants with added $\text{K}_4\text{Fe}(\text{CN})_6$ using the crystallographic $\text{Fe}(\text{CN})_6^{4-}$ radius of 4.24 Å.....	329
Figure 2.93	Experimental data and kinetic modeling results at 5.00 <u>mM</u> reactants with added $\text{K}_4\text{Os}(\text{CN})_6$ using the crystallographic $\text{Os}(\text{CN})_6^{4-}$ radius of 4.35 Å	330
Figure 2.94	Experimental data and kinetic modeling results at 5.00 <u>mM</u> reactants with added $\text{K}_4\text{Ru}(\text{CN})_6$ using crystallographic $\text{Ru}(\text{CN})_6^{4-}$ radius of 4.38 Å.....	331
Figure 2.95	The ratios of $k_{\text{ETX}}/k_{\text{ET}}$ arrived at for the halides studied at as a function of the reactants concentration using crystallographic radii (0.10 <u>mM</u> to 5.00 <u>mM</u> reactants).....	339
Figure 2.96	The ratios of $k_{\text{ETX}}/k_{\text{ET}}$ arrived at for the dicarboxylate salts studied as a function of the reactants concentration(0.10 <u>mM</u> to 5.00 <u>mM</u> reactants).....	340
Figure 2.97	The ratios of $k_{\text{ETX}}/k_{\text{ET}}$ arrived at for the halides studied at as a function of the reactants concentration using both crystallographic and hydrated radii.....	342
Figure 2.98	The log of the $k_{\text{ETX}}/k_{\text{ET}}$ ratios arrived at for the various hexacyano salts studied vs. the $\Delta E_{1/2}$	345

List of Tables

Chapter 1 - An Overview of Electron-Transfer Reactions

Table 1.1	A list of center-center and edge-edge distances for reaction (1-27) at various equimolar reactants concentrations, compared with center-center distances proposed by Robinson and Stokes.....	54
-----------	---	----

Chapter 2 - Kinetic Studies of Salt Effects and Concentration Effects of Reactants on Self-Exchange Reactions Monitored by ^{19}F NMR Spectroscopy

Table 2.1	The structures, names, and abbreviations for the dicarboxylate salts used in this work	64
Table 2.2	The structures, names, and abbreviations group VIII B hexacyano salts used in this work	65
Table 2.3	Comparison of T_2 relaxation times and $\Delta\nu_{1/2}$ values arrived at using both T_2 spin-echo measurement and experimental line-widths	92
Table 2.4	Spectroscopic and electroanalytical characterization data for the complexes used	105
Table 2.5	Instrumental readout temperatures and the actual sample temperatures calculated using equation (2-17).....	127
Table 2.6	The T_2 value of the proton of the methyl group on the methanol in the Autotest sample.....	141

Table 2.7	The measured ET self-exchange rates obtained for reaction (2-2) at different equimolar reactant concentrations through the T_2 spin-echo method, T_2 , and the line-broadening method, $\Delta\nu_{1/2}$	145
Table 2.8	Rates of reaction (2-2) at various concentrations of equimolar reactants showing the “self-salting” rate increase.....	147
Table 2.9	Previous rates obtained by stopped-flow at various concentrations of equimolar reactants showing the self-salting acceleration of reaction (2-1).....	147
Table 2.10	Self-salting slopes taken from Figure 2.25 for the various concentration ranges of reactants.....	149
Table 2.11	The effect of various added salts on k_{ex} for reaction (2-2) at a reactants concentration of 0.10 mM.....	153
Table 2.12	The effect of various added salts on k_{ex} for reaction (2-2) at a reactants concentration of 0.50 mM.....	160
Table 2.13	The effect of various added salts on k_{ex} for reaction (2-2) at a reactants concentration of 1.00 mM.....	165
Table 2.14	The effect of various added salts on k_{ex} for reaction (2-2) at a reactants concentration of 5.00 mM.....	168
Table 2.15	A summary of the measured early slopes for plots of $\log k_{ex}$ vs. GP for reaction (2-2) due to added inert salts at the various reactant concentrations investigated.....	173
Table 2.16	The rates of ET for to reaction (2-2) at a reactants concentration of 0.10 mM using the ^{19}F T_2 spin-echo method	177

Table 2.17	The effects of various degassing methods on the rate of exchange for reaction (2-2) at a reactants concentration of 0.10 <u>mM</u> with Na ₂ muc concentrations of 0 <u>M</u> and 0.004 <u>M</u>	180
Table 2.18	Kinetic data showing time-related decay of k_{ex} over a period of 25 minutes in the presence of K ₄ Fe ^{II} (CN) ₆ at a concentration of 0.01 <u>mM</u> for reaction (2-2) at an equimolar reactants concentration of 5.00 <u>mM</u>	187
Table 2.19	Kinetic data showing stability of catalyzed k_{ex} over a period of 25 minutes in the presence of K ₄ Fe ^{II} (CN) ₆ at a concentration of 0.39 <u>mM</u> for reaction (2-2) at an equimolar reactants concentration of 5.00 <u>mM</u>	187
Table 2.20	The effect of added [K ₄ M ^{II} (CN) ₆] on k_{ex} for reaction (2-2) at 5.00 <u>mM</u> reactants as measured by line-broadening	190
Table 2.21	The effect of added [K ₄ M ^{II} (CN) ₆] on k_{ex} for reaction (2-2) at 0.10 <u>mM</u> reactants as measured by T ₂	193
Table 2.22	Temperature dependent rate data obtained <i>via</i> T ₂ spin-echo at 0.10 <u>mM</u> , 0.50 <u>mM</u> , and 3.00 <u>mM</u> reactants.....	201
Table 2.23	Temperature dependent rate data obtained <i>via</i> NMR line-broadening at 5.00 <u>mM</u> , 5.30, <u>mM</u> , 5.50 <u>mM</u> , 6.50 <u>mM</u> , and 8.00 <u>mM</u> reactants	202
Table 2.24	The best-fit TST activation parameters, ΔH^\ddagger and ΔS^\ddagger , for reaction (2-2) at the various reactant concentrations	205

Table 2.25	Temperature dependent rate data at 0.10 mM reactants in the presence of various added salts making a total GP = 0.0494	212
Table 2.26	The activation parameters, ΔH^\ddagger and ΔS^\ddagger , for reaction (2-2) at 0.10 mM reactants in the presence of added electrolytes at “non-forcing conditions” (constant solution GP = 0.0767, except for the no-salt case)	215
Table 2.27	The activation parameters, ΔH^\ddagger and ΔS^\ddagger derived from the regression lines in Figure 2.46 for reactions (2-1) and (2-2) at 0.10 mM reactants in the presence of added salt at “non-forcing conditions”	217
Table 2.28	Temperature dependent rate data at 0.10 mM reactants in the presence of various added salts making a total GP = 0.0767 (0.006 M salt).....	222
Table 2.29	The activation parameters, ΔH^\ddagger and ΔS^\ddagger , for reaction (2-2) at 0.10 mM reactants in the presence of added electrolytes at “forcing conditions” (constant solution GP = 0.0767, except for the no-salt case)	224
Table 2.30	The activation parameters, ΔH^\ddagger and ΔS^\ddagger , for reactions (2-1) and (2-2) at 0.10 mM reactants in the presence of added salt at “forcing conditions” (constant solution GP = 0.0767, except for the no-salt case)	224
Table 2.31	Temperature dependent rate data at 5.00 mM reactants in the presence of the three hexacyano salts making a total GP = 0.181 (3.9x10 ⁻⁴ M salt) compared with previously obtained values from Qin.....	232

Table 2.32	The activation parameters, ΔH^\ddagger and ΔS^\ddagger , for reaction (2-2) at 0.10 mM reactants in the presence of added electrolytes at 3.9×10^{-4} M (constant solution GP = 0.181, except for the no salt case).....	235
Table 2.33	The activation parameters, ΔH^\ddagger and ΔS^\ddagger derived from the regression lines in Figure 2.51 for reaction (2-2) at 5.00 mM reactants in the presence of added hexacyano salts (constant solution GP = 0.0181, except for the no-salt case)	235
Table 2.34	Temperature dependent rate data at 0.10 mM reactants in the presence of $K_4Ru(CN)_6$ and $K_4Os(CN)_6$ making a total GP = 0.0295 (8×10^{-6} M salt).....	240
Table 2.35	The activation parameters, ΔH^\ddagger and ΔS^\ddagger , for reaction (2-2) at 0.10 mM reactants in the presence of added electrolytes at added hexacyano salts at a concentration of 8×10^{-6} M (constant solution GP = 0.0295, except for no-salt).....	242
Table 2.36	The experimental and calculated radii of the various added-salt and reactant ions used in kinetic simulations	252
Table 2.37	The calculated radii of various ion-pairs using values of bare radii listed in Table 2.36 and employing equation (2-40).....	253

Table 2.38	Best-fit k_{ET} , k_{ETX} , and k_{ETXX} rate constants for reaction (2-2) corresponding to first-order ET inside the presumed PC, PCX, and PCXX reactive intermediates (based on iterative fitting of the $\log k_{ex}$ vs. the self-salting curve over the reactants concentration range of 0.10 mM to 5.00 mM).....	257
Table 2.39	Experimental and calculated rate constants for reaction (2-2) as a function of GP arrived at using our three-channel model over a reactants concentration range of 0.10 mM – 5.00 mM.....	257
Table 2.40	Best-fit k_{ET} , k_{ETX} , and k_{ETXX} rate constants for reaction (2-2) corresponding to first-order ET inside the presumed PC, PCX, and PCXX reactive intermediates arrived at by iterative fitting of the $\log k_{ex}$ vs. salt curves measured at 0.10 mM reactants for the halide and dicarboxylate anions studied	261
Table 2.41	Experimental and calculated rate constants for reaction (2-2) as a function of GP arrived at using our three-channel model at 0.10 mM reactants.....	262
Table 2.42	Best-fit k_{ET} , k_{ETX} , and k_{ETXX} rate constants for reaction (2-2) corresponding to first-order ET inside the presumed PC, PCX, and PCXX reactive intermediates arrived at by iterative fitting of the $\log k_{ex}$ vs. salt curves measured at 0.50 mM reactants for the halide and dicarboxylate anions studied	283

Table 2.43	Experimental and calculated rate constants for reaction (2-2) as a function of GP arrived at using our three-channel model for reaction (2-2) at 0.50 mM reactants.....	284
Table 2.44	Best-fit k_{ET} , k_{ETX} , and k_{ETXX} rate constants for reaction (2-2) corresponding to first-order ET inside the presumed PC, PCX, and PCXX reactive intermediates arrived at by iterative fitting of the $\log k_{ex}$ vs. salt curves measured at 1.00 mM reactants for the halide and dicarboxylate anions studied	297
Table 2.45	Experimental and calculated rate constants for reaction (2-2) as a function of GP arrived at using our three-channel model for reaction (2-2) at 1.00 mM reactants.....	298
Table 2.46	Best-fit k_{ET} , k_{ETX} , and k_{ETXX} rate constants for reaction (2-2) corresponding to first-order ET inside the presumed PC, PCX, and PCXX reactive intermediates arrived at by iterative fitting of the $\log k_{ex}$ vs. salt curves measured at 5.00 mM reactants for the halide and dicarboxylate anions studied	308
Table 2.47	Experimental and calculated rate constants for reaction (2-2) as a function of GP arrived at using our three-channel model for reaction (2-2) at 5.00 mM reactants.....	309

Table 2.48	Best-fit k_{ET} , k_{ETX} , and k_{ETXX} rate constants for reaction (2-2) corresponding to first-order ET inside the presumed PC, PCX, and PCXX reactive intermediates arrived at by iterative fitting of the $\log k_{ex}$ vs. salt curves measured at 0.10 mM reactants for the various hexacyano salts studied.....	321
Table 2.49	Experimental and calculated rate constants for reaction (2-2) with various added hexacyano salts as a function of GP arrived at using our three-channel model for reaction (2-2) at 0.10 mM reactants	322
Table 2.50	Best-fit k_{ET} , k_{ETX} , and k_{ETXX} rate constants for reaction (2-2) corresponding to first-order ET inside the presumed PC, PCX, and PCXX reactive intermediates arrived at by iterative fitting of the $\log k_{ex}$ vs. salt curves measured at 5.00 mM reactants for the various hexacyano salts studied.....	327
Table 2.51	Experimental and calculated rate constants for reaction (2-2) with various added hexacyano salts as a function of GP arrived at using our three-channel model for reaction (2-2) at 5.00 mM reactants	328
Table 2.52	The ratios of k_{ETX}/k_{ET} arrived at for the F^- and Br^- anions at 0.10 mM and 5.00 mM reactants using both explicit integration limit values and infinite integration limits.....	336
Table 2.53	The computed k_{ai} and k_{di} values for the the F^- and Br^- anions at 0.10 mM reactants with 0.0005 M added salt.....	337
Table 2.54	The ratios of k_{ETX}/k_{ET} arrived at for the halides at the various reactants concentrations studied	338

Table 2.55	The ratios of $k_{\text{ETX}}/k_{\text{ET}}$ found for the various hexacyano salts at 5.00 mM reactants as well as their associated redox potentials (vs. SCE).....	344
------------	---	-----

Abstract

Kinetic salt effects on the bimolecular ET self-exchange reaction between pentaamineruthenium(II)(3-trifluoromethylpyridine)²⁺, (NH₃)₅Ru^{II}tfmp²⁺, and pentaamineruthenium(III)(3-trifluoromethylpyridine)³⁺, (NH₃)₅Ru^{III}tfmp³⁺, have been measured using both ¹⁹F NMR line-broadening and CPMG T₂ spin-echo relaxation techniques in H₂O and D₂O. Over the equimolar reactants concentration range of 0.10 mM – 8.00 mM there was a definite “self-salting” rate increase arising from the increased solution ionic strengths due to the reactants and counterions themselves. The magnitude of this effect diverged significantly, however, from predictions based on the classical Debye-Huckle-Bronsted theory of kinetic salt effects. In agreement with earlier stopped-flow work, addition of alkali-metal fluoride salts increased the rate of ET between the like-charged redox reactants in good quantitative agreement with the quantitative predictions of the Debye-Huckle-Bronsted theory of ion atmosphere charge screening effects, but the other halides exhibited progressively-increasing, non-linear upward deviations from theory in the order Cl⁻ < Br⁻ < I⁻. Catalytic effects on the rate of ET from the addition of various dicarboxylate salts were also found to deviate in a non-linear fashion from theory. In sharp contrast to previous stopped-flow work wherein addition of the trans,trans-muconate dianion showed a uniquely-large catalytic affect, NMR investigations established a complete loss in catalytic efficacy for muconate. Numerous control experiments force us to conclude that it is the presence of the magnetic field itself which quenches the catalysis as probed by NMR. Similar investigations showed that additions of even miniscule amounts of metal-hexacyano salts of formulation K₄M^{II}(CN)₆ (M = Fe, Os,

Ru) caused *much* larger ET catalytic effects than those seen with any of the added halides or dicarboxylates. Consideration of the redox thermodynamics of the metal centers involved supports an interpretation of the catalysis based on hole-transfer quantum super-exchange mediation by virtual states corresponding to hole creation on the bridging anions in presumed ternary ionic assemblies involved in the ET transition state.

Chapter 1

An Overview of Electron-Transfer Reactions

1.1 Introduction

Electron-transfer, ET, reactions have been widely studied over the past 60 years.¹⁻³ The underlying physical chemistry of ET reactions holds relevance to diverse areas of chemical reactivity including naturally-occurring biochemical and application-related chemistry such as battery and fuel cell technology. Some examples would include photosynthesis (the anabolic pathway which uses light energy to drive the catalytic conversion of carbon dioxide into sugars), the electron transport chain in human body (the metabolic pathway in the mitochondria which contributes to produce the enzyme ATP), and photovoltaic devices which use light to create electrical energy by exploiting the photo-physical and electron transport properties of semiconductors.⁴⁻⁶

All “redox” reactions imply the existence of an ET elementary step at some point in the mechanism. This is the point at which an electron (or some substantial fraction of a unit electron charge) is transferred from donor (reductant) to acceptor (oxidant). The work described in this thesis will involve a solution-phase sub-case of these reactions known as “bimolecular self-exchange reactions” in which, for example, two transition metal complexes in different oxidation states collide through diffusive encounter and then undergo an ET event over some narrow range of interreactant distance during the encounter.^{7, 8} Much of the work here will describe the effects of added salts on the rates of ET self-exchange reactions carried out in

water, as well as the possible role of specific anion catalysis due to enhanced quantum “super-exchange” mediation between the donor and acceptor in proposed ternary encounter assemblies (*vide infra*).^{9, 10}

The theoretical model pertaining to the details of how ET reactions take place was first established by Rudolph Marcus and Noel Hush beginning in 1956.¹¹⁻¹⁴ This model came to be known as the “Marcus-Hush theory.” It used a simplified model of the reactant structural characteristics and a polarizable dielectric continuum approximation of the surrounding solvent in order to arrive at the first quantitative understanding of ET reaction rates. Rudolph Marcus won the noble prize in chemistry for this model in 1992. The Marcus-Hush model of ET will be outlined below as a part of our description of the reactions studied in this work.

1.2 Complementary Aspects Between Thermal and Optical ET

1.2.1 Thermal ET

Thermally-induced or “activated” ET can take place in both intramolecular and intermolecular contexts. In the intermolecular (bimolecular) case, the donor, D, and acceptor, A, reactant species first diffuse together and upon encounter form what is known as the “precursor complex” (associated pair) as shown in Figure 1.1. In the classical picture, the precursor complex reorganizes its nuclear coordinates through a thermal activation barrier, ΔG_{th} , to form a transition state configuration relevant to the ET event. This transition state is located at, or near the intersection point of the corresponding reactant and product potential energy surfaces.

In the schematic illustration of the ET processes shown in Figure 1.1, a_2 and a_3 represent the average coordination sphere radii, assumed to be proportional to metal-ligand bond lengths, of the two reactant complexes involved in the ET reaction. M and M^+ represent the reactants respective oxidation states, and a^* represents the radii of the thermally activated reactants in which a_2 and a_3 have “compressed” or “expanded” respectively, such that the nuclear coordinates are equal at the intermediate, transition state geometry (independent of electronic state). In this representation, the reactants start in an already formed associated pair or “symmetric binuclear encounter complex” (labeled REACTANT). From this starting point, ET may occur through one of two pathways: thermal ET (lower pathway, represented by k_{th}) or optical ET (upper pathway, represented by $h\nu$, *vide infra*).

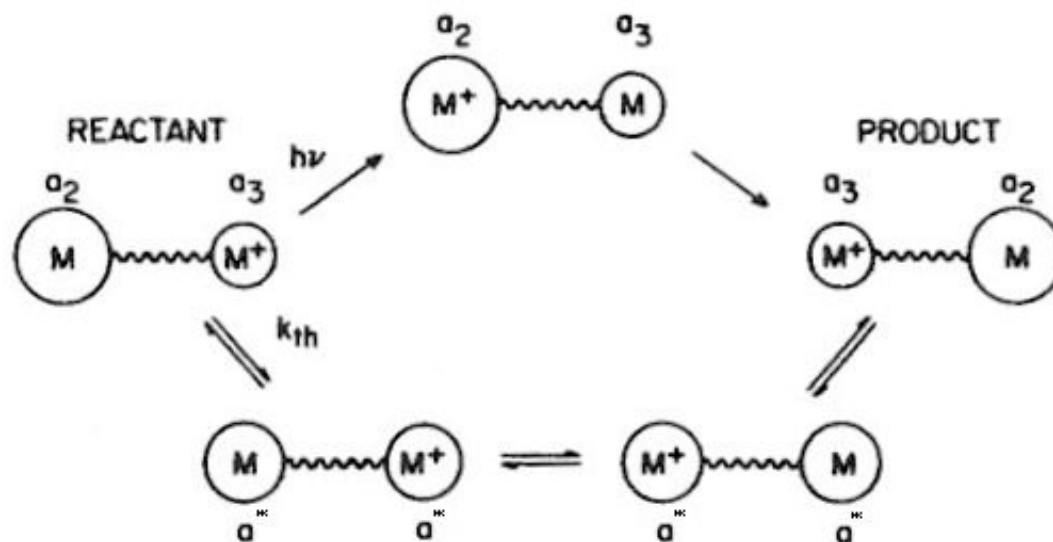


Figure 1.1 An illustration of optical (represented by “ $h\nu$ ”, upper pathway) and thermal (represented by “ k_{th} ”, lower pathway) ET processes relevant to a symmetric binuclear complex (or bimolecular encounter complex if the wavy “bridge” is omitted).¹⁵

At the transition state geometry, the electron is then able to be transferred on a rapid timescale (defined by a tunneling frequency, ν_{el} , *vide infra*), such that the nuclear coordinates and momenta are unchanged during the electronic transition as required by the Franck-Condon principle. The Franck-Condon principle comes from the fact that the time scales of electronic density fluctuations ($< 10^{-15}$ sec), and presumably any transitions between allowed electronic wavefunctions, ψ_{el} , are much faster than nuclear motion which occurs on the vibration/libration timescale of 10^{-13} - 10^{-11} sec. Therefore, it can be assumed that the nuclei remain “frozen” with respect to their positions and momenta during an electronic transition.^{11, 15} The Franck-Condon principle is also related to the Born-Oppenheimer approximation by which the wavefunction for some molecular system is divided into two parts; the separated electronic, ψ_{el} , and vibrational (or nuclear, χ_{nu}) wavefunctions. It is the probability density overlap between nuclear wavefunctions of two different electronic states which directly yields the quantity known as the Franck-Condon “factor”.^{16, 17} These are most often discussed with respect to spectroscopic (“vertical”) transitions between ground and excited electronic states, but they may be applied to thermally-induced barrier crossings as well. In our case, the nuclear coordinates, which remain frozen during the thermally-activated transition, would include both metal-ligand and all other skeletal bond lengths, as well as solvent shell configurations which are electrostatically coupled to the location of the probability density centroid of the “exchanging” electron (corresponding to the difference at the transition state between the system being on either the reactant’s or product’s electronic surface).

Once the electron is transferred within the encounter/precursor complex and some degree of vibrational relaxation has begun, the resulting successor complex is now considered to be “locked” in the products electronic configuration for at least some number of vibrations which can then lead to full relaxation in the thermally-equilibrated product state. This means that the bond lengths of the two complexes, as well as the “solvent shell” around the products now re-adjust to the new electrostatic field corresponding to the products electronic surface. The products then separate and diffuse apart. In the bimolecular thermal ET case, it should be noted that the displacement associated with nuclear relaxation from the activated precursor/successor intermediate nuclear configuration (transition state geometry) to the ET product state is about half of the total nuclear displacement corresponding to going from fully equilibrated reactants to equilibrated products (*vide infra*).

1.2.2 Optical ET

The two reactants, donor and acceptor, can exist together in close proximity in an electrostatically- disfavored “like-charged” encounter complex, a favored, unlike-charged “mixed-valence” ion pair, or in a covalently-bound bridged binuclear complex as shown in Figure 1.1 (where the wavy line represents the bridge). In some cases, the bimolecular, non-bridged encounter (or “precursor”) complex is a stable species, such as the known class of ion pairs of the composition $(\text{NH}_3)_5\text{Ru}^{\text{III}}\text{L}/\text{M}^{\text{II}}(\text{CN})_6$ where $\text{M} = \text{Fe}^{\text{II}}, \text{Ru}^{\text{II}}, \text{or Os}^{\text{II}}$. These strongly-charged (+3) and (-4) acceptor and donor ions are now electrostatically held in an overall (-1) mixed-valence pair.⁹ Photon absorption at the correct wavelength, either by the

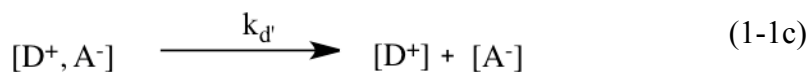
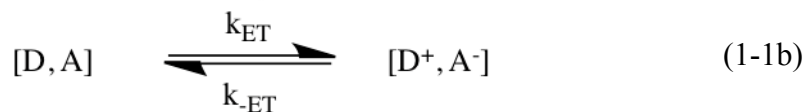
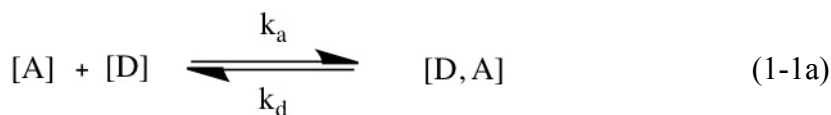
$M \sim M^+$ as in Figure 1.1 or by a general associated donor-acceptor pair $[D, A]$, can then result in sudden ET from donor to acceptor, and this vertical or “optical” ET transition necessarily occurs without any change in nuclear coordinates as required by the Franck-Condon principle (*vide supra*). In covalently linked D-A mixed-valence dimers as in Figure 1.1, the bridging group holds the two metal centers at a fixed distance and typically modulates the quantum interaction between D and A (or “M” and “M⁺”). Now both optical and thermal ET may occur just as in the case of an associated bimolecular ion pair, but now there is no associative step to form the precursor complex and spectroscopic study of the optical ET is facilitated.¹⁵

The “charge-transfer state” or “intervalence-transfer excited state” arrived at upon vertical transition caused by photon absorption is necessarily created in a vibrational excited state of the new electronic surface since nuclear positions are slow to adjust to the new charge distribution. In the case of symmetrical mixed-valence dimer systems where there is no driving force or “0-0” band energy, this Franck-Condon state (or initially-populated vibrational excited state) is at an energy λ above the ground state.¹⁵ The energy λ is known in the ET literature as the “nuclear reorganizational energy” (*vide infra*).¹⁸ The excited state thus formed can then relax to form the thermally-equilibrated products “redox isomer” of the former reactants ground state, now described by the product’s electronic distribution $[D^+, A^-]$ and with nuclear coordinates corresponding to, and in equilibrium with, the new electronic wavefunction.

1.3 The Outer-Sphere Mechanistic Pathway for Activated ET

The “outer-sphere” mechanism of thermally induced ET has been shown to underlie a large fraction of the ET reactions studied thus far.^{7-9, 19} In the work described here, all the reactions studied were outer-sphere reactions. The key defining feature of this mechanism is that no covalent bonds directly join the donor or acceptor sites at any point along the ET reaction coordinate. Therefore, all quantum interactions governing the rate of the elementary ET step are necessarily established by relatively weak and fleeting Van der Waals interactions taking place between the donor and acceptor species at contact during the lifetime of the encounter complex.

The outer-sphere mechanism can be divided into three identifiable steps as represented by equations (1-1a) to (1-1c). The basic mechanistic scheme is shown below, where A is the electron acceptor and D is the electron donor.



In this work, the electron acceptor was the $4d^5$ $(\text{NH}_3)_5\text{Ru}^{\text{III}}(3\text{-trifluoromethylpyridine})^{3+}$ ion in aqueous solution and the donor (or reducing agent) was the $4d^6$ $(\text{NH}_3)_5\text{Ru}^{\text{II}}(3\text{-trifluoromethylpyridine})^{2+}$ ion. Specifics of the reactants as well as their structures will be presented in section 1.7 (see reaction (1-27)).

In the initial, associative step, the two reactants diffuse together to form the encounter or precursor complex (also known as the reactants “ion pair”). In the formation of [A, D], the primary coordination spheres of both complexes remain unchanged. The association rate constant, k_a , for formation of the precursor complex has an upper bound at the maximum rate at which such reactants can diffuse through the solvent. This is known as the “diffusion-controlled limit” (*vide infra*).²⁰ In order for the elementary ET event to occur, as shown in step (1-1b), both the primary ligand sets (the “inner-spheres”) of the reactant ions and their solvation or “outer-sphere” molecular environments must be activated to some intermediate transition-state geometry such that ET may now occur without any change in energy (as required by the Franck-Condon principle in the context of activated rate processes, see the lower leg in Figure 1.1). This activation occurs as a result of stochastic thermal fluctuations of the metal-ligand bond lengths and other nuclear coordinates of the respective inner-coordination spheres along with simultaneous activation of the outer (solvent shell) coordinates. Due to the smaller quantum level spacing’s of the low-frequency solvent dipole librations involved, the rearrangement of the outer-sphere is generally the slower process.²¹ After fluctuations take the system to the correct set of nuclear coordinates, ET occurs *via* tunneling from D to A within the precursor complex and creates the successor complex $[D^+, A^-]$ as shown by step (1-1b). The successor complex can then relax and diffuse apart into separated products or revert back to reactants.

An expression for the bimolecular ET rate constant, k_{ex} , can be arrived at using a steady-state kinetic analysis of steps (1-1a) to (1-1c) based on the precursor [D, A] species as shown below,

$$k_{\text{ex}} = \frac{k_a}{1 + \frac{k_d}{k_{\text{ET}}} + \frac{k_{-\text{ET}} k_d}{k_{\text{ET}} k_{d'}}} \quad (1-2)^{20}$$

here k_a is the kinetically second-order association rate constant, k_d is the first-order rate of dissociation of [D,A] back to reactants, k_{ET} is the first-order rate of ET (see equation (1-16)), $k_{d'}$ is the rate of dissociation of $[D^+, A^-]$ to products and all other variables have been previously defined. If k_a and k_d are much greater than $k_{-\text{ET}}$, then the reaction is “activation” controlled and k_a / k_d can be treated as an association equilibrium constant, K_A . Equation (1-2) is then inverted (to aid in algebraic simplification^{20, 22-24}) and upon employing the pre-equilibrium constant form of k_a / k_d , equation (1-2) then transforms into,

$$\frac{1}{k_{\text{ex}}} = \frac{1}{k_a} + \frac{1}{K_A k_{\text{ET}}} \left(1 + \frac{k_{-\text{ET}}}{k_{d'}} \right) \quad (1-3)$$

If the rate of dissociation of the successor complex, $k_{d'}$, is also much larger than the backwards rate of ET, $k_{-\text{ET}}$, then $k_{-\text{ET}} / k_{d'}$ is negligible and equation (1-3) reduces to,

$$\frac{1}{k_{\text{ex}}} = \frac{1}{k_a} + \frac{1}{K_A k_{\text{ET}}} = \frac{1}{k_a} \left(1 + \frac{k_d}{k_{\text{ET}}} \right) \quad (1-4)$$

Furthermore, if the rate of dissociation of [D, A] back to reactants, k_d , is much larger than the forward rate of ET, k_{ET} , then equation (1-4) reduces to,

$$k_{ex} \cong K_A k_{ET} \quad (1-5)$$

This equation describes the commonly-encountered “pre-equilibrium” kinetic limit²⁵ and frequently applies in low-driving force bimolecular reactions between transition metal complexes such as the ones used in this work. On the other hand, if k_d is smaller than k_{ET} , then an important sub-case of equation (1-4) results,

$$k_{ex} \cong k_a \quad (1-6)$$

This represents the “diffusion-controlled” limit and we see that k_{ex} will not contain any direct information about the rate of the elementary ET step.²⁵ For all the reactions studied in this work, the driving force was zero and the formation/dissociation rates of the precursor complex are known to be fast compared to the rate of ET, therefore equation (1-5) can be rigorously applied.^{19, 24}

The association equilibrium constant, K_A , in equation (1-5) depends on the relative magnitudes of k_a and k_d since $K_A = k_a/k_d$. The factors governing k_a and k_d include, among other things, the sizes of the diffusing reactant species and their charge types. In all cases when the charge product of the reactants is not equal to zero, the magnitudes of k_a and k_d will depend on the ionic strength, μ , of the reactant solution. This is the underlying basis of the simplest type of “kinetic salt effect” and the studies to be reported in this thesis will address this behavior in depth. We will characterize both successes and spectacular failures of the longstanding mathematical

theories of this rate effect in the context of our NMR-based kinetic rate measurements.

1.4 The Reorganizational Energy Barrier, λ , Associated with ET

For optical ET in a symmetric system (*vide supra*), the reorganizational energy, λ , is a “pure” Franck-Condon energy (where symmetric refers to thermodynamically symmetrical cases where the relaxed $[D, A]$ and $[D^+, A^-]$ electronic states are energetically indistinguishable). In the case of transition metal complexes, the experimental λ or “ E_{op} ” (as seen later in Figure 1.3) will arise both from redox-state dependent structural shifts in the primary coordination sphere (ligand set) and in the secondary/tertiary coordination spheres (or first and second “hydration” shells) surrounding the reactant ions. Frequently it is assumed that the total nuclear reorganizational energy, λ , can be apportioned into separate “inner-sphere”, λ_{in} , and “outer-sphere”, λ_{out} , reorganizational energy contributions as described below,

$$\lambda = \lambda_{in} + \lambda_{out} \quad (1-7)^{19, 23}$$

where λ_o would presumably capture all reorganization exterior to the ligand sphere.

The Gibbs activation free energy for the thermal ET process, ΔG^* , is the energy required to reach transition state geometry through which reactants must pass on their way to products. This energy has been shown by Marcus and Hush²⁶⁻²⁸ to be described by equation (1-8) below,

$$\Delta G^* = \frac{\lambda}{4} \left[1 + \frac{\Delta_r G^\circ}{\lambda} \right]^2 \quad (1-8)^{19, 22, 23}$$

in the limit of linear solvent response to field fluctuations and strictly harmonic free-energy surfaces.^{25, 29} Here $\Delta_r G^\circ$ is the driving force (if any) for reaction (equivalent to the “standard reaction Gibbs’s free energy change” or $\Delta E_{1/2}$ as measured electrochemically). Equation (1-8) follows from the assumption of parabolic (harmonic) potential/free-energy surfaces as defining the shape of the reaction coordinate (with negligible departure due to resonance interactions) and in the limit of negligibly small changes in the harmonic oscillator force constants (of all relevant modes) upon going from $[D, A]$ to $[D^+, A^-]$.^{12, 26, 30} The activation free energy can also be apportioned into inner- and outer-sphere components by applying equation (1-7) to equation (1-8) and thus,

$$\Delta G^* = \Delta G_{in}^* + \Delta G_{out}^* \quad (1-9)$$

where ΔG_{in}^* is the inner-sphere (skeletal) part of the Gibbs activation energy and ΔG_{out}^* is the (presumably separable) outer-sphere (solvent) part. For ET self-exchange reactions such as the ones to be discussed here, the $[D, A]$ and $[D^+, A^-]$ ground state species are thermodynamically indistinguishable, therefore $\Delta_r G^\circ$ is necessarily zero and equation (1-8) simplifies to,

$$\Delta G^* = \frac{\lambda}{4} \quad (1-10)$$

1.4.1 The “inner-sphere” reorganizational energy, λ_{in}

In the case of ET between transition metal complexes, the “inner-sphere” reorganizational energy, λ_{in} , can sometimes be treated in an especially simple way if the reactant complexes contain identical small (or even mono-atomic) ligands which then carry the bulk λ_{in} simply in the metal-ligand equilibrium bond distance changes attending ET at each metal center. In such cases, λ_{in} can be expressed as,

$$\lambda_{in} = \frac{n f_1 f_2 (\Delta d_o)^2}{2 (f_1 + f_2)} \quad (1-11)^{22}$$

where n is the number of identical ligands coordinated to one of the reactant metals (typically six), f_1 and f_2 are the symmetric stretching force constants for these modes in the two different redox states at the metal center and Δd_o is the difference between the equilibrium metal-ligand bond distances in the two different redox states (as typically measured on separated reactant ions by crystallography). This expression for the inner-sphere reorganization energy is a highly simplified model in which the reactants are treated as two roughly spherical complexes with only one specific force constant being ascribed to each reactant ion. A more realistic portrayal of the inner-sphere reorganization energy encompasses the summation over all intramolecular vibrations of each complex involved in the reaction which change upon ET. In this more general approach, λ_{in} is described by,

$$\lambda_{in} = \frac{1}{2} \sum_i f_i (\Delta d_o)_i^2 \quad (1-12)^{23}$$

where $f_i = 2 f_1 f_2 / (f_1 + f_2)$ and is the “reduced” force constant for the i^{th} inner-sphere vibration, and $(\Delta d_{\circ})_i$ is the difference in the equilibrium metal-ligand bond distances in the two oxidation states.

1.4.2 The “outer-sphere” (solvent) reorganizational energy, λ_{out}

The energy required to reorganize the medium outside of the primary coordination spheres of the reactant ions is defined as the “outer-sphere” reorganizational energy, λ_{out} . It is related to the change in solvation due to solvent dipole electrostriction, orientation, libration, and other effects which contribute to the overall λ for reaction.³¹ Generally, the reactant with the higher charge (the species “A” in our notation thus far but soon to be specified as “Ru^{III}”) is more strongly solvated by the polar solvent molecules than its partner in the encounter complex, and this leads to significantly different degrees of polarization of the solvent medium exterior to the primary ligand sphere around A.

In the early model developed by Marcus and Hush, the medium outside of the inner-coordination sphere was treated as a “dielectric continuum” with two identifiable parts of the total polarization response assumed separable on the basis of their respective timescales. The rapid, smaller portion of the response was ascribed to the electronic polarizability of the molecules of the medium, and the slow, larger portion to the vibration-libration-orientation polarization of the molecular dipoles of the medium.²³ They used the fact that the rapid electronic polarizability of the medium, D_{op} , is proportional to the square of the refractive index, n^2 . The key

realization was that this “optical-frequency” electronic polarizability of the medium *remains in equilibrium* with the electrostatic change accompanying an ET event, while the slow vibration-orientation polarization of the medium has to fluctuate/adjust to a non-equilibrium value appropriate to the “averaged” charge distribution of the activated complex prior to a thermally-activated ET event. This is the constraint which governs whether the electronic ET transition is “allowed” within the zero-Franck-Condon energy or “isoenergetic” requirement for the elementary ET step.^{12, 32} The free-energy change necessary to produce the non-equilibrium polarization of the solvent appropriate to the transition state when the reactants are treated as spheres was then independently derived by Marcus and Hush as,

$$\lambda_{\text{out}} = (\Delta e)^2 \left(\frac{1}{2r_1} + \frac{1}{2r_2} + \frac{1}{d} \right) \left(\frac{1}{n^2} - \frac{1}{D_s} \right) \quad (1-13)^{12, 23, 26, 27}$$

where Δe is the amount of charge transferred in the reaction, r_1 and r_2 are the radii of the two reactant complexes, d is the distance between the centers of the two reactants, n is the refractive index (which upon squaring gives the “optical” dielectric constant, D_{op}), and D_s is the “static” dielectric constant of the medium (which describes the ability of any solvent or other condensed medium to screen electric fields at low frequency). In our case n^2 is 5.5³³ and D_s is 78.5 at 298 K for water (negligibly different at 298 K for D₂O). Equation (1-13) is rigorously valid only if,

$$d > (r_1 + r_2) \quad (1-14)$$

which implies that the “contacting spheres” idea is actually outside the range of allowed conditions (though metal complexes bound to the ends of a bridging ligand,

such as 4,4'-bipyridine, do fit the constraint).^{15, 34, 35} Extensive experimental work has shown, however, that the relation indeed predicts observed optical and thermal ET behavior even in cases where this condition is violated to a significant degree.^{9, 36}

1.5 Potential Energy Surfaces

Understanding of the interplay between the governing optical and thermal ET energetic quantities and the conceptual basis for the quantum rate theory of ET are facilitated by explicit consideration of the potential energy surfaces which describe the reactant and product states in nuclear configurational space. In the next sections we will develop these ideas more fully.

1.5.1 The harmonic oscillator approximation

In the most simplistic approach, we can think of a set of $3N-6$ degrees of freedom (from N total nuclei) behaving as “normal mode” harmonic oscillators contributing to the construction of the relevant hyper-surfaces *via* their mutually orthogonal (potential) energy *vs.* nuclear displacement functions. The classical one-dimensional harmonic oscillator is defined by a point mass bound at some equilibrium position to an infinite mass (wall) by a “spring like” restoring force whose magnitude is directly proportional to the particle’s displacement from equilibrium.³⁷ Noting that energy \equiv force \times distance, one can construct energy surfaces in their most basic form as the potential energy, $V(x)$, of the oscillator of interest using Hooke’s law,

$$V(x) = \frac{1}{2} k (x)^n \quad (1-15)^{37}$$

where k is the force constant and x is the displacement from equilibrium. The displacement coordinate x can be that either of a single particle relative to a point in space, or the idea can be extended to the distance along some “normal mode” of oscillation involving two or more bound masses. The exponent n is equal to 2 in the ideal, “harmonic”, case. The potential energy surfaces of the idealized harmonic oscillator are smooth and finite for all finite values of x , therefore the oscillators are always confined to the curve of the “potential well” function in equation (1-15). In the case of polyatomic reactants, it is a simple matter to extend the potential function to any number of vibrational degrees of freedom employing equation (1-12).

In order to understand the more-relevant quantum mechanical harmonic oscillator which would apply to bound atoms, one must solve the Schrödinger equation using equation (1-15), or its $3N-6$ dimension generalization, as the potential energy term in the molecular Hamiltonian. The energies of the allowed levels, E_v , in the potential well are then found as the eigenfunction/eigenvalue solutions of the Schrödinger equation. All of the energy levels are equally spaced in the harmonic case with the lowest state having zero nodes in its eigenfunction (these being in fact the “nuclear” or “vibrational” wavefunctions pertaining to the Born-Oppenheimer approximation and the Franck-Condon Principle mentioned in section 1.2). The first excited level has one node, the next two, and so on as shown in Figure 1.2. In the simplest case there is only one wavefunction for each allowed energy level and thus all of the levels are non-degenerate.

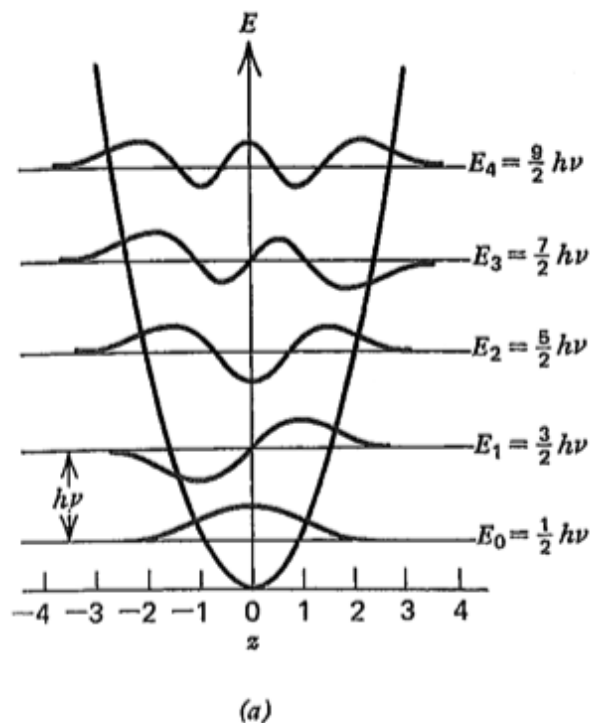


Figure 1.2 The quantum-mechanical solutions (vibrational energies and wavefunctions) for the parabolic potential function or “harmonic oscillator” (with energy levels, E_v , marked by the equally-spaced lines at $E_v = (1/2)(v + h\nu)$; v is the quantum number index for each vibrational level and h is plank’s constant). The superimposed wavefunction plots, $\psi_v(z)$, correspond to the nuclear probability amplitude vs. mode displacement coordinate, z , for each allowed E_v .³⁷

In the case of a spherical or an even higher multi-dimensional harmonic oscillator, the potential energy surfaces can be assumed to be symmetrical as a simplified starting point. If all vibrations are harmonic, a three-dimensional harmonic oscillator may be treated as three separable one-dimensional harmonic oscillators, therefore allowing the three-dimensional harmonic oscillator to be analyzed in terms

of a sum over three one-dimensional harmonic oscillators, whose mode-by-mode wavefunctions are combined by multiplication.³⁷

In the Marcus-Hush approach to ET in condensed phases, it is the “linear response” approximation which allows for generalization from potential energy surfaces (including solvent polarization) to parabolic *free-energy* surfaces and the familiar ET “reaction coordinate”.²⁹ This generalization can be applied in the most straight-forward way to $[D, A]$, $[D^+, A^-]$ reactions in the zero driving force limit (where the total free energy change between the minima of the reactant, $[D, A]$, and product, $[D^+, A^-]$, parabolas is equal to zero), and where the entropy of activation for ET, ΔS^* , within the precursor complex is negligible. These constraints are generally accepted as plausible for charge-symmetric systems with overall $\Delta S^0 \sim 0$ like the ones studied in this work, as well as to similar “low driving force” linking cases where $\Delta G_{\text{rxn}} \ll \lambda$.^{19, 25, 28, 38} Therefore, free-energy surfaces are often presumed and used analogously to potential energy surfaces by workers describing ET reactions in solution *via* application of Marcus-Hush theory, but it should be noted that the harmonic/free energy paradigm is often extended beyond its realm of rigorous applicability.

One major departure from the idealized harmonic oscillator model and equation (1-15) relative to real systems involves the sometimes significant degree of anharmonicity inherent in real vibration-libration energy manifolds of the surrounding solvent (or other) medium components in condensed-phase ET reactions. This reflects the fact that potential energy eventually goes up with inward

displacement, x , to the 6th-14th power as the nuclei are compressed, and also that it goes up as displacement to some power less than 2 once bonds are stretched more than 15-20% beyond their equilibrium values and thus start to break. This is especially true for the weaker, essentially electrostatic and dipolar, type of interactions (including H-bonding) which characterize the solvation sphere surrounding the associated reactants in the precursor complex. In the case pertaining to this work, these are predominately ion-dipole and H-bonding interactions with H₂O acting as an H-bond “acceptor” and the Ru-coordinated ammine ligands acting as H-bond “donors”. We note here that an alternative description of these interactions which focuses on H₂O as electron-density “donor” (Lewis base) and the ammine hydrogen’s as electron-density “acceptors” (Lewis acids) has been analyzed extensively in prior literature.^{1, 7} An important consequence of anharmonicity is that it causes the allowed quantum spacing’s between vibrational levels to narrow significantly at even moderate values of v (the vibrational quantum number), and this effectively blurs the vibrational manifold towards a very high density of states and “continuum-like” behavior at even moderate thermal energies.³⁷

An important aspect of the essential physics captured in Figure 1.2 involves the amplitude of the non-vanishing nuclear wavefunction extending past the classical oscillator “turning points” as described by the analytical and continuous E vs. displacement, z , potential function curve. This well-known quantum mechanical result applies whether the vibrational problem is treated approximately *via* the harmonic oscillator model or using full anharmonic potential functions in the nuclear

Hamiltonian.³⁹ Interestingly, penetration of the nuclear wavefunctions, χ_{nu} , into the classically-forbidden region implies the presence of “negative kinetic energy” for the system in these regions.³⁷ More importantly, in the context of ET reactions this exponential decay of nuclear probability amplitudes with distance allows for non-zero Franck-Condon overlap between vibrational levels in two neighboring such parabolas even at energies *below* that of the classical intersection/transition region. This forms the basis for activationless or “nuclear-tunneling limited” ET rates as will be discussed further on.^{26, 30}

1.5.2 Potential energy surfaces in the “zero-order” diabatic limit

The potential energy surfaces shown in Figure 1.3 are drawn in the diabatic, “zero-order” limit in which any degree of electronic coupling (resonance interaction), H_{AB} , between the redox sites is assumed to be energetically negligible. In such cases, the shapes of the diabatic curves are solely determined by the potential energy, E , vs. nuclear coordinates vibrational potential functions, and in this limit the intersection zone of the surfaces, as shown in Figure 1.3, retains a very sharp, “cusplike” character. A consequence of this limit involves the possibility for the “exchanging electron” to remain localized on the donor even as vibrations carry the entire system into and past the intersection region such that there is no longer any energetic or Franck-Condon overlap type reason for the $[\text{D}, \text{A}] \longrightarrow [\text{D}^+, \text{A}^-]$ transition not to occur.²³ In Figure 1.3, E is the potential energy, q is the nuclear configuration along the (presumably high-dimensional) reaction coordinate, E_{op} is the optical ET energy

(which in energetically-symmetric ET self-exchange cases is equal to the reorganizational energy λ), and E_{th} is the thermal ET activation energy (which is equal to $\lambda/4$ in the case of rigorously-parabolic surfaces, see equations (1-8) and (1-10)).

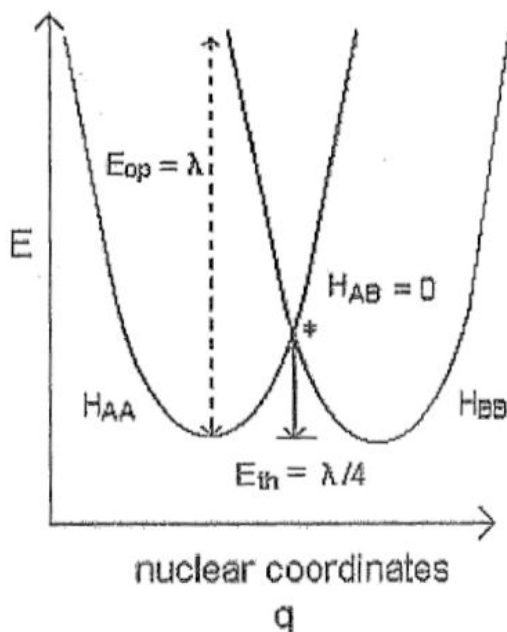


Figure 1.3 Zero-order (diabatic) potential energy surfaces describing reactants (denoted by H_{AA}) and the products (denoted by H_{BB}) corresponding ET reactions in the weak-coupling, non-adiabatic limit.⁴⁰

The expectation value, H_{AA} , of the reactant's energy $[D, A]$ at the minimum of the zero-order energy surface in the *absence* of any electronic resonance interaction with the $[D^+, A^-]$ state (a requirement of the diabatic limit) can be expressed as,

$$H_{AA} = \langle \psi_A | H | \psi_A \rangle \quad (1-16)^{23}$$

Where our focus here is on ψ_A , the electronic wavefunction of the initial state (reactants, $[D, A]$), and H is the Hamiltonian operator (there would also be nuclear/vibrational and spin wavefunction terms present in the full description). Similarly, the expectation value H_{BB} of the energy at the minimum of the product's, $[D^+, A^-]$, surface in the absence of any resonance interaction with the $[D, A]$ state is,

$$H_{BB} = \langle \psi_B | H | \psi_B \rangle \quad (1-17)^{23}$$

where now ψ_B denotes the product's electronic state. The cuspidity of the surfaces at the point where the product's and reactant's surfaces intersect is enforced by the diabatic requirement that the resonance coupling matrix element, $H_{AB} = 0$ (*vide infra*).

In semi-classical rate theories, this zero-interaction, diabatic constraint is relaxed such that the probability of ET occurring near the intersection point depends parametrically on the degree of electronic interaction (resonance coupling energy H_{AB}) between the two redox sites (or more formally, between the $[D, A]$ and $[D^+, A^-]$ electronic states). In real systems approaching the zero-interaction limit, the ET process is relatively slow due to the resulting very low probability (and hence low frequency) of the electron tunneling event during nuclear excursions into the intersection region. This so-called “non-adiabatic limit” (same as “diabatic” used above) is operationally characterized by the condition $H_{AB} \ll k_B T$ (which leads to the “transmission coefficient” κ_{el} , being $\ll 1$, *vide infra*).²³

1.5.3 Potential energy surfaces to first-order (adiabatic ET)

When resonance coupling is sufficient that the magnitude of H_{AB} becomes significant at the point of intersection of the two surfaces, then the potential energy surface profile shown in Figure 1.4 becomes relevant. The surfaces here are referred to as the “first-order” or “adiabatic” states of the system which describe the situation when electronic coupling energy H_{AB} is no longer energetically negligible on the scale of the zero-order barrier. This lowers the energy at the intersection point by an amount H_{AB} , and the total “splitting” between the lower and upper surfaces is then equal to $2H_{AB}$. The non-negligible H_{AB} decreases the magnitude of the thermal ET activation energy, E_{th} , to $\lambda/4 - H_{AB}$. This quantum interaction effectively stabilizes the transition state and leads to a rounding of the energy surfaces at the intersection region (as compared to the zero-order case, *vide supra*). A dynamical consequence of this resonance splitting is that as the system reaches the “intersection region” *via* nuclear fluctuations it will remain on the lower, continuous potential energy surface. Such cases where $H_{AB} \geq k_B T$, are said to be in the “adiabatic” ET limit, and in contrast to previous case, the transmission coefficient $\kappa_{el} \rightarrow 1$ (*vide infra*).

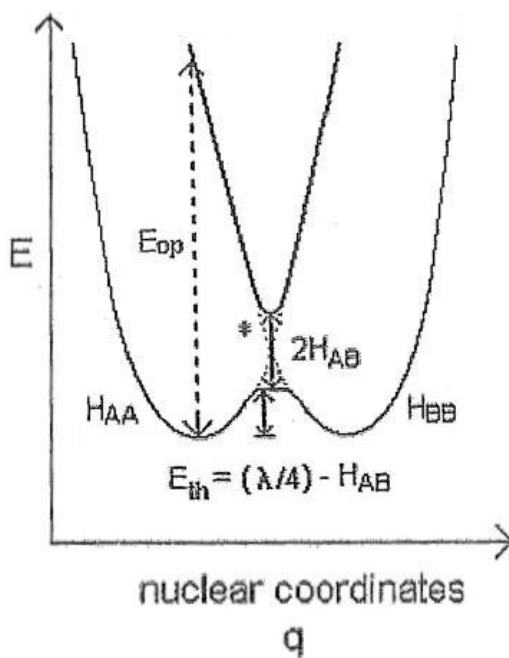


Figure 1.4 Illustration the of first-order potential energy surfaces for the reactants (denoted by H_{AA}) and the products (denoted by H_{BB}) corresponding to ET in the adiabatic limit where the coupling or “resonance” energy H_{AB} is no longer negligible.⁴⁰

1.5.4 The ET rate expression

According to classical barrier crossing theories, once the precursor complex has formed and has been thermally activated to the intersection region ET may occur. In the classical activated complex (or TST) formalism,²³ the reaction is assumed to be adiabatic ($\kappa_{el} = 1$) and nuclear tunneling effects (where the nuclear tunneling factor, $\Gamma_n = 1$, *vide infra*) are ignored. In this limit the first-order rate constant for activated ET, k_{ET} is,

$$k_{ET} = \nu_n e^{\frac{-\Delta G^*}{RT}} \quad (1-18)^{18, 22, 23}$$

where ν_n is the effective frequency of nuclear motion (which is assumed $\approx k_B T / h$ in transition state theory), R is the ideal gas constant, T is the absolute temperature, and ΔG^* is the Gibbs energy of activation as defined previously in equation (1-8) and (1-10).

The next level of refinement past the classical transition state theory expression is the “semi-classical” rate expression where the magnitude of the resonance interaction is incorporated by accounting for the probability of ET with each nuclear excursion into the intersection region. The electronic “transmission coefficient”, κ_{el} , parametrically describes this probability. It is derived to reflect the balance between the electron tunneling frequency and the amount of time the system spends at or near the potential surface intersection region.²² The magnitude of κ_{el} is proportional to the resonance energy squared, H_{AB}^2 , and approaches unity when this (off-diagonal) resonance coupling matrix element is large (thus $\kappa_{el} \cong 1$ for “adiabatic” ET and $\kappa_{el} \ll 1$ for “non-adiabatic” = “diabatic” ET).¹⁸ According to the Landau-Zener model, the electronic transmission coefficient in the high-temperature limit can be expressed as,

$$\kappa_{el} = \frac{2[1 - \exp(-\nu_{el} / 2\nu_n)]}{2 - \exp(-\nu_{el} / 2\nu_n)} \quad (1-19)^{18, 22, 23}$$

where ν_n has been previously defined and ν_{el} is the frequency of ET (tunneling) within the activated complex and is given by,

$$\nu_{el} = \frac{2H_{AB}^2}{h} \left[\frac{\pi^3}{(\Delta G_{out}^* + \Delta G_{in}^*)RT} \right]^{1/2} \quad (1-20)$$

where h is Plank's constant (all other variables have been previously defined). Modifying the rate expression in equation (1-18), we now include the probability of ET per passage into the intersection region as seen in equation (1-21).

Additional corrections to equation (1-18) must be made to capture quantum mechanical effects in cases of low temperature or high effective nuclear frequencies and hence vibrational level spacing's. This is accomplished by including the nuclear tunneling factor, Γ_n , which allows for a finite *nuclear* tunneling frequency through the potential energy barrier in cases where activated barrier passage is slow.²³ The rate constant for ET according to this extended semi-classical formalism is then given by,

$$k_{ET} = \nu_n \kappa_{el} \Gamma_n e^{\frac{-\Delta G^*}{RT}} \quad (1-21)^{22}$$

The nuclear factor is defined as the ratio of the nuclear frequency factor including tunneling effects (semi-classical treatment, κ_n) to the high-temperature limit (classical treatment, $(\kappa_n)_{T=\infty}$) as described by,

$$\Gamma_n = \frac{\kappa_n}{(\kappa_n)_{T=\infty}} \quad (1-22)^{22, 23}$$

$$\Gamma_n = \frac{\Delta G_{in}^* - \Delta G_{in}^*(T)}{RT} \quad (1-23)$$

where ΔG_{in}^* is the classical, temperature-independent, inner-shell reorganizational energy (coming from $(\kappa_n)_{T=\infty}$) and $\Delta G_{\text{in}}^*(T)$ is the temperature-dependent, inner-shell reorganization energy (coming from κ_n).²³ The temperature dependent, κ_n , term can be expressed in terms of temperature dependent reorganization energy as,

$$\kappa_n = e^{\left[\frac{-(\Delta G_{\text{out}}^* + \Delta G_{\text{in}}^*(T))}{RT} \right]} \quad (1-24)^{23}$$

At high-temperatures, $\Delta G_{\text{in}}^*(T)$, approaches the classical ΔG_{in}^* and Γ_n approaches unity. This quantum mechanical correction adjusts the rate expression to account for nuclear tunneling without abandoning the classical free-energy barrier.^{41, 42} When the ET reaction is adiabatic ($\kappa_{el}=1$), equation (1-21) then becomes,

$$k_{\text{ET}} = v_n \Gamma_n e^{\frac{-\Delta G^*}{RT}} \quad (1-25)$$

When the reaction is non-adiabatic and $\kappa_{el} \cong v_{el}/v_n \ll 1$, and equation (1-21) is now,

$$k_{\text{ET}} = v_{el} \Gamma_n e^{\frac{-\Delta G^*}{RT}} \quad (1-26)$$

In the classical non-adiabatic case, ET may *only* occur when the system vibrates into, or very near, the intersection region of the potential surfaces and quantum electron tunneling occurs. This does allow for the reactants to transition to the products surface, but it is a rare event when compared to the frequency of barrier “attempts” arising from the stochastic inner- and outer-sphere nuclear fluctuations. Marcus theory was originally derived for rigorous application to systems in this non-adiabatic regime, but subsequent experimental work has shown that it can also be

applied usefully to understand ET reaction dynamics, well up into the adiabatic regime as well.^{8, 18}

In order to more fully explain the rates of non-adiabatic ET reactions (over a larger temperature range) and the observed rates of ET at very low temperatures, a “full” quantum mechanical approach is needed which formally encompasses both nuclear and electronic tunneling probabilities.²⁰ Tunneling processes determine observed rates in the quantum non-adiabatic model in three identifiable ways. These are: I. electron tunneling at the transition state, II. Activated nuclear tunneling, and III. temperature-independent nuclear tunneling. We will discuss these in order here and make reference to Figure 1.5 which shows the relevant surfaces and nuclear wavefunctions.³⁰

When electron tunneling occurs at the transition state, the reactant and product states have the same nuclear configurations (as seen at the point of intersection of the surfaces in Figure 1.5). The $[D, A]$ and $[D^+, A^-]$ state have large vibrational wavefunction overlap at this point when the systems are in the high-lying vibrational state denoted by I. in Figure 1.5. There is a finite probability that an electron will tunnel from D to A and take the system from the reactants surface to the products surface even if H_{AB} is very small ($\kappa_{el} \ll 1$) but still greater than zero. The probability of tunneling at the intersection region is not temperature dependent, but the overall rate of reaction will be temperature dependent due to the activation energy required to reach the intersection region where the vibrational overlap (Franck-Condon) integrals are large.

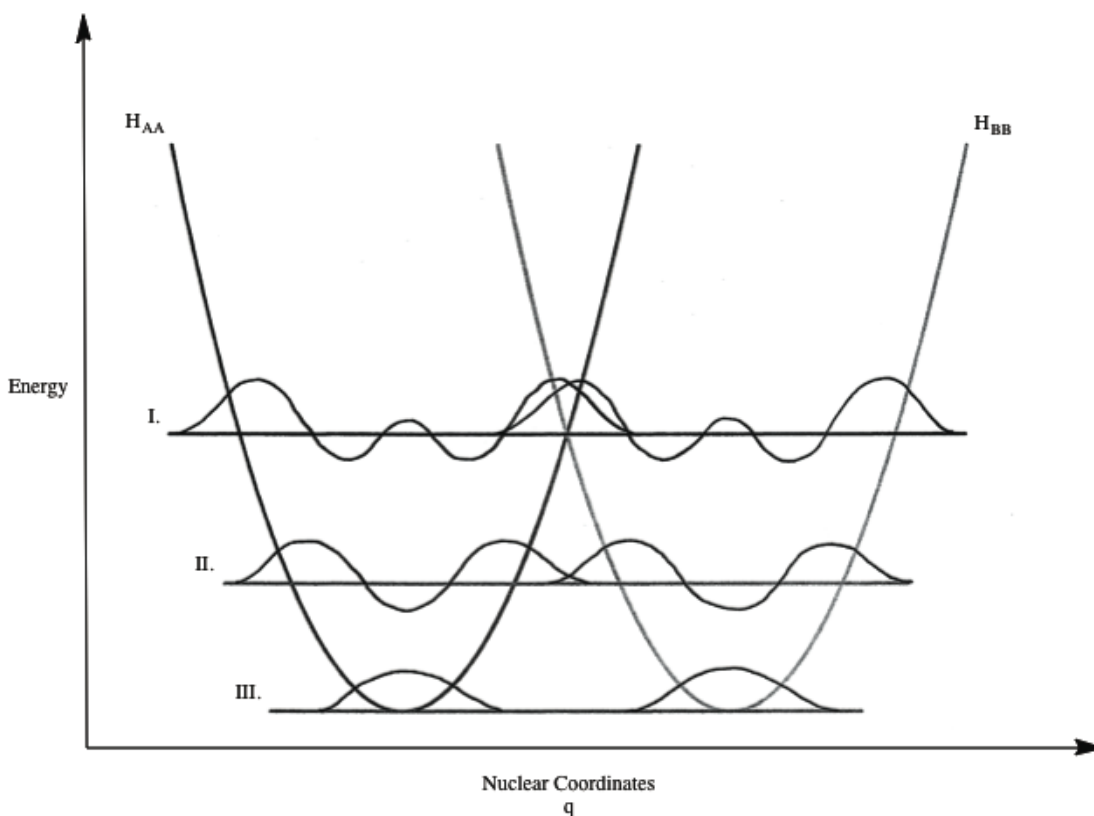


Figure 1.5 Surfaces and vibrational levels relevant to the three types of tunneling processes in the quantum non-adiabatic ET model. I. Electronic tunneling from a vibrational level with energy near that of the transition state. II. Activated nuclear tunneling. III. Temperature-independent nuclear and electron tunneling.

Activated nuclear tunneling involves the electron tunneling between intermediate vibrational levels, as shown by the energy level denoted II. in Figure 1.5. Although the system may not reach the intersection region, tunneling is still possible due to the potential energy surfaces being close enough in proximity to have some finite amount of vibrational wavefunction overlap (non-zero Franck-Condon factors). In this case, the rate of ET is also temperature dependent, but not as much so as in the

previous case since such activated nuclear tunneling does not require Boltzmann population as far up into the manifold as does tunneling at the transition state.

The third type of tunneling is temperature-independent tunneling, which involves tunneling between the ground vibrational states of the precursor complex and the successor complex as denoted by III. in Figure 1.5. If the χ_{nu} wavefunctions of the vibrational ground states of the precursor and successor complexes in their respective potential energy surfaces extend sufficiently close to each other, a small but finite possibility exists that the nuclei can tunnel from one ground state to the other. At very low temperatures, all activated ET events become negligible due to a lack of thermal energy to reach levels with $v > 0$ (much less the transition state itself), but nonetheless a small residual rate of ET due solely to combined nuclear and electron tunneling can be and has been measured in such cases.⁴³ The confirmed existence of this type of ET validates the full quantum-mechanical model of ET. This is more than a fine point since many biological ET rates require this level of treatment in order to quantitatively rationalize observed rates.⁴³⁻⁴⁵

1.6 Quantum Super-Exchange Theory of H_{AB} Modulation

The quantum super-exchange coupling (QSEC) formalism was first introduced by McConnell as a way to rationalize the measured rates of a certain category of chemical reactions.⁴⁶ His work involved the observation of the intramolecular ET between two phenyl groups in mononegative α,ω -diphenylalkanes, $[\text{phenyl}-(\text{CH}_2)_n\text{-phenyl}]^-$. The kinetics of this process was rationalized quantitatively by considering the electronic coupling between the two

redox-active sites being contingent on the energy of a virtual excited state on the methylene bridge connecting them. QSEC facilitates ET between identifiable donor and acceptor sites (situated in some condensed medium) and is known to facilitate long-distance hole and electron tunneling through the spatial region between the exchanging sites. This indirect mixing of the donor and acceptor electronic wavefunctions through participation of the HOMO and LUMO levels of the bridging group dramatically increases the tunneling frequency as compared to any through space interaction at similar distance. QSEC operates *via* the participation of “virtual” bridge states which can be constructed using bridge orbitals in combination with orbitals on D and A.⁴⁷

The “virtual bridge states” in QSEC refer to quantum states of indeterminate lifetime but estimatable energies corresponding to states wherein either a “hole” (or electron vacancy) moves from acceptor A onto the bridge (equivalent to moving an electron from the bridge to the Ru^{III} in our case) or an electron moves from donor D into an empty level on the bridge (equivalent to placing an electron from Ru^{II} into a π^* level of the bridge in our case). The effective height of the electron tunneling barrier between D and A at the intersection point, and thus the quantum tunneling frequency, is thus determined by the energy necessary to reach one or the other of these two virtual states. These energies are not just typical thermal energies, but rather can include gaps on the order of visible-wavelength photon energies and beyond. There is no measurable “lifetime” during which the electron resides in the virtual state on the bridging group. Electron tunneling through the D-Bridge-A assembly *via* quantum

super-exchange is thus a concerted process rather than a “hopping” one.⁴⁸ Figure 1.6 illustrates the “electron-transfer” and “hole-transfer” pathways schematically. Importantly, even though these seem and are very different in terms of the virtual state descriptions, real ET reactions are known to incorporate the action of either or both pathways in the manifestation of observed rates.

In the “electron-transfer” pathway (upper corridor in Figure 1.6), the electron is transferred (in a virtual, indefinite sense) from the donor, in our case Ru^{II} , through the LUMO of the bridging group and on to the acceptor (which was the Ru^{III} in the work done here). This process would correspond to virtual population of a π^* or σ^* anti-bonding orbital of the bridging group and creation of a hole on Ru^{III} . The energy required to populate the LUMO of the bridging group is then taken as defining the effective height of the tunneling barrier for “electron” super-exchange. This energy will be roughly equal to the MLCT (metal-ligand charge-transfer) absorption band energy in the context of the $(\text{NH}_3)_5\text{Ru-L}$ complexes used in this work.

The “hole-transfer” pathway (lower corridor in Figure 1.6) corresponds to an electron moving from the filled HOMO (or other level) of the bridging group into the LUMO of the acceptor (the “hole” corresponding to the $4d\ t_{2g}$ vacancy on the Ru^{III} in our case). The virtual hole created on the bridge is simultaneously filled with a higher-lying electron from the donor (Ru^{II}) site thus completing the full ET process. The energetic magnitude of the hole-transfer tunneling barrier in our context is roughly equal to LMCT (ligand to metal charge transfer) band energy of the

(NH₃)₅Ru-L complexes used in this work (or in some cases an ion-pair charge transfer from an associated anionic species such as Br⁻ or Fe^{III}(CN)₆⁴⁻, *vide infra*).

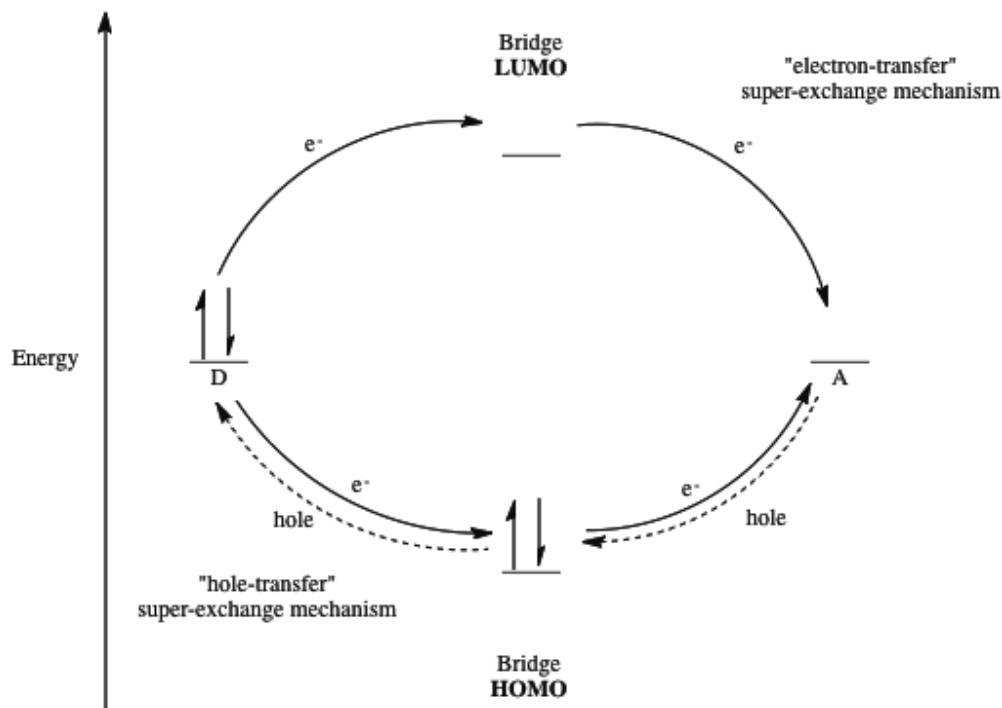


Figure 1.6 The “electron-transfer” (upper pathway) and “hole-transfer” (lower pathway) quantum super-exchange mechanisms, where A is the electron acceptor site and D is the donor site.

1.7 Debye-Hückel Theory and The Effects of Ionic Strength on Activity

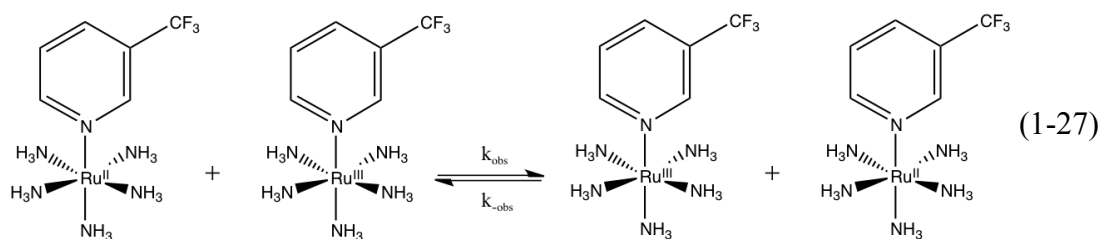
Coefficients

Since most of the kinetics to be described here focused on salt-induced ET rate variations, we will develop here some of the basic ideas and foundational principles of solution-phase electrolyte theory. The Debye-Hückel theory of ion atmospheres was the first successful model of electrolyte solutions and had its basis in treating ions as point charges distributed in a featureless dielectric continuum.⁴⁹

This model analyzes the distribution of ions in very dilute electrolyte solutions in order to characterize the “ionic atmosphere” or “cloud” of surrounding charges which build up near a charged solute (including charged reactant species) and results in the so-called “local potential”. From their treatment, quantitative predictions of salt effects on the rates of reaction between ionic reactants are possible, and these include the rates of bimolecular ET reactions in water such as those studied here (note the 2+ and 3+ reactant charges indicated in equation (1-27)).

The ET reaction kinetics studied in this work were measured in aqueous solutions. Due to the strongly-polar nature of water, each of the reactant ions will be surrounded by some number of “hydrating” water molecules (with a significant amount of the hydration energy arising from specific hydrogen bonding interactions between water, a Lewis base, and ruthenium ammine hydrogens acting as Lewis acids, *vide infra*). This dipolar solvation of the reactant ions partially screens their charges from the other ions present in solution. As Debye and Hückel showed, however, another significant increment in charge screening of an ionic reactant arises from the statistically-perturbed nature of the ion atmosphere which surrounds a charged reactant in the presence of some inert spectator electrolyte.⁵⁰ The cations and anions surrounding a charged reactant are “sorted” to some extent and migrate such that the counterion of opposite charge to the reactant is present at a concentration which is enhanced relative to its bulk value. This perturbation dies off with distance according to Poisson-Boltzmann statistics but has the effects of both screening the field and depressing the activity coefficient of the charged reactant.^{49, 51}

The work described in this thesis focused on specific instances of how added salts (some simple, as in alkali-halides, and some more complex) affected the measured rates of the aqueous bimolecular ET self-exchange reaction between pentaammineruthenium(II)(3-trifluoromethylpyridine)²⁺, $[(\text{NH}_3)_5\text{Ru}^{\text{II}}\text{tfmp}]^{2+}$, and pentaammineruthenium(III)(3-trifluoromethylpyridine)³⁺, $[(\text{NH}_3)_5\text{Ru}^{\text{III}}\text{tfmp}]^{3+}$, as shown in equation (1-27) below,



In agreement with prior observations made by Chun⁵², Inagaki⁴⁰, Sista³⁸, and Qin⁵³, we observed very divergent salt effects depending on the nature of the added anion. In some cases, variable degrees of super-exchange mediation must be invoked in order to rationalize the observed trends in the kinetic salt effects, but in some cases (especially for added fluoride), “simple” or “classical” salt effects in full agreement with theory were observed. These rate effects corresponded quantitatively to the behavior predicted by the Debye-Hückel-Bronsted equation^{19, 54} (*vide infra*) which flows directly from the (thermodynamically-derived) Debye-Hückel model of ion atmospheres mentioned above.⁴⁹ In what follows we will lay out a brief introduction to ion-atmospheres and prepare the way for analyzing the very strong and surprising (yet still systematic) deviations from classical behavior which we have uncovered.

Electrostatic interactions between ions in liquids are known to be much weaker than those in a vacuum or between ions in a lattice. This is an effect of Coulomb's Law which tells us that the interionic force, F , is described by,

$$F = \frac{q_1 q_2}{4\pi \epsilon_0 D_s r^2} \quad (1-28)$$

where q_1 and q_2 are the charges of the two ions (or charged complexes) separated by distance r (see Figure 1.7), D_s is the static dielectric constant, and ϵ_0 is the permittivity of vacuum. The D_s term arises from the collective action of solvent dipoles orienting to the electric field(s) associated with ionic species in solution including charged reactants.⁵⁵ The D_s term captures the extent of interionic charge screening, and because of its collective dipolar origin, D_s varies inversely with temperature on account of increased thermal randomization of the dipoles as T increases.

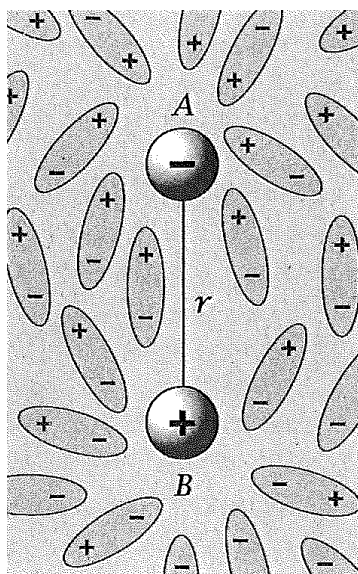


Figure 1.7 Charged ions, A and B at distance r , cause dipoles in the solvent to reorient according to their dipolar structure and this causes a net shielding of the ionic fields. The bulk dielectric constant, D_s , of a solvent captures the overall effect of this behavior as a single macroscopic observable.⁵⁵

As the like-charged reactant cations in our ET reaction approach each other to form the precursor complex (see equations (1-44) to (1-46)), they are doing so while working against an already partially-screened coulombic repulsive force (*vide supra*). Figure 1.8 illustrates the fact that there will be at least two levels of hydration surrounding the reactant cations (the secondary level is represented by the dipole arrow exterior to the dotted line in Figure 1.8). The primary hydration shell includes the neighboring solvent dipoles (also represented by arrows) which are oriented and essentially in contact with (or even hydrogen bonded to) the reactant cations at the boundary surface of their primary coordination spheres (shown here as the solid lined circles). The “secondary” hydration shell in our case refers to water dipoles which

are in the third coordination sphere out from the central ion since the ammine ligands comprise the primary coordination sphere. Moving beyond the second hydration sphere, the water structure returns to that of bulk water (which has an inherent dynamical structure of its own and has been the topic of intense investigation⁵⁶⁻⁶⁰).

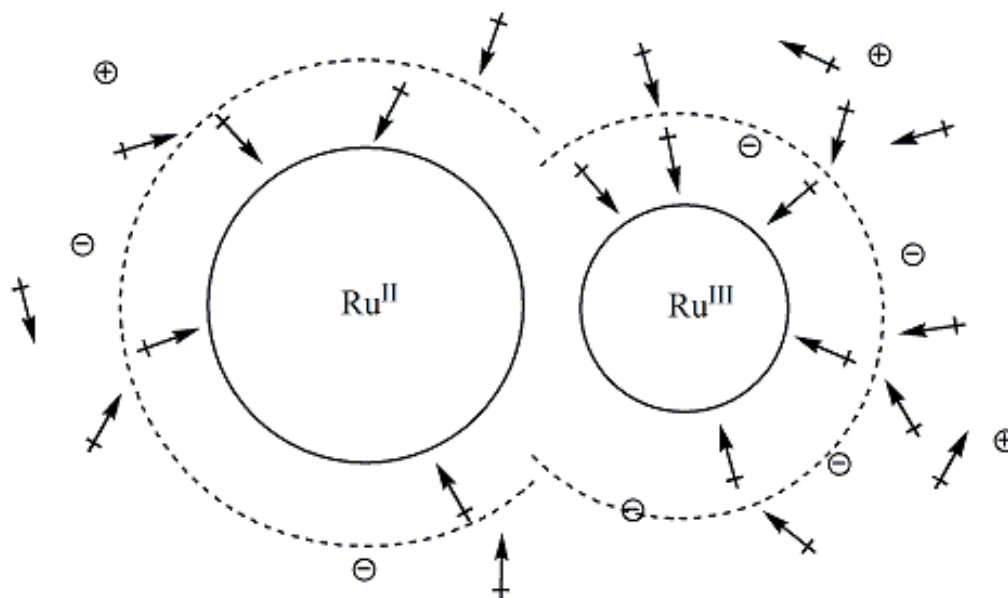


Figure 1.8 Solvent dipoles representing the first and second hydration spheres and the counter ions forming the Debye-Hückel “ion atmosphere” around the reactant ions, $[(\text{NH}_3)_5\text{Ru}^{\text{II}}\text{L}]^{2+}$ and $[(\text{NH}_3)_5\text{Ru}^{\text{III}}\text{L}]^{3+}$.

As noted previously, the concentration of the counter ions around reactant ions exponentially decays to the bulk value with increased distance from the reactant cation however, the electrical potential of the reactant ions is found to decrease with distance by Coulomb’s law and the effects of D_s (see Figure 1.7 and 1.8).⁴⁹ In the presence of the ion atmosphere formed in solutions of finite ionic strength however, the electrical potential decays significantly more rapidly. This added charge screening has the effect of decreasing the thermodynamic activity coefficients of

charged reactants in solution, and this realization was key in linking the theory of the ion atmosphere to our experiment.

An important quantity which follows from Debye-Hückel theory is the reciprocal distance or “inverse length”, κ . This quantity captures the effects of the Poisson-Boltzmann statistics on the charge density structures of the ion atmosphere (this usage of κ has nothing to do with the transmission coefficient or the “adiabatically parameter” shown in equations (1-18) to (1-24).^{49, 51} The effective “radius” of the ion atmosphere is then taken as the inverse of κ ,

$$\frac{1}{\kappa} = \left(\frac{D_s \varepsilon_o R T}{2 F^2 \mu} \right)^{1/2} \quad (\text{m}) \quad (1-29)^{49}$$

where D_s is the static dielectric constant, ε_o is the permittivity of vacuum, R is the ideal gas constant, T is the absolute temperature, F is Faraday’s constant, and μ is the ionic strength (*vide infra*) in units of mol/m³ (where 1 L = 0.001 m³). One can conclude from equation (1-29) that the Debye length (the effective size of the ion atmosphere) is inversely proportional to the square root of the ionic strength of a solution, and therefore electrostatic interactions between charged reactants can be modulated or deduced on the basis of ionic strength. As the ionic strength increases, reactions between liked charged particles will proceed faster and reactions between oppositely charged particles will become slower.⁶¹

The total ionic strength of a solution, μ , is a measure of the effective “iconicity” of a solution. It depends on both the concentrations and charge types of all the ionic species in a solution as shown in equation (1-30) below,

$$\mu = \frac{1}{2} \sum_{i=1}^n z_i^2 c_i \text{ (M)} \quad (1-30)^{62, 63}$$

where z_i is the charge of the ion and c_i is the concentration of the ion. This ionic strength thus reflects the total amount of mobile charge in a solution and is found to be the controlling variable in accounting for the interionic interactions in a solution and the resulting individual electrolyte ion thermodynamic activities.^{62, 64} In our work, the charges of the two ruthenium complexes, their counter ions, and then any added salts must all be accounted for when calculating the total ionic strength of a solution. Values of ionic strength are typically calculated in units of molarity, but when used in calculating dependent quantities such as the Columbic work term (*vide infra*) the units are subject to change.

When establishing the relationship between the electrostatic potential at a reference point in solution and the change in chemical potential of an ionic reactant arising from ion-ion interactions, Debye and Hückel showed that the activity coefficient of any charged species and the total ionic strength of the solution could be related using the “limiting law” which is defined as,

$$\log \gamma_{\pm} = -\alpha |Z^+ Z^-| \sqrt{\mu} \quad (1-31)^{49, 65, 66}$$

where γ_{\pm} is the stoichiometric “mean molar activity coefficient” for reactant ions in the medium, Z^+ and Z^- are the charges of the cation and anion respectively, α is a constant (which depends on the temperature and the relative permittivity, D_s , of the solution), and μ is the ionic strength. This equation was found to be quantitatively valid only for very dilute solutions with ionic strengths lower than $\sim 0.001 \text{ M}$.⁴⁹ The

Debye-Hückel limiting law was later modified in order to describe activity coefficients in terms of both the charge types and the sizes of the reactant ions, and this is modification (which works up to higher μ values) is known as the Debye-Hückel “extended law” as defined by,

$$\log \gamma_{\pm} = -\frac{\alpha |Z^+ Z^-| \sqrt{\mu}}{1 + \beta \sigma \sqrt{\mu}} \quad (1-32)$$

where σ is the center-center distance between a reference (or reactant) ion and an ion of the ion-atmosphere at contact. α and β are constants of the theory and are equal to 0.509 and 0.328 in water at a temperature of 298 K, respectively.^{19, 67} The β term depends on both the temperature and relative permittivity of the solution (static dielectric constant, D_s) and is defined as,

$$\beta = \left(\frac{8\pi N_A e^2 \rho}{4\pi \epsilon_0 D_s k_B T} \right)^{1/2} \left(\frac{\text{kg}^{1/2}}{\text{mol}^{1/2} \text{ m}} \right) \quad (1-33)^{68}$$

where N_A is Avogadro’s number ($6.022 \times 10^{23} \text{ mol}^{-1}$), e is the elementary charge of an electron ($1.602 \times 10^{-19} \text{ C}$), ρ is the density of the solvent in kg/m^3 , ϵ_0 is the permittivity in a vacuum ($8.854 \times 10^{-12} \text{ C}^2 \text{ J}^{-1} \text{ m}^{-1}$), k_B is Boltzman’s constant ($1.381 \times 10^{-23} \text{ J/K}$), and T is the temperature in K. In water at a temperature of 298 K, β is equal to $3.28 \times 10^9 \text{ kg}^{1/2} \text{ mol}^{-1/2} \text{ m}^{-1}$ (this number is large due to the use of meters instead of angstroms). The Debye inverse length, often denoted by κ , is then equal to $\beta \sqrt{\mu}$. The quantity $1/\kappa$ is interpreted as being the characteristic “thickness” of the ion atmosphere surrounding an ion of charge Z^+ at a given ionic strength.

In 1922, Johannes Bronsted proposed the following expression to describe general bimolecular reactions in terms of the rate constant to form an “associated pair”,

$$k_{\text{ex}} = k_{\mu=0} \frac{\gamma_A \gamma_D}{\gamma_{\text{AD}^\ddagger}} \quad (1-34)^{54, 69}$$

where γ_A is the activity coefficient of reactant A, γ_D is the activity coefficient of reactant D, $\gamma_{\text{AD}^\ddagger}$ is the activity coefficient of the activated/associated pair (corresponding to the “transition state” in modern terms), $k_{\mu=0}$ is then taken to be the rate constant at infinite dilution (where all $\gamma_i \rightarrow 1$), and k_{ex} is the now generalized rate constant at any given finite ionic strength. This expression explains quantitatively why the addition of inert, ionized salts to a solution typically causes reactions between oppositely charged ions (or molecular ions) to proceed more slowly and causes reactions between liked-charged species to proceed faster.⁵⁴ Using both the Debye-Hückel extended law and the Bronsted equation above, the kinetically relevant Debye-Hückel-Bronsted equation can be derived as shown below,

$$\log k_{\text{ex}} = \log k_{\mu=0} + \frac{2\alpha |Z_A Z_D| \sqrt{\mu}}{1 + \beta \sigma \sqrt{\mu}} \quad (1-35)^{19, 54}$$

where all quantities are as defined previously except the distance σ now refers to the center-center distance between the two reactant ions rather than the predominate counter ion in solution. This is an explicit, quantitative prediction of how the rate of any reaction between charged species will vary with ionic strength and is the origin of what are called “primary salt effects” on the inter-ionic reaction kinetics. This will be

a key equation in the analysis of the ET kinetics work to be described in this thesis. It was noted early on by Guggenheim⁷⁰ that the product of β and σ is approximately equal to 1 Å for many reactant ion/counterion combinations.⁷¹ This allows for equation (1-35) to be approximated by,

$$\log k_{\text{ex}} = \log k_{\mu=0} + \frac{2\alpha |Z_A Z_D| \sqrt{\mu}}{1 + \sqrt{\mu}} \quad (1-36)$$

From the form of equation (1-35), we see that it is useful to then define the general and very simple ionic strength-related quantity now known as the “Guggenheim parameter”, which we will denote as GP,

$$\text{GP} = \frac{\sqrt{\mu}}{1 + \sqrt{\mu}} \quad (1-37)^{19, 70}$$

Applying equation (1-37) to equation (1-36), the Debye-Hückel-Bronsted equation then becomes,

$$\log k_{\text{ex}} = \log k_{\mu=0} + 2\alpha Z_A Z_D (\text{GP}) \quad (1-38)$$

This is the version most-commonly used in studies of kinetic salt effect today. Using equation (1-38), kinetic data collected at different total ionic strengths are plotted as $\log k_{\text{ex}}$ vs. GP. The observed slopes are frequently very close to the simple $Z_A Z_D$ charge product since α in equation (1-38) is equal to 0.509 in water at 298 K. In the case of our reaction (see equation (1-27)) this would imply that the slope should be approximately equal to 6. As we will show, this “ideal” Debye-Hückel-Bronsted behavior is only observed for our reaction in the presence of alkali-metal salts of the fluoride anion, while all other salts investigated deviate from this linear prediction

and in fact present distinct curves (as will be presented and discussed later in chapter 2).^{38, 40, 53, 72}

1.8 Association Constants

From the treatment of outer-sphere ET reactions described previously we know that second-order bimolecular ET reactions occur *via* three identifiable component steps as represented by equations (1-1a) to (1-1c). It should be noted that in our work the reactants are both positively-charged ions (see equation (1-27)). If the formation of the precursor complex according to equation (1-1a) is not rate determining, then the “pre-equilibrium” limit applies and,

$$k_{\text{ex}} \cong K_A k_{\text{ET}} \quad (1-39)$$

$$K_A = \frac{k_a}{k_d} \quad (1-40)$$

From equation (1-39), we see that the observed rate constant, k_{ex} , depends solely on the product of the pre-equilibrium association constant, K_A , and the rate-determining first-order rate constant for ET inside the precursor complex, k_{ET} (as was derived in section 1.5.4 on the assumption that $k_d \gg k_{\text{ET}}$). From equation (1-40), it is clear that any solution condition- or composition-induced perturbations of *either* the second-order rate of association, k_a , or the unimolecular rate of dissociation, k_d , will then be directly reflected in a measured k_{ex} *if* k_{ET} itself is constant or relatively unperturbed. On this basis, we now need to introduce some of the known details of reactant encounter theory which underlie quantitative calculation of both k_a and k_d .

According to Kirk's presentation,⁶⁸ the second-order bimolecular rate constant for association by diffusional encounter can be taken from the Debye-Smoluchowski equation and expressed as,

$$k_a = \frac{2000N_A k_B T}{3\eta} \left[2 + \frac{r_A}{r_D} + \frac{r_D}{r_A} \right] \frac{1}{\sigma \int_{\sigma}^{\infty} r^{-2} \exp \left[\frac{w(r, \mu)}{k_B T} \right] dr} (\text{M}^{-1} \text{s}^{-1}) \quad (1-41)^{68}$$

where N_A is Avogadro's number ($6.022 \times 10^{23} \text{ mol}^{-1}$), k_B is Boltzman's constant ($1.381 \times 10^{-23} \text{ J/K}$), T is the temperature in K, η is the viscosity of the solvent ($1.002 \times 10^{-3} \text{ N s m}^{-2}$ for water at 298 K), r_A and r_D are the radii of the reactants A and D in meters, σ is the sum of the radii r_A and r_D in meters, r is the center-center distance between reactants in meters over which integration is carried out, and $w(r, \mu)$ is the Debye-Hückel work term in Joules as defined by equation (1-43).

Similarly, the first-order rate constant for the dissociation/separation of the associated encounter complex can be derived using the Debye-Eigen equation and is expressed by,

$$k_d = \frac{k_B T}{2\pi \eta a^2} \left[\frac{1}{r_A} + \frac{1}{r_D} \right] \left[\exp \left[\frac{w(\sigma, \mu)}{k_B T} \right] \right] \frac{1}{\sigma \int_{\sigma}^{\infty} r^{-2} \exp \left[\frac{w(r, \mu)}{k_B T} \right] dr} (\text{s}^{-1}) \quad (1-42)^{68, 73}$$

where $w(\sigma, \mu)$ is the Debye-Hückel work term in J as defined below by equation (1-43) only with a substitution of the quantity σ (the sum of the hard-sphere radii) for the variable r (the center-center distance). The Debye-Hückel electrostatic work of

association, $w(r, \mu)$, from bringing two ions together from infinity to s is expressed by,

$$w(r, \mu) = \frac{Z_A Z_D e^2}{8\pi \varepsilon_0 D_s} \left[\frac{\exp(\beta \sigma_A \sqrt{\mu})}{1 + \beta \sigma_A \sqrt{\mu}} + \frac{\exp(\beta \sigma_D \sqrt{\mu})}{1 + \beta \sigma_D \sqrt{\mu}} \right] \frac{\exp(-\beta r \sqrt{\mu})}{r} \quad (\text{J}) \quad (1-43)^{23, 68}$$

where e is the elementary charge of an electron (1.602×10^{-19} C), ε_0 is the permittivity in a vacuum (8.854×10^{-12} C² J⁻¹ m⁻¹), D_s is the static dielectric constant of the solvent (78.4 for water at 298 K), β is a constant defined by equation (1-33), μ is the total ionic strength in units of mol kg⁻¹, σ_A (or σ_D) is the sum of the radius of reactant ion A (or D) and the dominant counterion present in meters. Simplified work term expressions are available and will be presented in chapter 2.

If the formation of the precursor complex is less than diffusion controlled, the encounter pair equilibrium constant may then be calculated using a simple ratio of the Debye-Smoluchowski and Debye-Eigen values for k_a and k_d , which turns out to be equivalent to the thermodynamically-derived Eigen-Fuoss equation.^{68, 73} The association constant to form the precursor complex (see equations (1-1) and (1-27)) is thus equal to,

$$K_A = \frac{k_a}{k_d} = \frac{4000\pi N_A \sigma^3}{3} \exp\left[\frac{-w(\sigma, \mu)}{k_B T}\right] (\text{M}^{-1}) \quad (1-44)^{68, 73}$$

Either equations (1-40) to (1-43) using individual k_a and k_d values, or the Eigen-Fuoss expression above can be used to calculate an equilibrium association constant, K_A .

As we will show, the explicit calculations of the dynamics of reactant ion association/dissociation are necessary in order for us to successfully model our observed kinetic salt effects on bimolecular ET rates. As a prelude to this discussion, it is useful to consider an especially simple approach to calculating the average distance between reactant ions in solution. At the crudest level, we will assume a simple cubic model as describing the effective statistical distribution of ions in the solution. Ignoring ion atmosphere or other aggregation effects, this can be used to derive an idealized, statistical or “expectation” value for the average interreactant distance as a function of reactant concentration (see Figure 1.9). While clearly approximate, this approach has been used, for example, by Robinson and Stokes as a starting point in their classic treatment on electrolyte solutions.⁵¹ Figure 1.9 below illustrates this idea (with species A and D occupying alternate vertices in the lattice).

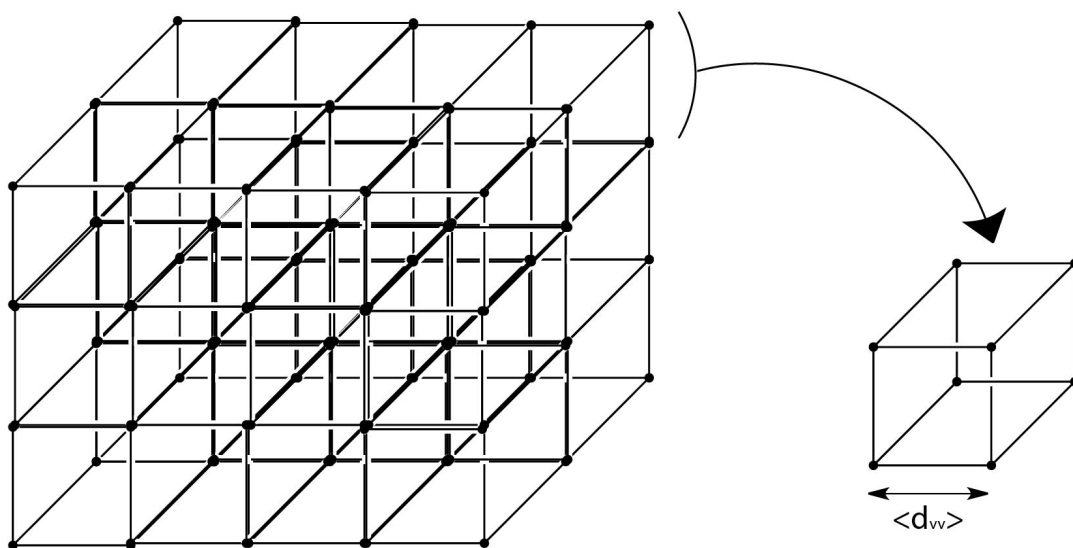


Figure 1.9 A simple cubic “lattice” model which can be used to calculate the effective center-center interreactant distance, $\langle d_{vv} \rangle$, between equivalent (like-charged) ionic species placed the vertices of an idealized solute lattice.

In order to calculate the effective center-center distance between the members of either the anionic or cationic statistical sub-lattices of ions in solution at a particular molar concentration, we need first recognize that the average distance between vertices of the simple cubic configuration will depend on the ratio of edge length to volume (presumed cubic) per reactant particle. To accomplish this we must first find the number of atoms in a set volume of, for example, 1L as shown below by,

$$\# \text{ of atoms in a Volume} = [A] \times N_A \times V \quad (1-45)$$

where $[A]$ is the molar concentration of species A in units of mol m^{-3} (recall that $1 \text{ L} = 0.001 \text{ m}^3$), N_A is Avogadro’s number in units of mol^{-1} , and V is the volume in L. Next, the number of atoms on an edge of this cubic volume is found to be,

$$\# \text{ of atoms on an edge of a cube} = \sqrt[3]{[A] \times N_A \times V} \quad (1-46)$$

Now, we can calculate the distance between two vertices in the cube, $\langle d_{vv} \rangle$, as shown below,

$$\langle d_{vv} \rangle = \frac{\sqrt[3]{V}}{\sqrt[3]{[A] N_A V}} = \sqrt[3]{\frac{1}{[A] N_A}} = 1.18 \times 10^{-8} \left(\sqrt[3]{\frac{1}{[A]}} \right) \text{ (m)} \quad (1-47)$$

If we convert equation (1-47) into units of Å ($11.8 \times [A]^{-1/3}$, where $[A]$ is expressed in M) and compare it with the equation for the anion-cation expectation value for the distance in solution presented by Robinson and Stokes⁵¹ ($\langle d_{\text{anion-cation}} \rangle \cong 9.4 \times [A]^{-1/3}$ Å) we find an overall difference of about 26%. This is because we need to correct our single-species lattice model to reflect the anion-cation (or as we will see, $\text{Ru}^{\text{II}}\text{-Ru}^{\text{III}}$) expectation distance rather than that for a single species with respect to itself. To do this we must apply the idea of interpenetrating sub-lattice structures, illustrated below in Figure 1.10. Here we present an illustration of an illustration of the prototypical CsCl body-centered crystal lattice (bcc) structure with the green spheres representing Cs and the grey spheres representing Cl. In our reactant solution the green spheres would represent either a cation or a Ru^{III} reactant ion and the grey spheres would represent an anion or an Ru^{II} reactant ion and the assumption now is that any given solution component would “see” an expectation distance to the vertices of another component’s sub-lattice. The corresponding distance between the grey and green sphere’s (our reactants) would be one-half of a cube diagonal away.

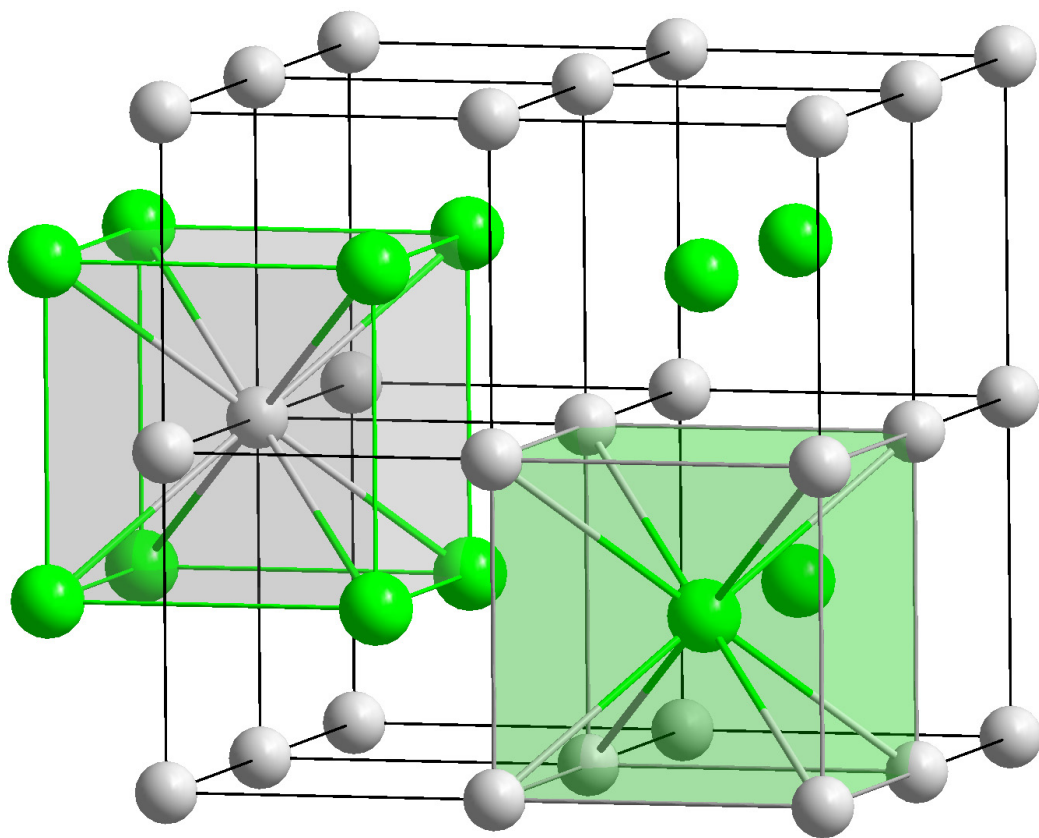


Figure 1.10 An illustration of the interpenetrating body-centered cubic crystal lattice sub-structures characteristic of CsCl, for example, which can be applied statistically to our reactant solutions.⁷⁴

From simple geometry, we see that a factor $\sqrt{3}/2 = 0.866$ now converts $\langle d_{vv} \rangle$ of equation (1-47) into $\langle d_{cv} \rangle$ corresponding to the average distance between the cube center (green sphere or Ru^{III}) and the vertex (grey sphere or Ru^{II} or dominant salt anion) as in equation (1-48) below,

$$\langle d_{cv} \rangle = 1.02 \times 10^{-8} \left(\sqrt[3]{\frac{1}{[A]}} \right) \text{ (m)} \quad (1-48)$$

If equation (1-48) is converted into units of Å and concentration is expressed in M units, then $\langle d_{cv} \rangle = 10.2 \times [A]^{-1/3}$ Å. We now find a difference of 9% with respect to the formula of Robinson and Stokes.⁵¹ While this difference might be considered negligible for practical purposes, we note that if instead a face-centered cubic (NaCl or “fcc”) lattice model is chosen to describe the ion distribution, then $\langle d'_{cv} \rangle$ works out to be $\langle d'_{cv} \rangle = (\sqrt{2}/2) \langle d_{vv} \rangle$. The Robinson and Stokes expression in fact derives from the averaging of these two limits. Given that our ET reactions are taking place on a timescale which is very long compared to diffusion times over tens of angstroms, we favor the slightly more expanded, but also more statistically sensible effective bcc lattice model for the electrolyte solutions.

A further refinement is to consider the average edge-edge distance between two reactant ions in the body-centered cubic model. Now the sum of the ionic radii must be subtracted from the average center-center distance between non-identical component positions as shown below,

$$\langle d'_{cv} \rangle = \langle d_{cv} \rangle - \sigma \text{ (m)} \quad (1-49)$$

$$\sigma = r_A + r_D \text{ (m)} \quad (1-50)$$

Lists of center-center reactant distances, as well as edge-edge reactant distances for our reactant system (where $\sigma = 4.48 \text{ Å} + 4.55 \text{ Å} = 9.03 \text{ Å}$) and those calculated using the Robinson and Stokes equation⁵¹ are shown in Table 1.1. As seen from the Table, the error introduced by ignoring the radii of the reactant themselves is on the order of ~8% at 1.00 mM reactant, but climbs rapidly to ~17% at 10.00 mM

reactants. Thus the radii of the reactants themselves cease to be negligible compared to $\langle d_{cv} \rangle$ from equation (1-48) at reactant concentrations much above 0.05 mM reactants (for reactant radii on the order of 4.5 Å such as our ruthenium complexes), as illustrated in Figure 1.11. These excluded-volume effects would presumably bring about deviations from models of diffusive encounter in solution such that non-ideal behavior would emerge at reactant concentrations much above 1.00 mM (possible evidence for such effects will be presented in Ch. 2). The individual behaviors of $\langle d_{cv} \rangle$, $\langle d_{cv, RS} \rangle$, and $\langle d'_{cv} \rangle$ are plotted in Figure 1.11, and the inset graph specifically illustrates the behavior relevant to our experiment concentration range.

Table 1.1 A list of center-center single-species distances, $\langle d_{vv} \rangle$, and center-center reactant distances, $\langle d_{cv} \rangle$, as well as edge-edge reactant distances, $\langle d'_{cv} \rangle$ (specific to reaction (1-27)) at various equimolar reactants concentrations, compared with center-center interreactant distances calculated according to Robinson and Stokes.⁵¹

Concentration of Reactants (<u>M</u>)	$\langle d_{vv} \rangle$ (Å) ^(a)	$\langle d_{cv} \rangle$ (Å) ^(b)	$\langle d_{cv}, RS \rangle$ (Å) ^(c)	$\langle d'_{cv} \rangle$ (Å) ^(d)
0.00005	321	278	255	269
0.0001	255	221	203	212
0.0005	149	129	118	120
0.001	118	102	94	94
0.005	69	60	55	51
0.01	55	48	44	39
0.1	26	22	20	13
1	12	10	9.4	1.2
1.5	10	8.9	8.2	N/A

(a) center-center single-component distances calculated *via* equation (1-47), (b) center-center cation-anion or inter-reactant distances calculated *via* (1-48), (c) center-center cation-anion distances proposed by Robinson and Stokes, (d) edge-edge inter-reactant distances calculated *via* equation (1-49) using the sum of radii from reaction (1-27) set equal to 9.03 Å.

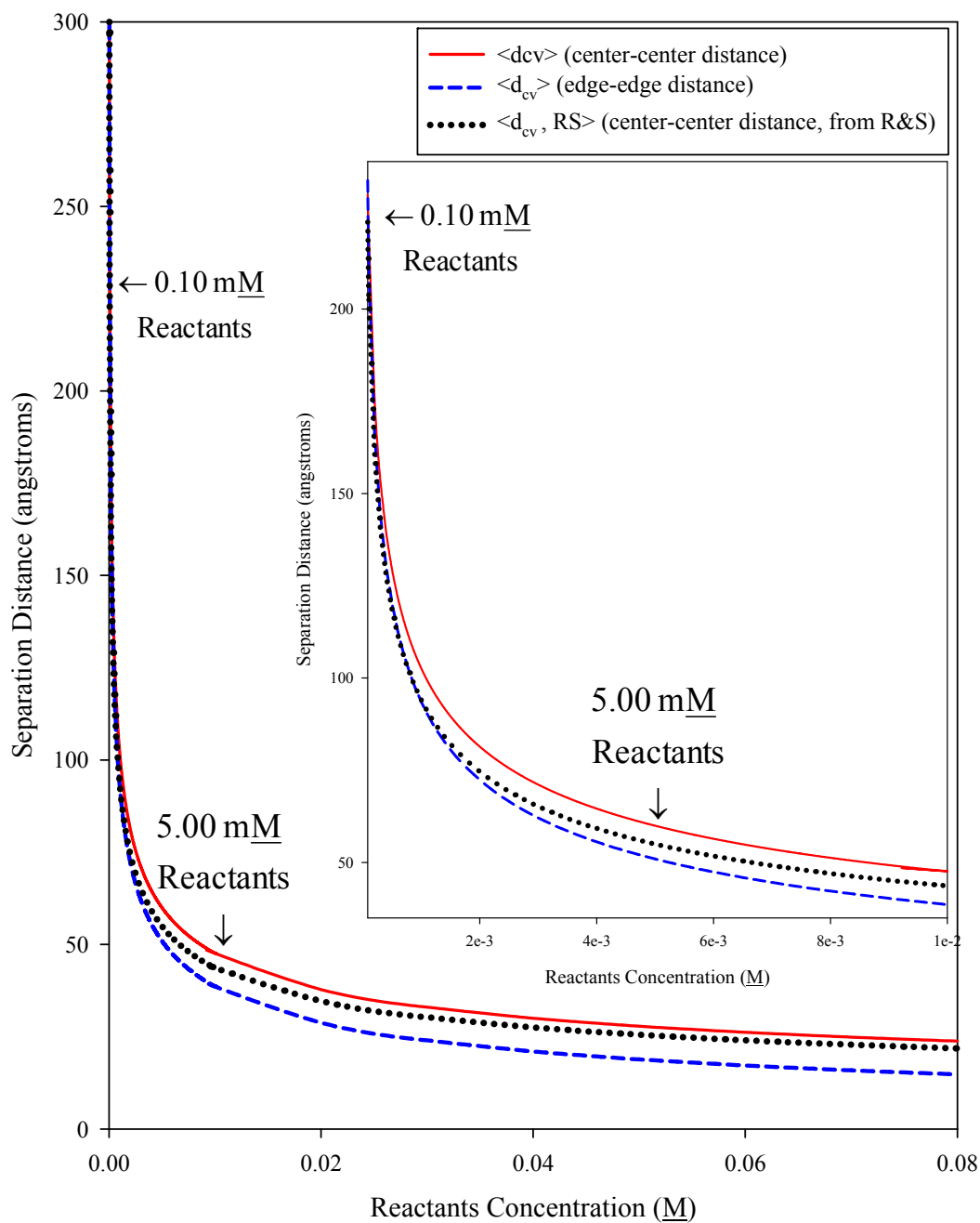


Figure 1.11 The change in the interreactant distance in solution vs. reactant concentration for reaction (1-27) applied for both center-center single-component distances, $\langle d_{vv} \rangle$ (red line, calculated *via* equation (1-47)) and center-center inter-reactant distances, $\langle d_{cv} \rangle$ (blue line, calculated *via* equation (1-48)) compared with the center-center distances $\langle d_{cv}, RS \rangle$ proposed by Robinson and Stokes.⁵¹

References

1. J. Curtis, J. Yang, D. Seneviratne, G. Arbatin, and A. Andersson. *J. Am. Chem. Soc.* 1997. 119. 5329.
2. J. M. Womick and A. M. Moran. *J. Phys. Chem. B.* 2011. 115. 1347.
3. R. Billing. *Coor. Chem. Rev.* 1997. 159. 257.
4. B. Wardle. Principles and Applications of Photochemistry. John Wiley and Sons, Ltd. 2009, 96
5. P. Ritter. Biochemistry, A Foundation. Brooks/Cole Publishing Company. 1996, 446-447
6. D. MacKay. Sustainable Energy, Without the Hot Air. UIT Cambrige, Ltd. 2008, 38
7. J. C. Curtis, et al. *Chem. Phys.* 2006. 326. 43-53.
8. J. C. Curtis, W. Mao, Z. Qian, and H. Yen. *J. Am. Chem. Soc.* 1996. 118. 3247.
9. J. Curtis and T. Meyer. *Inorg. Chem.* 1982. 21. 1562.
10. T. Meyer, J. Curtis, and P. Sullivan. *Inorg. Chem.* 1980. 19. 3833.
11. W. F. Libby. *J. Phys. Chem.* 1956. 56. 863.
12. R. A. Marcus. *J. Chem. Phys.* 1956. 24. 966.
13. H. Taube and H. Myers. *J. Am. Chem. Soc.* 1954. 76. 2103.
14. H. Taube. *Chem. Rev.* 1952. 50. 69.
15. C. Creutz. *Prog. Inorg. Chem.* 1983. 30. 1.
16. C. W. Brown. *J. Chem. Phys.* 1982. 77. 5379.
17. R. A. Marcus. *Rev. Phys. Chem.* . 1964. 15. 155.
18. N. Sutin. *Acc. Chem. Res.* 1982. 15. 275.
19. G. Brown and N. Sutin. *J. Am. Chem. Soc.* . 1979. 101. 883.

20. J. R. Bolton, N. Mataga, and G. McLendon. *Adv. In Chem. Series 228*. 1991. 8.
21. D. Shriver, P. Atkins, T. Overton, J. Rourke, M. Weller, and F. Armstrong. Inorganic Chemistry: Fourth Edition. W. H. Freeman and Company. 2006, 513-516
22. J. Zuckerman. Inorganic Reactions and Methods, Vol. 15. VCH Publishers Inc. 1986, 1-49
23. N. Sutin. *Prog. Inorg. Chem.* . 1983. 30. 441.
24. T. Meyer. *Prog. Inorg. Chem.* 1983. 30. 404.
25. R. A. Marcus and N. Sutin. *Comments Inorg. Chem.* . 1986. 5. 119.
26. N. Hush. *Trans. Faraday Soc.* . 1961. 57. 557.
27. R. A. Marcus. *J. Chem. Phys.* 1957. 26. 872.
28. M. Newton and N. Sutin. *Ann. Rev. Phys. Chem.* 1984. 35. 437.
29. A. Nitzan. Chemical Dynamics in Condensed Phases. Oxford University Press. 2006, 581-582
30. R. Marcus. *J. Chem. Phys.* 1965. 43. 679.
31. J. Curtis, K. Lau, A. Hu, M. Yen, and E. Fung. *Inorg. Chim. Acta.* . 1994. 226. 137.
32. R. A. Marcus. *J. Chem. Phys.* 1957. 26. 867.
33. C. H. Collie, J. B. Hasted, and D. M. Ritson. *Proc. Phys. Soc.* 1948. 60. 145.
34. T. J. Meyer, C. J.C, and J. S. Bernstein. *Inorg. Chem.* . 1985. 24. 385.
35. J. T. Hupp, Y. Dong, R. L. Blackburn, and H. Lu. *J. Phys. Chem.* 1993. 97. 3278-3282
36. M. J. Powers, R. W. Callahan, D. J. Salmon, and T. J. Meyer. *Inorg. Chem.* 1976. 15. 894.

37. S. Berry, A. Stuart, and J. Ross. Physical Chemistry, 2nd Ed.. Oxford University Press. 2000, 97-99, 184-187, 911-919
38. P. Sista. Master's Thesis. University of San Francisco, 2009.
39. P. F. Barbara, T. J. Meyer, and M. A. Ratner. *J. Phys. Chem.* 1996. 100. 13148.
40. M. Inagaki. Master's Thesis. University of San Francisco, 2006.
41. N. Sutin, M. D. Newton, B. S. Brunschwig, and J. Logan. *J. Am. Chem. Soc.* 1980. 102. 5798.
42. J. Hupp and M. Waeaver. *J. Electroanal. Chem.* 1983. 152. 1.
43. R. W. Murray, M. T. Michael T. Carter, G. K. Rowe, J. N. Richardson, L. M. Tender, and R. H. Terrill. *J. Am. Chem. Soc.* 1995. 117. 2896.
44. H. Bao, C. Zhang, Y. Ren, and J. Zhao. *Biochimica et biophysica acta.* 2010. 1797. 339-346.
45. J. Ankerhold and H. Lehle. *J Chem Phys.* 2004. 120. 1436-1449.
46. H. M. McConnell. *J. Chem. Phys.* 1961. 35. 508.
47. B. Paulson, J. Miller, W.-X. Gan, and G. Closset. *J. Am. Chem. Soc.* 2005. 127. 4860.
48. M. Todd, A. Nitzan, and M. Ratner. *J. Phys. Chem.* 1993. 97. 29.
49. R. W. Fawcett. Liquids, Solution, and Interferneces.. Oxford University Press. 2004, 96-145
50. M. Wright. An Introduction to Aqueous Electrolyte Solutions John Wilesey & Sons Ltd. 2007, 351-409
51. R. Robinson and R. Stokes. Electrolyte Solutions, 2nd Ed. Dover Publications Inc. 2002, 73-86
52. S. J. Chun. Master's Thesis. University of San Francisco, 2001.
53. A. Qin. Master's Thesis. University of San Francisco, 2012.
54. W. H. Koppenol. *Biophys. J.* 1980. 29. 493.

55. K. Dill and S. Bromberg. Molecular Driving Forces: Statistical Thermodynamics in Chemistry & Biology, 1st Ed.. Garland Science. 2002, 369-376
56. M. Berkowicz and R. Vacha. *Acc. Chem. Res.* 2011. 45. 74.
57. J. Li, H. Bian, X. Wen, H. Chen, K. Yuan, and J. Zheng. *The journal of physical chemistry. B.* 2012. 116. 12284-12294.
58. D. Laage, G. Stirnemann, F. Sterponem, and J. Hynes. *Acc. Chem. Res.* 2012. 45. 53.
59. Y. Marcus. *Pure Appl. Chem.* 2010. 82. 1889.
60. R. Dougherty. *J. Phys. Chem. B.* 2001. 105. 4514.
61. J. Burgess, F. Sanchez, and E. Morillo. *Transition Met. Chem.* 1986. 11. 166.
62. T. Solomon. *J. Chem Ed.* 2001. 78. 1691.
63. J. M. Walker and K. Wilson. Principles and Techniques of Biochemistry and Molecular Biology, 6th Ed.. Cambridge University Press. 2005, 7
64. T. Engel and P. R. Thermodynamics, Statistical Thermodynamics, and Kinetics. Benjamin Cummings. 2006, 232
65. J. Bockris and A. Reddy. Modern Electrochemistry: Ionics. Plenum Press. 1998, 281
66. P. Debye and E. Huckel. *Phys. Z.* 1923. 24. 185.
67. D. Skoog. Principles of Instrumental Analysis. CBS College Publishing 1985, 903
68. A. D. Kirk, L.-Z. Cai, and D. M. Kneeland. *J. Phys. Chem. A.* 1997. 101. 3871.
69. J. Bronsted. *Z. Phys. Chem.* 1922. 102. 169.
70. E. A. Guggenheim and J. C. Turgeon. *Trans. Faraday Soc.* 1955. 51. 747-761.

- 71. R. G. Mortimer. Physical Chemistry (2nd Edition). Academic Press. 2000, 233, 949
- 72. F. Mehmood. Master's Thesis. University of San Francisco, 2012.
- 73. C. Chiorboli, M. T. Indelli, M. A. R. Scandola, and F. Scandola. *J. Phys. Chem.* 1988. 92. 156.
- 74. H. Ehrenreich. Solid State Physics: advances in research and applications. Academic Press. 1984, 29-31

Chapter 2

Kinetic Studies of Salt Effects and Concentration Effects of Reactants on Self-Exchange Reactions Monitored by ^{19}F NMR Spectroscopy

2.1 Introduction

The previous chapter introduced the conceptual framework of bimolecular ET in solution and the basis of how added salts might be expected to affect ET rates between electron donor and acceptor complexes. Many studies have focused on how the rates of reactions between charged species in solution respond to the addition of added salts,¹⁻⁵ and previous studies conducted in this lab⁶⁻⁹ have focused specifically on measuring the ET kinetic effects arising from the addition of various “inert” or “spectator” salts. The bulk of that work concerned aqueous reaction mixtures involving the low-driving force “pseudo-self-exchange” reaction between pentaammineruthenium(II)(3-fluoropyridine)²⁺, $[(\text{NH}_3)_5\text{Ru}^{\text{II}}3\text{-fpy}]^{2+}$, and pentaammineruthenium(III)pyridine³⁺, $[(\text{NH}_3)_5\text{Ru}^{\text{III}}\text{py}]^{3+}$ (as described below in Figure 2.1), *via* the stopped-flow kinetic spectroscopy technique.^{1,6,7,9}

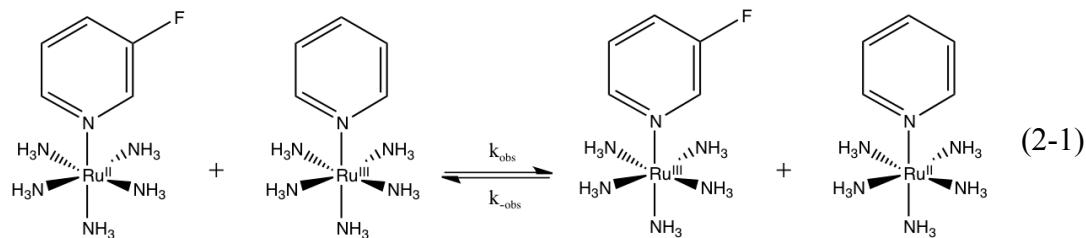


Figure 2.1 The low-driving force (69 mV in H_2O) “pseudo-self-exchange” reaction between $[(\text{NH}_3)_5\text{Ru}^{\text{II}}3\text{-Fpy}]^{2+}$ and $[(\text{NH}_3)_5\text{Ru}^{\text{III}}\text{py}]^{3+}$ studied in prior stopped-flow work.

Initial studies of salt effects on “true” (*i.e.* zero-driving force) self-exchange reactions were completed through ^{19}F NMR line-broadening techniques, and these studies have been continued and augmented by the work described in this thesis.⁸ We have investigated salt effects on the “true” ET self-exchange reaction between pentaamineruthenium(II)(3-trifluoromethylpyridine) $^{2+}$, $[(\text{NH}_3)_5\text{Ru}^{\text{II}}\text{tfmp}]^{2+}$, and pentaamineruthenium(III)(3-trifluoromethylpyridine) $^{3+}$, $[(\text{NH}_3)_5\text{Ru}^{\text{III}}\text{tfmp}]^{3+}$, as shown in Figure 2.2.

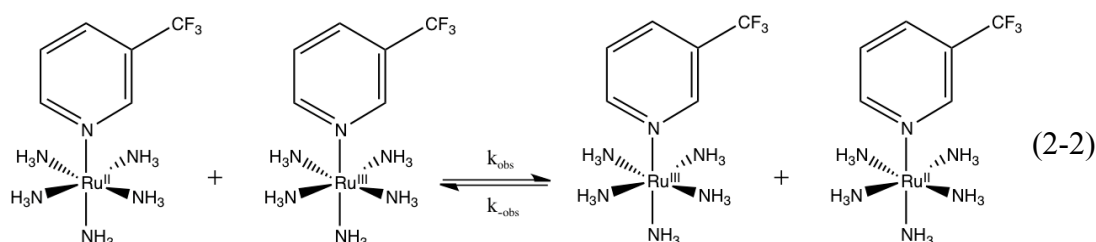


Figure 2.2 The “true” (zero-driving force) ET self-exchange reaction between $[(\text{NH}_3)_5\text{Ru}^{\text{II}}\text{tfmp}]^{2+}$ and $[(\text{NH}_3)_5\text{Ru}^{\text{III}}\text{tfmp}]^{3+}$ used in our NMR kinetics work.

The sensitivity of the spin- $\frac{1}{2}$ ^{19}F nucleus in NMR spectroscopy is almost equivalent to that of the ^1H isotope, and this has enabled us to obtain accurate kinetic data through NMR relaxation techniques using the ^{19}F nucleus from the workable line-broadening concentration range (5.00 mM and above) down to the previously-explored stopped-flow concentration range (~ 0.50 mM and below).¹⁰ The pentaamineruthenium(II/III)(3-trifluoromethylpyridine) $^{2+/3+}$ complexes shown in reaction (2-2) above have proven to be especially beneficial when studying salt effects on ET rates by NMR because the strong, singlet ^{19}F resonance which is

cleanly resolvable in both the ruthenium(II) and ruthenium(III) complexes (the chemical shift differential is ~ 5 ppm or ~ 2460 Hz in D_2O , *vide infra*). The appearance of these two peaks allows for simple verification of the necessary 50:50 redox state distribution between the two reactant ions in solution and for accurate kinetic rates to be calculated accurately from either peak.

The added inert salts previously studied included some “simple” salts (such as KF, NaCl, KI, KBr, *etc.*), as well as a selection of dicarboxylate salts (sodium muconate, sodium terephthalate, *etc.*) as shown in Table 2.1, and the three hexacyano- M^{II} group VIII B salts of the composition $K_4Fe^{II}(CN)_6$, $K_4Ru^{II}(CN)_6$, and $K_4Os^{II}(CN)_6$ as shown in Table 2.2. The concentration range of redox reactants used in the prior stopped-flow work on reaction (2-1) was between 0.06 mM and 0.30 mM, while the earlier ^{19}F NMR line-broadening work⁸ on reaction (2-2) was done with the redox reactants at 3.00 mM and above (with most of the work done at 5.00 mM). In the current work, we have optimized the NMR T_2 spin-echo experiment (*vide infra*) to now directly measure the rate of reaction (2-2) over the entire reactants concentration range from 0.10 mM up to 5.00 mM. This overlap between the stopped-flow and lower-end NMR reactants concentration ranges allows direct comparison of ET self-exchange kinetics as measured by NMR and the stopped-flow rates measured for reaction (2-1). As we will show, this experimental refinement has enabled investigation of the possible origins of the very significant deviations between salt-effect patterns mapped out by previous workers using the two kinetic methods which

were operationally constrained to measuring the ET rates at widely different reactant concentrations.

Table 2.1 The structures, names, and abbreviations for the dicarboxylate salts used in this work and earlier stopped-flow work.^{6,9}

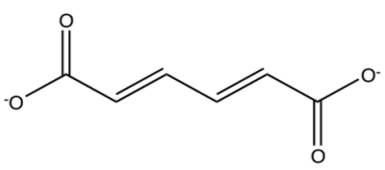
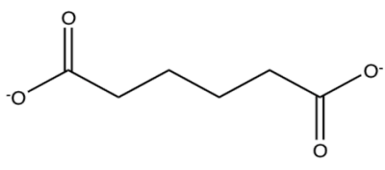
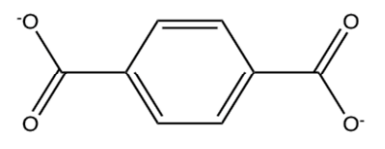
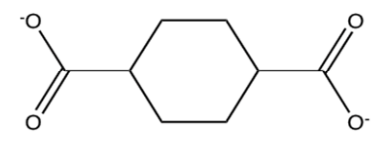
Name	Structure	Abbreviation
muconate		muc ²⁻
adipate		adip ²⁻
terephthalate		tere ²⁻
1,4-dicarboxylcyclohexane		1,4-dcch ²⁻

Table 2.2 The structures, names, and abbreviations of the group VIII B hexacyano salts used both in this work and previous stopped-flow as well as NMR line broadening work.^{8,9}

Name	Structure	Abbreviation
ferrocyanide		$[\text{K}_4\text{Fe}^{\text{II}}(\text{CN})_6]$
ruthenocyanide		$[\text{K}_4\text{Ru}^{\text{II}}(\text{CN})_6]$
osminocyanide		$[\text{K}_4\text{Os}^{\text{II}}(\text{CN})_6]$

2.1.1 Known effects of added simple salts on ET rates

Prior stopped-flow work in this lab has shown that added simple salts of the anions F^- , Cl^- , Br^- , I^- , NO_3^- , *etc.* enhance the rates of ET in reaction (2-1) in a way which routinely violates the quantitative predictions of Debye-Hückel theory^{6,9} (Debye-Hückel theory was introduced in chapter 1 (see section 1.7) and is used to characterize the ionic atmosphere near a charged solute in terms of “local potential” and the resulting effects on ionic activity coefficients^{2,5}). The stopped-flow work established that ET only in the presence of added F^- did the rate respond as would be predicted by Debye-Hückel theory. The rate acceleration due to added F^- salts agreed nearly perfectly with the theoretical Debye-Hückel-Bronsted $\log k_{\text{ex}}$ vs. GP slope of

6.12 (see equation (1-38))¹¹, while salts containing the other halide anions: Cl^- , I^- , Br^- , the dicarboxylate salts: muconate²⁻, adipate²⁻, terephthalate²⁻, and 1,4-dicarboxylcyclohexane²⁻ (see Table 2.1), and the hexacyano complexes: $\text{Fe}^{\text{II}}(\text{CN})_6^{4-}$, $\text{Ru}^{\text{II}}(\text{CN})_6^{4-}$, and $\text{Os}^{\text{II}}(\text{CN})_6^{4-}$ (see Table 2.2) deviated upward as shown in Figures 2.3 through 2.8.

From the stopped-flow work of Sista, as illustrated in Figure 2.3, we see that upon going from F^- to Cl^- , to Br^- , and then finally to I^- the observed early slope (first few points) of the graph of the $\log k_{\text{ex}}$ vs. GP for reaction (2-1) changes from 6.2 ± 0.1 for F^- , to 14.4 ± 0.5 for Cl^- , to 20.6 ± 1.2 for Br^- , and then to 21.6 ± 0.5 for I^- .⁶ This progressive deviation from the classical Debye-Hückel-Bronsted charge-product slope has been multiply-verified and is considered to be a real, anion-specific ET catalytic effect.^{1,6}

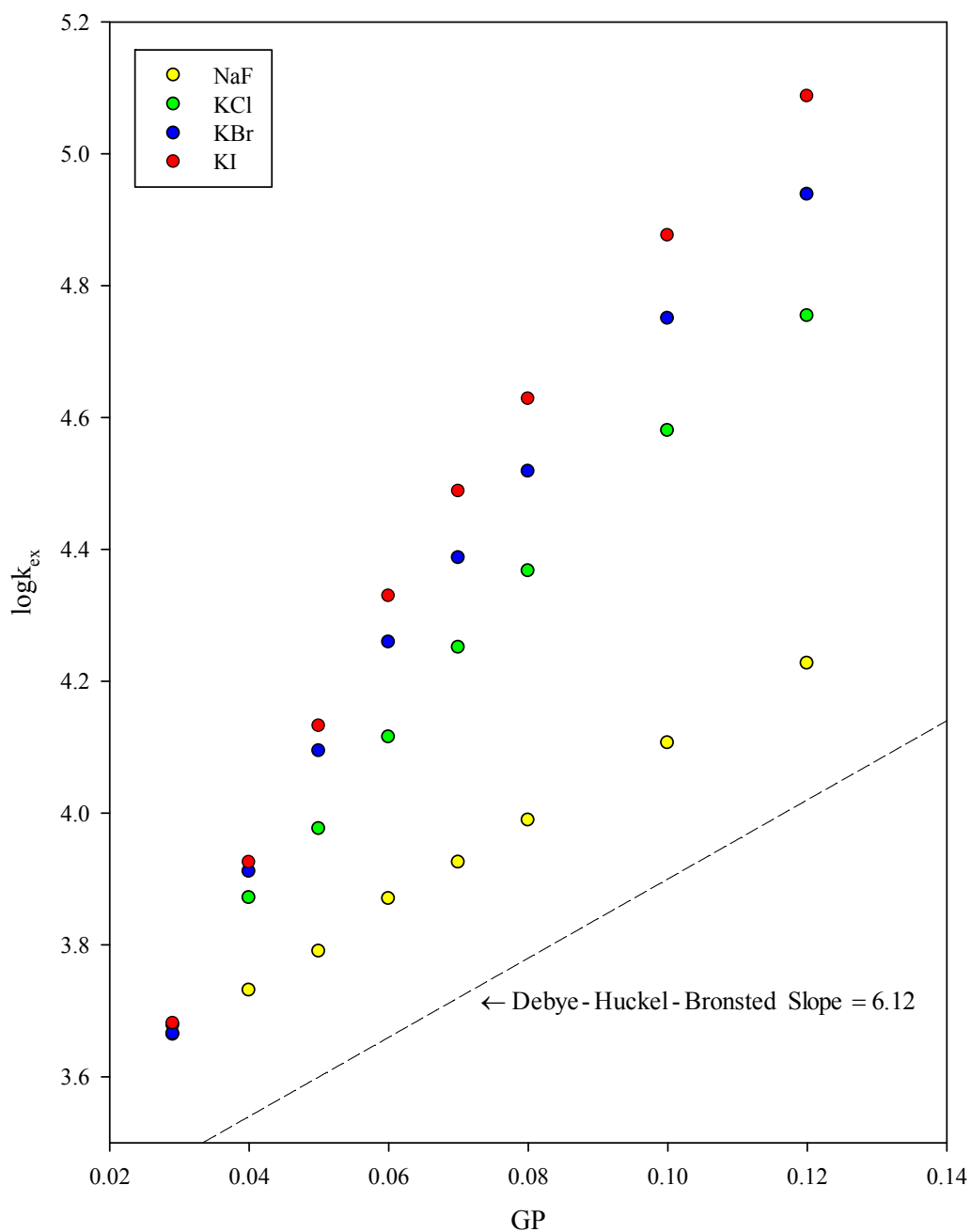


Figure 2.3 Log of the measured ET rate *vs.* added salt data from previous stopped-flow work done with equimolar reactant concentrations of 0.10 mM (see reaction (2-1)). Note the progressive deviation away from the theoretical Debye-Hückel-Bronsted slope (dotted line) as the identity of the added salt is varied over NaF, KCl, KBr, and KI.⁶

Figure 2.4 shows results from subsequent ^{19}F NMR line-broadening work by Qin measuring the kinetic salt effects due to added NaF, NaCl, and KBr on the rate of the true ET self-exchange reaction (2-2).⁸ Here we not only see a similar qualitative pattern of progressive change over the F^- to Br^- series found in Figure 2.3, but we also find that the magnitude of the ET rate accelerations due to all three salts deviate downward in a quantitative sense from what was observed in the stopped-flow work. The F^- anion is still “most-ideal” since it is the only one exhibiting strictly linear behavior, but with a slope of 0.92 ± 0.05 , while the observed early slopes due to adding Cl^- and Br^- fall to 8.2 ± 0.6 and 10.7 ± 0.7 , respectively.

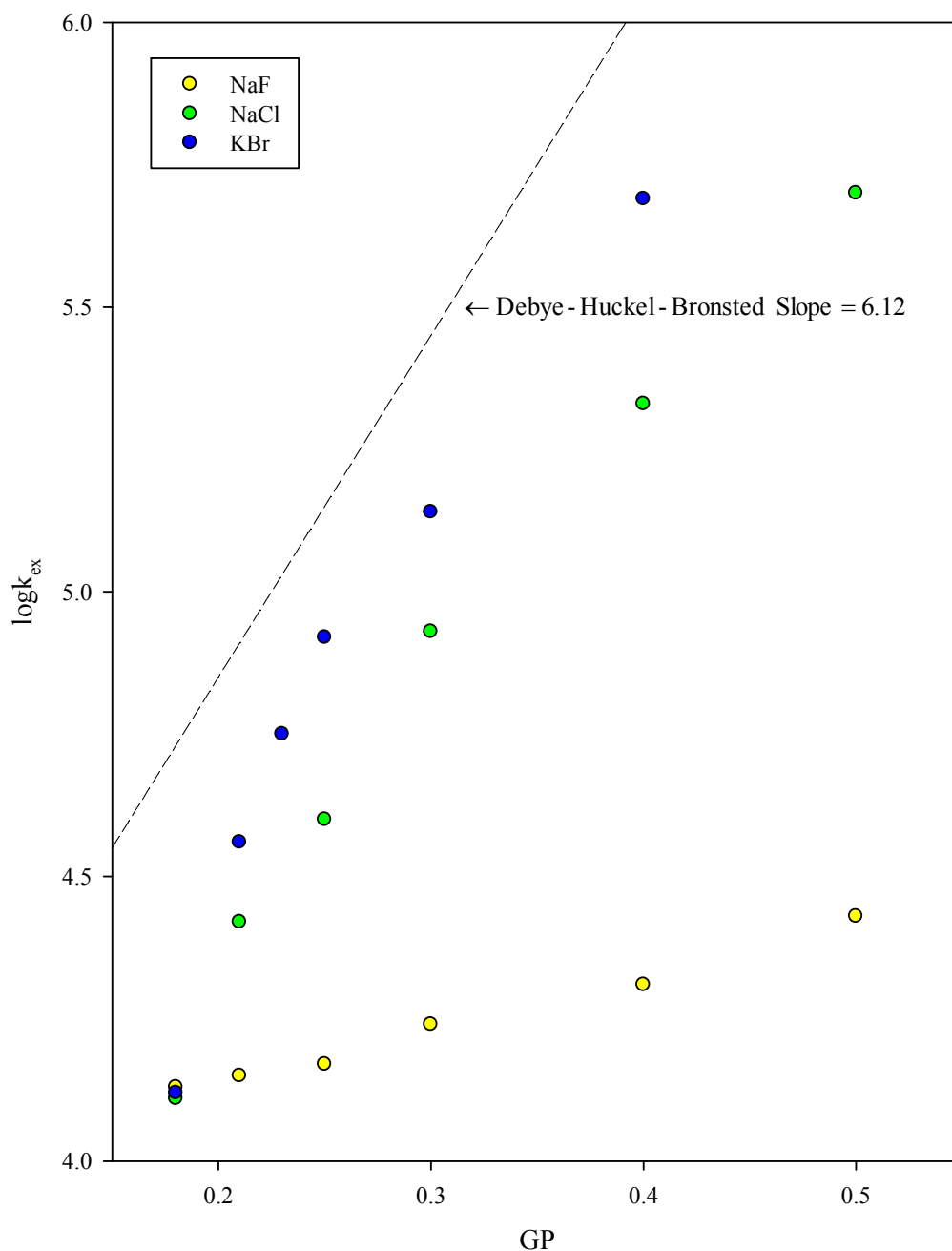


Figure 2.4 ^{19}F NMR line-broadening kinetic salt effects measured by Qin using equimolar reactant concentrations of 5.00 mM (see reaction (2-2)). There is qualitative similarity to the pattern of effects seen with added NaF, NaCl, and KBr obtained by stopped-flow (Figure 2.3), but the quantitative agreement with Debye-Hückel-Bronsted theory seen in stopped-flow for added F^- is lost.⁸

The large drop in the magnitude of the kinetic salt effects was provisionally linked to the fact that the NMR work was done at a reactants concentration of 5.00 mM, which is 50-fold higher than the reactants concentration of 0.10 mM used (for reasons of limited time-resolution) in the stopped-flow work. This increase of 50x in concentration translates into a significantly decreased average inter-reactant distance in solution (see Figure 1.11), and this might be expected to have ramifications regarding the quantitative applicability of the Debye-Hückel-Bronsted equation. Part of the motivation behind the work to be described here was to see if these decreases in kinetic salt effects at high reactant concentrations might simply be due to the change in average inter-reactant distance or if some other effect might be involved.

2.1.2 Known effects of added dicarboxylate salts on the rate of ET

In addition to the work completed on added “simple” salts, other kinetic work in this lab has focused on the salt effects arising upon the addition of the more complicated family of dicarboxylate salts shown in Table 2.1. The saturated dicarboxylate salts showed similar effects to those of the “simple” salt cases (*vide infra*).^{6,8,9} However, in the case of the *trans, trans*-diene “muconate” dianion, the observed rate effects are *greatly* enhanced when compared to the saturated dicarboxylates and the simple salts studied by stopped-flow at a 0.10 mM reactants concentration.

In Figure 2.5 (taken from stopped-flow work at 0.10 mM reactants), we see that while the adipate anion is more catalytic than F⁻ (behaving nearly equal to Br⁻), it lags muconate by about 1.4 log units at a GP of about 0.07. This reproducible, large

catalytic effect is unique to added muconate (nearly two orders of magnitude as compared to F⁻). This has been attributed to muconate acting as a “diffusive wire” and enhancing the ET process by an associative mechanism involving quantum “super-exchange” mediation (as explained in chapter 1, section 1.6) in a presumably H-bonded ternary assembly of the formulation [L-Ru^{II}(NH₃)₅, muc²⁻, (NH₃)₅Ru^{III}-L].^{1,6} In the case of sodium terephthalate and its saturated analog, sodium 1,4-dicarboxylcyclohexane (1,4-dcch²⁻), there was again a substantial acceleration for terephthalate (tere²⁻) over 1,4-dcch²⁻ by stopped-flow, but to a lesser degree than for the muc²⁻ and adip²⁻ pair.

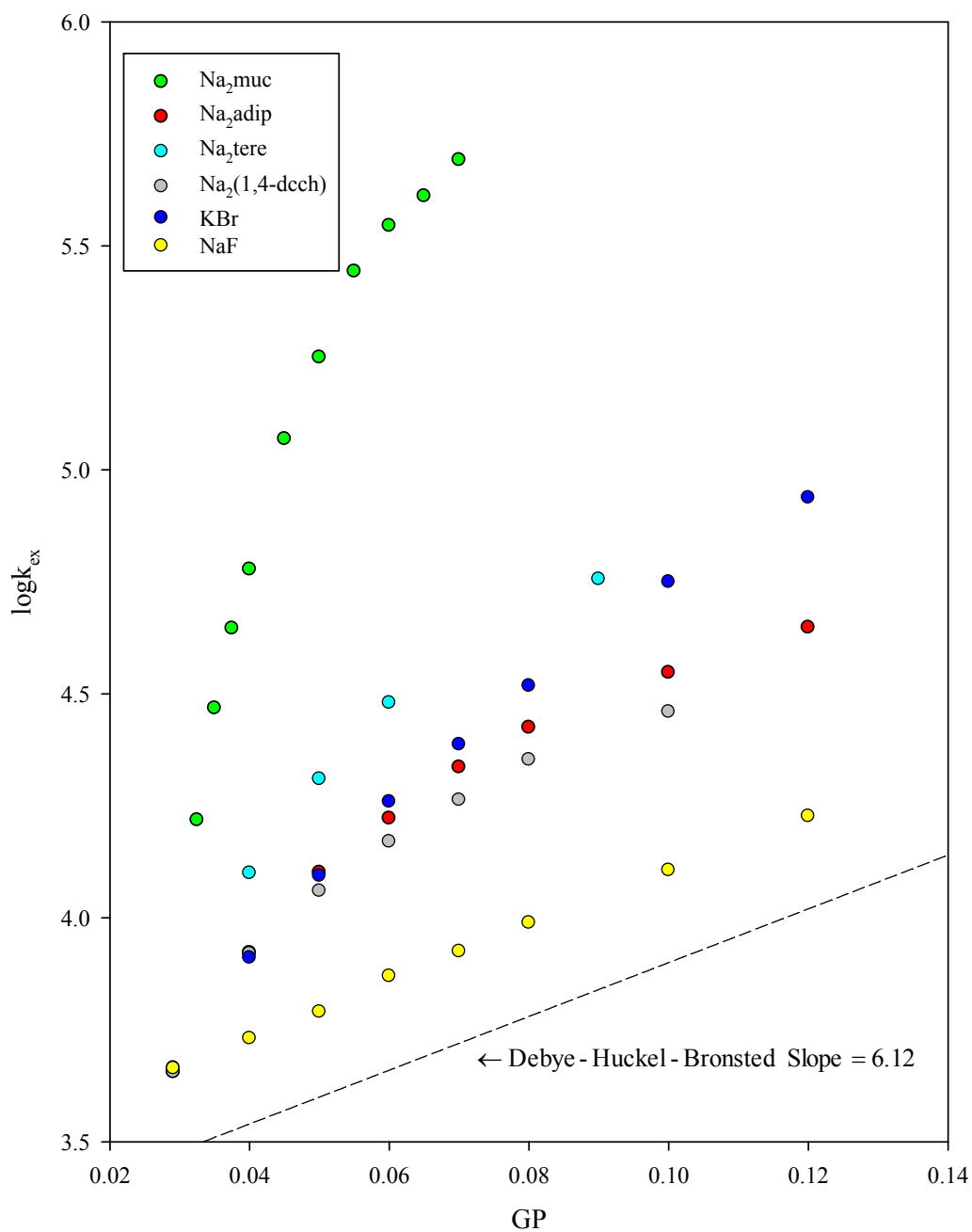


Figure 2.5 Kinetic data from previous stopped-flow work with equimolar reactant concentrations of 0.10 mM (see reaction (2-1)), showing the effects of added sodium muconate (Na_2muc), sodium adipate (Na_2adip), sodium terephthalate (Na_2tere), sodium 1,4-dicarboxylcyclohexane²⁻ ($\text{Na}_2(1,4\text{-dcch})$), KBr , and KF on the rate of ET.⁶

In surprising contrast, ^{19}F NMR line-broadening ET rate measurements at an equimolar reactants concentration of 5.00 mM in the presence of added muconate exhibited no such “special” catalytic effect, as can be seen in Figure 2.6.⁸ Here we see that muconate, while still slightly more accelerating than adipate, falls far below bromide as an ET catalyst when studied by NMR line-broadening. This puzzling loss in the catalytic efficacy of muconate in the NMR work was initially attributed to some unknown effect of the relatively high concentrations of reactants. One hypothesis in this regard hinged on possible effects arising from the “rod-like” (high aspect ratio) shape of the muconate dianion. Here it was thought that at the high reactant’s concentration of the NMR work, the anisotropic diffusion properties of muconate might impair its ability to get “in between” the redox reactants rapidly enough to enhance the ET process *via* the same “quantum super-exchange” mechanism hypothesized as being operative as in the stopped-flow work at 0.10 mM reactants concentration. A competing, though less-favored, hypothesis was that it may have in fact been the *magnetic field itself* which somehow attenuated muconate’s catalytic effectiveness. This latter idea was partially tested by performing stopped-flow measurements in the presence of a modest external magnetic field (obtained by stacking strong permanent magnets on the flow cell), but no attenuation of the catalytic efficacy of muconate was detected.¹² A third hypothesis was that the D_2O used in the NMR work was exchanging deuterons for the ammine protons of the reactant complexes (a known, rapid process) and that perhaps the ET catalysis by muconate relied on some degree of proton (in addition to electron) tunneling. The

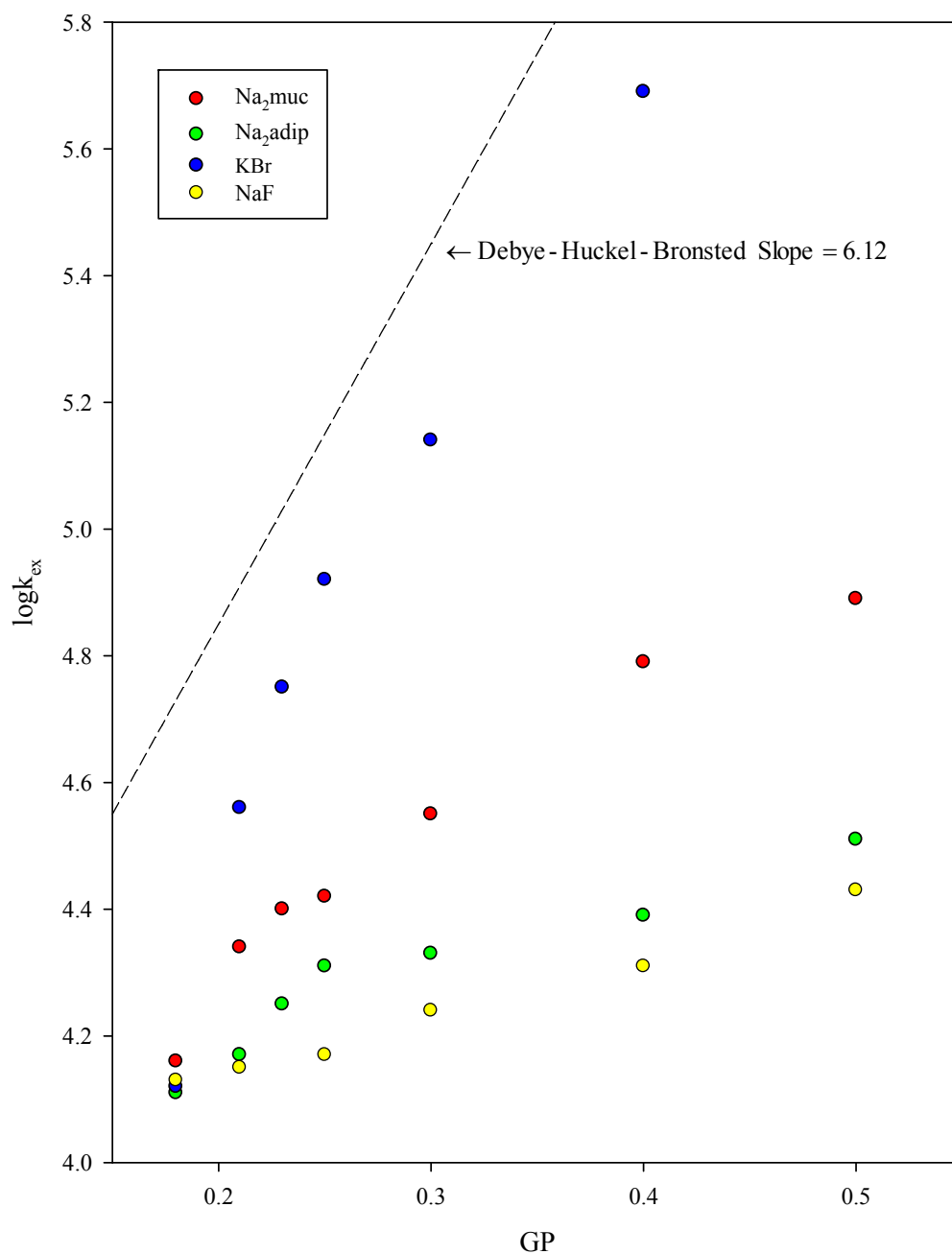


Figure 2.6 Results from previous ^{19}F NMR line-broadening work done with equimolar reactant concentrations of 5.00 mM (see reaction (2-2)). Here we see that added sodium muconate (Na_2muc), sodium adipate (Na_2adip) and KF give rise to very muted accelerations relative to theory and KBr (which in this case nearly matches theory).⁸

much lower tunneling probability of deuterons might then show up as a loss of catalytic efficacy.¹³ To this end, stopped-flow studies were conducted in D₂O, but the catalytic effect of muconate remained as high as in H₂O.^{6,12} This conundrum was another reason why we sought in this work to extend NMR rate measurements down in concentration far enough to overlap with the stopped-flow conditions. The surprising results of these studies and their bearing on the “muconate mystery” will be discussed in a later section.

2.1.3 Known effects of added hexacyano complexes (K₄M(CN)₆, where M = Fe^{II}, Ru^{II}, Os^{II}) on the rate of ET

Both stopped-flow⁹ and NMR line broadening work⁸ have shown that the rates of ET reactions (2-1) and (2-2) are most spectacularly catalyzed by the addition of very small amounts of the potassium hexacyano salts (from Table 2.2), as shown in Figures 2.7 and 2.8. Through both techniques, it was observed that the catalytic efficacy was greatest for K₄Fe^{II}(CN)₆, then K₄Os^{II}(CN)₆, and finally K₄Ru^{II}(CN)₆. This observed pattern of ET catalytic effects was linked to the known, thermodynamically favored ion-pair formation reactions of these species. For example, the series of ion-pairs formulated as (NH₃)₅Ru^{III}L/M^{II}(CN)₆, where L = substituted pyridine and M^{II} = Fe^{II}, Ru^{II}, or Os^{II}, are known to exhibit ion-pair intervalence-transfer transitions between the d⁶ and d⁵ redox centers.¹⁴ In the case of the bimolecular ET rate catalysis reported here, the [M^{II}(CN)₆]⁴⁻ salts are thought to facilitate “hole-transfer” quantum super-exchange mediation, the theoretical basis of which was discussed in chapter 1 (see section 1.6). The acceleration is thought to

again be due to enhanced donor/acceptor electronic coupling, in this case in presumed ternary association complexes of the general formulation, $[(\text{NH}_3)_5\text{Ru}^{\text{II}}\text{L}, \text{M}^{\text{II}}(\text{CN})_6, (\text{NH}_3)_5\text{Ru}^{\text{III}}\text{L}]^+$. The additional electronic coupling here would be provided by the virtual hole state of the $\text{M}^{\text{II}}(\text{CN})_6^{4-}$ bridging unit (in analogy to the ion-pair intervalence transitions mentioned above). Our current measurements of this effect and the extension to low-concentration NMR T_2 spin-echo kinetic measurements will be discussed in detail further on.^{8,9}

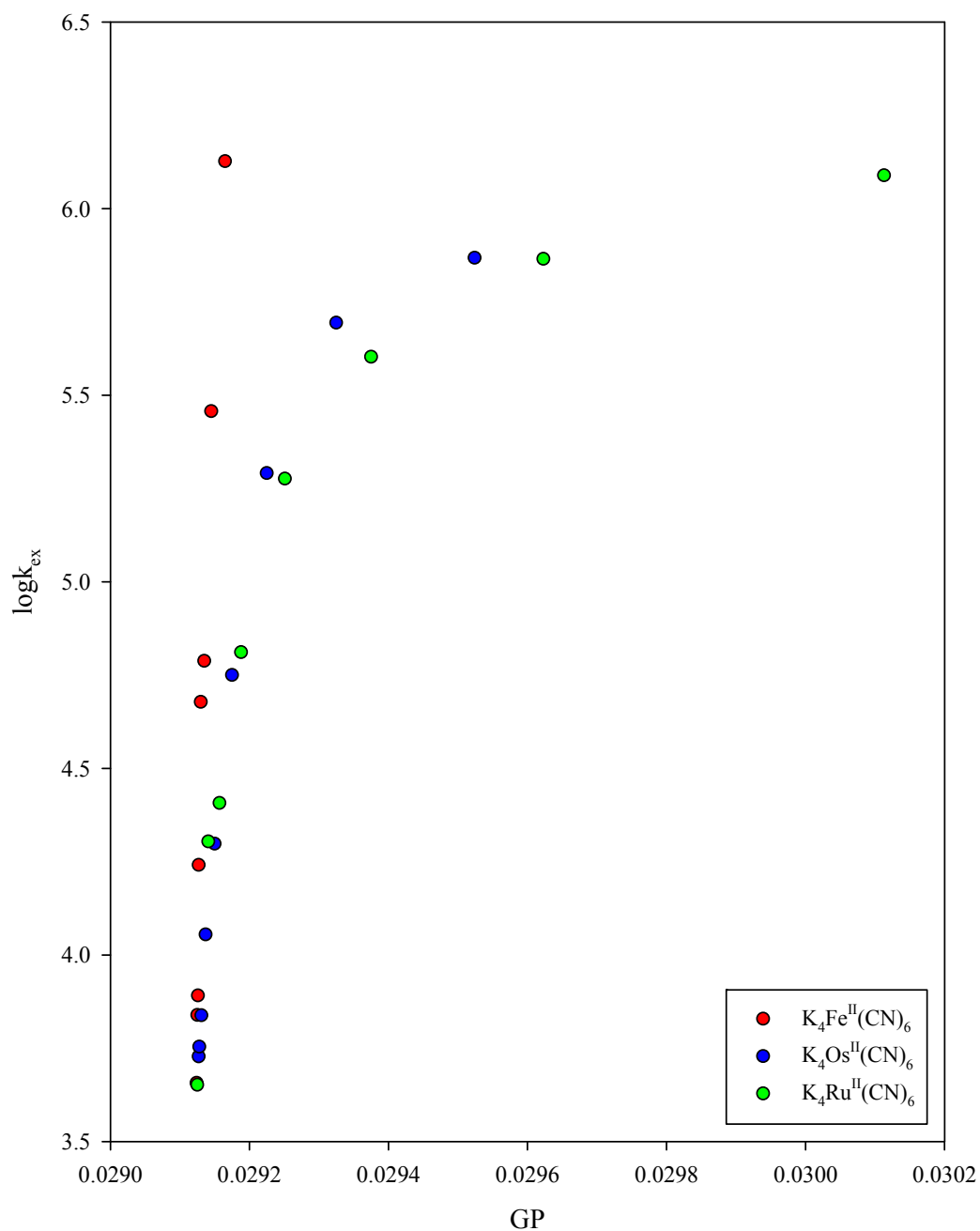


Figure 2.7 Data from stopped-flow work with equimolar reactants concentrations of 0.10 mM (see reaction (2-1)), showing the effects of added $\text{K}_4\text{Fe}^{\text{II}}(\text{CN})_6$, $\text{K}_4\text{Os}^{\text{II}}(\text{CN})_6$, and $\text{K}_4\text{Ru}^{\text{II}}(\text{CN})_6$ on the rate of ET. At the highest GP reached of 0.0301 with $\text{Ru}^{\text{II}}(\text{CN})_6^{4-}$ as a catalyst, the hexacyano complex is still only present at $6 \times 10^{-6} \text{ M}$, which is 6x lower in concentration than the reactants.⁹

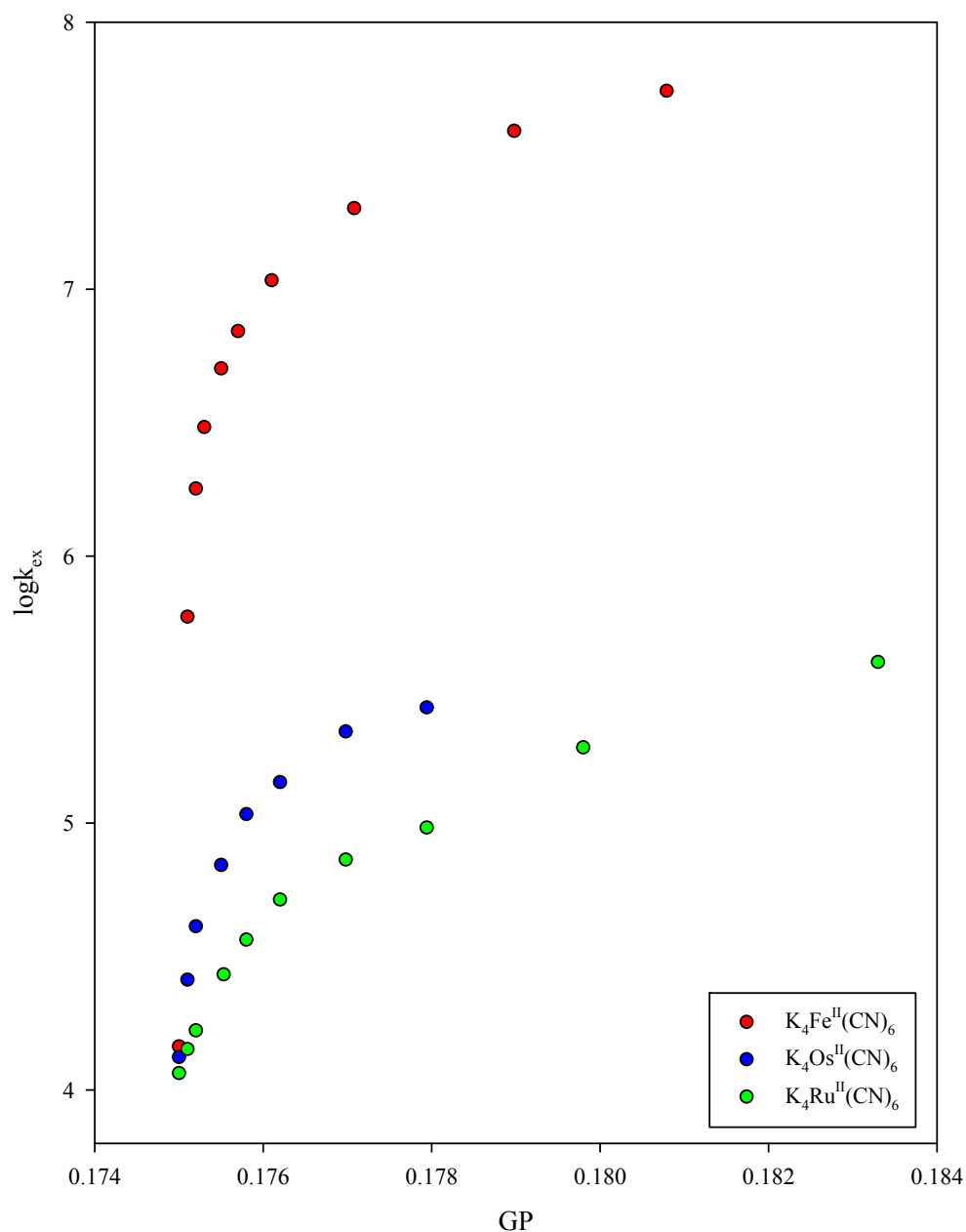


Figure 2.8 Data from previous ^{19}F NMR line-broadening work with equimolar reactants concentrations of 5.00 mM (see reaction (2-2)), showing the effects of added $\text{K}_4\text{Fe}^{\text{II}}(\text{CN})_6$, $\text{K}_4\text{Os}^{\text{II}}(\text{CN})_6$, and $\text{K}_4\text{Ru}^{\text{II}}(\text{CN})_6$ on the rate of ET. Here we see that at the highest GP reached of 0.1833 with $\text{Ru}^{\text{II}}(\text{CN})_6^{4-}$ as a catalyst, the hexacyano complex is still only present at 5.4×10^{-4} M, which is 10x lower in concentration than the reactants.⁸

2.2 Determination of Kinetic Rate Constants from NMR Line-Broadening and T_2

Measurements of the rates of the bimolecular ET self-exchange reaction (2-2) were executed using both ^{19}F NMR line-broadening and ^{19}F T_2 spin-echo (transverse) relaxation measurements.^{10,15} Rutheniumpentaammine-L complexes in both the Ru^{II} and Ru^{III} oxidation states are known to be “substitution inert” over moderate periods of time (4-6 hours) in aqueous solution, meaning that the ET reaction taking place is in all cases happening *via* the outer-sphere mechanism discussed in chapter 1 (see section 1.3).¹⁶ As is typical for 2nd and 3rd row transition metal complexes, the high-spin/low-spin characteristics of the electronic states of the Ru^{II} / Ru^{III} redox sites will not change during the course of an ET event since both are rigorously low-spin. The “extra” electron on the Ru^{II} center will exchange between one of the filled, mostly non-bonding, $d\pi$ or $(t_{2g})^6$ orbitals, of the low-spin Ru^{II} ion and the “hole” in the $d\pi$ or $(t_{2g})^5$ orbital set of the low-spin Ru^{III} ion.

NMR spectroscopy is a useful tool for measuring the rates of “chemical exchange” events if there is an observable resonance peak of both, or even just one, of the reactant ions, that shifts in resonance frequency due to a change in chemical environment; sometimes this can simply be a change in structural conformation, and/or a change in redox state (and therefore charge type), as in our work. If the chemical exchange dynamics of the spin system observed match the NMR timescale then rates can be obtained using either the exchange-induced NMR line-broadening values (which allow the relevant T_2 values to be *inferred* under certain assumptions)

or by *direct* determination of the kinetically-perturbed T_2 values *via* spin-echo relaxation methods (*vide infra*).¹⁰ It is the superiority of this latter approach in the “slow exchange” region which has allowed us to study the ET kinetics of reaction (2-2) by NMR in the stopped-flow concentration range at which reaction (2-1) was studied.

In the simplest cases, measured NMR line-widths depend directly on the dynamics of the free induction decay, FID, or “dephasing” of the post-pulse coherent spin-echo superposition in the x,y-plane (90° rotated net magnetization vector) as shown in Figure 2.9.

In step (a) the net magnetization vector arising from the unequal spin population in the sample at equilibrium (thick blue arrow) is “pushed” from its prior equilibrium along the z axis (the direction of the permanent magnetic field of the magnet, B_0) into the x,y-plane by a 90° radio frequency (RF) pulse along x, which is gated on for a very precisely defined amount of time. In step (b) the RF pulse is turned off once the net magnetization has precessed into the x,y-plane, and then the individual magnetization vectors (or “isochromats”), arising from the environmentally-different nuclei (in our case the magnetically-inequivalent fluorines on the Ru^{II} and Ru^{III} complexes in the sample), begin their respective dephasing processes in which they spread apart from each other as they precess in the x,y-plane (around B_0) according to their resonance frequencies and then ultimately relax back to their original orientation along z (re-establishing the previous equilibrium condition). During this time, the RF receiver coil is turned on and the amplified

voltage signal of the precessing isochromats is heterodyned against a pure sine wave reference or “observe” frequency. The intensity of the resulting “beats” decays due to

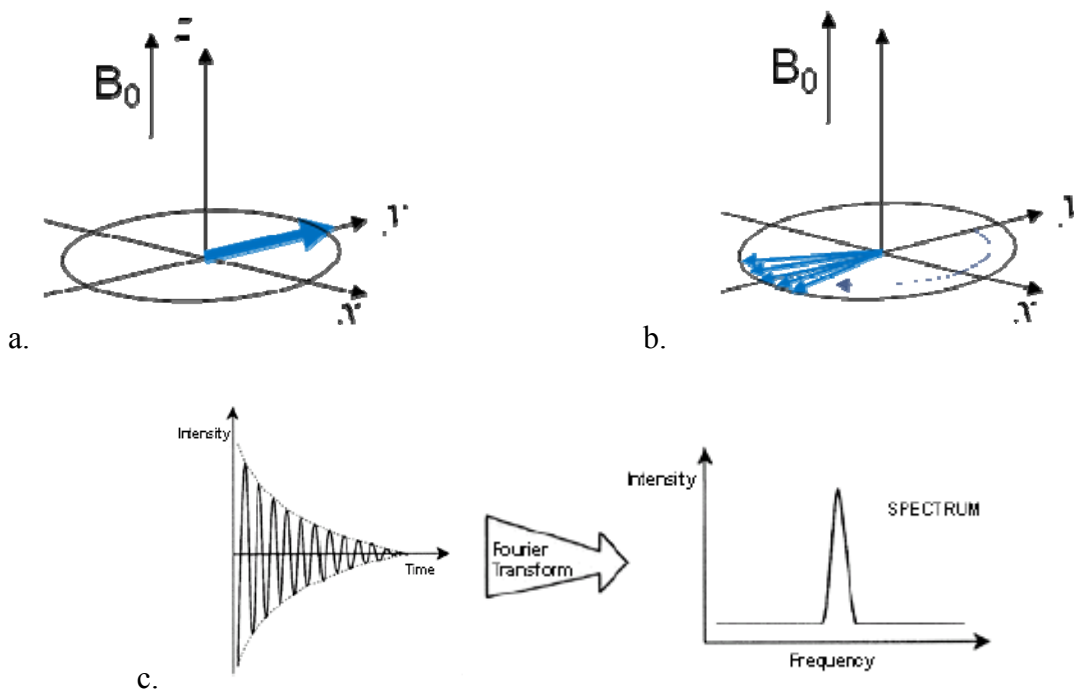


Figure 2.9 A schematic illustration of how NMR peak resonances arise. At point (a), the net magnetization vector (thick blue arrow) has been pushed 90° into the x, y -plane by a precisely-timed RF pulse. (b) Illustrates the dephasing of the “net magnetization vector” into the individual “fast” and “slow” spin system isochromats corresponding to different chemical environments and hence different resonance frequencies. (c) Illustrates the acquisition step wherein the FID signal from the heterodyned dephasing of the individual isochromats is recorded in the time domain. The spectral line-shape results when the FID is Fourier-Transformed so as to create a “spectrum” of intensity vs. frequency (showing here only as a single peak due to frequency axis truncation).

the aggregate dephasing processes creating the dynamic profile of the Free-Induction Decay, FID, as shown by part (c) in Figure 2.9. A Fourier transform algorithm is then

applied to the “time domain” FID which then produces a resonance peak in the frequency domain at a specific position and with a definable line-width. The transverse relaxation time, T_2 , of a given individual resonance peak will depend on the dynamics of the dephasing processes specific to that isochromat and will be encoded in the “true” line-width at half-height, $\Delta\nu_{1/2}$, for that resonance line (*vide infra*). The transverse, or spin-spin, relaxation time is defined as the rate at which phase coherence in the x,y-plane and the precession-induced NMR signal is lost after a 90° RF pulse is applied to the sample.^{10,17} The magnitude of T_2 in the simplest case is determined by “spin-spin” relaxation processes innate to the solvent/solute environment as well as coupling between the spin system being observed and nearby (but generally not directly bound) spin states. We will go into greater depth on this topic later.

In the most ideal case this innate spin-spin dephasing process would fully explain the measured line-widths of the resonances in an NMR spectrum, but in fact this is rarely the case. The total measured line-width often incorporates additional factors with the most common being “inhomogeneous broadening” due to small, but finite variations of the macroscopic magnetic fields which the instrument creates and manipulates throughout the sample.¹⁷ These derive from instrumental imperfections such as “bad shims” and unavoidable field inhomogeneity caused by sample magnetic susceptibility effects. Another factor which contributes to line-widths being larger than would be predicted from the innate or “natural” T_2 relaxation time alone (*vide infra*), stems from “homogenous” broadening. This is due to fluctuations of the

microscopic (local) magnetic field in the sample itself on the length scale of the molecules and nearby environments, and these effects cannot be avoided or corrected for. The measured line-width is necessarily due to contributions of all these effects and thus line-widths larger than what the underlying T_2 values alone would dictate are often observed experimentally.

When studying the kinetics of some chemical exchange process through NMR spectroscopy, the “mean kinetic lifetime”, τ_L , is defined as the average time the observed nucleus spends in the magnetic environment (local field strength and hence resonance frequency) corresponding to a given chemical environment (meaning conformer, redox state, state of association, *etc.*).^{10,15} In an exchanging or oscillating environment where a conformational change or other chemical process scrambles the spin-system isochromats during the FID acquisition time, there is now an additional dephasing mechanism which causes the FID to decay faster than the innate spin-spin relaxation in that solvent environment would otherwise dictate. It is this decrement in the measured T_2 which holds information relevant to the mean kinetic lifetimes of the exchanging species present. The details of the link between the kinetic rate of the stochastic scrambling event and the acceleration of the dephasing process will be explained below.

In the work done here the relevant exchange process was in all cases the second-order bimolecular ET reaction shown in equation (2-2). The mean kinetic lifetimes of the magnetically-inequivalent Ru^{II} and Ru^{III} species, $\tau_{\text{Ru}^{\text{II}}}$ and $\tau_{\text{Ru}^{\text{III}}}$ respectively, are directly related to the rate of scrambling during the x-y dephasing

period which determines to the FID curve shown in Figure 2.9 (b) and (c). The relevant expressions in terms of the ET self-exchange rate constant are,

$$\tau_{\text{Ru}^{\text{II}}} = \frac{[\text{Ru}^{\text{II}}]}{k_{\text{ex}}[\text{Ru}^{\text{II}}][\text{Ru}^{\text{III}}]} = \frac{1}{k_{\text{ex}}[\text{Ru}^{\text{III}}]} \quad (2-3)^{18}$$

and,

$$\tau_{\text{Ru}^{\text{III}}} = \frac{1}{k_{\text{ex}}[\text{Ru}^{\text{II}}]} \quad (2-4)$$

where $[\text{Ru}^{\text{II}}]$ corresponds to the concentration of $[(\text{NH}_3)_5\text{Ru}^{\text{II}}\text{tfmp}]^{2+}$, $[\text{Ru}^{\text{III}}]$ corresponds to the concentration of $[(\text{NH}_3)_5\text{Ru}^{\text{III}}\text{tfmp}]^{3+}$, and k_{ex} is the second-order ET self-exchange rate constant as described in chapter 1 (see section 1.3). When the concentrations are adjusted such that $[\text{Ru}^{\text{II}}]$ is equivalent to $[\text{Ru}^{\text{III}}]$, then the kinetic lifetimes of the two exchanging species will necessarily be equal.

The line-width at half-height of a given resonance, $\Delta\nu_{1/2}$, in the exchanging solution will thus be determined by the inherent contributors to dephasing discussed previously, as well as the additional dephasing caused by the chemical exchange process (ET in our case) depends on the chemical kinetics. Within certain limits, the line-widths of NMR resonance peaks are calculable using the following relation,

$$\Delta\nu_{\text{L}} = \frac{1}{\pi(\tau_{\text{L}})} \quad (2-5)^{18}$$

where $\Delta\nu_{\text{L}}$ (same as $\Delta\nu_{1/2}$) is the Lorentzian line-width at half-height of the peak corresponding to species L, and τ_{L} is the mean kinetic lifetime of species L. Importantly if one applies the Heisenberg energy-duration uncertainty relationship

from atomic spectroscopy using $\tau_L \cong T_2$ for Δt and the NMR Lorentzian line-width¹⁰ as a measure of ΔE , the one can write,

$$\Delta \nu_L = \frac{1}{\pi(T_2)} \quad (2-6)^{10,18}$$

where T_2 is the transverse relaxation time. In the presence of stochastic chemical exchange, the transverse relaxation (dephasing) time is shortened to some new value T_2' , and this in turn increases the line-width (energy uncertainty) of the NMR resonance peak. There are caveats involved in applying equations (2-5) and (2-6), and these will be addressed in detail in section 2.3

When the concentrations of both exchanging sites are equal as in our case, the total relaxation frequency, $1/T_2'$, which describes the dephasing rate seen in the FID can be decomposed into component relaxation frequencies according to,

$$\frac{1}{T_2'} = \frac{1}{T_2} + \frac{1}{\tau_L} \quad (2-7)^{19-22}$$

where T_2' is the measured transverse relaxation time in the presence of chemical exchange of the species being observed, T_2 is the transverse relaxation time of that species in absence of chemical exchange (pure Ru^{II} or Ru^{III} solutions in our case), and τ_L is the mean kinetic lifetime of the species being observed in the exchanging sample as in equation (2-5). The Lorentzian line-width expression defined by equation (2-6) can now be applied to equation (2-7) to obtain the following key relation,

$$\frac{1}{\tau} = \pi (\Delta \nu_{1/2}' - \Delta \nu_{1/2}) \quad (2-8)^{19}$$

where $\Delta \nu_{1/2}'$ is the line-width of the resonance peak in the presence of chemical exchange and $\Delta \nu_{1/2}$ is the line-width of the peak in the absence of chemical exchange. When equation (2-3) or (2-4) is combined with equation (2-8), the second-order rate constant for a bimolecular ET self-exchange reaction can be extracted from any measured line-broadening beyond the innate or “natural” line-width dictated by T_2 using equation (2-9) below,

$$k_{\text{ex}} = \frac{\pi (\Delta \nu_{1/2}' - \Delta \nu_{1/2})}{[C]} \quad (2-9)^{22}$$

where $[C]$ is the concentration of the ruthenium complex other than the one being observed ($[\text{Ru}^{\text{II}}]$ and $[\text{Ru}^{\text{III}}]$ were kept equal in all cases in the work done here).

The consequences of exchange processes on the observed line-shapes of NMR resonance peaks depend on how “fast” the kinetic rates are compared to the natural excited-state lifetime, as well as the difference in the NMR resonance peak frequencies of the nuclei in both exchanging and non-exchanging environments as seen in Figure 2.10. There are a variety of exchange rate “regions” ranging from the case of “very slow” exchange where isochromat scrambling barely increases the natural transverse dephasing rate, to “very fast” exchange where the mean kinetic lifetime, τ , is much less than the natural transverse relaxation lifetime, T_2 . Figure 2.10 illustrates how NMR line-shapes depend on exchange rate processes as the magnitudes of τ and T_2 are varied.

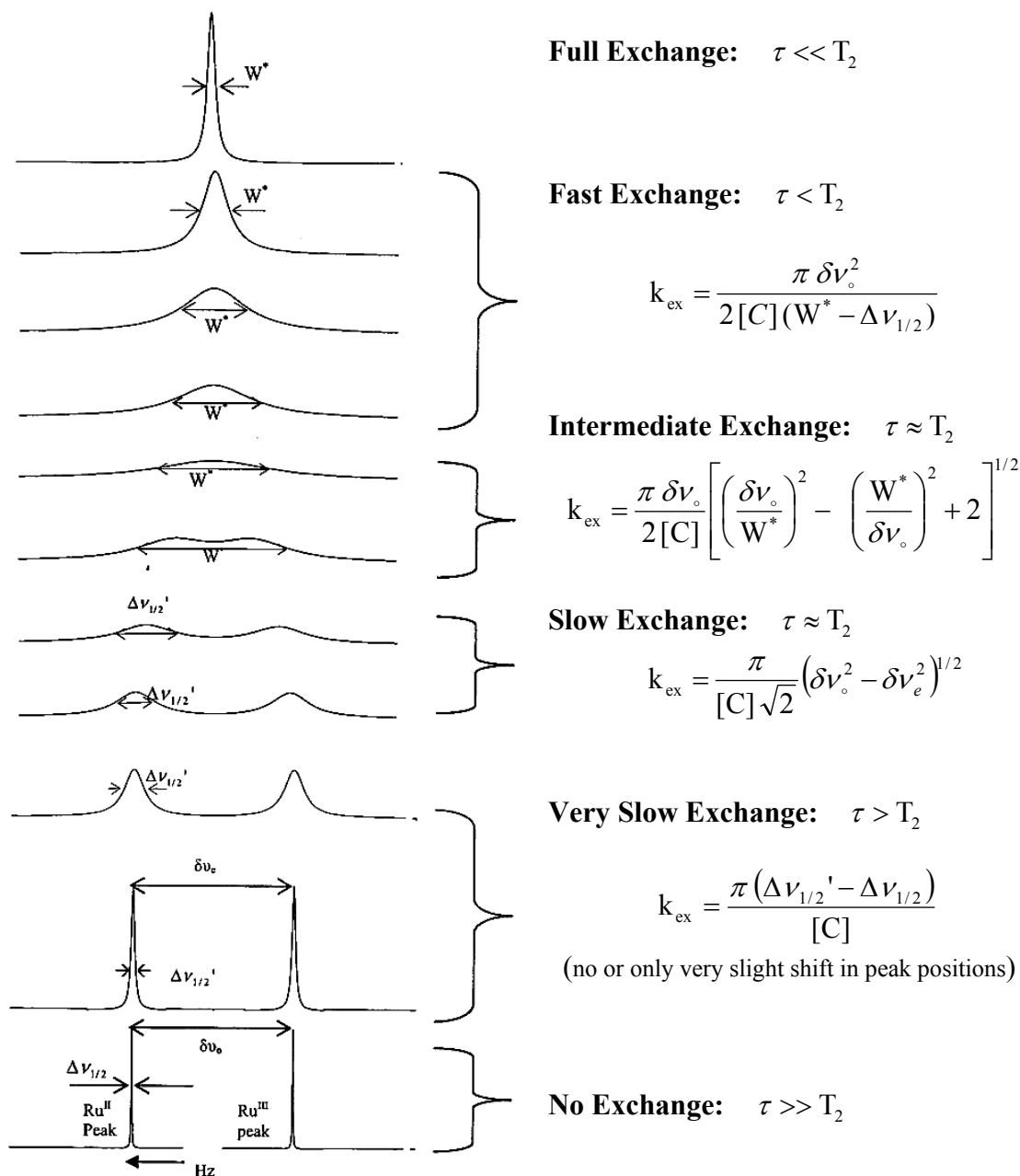


Figure 2.10 Illustration of how line-widths and shapes of exchange-coupled peaks respond to varying kinetic rates of scrambling. This general case diagram applies directly to our system for exchange of the ^{19}F 3-trifluoromethylpyridine singlets due to the ET self-exchange reaction shown in reaction (2-2).⁸

In Figure 2.10, $\delta\nu_0$ is the difference in chemical shift between the Ru^{II} and Ru^{III} NMR resonance frequencies in the absence of chemical exchange, $\delta\nu_e$ is the difference in chemical shift between the Ru^{II} and Ru^{III} resonance frequencies in the presence of chemical exchange, $\Delta\nu_{1/2}$ is the line-width at half-height of the resonance peak in the absence of chemical exchange, $\Delta\nu_{1/2}'$ is the line-width at half-height of the resonance peak in the presence of chemical exchange, and W^* is the line-width at half-height of the “merged” peaks in the presence of intermediate to fast chemical exchange.

In the “very slow” exchange region, the peaks become only slightly broadened and do not change frequencies relative to the non-exchanging case (*i.e.* solutions containing only pure Ru^{II} or Ru^{III}). As the rate of chemical exchange increases, more ET events take place during FID acquisition, and these stochastically scramble the “signals” of the two different peak resonances. As we go up the sequence in Figure 2.10, the rate of scrambling relative to $\delta\nu_0^{-1}$ goes up, and the peaks start to broaden as well as “move in” towards each other. In the intermediate region, peak overlap erases the return to baseline between the peaks, and the sequence finishes with coalescence of the two into a very broad, “merged” peak. In the fast exchange region, scrambling occurs on such a rapid timescale that only one peak will appear (which becomes sharp again in the limit where each nucleus spends exactly 50% of its time precessing as Ru^{II} and 50% as Ru^{III}).

Expressions for NMR spectrum-derived kinetic rate constants are not solely dependent on line-width. In the “slow exchange” region as labeled in Figure 2.10, another rate expression in replacement of equation (2-9) is derived from methods based on peak separation and is found to be,

$$k_{\text{ex}} = \frac{\pi}{[C]\sqrt{2}} (\delta\nu_o^2 - \delta\nu_e^2)^{1/2} \quad (2-10)^{15}$$

where $\delta\nu_o$ is the difference in chemical shift between the Ru^{II} and Ru^{III} resonance frequencies in the absence of chemical exchange, and $\delta\nu_e$ is the difference in chemical shift between the Ru^{II} and Ru^{III} resonance frequencies in the presence of chemical exchange.

Takeda and Stejskal derived a general bandwidth expression using the Bloch equations for an equally populated two-site case without any approximations.^{15,23} A slightly modified form of this equation can be written as,

$$\frac{W^*}{\delta\nu_o} = \{[(A+B)^2[2(2A+B)^{-1} - 8A]^2 + (4B[2A+B] + 1)^2]^{1/2} + (A+B)[2(2A+B)^{-1} - 8A]\}^{1/2} \quad (2-11)^{15,23}$$

$$A = \frac{k_{\text{ex}}}{2\pi \delta\nu_o} \quad B = \frac{\Delta\nu_{1/2}}{2 \delta\nu_o} \quad (2-12)^{15}$$

where W^* is the width at half-height of the broad peak in the presence of chemical exchange when the two previously-distinct peaks have merged, and A and B in equation (2-11) are defined in equation (2-12) (all other variables have been previously defined). Through the expansion of the term $(2A+B)^{-1}$ in a series and

neglecting all terms higher than second order in B, equation (2-11) can be solved for k_{ex} and is found to be,

$$k_{\text{ex}} = \frac{\pi \delta \nu_{\circ}^2 (W^* + \Delta \nu_{1/2}) \left[1 + 2 \left(\frac{W^*}{\delta \nu_{\circ}} \right)^2 - \left(\frac{\delta \nu_{\circ}}{W^*} \right)^4 \right]^{1/2}}{2[C][(W^*)^2 + (\Delta \nu_{1/2})^2]} \quad (2-13)^{15}$$

This equation is valid over the entire range of exchange broadening. If the natural line-width can be neglected when compared to the line-width in the presence of chemical exchange ($\Delta \nu_{1/2} \ll W^*$), equation (2-13) can be simplified as shown below and is valid in the “intermediate” exchange region as noted in Figure 2.10,

$$k_{\text{ex}} = \frac{\pi \delta \nu_{\circ}}{2[C]} \left[\left(\frac{\delta \nu_{\circ}}{W^*} \right)^2 - \left(\frac{W^*}{\delta \nu_{\circ}} \right)^2 + 2 \right]^{1/2} \quad (2-14)^{15}$$

Here W^* is more generally defined as being the width of the resonance at the intensity which is half the intensity at the center of the doublet. In the “fast” exchange region, ($W^* / \delta \nu_{\circ} \ll 1$), and equation (2-13) can be further simplified to the following,

$$k_{\text{ex}} = \frac{\pi \delta \nu_{\circ}^2}{2[C](W^* - \Delta \nu_{1/2})} \quad (2-15)^{15}$$

Equations (2-9), (2-10), (2-14), and (2-15) will be used to analyze the kinetic data collected in this thesis.

2.3 The T_2 Spin-Echo Experiment

As mentioned previously, the transverse relaxation time constant for any given non-exchanging resonance peak, T_2 , depends on the dynamics of transverse (x,y-plane) dephasing of that isochromat due to spin-spin relaxation (energy transfer)

processes with the nearby medium.¹⁷ Any operative chemical exchange processes will shorten T_2 in a way which can provide kinetic rate information. In ideally-behaving systems where homogeneous broadening is negligible, measured $\Delta\nu_{1/2}$ values will depend directly on the inverse of $\pi(T_2)$ as expressed by equation (2-6). In such cases, the experimental T_2 of a given peak is rigorously defined upon measuring the spectra line-width, but in practice this turns out not to be a universally-reliable linkage. The spectroscopic line-width can be larger than what would be predicted from the actual T_2 relaxation time due to the combination of both inhomogeneous broadening and homogenous broadening.¹⁷

For this reason, we undertook the challenge to optimize the “gold standard” spin-echo experiment for precise determination of T_2 itself. As we will show this enables measurements of more rigorously valid chemical exchange rates over a broader range (independent of any assumed linkage to line-width). An example of this divergence relative to our system is shown in Table 2.3 below.

Here we have listed the experimental spin-echo T_2 relaxation times, the experimental line-widths, the “calculated” line-widths arrived at from $T_{2\text{ (expt)}}$ using equation (2-6), and the “calculated” T_2 values which would be arrived at from $\Delta\nu_{1/2\text{ (expt)}}$, also employing equation (2-6). This table shows data for (a) the free-ligand 3-trifluoromethylpyridine (tfmp), (b) the pure $[(\text{NH}_3)_5\text{Ru}^{\text{II}}\text{tfmp}]^{2+}$ complex (as the Cl^- salt), and (c) the pure $[(\text{NH}_3)_5\text{Ru}^{\text{III}}\text{tfmp}]^{3+}$ (all in D_2O at concentrations of 5.00 mM). These values clearly illustrate the large error which can arise if line-widths alone are relied upon for estimation of T_2 *via* equation (2-6); clearly, heedless

application of equation (2-6) to experimental $\Delta \nu_{1/2}$ data could lead to vastly incorrect “measured” kinetic constants.

Table 2.3 Experimental T_2 values obtained using the spin-echo technique at 299 K (column 1) and the ideal, calculated $\Delta \nu_{1/2}$ values from equation (2-6) which *would* result (columns two) if equation (2-6) held rigorously. Columns 3 and 4 list the experimental line-widths and the incorrect T_2 (calc) values which would be inferred from them using equation (2-6). The free-ligand 3-trifluoromethylpyridine (tfmp), and the $[(\text{NH}_3)_5\text{Ru}^{\text{II}}\text{tfmp}]^{2+}$ and $[(\text{NH}_3)_5\text{Ru}^{\text{III}}\text{tfmp}]^{3+}$ complexes (as chloride salts) were all present (alone) at 5.00 mM in D_2O .

Compound	T_2 (expt) (sec)	$\Delta \nu_{1/2}$ (calc) (Hz)	$\Delta \nu_{1/2}$ (expt) (Hz)	T_2 (calc) (sec)
tfmp free ligand in D_2O	2.304 ± 0.003	0.14	4.47	0.071
$[(\text{NH}_3)_5\text{Ru}^{\text{II}}\text{tfmp}]^{2+}$ in D_2O	1.375 ± 0.006	0.23	3.87	0.082
$[(\text{NH}_3)_5\text{Ru}^{\text{III}}\text{tfmp}]^{3+}$ in D_2O	0.101 ± 0.003	3.17	6.74	0.047

In the “very slow exchange” rate region shown in Figure 2.10, the line-width based rate equation (2-9) may be transformed into the more rigorously-correct difference between contributing *dephasing times* as follows,

$$k_{\text{ex}} = \frac{\pi [(1/T_2') - (1/T_2)]}{[C]} \quad (2-16)$$

where T_2' is the experimental transverse relaxation time measured in the presence of chemical exchange and T_2 is the transverse relaxation time in its absence (that of either Ru^{II} or Ru^{III} alone in our case). We will use this more basic approach and experimental T_2 values to calculate ET rates in the “slow” exchange region and

thereby circumvent the difficulties in using line-widths to measure the slow rates at low concentrations of reactants (where homogeneous line-broadening effects place a “floor” under $\Delta\nu_{1/2}$ invalidate equations (2-5) and (2-6)).

The CPMG spin-echo pulse sequence allows for homogenous broadening (or spin coherence decay) due to spin-spin relaxation arising from fluctuating microscopic magnetic fields and/or chemical exchange broadening to be distinguished from inhomogeneous broadening arising from variations of the macroscopic magnetic field over the entire sample due to instrumental (shim) imperfections or sample magnetic susceptibility effects.¹⁷ This means that direct measurement of T_2 provides a more general and reliable approach to studying “slow” chemical exchange kinetics than methods relying solely on the line-shape. Importantly, in our work we find that we can extract ET rate constants at much lower reactant concentrations than in the previous NMR work done in this lab, including the 0.10 mM to 0.50 mM reactants concentration range explored the prior stopped-flow work but where the exchange broadening by NMR was too small to be measured.

Figure 2.11 illustrated the CPMG T_2 spin-echo pulse sequence in conventional NMR schematic notation.¹⁷ Here D1 is the relaxation delay between acquisitions which is used to insure that all magnetic vectors are longitudinally relaxed along z (the direction of the permanent magnetic field, B_0) before spin manipulation has begun. The first box represents the first RF-pulse applied to the equilibrated sample, and it is an exact 90° or $(\pi/2)$ pulse which, when properly calibrated (*vide infra*), will push the net magnetization vector precisely into the x,y-plane *via* precession

about x. The second box represents a precisely-timed 180° or π RF-pulse which has the effect of rotating the precessing sample isochromats by 180° about the same axis (typically “x”) as the initial 90° pulse was directed. The spin evolution interval between the two pulses, $\tau/2$, is kept at the same length as the one preceding signal acquisition (FID collection as symbolized by the decaying sine wave) which occurs when the RF receiver coil is gated “on”. Operationally, an “arrayed” experiment is performed by varying values of τ in such a way that τ starts small and becomes large compared to the actual T_2 value of the sample according to an automation routine. A Fourier transform is applied to the data collected at the end of each pulse train, and a stacked plot of these will give rise to a set of spectra peaks whose amplitudes vary with the values of τ with each going through a maximum-intensity “echo” (due to isochromat refocusing) at a certain value of τ , which then decays as τ increases.

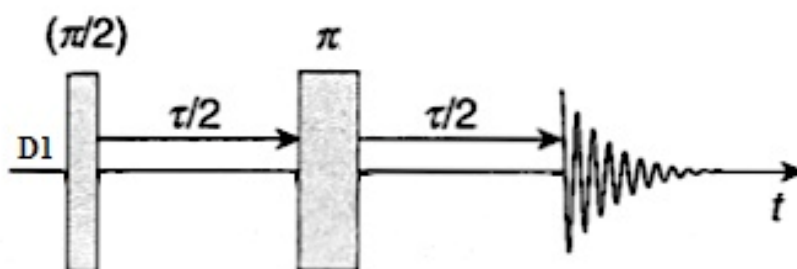


Figure 2.11 The CPMG T_2 spin-echo pulse sequence.¹⁷

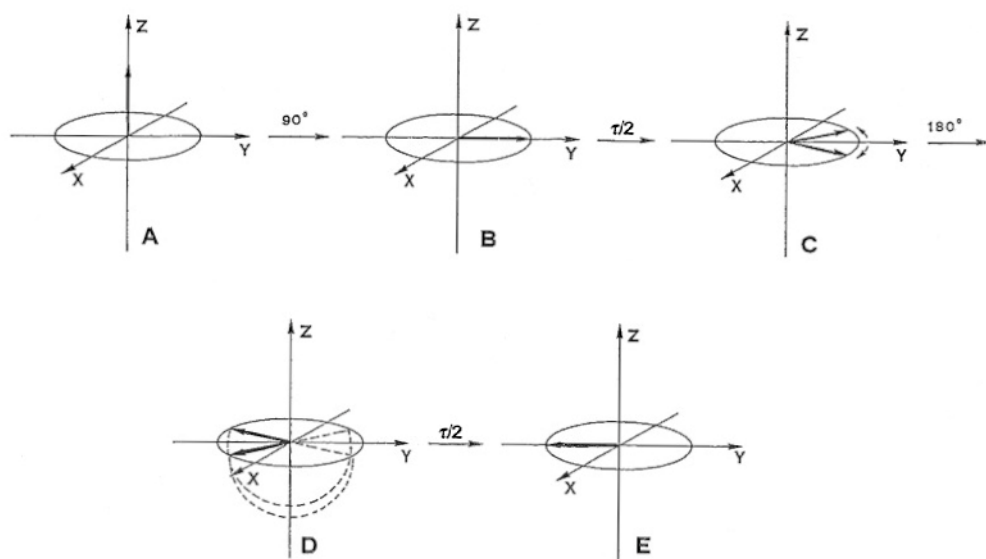


Figure 2.12 The rotating frame depiction the net of magnetization vector and isochromat behaviors during execution of the CPMG T_2 spin-echo pulse sequence shown in Figure 2.11.¹⁰

Figure 2.12 uses the “rotating frame” formalism to illustrate the specific magnetic spin vector manipulations. Step (A) shows the net magnetization vector at equilibrium (in the direction of the permanent magnetic field, B_0). The 90° pulse is then applied to the sample such that the net magnetization vector is rotated into the x,y-plane as shown in step (B). The spin evolution ($\tau/2$) delay then allows the individual magnetic vectors to begin the dephasing process (due to their different precession frequencies), as shown in step (C), where the various isochromats in the sample (denoted here by the spreading arrows) precess either more slowly or quickly than the Larmor frequency (which would lie stationary and exactly along y in the “rotating frame” formalism used here for analyzing the NMR spin dynamics).¹⁰ After

a delay of $(\tau/2)$, the 180° pulse is applied to rotate the spreading isochromats around x. This has the effect of reversing their relative spreading directions in the rotating frame as shown in panel (D) and herein lies the origin of the re-focusing towards the eventual “echo”. A second delay of $(\tau/2)$ is then applied before acquisition starts and if the timing is correct, the isochromats of the net magnetization vector will have now refocused along x in the x,y-plane and aligned (very briefly) in the opposite direction of where they had originally started out as shown in panel (E). During the precisely-gated acquisition period after (E), the “spin-echo” signal will be observed with peak now 180° out of phase with the respect to a “normal” 90° pulse-then-acquire spectrum. As spin-spin relaxation or other stochastic processes (such as chemical exchange) occur, phase coherence will be lost in the x,y-plane and a decay in the spin-echo peak intensities will result. The experimental T_2 value is obtained from analysis of the intensity vs. τ decay curve.

Experimental problems can arise when measuring the T_2 value of a particular resonance peak. Two of the more frequent problems are due to dissolved oxygen effects and an incorrectly calibrated 90° pulse-width, pw90 (*vide infra*). Oxygen present in the solvent can affect the measured T_2 relaxation by providing enhanced spin-spin relaxation (dephasing) resulting from the paramagnetic nature of the oxygen ground state.¹⁰ Paramagnetic molecules present in solution can greatly enhance spin-spin relaxation due to the quadrupole moments of the paramagnetic nuclei coupling with electric field gradients.¹⁷ This is known to produce larger line-widths in some cases and can even give rise to “paramagnetic shifts” in peak positions of open-shell

spin systems due to the very large magnetic moments associated with unpaired electrons. The importance of oxygen effects on T_2 varies depending on the nature of the spin system under investigation, but it is important to check for any such effects in a T_2 investigation since O_2 is present at 5×10^{-4} M in air-saturated D_2O at $25^\circ C$.^{24,25} In our case, multiple control experiments showed no significant effects due to dissolved oxygen on all of our measured T_2 values (details of these determinations will be discussed further on). Incorrectly calibrated pulse-widths can also lead to incorrect T_2 relaxation values since the net magnetization vector is not pushed precisely into the x,y-plane prior to further manipulation and acquisition. The effects of this error source on experimental T_2 decay curves will be discussed in the experimental section.²⁶

In the rest of this chapter we will show how the combined application of both line-width and carefully-optimized direct determinations of T_2 have allowed us to explore electrolyte and super-exchange catalytic effects on ET reaction (2-2) over a 50-fold range of concentration (0.10 mM to 5.00 mM) in our bimolecular reaction. In many cases, our results lead to very precise confirmation of the prior stopped-flow and NMR line-broadening based measurements carried out in this lab, while in other cases, new and interestingly divergent behaviors are encountered. In the case of ET catalysis by muconate in particular, we find that a longstanding mystery has in fact *deepened* upon closer examination.

2.4 Synthesis and Purification of Reactants and Salts

Synthesized (and purchased) compounds used in this work were characterized through NMR and UV-Vis spectroscopic techniques as well as by differential pulse voltammetry. The purities of the ruthenium complexes were verified through UV-Visible and DPV analysis as well as reference to known λ_{\max} , ϵ_{\max} , $E_{1/2}$ values. Purification procedures were repeated as necessary in order to obtain the highest purity.

2.4.1 Preparation of ruthenium(III)chloropentaaminedichloride,



Ruthenium(III)chloropentaaminedichloride, $[(\text{NH}_3)_5\text{Ru}^{\text{III}}\text{Cl}]\text{Cl}_2$, was synthesized from commercial rutheniumtrichloride hydrate, $\text{RuCl}_3 \cdot \text{H}_2\text{O}$ (Sigma Aldrich, CAS 14898-67-0), using a modification from the literature.²⁷ In a typical preparation, 5.00 g of $\text{RuCl}_3 \cdot \text{H}_2\text{O}$ were added to a 500 mL or 1000 mL round bottom flask containing 62.5 mL of commercial grade distilled water and was allowed to dissolve. The reactant solution was placed in an ice bath and then 62.5 mL of hydrazine monohydrate (Alfa Aesar, CAS 7803-57-8) were added dropwise with stirring to the solution (which was chilled by suspension in an ice bath before and during the addition). The resulting dark purple mixture was then allowed to stir at room temperature for at least 4 hours, but no longer than 24 hours. The final mixture was a dark red-purple color after reaction. The reaction flask was again placed in an ice bath and 125 mL of 12 M HCl were slowly added dropwise with stirring to the solution. The solution was then heated at reflux for 2 hours. The resulting yellow

product was isolated *via* filtration and washed with 20 mL of 0.1 M HCl, followed by 20 mL of reagent grade acetone (Pharmco-Aaper, CAS 67-64-1). The resulting product was dried in a vacuum (typical yields were 70%).

2.4.2 Recrystallization of ruthenium(III)chloropentaaminedichloride,



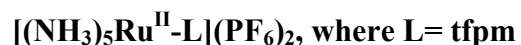
In order to ensure best results in subsequent synthesis, the crude product from above was added to about 125 mL of 0.1 M HCl and heated to about 70°C, or until all of the compound went into the solution. The solution was then cooled slowly to room temperature, placed in an ice-bath, and cooled to 0°C. The purified yellow crystalline product was isolated by filtration, washed with reagent grade acetone and allowed to dry by air suction for at least 30 minutes (typical yields were 85%).

2.4.3 Preparation of Zn/Hg amalgam

About 1.00 g of 20 mesh Zinc granules, Zn (Sigma Aldrich, CAS 7440-66-6), were added to a 25 mL round bottom flask. The Zn granules were briefly washed with about 5 mL of 1 M HCl to remove the oxide on the zinc surface. Hydrogen bubbles initially formed on the surface of the metal, but then dispersed when about 3 mg of mercuric chloride, HgCl₂ (EM Science, CAS 7487-94-7), were added to the solution with swirling agitation. Within about 30 seconds the bubbles were gone, and the Zn granules became noticeably shiny and clumped together indicating the presence of a thin layer of metallic mercury having been reduced onto the zinc particles. The resulting Zn/Hg amalgam was then washed three times with three small portions of

distilled water and henceforth carefully protected from exposure to air. The flask was then filled with 5 mL of distilled water and a small stir bar was added. Two pasteur pipets of trifluoroacetic acid vapor (Sigma-Aldrich, CAS 76-05-01) were then puffed into the flask to slightly acidify the solution. The flask was immediately sealed with parafilm and allowed to stir for a minimum of 2 minutes. The amalgam must be used for subsequent synthesis within a few minutes of preparation, and after use it must be removed from frits and flasks immediately so as to avoid the formation of problematic zinc oxide, ZnO, deposits (as these require soaking in acid in order to remove later).

2.4.4 Preparation of ruthenium(II)L-pentaamminehexafluorophosphate,



About 0.1 g of $[(\text{NH}_3)_5\text{Ru}^{\text{III}}\text{Cl}]\text{Cl}_2$ were added to a 25 mL round bottom flask containing fresh Zn/Hg amalgam (*vide supra*). 1.5 molar equivalents of the pyridyl ligand (tfmp: Aldrich, CAS 3796-23-4) were added to the flask, which was then sealed with parafilm and covered with foil to block ambient light. The solution was rapidly stirred at room temperature for 25 minutes (so as to tumble the Zn/Hg and poorly soluble Ru^{III} suspension) and was then filtered, using a coarse filter (to remove the amalgam) into a flask containing 3 molar equivalents of ammoniumhexafluorophosphate, NH_4PF_6 (Aldrich, CAS 16941-11-0). The filtrate mixture was then swirled, sealed, and placed into a -20°C freezer for at least 15 minutes and no longer than 30 minutes. The resulting suspension of crude $[(\text{NH}_3)_5\text{Ru}^{\text{II}}\text{L}](\text{PF}_6)_2$ product was then allowed to thaw if necessary and the yellow-

orange crystalline product was isolated by filtration. The product was allowed to drain under air suction for 20 minutes and was then dried in a vacuum desiccator (typical yields were 80%).

2.4.5 Acetone/Ether purification pentaammineruthenium(II)-L-hexafluorophosphate, $[(\text{NH}_3)_5\text{Ru}^{\text{II}}\text{-L}](\text{PF}_6)_2$ where L = tfpm

The crude pentaammineruthenium(II)L-hexafluorophosphate, $[(\text{NH}_3)_5\text{Ru}^{\text{II}}\text{-L}](\text{PF}_6)_2$, was dissolved in a minimal amount of reagent grade acetone (~3-7 mL) and was filtered using a fine frit to remove any undissolved solid. A three to five fold volume excess of diethylether was then slowly added to the filtrate in order to precipitate > 95% of the Ru^{II} product (the filtrate should be just barely colored a faint yellow for optimum results). The product was then isolated *via* filtration and dried in a vacuum desiccator (typical yields were about 90%).

2.4.6 Preparation of pentaammineruthenium(II)-L-chloride, $[(\text{NH}_3)_5\text{Ru}^{\text{II}}\text{-L}]\text{Cl}_2$ where L = tfmp

About 30 mg of the purified $[(\text{NH}_3)_5\text{Ru}^{\text{II}}\text{-L}](\text{PF}_6)_2$ (*vide supra*) were dissolved in a minimal amount of reagent grade acetone (~3-7 mL) and filtered using a fine frit to remove any undissolved solid. About 20 mL of reagent grade acetone were then added to the deep red (L = tfmp) colored filtrate. About 1 mL of HPLC grade methanol (Pharmco-Aaper, CAS 67-56-1) was mixed with about 1 mL of 1:8 saturated TEACl, tetra-ethyl-ammonium chloride, in rigorously dry 70:30 acetone/methanol. The TEACl/methanol mixture was then added dropwise (~25

drops) to precipitate the product out of solution. The red-orange colored crystalline product was obtained *via* vacuum filtration. The mother liquor should be slightly colored indicating no excess amount of TEACl was added (as removal of TEACl contamination of the product is very difficult). The precipitate was then washed twice with 5 mL of reagent grade acetone and was allowed to dry by air suction for at least 25 minutes (typical yields were about 80%). These chloride salts of the $(\text{NH}_3)_5\text{Ru}^{\text{II}}\text{-L}^{2+}$ are only stable for about 24 hours, and therefore should not be prepared in unnecessarily large amounts.

2.4.7 Preparation of pentaammineruthenium(III)-L-chloride, $[(\text{NH}_3)_5\text{Ru}^{\text{III}}\text{-L}]\text{Cl}_3$, where L = tfmp

About 30 mg of $[(\text{NH}_3)_5\text{Ru}^{\text{II}}\text{L}]\text{PF}_6$ (*vide supra*) were dissolved in a minimal amount of reagent grade acetone (~3-7 mL) and filtered using a fine frit to remove any undissolved solid. About 2-3 mL of commercial grade D.I. water were added to the filtrate. Then, 9 drops (~0.3 mL) of 1 M HCl were added to the solution in order to slightly acidify the reactant solution and provide the necessary additional Cl^- ions. After mixing, 8 drops (~0.4 mL) of 30% hydrogen peroxide, H_2O_2 , (EMD Chemicals, CAS 7722-84-1) were added to the reactant solution. The ruthenium(II) was considered to be completely oxidized when the color of the solution turned from red-orange to a persistent pale yellow. A fifteen-fold excess of reagent grade acetone was then added slowly to the solution. The yellow crystalline product was isolated by vacuum filtration, washed twice with 5 mL of reagent grade acetone, and was allowed to dry by air suction for at least 25 minutes (typical yields were around 80%). These

Ru^{III} products can be stable for more 24 hours but since they were generally used in a paired manner with the less-stable Ru^{II} chlorides, we in all cases prepared the Ru^{II} and Ru^{III} reactants in tandem.

2.4.8 Preparation of disodium dicarboxylate salts, $\text{Na}_2\text{-X}$, where X = muc, tere, 1,4-dcch, adip

1.00 g of the acid equivalent of the sodium dicarboxylate salt product sought, for example muconic acid, $\text{H}_2(\text{muc})$, was added to a 250 mL erlenmeyer flask containing 100 mL of D.I. water and a stir bar. A 1 M NaOH solution was then used to titrate the sodium dicarboxylate acid solution until a pH of 6.5 was reached using two-point a calibrated glass electrode pH meter (Beakman, Electrode Part # 511060, Lot #50088) to monitor the pH of the solution. During this titration process, the sparingly-soluble solid dicarboxylate acid dissolved as the pH approached 6.5. The solution was left to stir until the pH was maintained at 6.5. The resulting solution was then filtered using a fine frit, and 4 volumes of reagent grade acetone were added to the filtrate in order to precipitate out the sodium dicarboxylate salt. The precipitate was then isolated using a fine frit and dried in a vacuum desiccator (typical yields were about 90%). No further purification was needed for these salts.

2.4.9 Preparation of potassium ruthenocyanide, $\text{K}_4\text{Ru}^{\text{II}}(\text{CN})_6$

Potassium ruthenocyanide, $\text{K}_4\text{Ru}^{\text{II}}(\text{CN})_6$, was synthesized using the method according to Howe.²⁸ In a typical preparation, 2.00 g of ruthenium chloride, $\text{RuCl}_3 \cdot \text{H}_2\text{O}$, were added to a 125 mL erlynmeyer flask containing 50 mL of saturated

aqueous potassium cyanide, KCN (J.T. Baker, CAS 151-50-8, Lot # 41395), and allowed to dissolve. This solution was then heated at reflux for 24 hours. The reactant solution was then allowed to cool to 0°C overnight which resulted in a white crystalline precipitate. The crude crystalline product was then isolated by filtration, washed with several 5 mL portions of HPLC grade methanol, and dried in a vacuum desiccator (typical yields were 70%). Commercial $\text{K}_4\text{Ru}^{\text{II}}(\text{CN})_6$ (Aldrich, CAS 339268-21-2, Lot # MKBL1258V) was purchased as well to compare results with the “in-house” $\text{K}_4\text{Ru}^{\text{II}}(\text{CN})_6$.

2.4.10 Preparation of potassium osminocyanide, $\text{K}_4\text{Os}^{\text{II}}(\text{CN})_6$

Potassium osminocyanide, $\text{K}_4\text{Os}^{\text{II}}(\text{CN})_6$, was synthesized analogously to $\text{K}_4\text{Ru}^{\text{II}}(\text{CN})_6$, only using ammoniumhexachloroosmate, $(\text{NH}_4)_2\text{OsCl}_6$ (Engelhard Industries, CAS 12125-08-5, Lot # Os-70), as the starting material instead of ruthenium chloride.

2.4.11 Recrystallization of potassium ferrocyanide, $\text{K}_4\text{Fe}^{\text{II}}(\text{CN})_6$

In a typical recrystallization, about 1 g of potassium ferrocyanide, $\text{K}_4\text{Fe}^{\text{II}}(\text{CN})_6$ (Sigma-Aldrich, CAS 14459-95-1, Lot # SLBC1213V), was added to a 125 mL erlenmeyer flask. About 50 mL of distilled water were slowly added to the flask slowly so as to partially dissolve the $\text{K}_4\text{Fe}^{\text{II}}(\text{CN})_6$ complex. The solution was then slowly heated to about 45°C or until all of the $\text{K}_4\text{Fe}^{\text{II}}(\text{CN})_6$ complex went into solution. More $\text{K}_4\text{Fe}^{\text{II}}(\text{CN})_6$ complex was added to the heated solution until a saturated solution was obtained. The heated solution was then filtered using a fine frit

and cooled slowly to 0°C overnight. The microcrystalline precipitate was isolated via filtration, washed with HPLC grade methanol and dried in a vacuum desiccator.

2.4.12 Recrystallization of potassium hexacyano complexes, $K_4M(CN)_6$, where



About 0.2 g of the potassium hexacyano complex were added to a 125 mL erlynmeyer flask. About 15 mL of D.I. H_2O were added to the flask so as to dissolve the $K_4M(CN)_6$ complex (room temperature throughout). The resulting solution was then filtered to remove any undissolved solid. HPLC grade methanol was then added dropwise (~20 mL) so as to precipitate out the product. The white microcrystalline precipitate was isolated *via* filtration, washed with HPLC grade methanol and dried in a vacuum desiccator.

Table 2.4 Spectroscopic and electroanalytical characterization data for the complexes used.

Compound	λ_{max} (nm) in Acetone	ϵ_{max}	$E_{1/2}$	Solvent for $E_{1/2}$ measurement
$[A_5Ru^{II}tfmp](PF_6)_2$	450	9000	0.035 ^(a)	Acetone
$[A_5Ru^{II}tfmp]Cl_2$	436	8235	0.143 ^(b)	Water
$Fe(CN)_6$	-	-	0.2 ^(b)	Water
$Os(CN)_6$	213	47000	0.4 ^(b)	Water
$Ru(CN)_6$	-	-	0.7 ^(b)	Water

(a) The $E_{1/2}$ value was measured against an Ag/AgCl reference electrode and the fc/fc^+ couple was measured against the same Ag/AgCl reference during that same experimental session. (b) The $E_{1/2}$ value were measured against SCE in 0.1 M KCl.

2.5 Solution Preparation

Solutions for all NMR and UV-Vis spectroscopic work were prepared using the appropriate micropipette (calibrated by mass) and/or volumetric glassware (all solutions with concentrations $< 0.10 \text{ mM}$ were prepared in plastic glassware⁶). All quantities weighed were within the analytical specifications of the balance, which in our case required that quantities be no smaller than 3.5 mg in order to achieve ~5% precision.

2.5.1 Solution preparation of reactant solutions for NMR ET self-exchange measurements

For solutions with concentrations of reactants of 5.00 mM and above, reactants were weighed out directly in amounts which would correspond to the desired concentration of reactants in a 2.00 mL solution of D_2O . For solutions with concentrations of reactants between 1.00 mM and 5.00 mM , the reactants were weighed out in amounts which would correspond to the desired concentration of reactants in a 10.00 mL solution of D_2O . For solutions with concentrations of reactants between 0.50 mM and 1.00 mM , the reactants were weighed out in amounts which would correspond to the desired concentration of reactants in a 25.00 mL solution of D_2O . For all solutions with concentrations of reactants below 0.50 mM , a 25.00 mL stock with a concentration of reactants of 0.50 mM was first prepared. From this stock solution, a 2.00 mL solution of the desired concentration was prepared using appropriate dilution and analytical techniques (using plastic volumetric flasks and graduated cylinders).

2.5.2 Solution preparation for added-salt NMR kinetic measurements

The following method was used for all simple salts and dicarboxylate salts. Before preparation of the salt solutions; the concentrations, total ionic strength, overall GP, and volumes of the salt solution aliquots to be added to the reactant solution were first calculated such that the total volume of the salt solution added would be less than 8% of the total volume of the reactant solution and thus introduce negligible dilution error. We also note that no delivered volume of an added salt solution was ever smaller than 0.8 μL . Once the calculations of the volumes of the stock salt solution to be added to a given reactant solution were complete (so as to arrive at the desired total μ and GP), the amount of salt needed to make the desired concentration of the salt stock solution in 2.00 mL of D_2O was calculated and prepared using the appropriate analytical techniques as outlined above.

For the highly-catalytic hexacyano salts ($\text{K}_4\text{Fe}^{\text{II}}(\text{CN})_6$, $\text{K}_4\text{Os}^{\text{II}}(\text{CN})_6$, and $\text{K}_4\text{Ru}^{\text{II}}(\text{CN})_6$) a similar procedure was performed as in the simple and dicarboxylate salt cases, but with minor alterations due to the need for achieving exceptionally close control of the very low concentrations of $\text{M}(\text{CN})_6^{4-}$ required in these cases. To achieve controllable $\text{M}(\text{CN})_6^{4-}$ stock solution concentrations down in the range of 10^{-5} M salt in 2.00 mL, a 3.00 mM $\text{M}(\text{CN})_6^{4-}$ stock solution was first prepared and then diluted accordingly in order to achieve the desired final concentration using the appropriate size micropipette with plastic tip.

2.6 NMR Instrument Set-Up and Experiment Execution

All NMR measurements were made using a Varian 500 MHz NMR spectrometer (Part # MR0904W025, VNMRs, vnmrj 3.2). Before loading/acquiring any NMR data, the instrument must first be setup specifically for the nuclei of interest according to procedures outline in the USF vnmrj 4.2 user manual.²⁹ The nucleus of interest in the majority of the work to be reported here was the spin- $\frac{1}{2}$ ^{19}F nucleus of the CF_3 substituent on the 3-trifluoromethylpyrindine ligand (see Figure 2.2). Therefore, it was necessary to first set up the instrument for general 1-D ^{19}F NMR experiments before any pulse calibration, relaxation, kinetic, or temperature dependent experiments could be performed. We will include here a brief mention of some aspects of general set up, but will focus primarily on those aspects particularly important to ^{19}F NMR work.

The sample was inserted into the NMR and a “field frequency lock” was established on D_2O . The probe was tuned and matched to the ^{19}F nucleus according to the steps outlined in the USF vnmrj 4.2 user manual.²⁹ Due to the precise nature of the kinetic relaxation and temperature-dependent rate experiments of our work, we found it was necessary that the probe be tuned and matched using the “fine” criterion.

2.6.1 Setting up the ^{19}F NMR experiment

In order to set up and execute a 1-D ^{19}F NMR experiment, first the ^{19}F experiment was selected in the “Protocol” window, located on the left side of the screen. The “Liquids” tab was then opened, the “Std 1-D” button was selected, and “FLOURINE” was chosen. This action called up all necessary experimental

parameters for ^{19}F acquisition. Then the “Acquire” tab was opened (located at the top left in the parameter panel window). One may go at this point through and adjust any parameter desired, such as the relaxation delay (D1) which is the delay time before any pulse is applied and is typically set equal to $5 \times T_1$ (*vide infra*), the pulse width at 90° (pw90, *vide infra*), the number of scans (ns) which is the number of repetitions of the pulse sequence which will take place before the FID is Fourier transformed, and the block size (BS) which is how many scans must be taken before an updated FID is saved to the acquisition window. These are just a few of the parameters which may be adjusted in this window. The parameters were typically assigned as follows for our reactant solutions in D_2O ; D1 was set equal to 10 sec, the initial pw90 was 9.7 μsec at a power of 57 dB, and for simple 1-D spectra, the number of scans, ns, was typically set to 64 (except for dilute solutions) and the block size was 4.

2.6.2 NMR pulse calibration

Before any kinetic data can be obtained *via* the 1-D ^{19}F NMR line-broadening method or the ^{19}F spin-echo T_2 relaxation method (see section 2.7), careful calibration of the 90° pulse length, pw90, is required. The pw90 is defined as the duration, in microseconds, that an RF-signal of a given power level must irradiate a sample in order to tilt the net magnetization vector precisely into the x,y-plane, which is by definition 90° away from the z axis of the NMR’s magnetic field. This pulse is also often referred to as the $\pi/2$ pulse. Precise calibration of the pw90 ensures that the manipulations of the net magnetization of the ^{19}F spin system will be executed as intended in the pulse program and that the state of the spin system after evolution

delays will be well-defined. In addition to making the spin-echo (or any other) pulse sequence function properly, accurate pw90's are key to obtaining the optimum signal to noise ratio (S/N) in the final data collected. This is because of the cumulative coherence loss which accrues effect when multiple pulses are applied to the sample, such as 45°, 90°, and 180°, during the pulse program.

Each nucleus within a given compound has a distinct chemical environment, and in theory, each will have a unique 90° pulse width. However, since the chemical shift dispersions between different peaks in a sample are typically on the order of less than 1000 ppm, pw90 variations will be on the same order (0.1% or ~10 nsec) and thus fall below the level of settable precision on our instrument (0.1 µsec). The simplest pulse sequence of “irradiate-observe” on a one-peak spectrum will display maximum signal intensity when the pulse duration corresponds exactly to a 90° pulse, as seen in Figure 2.13. However, the difficulties in precisely measuring the maximum signal intensity by comparing similarly intense peaks, as would be obtained at 89° or 91° pulse width, results in it being more accurate to observe and calibrate the 180° pulse, or better still the 360° pulse. The 360° pulse measurement is therefore the most commonly-used method for calibrating the 90° pulse. If the 360° pw90 calibration curve is not a smooth and symmetrical sine curve (peak intensity vs. irradiation pulse length in µsec) like the one in Figure 2.13, then the four key things which must be adjusted are the initial guess for pw90 (or pw[1] in Varian notation), the pre-pulse (relaxation) delay time (D1), the probe tuning and matching, and the magnetic field homogeneity (shims).^{26,30}

Multiple determinations of pw90 (as $\text{pw360} / 4$) for ^{19}F using our tfmp complexes in D_2O consistently gave 9.7 μsec at a power level of 57 dB. This value was found to be adequate for all experiments involving reaction (2-2). Over an operating period of 26 months or so, we found no significant change in this pw90 for ^{19}F . By way of comparison, the standard pw90 for ^1H at a power level of 57 dB was found to be 7.5 μsec .

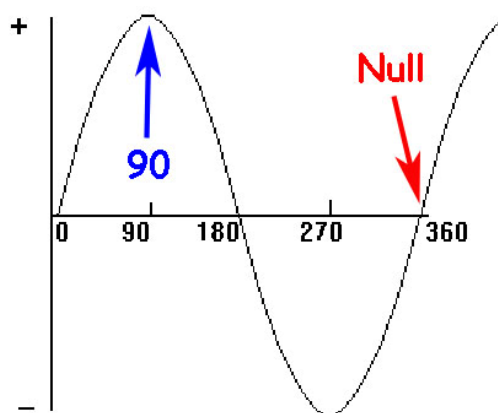


Figure 2.13 An illustration of a pw90 determination *via* peak intensity *vs.* angular rotation plot out past pw360. Note the maximum peak intensity at 90° , and the nulls at 180° , and 360° .³⁰

In practice, a quality 1-D ^{19}F NMR spectrum is obtained, the cursors are used to zoom in on the peak of interest, and this portion of the spectrum is carefully phased according to the USF vnmrj 4.2 user manual.²⁹ It is recommended that peaks used for pw90 calibrations be from a well-resolved singlet resonance of the sample. In order to initiate the Varian pw90 calibration utility, the following input was typed into the command line (with “enter” being pressed after each command):

- **nt=1** (stands for number transients = 1)
- **gain='y'** (stands for receiver gain = value in stored experiment)
- **ai vp=50** (stands for absolute intensity mode and spectrum vertical position = 50)
- **pw90?** (stands for the current pulse width at 90°)

Next, an array of values for the pulse width is created which brackets the expected 360° pulse width of 4 x pw90. In the case of our ET reaction (see Figure 2.2), the 360° pulse width was known to be around 39 µsec. To define the appropriate array for a “coarse” pw90 calibration, a large range of pw values were chosen by inputting:

- **array('pw',45,0,1)** (stands for array pw with 45 increments starting at 0µsec with a step size of 1µsec)

Next, the guessed pw90 was defined and the calibration was initiated by entering the following in the command line:

- **pw[1]=9.7** (stands for the first pw which is the current value of pw90 given when pw90? was typed in)
- **au** (stands for auto gain and go which will start the experiment)

Once the calibration had completed, in order to process, autophase, and stack the spectra the following must be typed into the command line:

- **wft(1)**
- **aph**
- **vsadj**
- **wft dssh**

At completion of the array of the pw values, a plot like the one in Figure 2.14 is displayed. Each intensity value in the plot corresponds to a different irradiation time. The first null represents the 180° pulse width and the second null represents the 360° pulse width. The time at where the 360° null is was divided by 4 and this number was then accepted as the coarse pw90 value specific to the sample being measured.

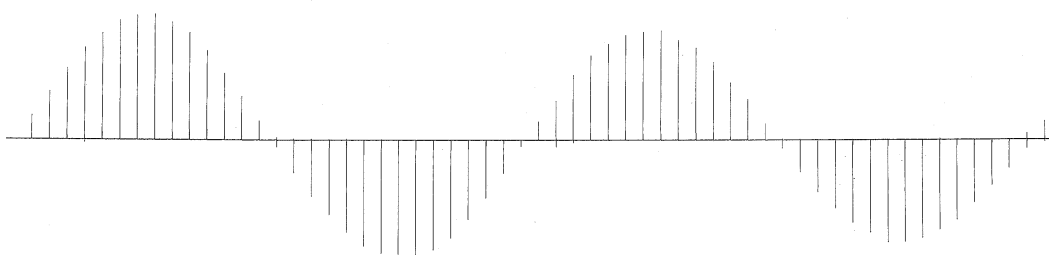


Figure 2.14 A coarse pw90 calibration curve for the complex $[(\text{NH}_3)_5\text{Ru}^{\text{II}}\text{tfmp}]\text{Cl}_2$ in D_2O at a concentration of 5.00 mM using the ^{19}F nucleus.

After a crude calibration of pw90 was completed, a more accurate value of pw90 is obtained. The same sequence of commands was used, only now the array of pulse widths used to acquire the first, crude calibration of the pw90 was adjusted to zoom in precisely on the region of the 360° null. This was achieved by adjusting the array to have smaller time increments between the different trial pulse widths and by re-defining the pw90 as the value obtained from the prior crude calibration as shown below:

- **array('pw',30,37,0.1)** (stands for array pw with 30 increments starting at 37 μsec with a step size of 0.1 μsec)

- **pw[1]=enter value obtained from first, crude calibration**

The new, more accurate value of pw90 obtained from the second calibration was used for all experiments involving that particular sample with the observable nucleus being ^{19}F of tfmp. In our experience (demonstrated stability of pw90 for greater than 28 months), there is no need for frequent recalibration when one is investigating similar systems in the same solvent. If, however, a T_2 spin-echo experiment were to be run on a significantly different molecular species or in a different solvent, or on a different nucleus, then checking of a pw90 would be strongly recommended.

2.6.3 Setting up the ^{19}F spin-lattice (longitudinal) relaxation, T_1 , experiment

The spin-lattice or “longitudinal” relaxation time, T_1 , is the characteristic first-order relaxation time constant for the spin system (and hence net magnetization vector) to re-establish its Boltzmann equilibrium distribution with the external magnetic field, B_0 (along z), after spin manipulations have taken it to some non-equilibrium state (*vide supra*).¹⁰ It is crucial to know this value prior to running the majority of pulse sequenced experiments since a relaxation delay on the order of $5 \times T_1$ is required in order to have a well-defined system prior to sequence initiation (for optimally valid results to be obtained). In order to set up and acquire a ^{19}F T_1 determination experiment, a 1-D ^{19}F NMR spectrum and the pw90 for the sample of interest must first be obtained as described above. To load the T_1 inversion-recovery experiment, the “Liquids” tab was opened in the “Protocol” window, then the “Std 1-D” button was chosen and “T1_MEASURE” was selected. The standard parameter set is commonly setup to acquire using the default ^1H nucleus parameters, therefore

these values must be changed in order to measure T_1 using ^{19}F (or any other nucleus) as the observe nucleus. The parameters which will be listed here apply to most of the samples used in this work, but some parameters apply specifically only to the $[(\text{NH}_3)_5\text{Ru}^{\text{II}}\text{tfmp}]\text{Cl}_2$ complex in D_2O at a concentration of 5.00 mM. These include the relaxation delay, the pw90, the first pulse, the observe pulse, and all parameters associated with the array of delays between pulses.

The observe nucleus is set to be the ^{19}F nucleus by opening the “Channels” sub-tab located on the left side of the parameter panel window under the “Acquire” tab. The following values are then entered in manually as shown in Figure 2.15: nucleus = F19, offset = 12349.5 Hz, and pw90 = 9.70 μsec at a power of 57 dB.

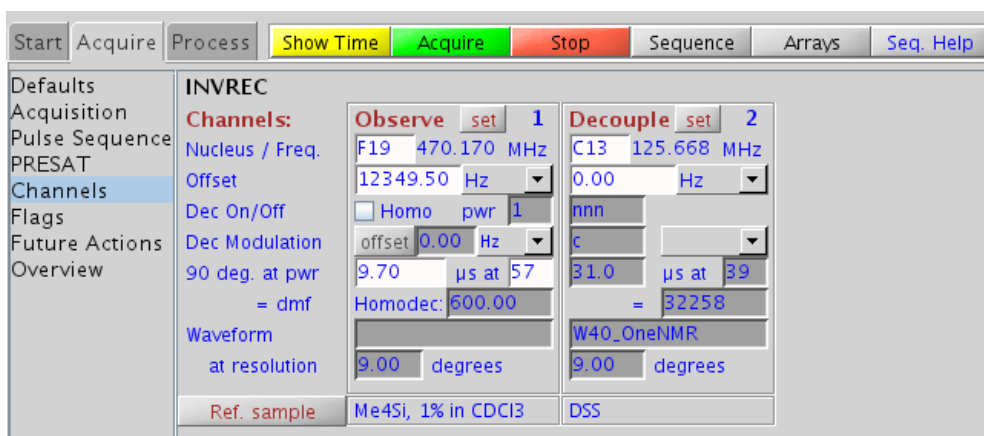


Figure 2.15 The setup of the “Channels” sub-tab under the “Acquire” tab in the parameter panel window showing the correct parameters for the ^{19}F T_1 inversion-recovery determination.

The general T_1 inversion-recovery sequence parameters to be adjusted next are located under the “Acquisition” sub-tab on the left side of the parameter panel

window under the “Acquire” tab. The following values were entered in manually as shown in Figure 2.16: spectral width = 18939.4 Hz (which is equivalent to a spectral width of -80.2 ppm to -39.9 ppm), acquisition time = 1.730 sec, complex points = 32768, number of scans = 4, number of steady state scans = 0, block size = 4, relaxation delay (which should be at least $5 \times T_1$) = 20 sec, first pulse (which is equivalent to a precise 180° pulse) = 19.4 μ sec, observe pulse (which is equivalent to a precise 90° pulse) = 9.7 μ sec, and the receiver gain = 40.

The screenshot shows the 'Acquire' sub-tab of a parameter panel window. The window has a top menu bar with buttons: Start, Acquire, Process, Show Time, Acquire, Stop, Sequence, Arrays, and Seq. Help. On the left is a sidebar with tabs: Defaults, Acquisition (selected), Pulse Sequence, PRESAT, Channels, Flags, Future Actions, and Overview. The main area is titled 'INVREC' and contains several sections:

- Data:** Spectral width (18939.4 Hz), Acquisition time (1.730 s), Complex points (32768).
- Scans:** Requested (4), Completed (0), ☐ Steady State (0), ☒ Block Size (4), ☐ Interleave.
- Excitation:** Relaxation delay (20.000 s), First pulse (19.40 μ s) or 180 degrees, Inter-pulse delay (array s), Observe Pulse (9.70 μ s) or 90 degrees, Calibration: pw90 9.70 μ s at Power 57 dB.
- Receiver:** Receiver Gain (40) ☐ Auto, Timing (μ s): rof2 25.03, alfa 10.0, ddrtc 41.2.

Figure 2.16 The setup of the “Acquisition” sub-tab under the “Acquire” tab in the parameter panel window displaying the correct parameters for the ^{19}F T_1 inversion-recovery specific to the $[(\text{NH}_3)_5\text{Ru}^{\text{II}}\text{tfmp}]\text{Cl}_2$ complex in D_2O at a concentration of 5.00 mM.

After establishing these programmed instructions, the “Defaults” sub-tab was then opened (located on the left side of the parameter panel window under the “Acquire” tab), and the spectral width was set to -80.2 ppm to -39.9 ppm. The array of delays between pulses was then setup by selecting the “Arrays” button at the top of

the parameter panel window. The array pop-up window (as shown in Figure 2.17) was then set up with the array size set equal to 12 starting at 0.06 seconds and ending at 15 seconds (with an exponential evolution delay incrementation applied).

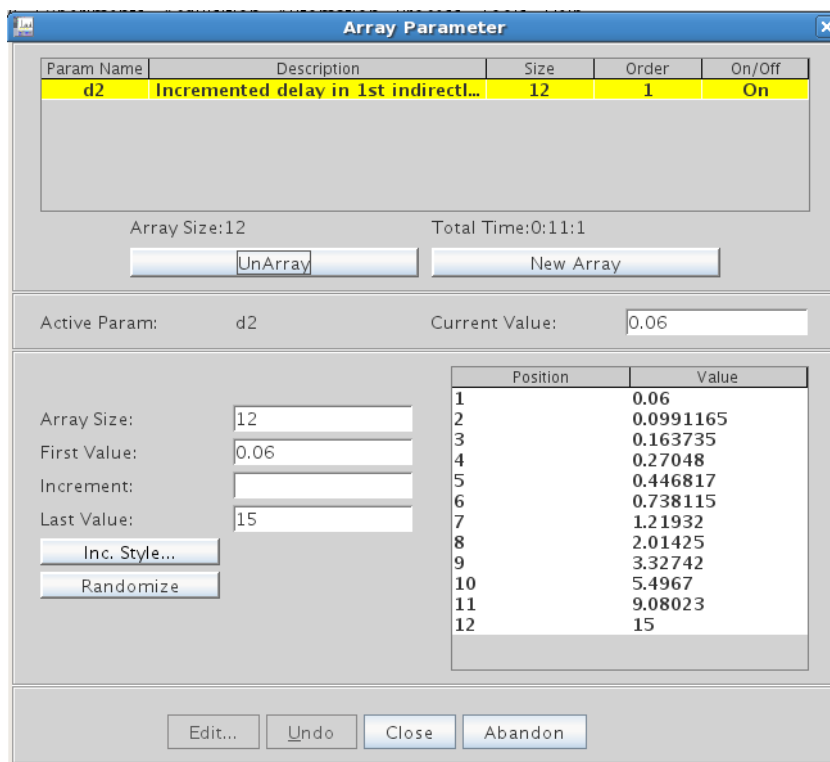


Figure 2.17 The setup of the “Array Parameter” window corresponding to the ^{19}F T_1 inversion-recovery experiment on the $[(\text{NH}_3)_5\text{Ru}^{\text{II}}\text{tfmp}]\text{Cl}_2$ complex in D_2O at a concentration of 5.00 mM.

Once all of the parameters for a given experiment have been entered, it is important to verify the programming by checking the pulse sequence as a visual display (since it will indicate currently set parameter values). This is done by selecting the grey box labeled as “Sequence”. The T_1 inversion-recovery pulse

sequence established according to the input in Figures 2.15 to 2.17 appears on the screen as shown in Figure 2.18, with key pulse widths and delay times placed appropriately.

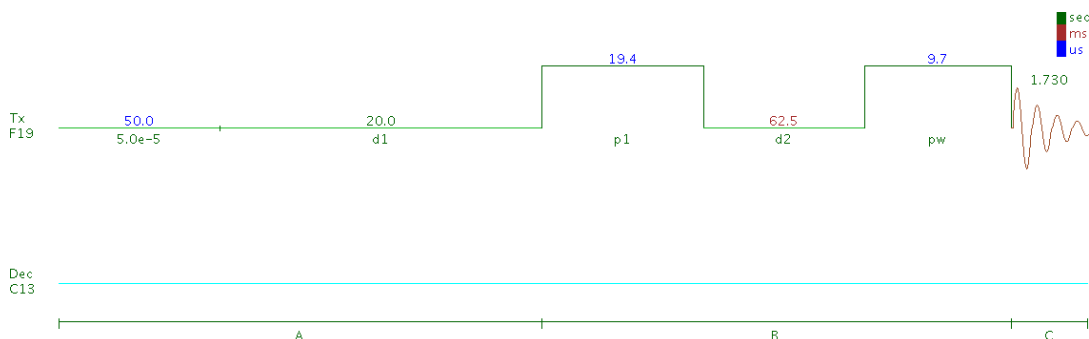


Figure 2.18 The ^{19}F T_1 inversion-recovery pulse sequence displaying parameters associated with the $[(\text{NH}_3)_5\text{Ru}^{\text{II}}\text{tfmp}]\text{Cl}_2$ complex in D_2O at a concentration of 5.00 mM.

After checking the pulse sequence for correctness, the ^{19}F T_1 inversion-recovery experimental acquisition was started by selecting the green “Acquire” button at the top of the parameter panel window. Once the experiment had completed, the spectral intensity vs. evolution time data were then analyzed under the “Process” tab by selecting the green box labeled “Auto Process”.

To improve the sensitivity of the T_1 sequence (and therefore the S/N), it is very common to apply “weighting functions” in the form of a small amount of line-broadening (exponential multiplication of the FID) to the spectrum in order to extract a more accurate value for T_1 from a “noisy” experiment. The amount of line-broadening applied to the sample should be no larger than the experimental line-width

of the peak under investigation, and this type of weighting function is known as a matched filter.^{31,32} If the applied line-broadening is larger than the actual line-width of the peak, then the sensitivity of the experiment actually degrades and the T_1 analysis leads to invalid relaxation data (T_1 values which are “shorter” than the real decay times and which would correspond to larger than true, natural line-widths). The optimum amount of matched-filter line-broadening to be applied to different samples will vary and must be chosen according to a 1-D spectrum obtained using little or no line-broadening in processing. To apply the matched-filter line-broadening to the T_1 data, the “Basic” sub-tab is opened (which is located on the left side of the parameter panel window under the “Process” tab), and then the box next to “linebroaden” was checked and the amount of line-broadening desired was entered in units of Hz (corresponding to the peak of interest). Optimum values in our experiments typically usually ranged between 1 Hz and 5 Hz.

The best-fit T_1 relaxation values corresponding to each peak (Ru^{II} or Ru^{III}) in the spectrum from the ^{19}F nuclei of the tfmp ligand were obtained by opening the “T1 Analysis” sub-tab located on the left side of the parameter panel window under the “Process” tab. Then the grey box labeled “Display Last Spectrum” was selected. At this point the final spectrum was phased and adjusted as necessary for good display. Then the grey button labeled “Do T1 Analysis” was selected, which causes the fitted T_1 values for all peaks visible in the spectrum to be listed. To illustrate all of the T_1 curves which were analyzed, the button labeled “Display All Fits” was selected. All T_1 values and the errors associated with these values were displayed on the right side

of the parameter panel window. If only one particular curve was sought to be displayed instead of all of the T_1 curves, the number of the desired peak was entered in the “Display Selected Fits” box and “enter” was pressed. An example ^{19}F T_1 inversion-recovery decay curve corresponding to the $[(\text{NH}_3)_5\text{Ru}^{\text{II}}\text{tfmp}]\text{Cl}_2$ complex in D_2O at 5.00 mM (using the parameters as stated here) is shown in Figure 2.19.

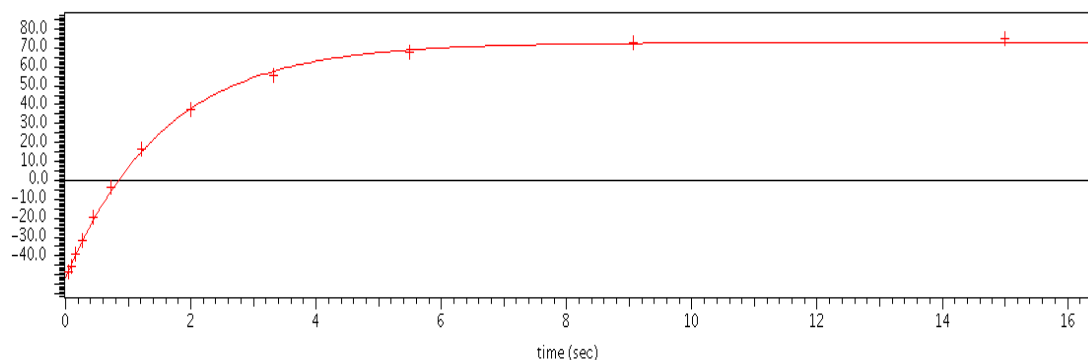


Figure 2.19 An example of the ^{19}F T_1 inversion-recovery curve corresponding to the spin-lattice relaxation of the $[(\text{NH}_3)_5\text{Ru}^{\text{II}}\text{tfmp}]\text{Cl}_2$ complex in D_2O at a concentration of 5.00 mM using the parameters stated.

2.6.4 Setting up the ^{19}F T_2 spin-echo experiment

The transverse relaxation time, T_2 , is the fundamental relaxation time constant related to the lifetime of the net magnetization (isochromat coherence time) in the x,y-plane after a well calibrated pw90 has brought it perpendicular to the external magnetic field, B_0 , along z. Another explanation for this defines T_2 as the time constant at which the intensity of the “beat signal” due to spin precession in the x,y-plane as referenced to the synthesized observe frequency decays to zero (*vide supra*).¹⁰ As such, it can be readily seen visually as the decay “envelope” containing

the interferogram pattern of the free induction decay (FID) which, upon Fourier transformation, yields the frequency spectrum. To set up and run the ^{19}F T_2 spin-echo experiment, a ^{19}F NMR spectrum, a pw90, and a T_1 value for the sample of interest must first be obtained as described above.

To bring up the standard parameter set for the T_2 spin-echo pulse sequence, the “Liquids” tab is opened in the “Protocol” window located on the left side of the screen. Then the “Std 1-D” button is opened and “T2_MEASURE” is selected. The standard parameter set contains the defaults to acquire using ^1H as the observe nucleus, therefore various parameters must be changed so as to measure T_2 for ^{19}F . Most of the parameters which will be listed here apply to most of the samples used in this work, but some specific parameters have been refined to apply to the $[(\text{NH}_3)_5\text{Ru}^{\text{II}}\text{tfmp}]\text{Cl}_2$ complex in D_2O at a solute concentration of 5.00 mM and these will be specified. The key parameters which must be adjusted, and one specific for each sample, are the relaxation delay (D1), the pw90, the observe pulse length, and all parameters associated with the array of spin system evolution delays between pulses.

The observe nucleus is changed to ^{19}F by opening the “Acquire” tab and selecting the “Channels” sub-tab located on the left side of the parameter panel window. The parameters for ^{19}F were entered analogously to the ^{19}F T_1 inversion-recovery sequence as already described.

The specific parameters for the ^{19}F T_2 spin-echo pulse sequence were adjusted by opening “Acquisition” sub-tab, and the following values were entered in manually: spectral width = 18939.4 Hz, acquisition time = 1.730 sec, complex points = 32768,

number of scans = 4, number of steady state scans = 0, block size = 4, relaxation delay = 10 sec, observable pulse (which is equivalent to a 90° pulse) = 9.7 μ sec, and the receiver gain = 40 or higher.

After this, the “Defaults” sub-tab was opened (located on the left side of the parameter panel window under the “Acquire” tab). The spectral width field was inspected to verify that it was equal to -80.2 ppm to -39.9 ppm. The array describing the series of spin evolution delays between pulses was then setup by selecting the “Arrays” button located at the top of the parameter panel window. A window appeared as in the T_1 experiment, and in this window the number of array values was generally set to equal to 10, starting at 0.025 seconds and ending at 13 seconds, in this case using linear increment spacing.

The correctness of the entered parameters was again verified by checking the displayed pulse sequence. This was done by selecting the grey box labeled “Sequence”. The T_2 spin-echo pulse sequence appeared on the screen showing the current parameters as in Figure 2.20 below.

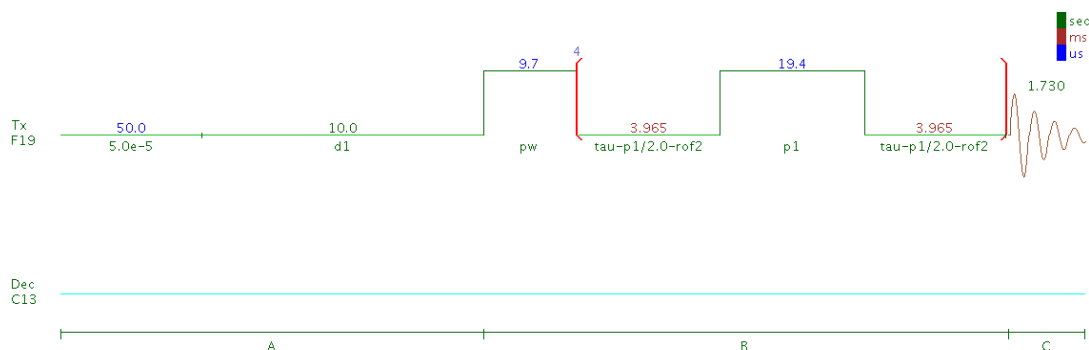


Figure 2.20 The ^{19}F T_2 spin-echo pulse sequence displaying the parameters associated with the $[(\text{NH}_3)_5\text{Ru}^{\text{II}}\text{tfmp}]\text{Cl}_2$ complex in D_2O at a concentration of 5.00 mM.

After verifying the pulse sequence, the T_2 spin-echo acquisition was initiated by selecting the green “Acquire” button at the top of the parameter panel window. Once the experiment had completed, the spectra were analyzed by opening the “Process” tab and selecting the green box labeled “Auto Process”. As in the T_1 inversion-recovery experiment, line-broadening may be applied to help with the signal-to-noise ratio as long as one adheres to the same validity constraints (*vide supra*).

The T_2 value of each peak in a multi-peak spectrum can be obtained by opening the “T2 Analysis” sub-tab (located on the left side of the parameter panel window under the “Process” tab). Once again, the grey field “Display Last Spectrum” is selected. During this time the spectrum should be phased, or adjusted in any way necessary. Then the grey button labeled “Do T2 Analysis” is selected and the T_2 relaxation values (and associated errors) will be displayed for all peaks present in the spectrum on the right side of the parameter panel window. The “Display All

Fits” button is then selected to display the all of the T_2 decay curves. If only one curve is sought for display, then instead of all of the T_2 curves being selected by default, the number of the desired peak for decay curve display should be entered in the “Display Selected Fits” box (followed by “enter”). The T_2 decay curve thus obtained for the $[(\text{NH}_3)_5\text{Ru}^{\text{II}}\text{tfmp}]\text{Cl}_2$ complex in D_2O at 5.00 mM is shown in Figure 2.21.

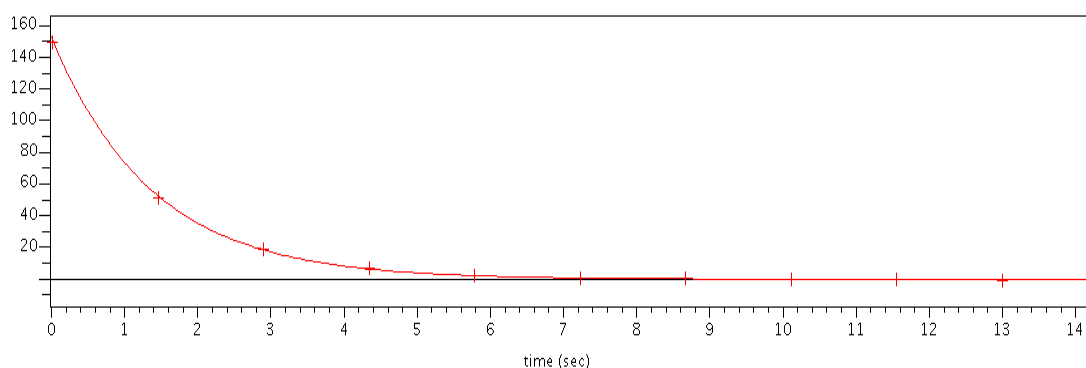


Figure 2.21 The ^{19}F T_2 spin-echo decay curve of the $[(\text{NH}_3)_5\text{Ru}^{\text{II}}\text{tfmp}]\text{Cl}_2$ complex in D_2O at a concentration of 5.00 mM as obtained using the parameters stated.

2.6.5 NMR probe/sample temperature calibration

The variable temperature, VT, control system of the NMR spectrometer adjusts and stabilizes the temperature of the system (probe and sample) at a constant, user defined value. The temperature readout comes from a factory calibrated thermocouple located in the probe, but, importantly, *not* in the sample itself. Therefore, a temperature differential can exist between the two, and in order to obtain an accurate reading of the temperature in the sample, a careful VT calibration curve must be constructed (this procedure is critically-important if valid kinetic activation

parameters are to be measured). The sample temperature in our work was calibrated vs. the thermocouple “readout temperature” using a standard 100% methanol sample (Varian, CAS 968120-80, Lot 8D-265-P) over a range of -10°C to 55°C. The two peaks which appear in the proton spectrum of the calibration standard represent the -OH peak located at ~4.5 ppm and the -CH₃ peak located at ~3.3 ppm, as shown in Figure 2.22.⁸

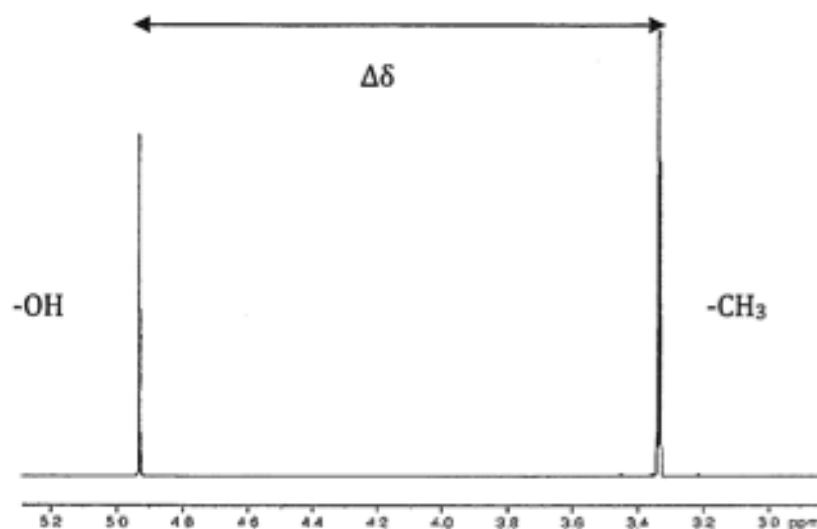


Figure 2.22 The ¹H NMR spectrum of the standard 100% methanol sample displaying the chemical shift difference between the two peaks, $\Delta\delta$, arising from the -OH and -CH₃ functional groups of the methanol.⁸

Using the distance between these two peaks, in units of ppm, the actual temperature of the system may be calculated using the published interpolation formula,

$$T(K) = 403.0 - 21.85\Delta\delta^2 - 36.54\Delta\delta \quad (2-17)^{33}$$

where $\Delta\delta$ is the distance between the two peaks in ppm, and T is the actual sample temperature in Kelvins. Equation (2-17) may be transformed to calculate the temperature in Celsius as shown below,

$$T(^{\circ}\text{C}) = 130.00 - 23.87\Delta\delta^2 - 29.53\Delta\delta \quad (2-18)^{34}$$

where again $\Delta\delta$ is the distance in ppm between the two peaks. After one compiles a number of data points for $\Delta\delta$ at varying readout temperatures into a table (being *very* careful to allow adequate equilibration time, *vide infra*), a graph may be constructed of the “true” sample temperature (T_{Sample}) vs. the instrumental “readout” temperature (T_{Readout}) using either of the interpolation formulae shown above (equation (2-17) was used to calculate values in Table 2.5 and then Figure 2.23).

If the VT control had no flaws, the “true” vs. “readout” temperature line would have a slope of one and a y-intercept of zero. In real cases, a best-fit equation of the line allows a very accurate sample temperature for any for any given readout temperature to be obtained over the calibrated range. The VT calibration curve created for the 500 MHz Varian NMR spectrometer and “ONE” probe used in the work is shown in Figure 2.23 (see also Table 2.5).

Table 2.5 Instrumental readout temperatures and the actual sample temperatures calculated using equation (2-17) from the VT calibration plot, as seen in Figure 2.23, and selected 95% confidence intervals (based on 5 replicate measurements).

Instrument Readout Temperature		Calculated Temperature, Avg		95% Confidence Interval
°C	K	°C	K	
-10.00	263.15	-11.92	261.23	--
0.00	273.15	-1.90	271.25	--
10.00	283.15	9.34	282.49	--
15.00	288.15	14.75	287.90	0.06
20.00	293.15	20.16	293.31	0.12
25.00	298.15	25.40	298.55	0.17
30.00	303.15	31.82	304.97	0.11
35.00	308.15	37.30	310.45	0.10
40.00	313.15	42.11	315.26	0.05
50.00	323.15	51.48	324.63	0.15
55.00	328.15	56.05	329.20	0.17

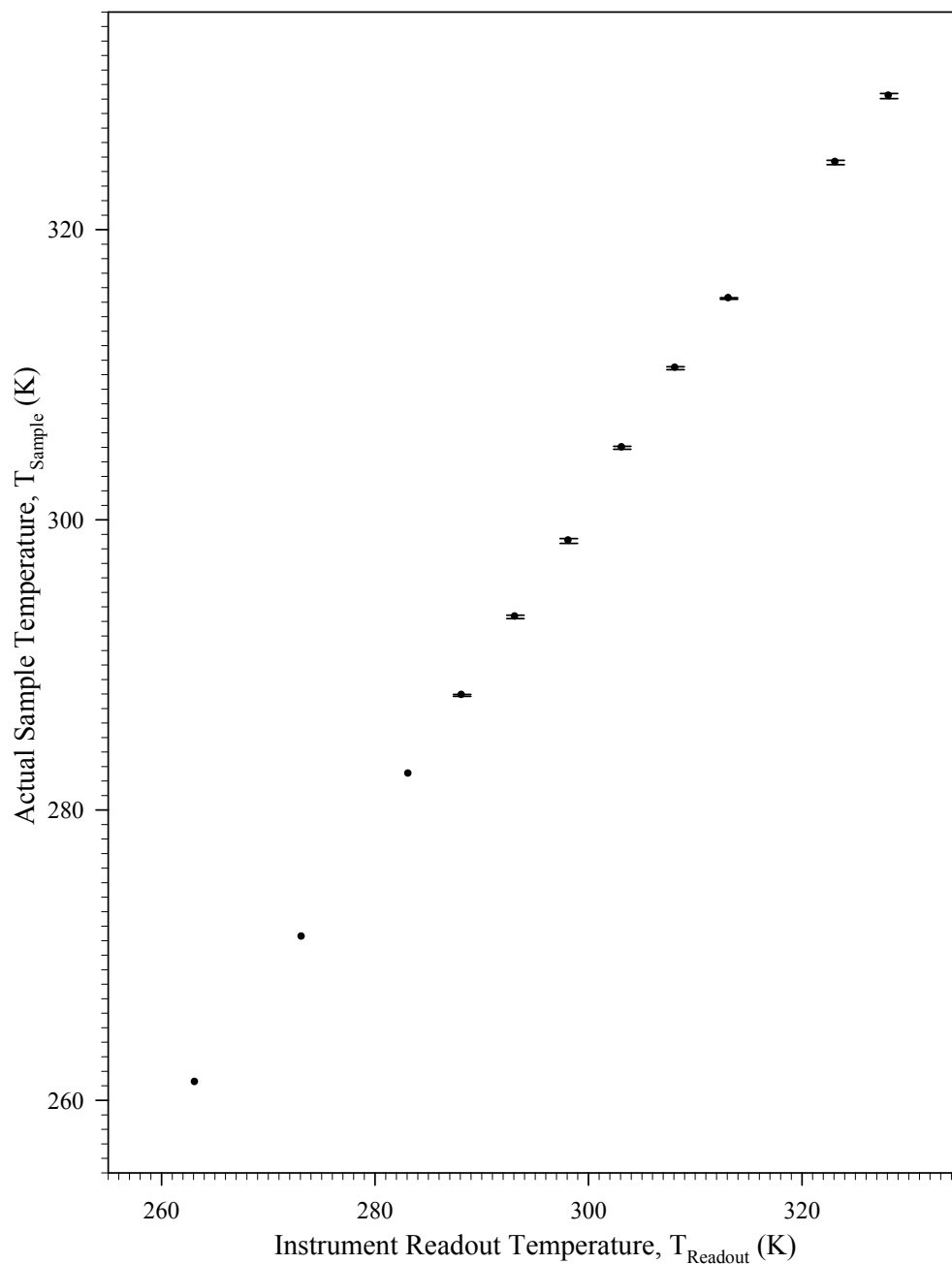


Figure 2.23 The temperature calibration curve obtained over the range of 263.15 K (-10°C) to 328.15 K (55°C) using the standard 100% methanol sample provided by Varian and applying equation (2-17) to the experimental $\Delta\delta$ values to generate “ T_{Sample} ”. The 95% confidence intervals shown for selected data points are taken from the entire data set listed in Table 2.5.

The thermocouple calibration data listed in Table 2.5 are plotted in Figure 2.23. The rough regression line which can be used to estimate the actual temperature of a given sample in the NMR T_{Readout} (in the linear approximation) was found to be,

$$T_{\text{Actual}} = (1.06) T_{\text{Readout}} - 18.62 \quad (2-19)$$

where T_{Actual} is now much closer to the temperature of the sample (in Kelvins). A graph of the error at each examined T_{Readout} of the VT control system is shown Figure 2.24. Applying the indicated (or visually interpolated) error increment ($T_{\text{Sample}} - T_{\text{Readout}}$) to T_{Readout} anywhere in this calibrated range will then give the most accurate T_{Sample} possible based on our calibration work (interpolation being assisted by referencing the dotted line in the figure).

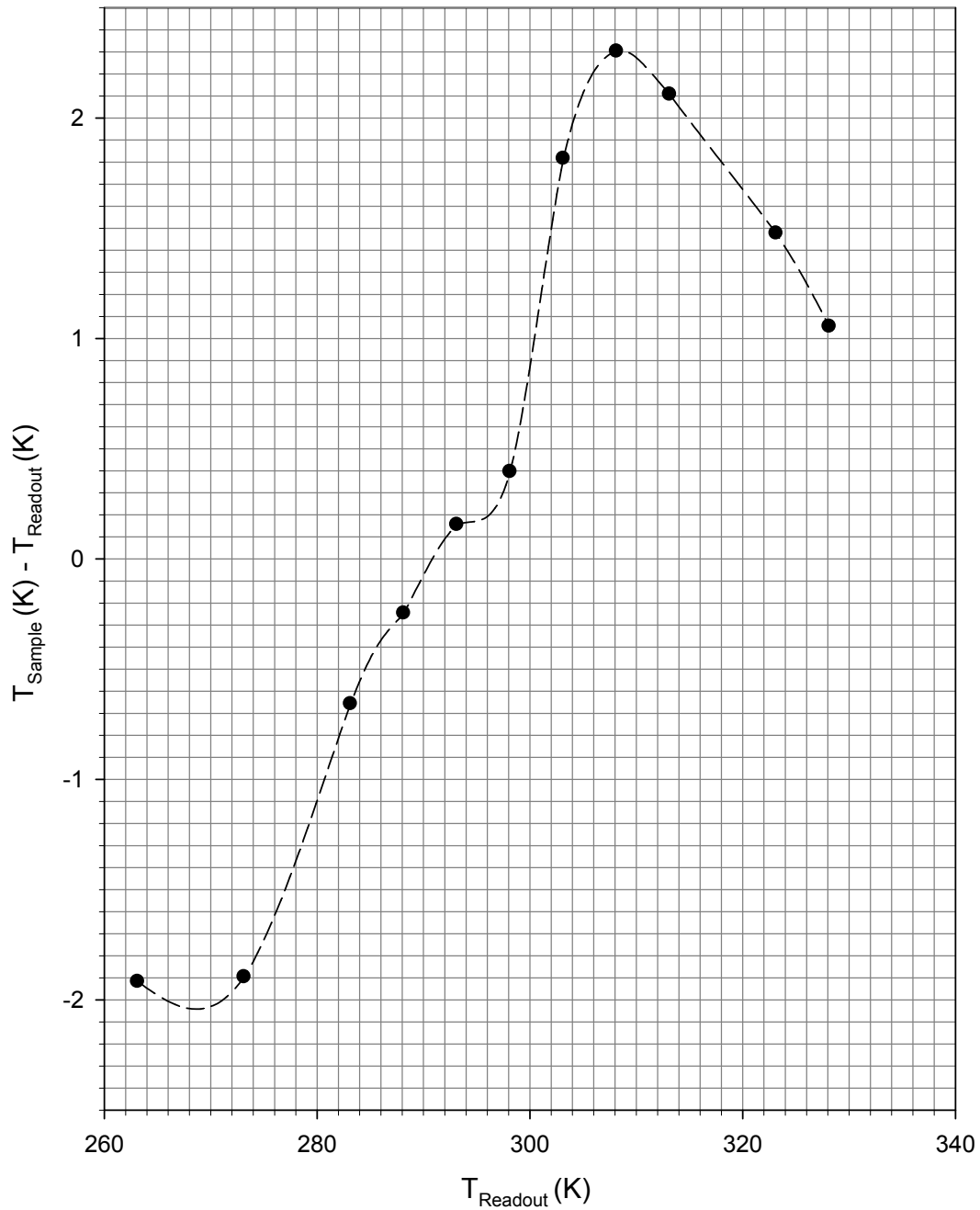


Figure 2.24 The instrument readout temperature error as the increment ($T_{\text{Sample}} - T_{\text{Readout}}$) over the temperature range 263.15 K (-10°C) to 328.15 K (55°C). From this graph, T_{Sample} at any given T_{Readout} can be obtained by adding the interpolated error increment value to T_{Readout} (or more approximately by using equation (2-19)).

In our subsequent work on temperature dependent kinetics difficulties were encountered relating to the temperature equilibration times of the system. It was discovered that even though the readout temperature had stabilized at some constant temperature, not all of the components of the system, most importantly the sample, were fully equilibrated at the “true” temperature which would be inferred from the readout T. We found that very careful temperature calibration of the instrument as well as equally careful (and slow) thermal equilibration of the probe and sample were crucial to the collection of valid, reproducible activation parameter data. An equilibration time of about 15 minutes was initially recommended by Varian as the wait period between experiments to be done at different sample temperatures. This value was found to be too short leading to irreproducible results. Additionally, we found that if the probe and sample are not allowed to fully equilibrate after a change in temperature, it becomes impossible to shim the magnetic field correctly and thus accurate line-widths are unobtainable (due to temperature gradients within the sample and probe leading to an additional source of inhomogeneous line-broadening). After extensive testing, the minimum equilibration time was found to be 25 minutes between experiments after any changes in temperature (after even a very modest 3°C change). It is important to note, however, that D₂O is notoriously slow to equilibrate, so the 25 minute equilibration time should not be taken as a global value; organic solvents may behave more according to the Varian recommendation (but caution is advised).

2.7 Experimental Methodology used in Measuring Kinetic Salt Effects

In all the NMR kinetic experiments done here all simple salts, sodium dicarboxylic salts, and metallic hexacyanide salts were added as concentrated (small volume) salt solutions directly to the NMR tube containing the verified equimolar mixture of $[(\text{NH}_3)_5\text{Ru}^{\text{II}}\text{tfmp}]\text{Cl}_2$ and $[(\text{NH}_3)_5\text{Ru}^{\text{III}}\text{tfmp}]\text{Cl}_3$ reactants in 2.00 mL D_2O . The 50:50 $\text{Ru}^{\text{II}}:\text{Ru}^{\text{III}}$ mixture was verified by noting the ^{19}F peak heights on the $[(\text{NH}_3)_5\text{Ru}^{\text{II}}\text{tfmp}]^{2+}$ and $[(\text{NH}_3)_5\text{Ru}^{\text{III}}\text{tfmp}]^{3+}$ resonances at -29547 Hz (-59 ppm) and -32010 Hz (-64 ppm), respectively. The stock salt solutions were prepared as described previously, and the volume of the added salt solution was calculated based on the desired total GP value. The salt solutions were added to the reactant solution using p-2, p-20, p-100, and p-200 micropipets. The total volume added to the 2.00 mL reactant solution was never larger than 8% of the volume of the reactant solution. The smallest volume added was never smaller than 0.08 μL .

In a typical experiment, the $[(\text{NH}_3)_5\text{Ru}^{\text{II}}\text{tfmp}]\text{Cl}_2$ complex was added to an 8 inch, 5 mm NMR tube so that a concentration in the range between 0.10 mM and 5.00 mM (for T_2 spin-echo determination) was established in 2.00 mL of 99.9% D_2O (Sigma Aldrich, CAS 7789-20-0). After proper temperature equilibration was attained, a well-shimmed ^{19}F NMR spectrum was acquired at the default running temperature of 26°C (*vide supra*). For the lower-concentration range work, T_2 spin-echo sequence was then loaded with the proper parameters as previously described for ^{19}F T_2 relaxation measurement on the $[(\text{NH}_3)_5\text{Ru}^{\text{II}}\text{tfmp}]^{2+}$ species in D_2O . A new solution was then prepared with equimolar amounts of $[(\text{NH}_3)_5\text{Ru}^{\text{II}}\text{tfmp}]\text{Cl}_2$ and

$[(\text{NH}_3)_5\text{Ru}^{\text{III}}\text{tfmp}]\text{Cl}_3$ and the T_2 was then re-measured on the exchanging mixture. Upon completion a specified amount of the given salt solution was then carefully added to the reactant solution (*vide supra*) and the solution was mixed in the NMR tube by inverting the tube a minimum of 20 times to ensure that the concentration of salt was uniform throughout the sample. After thermal equilibration and careful shimming (very important at higher ionic strengths), the T_2 of the exchanging solution was measured again. This procedure was repeated until all salt dependent rate data were collected. We found that the reactant solutions used here had an operational lifetime of 6 hours before measured rates would begin to drift due to sample degradation.

For exchanging mixtures with reactants concentrations less than 5.00 mM, the simple line-broadening method could not be used because the change in line-width due to ET exchange was too small to measure, but rates obtained *via* line-broadening checked well against T_2 rates collected at 5.00 mM as will be discussed further on. This experiment was performed using simple salts (KF, NaCl, and KBr), dicarboxylate salts (Na_2muc , Na_2tere , Na_2adip , and $\text{Na}_2(1,4\text{-dcch})$), and hexacyano salts ($\text{K}_4\text{Fe}^{\text{II}}(\text{CN})_6$, $\text{K}_4\text{Os}^{\text{II}}(\text{CN})_6$, and $\text{K}_4\text{Ru}^{\text{II}}(\text{CN})_6$). This procedure was also repeated for the salt Na_2muc using H_2O (running unlocked) instead of D_2O .

2.8 Sample Degassing

In general we found that degassing was not necessary in order to arrive at valid and reproducible rates. It was important however to carefully check into this since air-saturated D_2O contains about 5×10^{-4} M paramagnetic O_2 gas, and this can, in

some cases,^{25,35} lead to shortened T_1 and T_2 values and thus “paramagnetic broadening” which can invalidate chemical exchange rate measurements.

2.8.1 Degassing with argon

O₂ gas can be readily removed from a sample by a simply bubbling high-purity argon (or nitrogen) gas through the solution. We used scientific grade (grade 6) ultra high purity, UHP, argon gas (Airgas, CAS 7440-37-1, UN1006). All sample tubes which were degassed were placed in a 125 mL erlenmeyer flask for stability (with a layer of kimwipes on the bottom in order to protect the NMR tube from damage). A 12 inch, 18 gauge stainless steel needle was then attached to the gas line and placed well down into the solution in the NMR tube. The gas line was then turned on slowly, using a gas manifold to regulate the rate at which argon gas bubbles were allowed to come up through the solution (a rate of 1-3 bubbles per second was found to be ideal). This process was monitored for 20 minutes. The gas was then turned off slowly, and the needle was removed quickly and carefully followed by rapid placement of the tube cap on the Ar filled tube. As an added measure, a band of parafilm was then wrapped/stretched around the cap to prevent any O₂ gas from entering. If one seals the NMR tube using an oxygen/butane torch the degassed sample will not be exposed to air indefinitely.

2.8.2 Degassing by vacuum

The alternative, and generally superior, method of degassing is to employ the “freeze-pump-thaw” cycle wherein the sample is chilled to freezing, the headspace

gases are removed by brief exposure to vacuum, and the solution is thawed (vacuum off) so that dissolved gases now boil into the headspace. While this works well for organic solvents (after 2-3 cycles), it is impractical with D₂O since the tubes tend to break upon freezing. We were able to implement a modified version of this approach, however, by simply skipping the freezing step and keeping the evacuation step to a period of 4 seconds initially (the vacuum being delivered by inserting a sterile 5/8 inch, 25 gauge aluminum needle (Monoject 200, part # 8881-200466, Lot # 163791) through enough of a 5 mm white rubber septa (Aldrich, Catalog # Z10070-6) so that a vacuum can be applied). By gating the vacuum off quickly, vigorous solvent boiling was avoided and only the dissolved gases bubble out of the solution during equilibration. In order to achieve this level of control, the vacuum line from the manifold was attached to a 250 mL vacuum flask with a stop-cock, with the second line out of the vacuum flask being attached to the needle inserted into the headspace of the 8 inch, 5 mm NMR tube containing the reactant solution. The vacuum initially (first cycle) was turned on for 4 seconds using the gas line stop cock to control the vacuum. Bubbles containing “air” formed in the solution during this time. The solution was allowed to stand and outgas for 45 seconds, and then the headspace air was again evacuated another 4 seconds. This process was repeated until no air bubbles formed in the reactant solution upon standing after vacuum exposure. The vacuum was then applied to the sample for a final 25 seconds and the sample was allowed to stand for 1 minute. This process was repeated about 10 times over a

period of 20 minutes. Upon completion the needle was removed from the septum and the entire septum cap was quickly covered with multiple layers of stretched parafilm.

2.8.3 Saturation with oxygen

As part of our investigations into catalysis by muconate in particular a few such exchanging samples were saturated with O₂ by bubbling industrial grade compressed oxygen (Praxair, CAS #7782-447, UN1072), again using an 8 inch, 5 mm NMR tube containing the reactant solution and was placed in a 125 mL erlenmeyer flask with delicate kimwipes to prevent tube damage. A 12 inch, 18 gauge stainless steel needle was used to slowly bubble the O₂ gas up through the solution at a rate of 1-3 bubbles per second. This process was continued for 20 minutes and the gas was turned off, the needle was removed, the tube was capped with a polypropylene NMR tube cap, and finally wrapped with parafilm to further impede any gas exchange.

2.9 Methods for Assessing the Effects of Degassing on the ¹⁹F T₂ Spin-Echo ET Kinetics Measured with added Sodium Muconate

The T₂ spin-echo sequence was executed as described previously on the [(NH₃)₅Ru^{II}tfmp]²⁺ species by itself. A new solution was then prepared with equimolar amounts of [(NH₃)₅Ru^{II}tfmp]Cl₂ and [(NH₃)₅Ru^{III}tfmp]Cl₃ at a concentration of 0.10 mM in D₂O. A volume of 1.00 mL of this solution was inserted into an NMR tube and the T₂ value corresponding to the Ru^{II} peak was obtained as described previously. A 2.00 mL 0.125 M solution of sodium muconate in D₂O was then prepared and added to the reactant solution #1 so that the concentration of

sodium muconate in the reactant solution was 0.004 M (well up into the catalytic region in Figure 2.5) and the T_2 value was obtained corresponding to the Ru^{II} peak on this solution. A separate 1.00 mL solution was inserted into an NMR tube using the same solution as was prepared for solution #1. A T_2 value corresponding to the Ru^{II} peak was obtained for this new solution, solution #2, which contained reactants only. During this time, solution #1 was vacuum degassed and a T_2 value corresponding to Ru^{II} peak was obtained immediately after completion of degassing. During this time, solution #2 was vacuum degassed and a T_2 value corresponding to Ru^{II} peak was obtained immediately after completion of degassing. Next, solution #1 was argon degassed and a T_2 value corresponding to Ru^{II} peak was obtained immediately after completion of degassing. After, solution #2 was argon degassed and a T_2 value corresponding to Ru^{II} peak was obtained immediately after completion of degassing. Lastly, solution #1 was saturated with oxygen and a T_2 value corresponding to Ru^{II} peak was obtained immediately after completion of saturation. Solution #2 was saturated with oxygen as well and a T_2 value corresponding to Ru^{II} peak was obtained immediately after completion of saturation. It should be noted that the time of this experiment was well below the known aging time of our reactant solutions (about 6 hours at room temperature).

2.10 NMR Temperature Dependent Kinetic Experiments

2.10.1 Line-broadening measurements

In a typical experiment, the $[(\text{NH}_3)_5\text{Ru}^{\text{II}}\text{tfmp}]\text{Cl}_2$ complex was added at a specified concentration to an NMR tube, and a well shimmed ^{19}F 1-D spectrum was obtained at 26°C. The line-width of the ^{19}F peak of the $[(\text{NH}_3)_5\text{Ru}^{\text{II}}\text{tfmp}]^{2+}$ complex was then measured and recorded. An equimolar amount of the $[(\text{NH}_3)_5\text{Ru}^{\text{III}}\text{tfmp}]\text{Cl}_3$ complex was then added (as a solid) such that a 50:50 mixture of $[(\text{NH}_3)_5\text{Ru}^{\text{II}}\text{tfmp}]\text{Cl}_2$ and $[(\text{NH}_3)_5\text{Ru}^{\text{III}}\text{tfmp}]\text{Cl}_3$ was created. A new 1-D ^{19}F spectrum was then recorded and the new (exchanging) line-widths and peak positions corresponding to the $[(\text{NH}_3)_5\text{Ru}^{\text{II}}\text{tfmp}]^{2+}$ and $[(\text{NH}_3)_5\text{Ru}^{\text{III}}\text{tfmp}]^{3+}$ complexes were measured and recorded. A mixture of dry ice and chilled isopropanol (Sigma-Aldrich, CAS 67-63-0) was then added to the VT-dewar attached to the NMR probe assembly and dry air was driven through so as to allow precise temperature control of the probe and sample. For low temperature work, the temperature of the sample was lowered to 10°C (or sometimes 4°C) and allowed to equilibrate for a minimum of thirty-five minutes prior to initiating the temperature ramp to come. A 1-D ^{19}F spectrum was then acquired at 10°C (or 4°C), and the line-width of the $[(\text{NH}_3)_5\text{Ru}^{\text{II}}\text{tfmp}]^{2+}$ peak was measured and recorded. Spectra were then obtained at the following temperatures in this *specific order*: 26°C, 4°C, 7°C, 10°C, 15°C, 20°C, 26°C, 31°C, 37°C, (and 42°C, 48°C, and 53°C in some cases), and back to 26°C. The equilibration times were a minimum of twenty-five minutes for each change in temperature excluding the initial change in temperature which equilibrated for a minimum of thirty-five minutes due to the large

change in temperature. Solutions containing equimolar concentrations of $[(\text{NH}_3)_5\text{Ru}^{\text{II}}\text{tfmp}]\text{Cl}_2$ and $[(\text{NH}_3)_5\text{Ru}^{\text{III}}\text{tfmp}]\text{Cl}_3$ in D_2O were studied in this manner at concentrations of 5.00 mM, 5.30 mM, 5.50 mM, 6.50 mM, and 8.00 mM.

2.10.2 ^{19}F T_2 spin-echo measurements

These experiments were done analogously to the ^{19}F NMR line-broadening experiments but on samples at the low-end of the reactants concentration range where line-broadening is too small to allow for accurate rate measurement (any concentration below 5.00 mM). The ^{19}F T_2 spin-echo sequence was used to obtain rates at varying temperatures in the same manner as described above using a smaller set of temperatures. Temperature data were obtained in this *specific order*: 26°C, 10°C, 15°C, 20°C, 30°C, and 26°C. The concentrations of reactants studied using this technique were 3.00 mM, 1.00 mM, 0.50 mM, and 0.10 mM. Fewer temperatures were used here than in the line-broadening case because acquisition of precise T_2 values required longer experiment times. The final determination at 26°C was used as a necessary consistency check throughout the entire experiment (significant change compared to the initial determination would be a sign of sample decomposition). The upper end of the temperature range was truncated in the T_2 work because we found that Eyring plots were of sufficiently high quality over this smaller range.

Temperature dependent kinetic experiments were also completed with varying concentrations of added salts (KF, KBr, Na_2muc , Na_2adip , $\text{K}_4\text{Fe}^{\text{II}}(\text{CN})_6$, $\text{K}_4\text{Ru}^{\text{II}}(\text{CN})_6$, and $\text{K}_4\text{Os}^{\text{II}}(\text{CN})_6$) with a concentration of reactants being 0.10 mM (to match the conditions of the previous stopped-flow work^{6,9}).

2.11 Validation of the ^{19}F T_2 Spin-Echo Experiment

The T_2 spin-echo NMR experiment is a common technique used in a variety of ways including MRI¹⁷ and allows, in our case, for rates of ET (or other) chemical exchange processes to be measured (*vide supra*). Implementation of the technique in this work first required method validation in order to establish full confidence in the accuracy and precision of it for measuring our ET self-exchange rates. The ^{19}F nucleus has not been previously used in this lab for measuring T_2 relaxation rates, therefore a variety of samples and tests were conducted in the validation of the spin-echo pulse sequence over a broad range of conditions.

The T_2 spin-echo sequence itself was first validated using the ^1H nucleus as the observe nucleus in order to ensure the pulse sequence and data analysis routines were functioning properly. The Autotest sample (Varian, Lot # 9E-252-G), which consists of 1% H_2O , 99.8% D_2O , 0.1% ^{13}C -Methanol, 0.1% ^{15}N -Acetonitrile, and 0.30 mg/mL GdCl_3 , was used as the experimental standard. Our test value for T_2 relaxation of the CH_3 group on the methanol in the Autotest sample is presented in Table 2.6 along with the 0.0580 sec reference value given by the research NMR division at Agilent (formerly Varian) at the standard sample temperature of 299 K (26°C). Over fifty T_2 measurements on the Autotest sample were taken to compare with the Varian number. The T_2 measured with our instrument was found to be 0.0580 ± 0.0005 sec at 299 K, in perfect agreement with the accepted value.

Table 2.6 The T_2 value of the proton of the methyl group on the methanol in the Autotest sample.

Sample	$T_2^{(a)}$ (sec)	$T_2^{(b)}$ (sec)
Autotest Sample	0.0580 ± 0.0005	0.0580

(a) Obtained experimentally in this lab. (b) The reference T_2 value supplied by the NMR research division at Agilent.

The next step in our method validation was to apply the T_2 spin-echo sequence to a molecule containing the ^{19}F nucleus. The molecule used to initially validate the method was the free-ligand 3-trifluoromethylpyridine (tfmp) at a concentration of 5.00 mM in 2.00 mL of D_2O . Tfmp was chosen because it would later be present on both of the redox reactants shown in reaction (2-2) where changes in the T_2 values would then be used to measure the rate of ET self-exchange. Over a hundred T_2 relaxation measurements of this sample were obtained and the T_2 relaxation value of the fluorine substituent on the free ligand was determined to be 2.304 ± 0.003 sec at a temperature of 299 K (26°C) as shown previously in Table 2.3.

As part of our validation and control program, we undertook investigations of dissolved oxygen, shim settings, the pre-pulse relaxation delay time, and temperature effects on the measured T_2 value of the free ligand. The T_2 value was not affected by degassing the sample with Ar gas, which suggested that oxygen paramagnetic relaxation effects would most likely be insignificant when using the ^{19}F resonance line to measure ET rates, but further testing of this question was also carried out with respect to the complexes themselves and in the context of the “muconate effect” (these details will be described later. When examining how the shim settings (which

ensure the best-possible homogeneity of the magnetic field around the sample) affect the T_2 relaxation value, the magnetic field was intentionally made inhomogeneous by first establishing the best shims and then essentially degrading the condition by changing the z1 through z4 shims well away from the optimum setting. This was done in order to assess the degree that imperfect shims would affect the measured line-shape, but presumably not the T_2 relaxation value (on account of the cancellation of inhomogeneous broadening built into the T_2 CPMG sequence). We observed that the T_2 relaxation value was not affected to any significant degree by homogeneity of the magnetic field, even in cases where the measured line-width went from an optimized value 3 Hz to 6 Hz.

The relaxation delay time, D1, was then distorted such that it was no longer $5xT_1$. Shortening D1 from 10 seconds down to 5 seconds ($D1 \ll 5xT_1$) did indeed result in “invalid” T_2 relaxation values due to a “smooth” decay curve no longer being present for purposes of fitting and analysis. It was also established that as the delay time was increased to a value much longer than $5xT_1$ (on the order of $\sim 9xT_1$) the observed T_2 value diverged from the optimized value.

Temperature effects were investigated by both raising and lowering the temperature of the sample and then measuring the T_2 value. The T_2 was found to change with temperature as does the line-width, thus these free-ligand results suggest temperature dependent experiments can be conducted with high accuracy (using the T_2 method for measuring rates in order to obtain the necessary activation parameters, *vide infra*).

The T_2 relaxation values of both the Ru^{II} and Ru^{III} reactant species in reaction (2-2) alone and in conditions of ET self-exchange with each other were then measured in a similar manner as the tfmp sample (now adjusting the necessary experimental parameters in order to obtain valid T_2 values, *vide infra*). The rates obtained using the T_2 spin-echo experiment were then compared to rates obtained by line-broadening utilizing equation (2-9). In order to ensure a meaningful comparison, the concentrations of the reactants had to be large enough in order create measurable line-width increases under exchange conditions. We found that this required a minimum reactants concentration of 5.00 mM. Over fifty measurements of each reactant alone, $[(\text{NH}_3)_5\text{Ru}^{\text{II}}\text{tfmp}]^{2+}$ and $[(\text{NH}_3)_5\text{Ru}^{\text{III}}\text{tfmp}]^{3+}$, in D_2O were obtained and the ^{19}F T_2 relaxation values of the trifluoromethyl substituent of the Ru^{II} and Ru^{III} redox species alone were found to be 1.375 ± 0.006 sec and 0.101 ± 0.003 sec, respectively, at a temperature of 299 K (as reported previously in Table 2.3). The T_2 for the $[(\text{NH}_3)_5\text{Ru}^{\text{II}}\text{tfmp}]^{2+}$ complex in exchange with a reactants concentration of 5.00 mM was found to be 0.0181 ± 0.0002 . The $[(\text{NH}_3)_5\text{Ru}^{\text{III}}\text{tfmp}]^{3+}$ was not used to measure rates due to the paramagnetic nature of the Ru^{III} complex resulting in T_2 relaxation values which are too fast to measure at high concentrations of both reactants and added salts.

The line-widths of the same resonances measured by T_2 were also obtained in order to compare the exchange rates calculated from the two NMR based methods. The logarithm of the observed rate of ET obtained using the T_2 values, employing equation (2-16), was found to be 4.04 ± 0.05 for equimolar reactants in reaction (2-2)

with concentrations of 5.00 mM at 299 K. The logarithm of the observed rate of ET obtained using line-widths and employing equation (2-9) was found to be 4.12 ± 0.05 (see Table 2.7 below). While not identical, the k_{ex} values are nearly within error of each other and thus the two approaches are clearly convergent under these conditions. The calculated rate using T_2 was found to be consistently “smaller” at a reactants concentration of 5.00 mM than when using the line-broadening technique due to systematic errors that lie in line-width measurements and are not present in the T_2 measurement. This problem stems from homogenous and inhomogenous broadening (in the absence of chemical exchange) which does not affect measured T_2 values directly (*vide supra*). Therefore, the T_2 spin-echo method is a more accurate, precise, and broadly-applicable method for measuring exchange rates and offers the major advantage that when k_{ex} is slow enough (at reactants concentrations below about 5.00 mM in this work), then kinetic effects on the observed $\Delta\nu_{1/2}$ will become unmeasurably small whereas changes in T_2 are still able to yield valid exchange rates. On this basis, we proceeded to then “push” the T_2 method to both the slow and fast exchange rate regions so as to accurately determine k_{ex} by NMR with reactant concentrations in the stopped-flow concentration region and all the way into the very fast exchange region which occurs in the presence of highly-active ET catalysts like $\text{Fe}^{\text{II}}(\text{CN})_6^{-4}$.

When measuring the T_2 values of quickly exchanging samples (large reactants concentrations or strongly catalytic added salts), the time “tau” (as labeled in the Varian T_2 pulse sequence illustrated in Figure 2.20) was adjusted to a much shorter

time. In order to reassign this value, one must shorten the “Tau” value and array the “BigTau” in such a way that it captures the observed T_2 relaxation curve. This is done by typing the following in the command line:

BigTau array:(“number of points in array”, “starting value of array (sec)”,
“ending value of array (sec)”, tau value (sec))

DO NOT SET A VALUE FOR TAU SHORTER THAN **0.0005 sec** OR YOU WILL DAMANGE YOUR SPECTROMETER. DO NOT RUN EXPERIMENTS WITH SMALL VALUES FOR TAU OVER AN EXTENDED AMOUNT OF TIME. IF THE LOCK SIGNAL OF YOUR SAMPLE BEGINS TO CHANGE STOP ACQUISTION AND REMOVE SAMPLE IMMEDIATELY. THIS SHOULD NOT BE ATTEMPTED WITHOUT THE LABORATORY MANAGER OF THE NMR PRESENT AND AWARE.

Table 2.7 The measured ET self-exchange rates obtained for reaction (2-2) at different equimolar reactant concentrations through the T_2 spin-echo method, T_2 , and the line-broadening method, $\Delta\nu_{1/2}$.^{a,b}

Concentration (mM)	log k_{ex}	
	T_2 Method	$\Delta\nu_{1/2}$ Method ^(b)
5.00	4.04 ± 0.05	4.12 ± 0.05
1.00	3.71 ± 0.02	N/A
0.50	3.58 ± 0.04	N/A
0.10	3.32 ± 0.05	N/A

a) $[Ru^{II}] = [Ru^{III}]$ in D_2O at 299 K. b) See equation (2-9)

2.12 Reactant Concentration Effects on the Rate of ET (Self-Salting)

Due to the well-characterized added-salt and self-salting effects measured by Sista, Inagaki, and Mehmood in the stopped-flow ET work,^{6,9,36} we undertook investigation of whether the effect of changing the equimolar concentration of the two reactants on the T_2 -derived ET rate constant, k_{ex} , for reaction (2-2) over the reactant concentration range from 0.10 mM (the same as much of the prior stopped-flow work) all the way up to 5.00 mM (where T_2 and $\Delta\nu_{1/2}$ derived rates converge) would show the same “self-salting” pattern as seen previously. We also used $\Delta\Delta\nu_{1/2}$ (linebroadening) rates from 5.00 mM to 8.00 mM reactants since $k_{\text{obs}} = k_{\text{ex}}[\text{Ru}^{\text{II}}][\text{Ru}^{\text{III}}]$ in this region was too fast to measure by T_2 . The resulting $\log k_{\text{ex}}$ vs. GP data are listed in Table 2.8 and illustrated in Figure 2.25. This now allows for comparison between our T_2 -based “self-salting” curve (over a large concentration range) against both the classically-predicted Debye-Hückel behavior¹¹ and the previous body of stopped-flow data for reaction (2-1) collected in this lab^{6,8} (see chapter 1, section 1.7). The previous stopped-flow data are listed in Table 2.9 and are also shown in Figure 2.25 (the upper red triangles).

Table 2.8 Rates of reaction (2-2) at various concentrations of equimolar reactants showing the “self-salting” rate increase due to ionic strength of the reactants themselves.

Concentration (mM)	μ	GP	$\log k_{\text{ex}}$
0.10 ^(a)	0.0009	0.0291	3.318 ± 0.051
0.50 ^(a)	0.0045	0.0629	3.580 ± 0.039
1.00 ^(a)	0.0090	0.0866	3.708 ± 0.024
3.00 ^(a)	0.0270	0.1410	3.934 ± 0.071
5.00 ^(a)	0.0450	0.1750	4.039 ± 0.052
5.00 ^(b)	0.0450	0.1750	4.097
5.30 ^(b)	0.0477	0.1793	4.100
5.50 ^(b)	0.0495	0.1820	4.124
6.50 ^(b)	0.0585	0.1948	4.176
8.00 ^(b)	0.0720	0.2116	4.255

(a) Measured using the T₂ spin-echo method (with 95% confidence intervals as shown). (b) Measured by ¹⁹F NMR line-broadening (of the Ru(II) peak) in the slow-exchange region (see Figure 2.4).

Table 2.9 Previous rates obtained by stopped-flow at various concentrations of equimolar reactants showing the self-salting acceleration of reaction (2-1) and their respective 95% confidence intervals.⁶

Concentration (mM)	μ	GP	$\log k_{\text{ex}}$
0.10	0.0291	0.0291	3.656 ± 0.010
0.12	0.0318	0.0318	3.667 ± 0.030
0.14	0.0343	0.0343	3.695 ± 0.060
0.20	0.0407	0.0407	3.713 ± 0.010
0.25	0.0453	0.0453	7.807 ± 0.030
0.30	0.0494	0.0494	3.835 ± 0.040
0.35	0.0531	0.0531	3.856 ± 0.040
0.40	0.0566	0.0566	3.914 ± 0.040

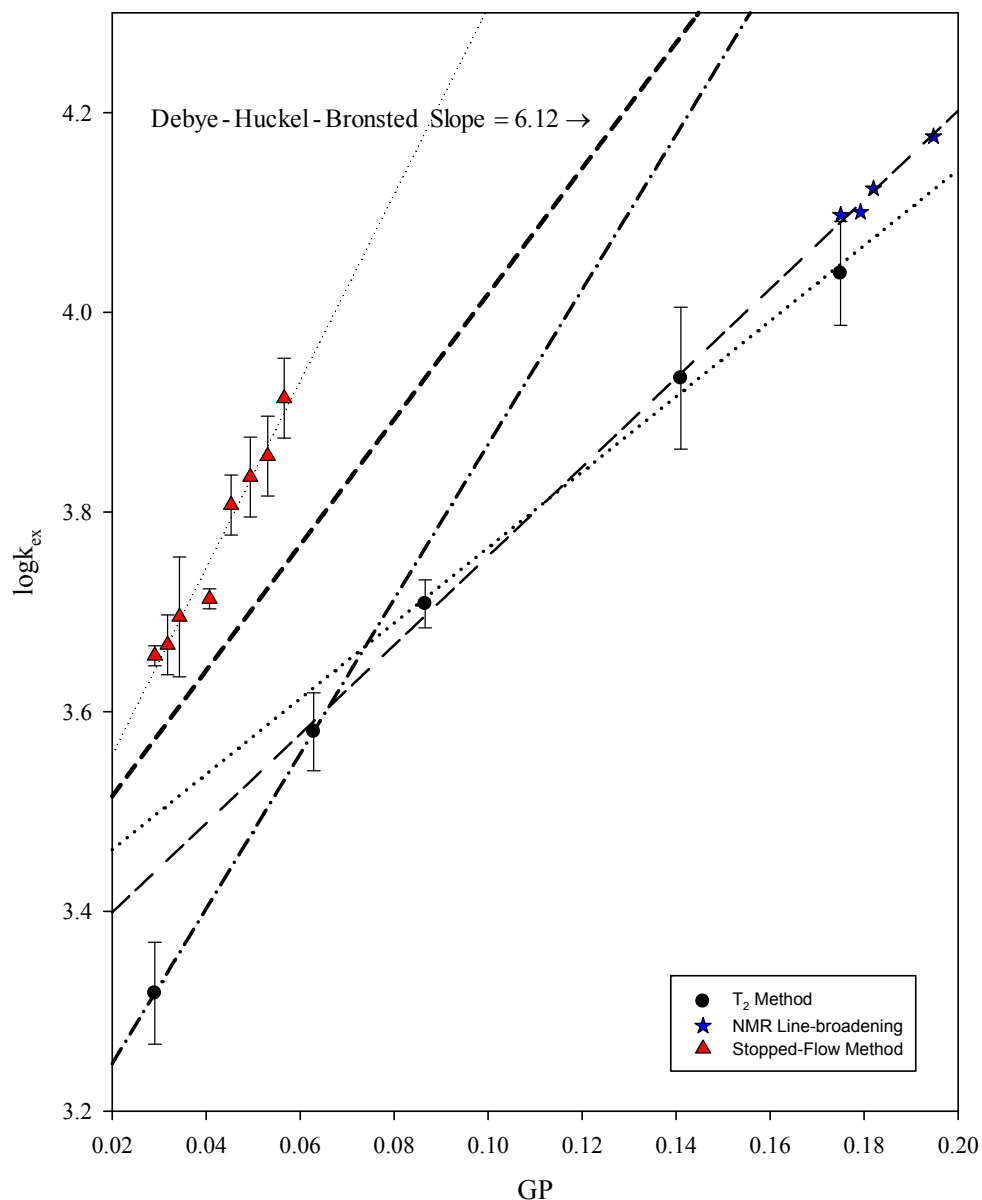


Figure 2.25 The measured $\log k_{ex}$ vs. GP behavior found for reaction (2-2) as measured by the T_2 spin-echo method (black circles) and NMR line-broadening data (blue stars) with error bars representing the 95% confidence intervals. The upper line (red triangles) is taken from stopped-flow data of Sista⁶ (see reaction (2-1)) and the central dashed line is the theoretical rate behavior predicted from the Debye-Hückle-Bronsted equation (see equation (1-40)).

Table 2.10 Self-salting slopes taken from Figure 2.25 for the various concentration ranges of reactants.

	Slope	Concentration Range of Reactants
Stopped-flow Slope ^(a)	9.36 ± 0.70	0.10 mM - 0.40 mM
NMR, T ₂ Early Slope ^(b)	7.75	0.10 mM - 0.50 mM
NMR, T ₂ Late Slope ^(b)	3.58 ± 0.41	1.00 mM - 5.00 mM
NMR, $\Delta\nu_{1/2}$ Slope ^(c)	4.46 ± 0.23	5.00 mM - 8.00 mM

(a) Using stopped-flow data (0.10 – 0.40 mM)⁶, (b) T₂ (0.10 – 5.00 mM), (c) and line-broadening (5.00 – 8.00 mM) techniques.

When compared to the rates obtained by T₂, we see that all of the rates are significantly larger in the stopped-flow case. This is expected due to the stopped-flow reaction being a “pseudo” (*i.e.* low-driving force) self-exchange reaction while the reaction studied by NMR is a “true” self-exchange reaction and has zero-driving force. In low-driving force reactions, the offset between the potential energy surface minima upon going from the reactants (H_{AA}) surface to the products (H_{BB}) surface slightly lowers the activation barrier for the stopped-flow reaction, and this accounts for their higher rates (since the reorganizational energy, λ , is effectively equal in these two closely-related types of ET reactions, see chapter 1, section 4).

In Table 2.10 we summarize the $\log k_{\text{ex}}$ vs. GP dependencies seen in Figure 2.25. The figure shows that the $\log k_{\text{ex}}$ vs. GP behavior measured by stopped-flow (hairline dotted) over the reactants concentration range of 0.10 mM to 0.40 mM matches fairly well with the low-concentration NMR data (dash-dot-dash line) with the slopes being 9.36 ± 0.70 and 7.75 by NMR (no error is stated with the low-

concentration NMR slope due to only 2 points being used). Interestingly, both sets of low concentration data show slightly steeper than theoretical behavior (note the heavy dashed Debye-Hückel reference line with a slope of 6.12 as produced by equation (1-40)). Looking at the full range of NMR data, we see that there are two identifiable slopes with the value dropping to 3.58 ± 0.41 in the higher reactants concentration range of 1.00 mM to 5.00 mM (as measured by T_2 , dotted line). The point at which the equimolar reactants concentration is equal to 1.00 mM would appear to be near the transition region from one slope region to the other. The dependence over the entire range also has some resemblance to the more-obviously curved dependences seen upon addition of “inert” salts at some constant reactants concentration as will be discussed in detail in later sections. The slightly smaller slope from the low-concentration T_2 measurements (as compared to stopped-flow rates) may simply be due to our having only two points to fit the T_2 data as well as the imperfect match to the stopped-flow data collection range (0.10 mM – 0.40 mM). The “late” self-salting slope from 1.00 mM – 5.00 mM as measured by T_2 is found to be 3.58 ± 0.41 . When compared with the self-salting slope of 4.46 ± 0.23 obtained using line-broadening measurements from 5.00 mM – 8.00 mM (dashed line), we see that the two slopes are nearly within error of each other. The aggregate high concentration slope is clearly lower than the expected slope of 6.12 from Debye-Hückel theory and possible reasons for this effect will be discussed further on.^{11,37}

2.13 Kinetic Salt Effects at Various (Constant) Reactant Concentrations

The rate of exchange for reaction (2-2) was measured by the ^{19}F T_2 spin-echo at constant reactant concentrations of 0.10 mM, 0.50 mM, 1.00 mM, and 5.00 mM as a function of the concentrations of various added “simple” (and supposedly inert) salts (KF, NaCl, KBr) and the disodium dicarboxylate salts Na_2muc , Na_2adip , Na_2tere , $\text{Na}_2(1,4\text{-dcch})$ as shown in Table 2.1. The early stopped-flow work has shown that Na_2muc and Na_2tere clearly act as catalytic for ET reaction (2-1) as studied by stopped-flow.^{6,9,36} The NMR kinetic results are listed in Tables 2.11 through 2.14 and illustrated in Figures 2.26 through 2.32.

The ET self-exchange reaction was first studied at a concentration of reactants of 0.10 mM so as to compare the NMR data against the largest body of previous stopped-flow⁶ data regarding salt effects on reaction (2-1). These results are presented in Table 2.11 and Figures 2.26 and 2.27. When compared to data obtained by NMR, the preliminary rates observed by stopped-flow (before any salt has been added) are significantly larger than those measured by NMR due to the accelerating effect of the non-zero driving force in the stopped-flow experiment (*vide supra*). In order to most informatively compare data between the two techniques, we must look at the *change* in the measured $\log k_{\text{ex}}$ as the concentration of added salt is increased; this is done by examining the resulting plots of $\log k_{\text{ex}}$ vs. GP. It should be noted that all of our experimentally derived $\log k_{\text{ex}}$ vs. GP salt curves were normalized to an average $\log k_{\text{ex}}$ starting value (reactants only) which was multiply-determined by a larger number (typically $N = 5$) of experiments. This was done by adjusting all the measured $\log k_{\text{ex}}$

values for a given salt run so that the initial point coincides with the highly-determined starting point (these minor, typically 2-5% adjustments were necessary to correct for jitter from run-to-run in the first point resulting from inevitable variations in reactant concentration and purities).

Table 2.11 The effect of various added salts on k_{ex} for reaction (2-2) at a reactants concentration of 0.10 mM displaying (a) raw $\log k_{\text{ex}}$ values and (b) $\log k_{\text{ex}}$ values normalized to the averaged (total N = 7) $\log k_{\text{ex}}$ starting value obtained across all trials for the initial no added salt point (with 95% confidence intervals as shown).

[KF]	GP	k_{ex}	$\log k_{\text{ex}}^{(a)}$	$\log k_{\text{ex}}^{(b)}$
0	0.0291	2060	3.313	3.318 ± 0.051
0.0005	0.0361	2270	3.356	3.361
0.0010	0.0418	2550	3.407	3.412
0.0020	0.0511	2770	3.442	3.447
0.0050	0.0713	3680	3.565	3.570
0.0120	0.1020	3820	3.582	3.587
0.0200	0.1263	4270	3.630	3.635
[NaCl]	GP	k_{ex}	$\log k_{\text{ex}}^{(a)}$	$\log k_{\text{ex}}^{(b)}$
0	0.0291	2450	3.388	3.318 ± 0.051
0.001	0.0418	3110	3.492	3.422
0.002	0.0511	5000	3.698	3.628
0.005	0.0713	9590	3.982	3.912
0.012	0.1020	19250	4.284	4.214
0.020	0.1263	29510	4.470	4.400
[KBr]	GP	k_{ex}	$\log k_{\text{ex}}^{(a)}$	$\log k_{\text{ex}}^{(b)}$
0	0.0291	2060	3.315	3.318 ± 0.051
0.001	0.0418	3610	3.557	3.560
0.002	0.0511	5630	3.751	3.754
0.005	0.0713	11130	4.047	4.050
0.012	0.1020	30580	4.485	4.488
0.020	0.1263	46960	4.671	4.674
[Na ₂ muc]	GP	k_{ex}	$\log k_{\text{ex}}^{(a)}$	$\log k_{\text{ex}}^{(b)}$
0	0.0291	2540	3.404	3.318 ± 0.051
0.00028	0.0400	6230	3.794	3.708
0.00083	0.0550	9620	3.983	3.897
0.00180	0.0735	14250	4.154	4.068
0.00400	0.1020	20690	4.316	4.230
0.00600	0.1209	24650	4.392	4.306

[Na₂adip]	GP	k_{ex}	logk_{ex}^(a)	logk_{ex}^(b)
0	0.0291	2610	3.417	3.318 ± 0.051
0.00083	0.0550	7240	3.860	3.761
0.00180	0.0735	11780	4.071	3.972
0.00400	0.1020	17320	4.239	4.140
0.00600	0.1200	18910	4.277	4.178
[Na₂tere]	GP	k_{ex}	logk_{ex}^(a)	logk_{ex}^(b)
0	0.0291	1900	3.279	3.318 ± 0.051
0.00028	0.0400	3460	3.539	3.578
0.00083	0.0550	7020	3.846	3.885
0.00180	0.0735	12070	4.082	4.121
0.00400	0.1020	18080	4.257	4.296
0.00600	0.1209	21170	4.326	4.365
[Na₂(1,4-dcch)]	GP	k_{ex}	logk_{ex}^(a)	logk_{ex}^(b)
0	0.0291	1540	3.187	3.318 ± 0.051
0.00028	0.0400	2990	3.476	3.607
0.00083	0.0550	4240	3.628	3.759
0.00180	0.0735	5830	3.766	3.897
0.00400	0.1020	9440	3.975	4.106
0.00600	0.1209	11040	4.043	4.174

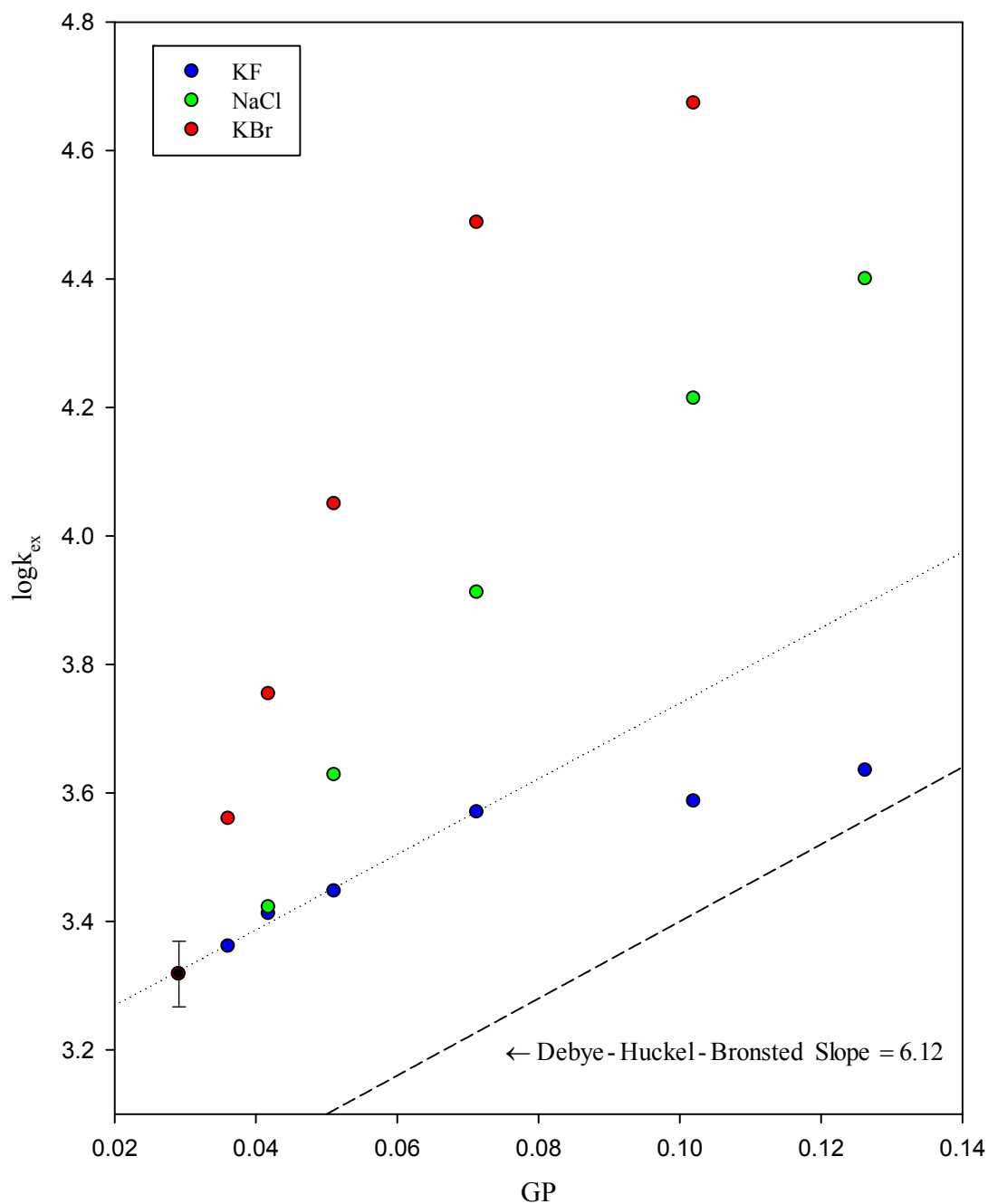


Figure 2.26 The effect of added KF (blue circles), NaCl (green circles), and KBr (red circles) on the measured k_{ex} for reaction (2-2) at 0.10 mM reactants. Only the “low” GP end of the KF data (slope = 5.9 ± 0.3) behaves in accordance with the predicted Debye-Hückel-Bronsted slope of 6.12.

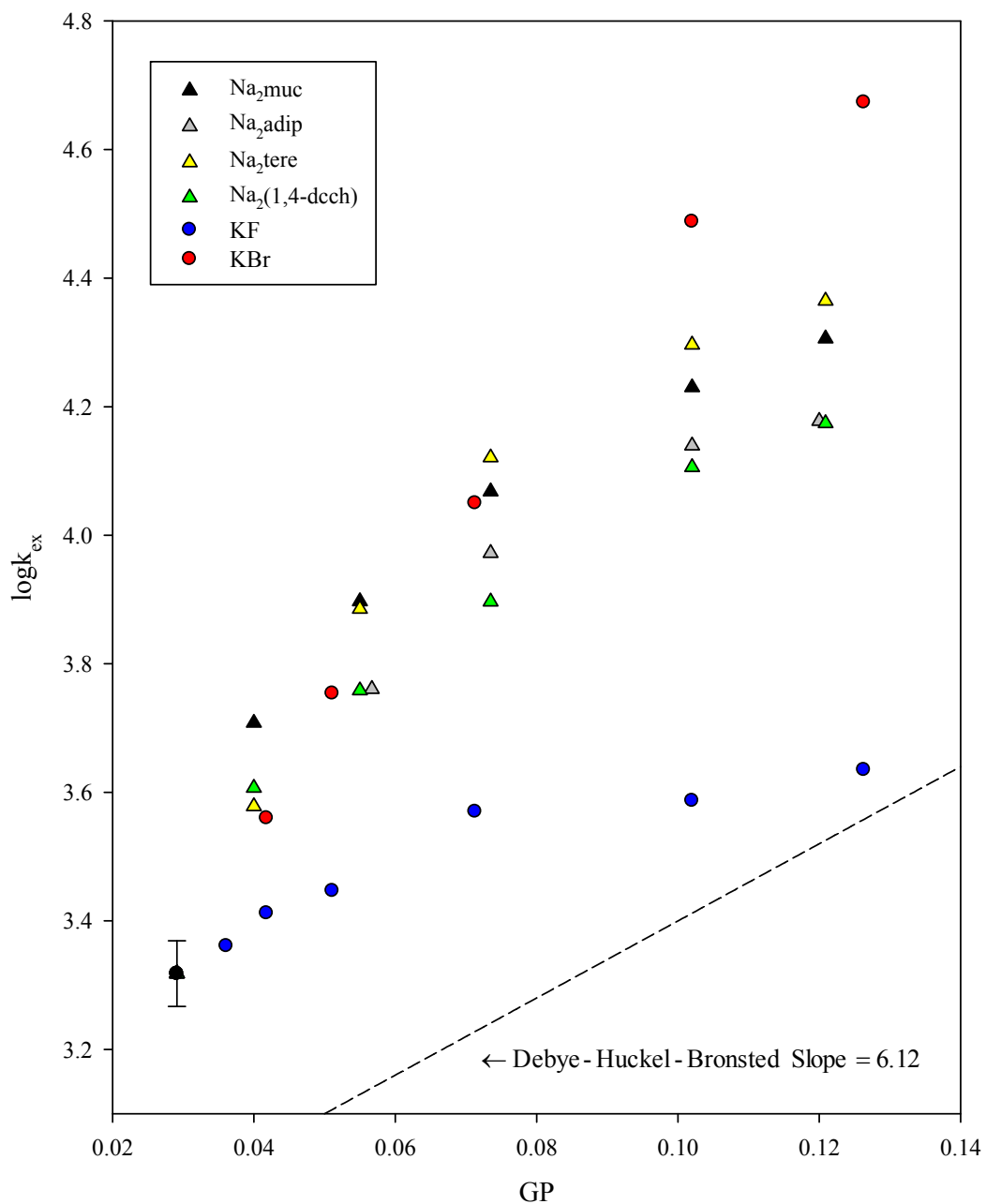


Figure 2.27 The effect of added Na_2muc (black triangles), Na_2adip (grey triangles), Na_2tere (yellow triangles), $\text{Na}_2(1,4\text{-dcch})$ (green triangles), KF (blue circles), and KBr (red circles) on the k_{ex} for reaction (2-2) at 0.10 mM reactants.

The F^- ion data were unique in that they exhibited linear behavior with a slope in agreement with classical Debye-Hückel theory over the range from $[KF] = 0 \text{ M}$ to 0.005 M ($GP = 0.0291$ to 0.0713). Our slope was 5.9 ± 0.3 , which is within error of both the theoretical Debye-Hückel-Bronsted slope of 6.12 , as well as the slope arrived at by previous stopped-flow work which was 6.2 ± 0.1 .^{6,11}

This now doubly-verified agreement with theory (by both stopped-flow and by NMR) is important because it establishes that the reactant concentration of 0.10 mM and the added-salt ranges of 0.50 mM to 5.00 mM with fluoride appears to behave in a way which matches the assumptions underlying the Debye-Hückel treatment and Guggenheim approximation (see chapter 1, section 7). This will now serve as the foundation from which we will describe our measured systematic deviations from theory observed with other (non-fluoride) supposedly “inert” salts. From here, we will go on to show salt effects on k_{ex} that also progressively deviate from theory upon increasing the reactants concentrations (even in the case of fluoride).¹¹

As we move to added Cl^- and Br^- salts, the $\log k_{ex}$ vs. GP plots become obviously curved, but we can still quantitate the “early” and “late” slopes for these anions for purposes of comparison. For chloride the early slope (as taken from the first four points in Figure 2.26) is 14.6 ± 1.4 and for bromide the early slope (first three points) is 19.8 ± 0.5 . In the previous stopped-flow work,⁶ the early slopes for Cl^- and Br^- were 14.4 ± 0.5 and 20.6 ± 1.2 , so we see again that the agreement between the two techniques is very good.

The rate effect data for the addition of the dicarboxylate salts (structures shown in Table 2.1) are also listed in Table 2.11 and are displayed in Figure 2.27 (with KF and KBr data still displayed as a visual reference). From the figure, we see that the dependences again give curved lines with the accelerations due to added adipate and 1,4-dicarboxycyclohexane falling somewhat below the muconate and terephthalate data. The differences over the entire range of GP, however, are just barely larger than the combined error limits, and none are as catalytic as bromide after $GP > 0.09$. These data were also compared to the stopped-flow data collected at the same reactants concentration.^{6,7,9} The early slopes for plots of $\log k_{\text{ex}}$ vs. GP (taken from the first 3 to 4 points) were found to be in good agreement for the adipate (adip^{2-}), terephthalate (tere^{2-}), and 1,4-dicarboxycyclohexane ($1,4\text{-dcch}^{2-}$) anions.⁹ By NMR, the early slope for the adip^{2-} anion was 14.9 ± 0.9 , and by stopped-flow it was 15.4 ± 0.5 .⁹ The early slope for the tere^{2-} anion was 21.8 ± 1 by NMR and was 27.8 ± 5.7 by stopped-flow. This would suggest less catalytic activity for tere^{2-} in the NMR case. For the $1,4\text{-dcch}^{2-}$ anion the early slope was 26.5 by NMR, but this was only in fair agreement with the stopped-flow work which yielded an early slope of 19.5 (no error is reported regarding the early slopes of the $\text{Na}_2(1,4\text{-dcch})$ data due to only the first two points being used to fit the data).

In the previously-unique case of muconate however, the rate acceleration measured by NMR deviated very strongly downward from the strong catalysis which was observed previously by stopped-flow (see Figure 2.4). For the muconate anion (muc^{2-}), the early slope measured by NMR was 35.8 while the early slope obtained by

stopped-flow was nearly three times as large at 102.9. This striking difference does not invalidate the NMR data presented here, nor does it cast doubt on the stopped-flow data (since the dramatic rate acceleration caused by muconate in the stopped-flow context has now been measured by multiple workers^{6,12,36,38,39}). Rather, this difference appears to point toward an interesting and surprising role being played by the *magnetic field itself*, and this development will be discussed in more detail further on.

These early-slope calculations will be used here simply as a quick index of a given salt's level of catalytic efficacy towards our ET reaction and are thus only useful as a crude guide. In a later section we will show how a detailed kinetic analysis and fitting of the entire $\log k_{\text{ex}}$ vs. GP *curve* using an extended kinetic model allows us to access directly the extent to which a particular anion modulates the quantity " k_{ETX} " (*vide infra*), which is the anion-enhanced version of the k_{ET} rate constant for electron-transfer now inside of a presumed tertiary-molecular encounter complex rather than the simple precursor complex as discussed previously in chapter 1.

Salt effects on reaction (2-2) were also studied at an equimolar reactant concentration of 0.50 mM, and these rate data are listed in Table 2.12 and displayed in Figures 2.28 and 2.29. As was done in the 0.10 mM reactants concentration case, the early slopes of the $\log k_{\text{ex}}$ vs. GP plots were measured and compared. As in our treatment of the added-salt data in the 0.10 mM reactants case, the experimentally measured $\log k_{\text{ex}}$ values from each run were normalized to the average $\log k_{\text{ex}}$ values obtained ($N \approx 5$) with no salt added.

Table 2.12 The effect of various added salts on k_{ex} for reaction (2-2) at a reactants concentration of 0.50 mM displaying (a) raw $\log k_{\text{ex}}$ values and (b) $\log k_{\text{ex}}$ values normalized to the averaged (total N = 5) $\log k_{\text{ex}}$ starting value obtained across trials for the initial, no-added salt point (with 95% confidence intervals as shown).

[KF]	GP	k_{ex}	$\log k_{\text{ex}}^{(a)}$	$\log k_{\text{ex}}^{(b)}$
0	0.0629	3660	3.563	3.580 ± 0.039
0.001	0.0690	3960	3.598	3.615
0.005	0.0888	4290	3.632	3.649
0.010	0.1075	4960	3.696	3.713
0.030	0.1566	6420	3.807	3.824
0.060	0.2025	7850	3.895	3.912
[NaCl]	GP	k_{ex}	$\log k_{\text{ex}}^{(a)}$	$\log k_{\text{ex}}^{(b)}$
0	0.0629	3490	3.543	3.580 ± 0.039
0.001	0.0690	4080	3.610	3.647
0.005	0.0888	7650	3.884	3.921
0.010	0.1075	12120	4.084	4.121
0.030	0.1566	31530	4.499	4.536
0.060	0.2025	59330	4.773	4.810
[KBr]	GP	k_{ex}	$\log k_{\text{ex}}^{(a)}$	$\log k_{\text{ex}}^{(b)}$
0	0.0629	3870	3.588	3.580 ± 0.039
0.001	0.0690	5420	3.734	3.726
0.005	0.0888	13840	4.141	4.133
0.010	0.1075	23750	4.376	4.368
0.030	0.1566	59210	4.772	4.764
0.060	0.2025	100470	5.002	4.994
[Na ₂ muc]	GP	k_{ex}	$\log k_{\text{ex}}^{(a)}$	$\log k_{\text{ex}}^{(b)}$
0	0.0629	4250	3.628	3.580 ± 0.039
0.00035	0.0693	6200	3.792	3.744
0.00160	0.0880	11070	4.044	3.996
0.00330	0.1071	14460	4.160	4.112
0.01000	0.1566	21620	4.335	4.287
0.02000	0.2025	29540	4.470	4.422

[Na₂adip]	GP	k_{ex}	logk_{ex}^(a)	logk_{ex}^(b)
0	0.0629	3770	3.577	3.580 ± 0.039
0.00035	0.0693	4550	3.658	3.661
0.00160	0.0880	7160	3.855	3.859
0.00330	0.1071	8640	3.937	3.940
0.01000	0.1566	13060	4.116	4.119
0.02000	0.2025	15420	4.182	4.186

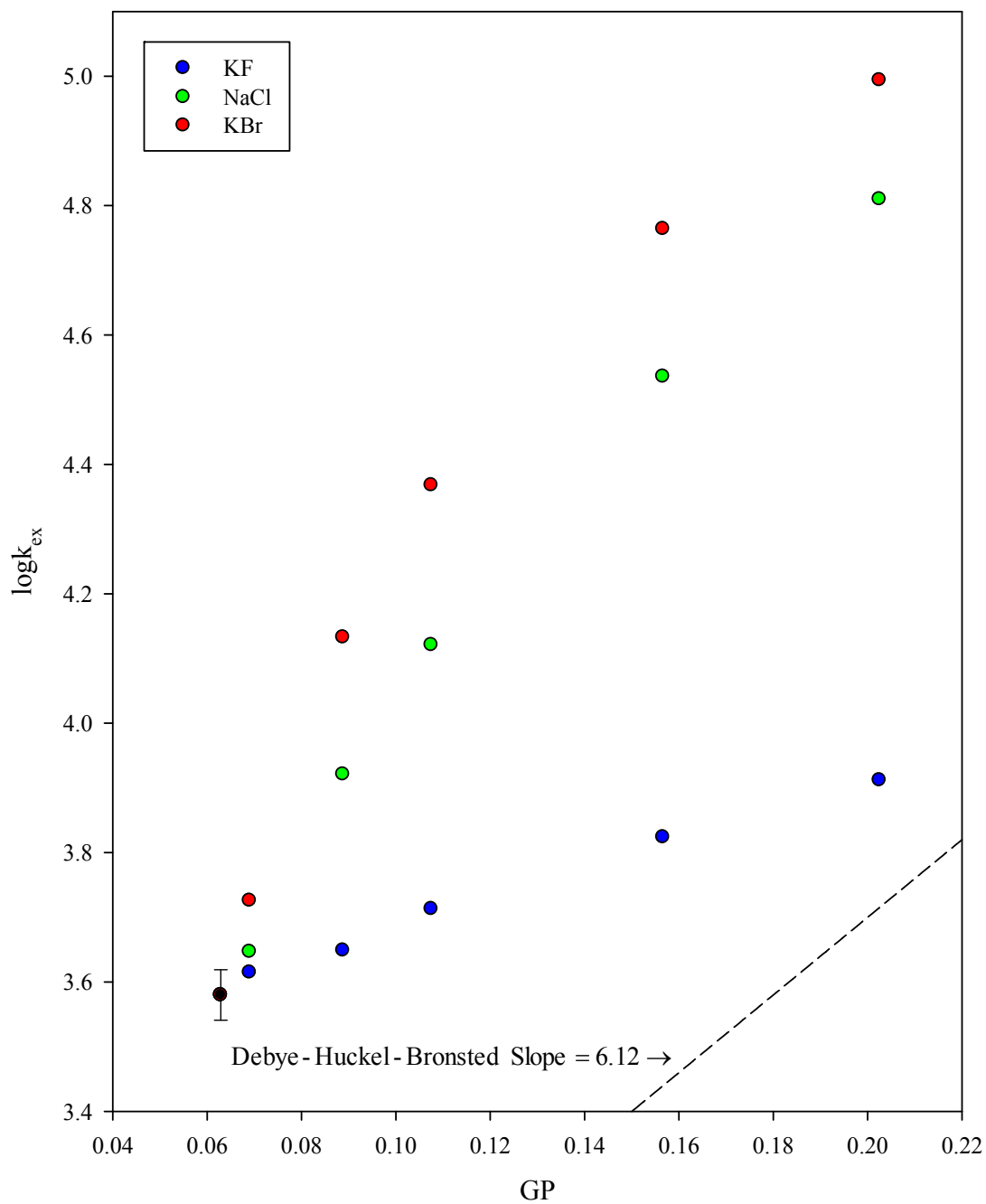


Figure 2.28 The effect of added KF (blue circles), NaCl (green circles), and KBr (red circles) on the measured $\log k_{\text{ex}}$ for reaction (2-2) at 0.50 mM reactants.

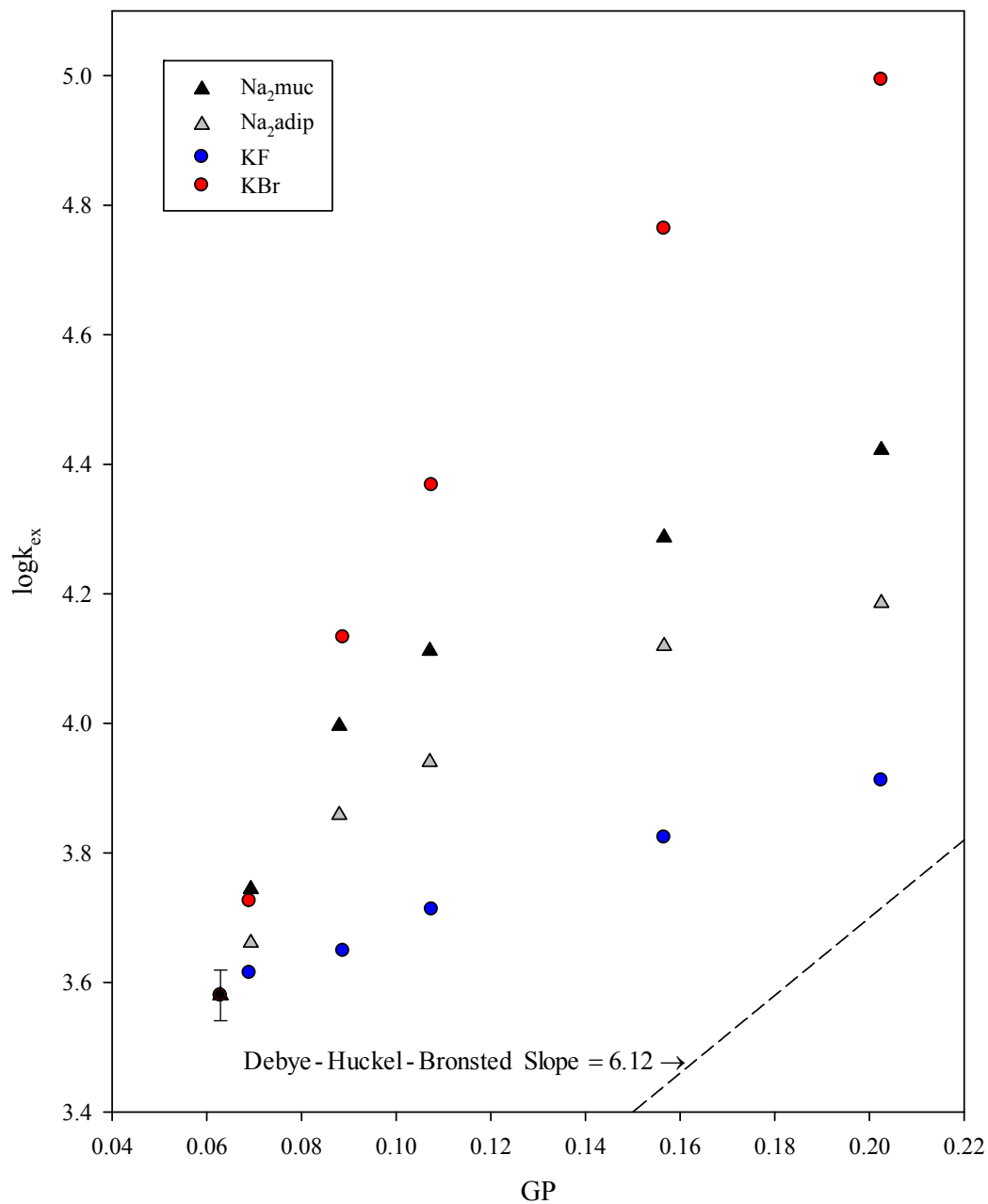


Figure 2.29 The effect of added Na₂muc (black triangles), Na₂adip (grey triangles) on the measured $\log k_{\text{ex}}$ for reaction (2-2) at 0.50 mM reactants (with KF (blue circles), and KBr (red circles) included for visual reference).

At this reactants concentration, we found that *no* anion exhibited a slope (in the early and presumably most-ideal part of the curve) which agreed with the theoretical Debye-Hückel-Bronsted slope of 6.12, and the early slopes all decreased significantly with this 5-fold increase in reactants concentration for F^- and Cl^- . The early slope for fluoride decreased from 5.9 ± 0.3 (0.10 mM reactants concentration) to 2.8 ± 0.3 . For chloride, the early slope fell from 14.6 ± 1.4 (0.10 mM reactants concentration) to 12.4 ± 0.3 . Bromide was unique in that it showed a slight increase from 19.8 ± 0.5 (0.10 mM reactants concentration) to 21.1 ± 0.7 (with the two slopes being essentially within error of each other).

The salt effects due to added sodium muconate and its saturated analog sodium adipate, also decreased as in the simple salt cases. For Na_2muc the early slope diminished from 35.8 (at 0.10 mM reactants) to 15.9 ± 2.5 , and the early slope for Na_2adip curve also decreased from 14.9 ± 0.9 to 11 ± 0.4 .

In order to further explore the effect of the reactants concentrations, reaction (2-2) was next studied at a reactants concentration of 1.00 mM. The rate data are listed in Table 2.13 and displayed in Figure 2.30. Again, all experimentally derived $\log k_{ex}$ values were normalized to the average ($N = 5$) $\log k_{ex}$ starting value (no salt added). Here we found that the kinetic salt effects were indeed further diminished upon doubling the reactants concentration to 1.00 mM (which can again be illustrated by taking the early slopes of the $\log k_{ex}$ vs. GP plots).

Table 2.13 The effect of various added salts on k_{ex} for reaction (2-2) at a reactants concentration of 1.00 mM displaying (a) raw $\log k_{\text{ex}}$ values and (b) $\log k_{\text{ex}}$ values normalized to the averaged (total N = 5) $\log k_{\text{ex}}$ starting value obtained across all trials for the initial no-added salt point (with 95% confidence intervals as shown).

[KF]	GP	k_{ex}	$\log k_{\text{ex}}^{(a)}$	$\log k_{\text{ex}}^{(b)}$
0	0.0866	4890	3.689	3.708 ± 0.024
0.006	0.1091	6310	3.800	3.819
0.030	0.1649	8280	3.918	3.937
0.100	0.2482	10960	4.040	4.059
0.200	0.3137	13500	4.130	4.149
[NaCl]	GP	k_{ex}	$\log k_{\text{ex}}^{(a)}$	$\log k_{\text{ex}}^{(b)}$
0	0.0866	5480	3.739	3.708 ± 0.024
0.002	0.0949	6630	3.822	3.791
0.006	0.1091	8440	3.926	3.895
0.010	0.1211	11990	4.079	4.048
0.030	0.1649	22540	4.353	4.322
0.060	0.2080	39850	4.600	4.569
0.100	0.2482	68220	4.834	4.803
[KBr]	GP	k_{ex}	$\log k_{\text{ex}}^{(a)}$	$\log k_{\text{ex}}^{(b)}$
0	0.0866	4940	3.694	3.708 ± 0.024
0.006	0.1091	12919	4.110	4.124
0.030	0.1649	53031	4.725	4.739
0.100	0.2482	150530	5.178	5.192
[Na ₂ muc]	GP	k_{ex}	$\log k_{\text{ex}}^{(a)}$	$\log k_{\text{ex}}^{(b)}$
0	0.0866	5110	3.709	3.708 ± 0.024
0.0007	0.0953	7320	3.865	3.864
0.0020	0.1091	9170	3.963	3.962
0.0033	0.1209	11430	4.058	4.057
0.0100	0.1649	13600	4.133	4.132
0.0200	0.2080	16300	4.212	4.211

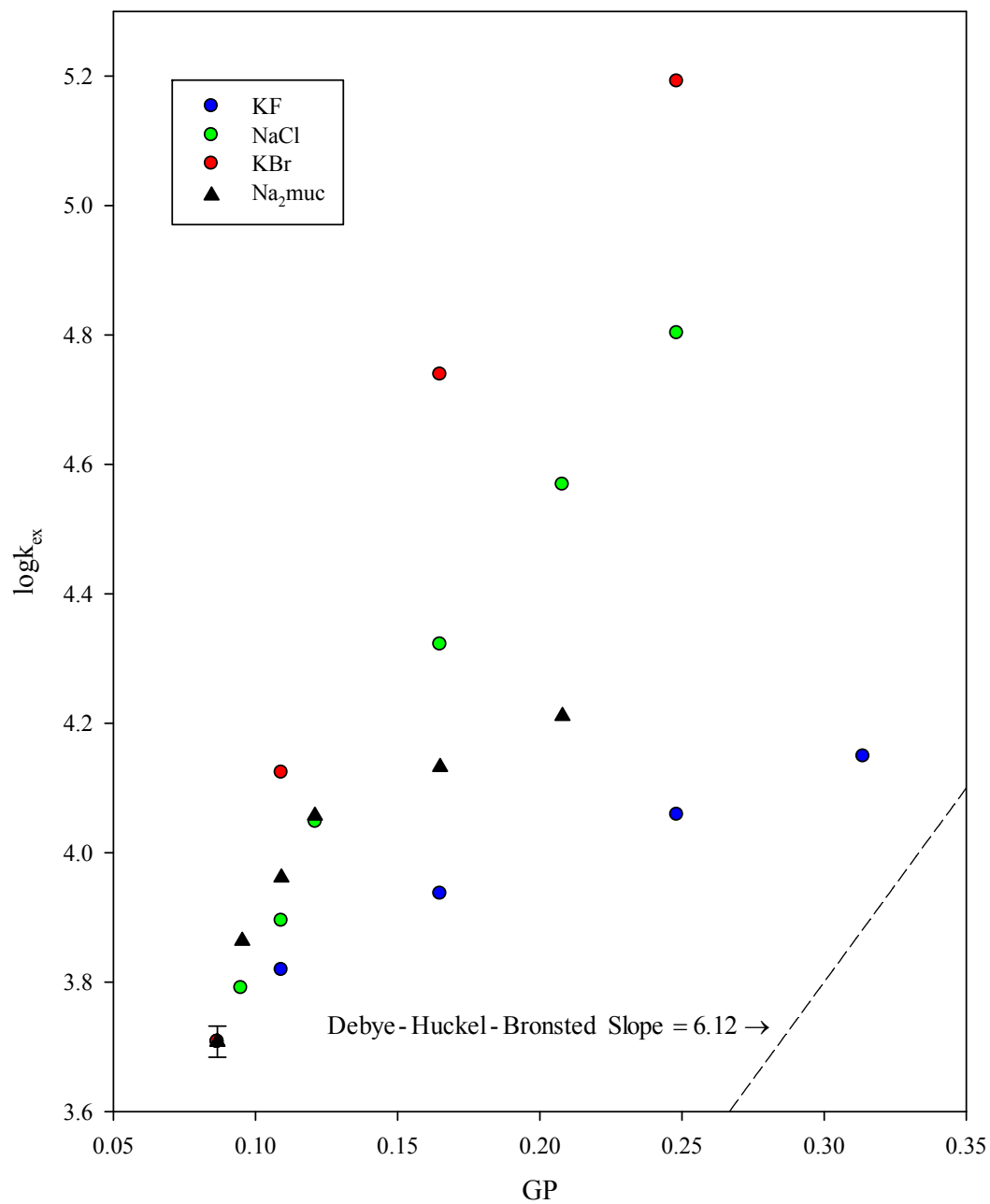


Figure 2.30 The effect of added KF (blue circles), NaCl (green circles), KBr (red circles), and Na_2muc (black triangles) on the measured $\log k_{\text{ex}}$ for reaction (2-2) at 1.00 mM reactants.

As was the case at reactants concentrations of 0.10 mM and 0.50 mM, the fluoride ion exhibited linear behavior over a significant range (see Figures 2.26 and 2.28), but now it was only in the latter part. The early slope for fluoride which had been 2.8 ± 0.3 (0.50 mM reactant concentration) decreased to 1.8 ± 0.2 . For chloride the early slope fell from 12.4 ± 0.5 (0.50 mM reactant concentration) to 9.5 ± 0.8 , and for bromide it reduced from 21.1 ± 0.7 to 12.8 ± 1.7 . In the case of Na₂muc, the early slope decreased from 15.9 ± 2.5 to now 9.7 ± 1.4 .

Lastly, salt effects on reaction (2-2) were measured at 5.00 mM reactants (again using the ¹⁹F T₂ spin-echo method) and the results are listed in Table 2.14 and displayed in Figures 2.31 and 2.32. As will be shown and discussed later, previous data obtained by ¹⁹F NMR line-broadening⁸ studies of reaction (2-2) at this concentration are also available, and these will allow for direct comparison between rate behaviors mapped out using both methods.

Table 2.14 The effect of various salts on k_{ex} for reaction (2-2) at a reactants concentration of 5.00 mM displaying (a) raw $\log k_{\text{ex}}$ values and (b) $\log k_{\text{ex}}$ values normalized to the averaged (total N = 5) $\log k_{\text{ex}}$ starting value obtained across all trials for the initial no-added salt point (with 95% confidence intervals as shown).

[KF]	GP	k_{ex}	$\log k_{\text{ex}}^{(a)}$	$\log k_{\text{ex}}^{(b)}$
0	0.175	10500	4.021	4.039 ± 0.052
0.03	0.215	12250	4.088	4.106
0.07	0.253	12800	4.107	4.125
0.14	0.301	13330	4.125	4.143
0.40	0.400	14240	4.154	4.172
[NaCl]	GP	k_{ex}	$\log k_{\text{ex}}^{(a)}$	$\log k_{\text{ex}}^{(b)}$
0	0.175	10530	4.022	4.039 ± 0.052
0.03	0.215	26850	4.423	4.440
0.07	0.253	35030	4.544	4.561
0.14	0.301	69470	4.842	4.859
[KBr]	GP	k_{ex}	$\log k_{\text{ex}}^{(a)}$	$\log k_{\text{ex}}^{(b)}$
0	0.175	10240	4.010	4.039 ± 0.052
0.03	0.215	37700	4.576	4.605
0.07	0.253	64220	4.808	4.837
0.14	0.301	159980	5.204	5.233
[Na ₂ muc]	GP	k_{ex}	$\log k_{\text{ex}}^{(a)}$	$\log k_{\text{ex}}^{(b)}$
0	0.175	10380	4.016	4.039 ± 0.052
0.01	0.215	16920	4.228	4.251
0.02	0.245	18880	4.276	4.299
0.05	0.306	20120	4.304	4.327
0.13	0.397	25460	4.406	4.429
[Na ₂ adip]	GP	k_{ex}	$\log k_{\text{ex}}^{(a)}$	$\log k_{\text{ex}}^{(b)}$
0	0.175	8560	3.932	4.039 ± 0.052
0.01	0.215	11320	4.054	4.161
0.02	0.245	12640	4.102	4.208
0.05	0.306	14010	4.146	4.253
0.13	0.397	15790	4.198	4.305

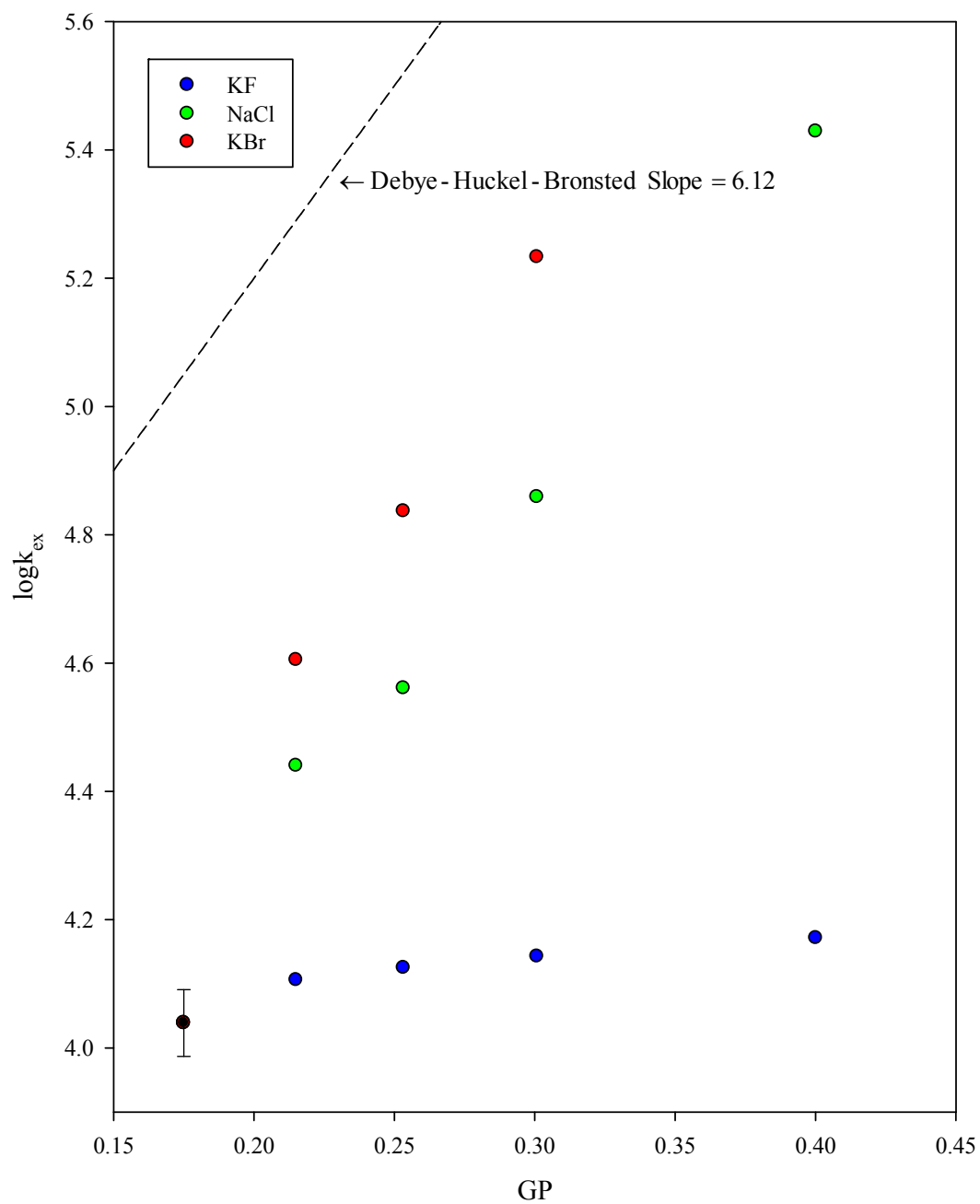


Figure 2.31 The effect of added KF (blue circles), NaCl (green circles), and KBr (red circles) on the measured $\log k_{\text{ex}}$ for reaction (2-2) at 5.00 mM reactants.

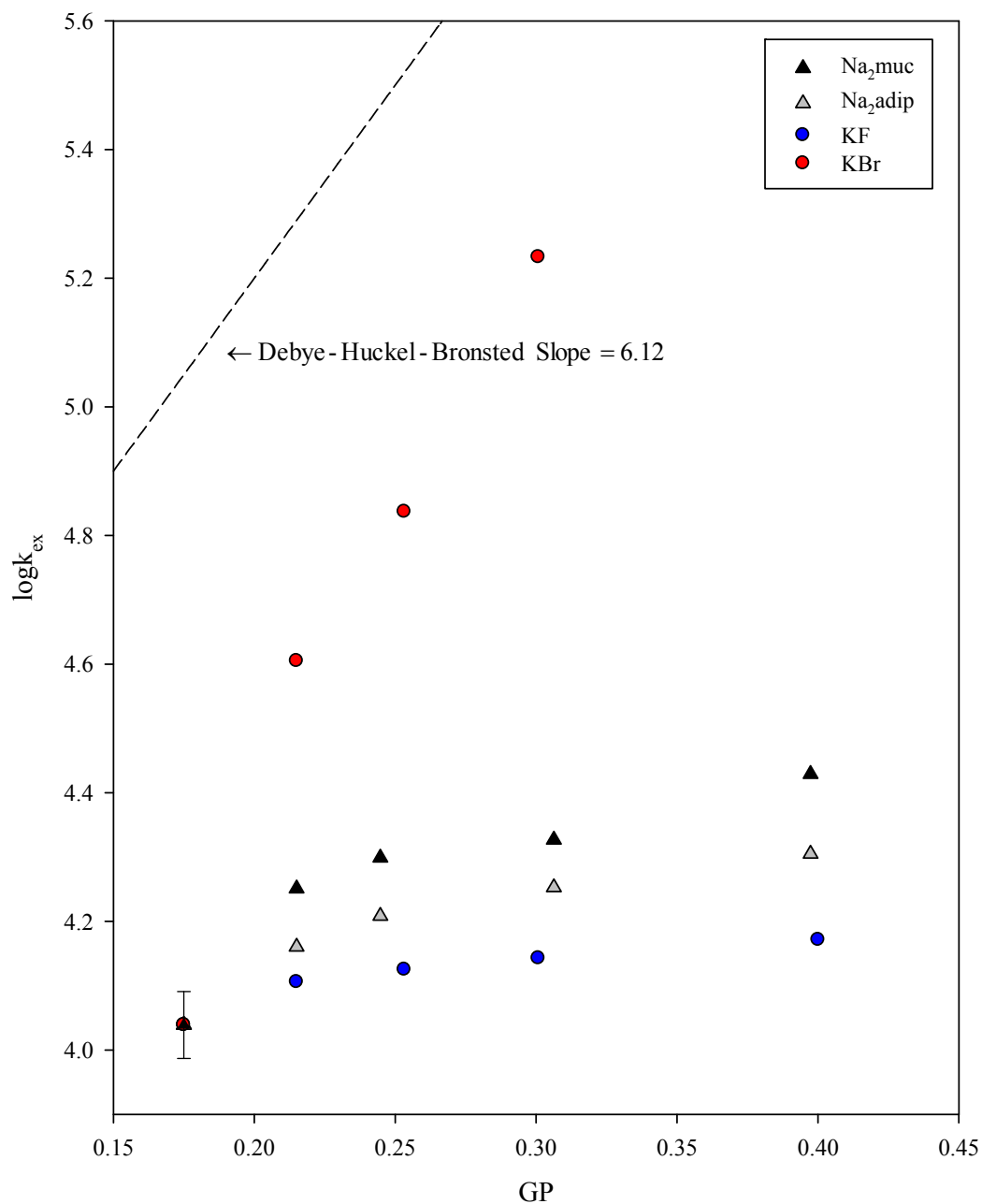


Figure 2.32 The effect of added Na₂muc (black triangles), Na₂adip (grey triangles), KF (blue circles), and KBr (red circles) on the measured $\log k_{\text{ex}}$ for reaction (2-2) at 5.00 mM reactants.

Here we see that the kinetic salt effects decrease again as the concentration of reactants is quintupled to 5.00 mM from 1.00 mM. Both the fluoride and chloride data exhibit linear behavior in their latter ranges, while all the ions continue to follow the same qualitative ranking in catalytic effect size as was observed at the reactant concentrations ($F^- < \text{adip}^{2-} \sim \text{muc}^{2-} < Cl^- < Br^-$). The fluoride slope from 1.8 ± 0.2 (1.00 mM reactants) to now 0.52 ± 0.14 . We note that the slope of the previous fluoride ion data gathered from ^{19}F NMR line-broadening (also with an equimolar reactant concentration of 5.00 mM)⁸ was 0.92 ± 0.05 , thus the measured early slopes are almost within error of each other.

The slope across the linear range of the chloride data drops from 9.5 ± 0.8 at 1.00 mM reactants concentration to now 5.92 ± 0.4 , which is within error of the Debye-Hückel-Bronsted slope of 6.12.¹¹ However, we see that the “early” slope using the first two points is 10.0. The previous chloride data gathered by ^{19}F NMR line-broadening at this concentration had an early slope of 8.2 ± 0.6 . The larger slope in the case of the ^{19}F NMR line-broadening data is due to the slight curvature the chloride data obtained by line-broadening (and therefore only the first few points were used to obtain the early slope). This deviation is probably due to the lesser accuracy and precision of the line-broadening method in this case. This is the only other case besides F^- at 0.10 mM in which a significant linear range in $\log k_{\text{ex}}$ vs. GP is observed in quantitative agreement with the Debye-Hückel-Bronsted slope, but given the non-linearity at the start, it is impossible to interpret as actually “following” the Debye-Huckel-Bronsted prediction.

The early slope for bromide drops from 12.8 ± 1.7 (1.00 mM reactants) to 10.2 ± 2.3 at 5.00 mM reactants. This slope is also within error of the previous bromide ion data gathered through ^{19}F NMR line-broadening which was 10.7 ± 0.7 .

Sodium muconate and its saturated analog sodium adipate exhibited similar decreases in rate acceleration found with the simple salts. The early slope of Na_2muc , dropped from 9.7 ± 1.4 (1.00 mM reactant concentration) to 3.8 ± 1.0 at 5.00 mM reactants (the line-broadening study gave an early slope of 3.8 ± 0.5). The early slope of Na_2adip which had been 11.0 ± 0.4 at 0.50 mM reactants fell to 2.5 ± 0.4 at 5.00 mM reactants. The early slope found using line-broadening was 2.6 ± 1.0 .

The generally close agreement between results acquired by the T_2 and line-broadening based measures of these kinetic salt effects systematic deviations from Debye-Hückel-Bronsted theory appear to start around an equimolar reactant concentration between 0.10 mM and 1.00 mM.

To summarize the foregoing results, we have listed the observed early slopes of the plots of $\log k_{\text{ex}}$ vs. GP for the various salts in Table 2.15. We focus on these since, as we will show in later sections, deviations upwards from the Debye-Hückel-Bronsted prediction of 6.1 correlate with the degree of “ET catalysis” exhibited by a given salt. One explanatory hypothesis we will discuss later for the drop in salt effects with increased reactants concentrations is that the progressive decrease in distance through which the Ru^{II} and Ru^{III} species must diffuse in order to form the ET precursor complex somehow invalidates the assumptions underlying the Debye-Hückel-Bronsted equation (see equation (1-40)). Even so, all added salts showed

significant and measureable catalytic effects on the rate of reaction (2-2) even at 5.00 mM reactants.

Table 2.15 A summary of the measured early slopes for plots of $\log k_{\text{ex}}$ vs. GP for reaction (2-2) due to added inert salts at the various reactant concentrations investigated.

Salt	Early Slopes from $\log k_{\text{ex}}$ vs. GP			
	0.10 <u>mM</u>	0.50 <u>mM</u>	1.00 <u>mM</u>	5.00 <u>mM</u>
KF	5.9 ± 0.3	2.8 ± 0.3	1.8 ± 0.2	0.52 ± 0.14
NaCl	14.6 ± 1.4	12.4 ± 0.3	9.5 ± 0.8	5.92 ± 0.4
KBr	19.8 ± 0.5	21.1 ± 0.7	12.8 ± 1.7	10.2 ± 2.3
Na ₂ muc	35.8	15.9 ± 2.5	9.7 ± 1.4	3.8 ± 1
Na ₂ adip	14.9 ± 0.9	11.0 ± 0.4	-	2.5 ± 0.4

2.14 Sodium Muconate Effects on the Rate of ET as Established by NMR

As already mentioned, previous stopped-flow work^{1,6,7} has reproducibly shown sodium muconate, in particular, to possess a uniquely-large catalytic effect on the rate of ET for reaction (2-1) at reactants concentration ranges in the region near 0.10 mM (which is where stopped-flow has optimum applicability in this case). The higher reactants concentrations of reactants (*e.g.* 1.00 – 8.00 mM) cannot be probed conventionally by stopped-flow due to its limited temporal resolution ($k_{\text{ex}} < \sim 10^3 \text{ s}^{-1}$). Surprisingly, even upon pushing the limits (of signal to noise) for T₂ based NMR kinetics measurements on reaction (2-2) down to the stopped-flow concentration range of 0.10 mM, the loss of ET catalysis by muconate first documented by Inagaki³⁶ and then verified by Qin⁸ using NMR line-broadening at equimolar reactants concentrations of 5.00 mM was found to persist. The magnitude of this

striking discrepancy between stopped-flow and T_2 NMR based measurements of the “muconate effect” at 0.10 mM reactants is illustrated in Figure 2.33.

We note also that while the data shown in Figure 2.27 leaves open the possibility for a very slight rate acceleration by tere^{2-} as compared to dcch^{2-} and adip^{2-} , it is at or near the noise level. In the stopped-flow work, however, it has been amply demonstrated^{6,36} that tere^{2-} is also significantly catalytic towards ET, though considerably less-so than muc^{2-} .

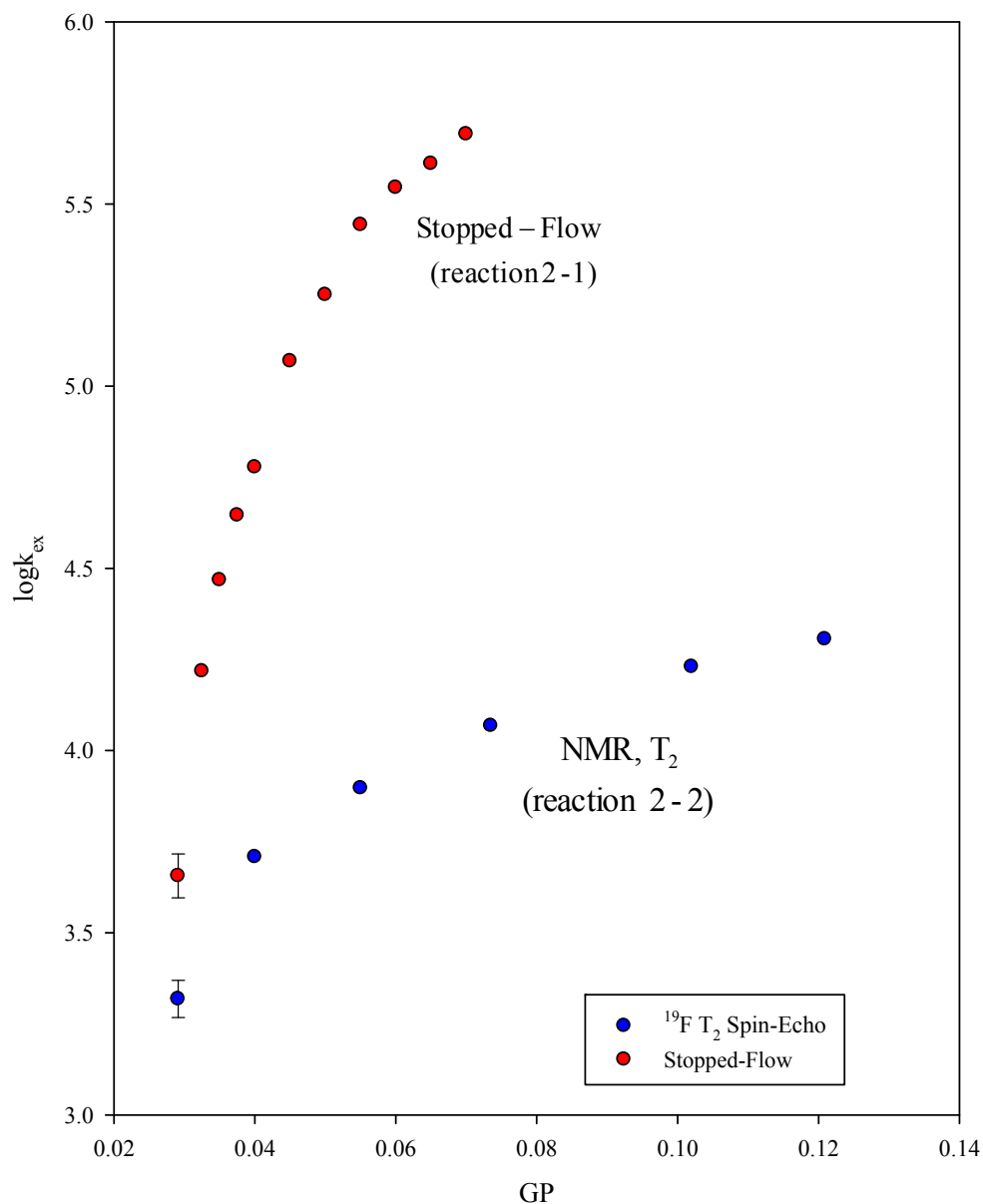


Figure 2.33 The catalytic effect of added Na_2muc on the rate of ET for the pseudo self-exchange reaction (2-1) as measured by stopped-flow⁶ (red circles) compared to its relatively-muted “normal salt” effect on the rate of reaction (2-2) measured using T_2 spin relaxation. Both experiments executed at the equimolar reactants concentration of 0.10 mM. The offset between the origin points at 0.0291 GP is due to the 65 mV driving force in reaction (2-1).

It was originally thought that the diminished catalytic effect of muconate observed by NMR 5.00 mM reactants was due to how the 50x concentration difference of the reactants changed the details of inter-reactant diffusive encounter to form a presumably tertiary-molecular encounter/precursor complex relevant to the catalyzed reaction. It was hypothesized that the “rod-like” shape of muconate might lead to especially-slow diffusion in solution and hence an early “drop out” of its catalytic effect on ET (thought to operate *via* quantum super-exchange mediation) at high reactant concentrations where the bimolecular encounter frequency between Ru^{II} and Ru^{III} naturally increases (by $\sqrt[3]{50}$ fold upon going from 0.10 mM to 5.00 mM reactants). Importantly, using the T₂ spin-echo technique, we have recovered here the same “nominal” muconate salt effect as was found using ¹⁹F NMR line-broadening⁸ at a reactants concentration of 5.00 mM. The T₂-based rate data rate data at 0.10 mM reactants show conclusively that the robust catalytic efficacy of sodium muconate seen by stopped-flow at 0.10 mM reactants is *not* regained (this comparison having only been possible due to careful optimization and validation of the T₂ spin-echo experiment). Therefore, we are forced to abandon our prior hypothesis implicating details of reactants concentration on diffusive encounter frequency as a possible basis for the “missing muconate effect” when the kinetic are probed by NMR.

After eliminating the reactant concentrations as a possible source of the loss of catalytic efficacy by muconate in the NMR work, we examined other possible factors which might explain it. These included solvent isotope and dissolved oxygen effects. To check for the former possibility, Eskandari¹² had already studied reaction (2-1)

by stopped-flow in both H₂O and D₂O and it was determined that D₂O had no affect on the strong catalytic efficacy of sodium muconate. There was no difference found in either the starting point or the effect on the rate of exchange when using D₂O instead of H₂O as the solvent. Even though no isotopic effect was found by stopped-flow the possibility of an isotope effect still had to be investigated as a possible factor in the puzzle presented by the NMR work. In Table 2.16 and Figure 2.34 the observed rates of reaction (2-2) in H₂O at various concentrations of added sodium muconate are compared to the rates obtained in D₂O. From the figure we see that while the rate acceleration may be marginally faster in H₂O, the rates at a given GP are still within error; therefore we conclude that solvent isotope effects are unrelated to the loss of the catalytic effect of muconate.

Table 2.16 The rates of ET for to reaction (2-2) at a reactants concentration of 0.10 mM using the ¹⁹F T₂ spin-echo method.

[Na ₂ muc]	GP	logk _{ex} (H ₂ O) ^(a)	logk _{ex} (H ₂ O) ^(b)	logk _{ex} (D ₂ O) ^(c)
0	0.0291	3.340	3.318 ± 0.051	3.318 ± 0.051
0.00028	0.0400	-	-	3.708
0.00083	0.0550	4.024	4.002	3.897
0.00180	0.0735	4.170	4.148	4.068
0.00400	0.1020	4.324	4.302	4.230
0.00600	0.1209	-	-	4.306

(a) Raw logk_{ex} values obtained in H₂O and (b) normalized H₂O logk_{ex} values shifted to match the average logk_{ex} starting value in D₂O (with 95% confidence intervals). This is then compared with (c) normalized logk_{ex} values to the average (total N = 5) logk_{ex} starting value with 95% confidence intervals in D₂O.

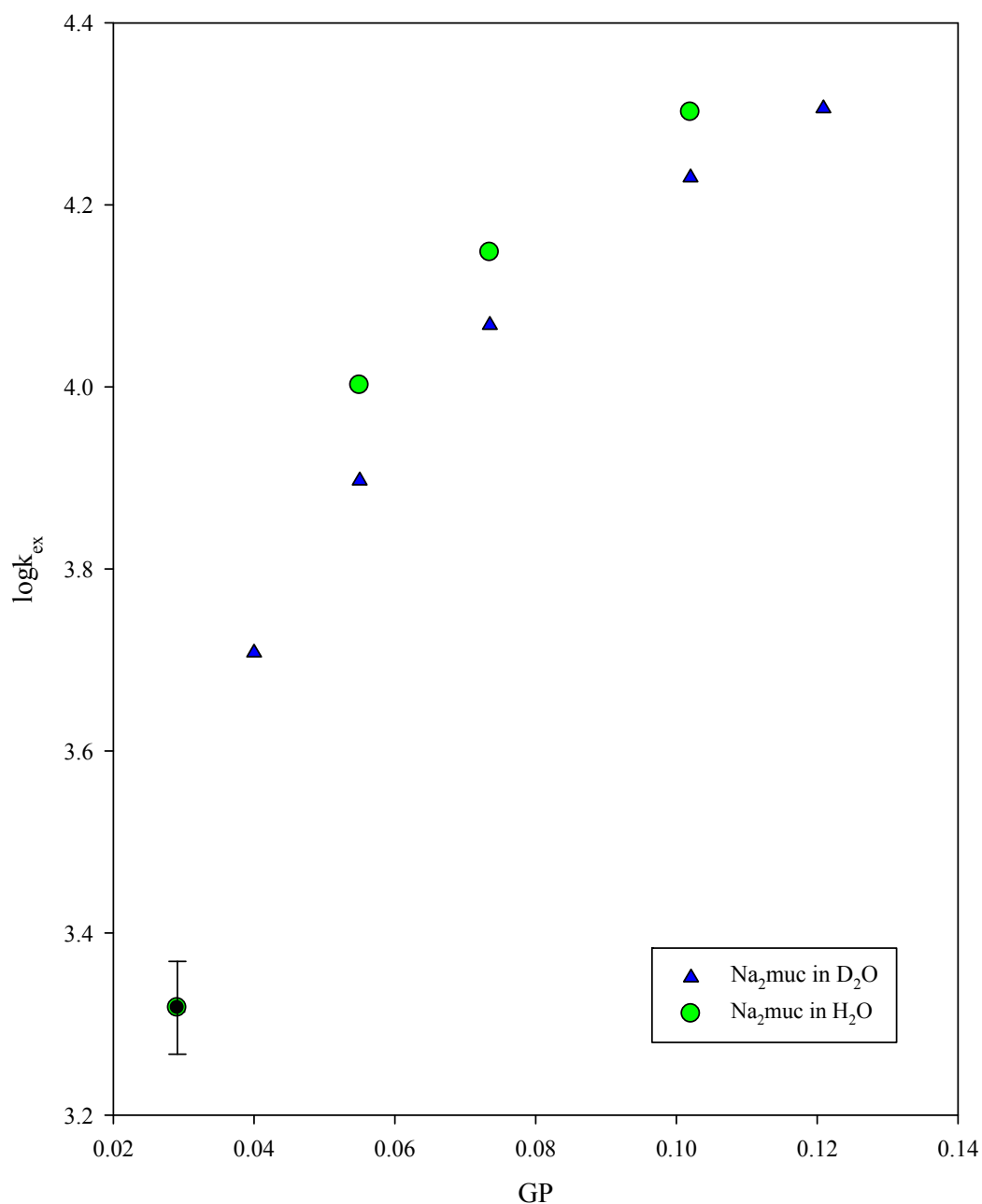


Figure 2.34 The effect of sodium muconate on the rate of ET for reaction (2-2) as measured by T_2 at 0.10 mM reactants in D_2O (blue triangles) and H_2O (green circles). In this plot the H_2O data have been normalized to match up with the highly-determined D_2O starting point indicated by the black circle for purpose of comparison.

A second possible reason for the divergence between the stopped-flow and NMR kinetic behaviors hinged on the paramagnetic relaxation effects of dissolved O₂ which are known to sometimes contaminate T₂ measurements by accelerating spin-spin relaxation (and even line-widths, *vide supra*).¹⁰ Since the concentration of O₂ in air-saturated H₂O is 5x10⁻⁴ M at 25°C (and presumably very close to that in D₂O),^{25,35} we hypothesized that some unknown paramagnetic effect might be specifically affecting the NMR relaxation-based kinetic measurements in a way which would not be operative in the stopped-flow work. It is not immediately obvious why this would show up specifically in the case of muconate, and systematically interfere with it, but not the other salts, but we nevertheless performed experiments to test this idea. We did this by studying reaction (2-2) both with and without added muconate in D₂O under conditions of air-saturation, vacuum degassing, Ar degassing, and 1.0 atm oxygen gas saturation. The data presented in Table 2.17 and Figures 2.35 and 2.36 show the rates of ET (measured by T₂) obtained upon degassing 0.10 mM reactant solutions alone as well as solutions containing Na₂muc at a concentration of 0.004 M (corresponding to GP = 0.102 which places the system well up into the catalytic region shown in Figure 2.33).

Table 2.17 The effects of various degassing methods on the rate of ET exchange reaction (2-2) at a reactants concentration of 0.10 mM with Na₂muc concentrations of 0 M and 0.004 M.

	[Na ₂ muc]	GP	logk _{ex} ^(a)	logk _{ex} ^(b)
No Degassing (air-saturated)	0	0.0291	3.309	3.318 ± 0.051
	0.004	0.102	4.242	4.251
Vacuum Degassing	0	0.0291	3.322	3.318 ± 0.051
	0.004	0.102	4.180	4.176
Ar Degassing	0	0.0291	3.187	3.318 ± 0.051
	0.004	0.102	4.110	4.241
O ₂ Saturated	0	0.0291	3.230	3.318 ± 0.051
	0.004	0.102	4.027	4.115

(a) Raw logk_{ex} values and (b) logk_{ex} values normalized to the study aggregate (total N = 5) averaged logk_{ex} starting value (with 95% confidence intervals as shown).

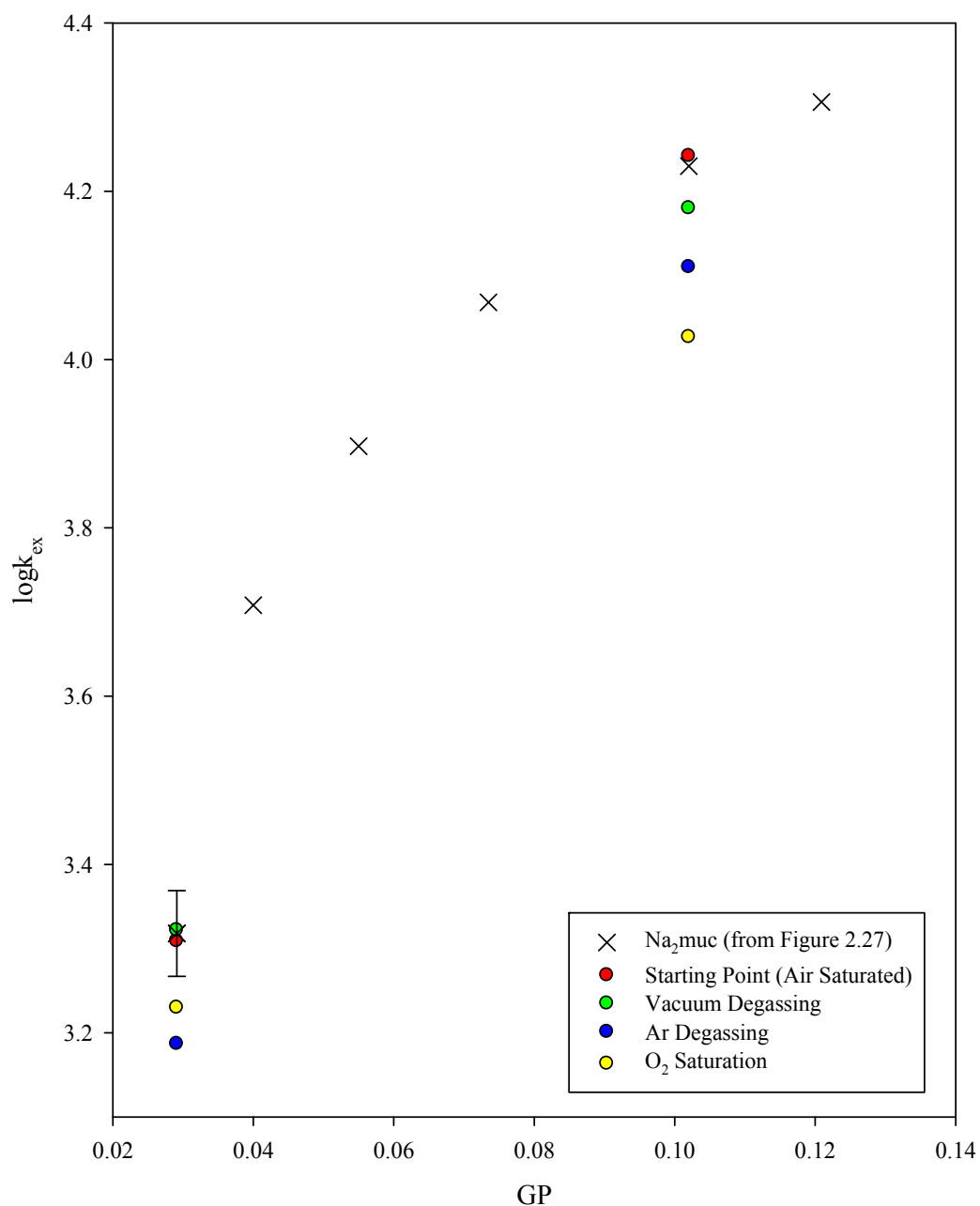


Figure 2.35 Degassing and O₂-saturation effects on the rate of reaction (2-2) in D₂O at a reactants concentration of 0.10 mM using raw $\log k_{ex}$ values for the effects of air-saturation (red circles), vacuum degassing (green circles), Ar degassing (blue circles), and O₂ saturation (yellow circles). The black cross marks are taken from the Na₂muc data previously presented in Table 2.11 and Figure 2.26.

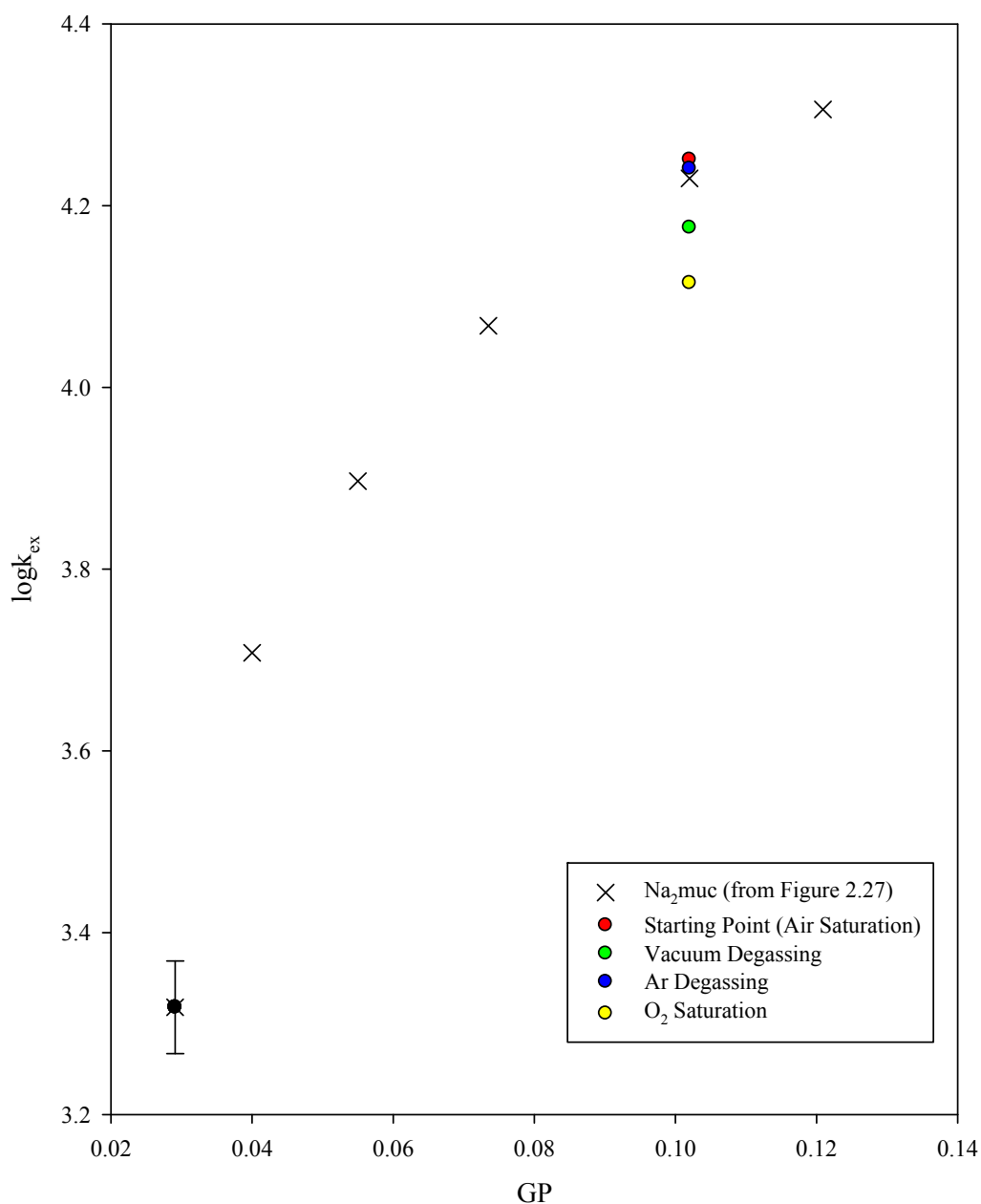


Figure 2.36 Degassing effects on reaction (2-2) at a reactants concentration of 0.10 mM using $\log k_{ex}$ values normalized to the average $\log k_{ex}$ starting value (with a 95% confidence interval, black circle) in D₂O for air-saturation (red circle), vacuum degassing (green circle), Ar degassing (blue circle), and 1.0 atm O₂ saturation (yellow circle). The black cross marks are taken from the Na₂muc data previously presented in Table 2.11 and Figure 2.26.

While Figure 2.35 does indicate some (typical) run-to-run jitter in the first point, when normalized together in Figure 2.35 we see that the ET rates in all cases fall within error of the air-saturated values, therefore ruling out the presence of oxygen (or not) as being a contributing factor to the puzzling loss of muconate's catalytic efficacy as probed by NMR (the solutions for each experiment were freshly prepared).

The negative results coming from the H₂O vs. D₂O and O₂-purged vs. air-saturated experiments force us to conclude that the loss of sodium muconate's catalytic efficacy has to be attributed to some factor not previously considered. This striking and unique loss of sodium muconate's catalytic efficacy specific to NMR is now taken as necessarily being due to some specific aspect of the technique/instrumentation/physical environment relevant to our kinetic investigations of reaction (2-2). The most obvious such possibility is at this point narrowed down to *the magnetic field itself*. This improbable-seeming idea was applied in previous stopped-flow work wherein a somewhat strong magnetic field was applied to the optical flow cell containing the reacting mixture through use of a stack of strong external disk magnets situated directly above the cell. No magnetic field effect was observed,^{6,9} but at the time this was considered inconclusive since the magnetic field present in an NMR is so much more powerful than the magnetic field that could be applied during the stopped-flow experiments.

The mechanism whereby the powerful magnetic field inside of the NMR might nullify the otherwise very strong "muconate effect" remains unclear at this

point. One speculation involves a possible field-dependent hindering of muconate's ability to freely diffuse through solution. The basis of this idea derives from the two negative charges on either end of muconate (see Table 2.1) and the possibility that the structured hydration spheres around them might interact in some unique way with similar qualities to diamagnetic ring currents (like those in benzene rings) in these "rod-tip" regions. If large-scale cooperative vibrational and nuclear tunneling effects were of sufficient magnitude, one can envision a way in which the magnetic moments at the rod "ends" might bring about an anisotropic ordering effect in the powerful NMR magnetic field so as to render the muconate dianion essentially "locked" into a specific orientation which might then constrain its diffusive behavior. Presumably, any such effect which impeded muconate's ability to freely diffuse through solution would severely hinder its ability to enhance the rate of ET *via* quantum super-exchange since it would have less of a chance to get in between the two reactants. A second possibility is that there may be a problem with our assumed mode of operation regarding the super-exchange mechanism. Previous workers measuring stopped-flow kinetics^{6,9,36} have invoked the typical "hole" + "electron" transfer pathways used in conceptualizing this fairly well-known phenomenon.²² Since the virtual "hole" and "electron" transfer quantum super-exchange states involve di-radical character in both cases, there may be some as yet unknown magnetic fields effect attenuating quantum super-exchange. Importantly, the stopped-flow work done by Pan³⁸ has shown that the same $(\text{NH}_3)_5\text{Ru}^{\text{III}}(\text{tfmp})^{3+}$ species used in our NMR work exhibits the very same catalysis by muconate as the $(\text{NH}_3)_5\text{Ru}^{\text{III}}(3\text{-fpy})^{3+}$ oxidant when used in

reaction (2-1), thus we know that this small difference in oxidant structure is immaterial to the quenching of the catalysis.

Whatever the eventual explanation, this observed effect is a real, verified, NMR-specific kinetic effect which can now only be attributed to the magnetic field itself. Further investigation will be needed to explore the possibilities regarding the mechanism of the surprising quenching of muconate's catalytic activity in magnetic field.

2.15 Effect of Added Group VIII Metal Hexacyano Salts on the Rate of ET

The catalytic rate effects arising upon addition of the group-VIII metal hexacyano salts $\text{K}_4\text{Fe}^{\text{II}}(\text{CN})_6$, $\text{K}_4\text{Ru}^{\text{II}}(\text{CN})_6$, and $\text{K}_4\text{Os}^{\text{II}}(\text{CN})_6$ (structures shown in Table 2.2) greatly exceed even those of muconate, and they strongly catalyze ET even when present at very low concentrations in the reactant solution.^{8,9,40,41} Reaction (2-1) has been studied in this lab by stopped-flow⁹ at a reactants concentration of 0.10 mM and reaction (2-2) has been studied by NMR line-broadening⁸ at a reactants concentration of 5.00 mM. Both the ^{19}F T_2 spin-echo method at 0.10 mM reactants and ^{19}F NMR line-broadening at 5.00 mM reactants have been used here to study reaction (2-2) so as to verify the previous 5.00 mM rate data and once again to extend the reach of NMR down to the stopped-flow concentration range.

The magnitude of the hexacyano-complex catalysis measured for reaction (2-2) 5.00 mM reactants was found to decay with time when using the line-broadening method in this work (only very small amounts of $\text{M}^{\text{II}}(\text{CN})_6^{4-}$, 0.01 mM salt, were present in these reactant solutions. This decay in k_{ex} (all the way back to the value

obtained with no added hexacyano salt) took place over a period of about 25 minutes as shown in Table 2.18 and Figure 2.37. When the concentrations of added hexacyano salts were higher ($> 0.39 \text{ mM}$), measured k_{ex} values held constant for periods up to 4-6 hours as shown in Table 2.19 and Figure 2.38. The decay presumably relates to reaction of the essentially trace amounts of catalyst in the former case to form inactive cyanide-bridged species.

Table 2.18 Kinetic data showing time-related decay of k_{ex} over a period of 25 minutes in the presence of $\text{K}_4\text{Fe}^{\text{II}}(\text{CN})_6$ at a concentration of 0.01 mM (calculated employing the “slow” rate equation (2-9)) for reaction (2-2) at an equimolar reactants concentration of 5.00 mM.

Time (min)	$\Delta\nu_{1/2}$ (Hz)	$\Delta\nu_{1/2}'$ (Hz)	k_{ex}	$\log k_{\text{ex}}$
4	3	28.92	16280	4.21
6	3	28.28	15880	4.20
9	3	25.60	14190	4.15
10.5	3	25.12	13890	4.14
12	3	24.38	13430	4.13
13	3	24.78	13680	4.14
15	3	23.76	13040	4.12
19	3	23.29	12740	4.11
22	3	23.14	12650	4.10
25	3	22.57	12290	4.09

Table 2.19 Kinetic data showing stability of catalyzed k_{ex} over a period of 25 minutes in the presence of $\text{K}_4\text{Fe}^{\text{II}}(\text{CN})_6$ at a concentration of 0.39 mM (calculated employing the “fast” rate equation (2-15)) for reaction (2-2) at an equimolar reactants concentration of 5.00 mM.

Time (min)	$\Delta\nu_{1/2}$ (Hz)	$\Delta\nu_{1/2}'$ (Hz)	k_{ex}	$\log k_{\text{ex}}$
4	3	115.29	16963200	7.23
6	3	119.29	16379700	7.21
8	3	114.26	17120200	7.23
10	3	112.89	17363600	7.24
12	3	115.80	16886500	7.23
15	3	112.76	17354200	7.24
20	3	115.85	16879000	7.23
25	3	109.41	17900500	7.25

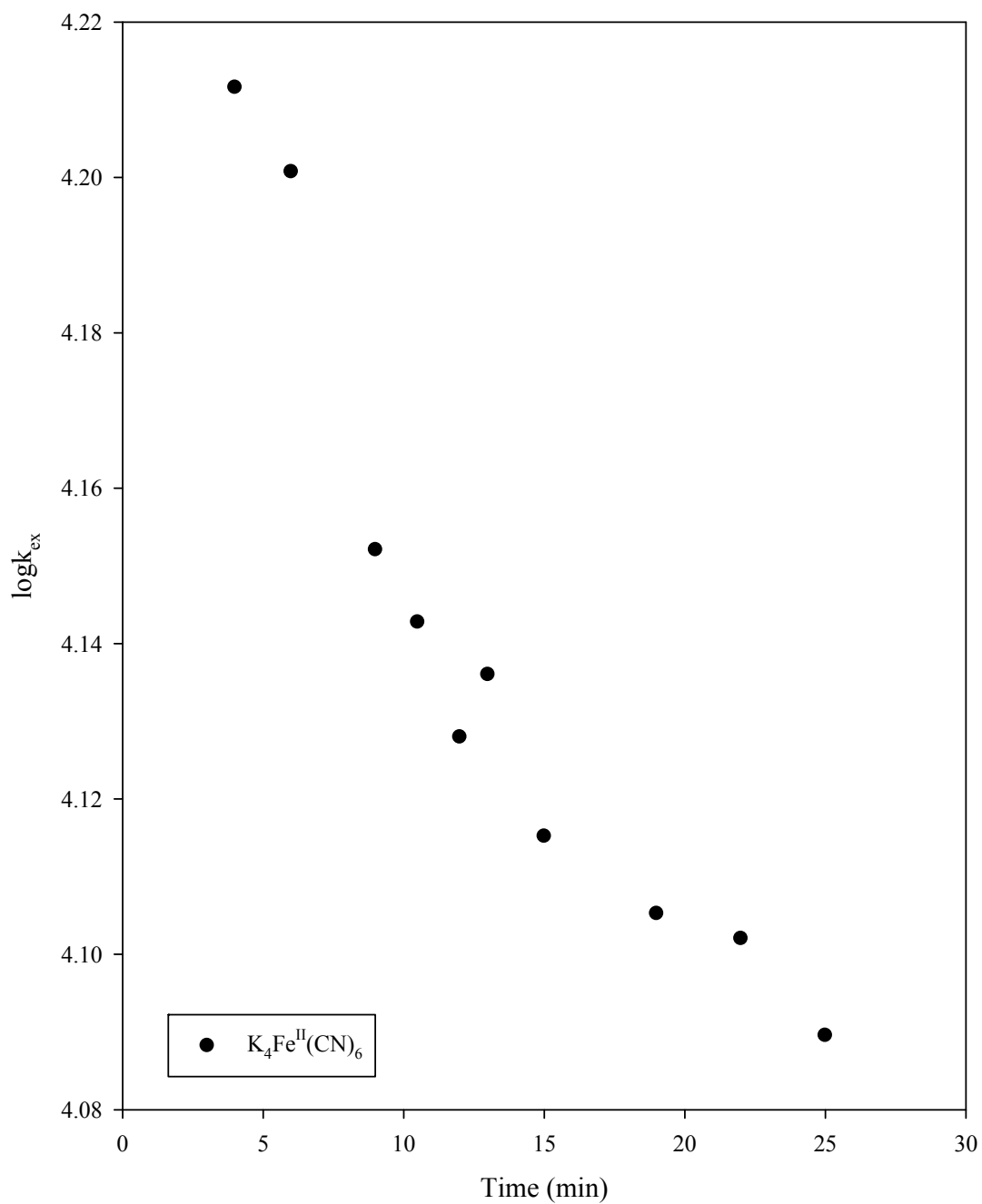


Figure 2.37 Data showing the temporal decay of the measured $\log k_{\text{ex}}$ over a period of 25 minutes for reaction (2-2) (calculated from $\Delta v_{1/2}$ values using the “slow” rate equation (2-9)) at a reactants concentration of 5.00 mM with the addition of $\text{K}_4\text{Fe}^{\text{II}}(\text{CN})_6$ at 0.01 mM.

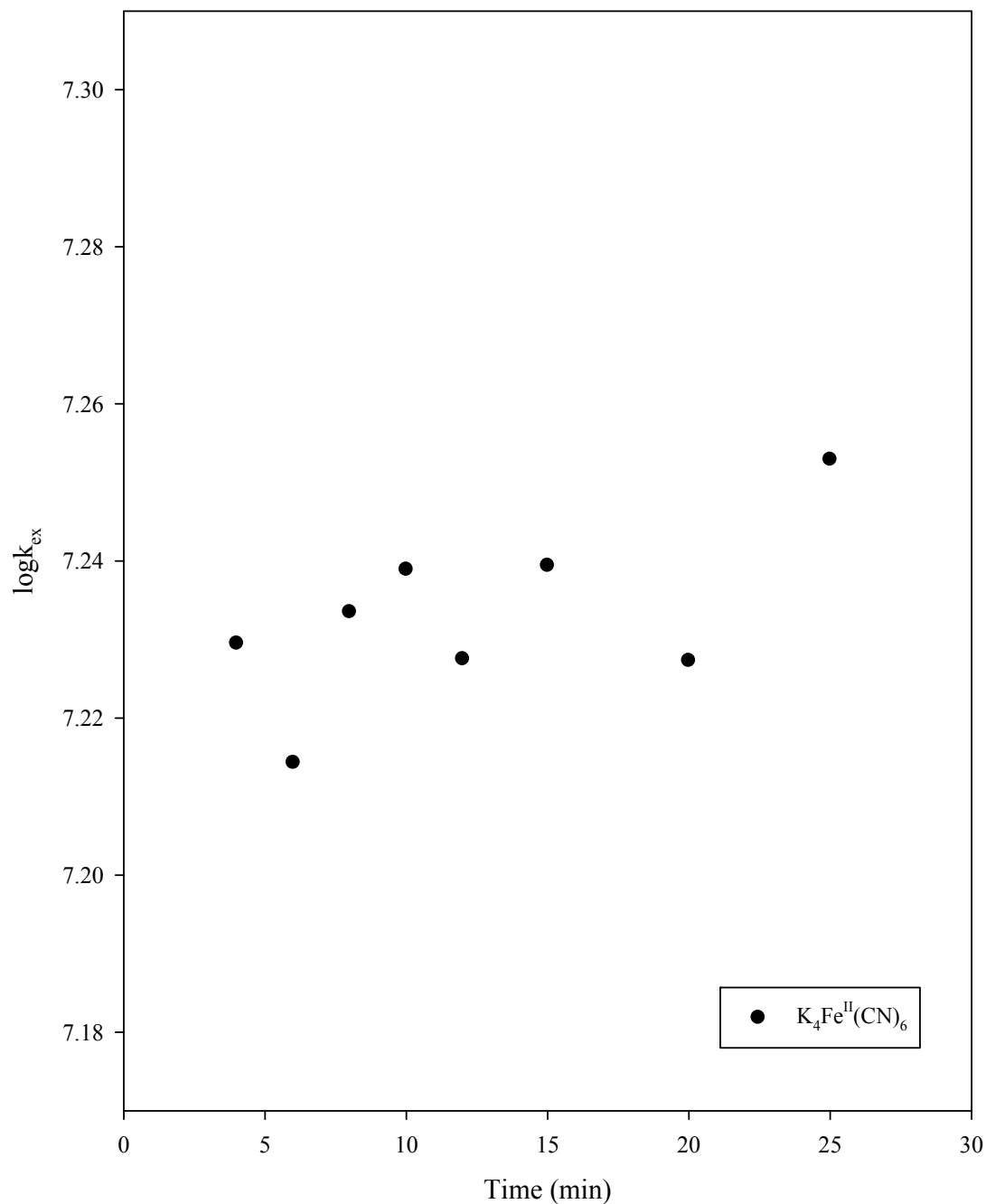


Figure 2.38 Data showing stability of the measured $\log k_{\text{ex}}$ over a period of 25 minutes for reaction (2-2) (calculated from $\Delta v_{1/2}$ values using the “fast” exchange equation (2-15)) at a reactants concentration of 5.00 mM with the addition of $\text{K}_4\text{Fe}^{\text{II}}(\text{CN})_6$ at 0.39 mM (note, the uncatalyzed rate is 4.04 ± 0.05).

The observed decay of k_{ex} at 5.00 mM reactants with the addition of $\text{K}_4\text{Fe}^{\text{II}}(\text{CN})_6$ at 0.01 mM is at variance with the prior work by Qin under the same conditions.⁸ While the reason for the variance is unknown, this instability compels us to ignore all previous data points at 5.00 mM reactants with low concentrations of added metallic hexacyano salts (< 0.39 mM added salt).⁸ Previous results are reproduced, however, at a reactants concentration of 5.00 mM with the addition of metallic hexacyano salts at a concentration of 0.39 mM where the measured k_{ex} is stable, as listed in Table 2.20 and displayed in Figure 2.39.

Table 2.20 The effect of added $\text{K}_4\text{M}^{\text{II}}(\text{CN})_6$ on k_{ex} for reaction (2-2) at 5.00 mM reactants as measured by line-broadening (with rates calculated using the “fast” rate equation (2-15) for added $\text{K}_4\text{Fe}^{\text{II}}(\text{CN})_6$ and the “slow” rate equation (2-9) for $\text{K}_4\text{Os}^{\text{II}}(\text{CN})_6$ and $\text{K}_4\text{Ru}^{\text{II}}(\text{CN})_6$). Current rates (a) are the raw $\log k_{\text{ex}}$ values obtained by us and column (b) lists the rates previously obtained by Qin.⁸

$[\text{K}_4\text{Fe}^{\text{II}}(\text{CN})_6]$	GP	k_{ex}	$\log k_{\text{ex}}^{(a)}$	$\log k_{\text{ex}}^{(b)}$
0	0.1750	13180	4.120	4.120
3.90E-04	0.1811	17334000	7.239	7.300
5.30E-04	0.1832	40657000	7.612	-
$[\text{K}_4\text{Os}^{\text{II}}(\text{CN})_6]$	GP	k_{ex}	$\log k_{\text{ex}}^{(a)}$	$\log k_{\text{ex}}^{(b)}$
0	0.1750	12080	4.082	4.120
3.90E-04	0.1811	47280	4.675	5.430
$[\text{K}_4\text{Ru}^{\text{II}}(\text{CN})_6]$	GP	k_{ex}	$\log k_{\text{ex}}^{(a)}$	$\log k_{\text{ex}}^{(b)}$
0	0.175	12890	4.110	4.120
3.90E-04	0.181	30870	4.489	4.980

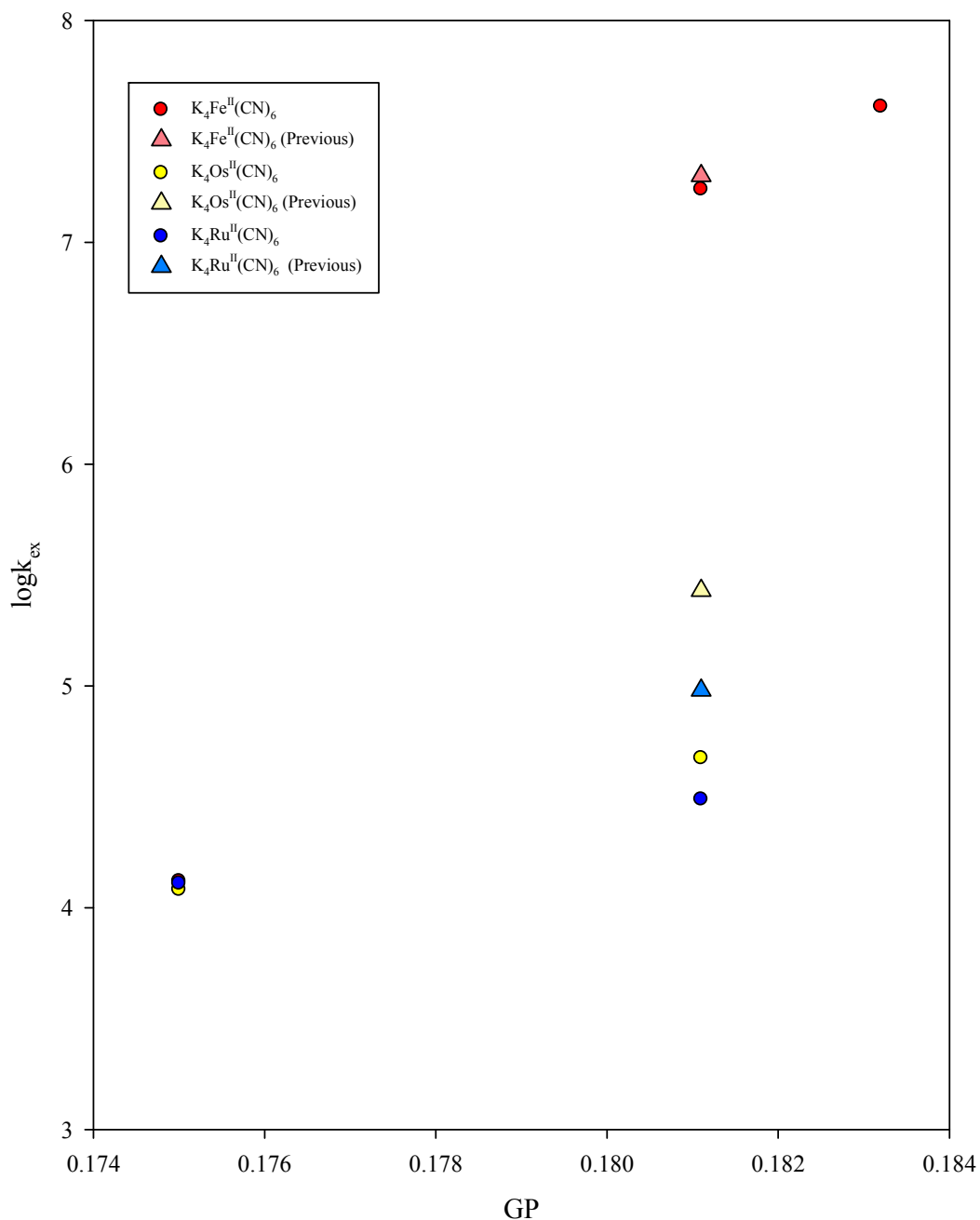


Figure 2.39 The effect of added $\text{K}_4\text{Fe}^{\text{II}}(\text{CN})_6$ (red circles), $\text{K}_4\text{Os}^{\text{II}}(\text{CN})_6$ (yellow circles), and $\text{K}_4\text{Ru}^{\text{II}}(\text{CN})_6$ (blue circles) on k_{ex} for reaction (2-2) at a reactants concentration of 5.00 mM along with previous results obtained by Qin (black, green, and grey triangles, respectively).⁸

The rate of reaction (2-2) was also measured at a reactants concentration of 0.10 mM (now using the ^{19}F T_2 spin-echo method) in the presence of $\text{K}_4\text{M}^{\text{II}}(\text{CN})_6$ ($\text{M} = \text{Fe}^{\text{II}}$, Os^{II} , and Ru^{II}), and the results are listed Table 2.21 and illustrated in Figure 2.40. This NMR data was compared with previous results obtained *via* stopped-flow by Mehmood⁹ (pertaining to reaction (2-1)). At the time the when the current NMR rate data was collected (T_2 method), the problem arising from time-dependent decay effects of k_{ex} as catalyzed by added $\text{K}_4\text{M}^{\text{II}}(\text{CN})_6$ was unknown. Therefore, current rate data here can presumably provide only lower bounds on the actual catalytic effects of the hexacyano salts on the rates of ET. The results obtained *via* stopped-flow should probably be considered a more accurate representation of these effects on k_{ex} since the solution standing time required for the stopped-flow measurement is much less than for determination using the T_2 spin-echo method (a few minutes by stopped-flow vs. > 10 minutes by T_2 spin-echo).

Table 2.21 The effect of added $[\text{K}_4\text{M}^{\text{II}}(\text{CN})_6]$ on k_{ex} for reaction (2-2) at 0.10 mM reactants as measured by T_2 (with rates calculated using the relaxation-based rate equation (2-16)). Displaying (a) raw $\log k_{\text{ex}}$ values and (b) $\log k_{\text{ex}}$ values normalized to the averaged (total $N = 5$) $\log k_{\text{ex}}$ starting value obtained across trials for the initial, no-added salt point (with 95% confidence intervals as shown).

$[\text{K}_4\text{Fe}^{\text{II}}(\text{CN})_6]$	GP	k_{ex}	$\log k_{\text{ex}}^{(a)}$	$\log k_{\text{ex}}^{(b)}$
0	0.0291262	2140	3.331	3.318 ± 0.051
4.00E-09	0.0291268	2830	3.452	3.439
1.60E-08	0.0291287	3630	3.560	3.547
6.40E-08	0.0291363	3150	3.498	3.485
8.00E-07	0.0292516	52250	4.718	4.705
1.60E-06	0.0293764	137800	5.139	5.126

$[\text{K}_4\text{Os}^{\text{II}}(\text{CN})_6]$	GP	k_{ex}	$\log k_{\text{ex}}^{(a)}$	$\log k_{\text{ex}}^{(b)}$
0	0.029126	1900	3.279	3.318 ± 0.051
1.00E-07	0.029142	2290	3.360	3.399
4.00E-07	0.029189	5380	3.731	3.770
8.00E-07	0.029252	25340	4.404	4.443
1.60E-06	0.029376	93460	4.971	5.010
3.20E-06	0.029624	268000	5.428	5.467

$[\text{K}_4\text{Ru}^{\text{II}}(\text{CN})_6]$	GP	k_{ex}	$\log k_{\text{ex}}^{(a)}$	$\log k_{\text{ex}}^{(b)}$
0	0.029126	1860	3.269	3.318 ± 0.051
4.00E-07	0.029189	2660	3.426	3.475
1.60E-06	0.029376	13460	4.129	4.178
3.20E-06	0.029624	25920	4.414	4.463
6.40E-06	0.030113	79100	4.898	4.947
1.28E-05	0.031066	195350	5.291	5.340

2.16 Temperature Dependent Kinetic Studies

As the temperature of a typical reacting chemical system and surroundings increase, the rates of any chemical reactions of the system will increase as well.^{11,42,43} This is due to a larger number of reactant molecules in solution possessing the necessary Boltzman activation energy such that, in the case of bimolecular reactions, there will be both more frequent collisions between reactant molecules as well as a greater fraction of these collisions possessing the necessary threshold (or activation) energy required for reaction. The influence of temperature on the rate of reaction was originally noted and quantitatively assessed by Arrhenius, and his detailed analyses of the available data led him to propose the following empirical expression,

$$k = Ae^{-E_a / RT} \quad (2-20)^{18,19,44}$$

where k is a measured “rate constant”, A is the pre-exponential factor or “frequency” factor ($A \approx k_B T/h$ in the classical transition theory⁴⁵), E_a is the “activation” energy which is the energy input required for the reactants to surmount the activation barrier of the reaction, R is the universal gas constant, and T is the temperature in Kelvins. Much later, a more “first principles approach known as ”transition state theory” (TST or also “activated rate theory”) was developed, and this allowed reaction rates and mechanisms to be more fully analyzed in the context of the now separable “activation parameters” associated with a particular reaction; those being the enthalpy of activation, ΔH^\ddagger , and the entropy of activation, ΔS^\ddagger .^{19,44,46,47} From the transition state theory of activated rate processes, the rate constant, k_{ex} , is most compactly given by the Eyring equation,

$$k_{\text{ex}} = \frac{k_B T}{h} e^{\left(\frac{-\Delta G^\ddagger}{RT}\right)} \quad (2-21)^{11,19,44,46,47}$$

where k_B is Boltzmann's constant, h is Plank's constant, and ΔG^\ddagger is now the Gibbs free energy of activation which formally corresponds to the free energy difference between reactants and the "transition state" through which the system must pass on its way to products. The Gibbs free energy of activation can be apportioned into both enthalpic (\sim work against forces) and entropic (\sim statistical improbability of the transition state configuration) "barriers" using the Gibbs equation,

$$\Delta G^\ddagger = \Delta H^\ddagger - T\Delta S^\ddagger \quad (2-22)^{44,47}$$

Therefore, by substitution of equation (2-22) into (2-21), the rate expression can be expressed as,

$$k_{\text{ex}} = \frac{k_B T}{h} e^{\left(\frac{-\Delta H^\ddagger}{RT}\right)} e^{\left(\frac{\Delta S^\ddagger}{R}\right)} \quad (2-23)$$

In order to experimentally determine the activation parameters for a particular reaction, the Eyring formalism⁴⁸ is typically applied, wherein equation (2-23) is divided by T and the natural log is taken of both sides,

$$\ln\left(\frac{k_{\text{ex}}}{T}\right) = \ln\left(\frac{k_B}{h}\right) - \left(\frac{\Delta H^\ddagger}{RT}\right) + \left(\frac{\Delta S^\ddagger}{R}\right) \quad (2-24)$$

Equation (2-24) is known as the Eyring equation, and a plot of experimental kinetic rates in the form of $\ln(k_{\text{ex}}/T)$ vs. $1/T$ is known as an "Eyring plot".^{19,47} The enthalpy of activation is thus derived from the slope of the curve and the entropy of activation is derived from the y-intercept as shown below,

$$\text{Slope} = -\frac{\Delta H^\ddagger}{R} \quad (2-25)$$

$$\text{y - intercept} = \ln\left(\frac{k_B}{h}\right) + \left(\frac{\Delta S^\ddagger}{R}\right) \quad (2-26)$$

For bimolecular ET reactions in the pre-equilibrium limit, such as the reactions studied in this work (see Chapter 1), the overall second-order ET rate constant, k_{ex} , can be more informatively expressed as,

$$k_{\text{ex}} = K_A k_{\text{ET}} \quad (2-27)^{11}$$

where K_A is the encounter pair equilibrium association constant as defined by equation (1-40) in chapter 1 (see section 1.8), and k_{ET} is a first-order rate constant of electron exchange within the associated pair (as defined previously in equation (1-18) in chapter 1, section 1.5.4). Expanding K_A and replacing k_{ET} with equation (1-21), equation (2-27) becomes,

$$k_{\text{ex}} = \left(\frac{4000\pi N_A a^3}{3}\right) \exp\left[\frac{-w(a, \mu)}{k_B T}\right] \left[\nu_n \kappa_{el} e^{\left(\frac{-\Delta H^\ddagger}{RT}\right)} e^{\left(\frac{\Delta S^\ddagger}{R}\right)} \right] \quad (2-28)$$

Where we have now replaced the \ddagger superscript of absolute rate theory with the more general $*$ superscript as is required by the non-standard pre-exponential we are using here. If the Debye-Hückel work of association, $w(a, \mu)$, is broken down into its enthalpic and entropic components which are then merged into ΔH^\ddagger and ΔS^\ddagger , equation (2-28) becomes,

$$k_{\text{ex}} = \left(\frac{4000\pi N_A a^3}{3} \right) \left(\nu_n \kappa_{el} e^{\left(\frac{-\Delta H^*}{RT} \right)} e^{\left(\frac{\Delta S^*}{R} \right)} \right) \quad (2-29)$$

If it is assumed that $\nu_n \cong k_B T / h$ and the reaction is adiabatic (meaning that electron tunneling is facile and $\kappa_{el} \cong 1$, see chapter 1.5), then equation (2-29) further simplifies to,

$$k_{\text{ex}} = \left(\frac{4000\pi N_A a^3}{3} \right) \left(\frac{k_B T}{h} \right) e^{\left(\frac{-\Delta H^*}{RT} \right)} e^{\left(\frac{\Delta S^*}{R} \right)} \quad (2-30)$$

Now the Eyring formalism can be applied to equation (2-30) as was done in equation (2-24), and equation (2-30) becomes,

$$\ln\left(\frac{k_{\text{ex}}}{T}\right) = \ln\left(\frac{4000\pi N_A a^3}{3}\right) + \ln\left(\frac{k_B T}{h}\right) - \left(\frac{-\Delta H^*}{RT}\right) + \left(\frac{\Delta S^*}{R}\right) \quad (2-31)$$

A plot of $\ln(k_{\text{ex}}/T)$ vs. $1/T$ can in principle then yield the model-specific enthalpy of activation, ΔH^* , and entropy of activation, ΔS^* , as was explained previously (*vide supra*).

2.16.1 Reactant concentration effects on activation parameters

Due to the good agreement of our data presented in section 2.12 with the similar kinetic “self-salting” effects previously reported by Eskandari¹² and Sista⁶, we undertook experiments to see if any insight into the mechanism of this effect might be gained by measuring the activation parameters for reaction (2-2) at various reactant concentrations with no other added salt (utilizing both the ¹⁹F T₂ spin-echo and ¹⁹F NMR line-broadening methods for measuring rates of ET). The TST activation

parameters were derived from standard plots of $\ln(k_{\text{ex}} / T)$ vs. $1/T$, utilizing equations (2-25) and (2-26). Temperature-dependent rate data obtained using the ^{19}F T_2 spin-echo method at equimolar reactant concentrations of 0.10 mM, 0.50 mM, and 3.00 mM are listed in Table 2.22 and displayed in Figure 2.41. Line-broadening rate data at 5.00 mM, 5.30 mM, 5.50 mM, 6.50 mM, and 8.00 mM reactants are listed in Table 2.23 and displayed in Figure 2.42. The Eyring activation parameters at all reactant concentrations are presented in Table 2.24.

It should be noted that all values of $\ln(k_{\text{ex}} / T)$ obtained in a given experimental run were normalized so as to match the average k_{ex} value obtained at that reactant concentration at the intermediate temperature of 299 K (this was necessary to account for the small run-to-run variations in starting point rates due to unavoidable small errors ($< 10\%$) in reactant concentrations and purities). In order to do this, the following relationship was applied to all measured k_{ex} values of a given temperature variation experiment,

$$k_{\text{ex}}^T(\text{normalized}) = k_{\text{ex}}^T(\text{measured}) \left(\frac{k_{\text{ex}}^{299\text{K}}(\text{average})}{k_{\text{ex}}^{299\text{K}}(\text{measured})} \right) \quad (2-32)$$

where $k_{\text{ex}}^T(\text{measured})$ is the experimental k_{ex} value at a given temperature in that series, $k_{\text{ex}}^{299\text{K}}(\text{average})$ is the average k_{ex} value ($N \geq 5$) with no salt added at 299 K at a given reactants concentration, and $k_{\text{ex}}^{299\text{K}}(\text{measured})$ is the experimentally derived k_{ex} value at 299K obtained in that particular set of measurements. The set of normalized k_{ex}^T values are then used to calculate the set of $\ln(k_{\text{ex}}^T / T)$ values used in constructing the final Eyring plot. This normalization procedure was only applied to T_2 rate data

where we had multiple measurements to work with at 299 K. Because of the inherently better S/N and less jitter, line-broadening temperature studies were conducted using only 1 trial.

Table 2.22 Temperature dependent T_2 rate data obtained at 0.10 mM, 0.50 mM, and 3.00 mM reactants. Column (a) lists the values of $\ln(k_{\text{ex}} / T)$ obtained from the raw k_{ex} values, and (b) shows the same data after normalizing all runs to the average k_{ex} value at each reactant concentration (where the average k_{ex}^T is taken from ≥ 5 measurements at 299 K).

0.10 mM (GP = 0.0291)

Temperature (K)	1/T (K^{-1})	k_{ex} ($\text{M}^{-1} \text{s}^{-1}$)	$\ln(k_{\text{ex}} / T)^{(a)}$	$\ln(k_{\text{ex}} / T)^{(b)}$
283	0.00353	1520	1.68	1.65
288	0.00347	2190	1.84	1.80
293	0.00341	1810	1.81	1.77
299	0.00334	1930	1.98	1.94 ± 0.12
303	0.00330	2690	2.18	2.14
299	0.00334	2450	2.10	2.06

0.50 mM (GP = 0.0628)

Temperature (K)	1/T (K^{-1})	k_{ex} ($\text{M}^{-1} \text{s}^{-1}$)	$\ln(k_{\text{ex}} / T)^{(a)}$	$\ln(k_{\text{ex}} / T)^{(b)}$
283	0.00353	2670	2.25	2.23
288	0.00347	2960	2.33	2.32
293	0.00341	3330	2.43	2.42
299	0.00334	3850	2.56	2.54 ± 0.09
303	0.00330	4520	2.70	2.69
299	0.00334	3900	2.57	2.56

3.00 mM (GP = 0.1411)

Temperature (K)	1/T (K^{-1})	k_{ex} ($\text{M}^{-1} \text{s}^{-1}$)	$\ln(k_{\text{ex}} / T)^{(a)}$	$\ln(k_{\text{ex}} / T)^{(b)}$
283	0.00353	5250	2.92	3.05
288	0.00347	6120	3.06	3.19
293	0.00341	7060	3.18	3.32
299	0.00334	7520	3.23	3.36 ± 0.06
303	0.00330	9390	3.43	3.57
299	0.00334	7460	3.22	3.35

Table 2.23 Temperature dependent rate data obtained *via* NMR line-broadening at 5.00 mM, 5.30, mM, 5.50 mM, 6.50 mM, and 8.00 mM reactants, showing values of $\ln(k_{\text{ex}} / T)$ obtained from raw k_{ex} values. Only one trial was executed at these reactants concentrations.

5.00 mM (GP = 0.1750)

Temperature (K)	1/T (K ⁻¹)	k_{ex} (M ⁻¹ s ⁻¹)	$\ln(k_{\text{ex}} / T)$
277	0.00361	7130	3.248
280	0.00357	7170	3.243
283	0.00353	7210	3.238
288	0.00347	8070	3.333
293	0.00341	9370	3.465
299	0.00334	12520	3.734
304	0.00329	15390	3.924
310	0.00323	20100	4.172
315	0.00317	22390	4.264
321	0.00312	24590	4.339

5.30 mM (GP = 0.1793)

Temperature (K)	1/T (K ⁻¹)	k_{ex} (M ⁻¹ s ⁻¹)	$\ln(k_{\text{ex}} / T)$
283	0.00353	7630	3.294
288	0.00347	8830	3.423
293	0.00341	10500	3.579
299	0.00334	12600	3.741
304	0.00329	15300	3.919
310	0.00323	17900	4.056

5.50 mM (GP = 0.1820)

Temperature (K)	1/T (K ⁻¹)	k_{ex} (M ⁻¹ s ⁻¹)	$\ln(k_{\text{ex}} / T)$
283	0.00353	8150	3.360
288	0.00347	9390	3.484
293	0.00341	10900	3.616
299	0.00334	13300	3.795
304	0.00329	15200	3.912
310	0.00323	18300	4.078

6.50 mM (GP = 0.1948)

Temperature (K)	1/T (K ⁻¹)	k _{ex} (M ⁻¹ s ⁻¹)	ln(k _{ex} / T)
277	0.00361	7360	3.280
280	0.00357	7700	3.314
283	0.00353	8380	3.388
288	0.00347	9680	3.515
293	0.00341	11600	3.679
299	0.00334	15000	3.915
304	0.00329	18800	4.125
310	0.00323	22700	4.294
315	0.00317	25500	4.394
321	0.00312	28900	4.500

8.00 mM (GP = 0.2116)

Temperature (K)	1/T (K ⁻¹)	k _{ex} (M ⁻¹ s ⁻¹)	ln(k _{ex} / T)
280	0.00357	7700	3.314
283	0.00353	8380	3.388
288	0.00347	9680	3.515
293	0.00341	11600	3.679
299	0.00334	15000	3.915
304	0.00329	18800	4.125

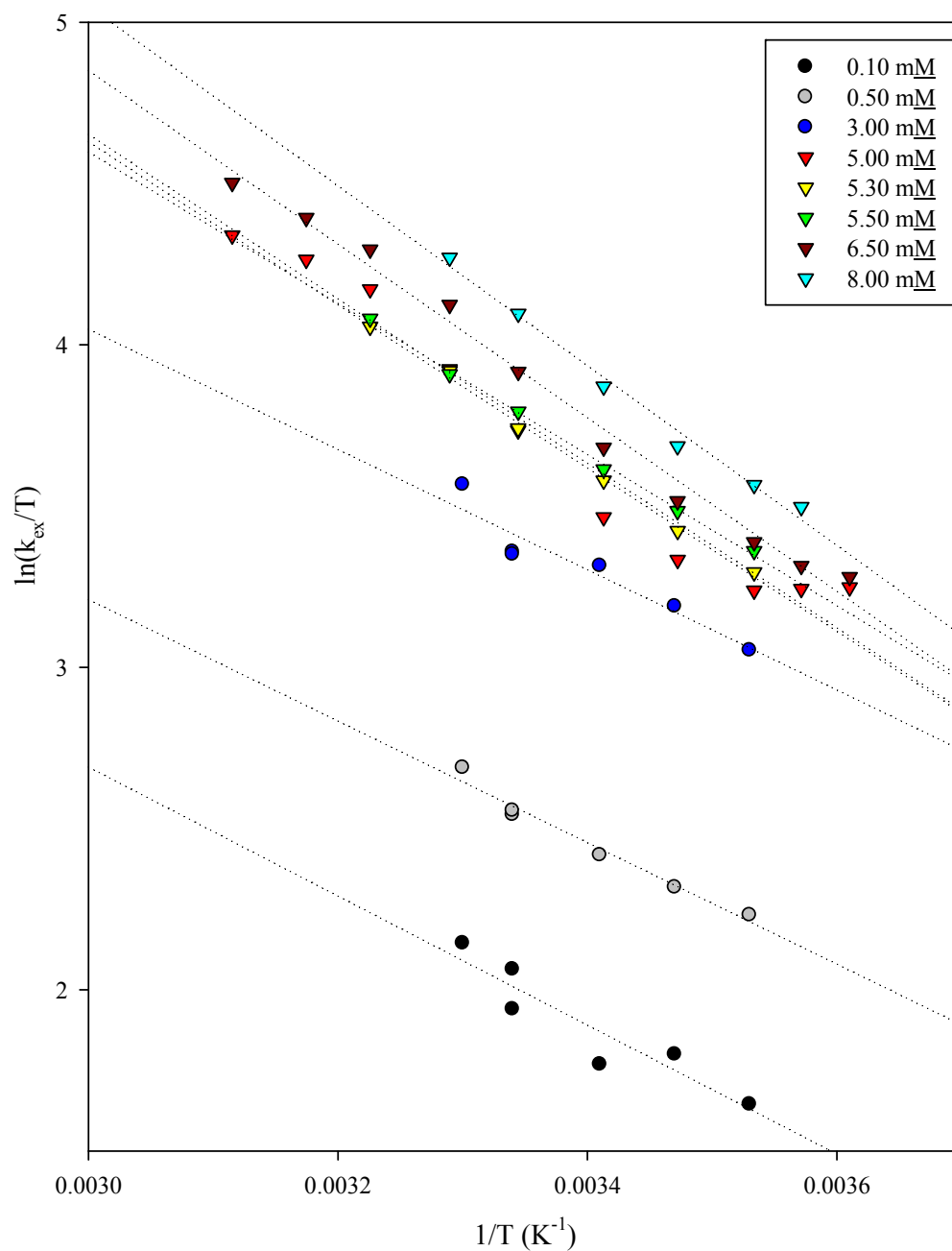


Figure 2.41 Eyring plots of the data in Tables 2.21 and 2.22 at equimolar reactants concentrations of 0.10 mM, 0.50 mM, 3.00 mM (using T_2 spin-echo ; black, grey, and blue circles, respectively); and at 5.00 mM, 5.30 mM, 5.50 mM, 6.50 mM, and 8.00 mM (using line-broadening; red, yellow, green, light blue, and dark red triangles, respectively).

Table 2.24 The best-fit TST activation parameters, ΔH^\ddagger and ΔS^\ddagger , for reaction (2-2) at the various equimolar reactant concentrations taken from the Eyring plots shown in Figure 2.41.

Concentration (mM)	Slope	y-intercept	ΔH^\ddagger (kJ/mol)	ΔS^\ddagger (J/K mol)	ΔG^\ddagger_{298} (kJ/mol)
0.10 (GP = 0.0291)	-2000 \pm 390	8.7 \pm 1.3	16.6 \pm 3.2	-125 \pm 11	53.9
0.50 (GP = 0.0628)	-1880 \pm 150	8.9 \pm 0.5	15.7 \pm 1.3	-124 \pm 4	52.7
3.00 (GP = 0.1411)	-1860 \pm 310	9.6 \pm 1.0	15.5 \pm 2.6	-118 \pm 9	50.7
5.00 (GP = 0.1750)	-2550 \pm 190	12.3 \pm 0.6	21.2 \pm 1.5	-95 \pm 5	49.5
5.30 (GP = 0.1793)	-2530 \pm 70	12.2 \pm 0.2	21.0 \pm 0.6	-96 \pm 2	49.6
5.50 (GP = 0.1820)	-2340 \pm 50	11.9 \pm 0.2	19.5 \pm 0.4	-98 \pm 2	48.7
6.50 (GP = 0.1948)	-2690 \pm 100	12.9 \pm 0.3	22.4 \pm 0.8	-90 \pm 3	49.2
8.00 (GP = 0.2126)	-2790 \pm 150	13.4 \pm 0.5	23.2 \pm 1.3	-86 \pm 4	48.8

Derived from linear least-squared fits of the kinetic data in Tables 2.22 and 2.23 utilizing equation (2-24).

The activation parameters in Table 2.24 show that the largest (most positive) enthalpy of activation, $\Delta H^\ddagger = 23.3 \pm 1.3$ kJ/mol, occurs at the high end of the “self-salting” reactants concentration range studied, 8.00 mM. Interestingly, the largest (meaning “least negative”) entropy of activation, ΔS^\ddagger , with a value of -86 ± 4 J/K mol occurs at 8.00 mM reactants as well. Correspondingly, both the smallest ΔH^\ddagger and most negative ΔS^\ddagger values occurred at 0.10 mM reactants, the low end of the concentration range studied. The respective values are $\Delta H^\ddagger = 16.6 \pm 3.2$ kJ/mol and $\Delta S^\ddagger = -125 \pm 11$ J/K mol. All reactants concentrations studied between these two extremes follow the trend with both ΔH^\ddagger and ΔS^\ddagger becoming more positive/less

negative as the concentration of reactants is increased. ΔH^\ddagger as a function of GP is displayed in Figure 2.42 and ΔS^\ddagger as a function of GP is illustrated in Figure 2.43.

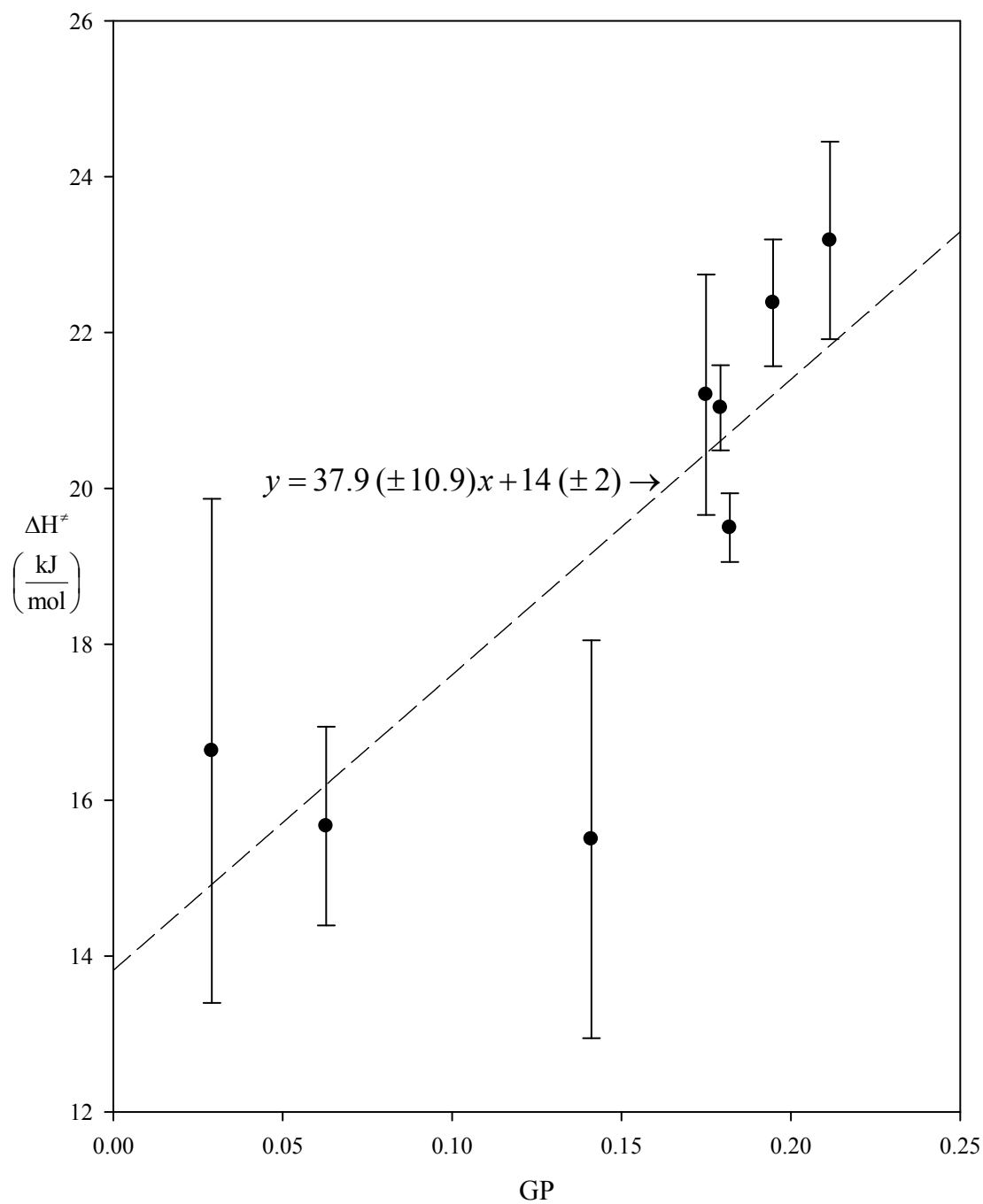


Figure 2.42 The approximately linear relationship between ΔH^\ddagger vs. GP (reactant concentrations ranging from 0.10 mM to 8.00 mM) for reaction (2-2) as taken from Table 2.24. The equation of the regression line is $y = 37.9(\pm 10.9)x + 14(\pm 2)$.

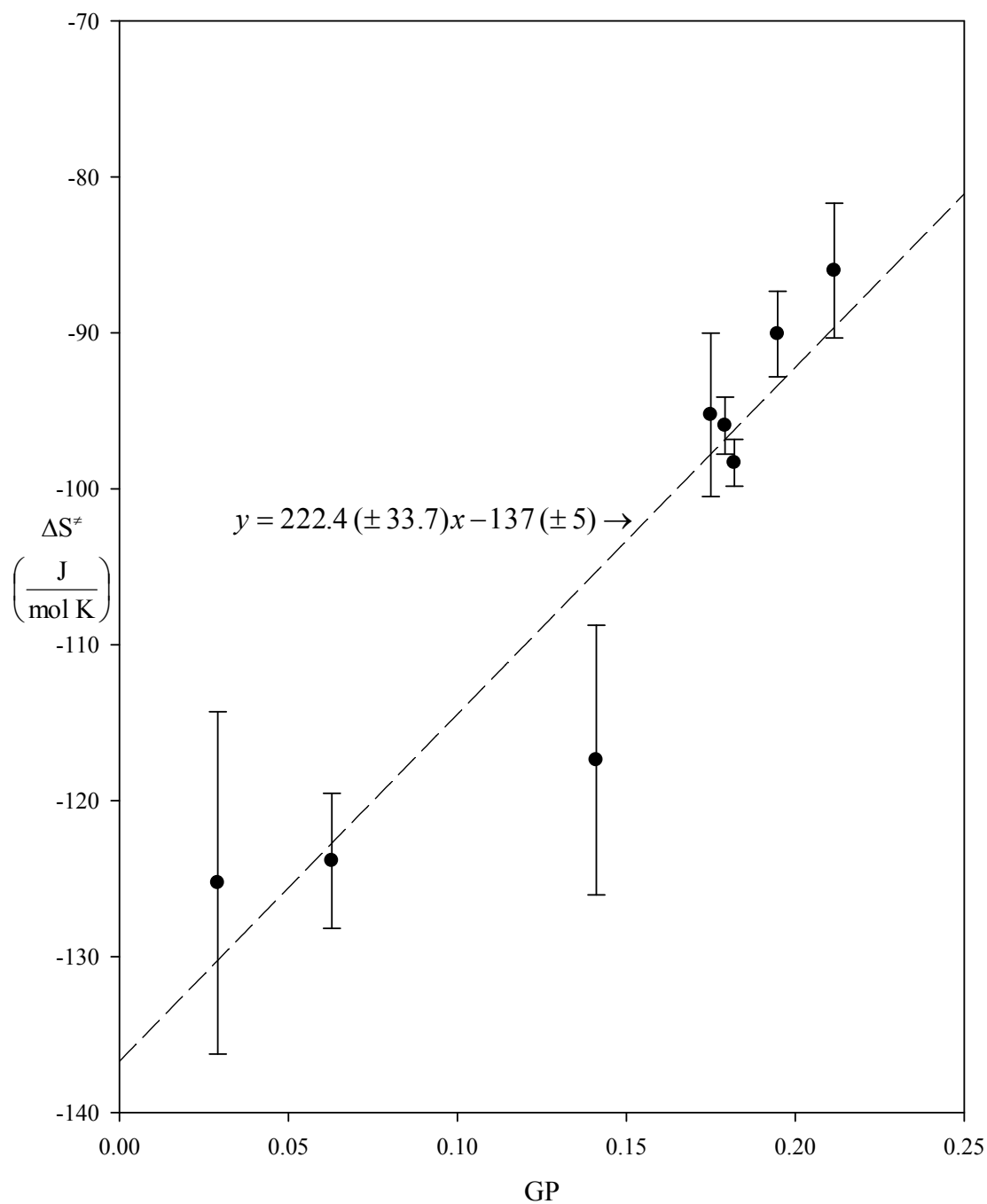


Figure 2.43 The approximately linear relationship between ΔS^\ddagger vs. GP (reactant concentrations ranging from 0.10 mM to 8.00 mM) for reaction (2-2) as taken from Table 2.24. The equation of the regression line is $y = 222.4 (\pm 33.7)x + 137 (\pm 5)$.

The positive slope of the regression line between ΔH^\ddagger and GP as the reactants concentration is increased (Figure 2.42) implies that the energy required to drive the reactants to the transition state *increases* as the reactant concentrations become larger. This is a surprising result since one might expect the enthalpic barrier to not change much, or perhaps even to become smaller as the reactants concentration is increased due to the presumably higher interreactant coulombic screening which would be expected at higher GP (since the total ionic strength is higher; see also section 2.12).

From the linear fit of the data in Figure 2.42 over the experimental GP range of 0.0291 to 0.2126 ($\Delta GP = 0.1835$) we see a change in ΔH^\ddagger of +6.6 kJ/mol. Over the same range, Figure 2.43 shows that ΔS^\ddagger decreases from -125.3 to -86.0 J/K mol (a change of +39.3 J/K mol).

Figure 2.44 shows a plot ΔH^\ddagger vs. ΔS^\ddagger at the various reactant concentrations. In this case, a positive and more-obviously linear relationship is found. Activational data often lead to such “enthalpy-entropy compensation” or “isokinetic” relationships when activational barriers are compared for closely related reactions and much has been written on this topic in the literature.^{43,49} The molecular origins of these relationships are notoriously difficult to establish, but the fact that we arrive at this particular one using two different NMR techniques over an uncommonly-large range of reactants concentrations supports its validity (as does the strongly-confirming nature of related temperature-dependent stopped-flow studies conducted by Sista and Mehmood.^{6,9}

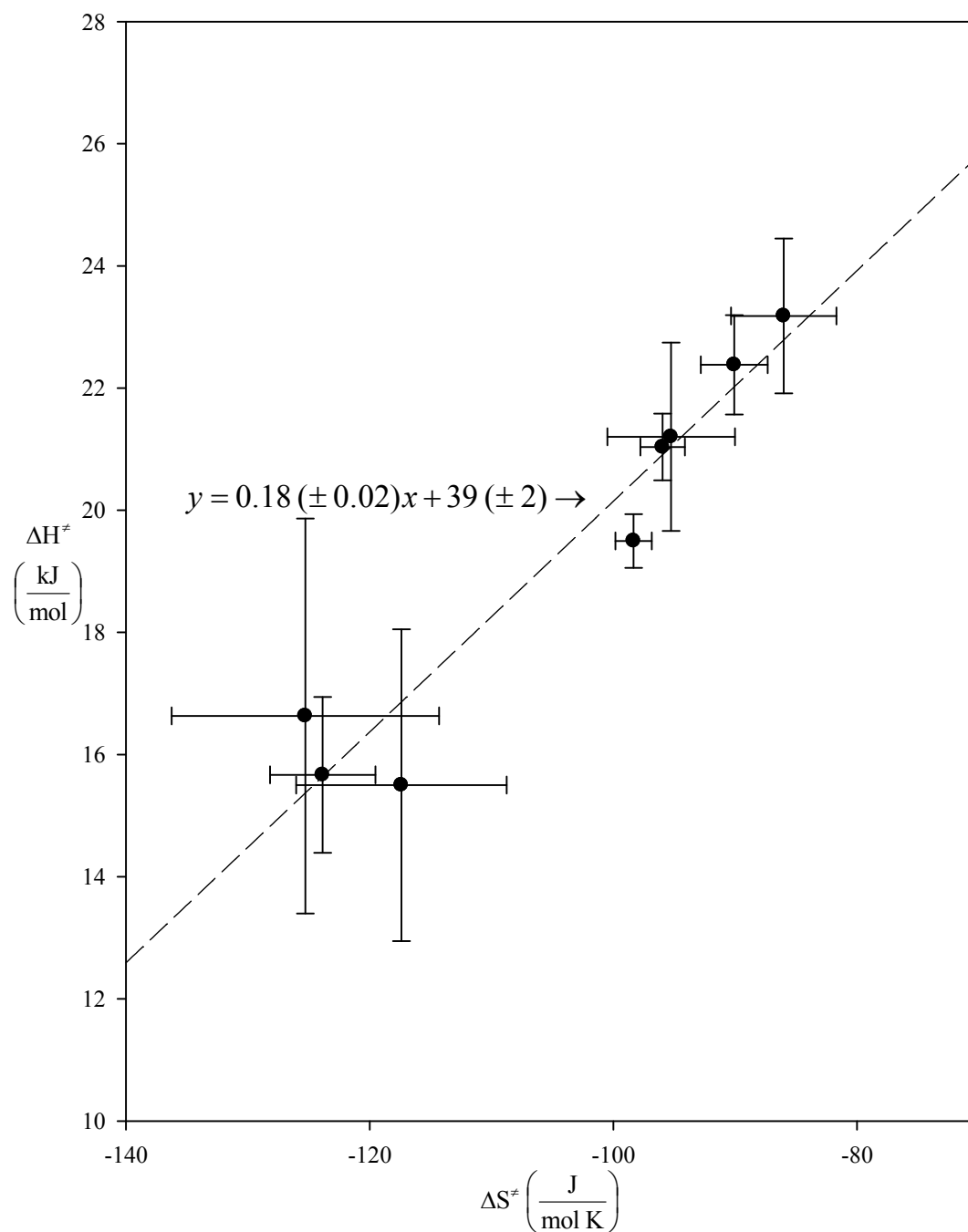


Figure 2.44 ΔH^\ddagger vs. ΔS^\ddagger for reaction (2-2) at reactant concentrations ranging from 0.10 mM to 8.00 mM showing evidence for enthalpy-entropy compensation.⁴³ The equation of the regression line is $y = 0.18 (\pm 0.02) x + 39 (\pm 2)$.

In this case the slope of the plot gives an isokinetic temperature of ~ 187 K, which is well-away from the experimental temperature range. We will return to our discussion of these observations in a later section.

2.16.2 The effects of added salts on activation parameters

The temperature dependent kinetic work was next extended to study the effects of the added salts KF, KBr, Na₂muc, and Na₂adip on the entropic and enthalpic barriers of reaction (2-2) using T₂ at the constant reactants concentration of 0.10 mM. The effects of these salts were first studied at modest added salt concentrations which we consider as being the “non-forcing” condition with a total solution GP of 0.0494 (the initial GP of 0.0494 being due to the 0.10 mM reactants with the rest coming added salt concentrations of 1.80 mM for KF and KBr, and from added concentrations of Na₂muc and Na₂adip equal to 0.60 mM). The results are listed in Table 2.25 and illustrated in Figure 2.45. The activation parameters derived from the linear fit of the data plotted in Figure 2.45 are listed in Table 2.26. As was done for the previous temperature-dependent rates acquired using T₂ at various equimolar reactants concentrations, equation (2-32) was applied to all experimental runs in order to normalize the starting point jitter in the $\ln(k_{\text{ex}}/T)$ data sets.

Table 2.25 Temperature dependent T_2 rate data at 0.10 mM reactants in the presence of various added salts making a total GP = 0.0494 (0.0018 M salt for KF and KBr, and 0.0006 M salt for Na₂muc and Na₂adip). Column (a) lists the values of $\ln(k_{\text{ex}} / T)$ obtained from raw k_{ex} values, and (b) shows the same data after normalizing all runs to an average k_{ex} value at a reactants concentration of 0.10 mM with no salt added (where the average k_{ex}^T is taken from ≥ 5 measurements at 299 K).

KF (0.0018 M)

Temperature (K)	1/T (K ⁻¹)	k_{ex} (M ⁻¹ s ⁻¹)	$\ln(k_{\text{ex}} / T)^{(a)}$	$\ln(k_{\text{ex}} / T)^{(b)}$
283	0.00353	1940	1.93	1.94
288	0.00347	2840	2.29	2.30
293	0.00341	3130	2.37	2.38
299	0.00334	3110	2.34	2.35 ± 0.12
303	0.00330	4510	2.70	2.71

KBr (0.0018 M)

Temperature (K)	1/T (K ⁻¹)	k_{ex} (M ⁻¹ s ⁻¹)	$\ln(k_{\text{ex}} / T)^{(a)}$	$\ln(k_{\text{ex}} / T)^{(b)}$
283	0.00353	3640	2.56	2.38
288	0.00347	4070	2.67	2.49
293	0.00341	4580	2.75	2.57
299	0.00334	5650	2.94	2.76 ± 0.12
303	0.00330	6100	3.00	2.83

Na₂muc (0.0006 M)

Temperature (K)	1/T (K ⁻¹)	k_{ex} (M ⁻¹ s ⁻¹)	$\ln(k_{\text{ex}} / T)^{(a)}$	$\ln(k_{\text{ex}} / T)^{(b)}$
283	0.00353	6890	3.19	3.05
288	0.00347	8750	3.41	3.27
293	0.00341	10450	3.57	3.43
299	0.00334	12550	3.74	3.59 ± 0.12
303	0.00330	14000	3.83	3.69

Na₂adip (0.0006 M)

Temperature (K)	1/T (K ⁻¹)	k _{ex} (<u>M</u> ⁻¹ s ⁻¹)	ln(k _{ex} / T) ^(a)	ln(k _{ex} / T) ^(b)
283	0.00353	7070	3.22	3.19
288	0.00347	7540	3.32	3.29
293	0.00341	8080	3.34	3.31
299	0.00334	8830	3.47	3.44 ± 0.12
303	0.00330	9320	3.76	3.73

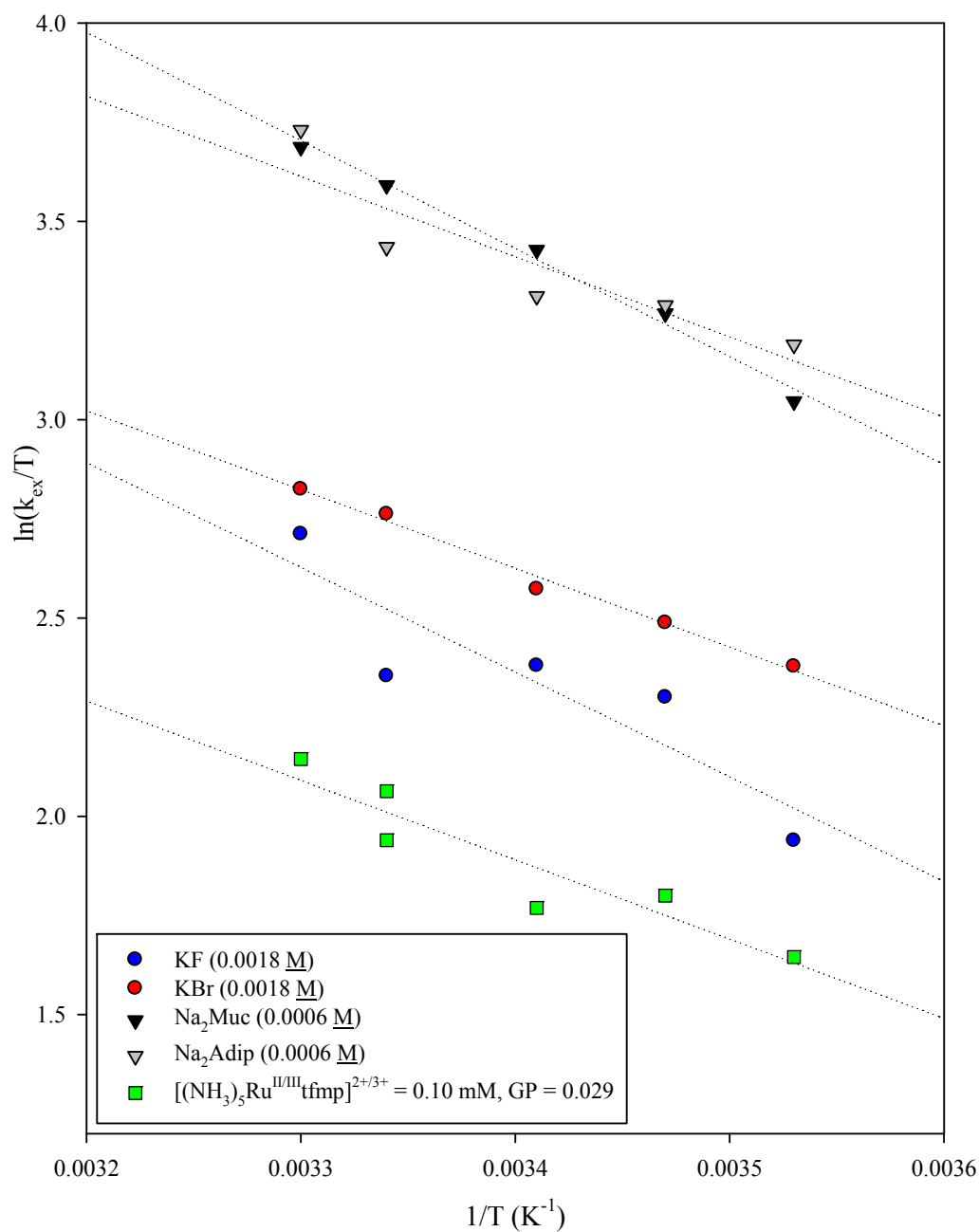


Figure 2.45 Temperature dependent normalized rate data for reaction (2-2) at 0.10 mM reactants with no added salt (green squares), added KF (1.80 mM, blue circles), KBr (1.80 mM, red circles), Na_2muc (0.60 mM, black triangles), and Na_2adip (0.60 mM, grey triangles). This equates to a total solution GP of 0.0494 (“non-forcing conditions”) for all but the bottom line.

Table 2.26 The activation parameters, ΔH^\ddagger and ΔS^\ddagger , for reaction (2-2) at 0.10 mM reactants in the presence of added electrolytes at “non-forcing conditions” (constant solution GP = 0.0494, except for the no-salt case) derived from the linear fit of the normalized temperature-dependent rate data presented in Table 2.25 (illustrated in Figure 2.45).

Electrolyte	Slope	y-intercept	ΔH^\ddagger (kJ/mol)	ΔS^\ddagger (J/K mol)	ΔG^\ddagger_{298} (kJ/mol)
No Salt	-2000 ± 390	8.7 ± 1.3	16.6 ± 3.2	-125 ± 11	53.9
KF	-2640 ± 750	11.3 ± 2.5	22.0 ± 6.2	-103 ± 21	46.4
KBr	-1990 ± 120	9.1 ± 0.4	16.5 ± 1.0	-120 ± 3	52.3
Na ₂ muc	-2720 ± 160	12.7 ± 0.5	22.7 ± 1.3	-92 ± 5	50.1
Na ₂ adip	-2020 ± 550	10.3 ± 1.9	16.8 ± 4.5	-112.0 ± 15.5	50.2

Previous temperature-dependent stopped-flow work⁶ on reaction (2-1) at 0.10 mM reactants upon addition of the same salts in the same amounts (total solution GP = 0.0494) showed a very similar pattern. The stopped-flow data are compared with the current T₂ data in Figure 2.46, and the activation parameters derived from linear fits of these data as well are presented in Table 2.27.

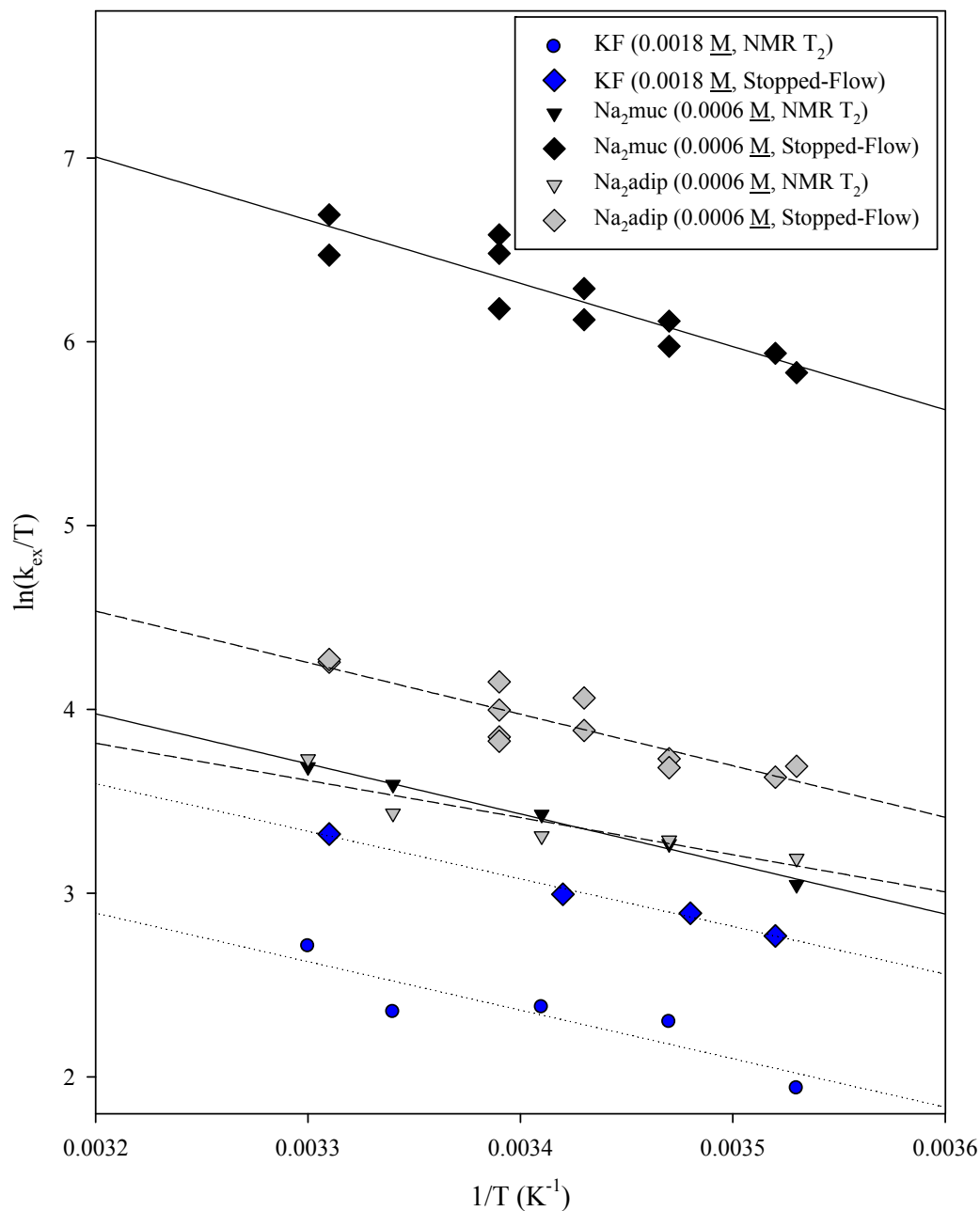


Figure 2.46 Temperature dependent rate data for reactions (2-1) and (2-2) measured by stopped-flow and T₂, respectively, at 0.10 mM reactants with added KF (1.80 mM, blue circles = NMR, blue diamonds = stopped-flow), Na₂muc (0.60 mM, black triangles = NMR, black diamonds = stopped-flow), and Na₂adip (0.60 mM, grey triangles = NMR, grey diamonds = stopped-flow) such that the total solution GP was 0.0494 (“non-forcing conditions”).

Table 2.27 The activation parameters, ΔH^\ddagger and ΔS^\ddagger derived from the regression lines in Figure 2.46 for reactions (2-1) and (2-2) at 0.10 mM reactants in the presence of added salt at “non-forcing conditions” (constant solution GP = 0.0494, except for the no-salt case).

Electrolyte	Conc. Salt (mM)	ΔH^\ddagger (kJ/mol)		ΔS^\ddagger (J/K mol)	
		Reaction (2-2) ^(a)	Reaction (2-1) ^(b)	Reaction (2-2) ^(a)	Reaction (2-1) ^(b)
No Salt	N/A	16.6 ± 3.2	20.1 ± 2.3	-125 ± 11	-106 ± 8
KF	1.80	22.0 ± 6.2	21.2 ± 0.9	-103 ± 21.2	-100 ± 3
KBr	1.80	16.5 ± 1.0	16.6 ± 0.9	-120 ± 3	-111 ± 3
Na ₂ Muc	0.60	22.7 ± 1.3	28.3 ± 4.9	-92 ± 5	-49 ± 17
Na ₂ Adip	0.60	16.8 ± 4.5	23.5 ± 3.9	-112 ± 16	-85 ± 13

(a) For reaction (2-2) as measured by T₂ relaxation. (b) For reaction (2-1) as measured by stopped-flow.⁶

Comparing the activation parameters obtained by stopped-flow and NMR in Table 2.27, we see that the ΔH^\ddagger values are identical within error for added KF and KBr. For Na₂muc and Na₂adip, we see a consistent upwards bias in the stopped-flow data, but the difference is not rigorously above experimental error. The ΔS^\ddagger values for KF and KBr are again very close, but for muc²⁻ and adip²⁻ we see a consistently lower entropic barrier by stopped-flow (especially for muc²⁻ where the difference is 43 J/ mol K). The higher *rate* for the stopped-flow *pseudo* self-exchange reaction (2-1) (which has a 69 mV driving force) as compared to the *true* self-exchange reaction (2-2) (with zero driving force) is to be expected on the basis of the following equation from Marcus-Hush theory,

$$\Delta G^* = \frac{\lambda}{4} \left(1 + \frac{\Delta G^\circ}{\lambda} \right)^2 \quad (2-33)$$

which shows how ΔG^* (a key component of ΔG^\ddagger) decreases when $\Delta G^\circ < 0$. Given that the ΔH^\ddagger values are larger for the no-salt, muc²⁻, and adip²⁻ cases by stopped-flow, however, the form of equation (2-33) would suggest that the “driving force effect” speeding up the stopped-flow rates must be due to more-than-compensating decrements in the entropic barriers for these cases. While the data in the last two columns of Table 2.27 do bear this out, the very surprising implication for this subset of cases is that the driving force manifests primarily in the *entropic barrier*. To our knowledge this is a novel finding, especially for the “no-salt” case where no possibility of anion-specific mediation exists (though we must again note the “not quite 95%” confidence level of the difference). These observations present us with a fundamental question regarding how to interpret the activation barriers derived from the Eyring/TST formalism and how compatible this (necessarily approximate) formalism is with even our relatively simple ET reaction.

If we look closely at the fluoride anion data in Figure 2.46 (blue circles = NMR, and blue diamonds = stopped-flow) we see that the slopes (dotted-line) arrived at by both methods are identical while the y-intercepts slightly differ (*ie.* ΔS^\ddagger values, although still within error). The drop in the entropic barrier is even more pronounced for bromide, muconate, and adipate anion data (best seen in Table 2.27).

The most striking difference between stopped-flow and NMR data was in the measured entropic barrier due to added sodium muconate: ΔS^\ddagger is more positive by 43

J/K mol as measured by stopped-flow (where the “muconate effect” is relevant) compared to that measured by NMR (see Table 2.27). The exceptionally-low entropic barrier (multiply-verified)^{6,9,36} for added muconate in the context of reaction (2-1) has been attributed to its ability to ET by virtue of quantum super-exchange mediation.²² While our NMR data does show a slightly smaller entropic barrier for muconate (as compared to KF and KBr), the relative sizes of the deviations further support the earlier observations of muconate reverting to a “normal” (or “inert”) salt behavior when observed by NMR.⁸

As was done for the activation parameters obtained at differing reactants concentrations as measured by NMR, we have constructed a plot of ΔH^\ddagger vs. ΔS^\ddagger in Figure 2.47. We have included both the current NMR-derived activation parameters and the corresponding ones from Sista using stopped-flow in the non-forcing condition case.⁶ The very similar isokinetic^{43,49,50} (ΔH^\ddagger vs. ΔS^\ddagger) correlations obtained using both techniques supports the idea of a common salt-induced rate effect underlying the enthalpy-entropy compensation in both cases.

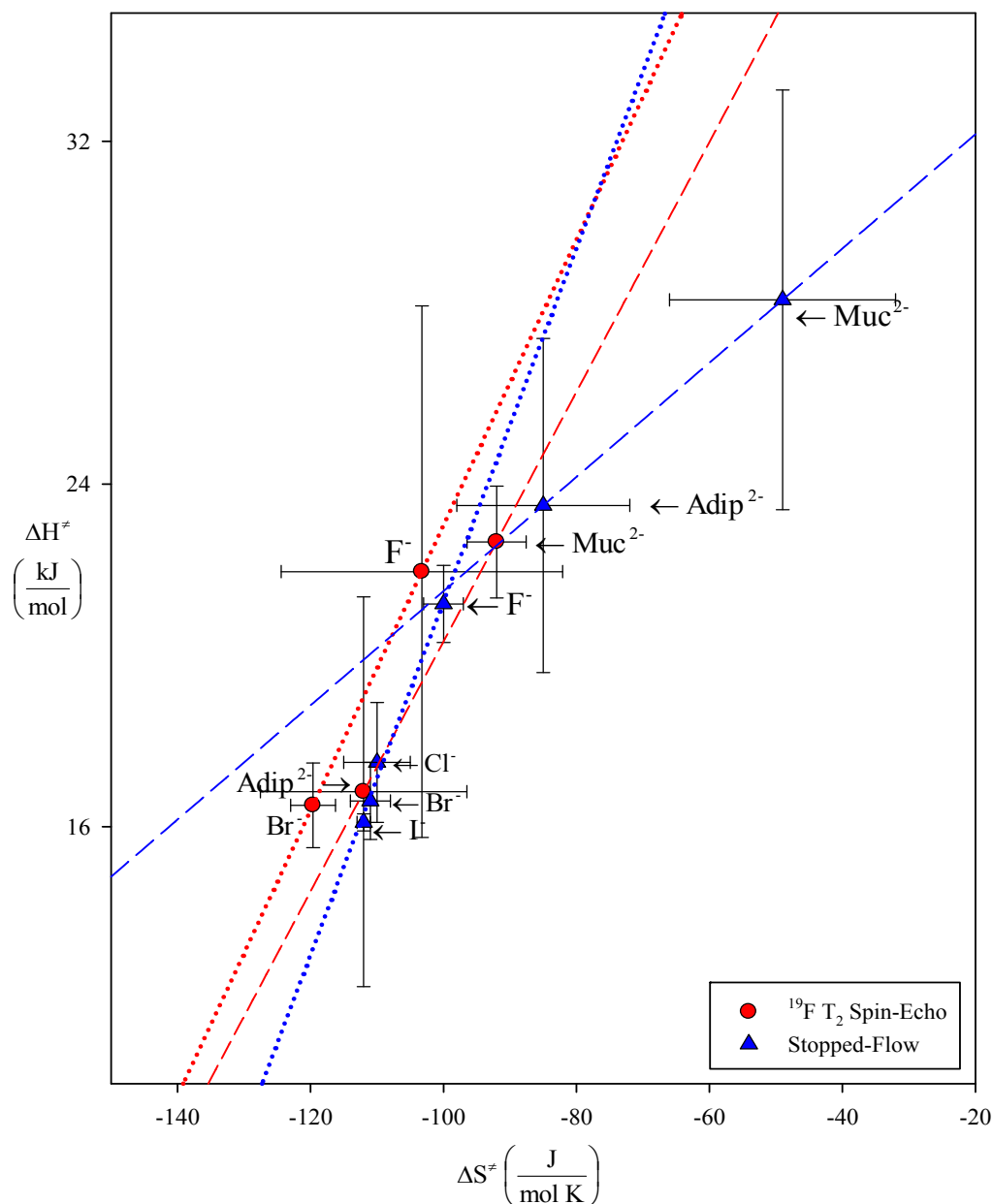


Figure 2.47 Enthalpy-Entropy compensation at a 0.10 mM reactants in the presence of KF (0.0018 M), KBr (0.0018 M), Na₂Muc (0.0006 M), and Na₂Adip (0.0006 M) (non-forcing conditions, GP = 0.0494) for reaction (2-2) studied by NMR (red circles) compared with the entire halide series and dicarboxylate salts for reaction (2-1) studied by stopped-flow⁶ (blue circles). The error bars represent the standard deviations associated with the linear fits of the temperature dependent data (see Table 2.27).

When we compare the slopes of the isokinetic plots shown in Figure 2.47 arrived at by NMR and stopped flow, we find the slopes of the halide series to be 333 K and 412 ± 32 K as measured by NMR and stopped-flow, respectively. These slopes can be considered identical given the large relative errors because only two points being used to fit the NMR data. When we compare the two-point slopes arrived at using the dicarboxylate data however, we find slopes of 291 K and 133 K by NMR and stopped-flow respectively. Although only two points are used to fit these data the slope arrived at by NMR closely resembles that of the halides while that found by stopped-flow deviates strongly. Importantly, muconate as measured by stopped-flow appears to occupy a separate region of the graph, and this again supports the idea that the muconate effect seen by stopped-flow is lost when measured by NMR.

Temperature dependent rate measurements were repeated at 0.10 mM reactants but now with larger concentrations of added salts with the intention of mimicking the more “forcing” conditions (0.006 M salt, total GP = 0.0767) used in the stopped-flow work conducted by Sista. Both the fluoride and bromide anions were studied at these conditions and these data are presented in Table 2.28 and illustrated in Figure 2.48. The activation parameters derived from Figure 2.49 are listed in Table 2.29. As in the “non-forcing” conditions case, equation (2-32) was applied to all experimental k_{ex} values in order to normalize experimental $\ln(k_{\text{ex}} / T)$ values.

Table 2.28 Temperature dependent rate data at 0.10 mM reactants in the presence of various added salts making a total GP = 0.0767 (0.006 M salt). Column (a) lists the values of $\ln(k_{\text{ex}} / T)$ obtained from raw k_{ex} values, and (b) shows the same data after normalizing all runs to an average k_{ex} value at a reactants concentration of 0.10 mM with no salt added (where the average k_{ex}^T is taken from ≥ 5 measurements at 299 K).

KF (0.006 M)

Temperature (K)	1/T (K ⁻¹)	k_{ex} (M ⁻¹ s ⁻¹)	$\ln(k_{\text{ex}} / T)$ ^(a)	$\ln(k_{\text{ex}} / T)$ ^(b)
283	0.00353	3730	2.57	2.59
288	0.00347	4630	2.78	2.80
293	0.00341	5560	2.94	2.97
299	0.00334	5740	2.95	2.98 ± 0.12
303	0.00330	8650	3.35	3.37

KBr (0.006 M)

Temperature (K)	1/T (K ⁻¹)	k_{ex} (M ⁻¹ s ⁻¹)	$\ln(k_{\text{ex}} / T)$ ^(a)	$\ln(k_{\text{ex}} / T)$ ^(b)
283	0.00353	15610	4.01	3.95
288	0.00347	17410	4.10	4.04
293	0.00341	19200	4.18	4.12
299	0.00334	21030	4.25	4.20 ± 0.12
303	0.00330	23500	4.35	4.29

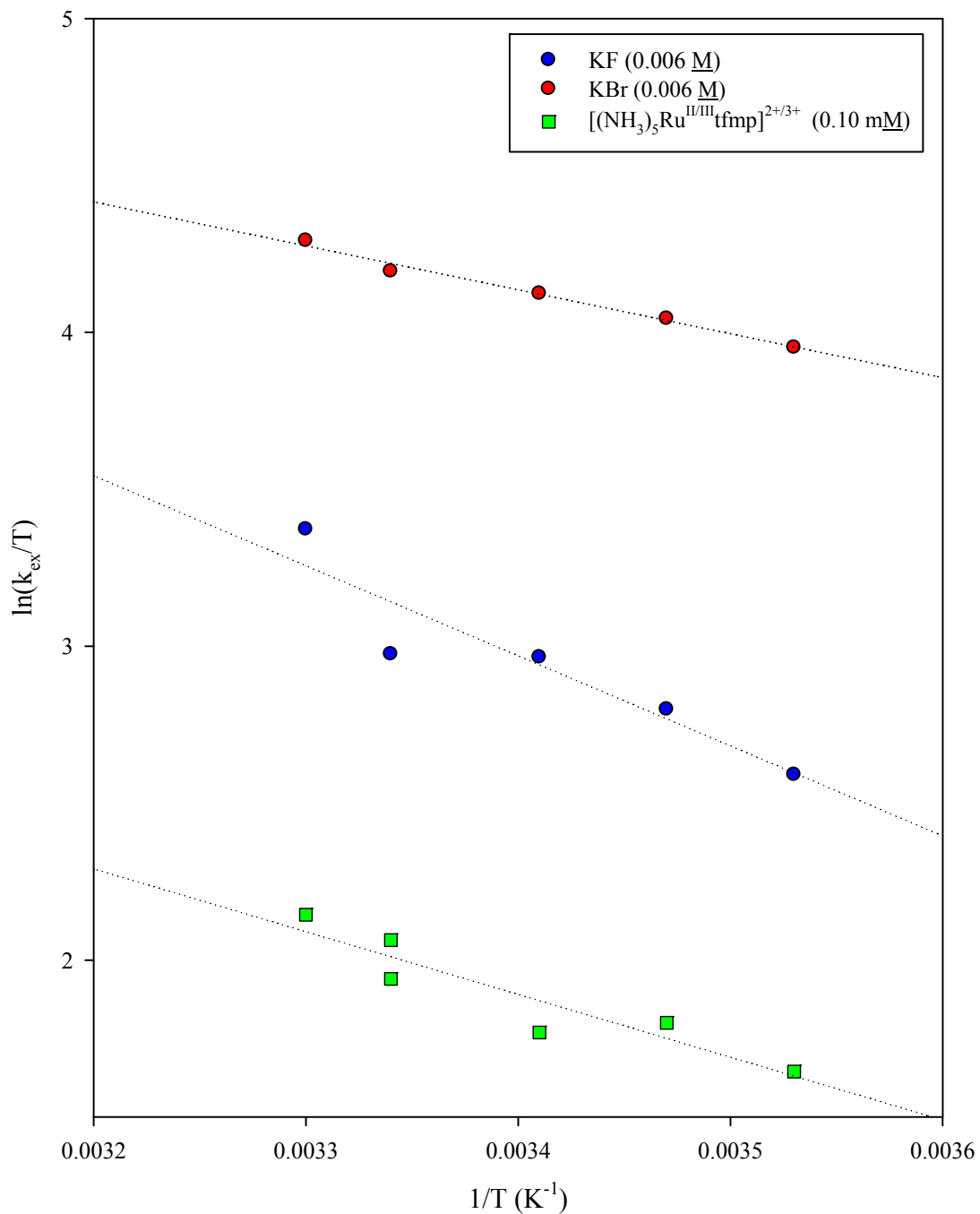


Figure 2.48 Temperature dependent normalized rate data for reaction (2-2) at 0.10 mM reactants with no added salt (green squares, GP=0.0291), added KF (6.00 mM, blue circles), and KBr (6.00 mM, red circles) such that the total solution GP was 0.0767 (“forcing conditions”) for all but the bottom line.

Table 2.29 The activation parameters, ΔH^\ddagger and ΔS^\ddagger , for reaction (2-2) at 0.10 mM reactants in the presence of added electrolytes at “forcing conditions” (constant solution GP = 0.0767, except for the no-salt case) derived from the linear fit of the normalized temperature-dependent rate data presented in Table 2.28 (illustrated in Figure 2.48).

Electrolyte	Slope	y-intercept	ΔH^\ddagger (kJ/mol)	ΔS^\ddagger (J/K mol)	ΔG^\ddagger_{298} (kJ/mol)
No Salt	-2000 ± 390	8.7 ± 1.3	16.6 ± 3.2	-125 ± 11	53.9
KF	-2870 ± 640	12.7 ± 2.2	23.9 ± 5.3	-92 ± 18	51.3
KBr	-1400 ± 95	8.9 ± 0.3	11.6 ± 0.8	-124 ± 3	48.6

As in the non-forcing condition case, we also have previous temperature dependent stopped-flow work on reaction (2-1)⁶ at 0.10 mM reactants in the presence of the same added salts for comparison; the activation parameters arrived at by both methods are listed in Table 2.30.

Table 2.30 The activation parameters, ΔH^\ddagger and ΔS^\ddagger , for reactions (2-1) and (2-2) at 0.10 mM reactants in the presence of added salt at “forcing” conditions” (constant solution GP = 0.0767, except for no-salt).

Electrolyte	ΔH^\ddagger (kJ/mol)		ΔS^\ddagger (J/K mol)	
	Reaction (2-2) ^(a)	Reaction (2-1) ^(b)	Reaction (2-2) ^(a)	Reaction (2-1) ^(b)
No Salt	16.6 ± 3.2	20.1 ± 2.3	-125 ± 11	-106 ± 8
KF	23.9 ± 5.3	24.5 ± 2.1	-92 ± 18	-86 ± 7
KBr	11.6 ± 0.8	13.3 ± 3.3	-124 ± 3	-115 ± 11

(a) For reaction (2-2) measured *via* T₂ spin-echo and (b) for reaction (2-1) measured *via* stopped-flow.⁶

Similar to what we saw at “non-forcing conditions”, when comparing the activation parameters obtained by both NMR and stopped-flow, we find that the ΔH^\ddagger values are consistently higher by stopped-flow but still within error of each other (see also Table 2.27). The ΔS^\ddagger values arrived at by NMR differ in an opposite manner with the entropic barrier being consistently lower decreasing in the stopped-flow case (where there is a driving force present). The significance relative to experimental error limits is again unclear due to the large extrapolation involved in assessing ΔS^\ddagger .

Specific to the data in Table 2.30, we see that upon going from the “no salt” case (at 0.10 mM reactants) to the forcing condition of 6.00 mM of added F^- (total solution GP = 0.0767) causes ΔH^\ddagger as measured by NMR to increase by 44% (going from 16.6 to 23.9 kJ/mol). In the non-forcing case (see Table 2.27) the increase was only 33%. On the other hand, ΔS^\ddagger becomes less negative by 33 J/K mol in the forcing conditions case (a 27% drop in the barrier which corresponds to 10 kJ/mol using $-T\Delta S^\ddagger$ with $T = 299$ K). These compensating changes, $\Delta\Delta H^\ddagger = +7.3$ kJ/mol and $-\Delta\Delta S^\ddagger (299\text{ K}) = - (33\text{ J/ mol K})(299\text{K}) = -10.0$ kJ/mol, mirror the changes seen in the stopped-flow data upon adding fluoride. The change in the F^- vs. no-added salt barriers at non-forcing (0.0018 M F^-) conditions (see Table 2.27) were $\Delta\Delta H^\ddagger = +5.4$ kJ/mol and $-\Delta\Delta S^\ddagger (299\text{ K}) = - (+22\text{ J/mol K})(299\text{ K}) = -6.7$ kJ/mol thereby confirming the progressive change with increasing $[F^-]$. The NMR data then clearly confirm Sista’s conclusion⁶ that the rate acceleration due to added F^- vs. no-added salt is due to the dominating (and compensating) decrease in the entropic barrier.

Upon going from no-added salt to added Br^- , we find $\Delta\Delta H^\ddagger = -5.5 \text{ kJ/mol}$ and $-\Delta\Delta S^\ddagger = +5 \text{ J/mol K}$. At 299 K this equates to $\Delta\Delta G^\ddagger = -1.5 \text{ kJ/mol}$, meaning that the modest rate increase for Br^- is due to a small, drop in the entropic barrier. At forcing conditions of added Br^- we find $\Delta\Delta H^\ddagger = -4 \text{ kJ/mol}$ and $-(\Delta\Delta S^\ddagger)(299 \text{ K}) = +9.6 \text{ kJ/mol}$. While this pattern is rather confusing it does at least agree with Sista's results, in that the dominating source of the rate increase due to Br^- at forcing conditions is in the enthalpic term.⁶ These results suggest that the dominating kinetic factor in the salt effect on the reaction rate can vary from primarily entropic (F^-) to primarily enthalpic (Br^-) depending on the nature of the salt. Overall, we find that the trends observed previously by stopped-flow on reaction (2-1)⁶ are validated by this NMR work on added fluoride and bromide.

As was done in our analysis of the non-forcing data, we have constructed an isokinetic plot of ΔH^\ddagger vs. ΔS^\ddagger in Figure 2.49. Again we have included both the current NMR-derived activation parameters and the corresponding ones from Sista's stopped-flow work.⁶ The very similar isokinetic^{43,49,50} (ΔH^\ddagger vs. ΔS^\ddagger) correlation again observed by both techniques supports the idea of a common mechanism underlying the salt-induced rate effects. There is clearly a very strong enthalpy-entropy compensation at work in both cases.

In Figure 2.50 we present a too busy, but nonetheless instructive view of the aggregate NMR and stopped-flow salt-specific activation data. The resulting isokinetic plot clearly shows the overall agreement in the salt-specific trends at

similar conditions between the two techniques except for added muconate as measured by stopped-flow.

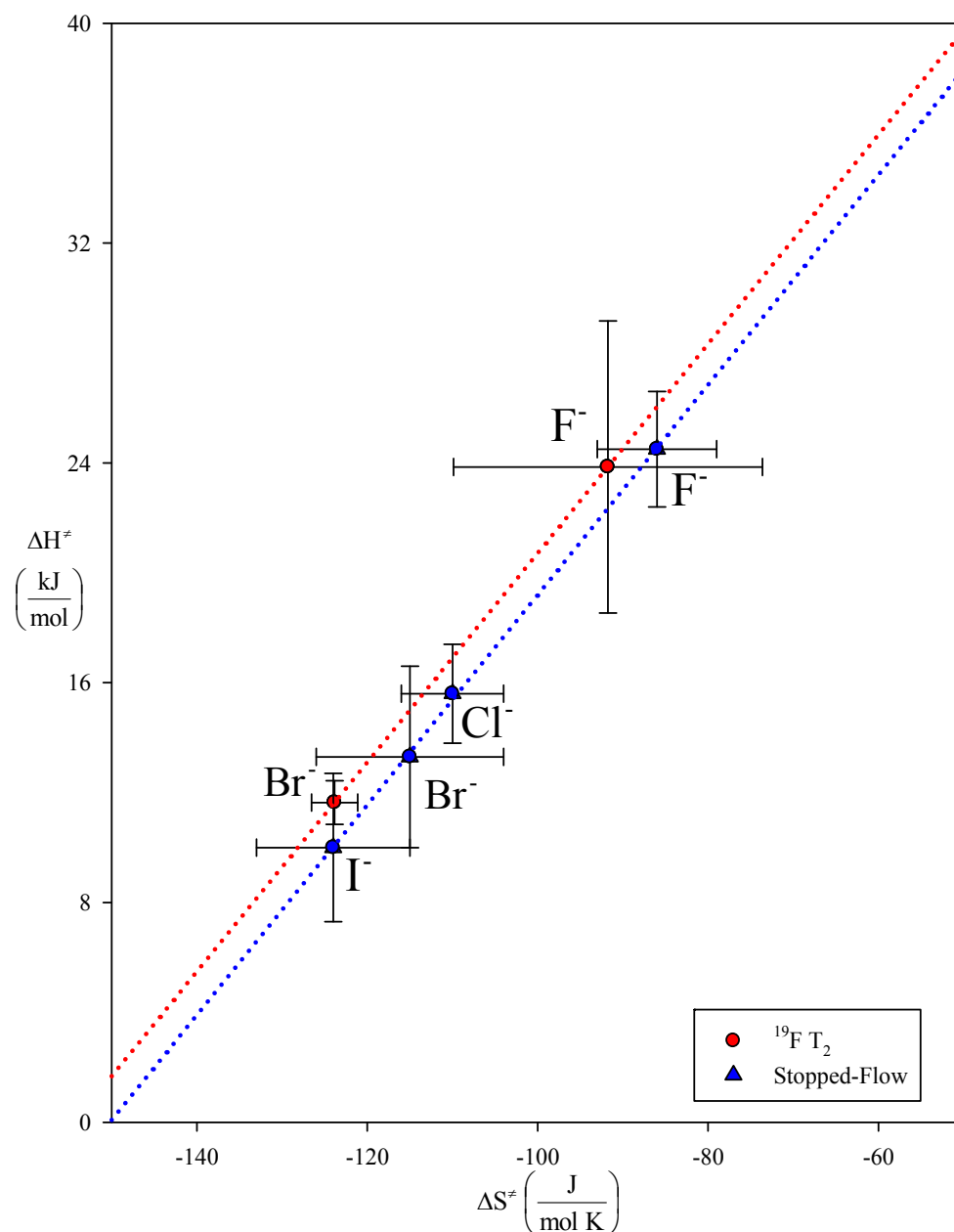


Figure 2.49 Enthalpy-Entropy compensation at 0.10 mM reactants in the presence of KF and KBr (forcing conditions, $[X^-] = 0.006 \text{ M}$) for reaction (2-2) studied by NMR (red circles) compared with kinetic data for the entire halide series obtained in studies of reaction (2-1) by stopped-flow⁶ (blue circles). The error bars represent the standard deviations associated with the linear fits of the temperature dependent data (listed in Table 2.30).

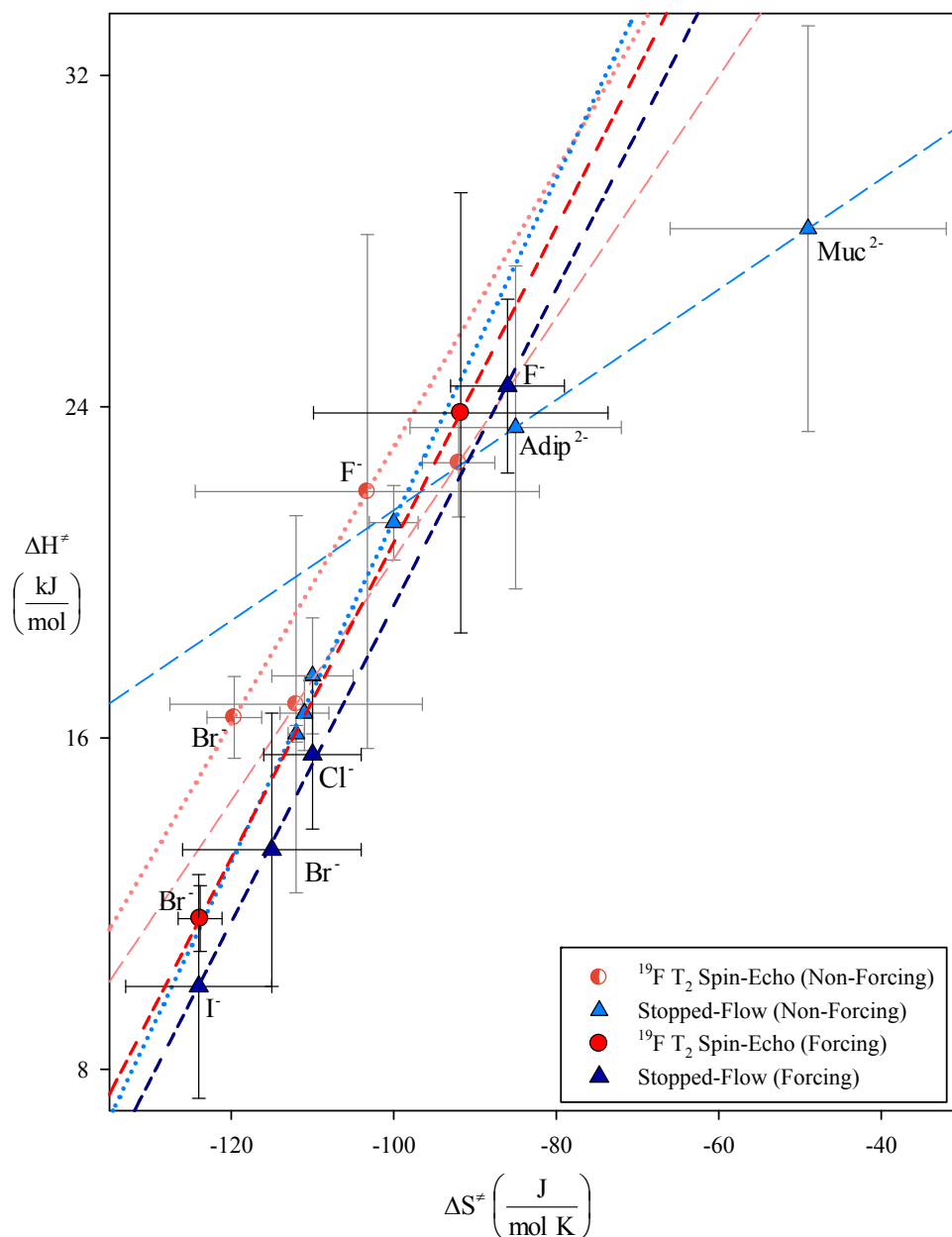


Figure 2.50 Enthalpy-Entropy compensation at 0.10 mM reactants in the presence of the halides and dicarboxylate salts for reaction (2-2) studied by NMR (red circles) compared with kinetic data for the entire halide series and dicarboxylate salts obtained in studies of reaction (2-1) by stopped-flow⁶ (blue circles) at both non-forcing conditions (GP = 0.0494) and forcing conditions (GP = 0.0767). The error bars represent the standard deviations associated with the linear fits of the temperature dependent data (listed in Tables 2.27 and 2.30).

When we compare the slopes of the plots generated in Figure 2.49 arrived at by NMR and stopped-flow, we find essentially identical isokinetic temperature slopes of 380 K and 382 ± 7 K, respectively. This observation supports the tentative explanation previously proposed on the basis of the stopped-flow work that the known variations in the hydration energies of the halide ions (due to the progressive change in radii) may be playing a dominate role in modulating how the entropic and enthalpic barriers of the ET reaction responds to added halide salts. Clearly the two closely-related reactions (2-1) and (2-2) are behaving similarly upon addition of salt.⁶ The decrease in solvation (as reflected in dropping hydration energies)⁵¹ of the halides as we move from F^- to Br^- , would imply that during the formation of an ion-pair between the anion and the 3+ oxidant (the ruthenium(III) complex) fewer and/or less tightly-bound waters of hydration would be lost in the process of forming that ion-pair. The same logic would apply to the step in which the (presumed) ternary precursor complex which leads to ET (see Chapter 1, section 1.2). The enthalpically-unfavorable dehydration at X^- would be lower in magnitude for the larger (and less hydrated) halide ions like Br^- and I^- , and this would logically be expected to show up as a decrement in the overall ΔH^\ddagger . At the same time, the smaller entropy gain upon desolvation of I^- and Br^- (as compared to the strongly-hydrated F^-) ion would provide less compensation for the typically-large entropic barrier expected in a bimolecular reaction which requires association of like-charged reactants (and possibly specific orientation) to reach the transition state.

2.16.3 Effects of added Group VIIIb hexacyano salts on reaction (2-2) activation parameters

The temperature-dependent NMR kinetic work conducted by Qin⁸ on reaction (2-2) using NMR line-broadening (at 5.00 mM reactants) showed that added iron(II), ruthenium(II), and osmium(II) hexacyano salts (see Table 2.2) catalyze ET reaction (2-2) to an extent even far beyond muconate with respect to reaction (2-1) observed by stopped-flow. Their profound catalytic activity increased in the order $\text{Ru}^{\text{II}}(\text{CN})_6^{4-} < \text{Os}^{\text{II}}(\text{CN})_6^{4-} < \text{Fe}^{\text{II}}(\text{CN})_6^{4-}$. A similar pattern was found by Mehmood⁹ in his stopped-flow investigations (including temperature-dependent rate measurements) of reaction (2-1) by stopped-flow. The ordering of the catalytic efficacy was explained on the basis of a redox-potential dependent virtual “hole-transfer” super-exchange mechanism since the $\text{M}^{\text{II/III}}(\text{CN})_6^{4-/3-}$ redox potentials decrease in the order $\text{Fe} < \text{Os} < \text{Ru}$.⁴¹ In the current work, we have sought to verify Qin’s measurements at 5.00 mM reactants under the same conditions using the same ¹⁹F NMR line-broadening method as she did (although now using a Varian 500 MHz NMR spectrometer rather than the previous Bruker 400 MHz spectrometer). We have also extended the NMR work to probe the catalysis at 0.10 mM reactants using T₂ relaxation. The 5.00 mM reactants results are presented in Table 2.31 and illustrated in Figure 2.51. The concentrations of the added potassium hexacyano salts in the exchanging solutions were held constant at $[\text{M}^{\text{II}}(\text{CN})_6]^{4-} = 3.9 \times 10^{-4} \text{ M}$, which was sufficiently enough to be well up into the “catalytic region” (see Figure 2.40). This catalyst concentration was also helpful in minimizing any tendency towards decay in the ET catalytic effect simply

due to standing (*vide supra*, section 2.15). The line-broadening derived rates listed in Table 2.30 were calculated using the “fast-exchange” equation (2-13) for the $\text{K}_4\text{Fe}^{\text{II}}(\text{CN})_6$ salt and the “slow exchange” equation (2-7) for the $\text{K}_4\text{Os}^{\text{II}}(\text{CN})_6$ and $\text{K}_4\text{Ru}^{\text{II}}(\text{CN})_6$ salts (see Figure 2.9).

Table 2.31 Temperature dependent rate data at 5.00 mM reactants in the presence of the three hexacyano salts making a total GP = 0.181 (3.9×10^{-4} M salt). Column (a) shows values of $\ln(k_{\text{ex}} / T)$ obtained from raw k_{ex} values compared with (b) previously obtained values of $\ln(k_{\text{ex}} / T)$.⁸

$\text{K}_4\text{Fe}(\text{CN})_6$ (3.9×10^{-4} M)

Temperature (K)	1/T (K^{-1})	k_{ex} ($\text{M}^{-1} \text{s}^{-1}$)	$\ln(k_{\text{ex}} / T)$ ^(a)	$\ln(k_{\text{ex}} / T)$ ^(b)
283	0.00353	4.503×10^6	9.67	9.79
288	0.00347	6.546×10^6	10.03	10.19
293	0.00341	1.146×10^7	10.57	10.75
299	0.00334	2.095×10^7	11.16	11.13
304	0.00329	2.095×10^7	11.66	11.62

$\text{K}_4\text{Ru}(\text{CN})_6$ (3.9×10^{-4} M)

Temperature (K)	1/T (K^{-1})	k_{ex} ($\text{M}^{-1} \text{s}^{-1}$)	$\ln(k_{\text{ex}} / T)$ ^(a)	$\ln(k_{\text{ex}} / T)$ ^(b)
283	0.00353	2.967×10^4	4.65	5.50
288	0.00347	3.480×10^4	4.79	5.67
293	0.00341	4.253×10^4	4.98	5.77
299	0.00334	4.983×10^4	5.12	6.05
304	0.00329	7.281×10^4	5.48	6.34

K₄Os(CN)₆ (3.9x10⁻⁴ M)

Temperature (K)	1/T (K⁻¹)	k_{ex} (<u>M</u>⁻¹ s⁻¹)	ln(k_{ex} / T) ^(a)	ln(k_{ex} / T) ^(b)
283	0.00353	3.270x10 ⁴	4.75	5.88
288	0.00347	6.509x10 ⁴	5.42	5.98
293	0.00341	9.682x10 ⁴	5.80	6.56
299	0.00334	1.213x10 ⁵	6.01	6.73

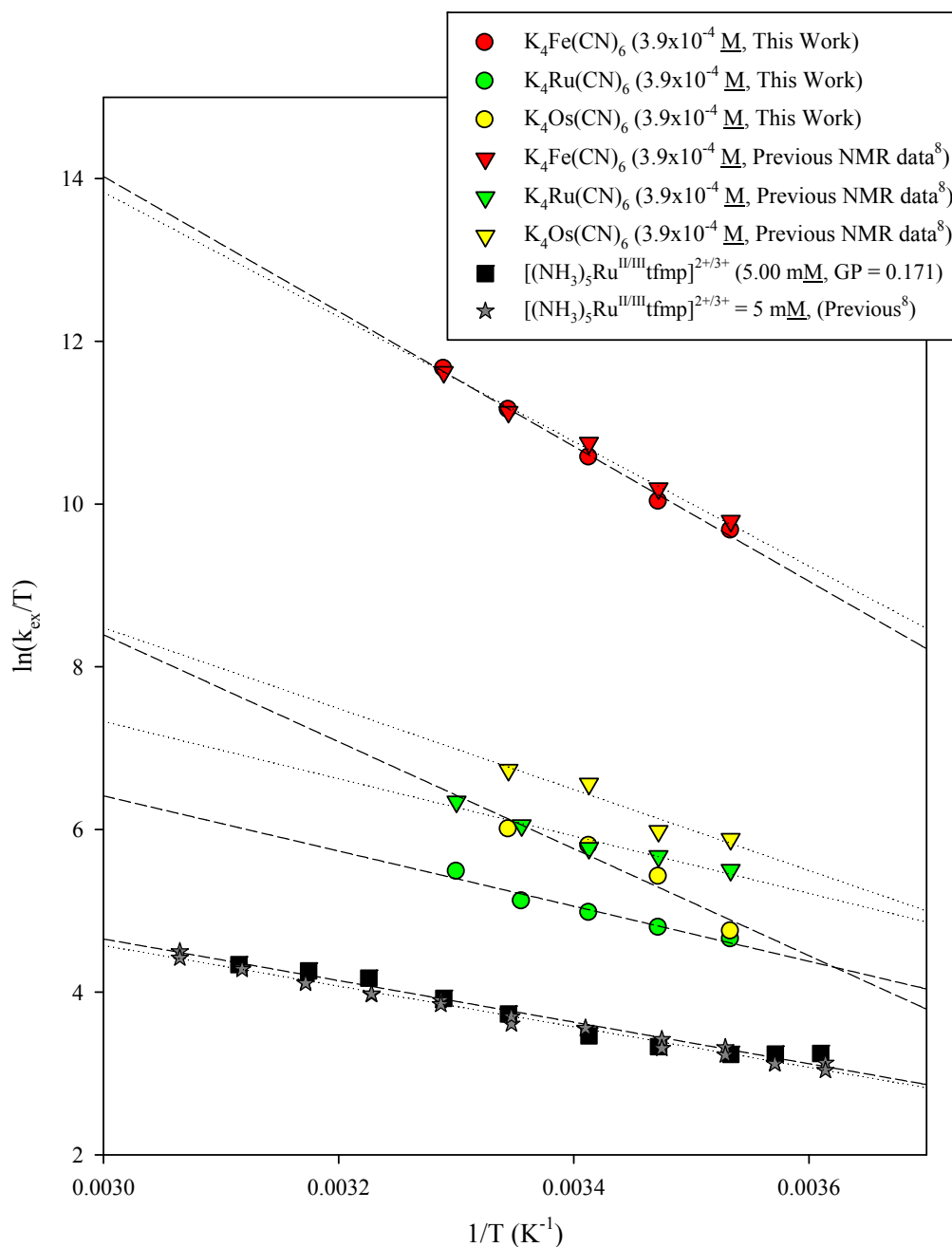


Figure 2.51 Temperature dependent line-broadening data for reaction (2-2) obtained at 5.00 mM reactants with no added salt (this work, black squares; Qin, grey stars; GP = 0.171), and $3.9 \times 10^{-4} \text{ M}$ added $\text{K}_4\text{Fe}^{\text{II}}(\text{CN})_6$ (red circles), $\text{K}_4\text{Ru}^{\text{II}}(\text{CN})_6$ (green circles), and $\text{K}_4\text{Os}^{\text{II}}(\text{CN})_6$ (yellow circles) such that the total solution GP = 0.181. The corresponding data obtained previously by Qin are plotted as red, green, and yellow triangles, respectively.⁸

Table 2.32 The activation parameters, ΔH^\ddagger and ΔS^\ddagger , for reaction (2-2) at 0.10 mM reactants in the presence of added electrolytes at 3.9×10^{-4} M (constant solution GP = 0.181, except for the no salt case) derived from linear fits of the temperature-dependent rate data presented in Table 2.31 (illustrated in Figure 2.51).

Electrolyte	Slope	y-intercept	ΔH^\ddagger (kJ/mol)	ΔS^\ddagger (J/K mol)	ΔG^\ddagger_{298} (kJ/mol)
No Salt	-2550 ± 190	12.3 ± 0.6	21.2 ± 1.5	-95 ± 5	49.5
$K_4Fe(CN)_6$	-8300 ± 350	38.9 ± 1.2	68.9 ± 2.9	126 ± 10	31.4
$K_4Os(CN)_6$	-6600 ± 1300	28.1 ± 4.5	54.7 ± 10.8	36 ± 27	44.0
$K_4Ru(CN)_6$	-3400 ± 430	16.6 ± 1.5	28.2 ± 3.6	-59.7 ± 12.3	46.0

In Figure 2.51 we see that there is good agreement between the two studies for added ferrocyanide and no-added salt cases, but for added rutheno- and osminocyanide the current results deviate downwards from Qin's.⁸ Table 2.33 below compares the two studies.

Table 2.33 The activation parameters, ΔH^\ddagger and ΔS^\ddagger derived from the regression lines in Figure 2.51 for reaction (2-2) at 5.00 mM reactants in the presence of the added hexacyano salts (constant solution GP = 0.0181, except for the no-salt case).

Electrolyte	ΔH^\ddagger (kJ/mol)		ΔS^\ddagger (J/K mol)	
	Reaction (2-2) ^(a)	Reaction (2-2) ^(b)	Reaction (2-2) ^(a)	Reaction (2-2) ^(b)
No Salt	21.2 ± 1.5	20.8 ± 0.8	-95 ± 5	-97 ± 3
$K_4Fe(CN)_6$	68.9 ± 2.9	59.5 ± 1.1	126 ± 10	94 ± 4
$K_4Os(CN)_6$	54.7 ± 10.8	46.3 ± 1.9	36 ± 27	15 ± 6
$K_4Ru(CN)_6$	28.2 ± 3.6	33.3 ± 1.3	-60 ± 12	-35 ± 5

(a) Values obtained by this work using a 500 MHz NMR spectrometer compared with (b) those previously obtained by Qin on a 400 MHz NMR spectrometer.⁸

When comparing the activation parameters from the two studies side by side in Table 2.32, we see that both the ΔH^\ddagger and ΔS^\ddagger values are within error of each other for the first row (no added salt) but somewhat divergent for the catalyzed reactions. In both studies, however, we see that added $\text{K}_4\text{Fe}(\text{CN})_6$ had the largest catalytic effect and that the origin appears to be in the profound reduction in the entropic barrier (from -95 J/mol K to $+126 \text{ J/mol K}$) since ΔH^\ddagger actually increases by 47.7 kJ/mol compared to the no-salt case (this work). In fact, this remarkable change in the entropic “barrier” from -95 J/K mol with no catalyst to $+126 \text{ J/K mol}$ ($+97 \text{ J/K mol}$ in Qin’s work⁸) indicates that there is *no* entropic barrier at all and when $\text{Fe}^{\text{II}}(\text{CN})_6^{4-}$ is present there actually is an entropic “payoff” to forming the transition state. This situation occurs, though to a less extreme degree, with added osiminocyanide where once again the rate goes up due to large, positive $\delta\Delta S^\ddagger$ in spite of a significant positive $\delta\Delta H^\ddagger$ with respect to no catalyst. With added ruthenocyanide we see an entropic barrier again, but it is 35.6 J/K mol more favorable than the no-salt reference case (62 J/K mol less unfavorable in Qin’s work). In the now-familiar trend, this positive $\delta\Delta S^\ddagger$ due to catalysis over-shadows the modest $\delta\Delta H^\ddagger$ of $+7 \text{ kJ/mol}$ ($+13 \text{ kJ/mol}$, Qin⁸).

We note the rate acceleration afforded by these catalysts, even the “weakest” one (rutheniumcyanide), far surpassed any simple GP effect as was seen with added simple salts. While the addition of $3.9 \times 10^{-4} \text{ M}$ $\text{K}_4\text{M}(\text{CN})_6$ salt to 5.00 mM reactants increases the solution GP from $\text{GP}_{\text{rcts}} = 0.171$ to a new value of $\text{GP}_{\text{total}} = 0.181$, this increment in GP would have negligible Debye-Hückle-Bronsted type kinetic

consequences (see, for example, Figure 2.40). Thus we know that the origin of the catalysis must lay elsewhere. Since the sizes of the hexacyanide ions are roughly the same (see Table 2.36), the spectacular variation with central metal ion implies that some aspect of electronic structure and/or redox thermodynamics must be involved.

As was done in our analysis of the halide and dicarboxylate temperature data, we have constructed an isokinetic plot of ΔH^\ddagger vs. ΔS^\ddagger in Figure 2.52. Again we have included both the current NMR-derived activation parameters and the corresponding ones from Qin.⁸ The very similar isokinetic^{43,49,50} (ΔH^\ddagger vs. ΔS^\ddagger) correlation again observed by both trials validates both previous and current work.

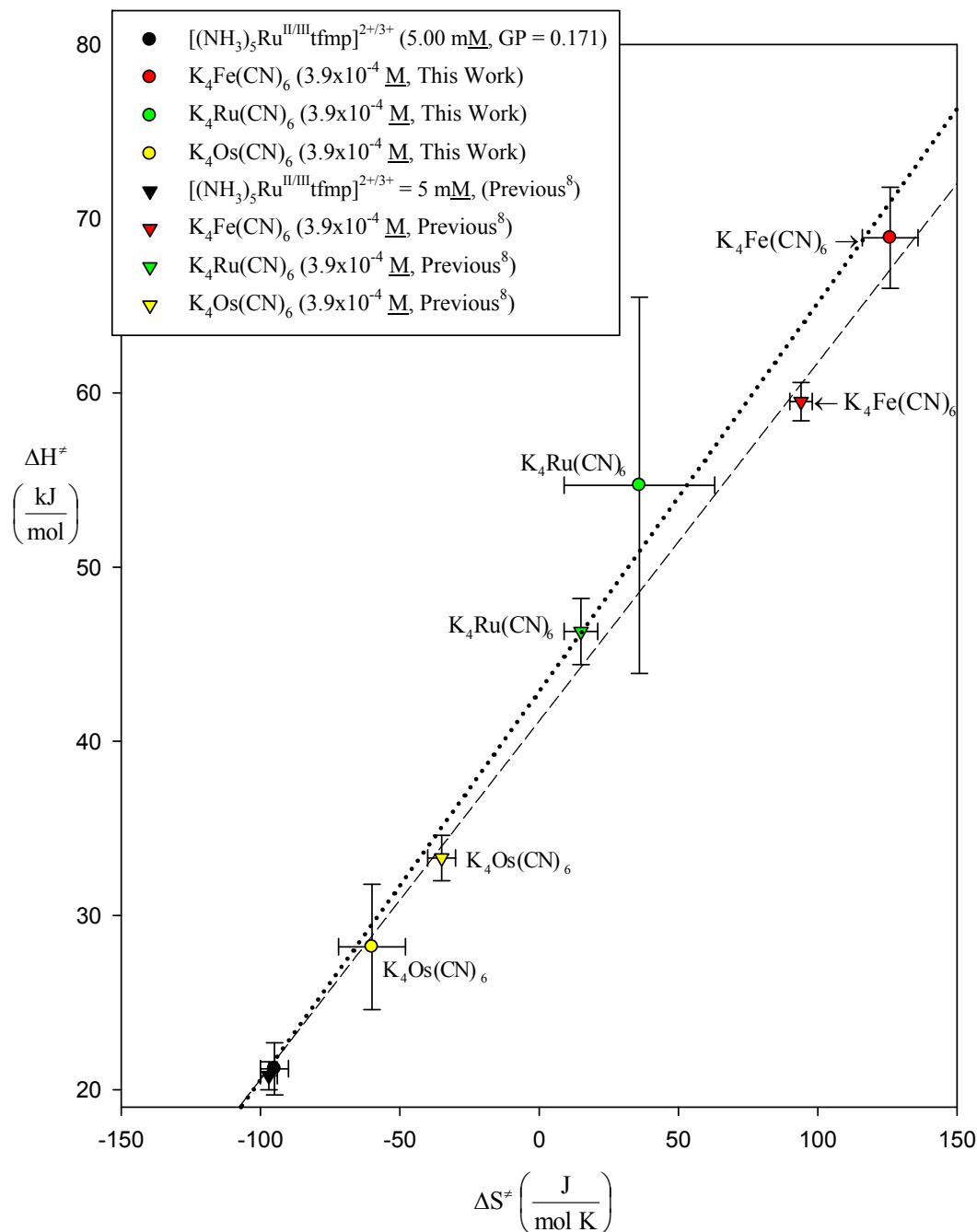


Figure 2.52 Enthalpy-Entropy compensation at 5.00 mM reactants in the presence of the hexacyano salts (at 3.9×10^{-4} M) for reaction (2-2) (red, green, and yellow circles, dotted line) compared with previous data obtained by Qin (red, green, and yellow triangles, dashed line).⁸ The error bars represent the standard deviations associated with the linear fits of the temperature dependent data (listed in Table 2.33).

When the slopes of the plots generated in Figure 2.52 are compared, we find slopes of 223 ± 19 K for the current work and 206 ± 12 K for Qin's work.⁸ These slopes, and hence isokinetic temperatures, are within error of each other and are both well-removed from the experimental temperature range. It is surprising that the no added salt points line up so well with the hexacyano series since the presumed mechanism and transition states are so different.

Temperature dependent kinetic measurements of reaction (2-2) with added $K_4M(CN)_6$ salts (at 8×10^{-6} M salt) were also conducted at 0.10 mM reactants using T_2 . These data are presented in Table 2.34 and illustrated in Figure 2.53. The $K_4Fe(CN)_6$ salt was not studied at this reactants concentration due to the rate enhancement being too large to observe in the “stable” region (*vide supra* section 2.15). As in all the previous activation parameter work acquired by T_2 , equation (2-32) was applied to all experimental k_{ex} values in order to normalize the run-to-run jitter in the $\ln(k_{ex} / T)$ datasets.

Table 2.34 Temperature dependent rate data at 0.10 mM reactants in the presence of $\text{K}_4\text{Ru}(\text{CN})_6$ and $\text{K}_4\text{Os}(\text{CN})_6$ making a total GP = 0.0295 (8×10^{-6} M salt). Column (a) lists the values of $\ln(k_{\text{ex}} / T)$ obtained from raw k_{ex} values, and (b) shows the same data after normalizing all runs to an average k_{ex} value at a reactants concentration of 0.10 mM with no salt added (at 299 K based off 5 measurements at this temperature).

$\text{K}_4\text{Ru}(\text{CN})_6$ (8×10^{-6} M)

Temperature (K)	1/T (K^{-1})	k_{ex} ($\text{M}^{-1} \text{s}^{-1}$)	$\ln(k_{\text{ex}} / T)$ ^(a)	$\ln(k_{\text{ex}} / T)$ ^(b)
283	0.00353	3.686×10^4	4.87	4.69
288	0.00347	4.623×10^4	5.08	4.90
293	0.00341	6.280×10^4	5.37	5.19
299	0.00334	7.864×10^4	5.57	5.39 ± 0.12
304	0.00329	9.174×10^4	5.71	5.53

$\text{K}_4\text{Os}(\text{CN})_6$ (8×10^{-6} M)

Temperature (K)	1/T (K^{-1})	k_{ex} ($\text{M}^{-1} \text{s}^{-1}$)	$\ln(k_{\text{ex}} / T)$ ^(a)	$\ln(k_{\text{ex}} / T)$ ^(b)
283	0.00353	1.190×10^4	3.74	3.83
288	0.00347	1.649×10^4	4.05	4.14
293	0.00341	2.341×10^4	4.38	4.47
299	0.00334	3.590×10^4	4.79	4.88 ± 0.12

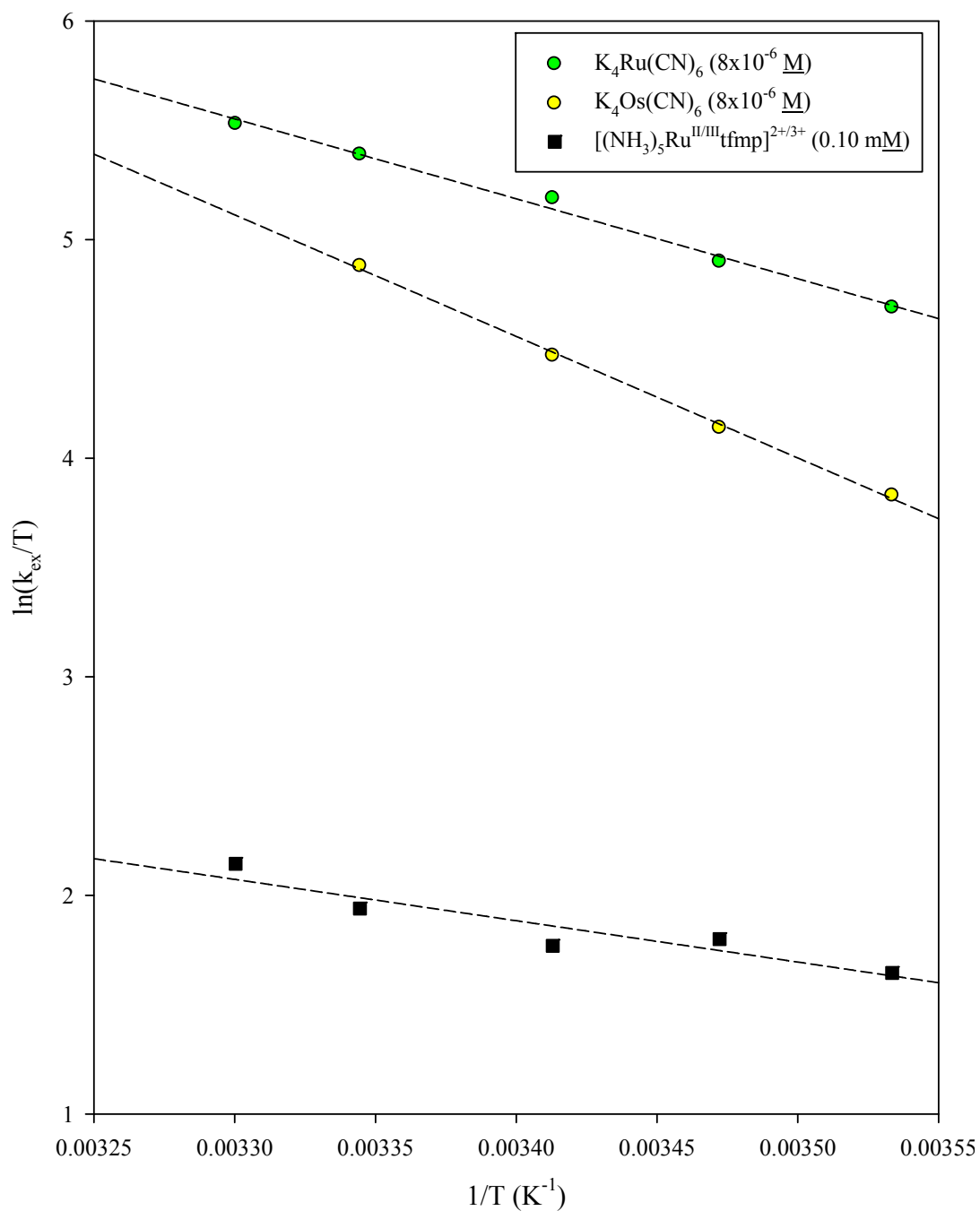


Figure 2.53 Temperature dependent rate data for reaction (2-2) at 0.10 mM reactants with no added salt (black squares, GP = 0.0291), added K₄Ru^{II}(CN)₆ (8x10⁻⁶ M, green circles), and K₄Os^{II}(CN)₆ (8x10⁻⁶ M, yellow circles) making a total solution GP = 0.0295.

Table 2.35 The activation parameters, ΔH^\ddagger and ΔS^\ddagger , for reaction (2-2) at 0.10 mM reactants in the presence of added hexacyano salts at a concentration of 8×10^{-6} M (constant solution GP = 0.0295, except for no-salt) derived from linear fits of the temperature-dependent rate data presented in Table 2.34 (illustrated in Figure 2.53).

Electrolyte	Slope	y-intercept	ΔH^\ddagger (kJ/mol)	ΔS^\ddagger (J/K mol)	ΔG^\ddagger_{298} (kJ/mol)
No Salt	-2000 ± 389	8.7 ± 1.3	16.6 ± 3.2	-125 ± 11	53.9
$K_4Os(CN)_6$	-5560 ± 152	23.5 ± 0.5	46.2 ± 1.3	-2.5 ± 4.3	46.9
$K_4Ru(CN)_6$	-3390 ± 433	17.6 ± 0.6	30.4 ± 1.5	-51 ± 5	45.6

As was observed by line-broadening at 5.00 mM reactants, both the entropy and enthalpy of activation become larger (more positive) as we go from $K_4Ru^{II}(CN)_6$ to $K_4Os^{II}(CN)_6$. The enthalpy of activation with added $K_4Os^{II}(CN)_6$ is 46.2 ± 1.3 kJ/mol and 30.4 ± 1.5 kJ/mol with $K_4Ru^{II}(CN)_6$. Interestingly, the entropy of activation with added $K_4Os^{II}(CN)_6$ is -2.5 ± 4.3 J/K mol, now a just-finite “barrier” again, and it is -51.1 ± 5.2 J/mol in the presence of added $K_4Ru^{II}(CN)_6$.¹⁴ The values of ΔH^\ddagger and ΔS^\ddagger obtained for added $K_4M^{II}(CN)_6$ salts support the notion that quantum super-exchange is still the source of the observed rate enhancement at extremely low concentrations of salt, but the effects are less dramatic and clearly supportive of the quantum super-exchange picture than in the 5.00 mM reactants work.

2.17 Kinetic Modeling

As noted in previous sections, the measured salt effects on the rate of bimolecular ET between our like-charged complexes diverge significantly from what the Debye-Hückel-Bronsted theory would predict¹¹ for *all* salts studied except for added KF at 0.10 mM reactants (as shown by the $\log k_{\text{ex}}$ vs. GP plots in Figures 2.27 through 2.33). To develop a deeper understanding of this surprising range of behavior in the observed kinetic salt effects, we have applied a simple extension of the “pre-equilibrium” kinetic model based on assumed ionic associations followed by first-order (intramolecular) ET reactive steps inside three identifiable reactive intermediates. In this section we will explain the details of the model and our results thus far in using it to fit our salt-dependent rate data. We will show how this model substantially succeeds in explaining the “classical” Debye-Hückel behavior observed for added fluoride (see equation (1-35)^{11,37}) and how we can at least partially account for the observed divergences for other salts. These modeling studies of kinetic salt effects will be compared with those arrived at previously using the same formalism (and effectively equivalent mathematical methods) already employed by Sista⁶, Inagaki⁷, and Mehmood⁹ using stopped-flow, and by Qin⁸ using line-broadening.

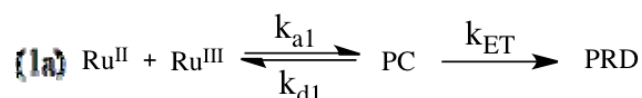
Our approach is to consider the simplest-plausible mechanistic scheme which might capture the bases of the measured kinetic salt effects. We postulate two fundamental types of reaction steps which would respond to the presence of added electrolytes and thereby modulate the rate of reaction (2-2). The first and simplest of these steps consist of the second-order associative encounter of reactants to form, and

the first-order dissociation to destroy, the ET “precursor complex” (PC) as explained in chapter 1, section 1.3. Studying equations (1-40) to (1-42) in chapter 1 (see section 1.8), and looking at the expression for the electrostatic “work term”, $w(r,\mu)$, defined by equation (1-43), we see that an added salt would ease the work of association between Ru^{II} and Ru^{III} (for convenience, the two ruthenium-pentaammine pyridyl reactants in reaction (2-2) will be denoted by Ru^{II} and Ru^{III} , respectively) simply on the basis of the corresponding increments in ionic strength μ (and also the corresponding GP function from Debye-Hückel theory, see equation (1-37)^{11,52}). We will explicitly consider ionic strength effects on the rates of association/dissociation relevant to PC as well as on association/dissociation rates to form various ion-paired reactive species such as $\text{Ru}^{\text{III}}\cdot\text{X}$, which become important at higher $[\text{X}^-]$ (see equations (1-41) to (1-42)). The second category of reactive steps are those which involve the fundamental first-order act of activated ET from donor to acceptor within the PC or some higher-order assembly such as “PCX” (see Channel 1, step (1a) below). Here, our salt-specific predictive capability is minimal and in fact the major goal of our modeling work was to discover what can be inferred about specific anion differences on these elementary steps.

The first and simplest kinetic pathway contributing to k_{ex} for reaction (2-2) will be denoted below as Channel 1. It involves the Ru^{II} and Ru^{III} reactant ions diffusive encounter to form the precursor complex, PC (this is a reversible step favoring the non-associated reactants due to the high coulombic repulsion between the like-charged reactants; see also equations (1-41) to (1-42) in section 1.8). After

formation of the precursor complex, activated ET occurs (see equations (1-18) to (1-26) in section 1.5.4) to form the successor complex which then dissociates into products on a timescale fast compared to the reverse ET reaction (which is simply another manifestation of the “pre-equilibrium” kinetic limit discussed in section 1.3, equations (1-2) to (1-6)).

Channel 1: Reactive Flux Through “PC”

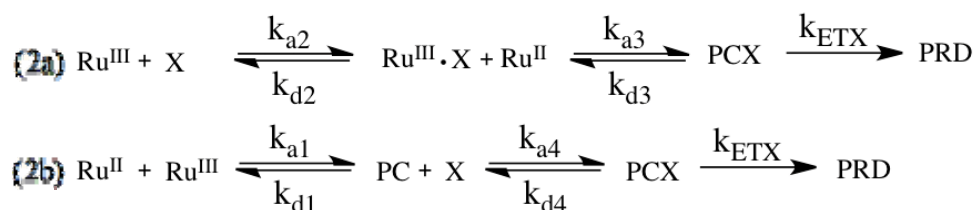


Channel 1 can be expected to predominate the reactive flux at low (or no) added-salt conditions where ion-pairing between reactants and salt anions, X, will be negligible. In this case, we model the kinetic salt effects under the assumptions that k_{a1} and k_{d1} will respond to changes in ionic strength as predicted by equations (1-41) and (1-42) and that “spectator” salt effects on the magnitude of k_{ET} taking PC on to products are negligible (we will return to and discuss this latter assumption later in this chapter).

When the concentration of added salt is sufficient however, ion-pairing can no longer be neglected and the second kinetic pathway (denoted below by Channel 2) becomes operative. This opens up the possibility for anion-specific rate effects to arise since the amounts of reactive flux being carried through the transient, ternary PCX species would be expected to depend on the identity of X at least in principle. When this occurs, Channel 1 and Channel 2 operate simultaneously at low [X], but then there will be a shifting competition regarding how the reactive flux partitions

between the channels in establishing the measured k_{ex} at a particular reactants concentration and added salt concentration. In our treatment of Channel 2, all ion-pairing between Ru^{II} and X has been neglected due to the higher charge on the Ru^{III} complex with its more lewis-acidic nature making it the more favorable partner for association with X at modest $[\text{X}]$.⁵³ Any finite equilibrium concentration of the ion-pair $\text{Ru}^{\text{III}} \cdot \text{X}$ is assumed by the model to reversibly associate with a free Ru^{II} complex and form the ternary, anion-containing precursor complex, PCX as shown in step (2a). A competing route to PCX is also considered in this Channel *via* step (2b), which requires association of the precursor complex formed in Channel 1, PC, with a free salt anion, X. Analogous to Channel 1, precursor complex formation is followed by activated ET within PCX (with rate k_{ETX}) to form the successor complex which then dissociates to products, PRD.

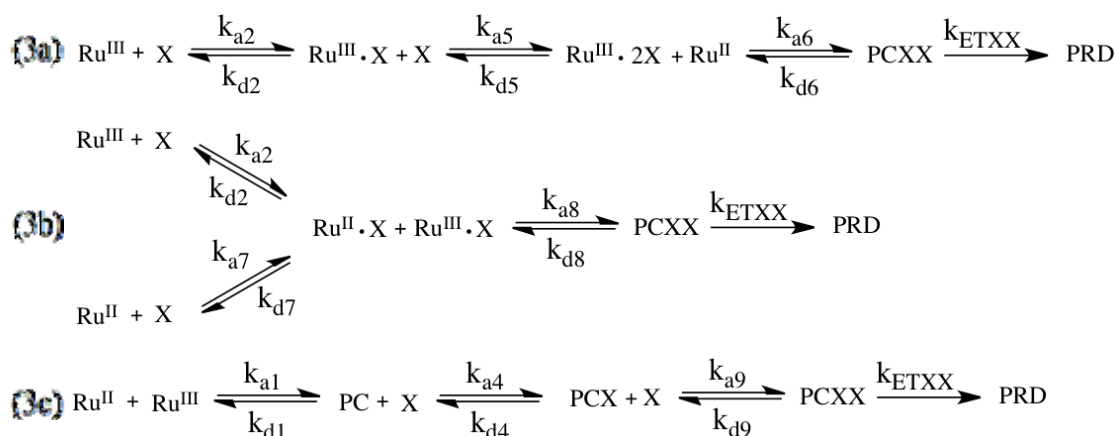
Channel 2: Reactive Flux Through “PCX”



At still higher salt concentrations, Channel 3 becomes active as shown below. Now associative equilibria to form the quaternary reactive intermediate, PCXX, are assumed to be a necessary source of the reactive flux leading to our observed rates at high $[\text{X}]$ (which topped out at 0.14 M in the bulk of our experiments). It can now be considered that there will be shifting contributions among Channels 1, 2, and 3 in carrying the overall ET reactive flux giving rise to our measured k_{ex} . In Channel 3 we

have considered multiple associative routes to formation of the precursor complex, PCXX. These include the possibility of two anions associating with the Ru^{III} complex to form the ion-pair $\text{Ru}^{\text{III}} \cdot 2\text{X}$ (as in step (3a)), as well as the association of X twice with the precursor complex formed in Channel 1, PC, making the ion-pair PCXX (note step (3c) below). At sufficiently large $[\text{X}]$ in the exchanging solution, the association of the Ru^{II} complex with X must be considered in this channel as well (note the lower entering branch for (3b) below). As was assumed in both Channel 1 and Channel 2, once the precursor complex has formed, activated ET occurs as a first-order process and the successor complex then dissociates to products.

Channel 3: Reactive Flux Through “PCXX”



In order to apply the kinetic model developed here to our system some simplifying assumptions are required. Channel 1 is assumed to respond to added salt only through the $k_{\text{a}1}$ and $k_{\text{d}1}$ associative/dissociative rate constants due to the presence of the solution ionic strength in the $w(\sigma, \mu)$ expression as presented in chapter 1 (see section 1.8; equation (1-43)). We will further assume that k_{ET} has no or only negligible dependence on the ionic strength therefore making it the only “adjustable”

parameter in our kinetic simulation of Channel 1 (the validity of this simplification will be addressed further on). In Channels 2 and 3, “ion-pairing” events are sequentially incorporated, with first one and then two of the added salt anions. Here, equations (1-41) and (1-42) (and the ionic radii taken either from the literature or computed from calculated reactant volumes, *vide infra*) was applied in order to compute values of the various k_{ai} and k_{di} as ionic strength increases. As in the case for Channel 1, the only adjustable parameters are k_{ETX} and k_{ETXX} and these are the key “fit-parameters” altered in bringing the simulated kinetic rates into agreement with our experimentally-determined $\log k_{ex}$ vs. GP curves (with our k_{ETX} and k_{ETXX} also assumed to be independent of ionic strength).

In the typical model for bimolecular ET, it is usually assumed that the pathway we are calling Channel 1 carries the entire reactive flux and that the observed rate constant in the “rapid pre-equilibrium” limit can be expressed as follows,

$$k_{ex} = K_A k_{ET} = \frac{k_a}{k_d} k_{ET} \quad (2-33)$$

where K_A is defined by equation (1-40) in chapter 1 (see section 1.8) and k_{ET} is the first-order rate of ET (see also equations (1-41) and (1-42) regarding computation of the component k_a and k_d values at a given ionic strength). As we show, equation (2-33) becomes secondary to more complex expressions for the reactive flux at high $[X]$ when Channels 2 and 3 “turn on” and must be incorporated in the overall rate calculation to account for the observed rate, k_{ex} (*vide infra*).

We have calculated the various k_{ai} and k_{di} values using the slightly-simplified work term expression, $w(r, \mu)$, as shown below,

$$w(r, \mu) = \frac{Z_A Z_D e^2}{4\pi \epsilon_0 D_s r(1 + \beta r \sqrt{\mu})} \quad (J) \quad (2-34)^{54}$$

where Z_A and Z_B are the charges of the two associating ions (for ion assemblies), e is the elementary charge of an electron, ϵ_0 is the permittivity of free space, D_s is the dielectric constant, r is the center-center distance of the ions in solution, β is Debye-inverse length defined by equation (1-33), and μ is the ionic strength defined by equation (1-30). When the values of the elementary charge of an electron, the permittivity of free space, and the dielectric constant of water are inserted into equation (2-33), the following expression is obtained,

$$w(s, \mu) = 2.9384 \times 10^{-20} \frac{Z_A Z_D}{s(1 + \beta s \sqrt{\mu})} \quad (J) \quad (2-35)$$

where s is expressed in Å.

In order to implement the three-channel kinetic model developed above, a rate expression specific to each channel was derived using the steady-state approximation (for the separate fluxes through intermediates PC, PCX, and PCXX).⁵⁰ These rate expressions were then simply added together at each experimental value used in the concentration range of added X (and hence total solution μ and GP), to arrive at a calculated best-fit value, $k_{ex} \text{ (calc.)}$, to the experimental rate, $k_{ex} \text{ (measured)}$.

To account for the progressive shift in reactive flux away from Channel 1 thru “PC” and toward Channel 2 thru “PCX” as $[X]$ increases, the previous rate expression

for Channel 1 defined by equation (2-33) was adjusted at low-to-moderate $[X]$ in order to account for the formation of the ion-pair $\text{Ru}^{\text{III}}\cdot\text{X}$. The initial reactive flux through PC (formed from $[\text{Ru}^{\text{III}}]$) is now replaced by flux through PCX which is formed from $[\text{Ru}^{\text{III}}\cdot\text{X}]$ as Channel 2 opens up. In this limit, equation (2-33) becomes,

$$k_1 = k_{\text{ET}} K_{\text{A1}} (1 - K_{\text{A2}}[X]) \quad (2-36)$$

where $K_{\text{A1}} = k_{\text{a1}}/k_{\text{d1}}$ and $K_{\text{A2}} = k_{\text{a2}}/k_{\text{d2}}$ (see (2a) of Channel 2 and (3a) of Channel 3 above). The steady-state derived rate expressions (*vide infra*) become significantly more complex as we account for the reactive fluxes thru Channels 2 and 3. The rate expression for reactive flux thru PCX of Channel 2 (which still retains an aspect of Channel 1 in (2b) and also accounts for loss of $[\text{Ru}^{\text{III}}\cdot\text{X}]$ due to the formation of the ion-triplet $\text{Ru}^{\text{III}}\cdot 2\text{X}$ in (3a)) is found to be,

$$k_2 = k_{\text{ETX}}[X] \left(\frac{k_{\text{a3}} K_{\text{A2}} (1 - K_{\text{A5}}[X]) + k_{\text{a4}} K_{\text{A1}} (1 - K_{\text{A2}}[X])}{k_{\text{d3}} + k_{\text{d4}}} \right) \quad (2-37)$$

where all variables have been previously defined. The rate expression for reactive flux through PCXX of Channel 3, now accounts for rates of all the pre-steps in Channels 1 and 2, leading to PC, PCX and $\text{Ru}^{\text{III}}\cdot\text{X}$, written as,

$$k_3 = k_{\text{ETXX}}[X]^2 \times Y \quad (2-38)$$

where Y is defined by,

$$Y = \left(\frac{k_{\text{a6}} K_{\text{A2}} K_{\text{A5}} + k_{\text{a8}} K_{\text{A2}} K_{\text{A7}} + k_{\text{a9}} \left(\frac{k_{\text{a3}} K_{\text{A2}} (1 - K_{\text{A5}}[X]) + k_{\text{a4}} K_{\text{A1}} (1 - K_{\text{A2}}[X])}{k_{\text{d3}} + k_{\text{d4}}} \right)}{k_{\text{d6}} + k_{\text{d8}} + k_{\text{d9}}} \right) \quad (2-39)$$

The full details of these steady-state deviations are derived in Appendix 1. Equations (2-36) to (2-38) were then used to calculate the overall rate constant for reaction (2-2) as a function of added-salt concentration (and hence total ionic strength and solution GP) as the sum of reactive fluxes thru the PC, PCX, and PCXX reactive intermediates. The values of the adjustable constants k_{ETX} and k_{ETXX} were iteratively varied to achieve best-fit to the experimentally $\log k_{\text{ex}}$ vs. GP curves. All the various k_{ai} and k_{di} calculations were completed using MathCad 14.0 (Parametric Technology Corporation). The radii used are listed in Tables 2.36 and 2.37. In all cases, all variables associated with distance/length which are defined in units of meters in the literature-sourced expressions used were converted into units of Angstroms in our calculations. Any constants in the relevant rate expressions were adjusted to reflect this as well.

Table 2.36 The experimental^(a) and calculated radii of the various added-salt and reactant ions used in kinetic simulations.

Ion	Radius (Å)
F ⁻	1.50 ^(a) , 3.89 ^(c)
Cl ⁻	1.90 ^(a) , 4.41 ^(c)
Br ⁻	2.61 ^(b) , 4.08 ^(c)
muc ²⁻	3.86 ^(b)
adip ²⁻	3.97 ^(b)
tere ²⁻	4.13 ^(b)
1,4-dcch ²⁻	4.11 ^(b)
Fe ^{II} (CN) ₆ ⁴⁻	4.24 ^(b)
Ru ^{II} (CN) ₆ ⁴⁻	4.38 ^(b)
Os ^{II} (CN) ₆ ⁴⁻	4.35 ^(b)
[(NH ₃) ₅ Ru ^{II} tfmp] ²⁺	4.55 ^(b)
[(NH ₃) ₅ Ru ^{III} tfmp] ³⁺	4.48 ^(b)

(a) The crystallographic radii values were obtained from Kielland⁵⁵, (b) calculated using B3LYP, 6-311+(2d,p)/sdd level using the “genecp” ad “volume=tight” keywords along with the PCM solvation model in Gaussian 09 W⁵⁶, and (c) the approximate hydrated radii of the halides were calculated at the same level but including six explicit waters in the primary shell.

The radii of the various ion-pairs and associated precursor species (PC, PCX, and PCXX) which were used in subsequent calculations are listed in Table 2.37. These were calculated using the component radii listed above to compute and add up the component volumes followed by a computation of the radius of a sphere of equal volume to the relevant composite species.¹¹ For example, the sphere of equivalent volume for the ion-pair Ru^{III}•F⁻ is calculated as follows,

$$V_{\text{Ru}^{\text{III}} \bullet \text{F}^-} = \frac{4}{3} \pi (r_{\text{Ru}^{\text{III}}}^3 + r_{\text{F}^-}^3) = \frac{4}{3} \pi (4.48^3 + 1.50^3) \Rightarrow r_{\text{Ru}^{\text{III}} \bullet \text{F}^-} = 4.54 \quad (2-40)$$

where $V_{\text{Ru}^{\text{III}} \cdot \text{F}^-}$ is the simple sum volume of the ion-pair $\text{Ru}^{\text{III}} \cdot \text{F}^-$ at contact and the 4.54 Å radius results from the calculation of the radius of a (presumed) single sphere of equal volume to that of the merged constituents.¹¹

Table 2.37 The calculated radii of various ion-pairs using values of bare radii listed in Table 2.36 and employing equation (2-40).

Ion	Radius (Å)	Ion	Radius (Å)
$\text{Ru}^{\text{II}} \cdot \text{F}^-$	4.60 ^(a) , 5.35 ^(b)	$\text{Ru}^{\text{III}} \cdot 2 \text{F}^-$	4.59 ^(a) , 5.92 ^(b)
$\text{Ru}^{\text{III}} \cdot \text{F}^-$	4.54 ^(a) , 5.30 ^(b)	$\text{Ru}^{\text{III}} \cdot 2 \text{Cl}^-$	4.70 ^(a) , 6.39 ^(b)
$\text{Ru}^{\text{II}} \cdot \text{Cl}^-$	4.66 ^(a) , 5.65 ^(b)	$\text{Ru}^{\text{III}} \cdot 2 \text{Br}^-$	5.01 ^(a) , 6.09 ^(b)
$\text{Ru}^{\text{III}} \cdot \text{Cl}^-$	4.59 ^(a) , 5.60 ^(b)	$\text{Ru}^{\text{III}} \cdot 2 \text{muc}^{2-}$	5.90 ^(a)
$\text{Ru}^{\text{II}} \cdot \text{Br}^-$	4.82 ^(a) , 5.45 ^(b)	$\text{Ru}^{\text{III}} \cdot 2 \text{adip}^{2-}$	5.99 ^(a)
$\text{Ru}^{\text{III}} \cdot \text{Br}^-$	4.76 ^(a) , 5.40 ^(b)	$\text{Ru}^{\text{III}} \cdot 2 \text{tere}^{2-}$	6.13 ^(a)
$\text{Ru}^{\text{II}} \cdot \text{muc}^{2-}$	5.33 ^(a)	$\text{Ru}^{\text{III}} \cdot 2 (1,4\text{-dcch})^{2-}$	6.12 ^(a)
$\text{Ru}^{\text{III}} \cdot \text{muc}^{2-}$	5.28 ^(a)	$\text{Ru}^{\text{III}} \cdot 2 [\text{K}_4\text{Fe}^{\text{II}}(\text{CN})_6]$	6.23 ^(a)
$\text{Ru}^{\text{II}} \cdot \text{adip}^{2-}$	5.39 ^(a)	$\text{Ru}^{\text{III}} \cdot 2 [\text{K}_4\text{Ru}^{\text{II}}(\text{CN})_6]$	6.37 ^(a)
$\text{Ru}^{\text{III}} \cdot \text{adip}^{2-}$	5.34 ^(a)	$\text{Ru}^{\text{III}} \cdot 2 [\text{K}_4\text{Os}^{\text{II}}(\text{CN})_6]$	6.34 ^(a)
$\text{Ru}^{\text{II}} \cdot \text{tere}^{2-}$	5.48 ^(a)	$\text{Ru}^{\text{II}} \cdot \text{Ru}^{\text{III}} \cdot \text{F}^-$	5.72 ^(a) , 6.24 ^(b)
$\text{Ru}^{\text{III}} \cdot \text{tere}^{2-}$	5.43 ^(a)	$\text{Ru}^{\text{II}} \cdot \text{Ru}^{\text{III}} \cdot \text{Cl}^-$	5.76 ^(a) , 6.46 ^(b)
$\text{Ru}^{\text{II}} \cdot 1,4\text{-dcch}^{2-}$	5.47 ^(a)	$\text{Ru}^{\text{II}} \cdot \text{Ru}^{\text{III}} \cdot \text{Br}^-$	5.75 ^(a) , 6.32 ^(b)
$\text{Ru}^{\text{III}} \cdot 1,4\text{-dcch}^{2-}$	5.42 ^(a)	$\text{Ru}^{\text{II}} \cdot \text{Ru}^{\text{III}} \cdot \text{muc}^{2-}$	6.27 ^(a)
$\text{Ru}^{\text{II}} \cdot \text{Fe}^{\text{II}}(\text{CN})_6^{4-}$	5.54 ^(a)	$\text{Ru}^{\text{II}} \cdot \text{Ru}^{\text{III}} \cdot \text{adip}^{2-}$	6.23 ^(a)
$\text{Ru}^{\text{III}} \cdot \text{Fe}^{\text{II}}(\text{CN})_6^{4-}$	5.50 ^(a)	$\text{Ru}^{\text{II}} \cdot \text{Ru}^{\text{III}} \cdot \text{tere}^{2-}$	6.34 ^(a)
$\text{Ru}^{\text{II}} \cdot \text{Ru}^{\text{II}}(\text{CN})_6^{4-}$	5.63 ^(a)	$\text{Ru}^{\text{II}} \cdot \text{Ru}^{\text{III}} \cdot (1,4\text{-dcch})^{2-}$	6.33 ^(a)
$\text{Ru}^{\text{III}} \cdot \text{Ru}^{\text{II}}(\text{CN})_6^{4-}$	5.58 ^(a)	$\text{Ru}^{\text{II}} \cdot \text{Ru}^{\text{III}} \cdot \text{Fe}^{\text{II}}(\text{CN})_6^{4-}$	6.39 ^(a)
$\text{Ru}^{\text{II}} \cdot \text{Os}^{\text{II}}(\text{CN})_6^{4-}$	5.61 ^(a)	$\text{Ru}^{\text{II}} \cdot \text{Ru}^{\text{III}} \cdot \text{Ru}^{\text{II}}(\text{CN})_6^{4-}$	6.45 ^(a)
$\text{Ru}^{\text{III}} \cdot \text{Os}^{\text{II}}(\text{CN})_6^{4-}$	5.56 ^(a)	$\text{Ru}^{\text{II}} \cdot \text{Ru}^{\text{III}} \cdot \text{Os}^{\text{II}}(\text{CN})_6^{4-}$	6.43 ^(a)
$\text{Ru}^{\text{II}} \cdot \text{Ru}^{\text{III}}$	5.69 ^(a)		

(a) with no waters of hydration and (b) with waters of hydration included in the halide ion radii.

One aspect of the fitting strategy used to arrive at the optimum set of k_{ET} , k_{ETX} , and k_{ETXX} values for a given salt, radii set, and anion was to first postulate that k_{ET} , the uncatalyzed first-order rate constant inside the $[\text{Ru}^{\text{II}}, \text{Ru}^{\text{III}}]$ precursor complex, PC, should be common to all runs and invariant with ionic strength (to within our experimental precision) across our dataset collected at 26°C. The well-defined experimental second-order k_{ex} value at 0.10 mM reactants with no added salt of $k_{\text{ex}} = 2080 \pm 1.12 \text{ M}^{-1} \text{ sec}^{-1}$ was used to calculate k_{ET} (using equation (2-36)) which gave a value of $k_{\text{ET}} = 8.60 \times 10^4$. Please note that the value of k_{ET} is only as accurate as the k_{a} and k_{d} values in equation (2-33) are and hence, in the modeling work to follow everything was contingent on this one “foundational” rate, but in an absolute sense its value could easily be off by a factor of 5 or even 10.¹¹

2.17.1 Application of our model to self-salting data

An immediate complication which our model encounters is in how predictions made using it (and also the simple Debye-Huckle-Bronsted model) compare with the reactants-concentration only “self-salting” rate variations documented in Table 2.10 and Figure 2.25. In Figure 2.54 we plotted our experimental reactants-only $\log k_{\text{ex}}$ vs. GP data and compared them with predictions based on the simple Debye-Huckle-Bronsted model (equation (1-36), red dotted line), and the simplest case of equation (2-33) where only the ionic strength dependencies of k_{a} and k_{d} are accounted for (see the blue line). For the linear plots we have used the experimental $\log k_{\text{ex}}$ value at 0.10 mM with no salt added as the anchor point from which equation (1-36) and (2-33) were applied.

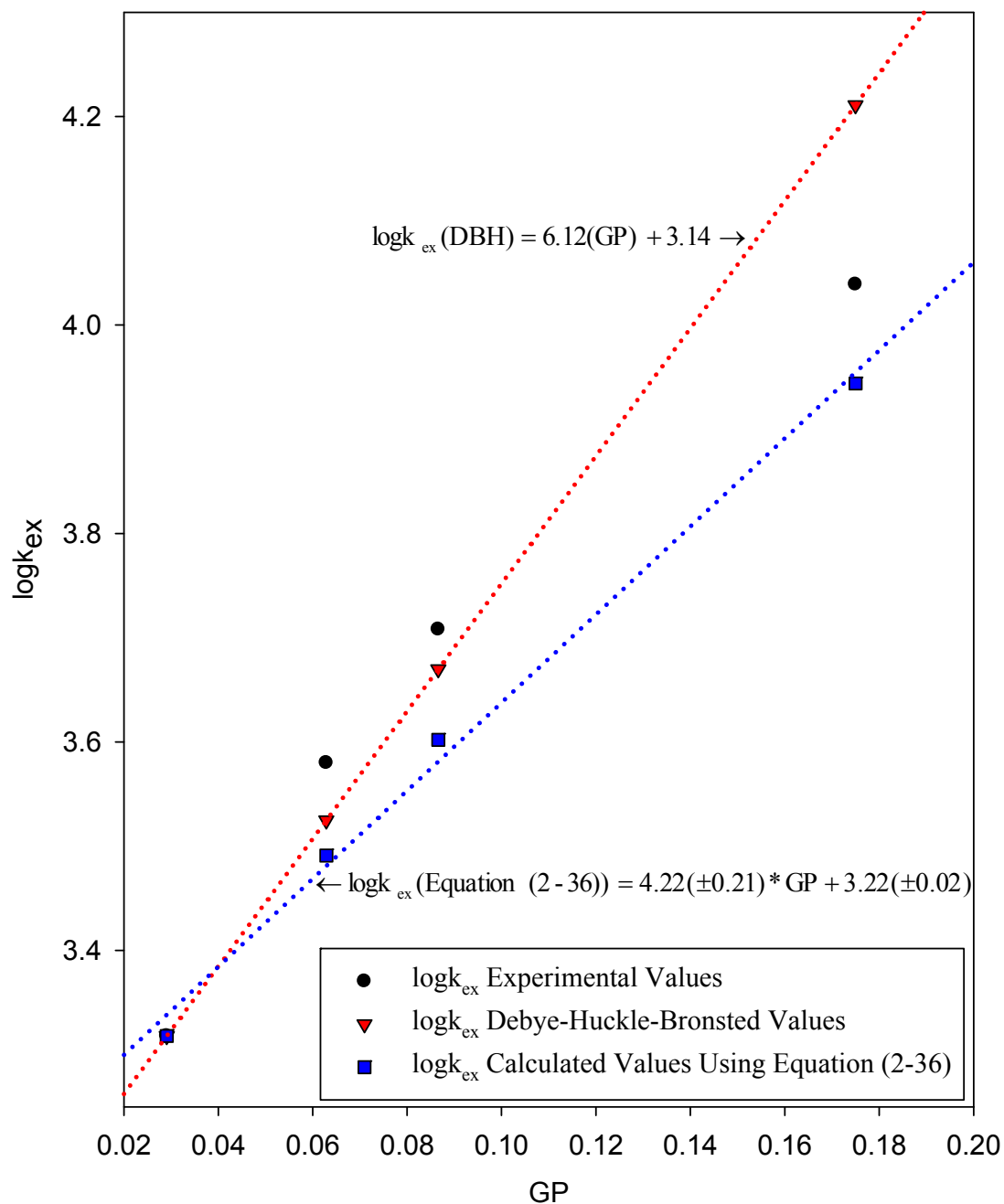


Figure 2.54 The experimentally measured $\log k_{\text{ex}}$ values vs. GP data compared with calculated values of $\log k_{\text{ex}}$ theoretically predicted by both the Debye-Hückle-Bronsted equation (1-38) and equation (2-36).

From the Figure we see that neither the simple Debye-Huckle-Bronsted linear plot with slope 6.1 or the equation (2-33) plot with slope 4.2 ± 0.21 adequately fits the data. This difference in slopes appears to derive from a small systematic deviation in the Debye-Smoluchowski/Debye-Eigen treatments of k_a and k_d (see equations (1-41) and (1-42)) and the older Debye-Hückle-Bronsted equation. The blue squares calculated from equation (2-36), however, do match the qualitative curve of the experimental data, but a consistent offset remains. In order to address this deviation in the salt-specific modeling work to follow at reactant concentrations $> 0.10 \text{ mM}$, we modeled our experimental rate data by using the k_{ex} values (plotted as $\log k_{ex}$ values) generated using our constrained k_{ET} value at the anchor points (k_{ex} values at each reactants concentration with no salt added) from which to then model our experimental salt-specific rate data. Therefore, there is small offset in the initial starting point when comparing our modeled data with experimental data. Following this, we obtained an initial value for k_{ETX} by adjusting it such that the calculated rate using only Channels 1 and 2 (equations (2-36) and (2-37), respectively) matched the early part of the $\log k_{ex}$ vs. GP experimental curve. Inclusion of Channel 3 then allowed a first-pass attempt at modeling the entire experimental curve in the initial (crude) limit of $k_{ETXX} = k_{ETX}$. This computed curve typically rises too quickly in the early portion, therefore k_{ETX} was decreased and k_{ETXX} was adjusted iteratively until stable and best-fit values were obtained. The best-fit rate constants calculated using equations (2-36) to (2-38) as a function of self-salting are listed in Table 2.39 along with the experimental data for comparison. Figure 2.55 illustrates the level of

agreement between the simulated and actual $\log k_{\text{ex}}$ vs. reactants curves obtained over our studied reactants concentration range.

Table 2.38 Best-fit k_{ET} , k_{ETX} , and k_{ETXX} rate constants for reaction (2-2) corresponding to first-order ET inside the presumed PC, PCX, and PCXX reactive intermediates (based on iterative fitting of the $\log k_{\text{ex}}$ vs. the self-salting curve over the reactants concentration range of 0.10 mM to 5.00 mM). These optimized values lead to the model-calculated rates listed in Table 2.39. The $k_{\text{ETX}}/k_{\text{ET}}$ and $k_{\text{ETXX}}/k_{\text{ETX}}$ ratios are listed in the final two columns.

$k_{\text{ET}}^{(a)}$	$k_{\text{ETX}}^{(b)}$	$k_{\text{ETXX}}^{(c)}$	$k_{\text{ETX}}/k_{\text{ET}}^{(d)}$	$k_{\text{ETXX}}/k_{\text{ETX}}^{(e)}$
8.6×10^4	1.5×10^5	1.0×10^5	1.7	0.7

(a) Estimated uncertainty $\pm 5\%$, (b) Estimated uncertainty of $\pm 5\text{-}10\%$, (c) estimated uncertainty of $\pm 30\%$, (d) estimated uncertainty of $\pm 7\text{-}10\%$, and (e) estimated uncertainty of $\pm 12\%$.

Table 2.39 Experimental and model-calculated rate constants for reaction (2-2) as a function of GP arrived at using the three-channel model summarized in equations (2-36) through (2-38) and the best-fit rate constants listed in Table 2.38. The data fitted curves are illustrated in Figure 2.55.

Reactants conc. (mM)	GP	$\log k_{\text{ex}}$ (expt.)	$\log k_{\text{ex}}$ (calc.) Channel 1 Only	$\log k_{\text{ex}}$ (calc.) Channels 1 and 2	$\log k_{\text{ex}}$ (calc.) Channels 1, 2, and 3
0.10	0.0291	3.32 ± 0.05	3.32	3.34	3.34
0.50	0.0629	3.58 ± 0.04	3.48	3.57	3.57
1.00	0.0866	3.71 ± 0.02	3.58	3.71	3.72
5.00	0.1800	4.04 ± 0.05	3.87	4.15	4.18

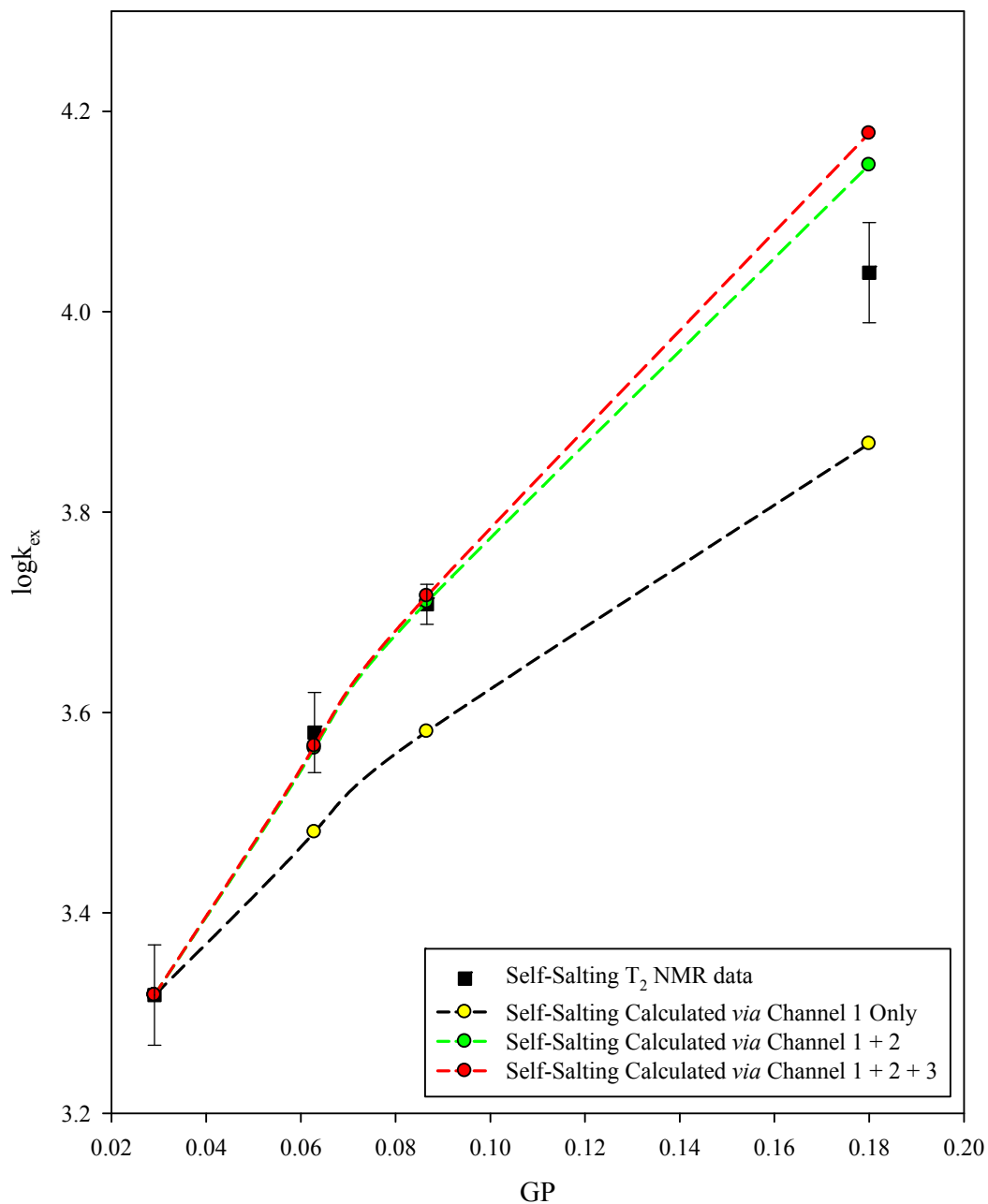


Figure 2.55 Experimental data and kinetic modeling results for the self-salting curve (reactants concentration 0.10 mM – 5.00 mM). The T_2 NMR data (black squares) are compared with modeling results using Channel 1 (yellow circles), Channels 1 + 2 (green circles), and Channels 1 + 2 + 3 (red circles).

Through the application of our model to our self-salting data (reactants only) we are able to better understand why a linear curve is found with a slope of 6 as would be predicted from the Debye-Huckel-Bronsted equation.¹¹ The k_{ET} and k_{ETX} values necessary to fit the data were 8.6×10^4 and 1.5×10^5 , respectively, giving a ratio of $k_{\text{ETX}}/k_{\text{ET}}$ equal to 1.74. This result suggests ion-pairing with the Cl^- ions is occurring in the reactant solution and this result will be discussed further on.

2.17.2 Salt-specific kinetic modeling at $[\text{Ru}^{\text{II}}] = [\text{Ru}^{\text{III}}] = 0.10 \text{ mM}$

Kinetic simulations of reaction (2-2) based on our three-channel model were first carried out at the relatively-low (stopped-flow equivalent) reactants concentration of 0.10 mM in the presence of progressively increasing concentrations of added simple salts, dicarboxylate salts, and the ferro-, osmino-, and rutheno-hexacyano species. The k_{ET} , k_{ETX} , and k_{ETXX} values necessary to fit the data are listed in Table 2.40 along with the best-fit $k_{\text{ETX}}/k_{\text{ET}}$ and $k_{\text{ETXX}}/k_{\text{ETX}}$ ratios. The best-fit rate constants calculated using equations (2-36) to (2-38) as a function of added-salt concentration are listed in Table 2.41 along with the experimental data for comparison. Figures 2.56 to 2.65 illustrate the level of agreement between the simulated and actual $\log k_{\text{ex}}$ vs. [salt] curves obtained at 0.10 mM reactants.

One of our primary concerns for measuring and interpreting the ET catalytic effect of the various added-salt anions investigated was to see how k_{ETX} for catalyzed ET compared to the k_{ET} for uncatalyzed rate of ET inside the more typical $\text{Ru}^{\text{II}} \cdot \text{Ru}^{\text{III}}$ bimolecular precursor complex, PC (note the $k_{\text{ETX}}/k_{\text{ET}}$ ratio listed in the fifth column of Table 2.40). In the case of F^- only Channels 1 and 2 were required to fit the data at

0.10 mM reactants and in all other cases Channels 1 to 3 were necessary. In all cases beyond F^- we found that the best-fit values for k_{ETX} were not very sensitive (showing only small variations of $< \sim 5\text{-}10\%$) to whether the k_{ETXX} values were in fact varied to optimize fit in the high $[X]$ region or simply kept at $k_{ETXX} \sim k_{ETX}$ (even when optimized to best-fit, the k_{ETXX} values themselves were considered to be too uncertain for detailed interpretation). In Table 2.41 (and the subsequent ones like it at higher reactant concentrations) we have listed the best-fit $\log k_{ex (calc.)}$ values resulting from fits calculated assuming reactive flux thru Channel 1 only and from fits using the sum of the fluxes thru Channels 1 and 2 as applied to the early ($GP < \sim 0.0713$) part of the experimental curves (see the fourth and fifth columns in Table 2.41). The most-informative k_{ETX}/k_{ET} ratios listed, however, are the ones in the fifth column of Table 2.40 which were arrived at using the “full” model based on the sum of the computed reactive fluxes through Channels 1-3 (see the last column in Table 2.41, except for fluoride).

Table 2.40 Best-fit k_{ET} , k_{ETX} , and k_{ETXX} rate constants for reaction (2-2) corresponding to first-order ET inside the presumed PC, PCX, and PCXX reactive intermediates (based on iterative fitting of the $\log k_{\text{ex}}$ vs. added salt curves measured at $[\text{Ru}^{\text{II}}] = [\text{Ru}^{\text{III}}] = 0.10 \text{ mM}$ for the halide and dicarboxylate anions studied). These optimized values lead to the model-calculated rates listed in Table 2.41. The $k_{\text{ETX}}/k_{\text{ET}}$ and $k_{\text{ETXX}}/k_{\text{ETX}}$ ratios are listed in the final two columns.

Ion	$k_{\text{ET}}^{(a)}$	$k_{\text{ETX}}^{(b)}$	$k_{\text{ETXX}}^{(c)}$	$k_{\text{ETX}}/k_{\text{ET}}^{(d)}$	$k_{\text{ETXX}}/k_{\text{ETX}}^{(e)}$
F^- ($r = 1.50 \text{ \AA}$)	8.6×10^4	8.2×10^4	-	0.9	-
F^- ($r = 3.89 \text{ \AA}$)	8.6×10^4	5.1×10^4	-	0.6	-
Cl^- ($r = 1.90 \text{ \AA}$)	8.6×10^4	4.6×10^5	5.1×10^5	5.3	1.1
Cl^- ($r = 4.41 \text{ \AA}$)	8.6×10^4	2.5×10^5	1.5×10^5	2.9	0.6
Br^- ($r = 2.61 \text{ \AA}$)	8.6×10^4	7.5×10^5	1.2×10^6	8.7	1.6
Br^- ($r = 4.08 \text{ \AA}$)	8.6×10^4	4.3×10^5	7.1×10^5	5.0	1.6
muc^{2-} ($r = 3.86 \text{ \AA}$)	8.6×10^4	6.0×10^4	1.0×10^4	0.7	0.2
adip^{2-} ($r = 3.97 \text{ \AA}$)	8.6×10^4	4.2×10^4	5.0×10^3	0.5	0.1
tere^{2-} ($r = 4.13 \text{ \AA}$)	8.6×10^4	6.6×10^4	1.8×10^4	0.8	0.3
$(1,4\text{-dcch})^{2-}$ ($r = 4.11 \text{ \AA}$)	8.6×10^4	5.6×10^4	3.0×10^4	0.7	0.5

(a) Estimated uncertainty $\pm 5\%$, (b) Estimated uncertainty of $\pm 5\text{-}10\%$, (c) estimated uncertainty of $\pm 30\%$, (d) estimated uncertainty of $\pm 7\text{-}10\%$, and (e) estimated uncertainty of $\pm 12\%$.

Table 2.41 Experimental and model-calculated rate constants at 0.10 mM for reaction (2-2) as a function of GP arrived at using the three-channel model summarized in equations (2-36) through (2-38) and the best-fit rate constants listed in Table 2.38 (the relevant ionic radii are taken from Tables 2.36 and 2.37). The data fitted curves are illustrated in Figures 2.56 and 2.65.

KF

r = 1.50 Å	GP	logk_{ex} (expt.)	logk_{ex} (calc.) Channel 1 Only	logk_{ex} (calc.) Channels 1 and 2	logk_{ex} (calc.) Channels 1, 2, and 3
	0.0291	3.318 ± 0.051	3.318	3.318	-
	0.0361	3.361	3.352	3.365	-
	0.0418	3.412	3.380	3.403	-
	0.0511	3.447	3.422	3.464	-
	0.0713	3.570	3.507	3.590	-
	0.1020	3.587	3.617	3.762	-
	0.1263	3.635	3.689	3.881	-

KF

r = 3.89 Å	GP	logk_{ex} (expt.)	logk_{ex} (calc.) Channel 1 Only	logk_{ex} (calc.) Channels 1 and 2	logk_{ex} (calc.) Channels 1, 2, and 3
	0.0291	3.318 ± 0.051	3.318	3.318	-
	0.0361	3.361	3.352	3.365	-
	0.0418	3.412	3.379	3.403	-
	0.0511	3.447	3.421	3.465	-
	0.0713	3.570	3.504	3.590	-
	0.1020	3.587	3.611	3.759	-
	0.1263	3.635	3.679	3.874	-

NaCl

r = 1.90 Å	GP	logk_{ex} (expt.)	logk_{ex} (calc.)	logk_{ex} (calc.)	logk_{ex} (calc.)
			Channel	Channels	Channels
			1 Only	1 and 2	1, 2, and 3
	0.0291	3.318 ± 0.051	3.318	3.318	3.318
	0.0361	-	3.352	3.423	3.423
	0.0418	3.422	3.379	3.504	3.506
	0.0511	3.628	3.422	3.628	3.635
	0.0713	3.912	3.505	3.862	3.885
	0.1020	4.214	3.614	4.143	4.199
	0.1263	4.400	3.685	4.321	4.407

KBr

r = 2.61 Å	GP	logk_{ex} (expt.)	logk_{ex} (calc.)	logk_{ex} (calc.)	logk_{ex} (calc.)
			Channel	Channels	Channels
			1 Only	1 and 2	1, 2, and 3
	0.0291	3.318 ± 0.051	3.318	3.318	3.318
	0.0361	-	3.352	3.470	3.472
	0.0418	3.560	3.379	3.581	3.587
	0.0511	3.754	3.422	3.740	3.757
	0.0713	4.050	3.506	4.018	4.065
	0.1020	4.488	3.614	4.332	4.434
	0.1263	4.674	3.685	4.524	4.673

KBr

r = 4.08 Å	GP	logk_{ex} (expt.)	logk_{ex} (calc.)	logk_{ex} (calc.)	logk_{ex} (calc.)
			Channel	Channels	Channels
			1 Only	1 and 2	1, 2, and 3
	0.0291	3.318 ± 0.051	3.318	3.318	3.318
	0.0361	-	3.352	3.457	3.460
	0.0418	3.560	3.379	3.560	3.570
	0.0511	3.754	3.421	3.711	3.734
	0.0713	4.050	3.504	3.977	4.045
	0.1020	4.488	3.610	4.279	4.428
	0.1263	4.674	3.677	4.463	4.681

Na₂muc					
r = 3.86 Å	GP	logk_{ex} (expt.)	logk_{ex} (calc.) Channel 1 Only	logk_{ex} (calc.) Channels 1 and 2	logk_{ex} (calc.) Channels 1, 2, and 3
	0.0291	3.318 ± 0.051	3.318	3.318	3.318
	0.0400	3.708	3.358	3.591	3.592
	0.0550	3.897	3.407	3.831	3.835
	0.0735	4.068	3.458	4.032	4.040
	0.1020	4.230	3.519	4.239	4.254
	0.1209	4.306	3.551	4.339	4.359
Na₂adip					
r = 3.97 Å	GP	logk_{ex} (expt.)	logk_{ex} (calc.) Channel 1 Only	logk_{ex} (calc.) Channels 1 and 2	logk_{ex} (calc.) Channels 1, 2, and 3
	0.0291	3.318 ± 0.051	3.318	3.318	3.318
	0.0550	3.761	3.408	3.742	3.744
	0.0735	3.972	3.460	3.925	3.930
	0.1020	4.140	3.524	4.120	4.130
	0.1209	4.178	3.556	4.215	4.229
Na₂tere					
r = 4.13 Å	GP	logk_{ex} (expt.)	logk_{ex} (calc.) Channel 1 Only	logk_{ex} (calc.) Channels 1 and 2	logk_{ex} (calc.) Channels 1, 2, and 3
	0.0291	3.318 ± 0.051	3.318	3.318	3.318
	0.0400	3.578	3.360	3.610	3.612
	0.0550	3.885	3.410	3.860	3.866
	0.0735	4.121	3.463	4.065	4.079
	0.1020	4.296	3.529	4.277	4.303
	0.1209	4.365	3.563	4.378	4.412

Na₂(1,4-dcch)

r = 4.11 Å	GP	logk_{ex} (expt.)	logk_{ex} (calc.) Channel 1 Only	logk_{ex} (calc.) Channels 1 and 2	logk_{ex} (calc.) Channels 1, 2, and 3
	0.0291	3.318 ± 0.051	3.318	3.318	3.318
	0.0400	3.738	3.360	3.579	3.581
	0.0550	3.890	3.410	3.813	3.819
	0.0735	4.028	3.463	4.013	4.025
	0.1020	4.237	3.529	4.218	4.242
	0.1209	4.305	3.563	4.318	4.351

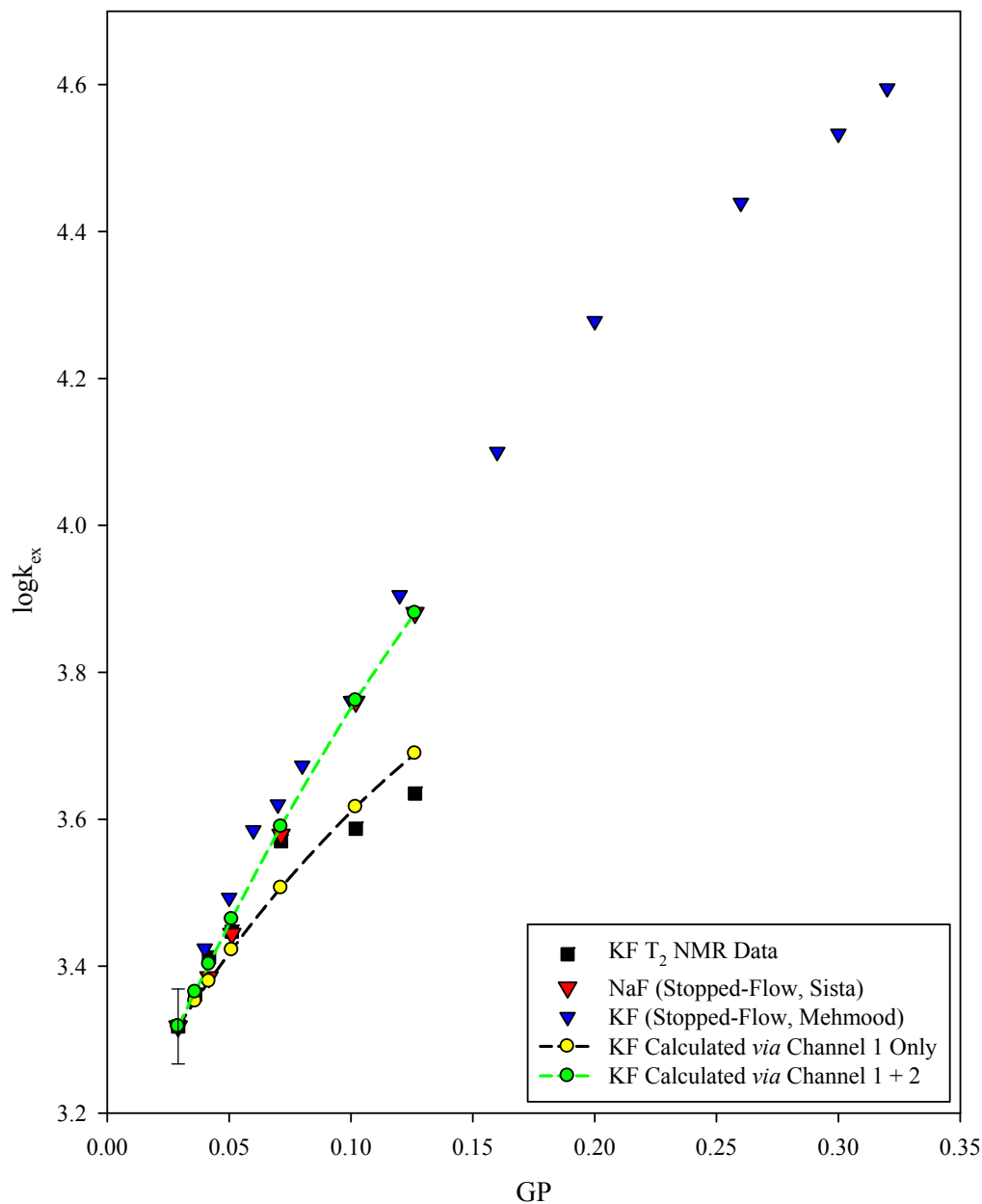


Figure 2.56 Experimental data and kinetic modeling results at 0.10 mM reactants with added KF (presumed crystallographic F^- radius of 1.50 Å). The T_2 NMR data (black squares) are compared with modeling results using Channel 1 (yellow circles) and Channels 1 + 2 (green circles). Also shown are Sista and Mehmood's stopped flow data for added NaF (red triangles)⁶ and KF (blue triangles)⁹ with their initial points normalized along y to the starting $\log k_{\text{ex}}$ value of the NMR data for purposes of comparison. In the Channel 1+2 fit the final two block squares data were ignored.

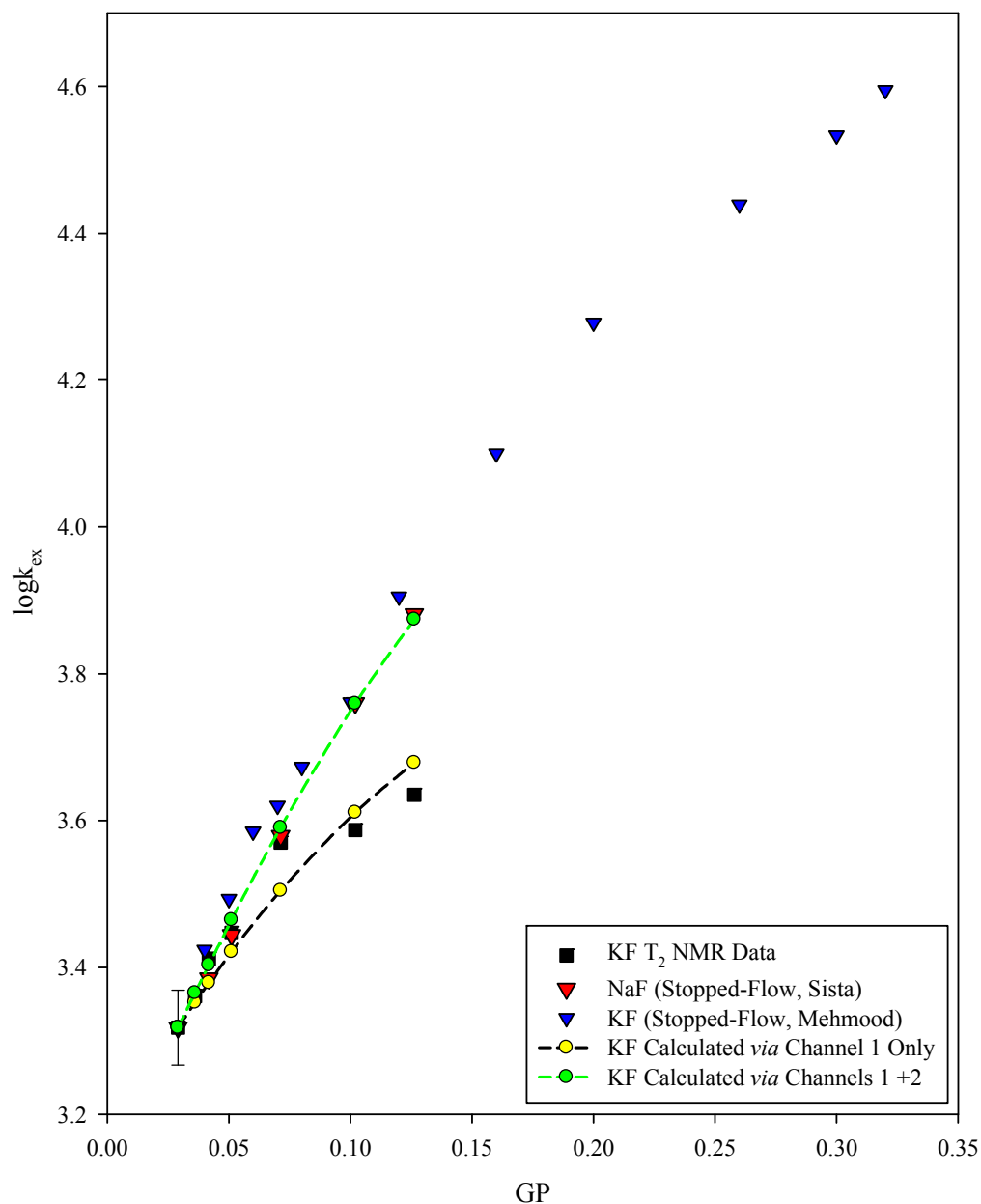


Figure 2.57 Experimental data and kinetic modeling results at 0.10 mM reactants with added KF now using the hydrated F^- radius of 3.89 Å. The T_2 NMR data (black squares) are compared with modeling results using Channel 1 (yellow circles) and Channels 1 + 2 (green circles). Also shown are Sista and Mehmood's stopped flow data for added NaF (red triangles)⁶ and KF (blue triangles)⁹ with their initial points normalized along y to the starting $\log k_{\text{ex}}$ value of the NMR data for purposes of comparison. In the Channel 1+2 fit the final two block squares data were ignored.

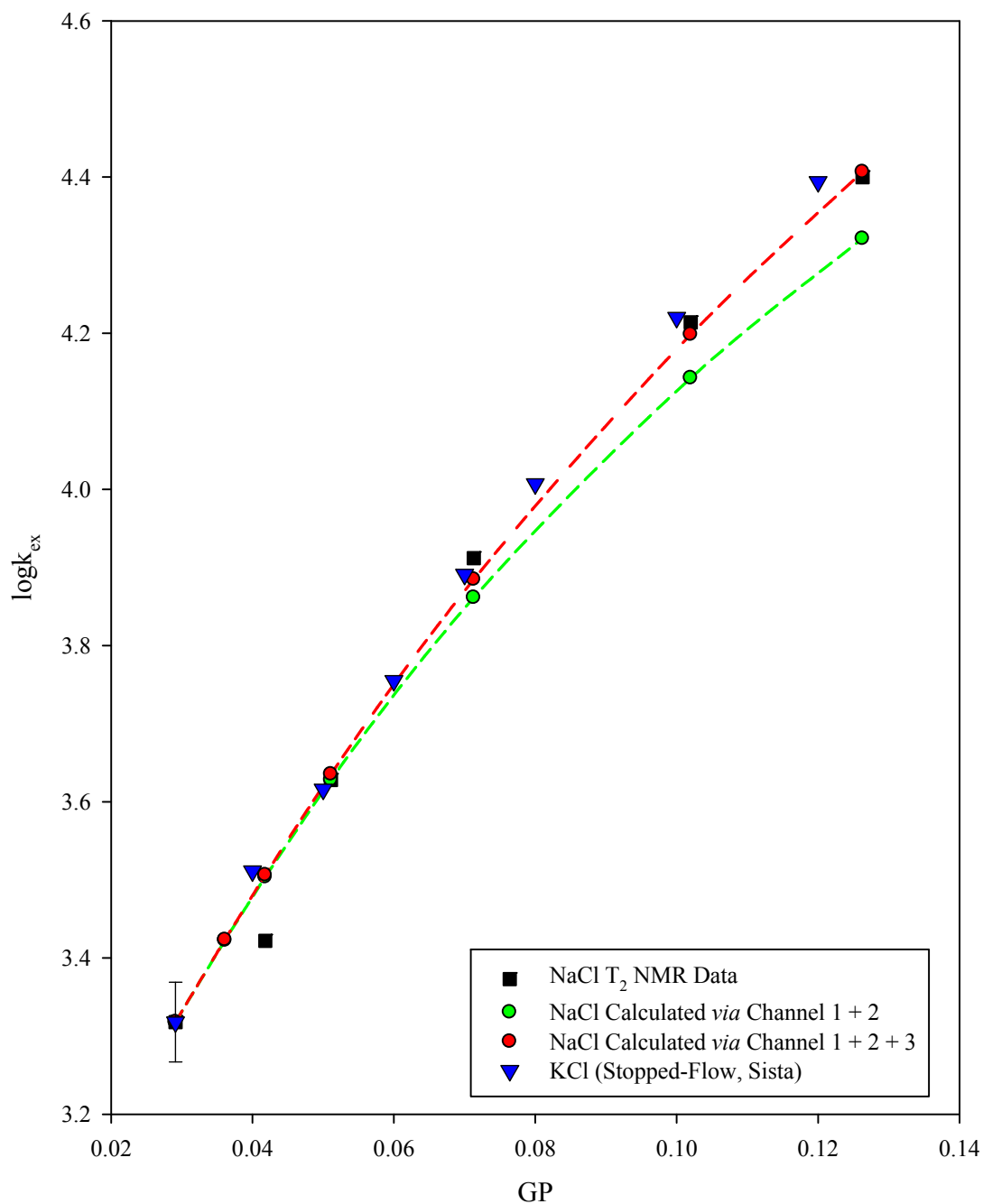


Figure 2.58 Experimental data and kinetic modeling results at 0.10 mM reactants with added NaCl using the crystallographic Cl^- radius of 1.90 Å. The T_2 NMR data (black squares) and stopped-flow data (blue triangles)⁶ are compared with modeling results using Channels 1 + 2 (green circles) and Channels 1 + 2 + 3 (red circles).

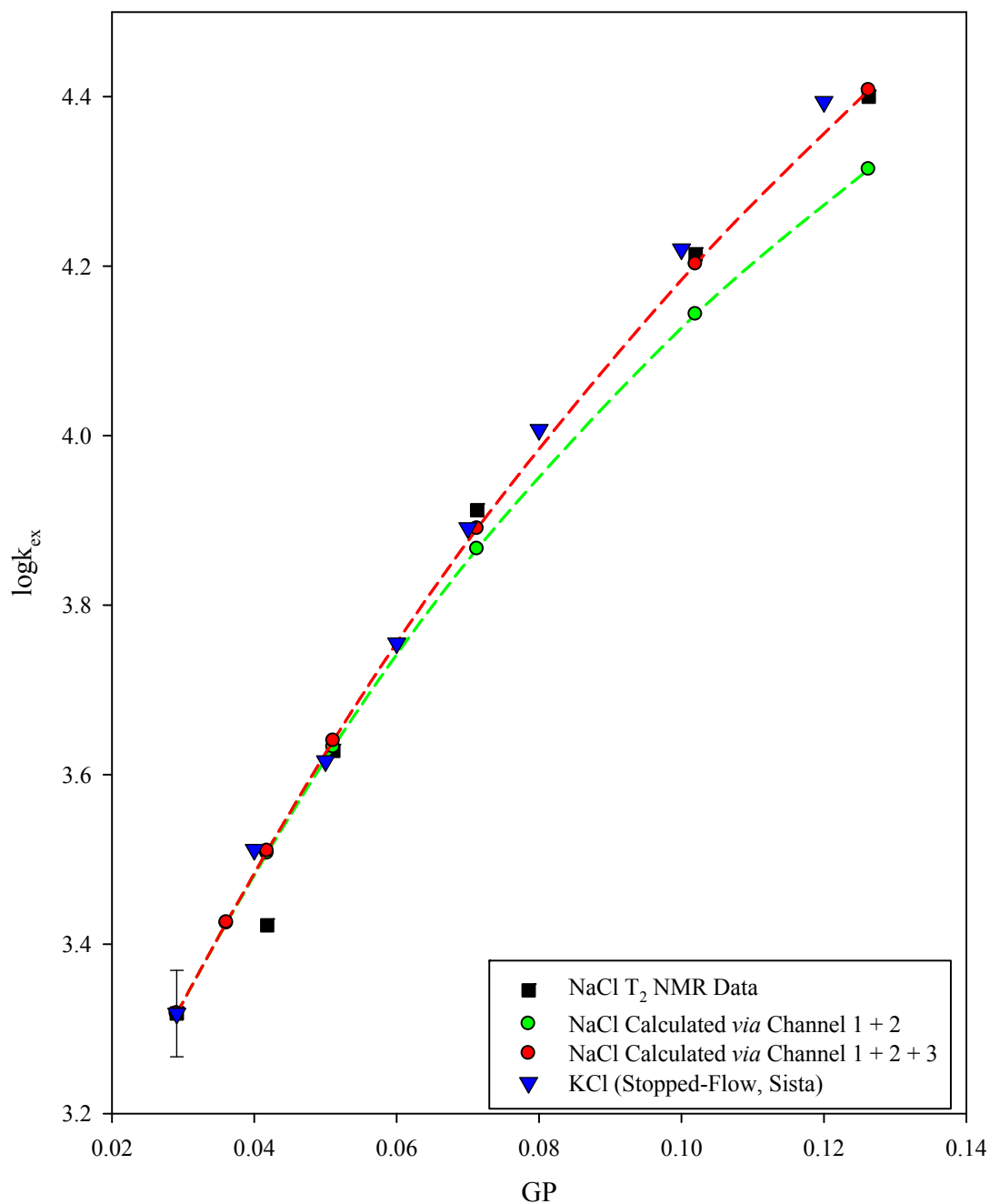


Figure 2.59 Experimental data and kinetic modeling results at 0.10 mM reactants with added NaCl now using the hydrated Cl^- radius of 4.41 Å. The T_2 NMR data (black squares) and stopped-flow data (blue triangles)⁶ are compared with modeling results using Channels 1 + 2 (green circles) and Channels 1 + 2 + 3 (red circles).

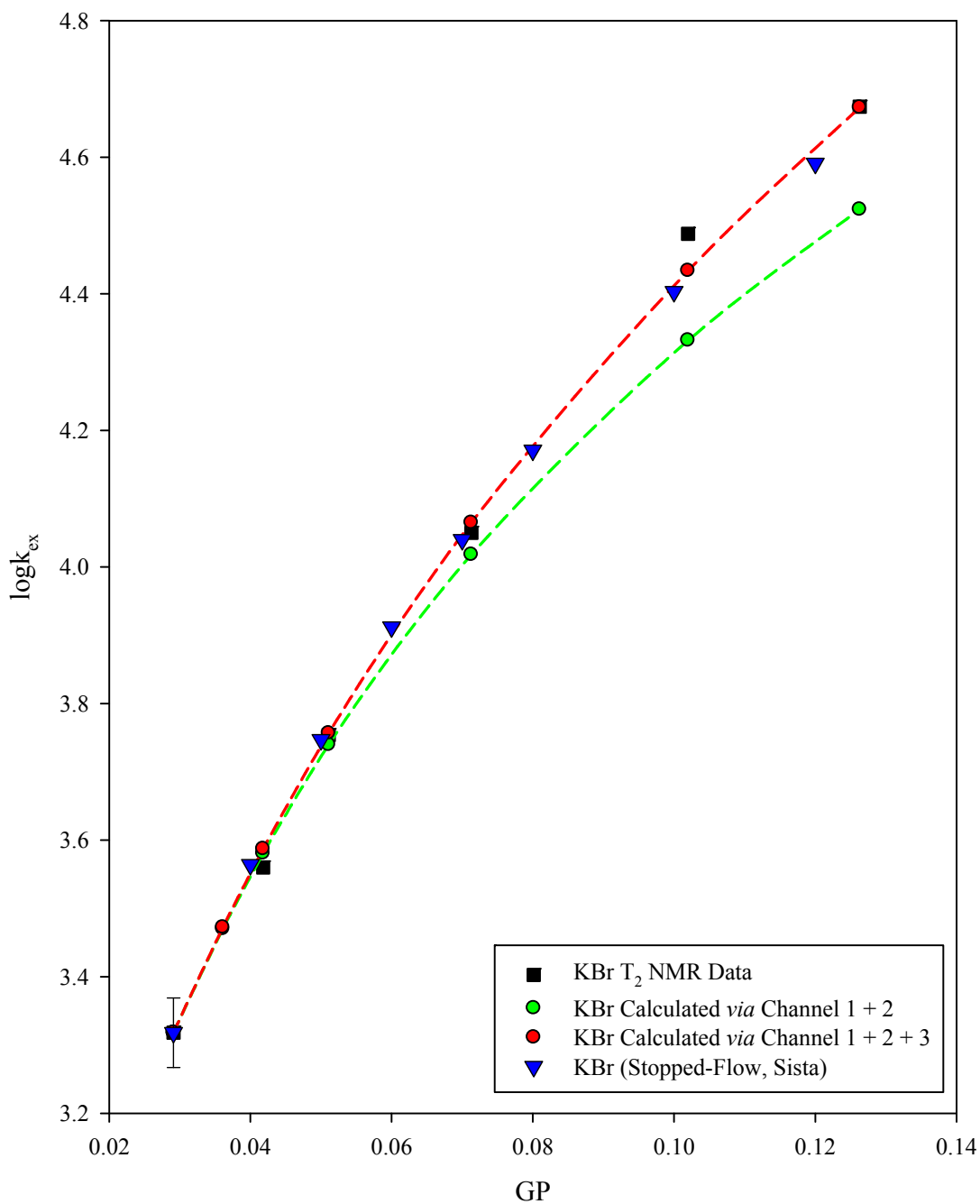


Figure 2.60 Experimental data and kinetic modeling results at 0.10 mM reactants with KBr (presumed crystallographic Br^- radius of 2.61 Å). The T_2 NMR data (black squares) and stopped-flow data (blue triangles)⁶ are compared with modeling results using Channels 1 + 2 (green circles) and Channels 1 + 2 + 3 (red circles).

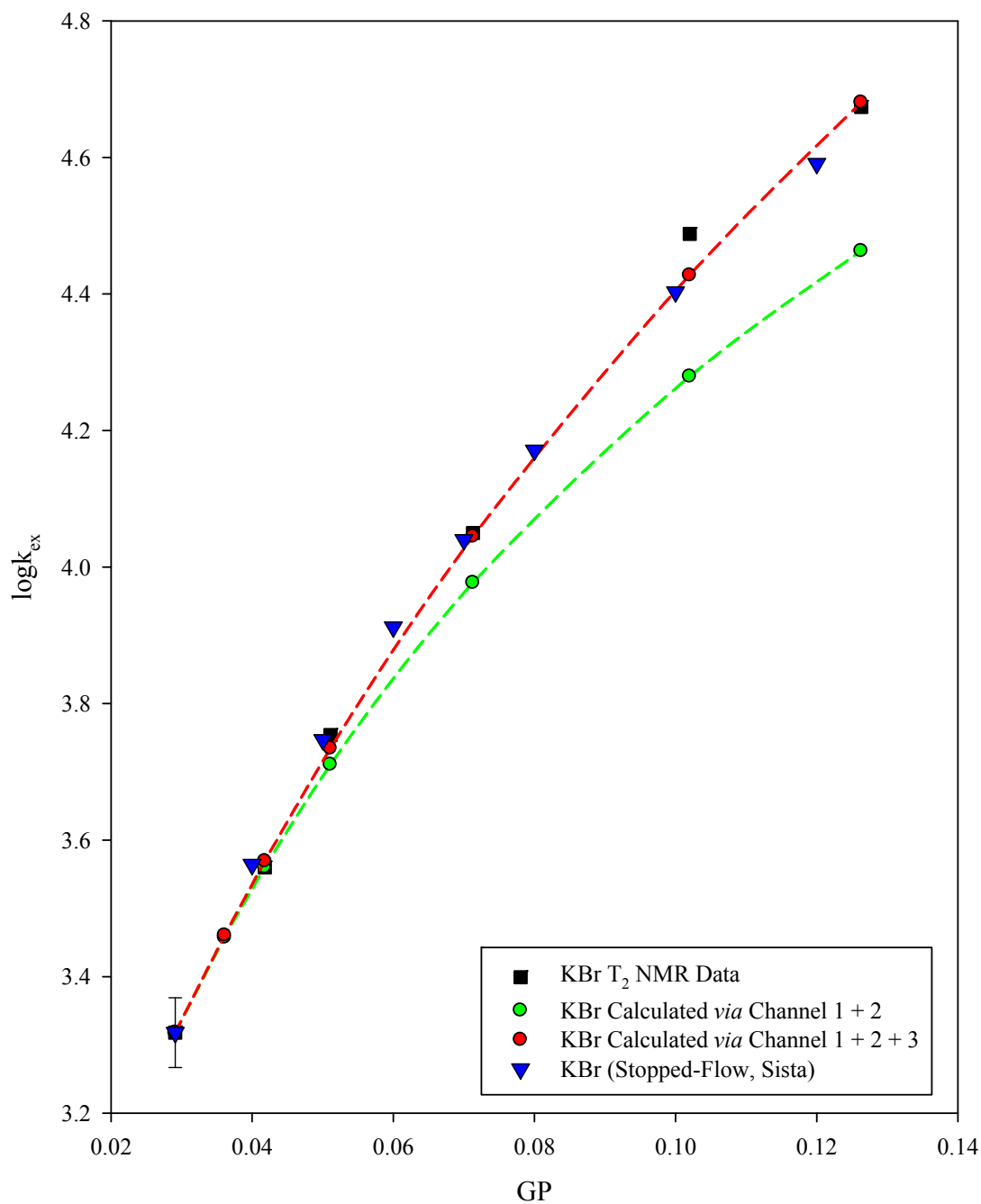


Figure 2.61 Experimental data and kinetic modeling results at 0.10 mM reactants with added KBr now using the hydrated Br⁻ radius of 4.08 Å. The T₂ NMR data (black squares) and stopped-flow data (blue triangles)⁶ are compared with modeling results using Channels 1 + 2 (green circles) and Channels 1 + 2 + 3 (red circles).

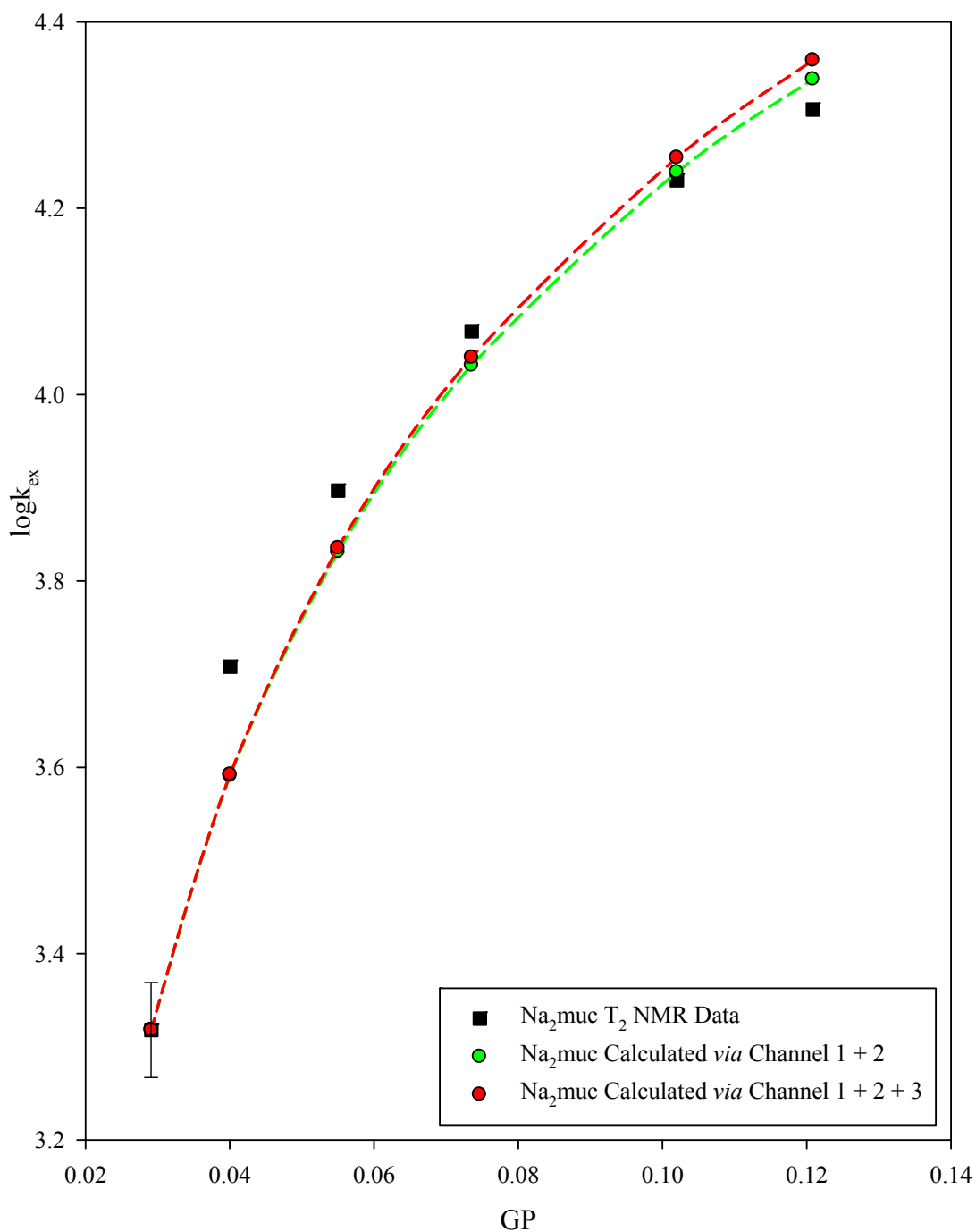


Figure 2.62 Experimental data and kinetic modeling results at 0.10 mM reactants with added Na_2muc using the crystallographic muc^{2-} radius of 3.86 Å. The T_2 NMR data (black squares) is compared with modeling results using Channels 1 + 2 (green circles) and Channels 1 + 2 + 3 (red circles).

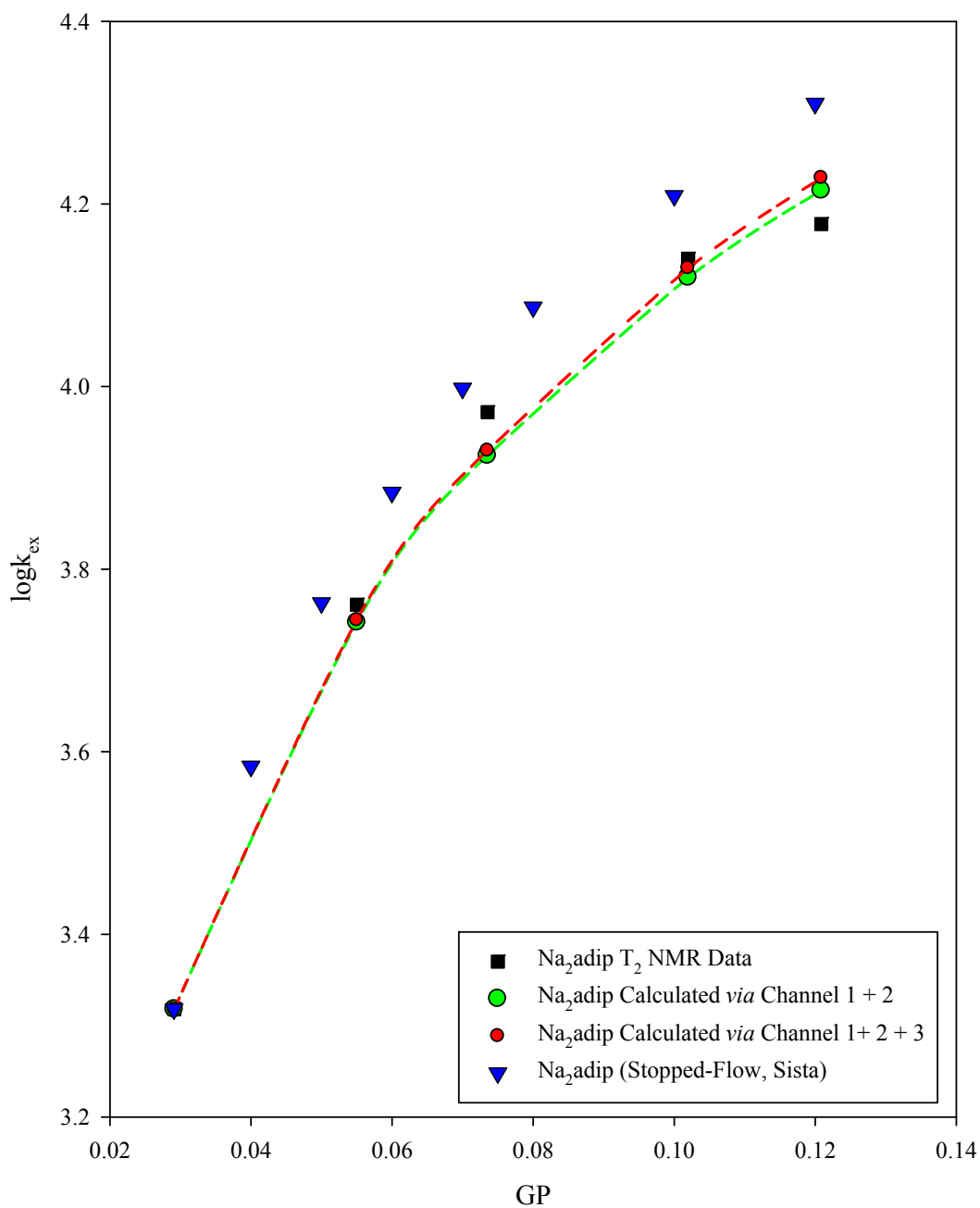


Figure 2.63 Experimental data and kinetic modeling results at 0.10 mM reactants with added Na₂adip using the crystallographic adip²⁻ radius of 3.97 Å. The T₂ NMR data (black squares) and stopped-flow data (blue triangles)⁶ are compared with modeling results using Channels 1 + 2 (green circles) and Channels 1 + 2 + 3 (red circles).

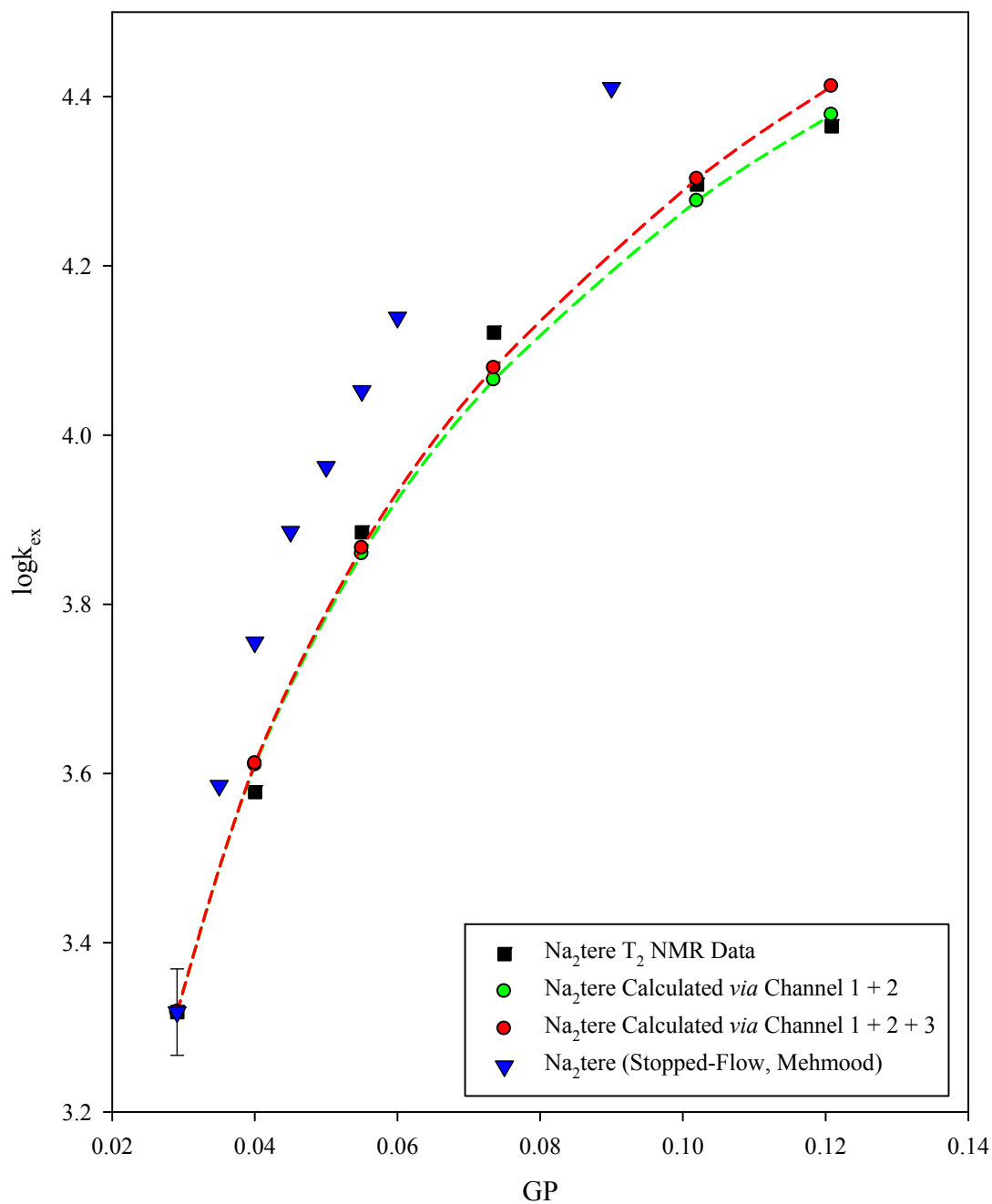


Figure 2.64 Experimental data and kinetic modeling results at 0.10 mM reactants with added Na_2tere using the crystallographic tere^{2-} radius of 4.13 Å. The T_2 NMR data (black squares) and stopped-flow data (blue triangles)⁹ are compared with modeling results using Channels 1 + 2 (green circles) and Channels 1 + 2 + 3 (red circles).

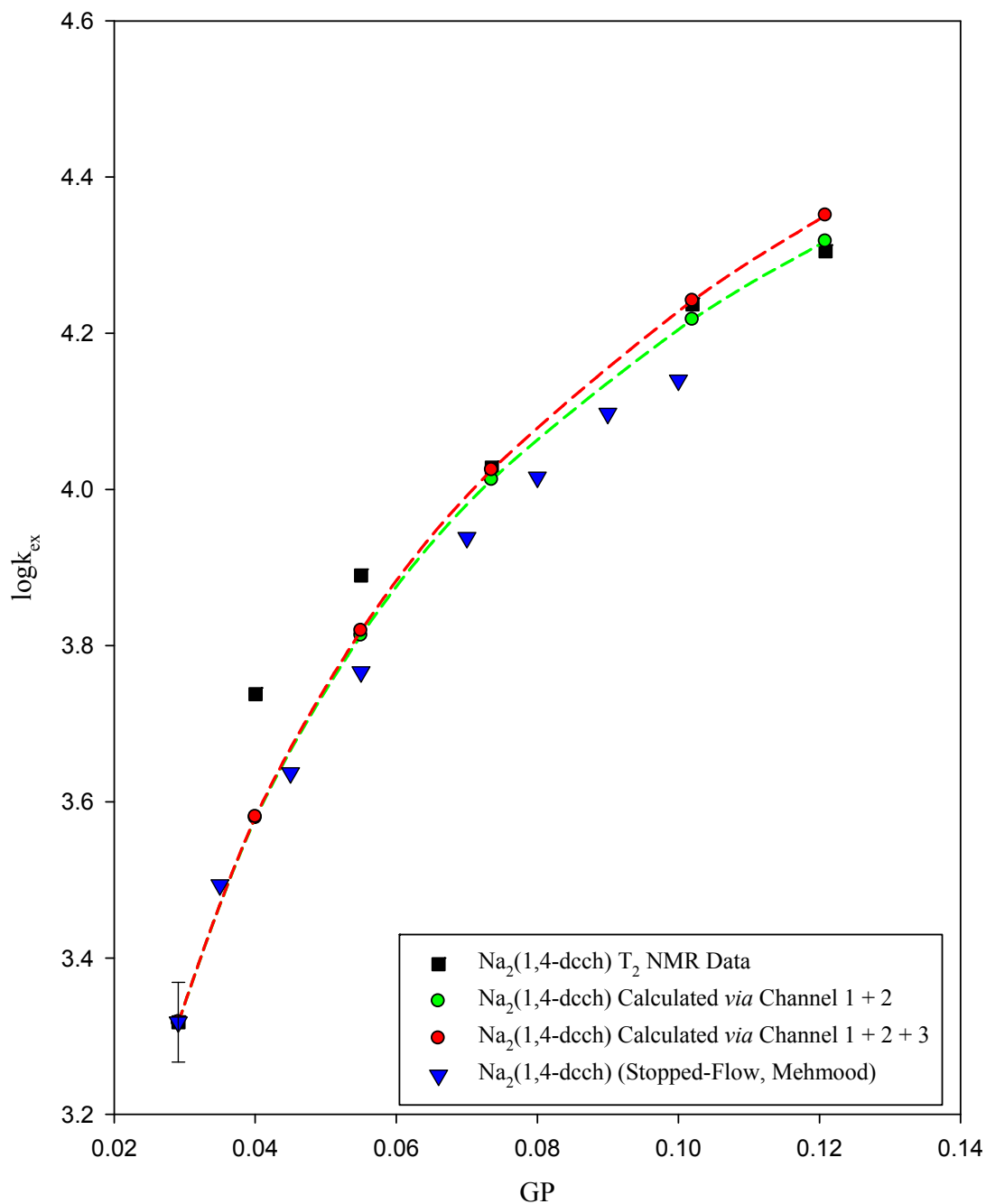


Figure 2.65 Experimental data and kinetic modeling results at 0.10 mM reactants with added Na₂(1,4-dcch) using the crystallographic 1,4-dcch²⁻ radius of 4.11 Å. The T₂ NMR data (black squares) and stopped-flow data (blue triangles)⁹ are compared with modeling results using Channels 1 + 2 (green circles) and Channels 1 + 2 + 3 (red circles).

To assess the sensitivity of our model to variations in inputted ionic radii, we applied it to the experimental $\log k_{\text{ex}}$ vs. GP curves for reaction (2-2) using both hydrated and crystallographic radii for the F^- , Cl^- , and Br^- anions as noted in Table 2.36. Previous kinetic modeling studies on the stopped-flow data^{6,9} on reaction (2-1) used only the unhydrated or “bare” crystallographic radii⁵⁵ of the various halides ions (these data were modeled using the SpecFit program to predicatively model stopped-flow absorbance vs. time-kinetic data according to the same kinetic scheme used here). Therefore, our conclusions are only directly comparable using the common set of crystallographic radii for the F^- , Cl^- , and Br^- .

Figure 2.55 shows the data and fit based on the crystallographic fluoride ion with $r = 1.50 \text{ \AA}$ at 0.10 mM reactants. We note that while the very early part of the data exhibit linear behavior and give a slope of 6 (in good agreement with the Debye-Huckel-Bronsted slope), the full-range is clearly curved downwards. The stopped-flow data shown here were normalized to the NMR starting $\log k_{\text{ex}}$ value to allow for direct comparison of the salt effect on rate (this is necessary since stopped-flow reaction (2-1) is a *pseudo* self-exchange reaction with a 69 mV driving force and thus starts off with a slightly higher rate; about $+0.34 \log k_{\text{ex}}$ units at 0.10 mM reactants). We find that reactive fluxes through both Channel 1 and Channel 2 were necessary in order for the modeled rates to match the experimental data, as was previously shown to be the case in modeling the stopped-flow data.⁶ The k_{ET} and k_{ETX} values necessary to fit the data using the crystallographic fluoride radius were 8.6×10^4 and 8.2×10^4 , respectively, giving a ratio of $k_{\text{ETX}}/k_{\text{ET}}$ equal to 0.9. A similar result was also found

by Sista for reaction (2-1) where k_{ET} and k_{ETX} were 2.7×10^5 and 2.5×10^5 , respectively (giving a ratio of $k_{\text{ETX}}/k_{\text{ET}}$ equal to 0.9 as well). From the computed values of k_{a2} and k_{d2} at an intermediate GP of 0.0713 ($[\text{F}^-] = 0.005 \text{ M}$) were 2.61×10^{10} and 2.34×10^9 , and from $K_{\text{A2}} = k_{\text{a2}}/k_{\text{d2}} = 11.19$ we conclude that significant ion-pairing must be occurring over most of the GP range even for this “simplest” and most ideal behaving case of added fluoride-the only one which quantitatively agrees with the Debye-Hückel-Bronsted equation (1-38) at the low $[\text{F}^-]$ end. The nearly-identical NMR and stopped-flow kinetic salt effect with F^- validate the presumed close relationship between the *true* self-exchange and the *pseudo* self-exchange ET energy barriers governing the two reactions.

A similar comparison holds between our modeling work for the salt effects using unhydrated radii for the Cl^- and Br^- ions and the earlier SpecFit modeling work on reaction (2-1). When comparing the k_{ET} , k_{ETX} , and the (now necessary) k_{ETXX} values for the Cl^- and Br^- ions listed in Table 2.38 (and shown in Figures 2.57 to 2.60), we now see that the k_{ETX} values of 4.6×10^5 and 7.5×10^5 are significantly larger than the “anchor” k_{ET} value of 8.6×10^4 . This indicates that Pathway 2 (using Channels 2 and 3) is the predominating pathway early on in the experimental range for the added halides beyond F^- . The computed ion-pair formation constants, K_{A2} , at a GP = 0.0713 ($[\text{X}] = 0.005 \text{ M}$) using the crystallographic radii for Cl^- and Br^- are 11.68 and 11.56 respectively. These magnitudes mean that ion-pairing is both important in the solution as well as, evidently, catalytic towards, ET in a manner which transcends the simple Debye-Huckel-Bronsted model. We again find a sequential increase in the

$k_{\text{ETX}}/k_{\text{ET}}$ ratio which now goes from 5.3 to 8.7 for Cl^- and Br^- respectively. Sista's work on reaction (2-1) yielded ratios of 5.06 for Cl^- and 10.09 for Br^- , which is again in very good agreement with our NMR results. This trend in $k_{\text{ETX}}/k_{\text{ET}}$ ratios for the F^- , Cl^- , Br^- series might be due to an unaccounted for increase in the thermodynamic favorability for ion-pairing (beyond what the computed K_{A} values would predict) along the series. However, prior work using ion-pair charge-transfer absorption studies have shown that the K_{IP} values formation of the $[(\text{NH}_3)_5\text{Ru}^{\text{III}}\text{py}\cdot\text{Cl}]^{2+}$ and $[(\text{NH}_3)_5\text{Ru}^{\text{III}}3\text{Fpy}\cdot\text{Br}]^{2+}$ ion-pairs are 15.9 ± 0.6 and 10.3 ± 0.8 which are approximately within error of each other and the Fuoss equation predictions of 14 and 11 (based on crystallographic radii).⁵⁷ The similarity in the measured $K_{\text{A}2}$ (same as K_{IP}) values for both Cl^- and Br^- , and their closeness to theory would then support the idea that electron-transfer inside the ternary PCX assembly is somehow catalyzed such that k_{ETX} is larger (more influential) than simply k_{ET} inside the bimolecular encounter complex, PC.

Upon fitting NMR data using the hydrated radius of 3.89 Å for F^- , we obtain Channel 2 $k_{\text{a}2}$ and $k_{\text{d}2}$ values (at a GP = 0.0713, $[\text{F}^-] = 0.005 \text{ M}$) of 1.57×10^{10} and 1.29×10^9 respectively, which yields an ion-pairing constant $K_{\text{A}2}$ of 12.17. Now the best-fit k_{ETX} value is 5.1×10^4 , which is significantly smaller than the “anchor” k_{ET} value of 8.6×10^4 . This smaller ratio suggests that Pathway 1 is the predominate pathway with higher $[\text{F}^-]$ than was found for the “naked” or unhydrated F^- ion. The slightly smaller value of the k_{ETX} relative to k_{ET} is a bit surprising, but it is necessary to account for the downward curvature of the $\log k_{\text{ex}}$ vs. GP plot in Figure 2.56 in the

case of the more realistic, larger radius for hydrated fluoride (which is known to strongly bind waters of hydration in solution).^{2,58} Interestingly, even though ion-pairing and flux through Channel 2 (PCX) is necessary to obtain the best-fit of the experimental data, we see that the fluoride ion itself is *not* acting as a catalyst to the ET event in sharp contrast to Cl^- and Br^- . Therefore, the full range of fluoride's effect on ET rate can only be explained by a combination of the ion-atmosphere type model proposed by Debye and Hückel^{11,59} as it affects k_{ex} through ionic strength at very low $[\text{F}^-]$ and the formation/reaction of ion-pairs and impeded ET within PCX at large $[\text{F}^-]$. That ET in the ternary $[\text{Ru}^{\text{II}}, \text{F}^-, \text{Ru}^{\text{III}}]$ encounter complex would actually be slower than it is in the simple $[\text{Ru}^{\text{II}}, \text{Ru}^{\text{III}}]$ precursor complex is not unreasonable given its strong hydration and the energetic unavailability of hole-transfer virtual states for quantum super-exchange mediation (as will be discussed in a later section).

For the hydrated Cl^- ($r = 4.41 \text{ \AA}$) and Br^- ($r = 4.08 \text{ \AA}$) ions progressive increases in the anion catalysis and the best-fit k_{ETX} values were again found upon going from chloride to bromide. The implied k_{ETX} values were significantly larger than the uncatalyzed k_{ET} value (or the GP-matched fluoride rates) further indicating that Channels 1 and 2 (at least) must be taken into account in modeling the reaction in the presence of these anions. The best-fit $k_{\text{ETX}}/k_{\text{ET}}$ ratios for the hydrated chloride and bromide ions are 2.9 and 5.0 respectively (see Table 2.40), whereas those obtained using the unhydrated radii were somewhat greater at 5.3 and 8.7 respectively (which is similar to the observed trend for F^- as well). This result is non-intuitive and

will be discussed further on. Looking at Table 2.40, we see that the same trends with halide radii are also obtained for the implied k_{ETX} values.

With the dicarboxylate anions (muc^{2-} , adip^{2-} , tere^{2-} , and $1,4\text{-dcch}^{2-}$), we find quite different behavior. Now the best-fit k_{ETX} values are on the order of about 75% of k_{ET} , as seen in the $k_{\text{ETX}}/k_{\text{ET}}$ ratios listed in Table 2.40. This implies a return to the fluoride case of ET “un-catalysis” by the anion, where Channel 2 through the PCX triplet is slower than what the ionic strength - and hence GP - enhanced flux thru Channel 1 would suggest. When we contrast our $k_{\text{ETX}}/k_{\text{ET}}$ ratios with those obtained previously for reaction (2-1) (with the current ratios from this thesis shown in parenthesis), the comparative ratios for adip^{2-} , tere^{2-} and $1,4\text{-dcch}^{2-}$ are 0.6 (0.5), 1.2 (0.8), and 0.3 (0.7) respectively.^{6,9} The best-fit k_{ETX} value for muconate was the only one which significantly deviated in our work from what was seen previously for reaction (2-1).^{6,9} The stopped-flow work yielded $k_{\text{ETX}}/k_{\text{ET}} = 6.7$, but in our NMR (T_2) work the ratio dropped to 0.7 which is exactly in the range of the other ones measured for the other dicarboxylate salts and thus showing *no sign* of any special “muconate effect” on the ET rate. This divergence in the $k_{\text{ETX}}/k_{\text{ET}}$ ratio specific to muconate as probed by NMR further validates the surprising and dramatic loss of catalytic efficacy for muconate already discussed on the basis of the salt curves and the isokinetic analysis.

The first observation of muconate’s collapse to a “simple-salt” behavior when studied by NMR was in Qin’s line-broadening ET rate measurements at 5.00 mM reactants.^{1,8} She also noted very shallow Debye-Hückel-Bronsted slopes upon adding

various simple salts including the halides. An initial hypothesis regarding the divergence from the stopped-flow work held that the 50-fold difference in reactants concentration was the probable reason. To explore this idea, we undertook detailed kinetic modeling of our measured salt effects on reaction (2-2) at reactants concentrations of 0.50 mM, 1.00 mM, and 5.00 mM with the added simple and dicarboxylate salts. In order to fit our experimental data with the model developed here, we again iteratively determined the optimum k_{ETX} and k_{ETXX} values for each specific added electrolyte at each specific reactants concentration while holding k_{ET} constant at the value determined from the multiply-determined 0.10 mM reactants only “anchor point” (which gave a $k_{ET} = 8.6 \times 10^4$).

2.17.3 Salt-specific kinetic modeling at $[Ru^{II}] = [Ru^{III}] = 0.50 \text{ mM}$

The best-fit k_{ET} , k_{ETX} , and k_{ETXX} values and the k_{ETX}/k_{ET} and k_{ETXX}/k_{ETX} ratios arrived at for 0.50 mM reactants are listed in Table 2.42. The experimental and best-fit calculated rate constants obtained using equations (2-36) to (2-38) are listed in Table 2.43 and the fits are illustrated in Figures 2.66 to 2.73.

As was noted previously, when applying our model to the reactants-only concentrations above 0.10 mM, the calculated $\log k_{ex}$ value with no added salt obtained using equation (2-33) (while keeping k_{ET} constant at 8.6×10^4) deviates not only from experiment, but also from what is predicted by the Debye-Hückel-Bronsted equation. In order to fit our experimental curves at these larger reactants concentrations, we split the difference between the implied starting $\log k_{ex}$ value (no added salt) arrived at using equation (2-33) and our experimentally measured $\log k_{ex}$

value. For example, at 0.50 mM reactants the calculated $\log k_{\text{ex}}$ value found is 3.49 while our experimental $\log k_{\text{ex}}$ value is 3.58 ± 0.04 , therefore, when fitting our experimental data we adjusted all calculated $\log k_{\text{ex}}$ values by adding 0.045 log units to the calculated values ($3.58 - 3.49 = 0.09$, $0.09/2 = 0.045$ log units) after all adjustments were applied to the k_{ETX} and k_{ETXX} values while keeping k_{ET} constant. The reported values in Table 2.43 contain only the adjusted $\log k_{\text{ex}}$ values (+0.045 log units from what would be obtained solely using equation (2-36) while keeping k_{ET} constrained).

Table 2.42 Best-fit k_{ET} , k_{ETX} , and k_{ETXX} rate constants for reaction (2-2) corresponding to first-order ET inside the presumed PC, PCX, and PCXX reactive intermediates (based on iterative fitting of the $\log k_{\text{ex}}$ vs. added salt curves measured at $[\text{Ru}^{\text{II}}] = [\text{Ru}^{\text{III}}] = 0.50 \text{ mM}$ for the halide and dicarboxylate anions studied. These values lead to the model-calculated rates listed in Table 2.43. The $k_{\text{ETX}}/k_{\text{ET}}$ and $k_{\text{ETXX}}/k_{\text{ETX}}$ ratios are listed in the final two columns.

Ion	$k_{\text{ET}}^{(a)}$	$k_{\text{ETX}}^{(b)}$	$k_{\text{ETXX}}^{(c)}$	$k_{\text{ETX}}/k_{\text{ET}}^{(d)}$	$k_{\text{ETXX}}/k_{\text{ETX}}^{(e)}$
F^- ($r = 1.50 \text{ \AA}$)	8.6×10^4	1.6×10^3	-	0.02	-
F^- ($r = 3.89 \text{ \AA}$)	8.6×10^4	2.4×10^3	-	0.03	-
Cl^- ($r = 1.90 \text{ \AA}$)	8.6×10^4	3.9×10^5	2.6×10^5	4.5	0.7
Cl^- ($r = 4.41 \text{ \AA}$)	8.6×10^4	2.0×10^5	1.0×10^5	2.3	0.5
Br^- ($r = 2.61 \text{ \AA}$)	8.6×10^4	8.0×10^5	2.0×10^4	9.3	0.03
Br^- ($r = 4.08 \text{ \AA}$)	8.6×10^4	5.5×10^5	4.0×10^3	6.4	0.1
muc^{2-} ($r = 3.86 \text{ \AA}$)	8.6×10^4	4.0×10^4	1.0×10^3	0.5	0.03
adip^{2-} ($r = 3.97 \text{ \AA}$)	8.6×10^4	2.0×10^4	1.0×10^3	0.2	0.05

(a) Estimated uncertainty of $\pm 5\%$, (b) Estimated uncertainty of $\pm 2\%$, (c) estimated uncertainty of $\pm 5\%$, (d) estimated uncertainty of $\pm 3\%$, and (e) estimated uncertainty of $\pm 2.5\%$.

Table 2.43 Experimental and model-calculated rate constants at 5.00 mM reactants for reaction (2-2) as a function of GP arrived at using the three-channel model summarized in equations (2-36) through (2-38) and the best-fit rate constants listed in Table 2.42 (the relevant ionic radii are taken from Tables 2.36 and 2.37). The data and fitted curves are illustrated in Figures 2.66 to 2.73.

KF

r = 1.50 Å	GP	logk_{ex} (expt.)	logk_{ex} (calc.) Channel 1 Only	logk_{ex} (calc.) Channels 1 and 2	logk_{ex} (calc.) Channels 1, 2, and 3
	0.0629	3.580 ± 0.039	3.536	3.536	-
	0.0690	3.615	3.561	3.561	-
	0.0888	3.649	3.634	3.636	-
	0.1075	3.713	3.695	3.699	-
	0.1566	3.824	3.824	3.832	-
	0.2025	3.912	3.903	3.916	-

KF

r = 3.89 Å	GP	logk_{ex} (expt.)	logk_{ex} (calc.) Channel 1 Only	logk_{ex} (calc.) Channels 1 and 2	logk_{ex} (calc.) Channels 1, 2, and 3
	0.0629	3.580 ± 0.039	3.536	3.536	-
	0.0690	3.615	3.560	3.563	-
	0.0888	3.649	3.631	3.642	-
	0.1075	3.713	3.690	3.708	-
	0.1566	3.824	3.806	3.844	-
	0.2025	3.912	3.858	3.914	-

NaCl

r = 1.90 Å	GP	logk_{ex} (expt.)	logk_{ex} (calc.) Channel 1 Only	logk_{ex} (calc.) Channels 1 and 2	logk_{ex} (calc.) Channels 1, 2, and 3
	0.0629	3.580 ± 0.039	3.536	3.536	3.536
	0.0690	3.647	3.561	3.645	3.646
	0.0888	3.921	3.633	3.914	3.924
	0.1075	4.121	3.693	4.104	4.128
	0.1566	4.536	3.818	4.462	4.529
	0.2025	4.810	3.892	4.690	4.805

NaCl

r = 4.41 Å	GP	logk_{ex} (expt.)	logk_{ex} (calc.) Channel 1 Only	logk_{ex} (calc.) Channels 1 and 2	logk_{ex} (calc.) Channels 1, 2, and 3
	0.0629	3.580 ± 0.039	3.536	3.536	3.536
	0.0690	3.647	3.560	3.643	3.644
	0.0888	3.921	3.630	3.906	3.921
	0.1075	4.121	3.688	4.091	4.126
	0.1566	4.536	3.799	4.426	4.532
	0.2025	4.810	3.840	4.614	4.813

KBr

r = 2.61 Å	GP	logk_{ex} (expt.)	logk_{ex} (calc.) Channel 1 Only	logk_{ex} (calc.) Channels 1 and 2	logk_{ex} (calc.) Channels 1, 2, and 3
	0.0629	3.580 ± 0.039	3.536	3.536	3.536
	0.0690	3.726	3.561	3.731	3.731
	0.0888	4.133	3.633	4.115	4.115
	0.1075	4.368	3.693	4.349	4.350
	0.1566	4.764	3.817	4.751	4.755
	0.2025	4.994	3.886	4.994	5.001

KBr

r = 4.08 Å	GP	logk_{ex} (expt.)	logk_{ex} (calc.) Channel 1 Only	logk_{ex} (calc.) Channels 1 and 2	logk_{ex} (calc.) Channels 1, 2, and 3
	0.0629	3.580 ± 0.039	3.536	3.536	3.536
	0.0690	3.726	3.560	3.738	3.738
	0.0888	4.133	3.631	4.128	4.131
	0.1075	4.368	3.690	4.361	4.368
	0.1566	4.764	3.804	4.752	4.772
	0.2025	4.994	3.852	4.970	5.009

Na₂muc					
r = 3.86 Å	GP	logk_{ex} (expt.)	logk_{ex} (calc.)	logk_{ex} (calc.)	logk_{ex} (calc.)
			Channel	Channels	Channels
			1 Only	1 and 2	1, 2, and 3
	0.0629	3.580 ± 0.039	3.536	3.536	3.536
	0.0693	3.744	3.551	3.676	3.676
	0.0880	3.996	3.590	3.932	3.933
	0.1071	4.112	3.623	4.095	4.096
	0.1566	4.287	3.678	4.347	4.351
	0.2025	4.220	3.683	4.481	4.486
Na₂adip					
r = 3.97 Å	GP	logk_{ex} (expt.)	logk_{ex} (calc.)	logk_{ex} (calc.)	logk_{ex} (calc.)
			Channel	Channels	Channels
			1 Only	1 and 2	1, 2, and 3
	0.0629	3.580 ± 0.039	3.536	3.536	3.536
	0.0693	3.661	3.552	3.618	3.619
	0.0880	3.859	3.591	3.795	3.796
	0.1071	3.940	3.626	3.923	3.925
	0.1566	4.119	3.684	4.134	4.140
	0.2025	4.186	3.693	4.248	4.258

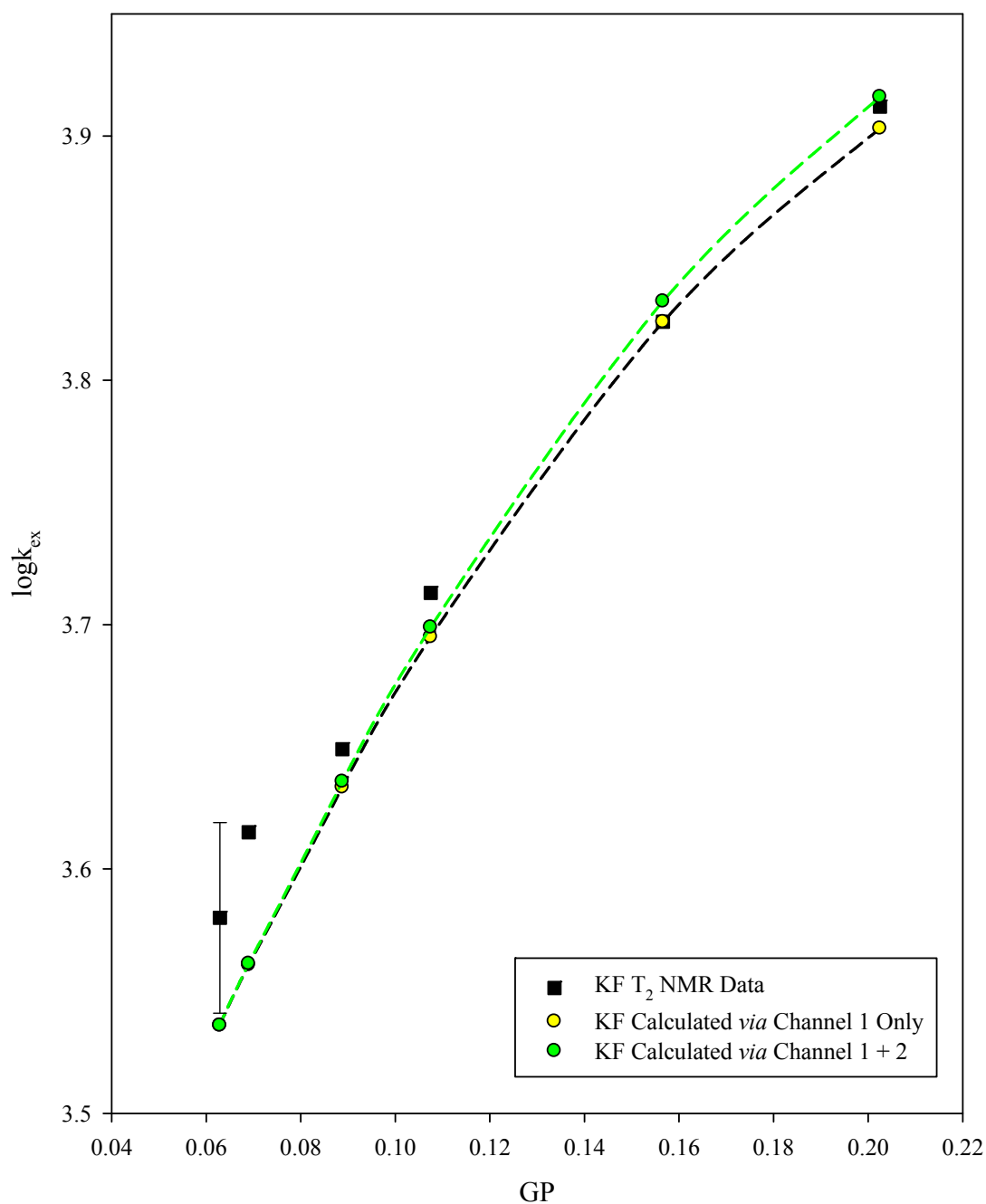


Figure 2.66 Experimental data and kinetic modeling results at 0.50 mM reactants with added KF using the crystallographic F^- radius of 1.50 Å. The T_2 NMR data (black squares) is compared with modeling results using Channel 1 (yellow circles) and Channels 1 + 2 (green circles).

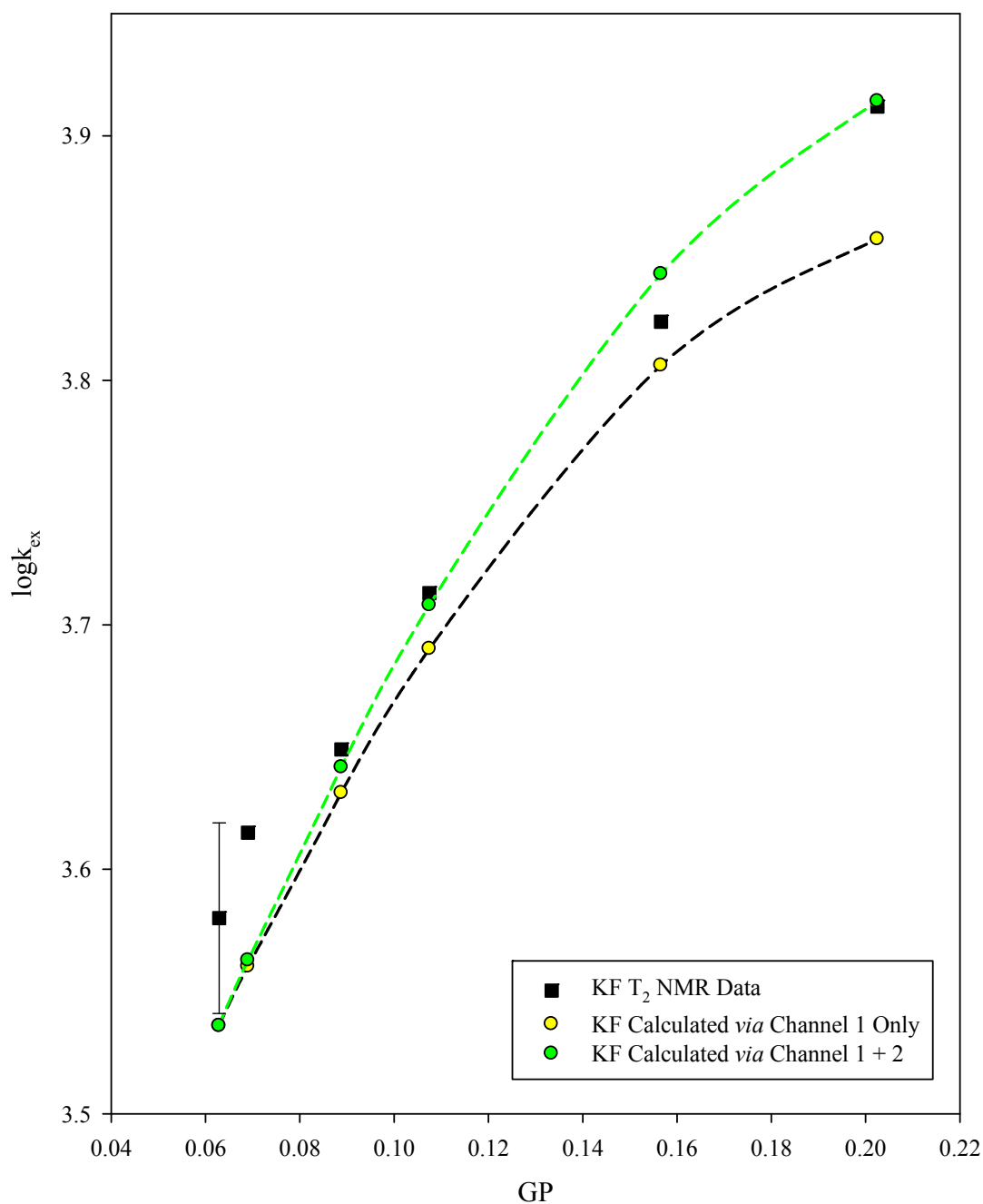


Figure 2.67 Experimental data and kinetic modeling results at 0.50 mM reactants with added KF now using the hydrated F^- radius of 3.89 Å. The T_2 NMR data (black squares) is compared with modeling results using Channel 1 (yellow circles) and Channels 1 + 2 (green circles).

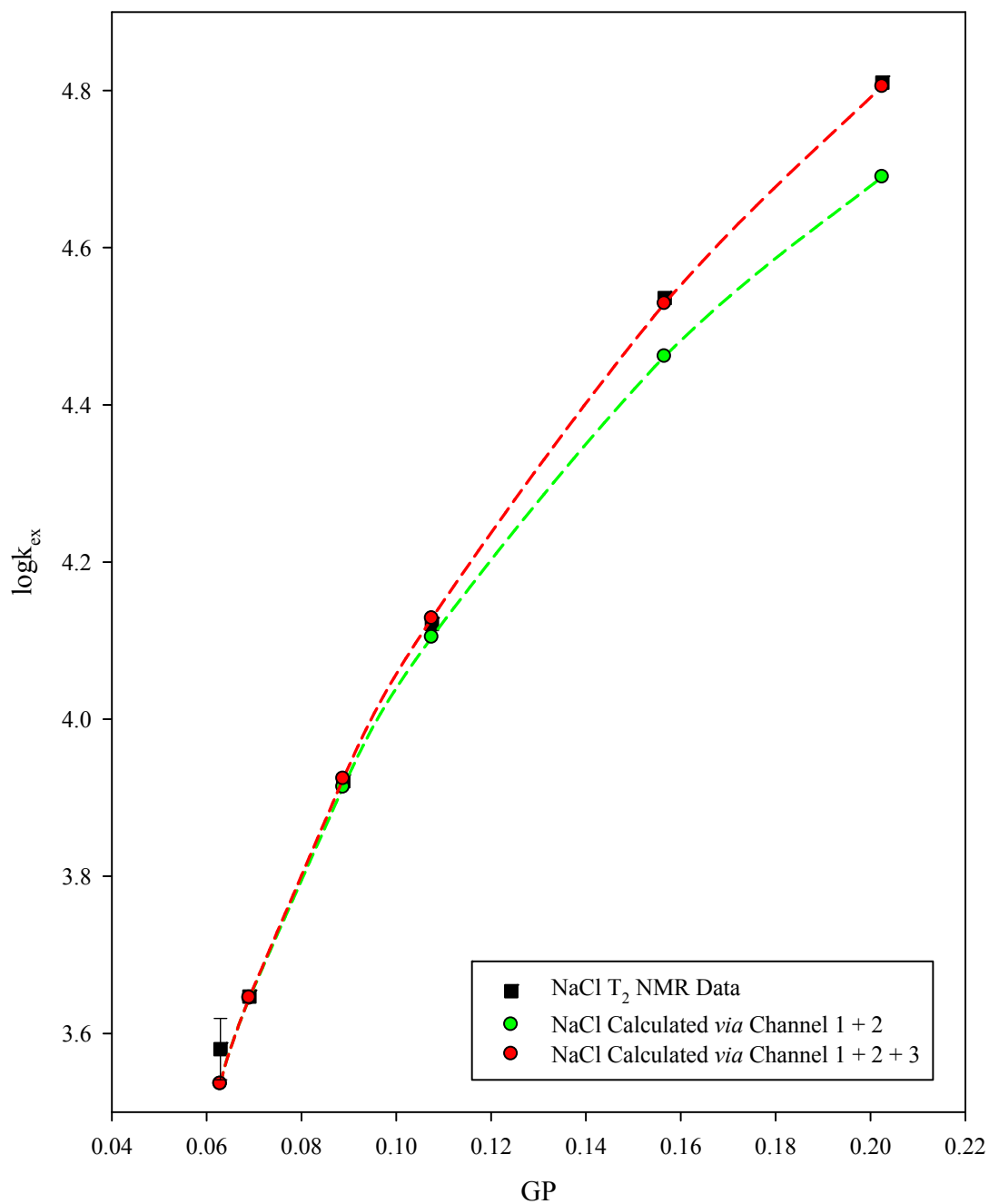


Figure 2.68 Experimental data and kinetic modeling results at 0.50 mM reactants with added NaCl using the crystallographic Cl^- radius of 1.90 Å. The T_2 NMR data (black squares) is compared with modeling results using Channels 1 + 2 (green circles) and Channels 1 + 2 + 3 (red circles).

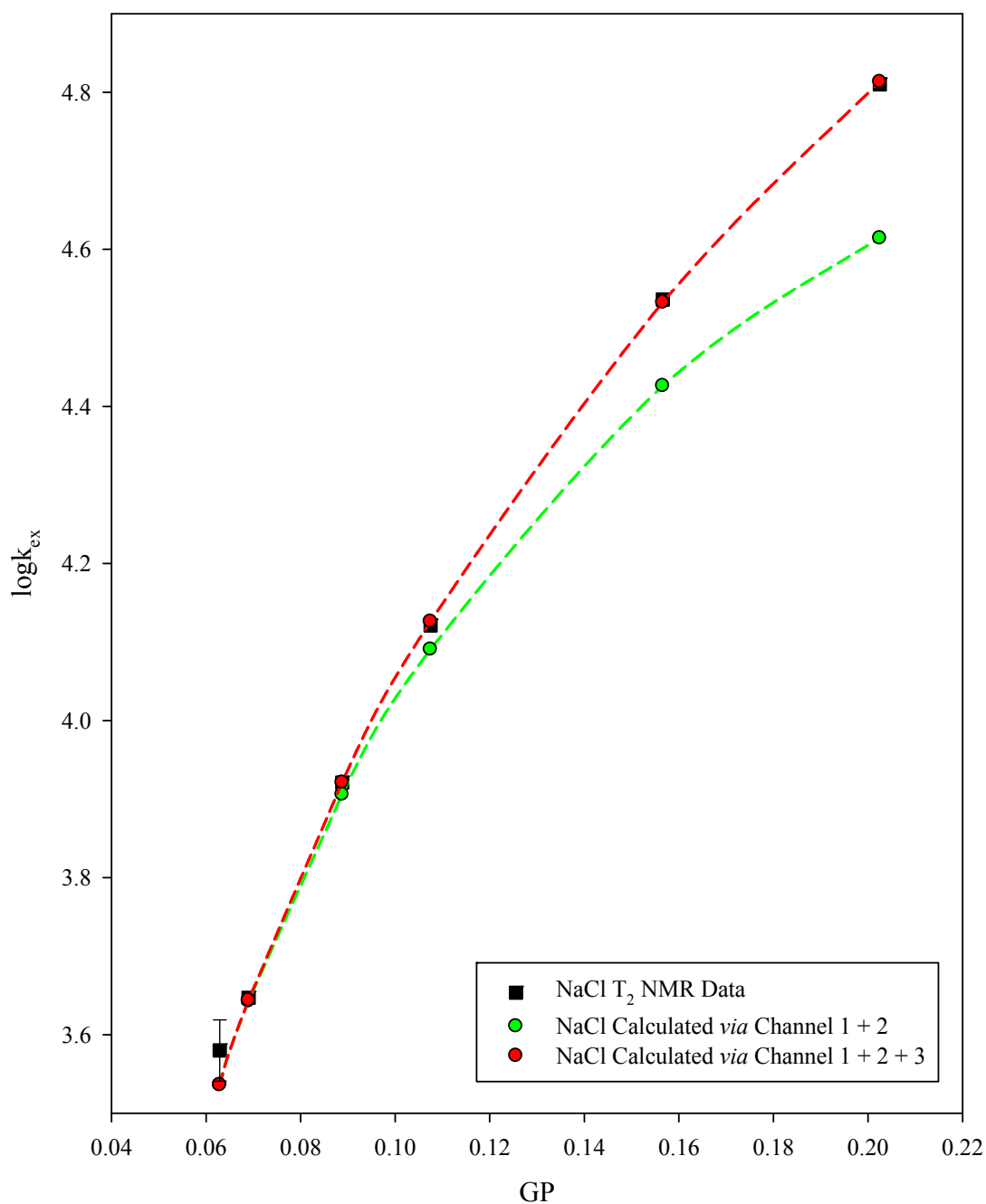


Figure 2.69 Experimental data and kinetic modeling results at 0.50 mM reactants with added NaCl now using the hydrated Cl^- radius of 4.41 Å. The T_2 NMR data (black squares) is compared with modeling results using Channels 1 + 2 (green circles) and Channels 1 + 2 + 3 (red circles).

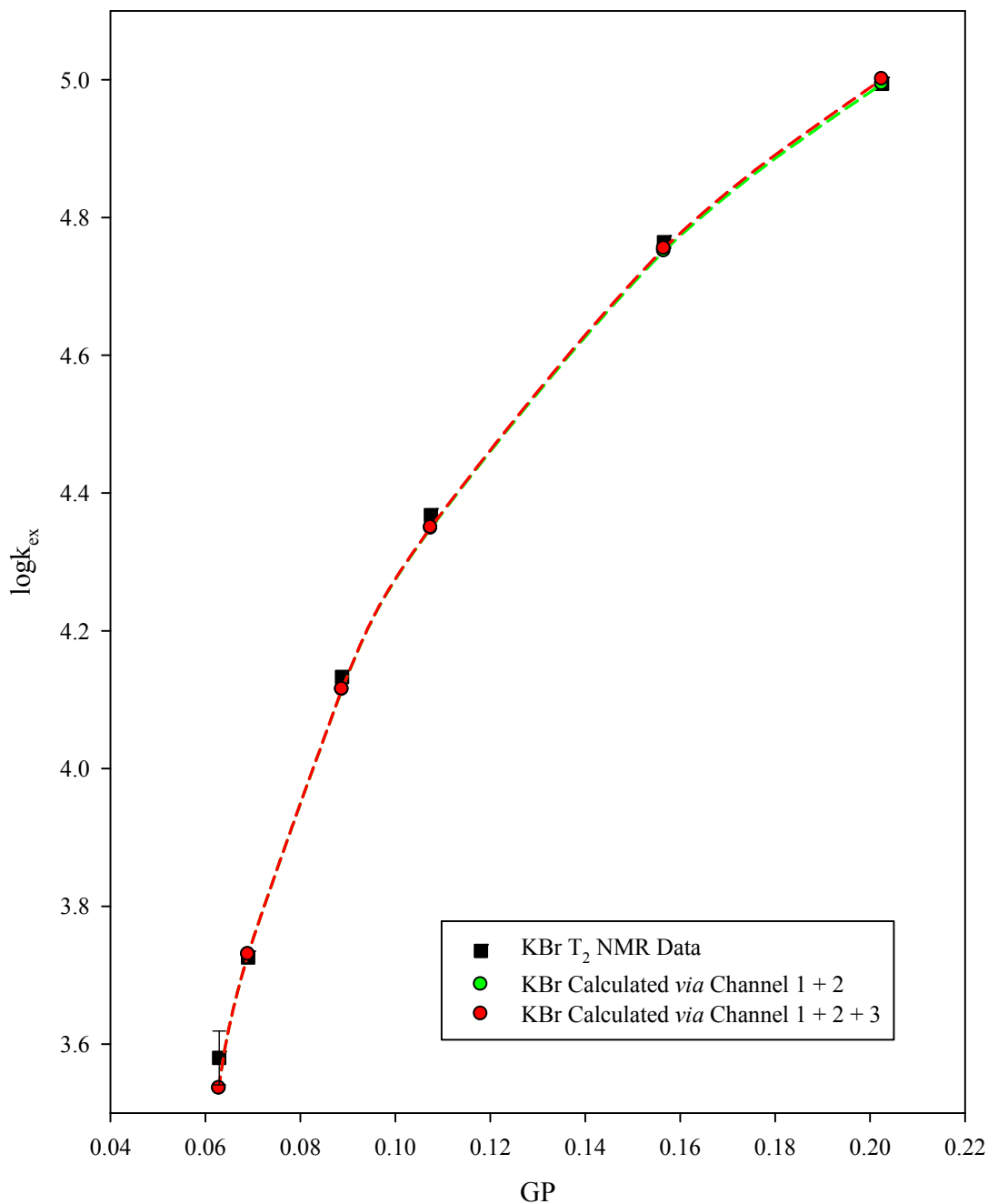


Figure 2.70 Experimental data and kinetic modeling results at 0.50 mM reactants with added KBr using the crystallographic Br⁻ radius of 2.61 Å. The T₂ NMR data (black squares) is compared with modeling results using Channels 1 + 2 (green circles) and Channels 1 + 2 + 3 (red circles).

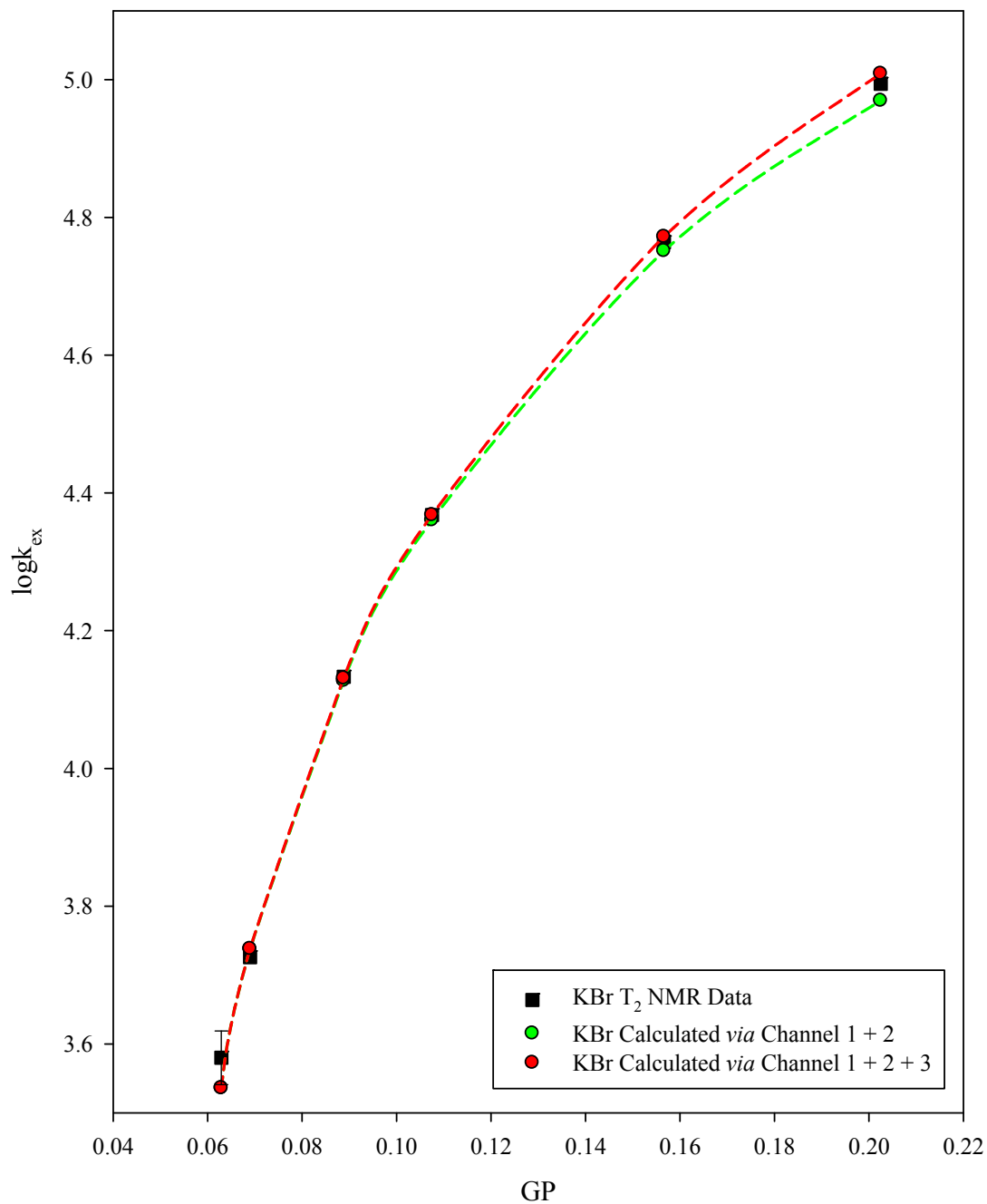


Figure 2.71 Experimental data and kinetic modeling results at 0.50 mM reactants with added KBr now using the hydrated Br⁻ radius of 4.08 Å. The T₂ NMR data (black squares) is compared with modeling results using Channels 1 + 2 (green circles) and Channels 1 + 2 + 3 (red circles).

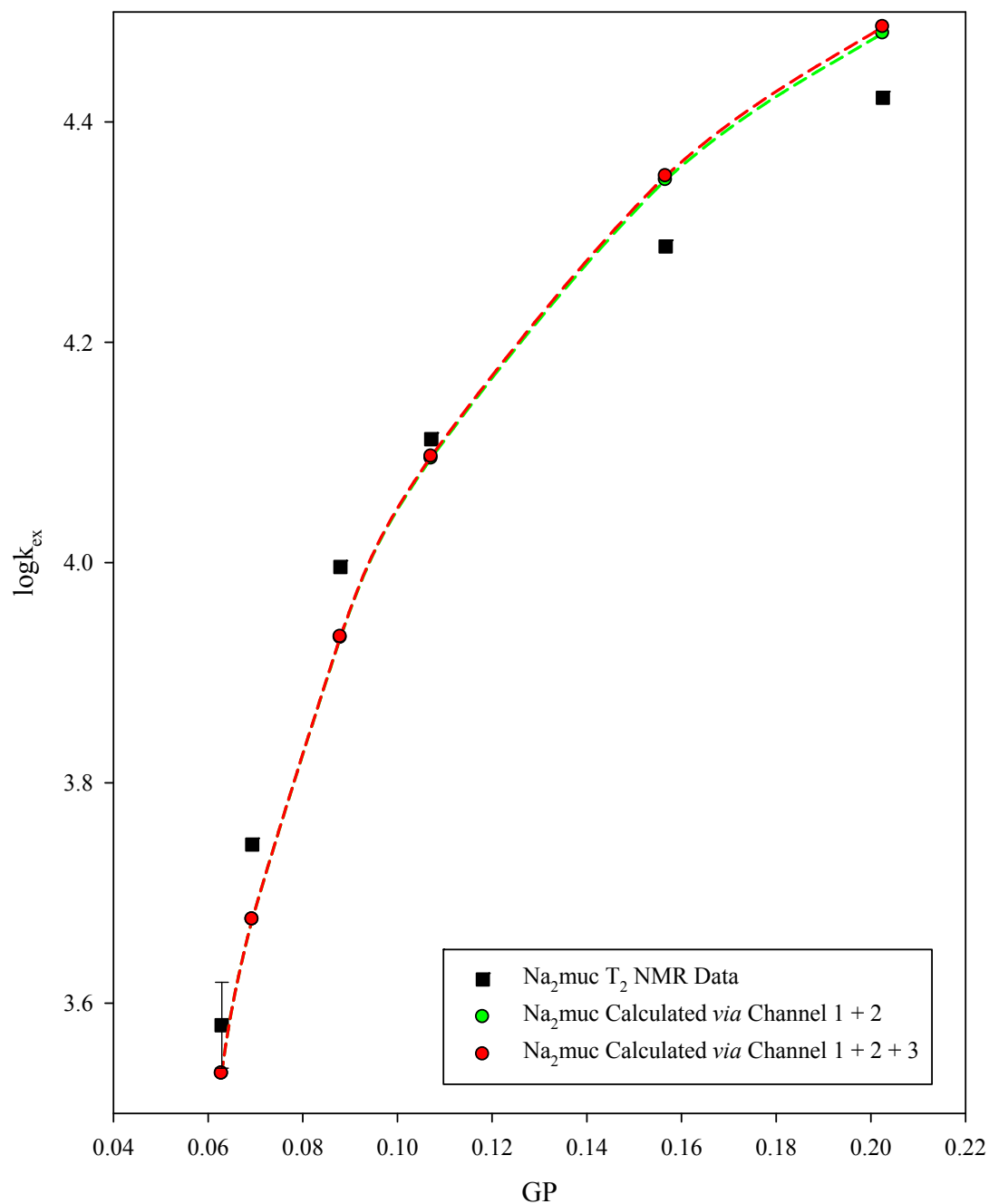


Figure 2.72 Experimental data and kinetic modeling results at 0.50 mM reactants with added Na_2muc using the crystallographic muc^{2-} radius of 3.86 Å. The T_2 NMR data (black squares) is compared with modeling results using Channels 1 + 2 (green circles) and Channels 1 + 2 + 3 (red circles).

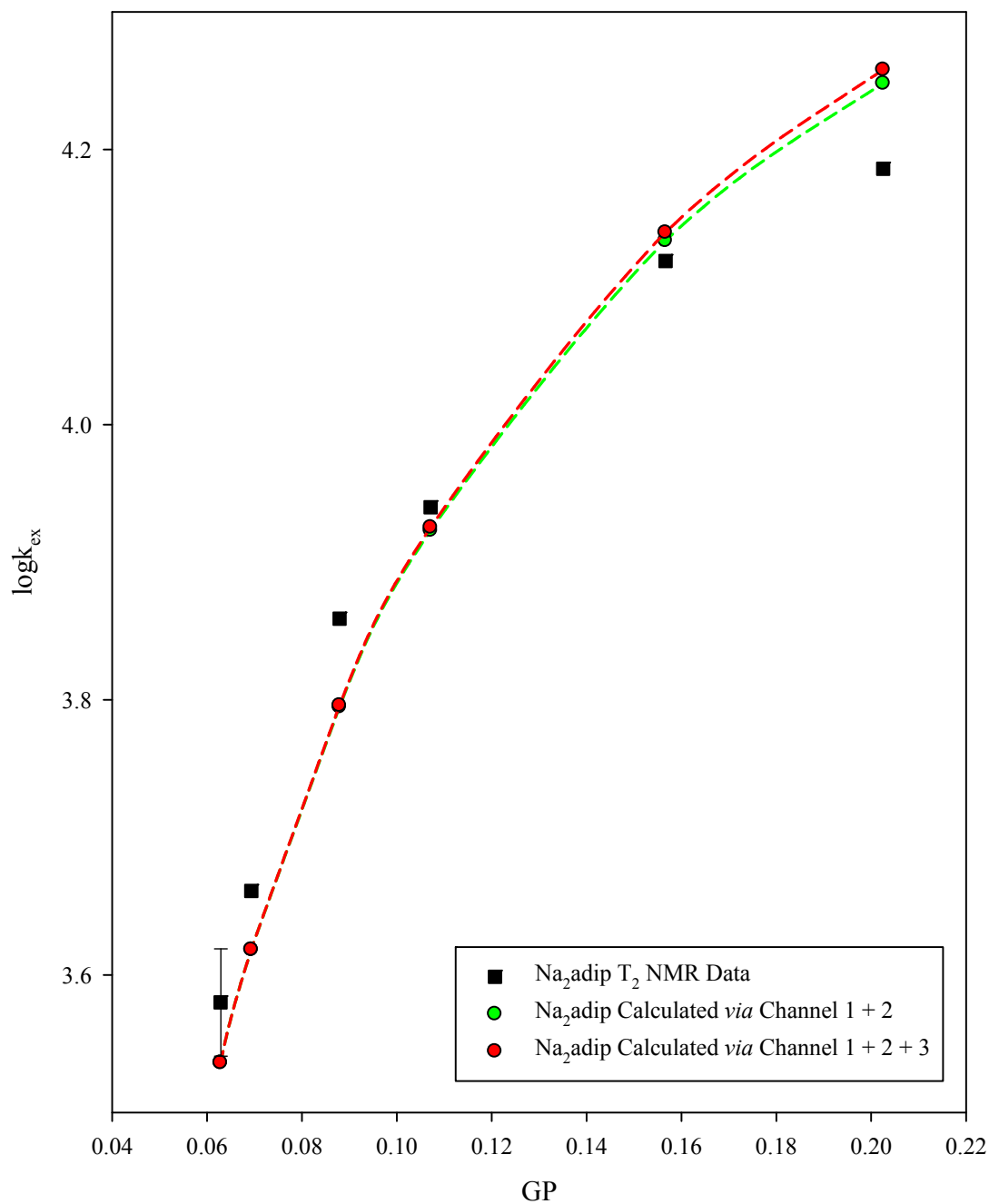


Figure 2.73 Experimental data and kinetic modeling results at 0.50 mM reactants with added Na₂adip using the crystallographic adip²⁻ radius of 3.97 Å. The T₂ NMR data (black squares) is compared with modeling results using Channels 1 + 2 (green circles) and Channels 1 + 2 + 3 (red circles).

Kinetic simulations of the data measured for reaction (2-2) at 0.50 mM reactants were again first conducted using the crystallographic radii of $r = 1.50 \text{ \AA}$, $r = 1.9 \text{ \AA}$, $r = 2.61 \text{ \AA}$ (see also Table 2.36) for F^- , Cl^- , and Br^- respectively. The $k_{\text{ETX}}/k_{\text{ET}}$ ratios found for F^- at 0.1 mM and 0.5 mM reactants were 0.95 and 0.03 respectively. This large drop in best-fit k_{ETX} upon going to the higher reactants concentration suggests that there may be some inadequacy in our model or violation of a basic assumption; possible explanations will be addressed later. A progressive increase in k_{ETX} is again found upon comparing the unhydrated chloride and bromide ion fits. Now the $k_{\text{ETX}}/k_{\text{ET}}$ ratios are 4.5 and 9.3, respectively. At 0.10 mM reactants the ratios were 5.3 for Cl^- and 8.7 for Br^- . So for these two halides, the 0.10 mM and 0.50 mM ratios are essentially within error of each other.

The model was next applied to reaction (2-2) using the hydrated radii for the F^- (3.89 Å), Cl^- (4.41 Å), and Br^- (4.08 Å) ions. A progressive increase is again found in the $k_{\text{ETX}}/k_{\text{ET}}$ ratios. For the hydrated F^- , Cl^- , and Br^- ions we obtain ratios of 0.1, 2.3, and 6.4 respectively. Compared to the corresponding ratios 0.10 mM ratios of 0.6 for F^- , 2.9 for Cl^- , and 5.0 for Br^- we again find agreement within error except for fluoride. When the ratios of $k_{\text{ETX}}/k_{\text{ET}}$ for the hydrated radii are compared to those for the crystallographic radii it is again found that the ratios are consistently lower when the fitting is done using the hydrated radii.

Applying our model to the rate effects from the dicarboxylate anions (muc^{2-} and adip^{2-}) value significantly different results are again obtained as compared to the halides. The best-fit $k_{\text{ETX}}/k_{\text{ET}}$ ratios found for the muc^{2-} and adip^{2-} anions are 0.5 and

0.2, respectively. While there is a slight drop as compared to the corresponding ratios at 0.10 mM reactants (0.7 for muc²⁻ and 0.5 for adip²⁻) the pattern persists and “uncatalysis” for the rate of ET through the Channel 2 intermediate PCX is again established.

2.17.4 Salt-specific kinetic modeling at [Ru^{II}] = [Ru^{III}] = 1.00 mM

Continuing our program to map and understand the kinetic salt effects the model was again applied to the data obtained at 1.00 mM reactants. The resulting best-fit k_{ET} , k_{ETX} , and k_{ETXX} values arrived at are listed in Table 2.44. The experimental and best-fit calculated rate constants obtained using equations (2-36) to (2-38) are listed in Table 2.45 and illustrated in Figures 2.74 to 2.80. As noted previously, in order to fit our experimental curves at these larger reactants concentrations, we split the difference between the implied starting $\log k_{ex}$ value (no added salt) calculated using equation (2-36) and our measured $\log k_{ex}$ value, which resulted in adding +0.053 log units to our calculated $\log k_{ex}$ values at 1.00 mM reactants ($3.708 - 3.602 = 0.106$, $0.106/2 = +0.053$ log units).

Table 2.44 Best-fit k_{ET} , k_{ETX} , and k_{ETXX} rate constants for reaction (2-2) corresponding to first-order ET inside the presumed PC, PCX, and PCXX reactive intermediates (based on iterative fitting of the $\log k_{ex}$ vs. added salt curves measured at $[Ru^{II}] = [Ru^{III}] = 1.00 \text{ mM}$ for the halide and dicarboxylate anions studied). These optimized values lead to the model-calculated rates listed in Table 2.45. The k_{ETX}/k_{ET} and k_{ETXX}/k_{ETX} ratios are listed in the final two columns.

Ion	$k_{ET}^{(a)}$	$k_{ETX}^{(b)}$	$k_{ETXX}^{(c)}$	$k_{ETX}/k_{ET}^{(d)}$	$k_{ETXX}/k_{ETX}^{(e)}$
F^- ($r = 1.50 \text{ \AA}$)	8.6×10^4	2.0×10^4	9.0×10^3	0.2	0.5
F^- ($r = 3.89 \text{ \AA}$)	8.6×10^4	1.2×10^4	9.5×10^3	0.1	0.8
Cl^- ($r = 1.90 \text{ \AA}$)	8.6×10^4	1.8×10^5	2.5×10^5	2.1	1.4
Cl^- ($r = 4.41 \text{ \AA}$)	8.6×10^4	1.0×10^5	7.3×10^4	1.2	0.7
Br^- ($r = 2.61 \text{ \AA}$)	8.6×10^4	5.7×10^5	3.0×10^5	6.6	0.5
Br^- ($r = 4.08 \text{ \AA}$)	8.6×10^4	3.8×10^5	1.7×10^5	4.4	0.5
muc^{2-} ($r = 3.86 \text{ \AA}$)	8.6×10^4	2.3×10^4	2.0×10^3	0.3	0.1

(a) Estimated uncertainty of $\pm 5\%$ (b) Estimated uncertainty of $\pm 7-11\%$, (b) estimated uncertainty of $\pm 30-35\%$, (c) estimated uncertainty of $\pm 9-11\%$, and (d) estimated uncertainty of $\pm 14\%$.

Table 2.45 Experimental and model-calculated rate constants at 5.00 mM reactants for reaction (2-2) as a function of GP arrived at using the three-channel model summarized in equations (2-36) through (2-38) and the best-fit rate constants listed in Table 2.44 (the relevant ionic radii are taken from Tables 2.36 and 2.37). The data and fitted curves are illustrated in Figures 2.74 to 2.80.

KF

r = 1.50 Å	GP	logk_{ex} (expt.)	logk_{ex} (calc.)	logk_{ex} (calc.)	logk_{ex} (calc.)
			Channel 1 Only	Channels 1 and 2	Channels 1, 2, and 3
	0.0866	3.708 ± 0.024	3.655	3.655	3.655
	0.1091	3.819	3.727	3.745	3.746
	0.1649	3.937	3.866	3.927	3.934
	0.2482	4.059	3.961	4.087	4.121
	0.3137	4.149	3.886	4.088	4.173

KF

r = 3.89 Å	GP	logk_{ex} (expt.)	logk_{ex} (calc.)	logk_{ex} (calc.)	logk_{ex} (calc.)
			Channel 1 Only	Channels 1 and 2	Channels 1, 2, and 3
	0.0866	3.708 ± 0.024	3.655	3.655	3.655
	0.1091	3.819	3.724	3.743	3.745
	0.1649	3.937	3.848	3.909	3.933
	0.2482	4.059	3.861	3.988	4.122
	0.3137	4.149	-	-	4.162

NaCl

r = 1.90 Å	GP	logk_{ex} (expt.)	logk_{ex} (calc.)	logk_{ex} (calc.)	logk_{ex} (calc.)
			Channel 1 Only	Channels 1 and 2	Channels 1, 2, and 3
	0.0866	3.708 ± 0.024	3.655	3.655	3.655
	0.1091	3.895	3.726	3.878	3.893
	0.1649	4.322	3.860	4.251	4.350
	0.2482	4.834	3.942	4.574	4.838

NaCl					
r = 4.41 Å	GP	logk_{ex} (expt.)	logk_{ex} (calc.) Channel 1 Only	logk_{ex} (calc.) Channels 1 and 2	logk_{ex} (calc.) Channels 1, 2, and 3
	0.0866	3.708 ± 0.024	3.655	3.655	3.655
	0.1091	3.895	3.723	3.883	3.898
	0.1649	4.322	3.841	4.241	4.352
	0.2482	4.834	-	4.455	4.829
KBr					
r = 2.61 Å	GP	logk_{ex} (expt.)	logk_{ex} (calc.) Channel 1 Only	logk_{ex} (calc.) Channels 1 and 2	logk_{ex} (calc.) Channels 1, 2, and 3
	0.0866	3.708 ± 0.024	3.655	3.655	3.655
	0.1091	4.124	3.726	4.116	4.128
	0.1649	4.739	3.859	4.640	4.705
	0.2482	5.192	3.925	5.021	5.192
KBr					
r = 4.08 Å	GP	logk_{ex} (expt.)	logk_{ex} (calc.) Channel 1 Only	logk_{ex} (calc.) Channels 1 and 2	logk_{ex} (calc.) Channels 1, 2, and 3
	0.0866	3.708 ± 0.024	3.655	3.655	3.655
	0.1091	4.124	3.724	4.119	4.135
	0.1649	4.739	3.846	4.629	4.717
	0.2482	5.192	3.847	4.939	5.201
Na₂muc					
r = 3.86 Å	GP	logk_{ex} (expt.)	logk_{ex} (calc.) Channel 1 Only	logk_{ex} (calc.) Channels 1 and 2	logk_{ex} (calc.) Channels 1, 2, and 3
	0.0866	3.708 ± 0.024	3.655	3.655	3.655
	0.0953	3.864	3.668	3.763	3.764
	0.1091	3.962	3.688	3.892	3.894
	0.1183	4.057	3.700	3.959	3.962
	0.1649	4.132	3.737	4.182	4.192
	0.2080	4.211	3.733	4.298	4.315

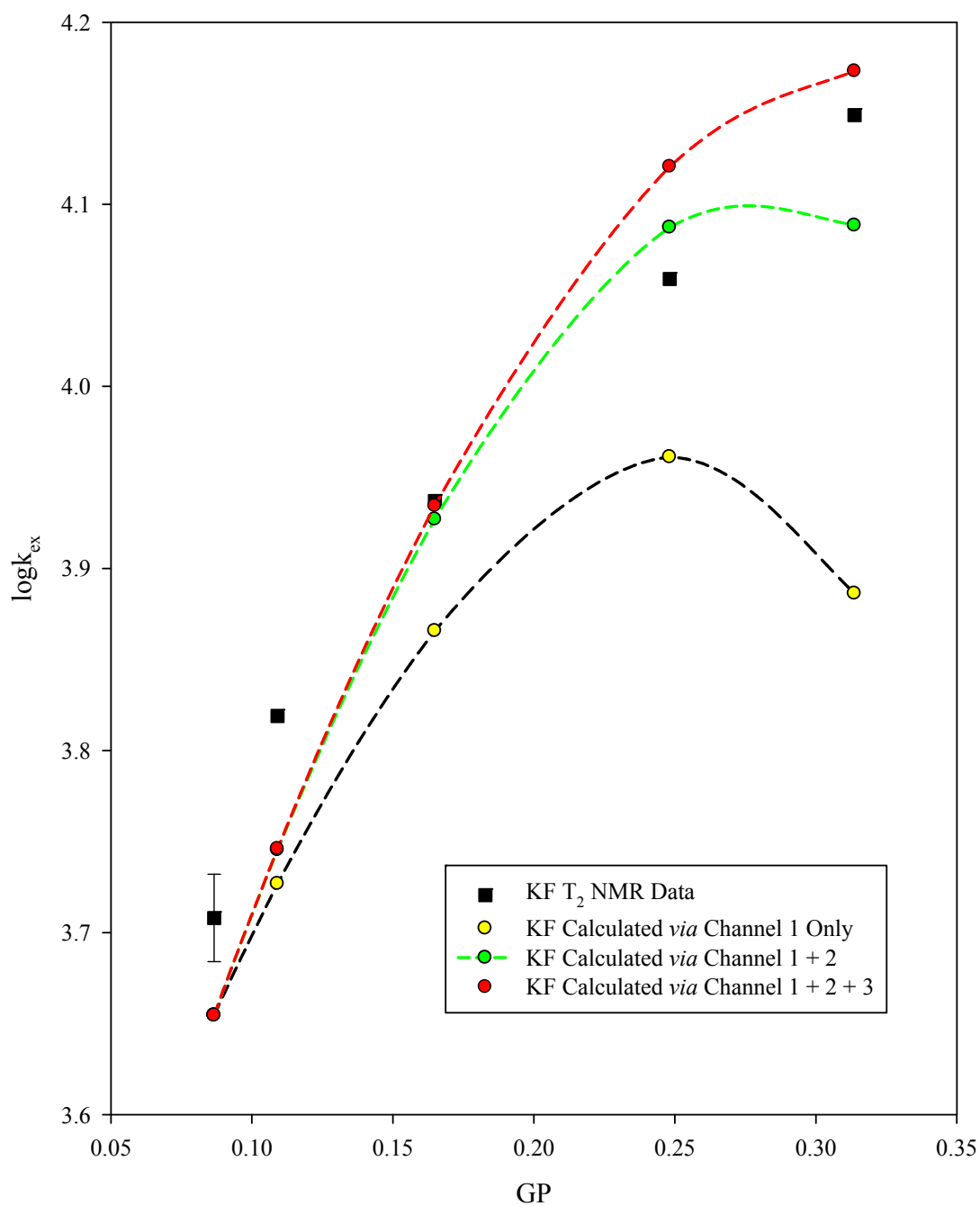


Figure 2.74 Experimental data and kinetic modeling results at 1.00 mM reactants with added KF using the crystallographic F^- radius of 1.50 Å. The T_2 NMR data (black squares) is compared with modeling results using Channel 1 (yellow circles), Channels 1 + 2 (green circles), and Channels 1 + 2 + 3 (red circles).

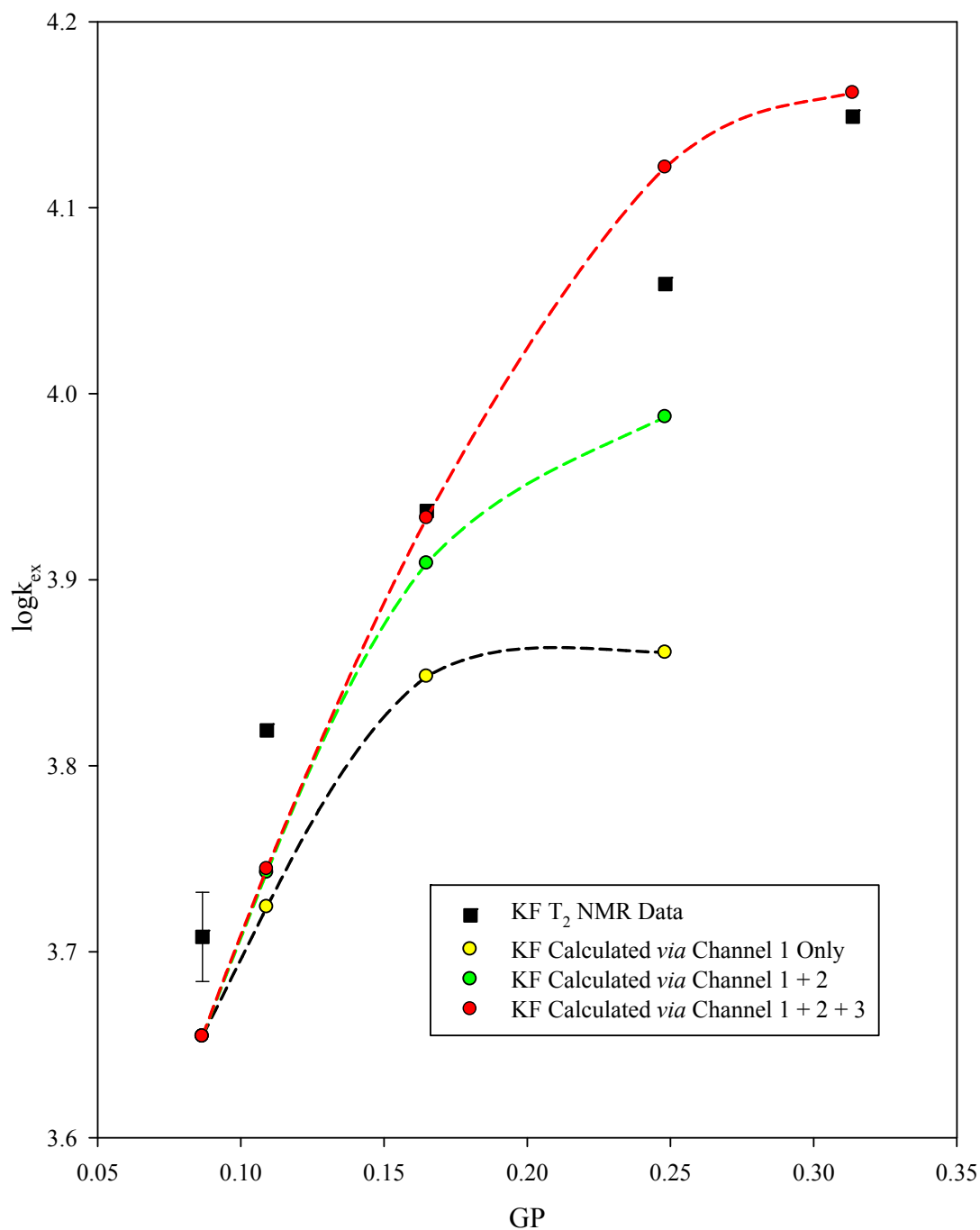


Figure 2.75 Experimental data and kinetic modeling results at 1.00 mM reactants with added KF now using the hydrated F⁻ radius of 3.89 Å. The T₂ NMR data (black squares) is compared with modeling results using Channel 1 (yellow circles), Channels 1 + 2 (green circles), and Channels 1 + 2 + 3 (red circles).

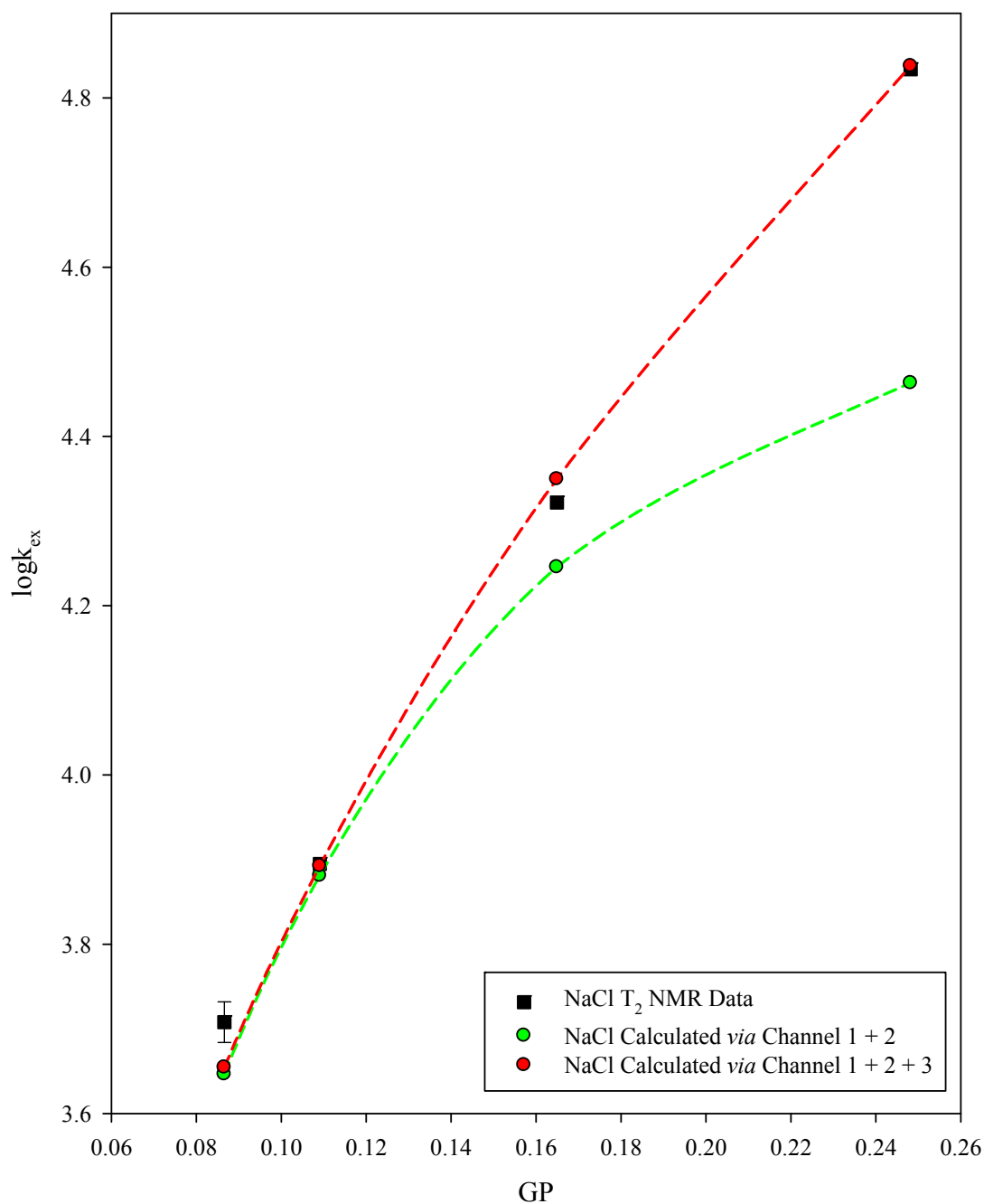


Figure 2.76 Experimental data and kinetic modeling results at 1.00 mM reactants with added NaCl using the crystallographic Cl⁻ radius of 1.90 Å. The T₂ NMR data (black squares) is compared with modeling results using Channels 1 + 2 (green circles) and Channels 1 + 2 + 3 (red circles).

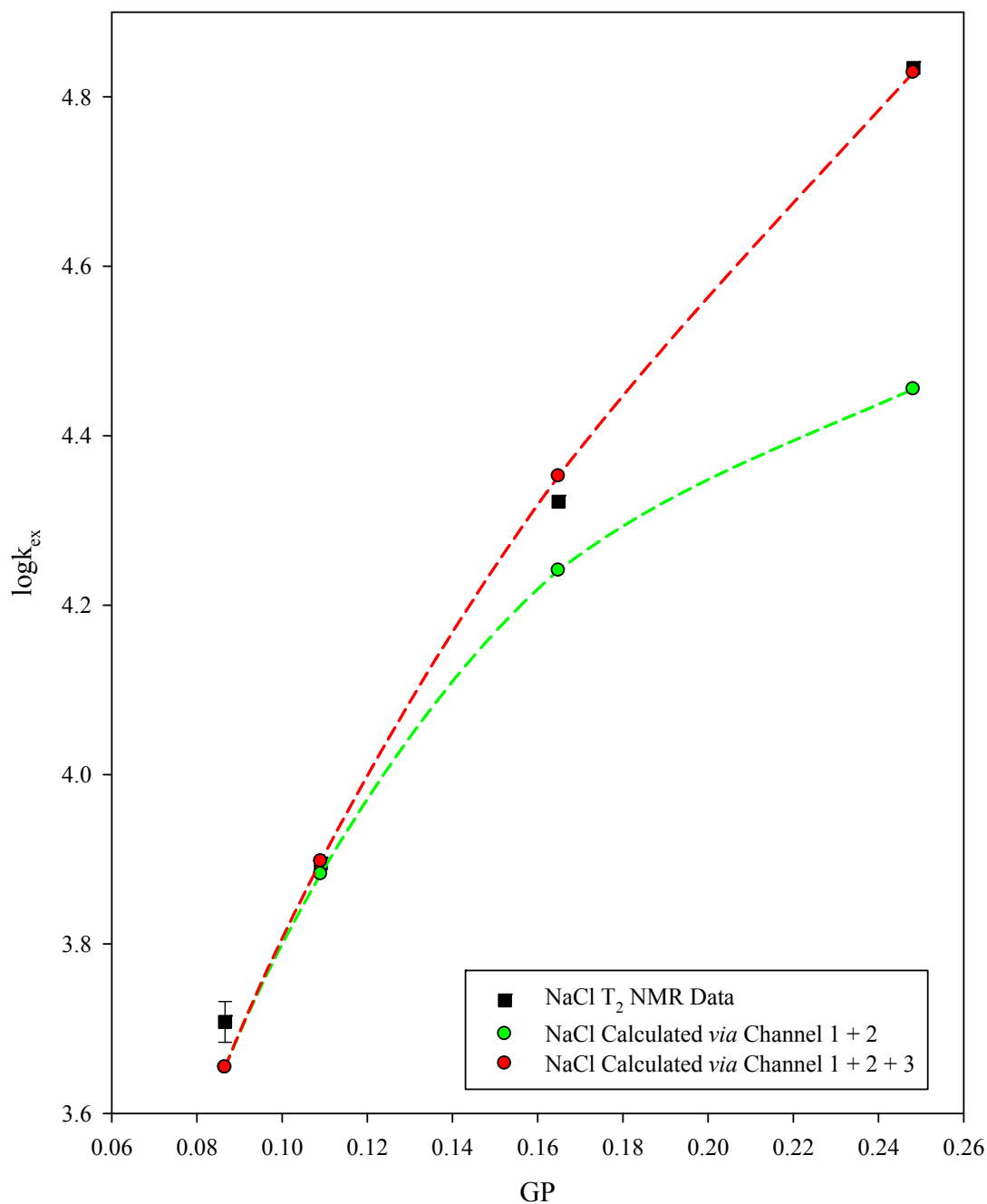


Figure 2.77 Experimental data and kinetic modeling results at 1.00 mM reactants with added NaCl now using the hydrated Cl^- radius of 4.41 Å. The T_2 NMR data (black squares) is compared with modeling results using Channels 1 + 2 (green circles) and Channels 1 + 2 + 3 (red circles).

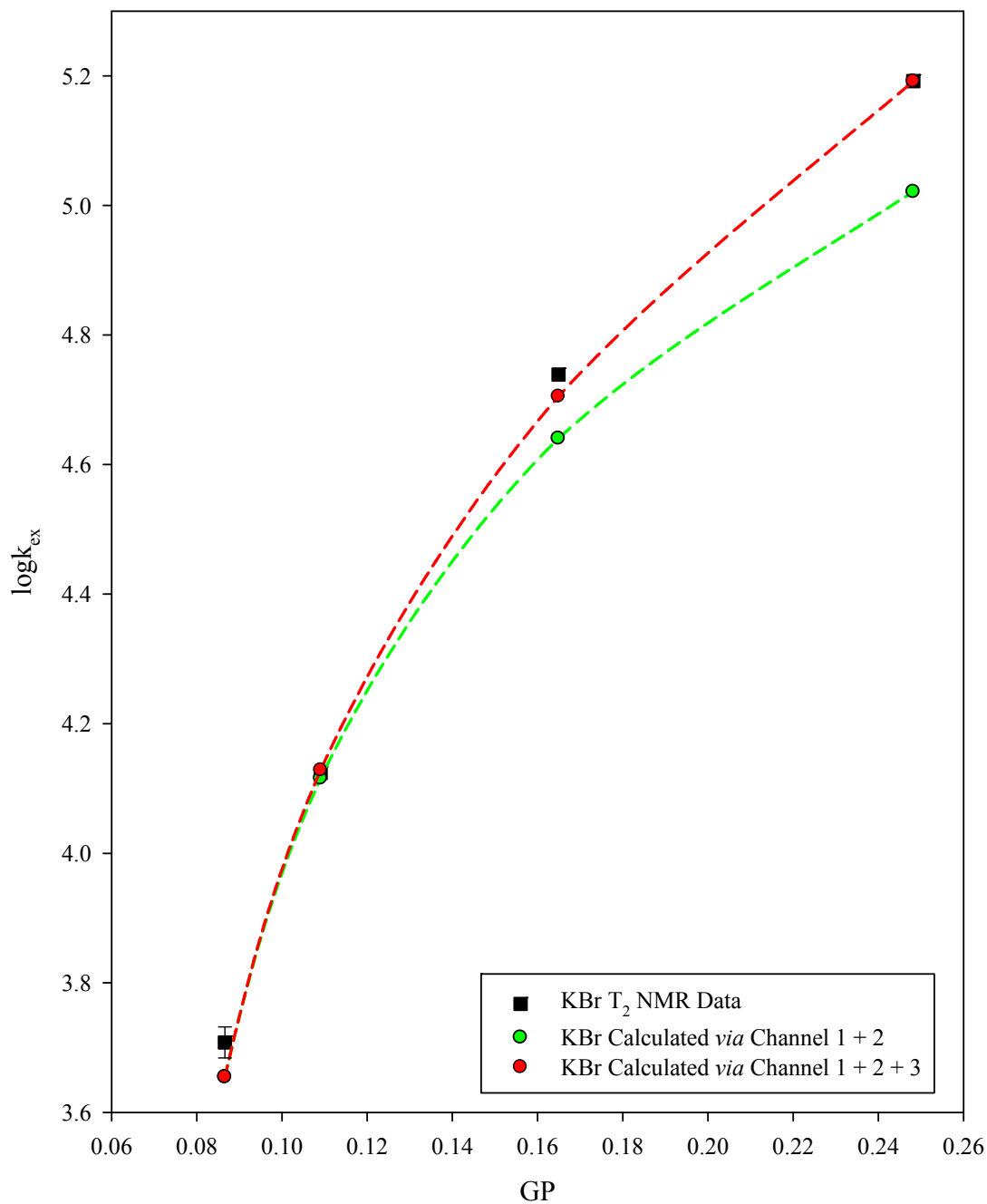


Figure 2.78 Experimental data and kinetic modeling results at 1.00 mM reactants with added KBr using the crystallographic Br^- radius of 2.61 Å. The T_2 NMR data (black squares) is compared with modeling results using Channels 1 + 2 (green circles) and Channels 1 + 2 + 3 (red circles).

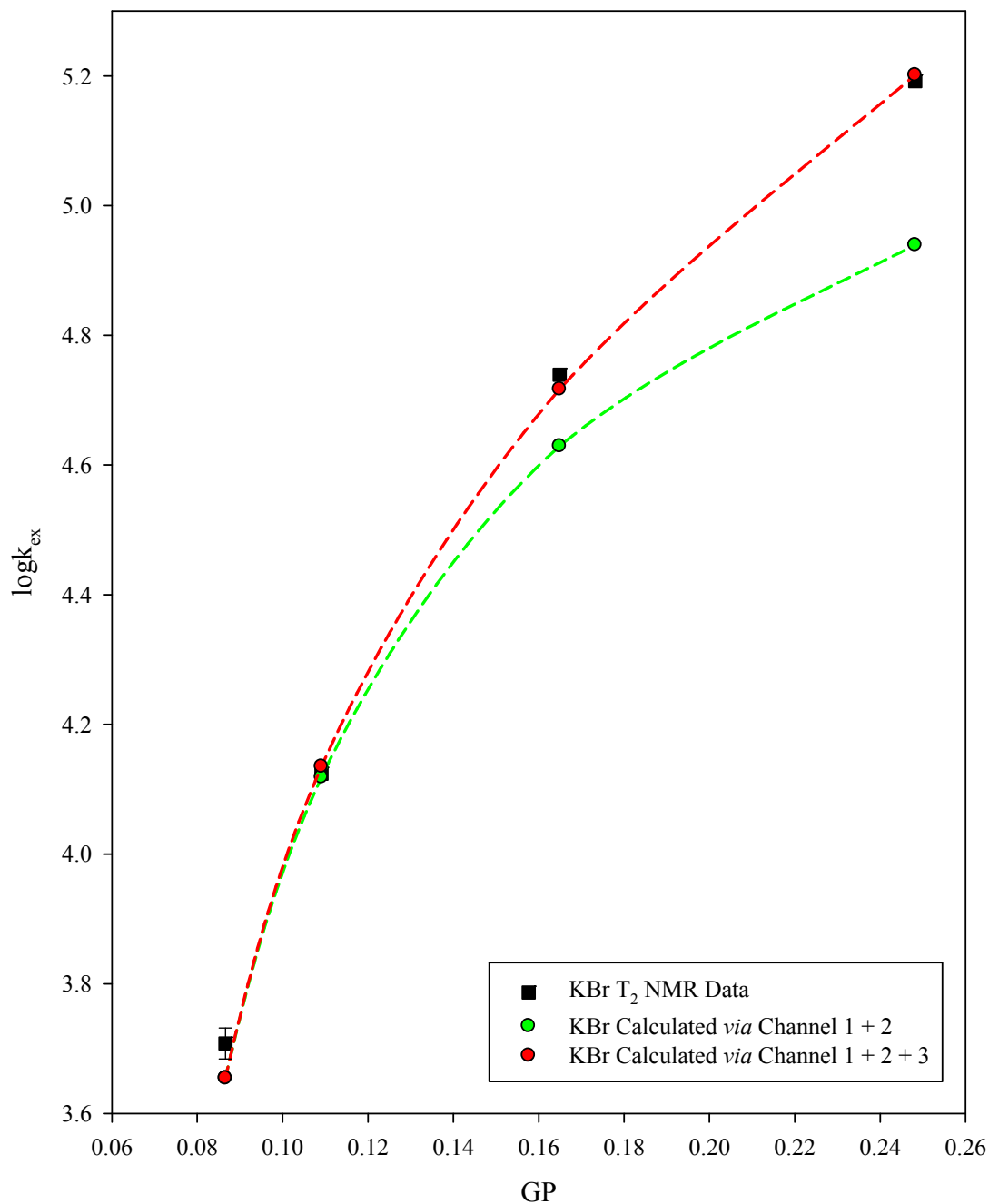


Figure 2.79 Experimental data and kinetic modeling results at 1.00 mM reactants with added KBr now using the hydrated Br^- radius of 4.08 Å. The T_2 NMR data (black squares) is compared with modeling results using Channels 1 + 2 (green circles) and Channels 1 + 2 + 3 (red circles).

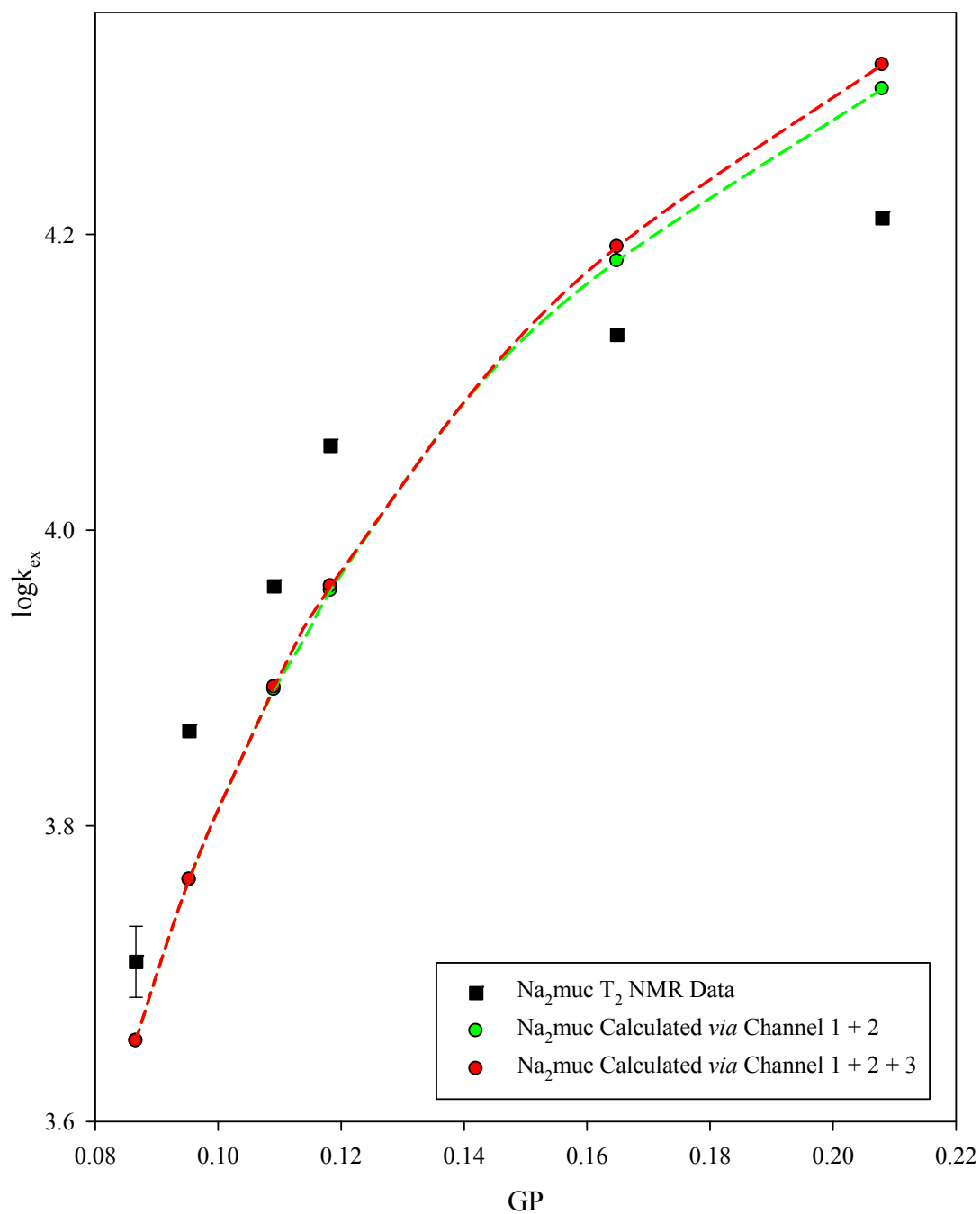


Figure 2.80 Experimental data and kinetic modeling results at 1.00 mM reactants with added Na₂muc using the crystallographic muc²⁻ radius of 3.86 Å. The T₂ NMR data (black squares) is compared with modeling results using Channels 1 + 2 (green circles) and Channels 1 + 2 + 3 (red circles).

The simulations for reaction (2-2) at 1.00 mM reactants were again first conducted using the crystallographic F⁻, Cl⁻, and Br⁻ radii. These $k_{\text{ETX}}/k_{\text{ET}}$ ratios were 0.2 for F⁻, 2.1 for Cl⁻, and 6.6 for Br⁻ (at 0.50 mM reactants the ratios were 0.03, 4.5, and 9.3). It is interesting to note that Channel 3 is now required in order to model the F⁻ data due to the significant fraction of reactive flux now carried by the PCXX intermediate. The apparent drop in k_{ETX} for both Cl⁻ and Br⁻ could be an indication that we are reaching the limits of the assumptions underlying of our model; this idea will be discussed in detail later on.

Upon using the hydrated radii for F⁻, Cl⁻, and Br⁻ the best-fit $k_{\text{ETX}}/k_{\text{ET}}$ values were 0.14, 1.2, and 4.42, respectively. So again we see a small decrease in k_{ETX} for the larger radii but the same progressive increase with halide ion identity.

Fitting the muc^{2-} data yielded $k_{\text{ETX}}/k_{\text{ET}} = 0.3$ which is only slightly lower than what was found at 0.10 mM and 0.50 mM reactants concentrations.

2.17.5 Salt-specific kinetic modelling at $[\text{Ru}^{\text{II}}] = [\text{Ru}^{\text{III}}] = 5.00 \text{ mM}$

Kinetic modeling of reaction (2-2) was concluded using the data collected at 5.00 mM reactants upon addition of both halide and dicarboxylate salts. The best-fit k_{ET} , k_{ETX} , and k_{ETXX} values arrived at are listed in Table 2.46. The experimental and best-fit calculated rate constants obtained using equations (2-36) to (2-38) are listed in Table 2.47 and illustrated in Figures 2.81 to 2.88. As was done previously at both 0.50 mM and 1.00 mM reactants, in order to fit our experimental $\log k_{\text{ex}}$ vs. GP plots at these larger reactants concentrations, we split the difference between the implied starting $\log k_{\text{ex}}$ value (no added salt) calculated using equation (2-33) and our

measured $\log k_{\text{ex}}$ value which resulted in adding +0.0475 log units to our calculated $\log k_{\text{ex}}$ values at 1.00 mM reactants ($4.04 - 3.94 = 0.095$, $0.095/2 = +0.0475$ log units).

Table 2.46 Best-fit k_{ET} , k_{ETX} , and k_{ETXX} rate constants for reaction (2-2) corresponding to first-order ET inside the presumed PC, PCX, and PCXX reactive intermediates (based on iterative fitting of the $\log k_{\text{ex}}$ vs. added salt curves measured at 5.00 mM reactants for the halide and dicarboxylate anions studied). These optimized values lead to the model-calculated rates listed in Table 2.47. The $k_{\text{ETX}}/k_{\text{ET}}$ and $k_{\text{ETXX}}/k_{\text{ETX}}$ ratios are listed in the final two columns.

Ion	$k_{\text{ET}}^{(a)}$	$k_{\text{ETX}}^{(b)}$	$k_{\text{ETXX}}^{(c)}$	$k_{\text{ETX}}/k_{\text{ET}}^{(d)}$	$k_{\text{ETXX}}/k_{\text{ETX}}^{(e)}$
F ⁻ ($r = 1.50 \text{ \AA}$)	8.6×10^4	1.0×10^4	6.0×10^3	0.1	0.6
F ⁻ ($r = 3.89 \text{ \AA}$)	8.6×10^4	1.0×10^4	7.0×10^3	0.1	0.7
Cl ⁻ ($r = 1.90 \text{ \AA}$)	8.6×10^4	1.8×10^5	1.6×10^5	2.1	0.9
Cl ⁻ ($r = 4.41 \text{ \AA}$)	8.6×10^4	1.0×10^5	5.3×10^4	1.2	0.5
Br ⁻ ($r = 2.61 \text{ \AA}$)	8.6×10^4	2.8×10^5	4.1×10^5	3.3	1.5
Br ⁻ ($r = 4.08 \text{ \AA}$)	8.6×10^4	1.9×10^5	1.7×10^5	2.2	0.9
muc ²⁻ ($r = 3.86 \text{ \AA}$)	8.6×10^4	9.0×10^3	1.4×10^4	0.1	1.5
adip ²⁻ ($r = 3.97 \text{ \AA}$)	8.6×10^4	9.0×10^3	7.7×10^3	0.1	0.9

(a) Estimated uncertainty of $\pm 7\%$, (b) Estimated uncertainty of $\pm 8\text{-}12\%$, (c) estimated uncertainty of $\pm 30\text{-}35\%$, (d) estimated uncertainty of $\pm 15\%$, and (e) estimated uncertainty of $\pm 18\%$

Table 2.47 Experimental and model-calculated rate constants at 5.00 mM reactants for reaction (2-2) as a function of GP arrived at using the three-channel model summarized in equations (2-36) through (2-38) and the best-fit rate constants listed in Table 2.47 (the relevant ionic radii are taken from Tables 2.36 and 2.37). The data and fitted curves are illustrated in Figures 2.81 to 2.88.

KF

r = 1.50 Å	GP	logk_{ex} (expt.)	logk_{ex} (calc.)	logk_{ex} (calc.)	logk_{ex} (calc.)
			Channel 1 Only	Channels 1 and 2	Channels 1, 2, and 3
	0.1750	4.039 ± 0.051	3.991	3.991	3.991
	0.2150	4.106	4.045	4.067	4.069
	0.2532	4.125	4.069	4.111	4.121
	0.3008	4.143	4.045	4.116	4.146
	0.4001	4.172	-	-	-

KF

r = 3.89 Å	GP	logk_{ex} (expt.)	logk_{ex} (calc.)	logk_{ex} (calc.)	logk_{ex} (calc.)
			Channel 1 Only	Channels 1 and 2	Channels 1, 2, and 3
	0.1750	4.039 ± 0.051	3.991	3.991	3.991
	0.2150	4.106	4.027	4.063	4.073
	0.2532	4.125	4.016	4.084	4.126
	0.3008	4.143	-	-	4.140
	0.4001	4.172	-	-	-

NaCl

r = 1.90 Å	GP	logk_{ex} (expt.)	logk_{ex} (calc.)	logk_{ex} (calc.)	logk_{ex} (calc.)
			Channel 1 Only	Channels 1 and 2	Channels 1, 2, and 3
	0.1750	4.039 ± 0.051	3.991	3.991	3.991
	0.2150	4.440	4.041	4.338	4.380
	0.2532	4.561	4.058	4.529	4.638
	0.3008	4.859	-	4.668	4.882

NaCl					
r = 4.41 Å	GP	logk_{ex} (expt.)	logk_{ex} (calc.) Channel 1 Only	logk_{ex} (calc.) Channels 1 and 2	logk_{ex} (calc.) Channels 1, 2, and 3
	0.1750	4.039 ± 0.051	3.991	3.991	3.991
	0.2150	4.440	4.041	4.330	4.387
	0.2532	4.561	4.058	4.475	4.639
	0.3008	4.859	-	4.454	4.863
KBr					
r = 2.61 Å	GP	logk_{ex} (expt.)	logk_{ex} (calc.) Channel 1 Only	logk_{ex} (calc.) Channels 1 and 2	logk_{ex} (calc.) Channels 1, 2, and 3
	0.1750	4.039 ± 0.051	3.991	3.991	3.991
	0.2150	4.605	4.038	4.467	4.565
	0.2532	4.837	4.049	4.689	4.914
	0.3008	5.233	-	4.835	5.237
KBr					
r = 4.08 Å	GP	logk_{ex} (expt.)	logk_{ex} (calc.) Channel 1 Only	logk_{ex} (calc.) Channels 1 and 2	logk_{ex} (calc.) Channels 1, 2, and 3
	0.1750	4.039 ± 0.051	3.991	3.991	3.991
	0.2150	4.605	4.025	4.505	4.556
	0.2532	4.837	4.009	4.655	4.903
	0.3008	5.233	-	4.703	5.212
Na₂muc					
r = 3.86 Å	GP	logk_{ex} (expt.)	logk_{ex} (calc.) Channel 1 Only	logk_{ex} (calc.) Channels 1 and 2	logk_{ex} (calc.) Channels 1, 2, and 3
	0.1750	4.039 ± 0.051	3.944	3.991	3.991
	0.2150	4.251	-	4.094	4.135
	0.2447	4.299	-	4.134	4.231
	0.3063	4.327	-	4.130	4.389

Na₂adip					
r = 3.97 Å	GP	logk_{ex} (expt.)	logk_{ex} (calc.)	logk_{ex} (calc.)	logk_{ex} (calc.)
			Channel	Channels	Channels
			1 Only	1 and 2	1, 2, and 3
	0.1750	4.039 ± 0.051	3.991	3.991	3.991
	0.2150	4.161	-	4.094	4.117
	0.2447	4.209	-	4.136	4.192
	0.3063	4.253	-	4.133	4.296
	0.3974	4.305	-		4.304

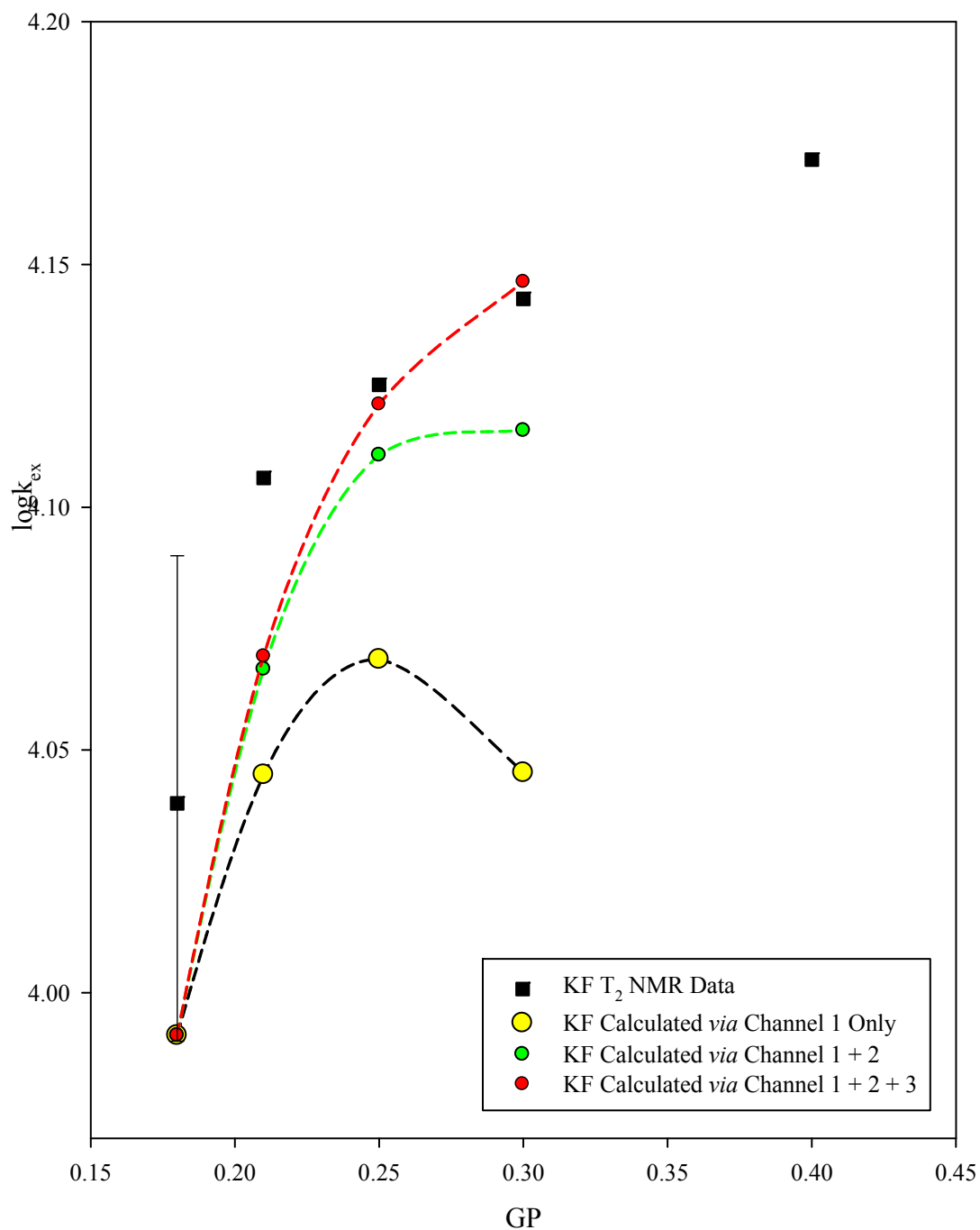


Figure 2.81 Experimental data and kinetic modeling results at 5.00 mM reactants with added KF using the crystallographic F⁻ radius 1.50 Å. The T₂ NMR data (black squares) is compared with modeling results using Channel 1 (yellow circles), Channels 1 + 2 (green circles), and Channels 1 + 2 + 3.

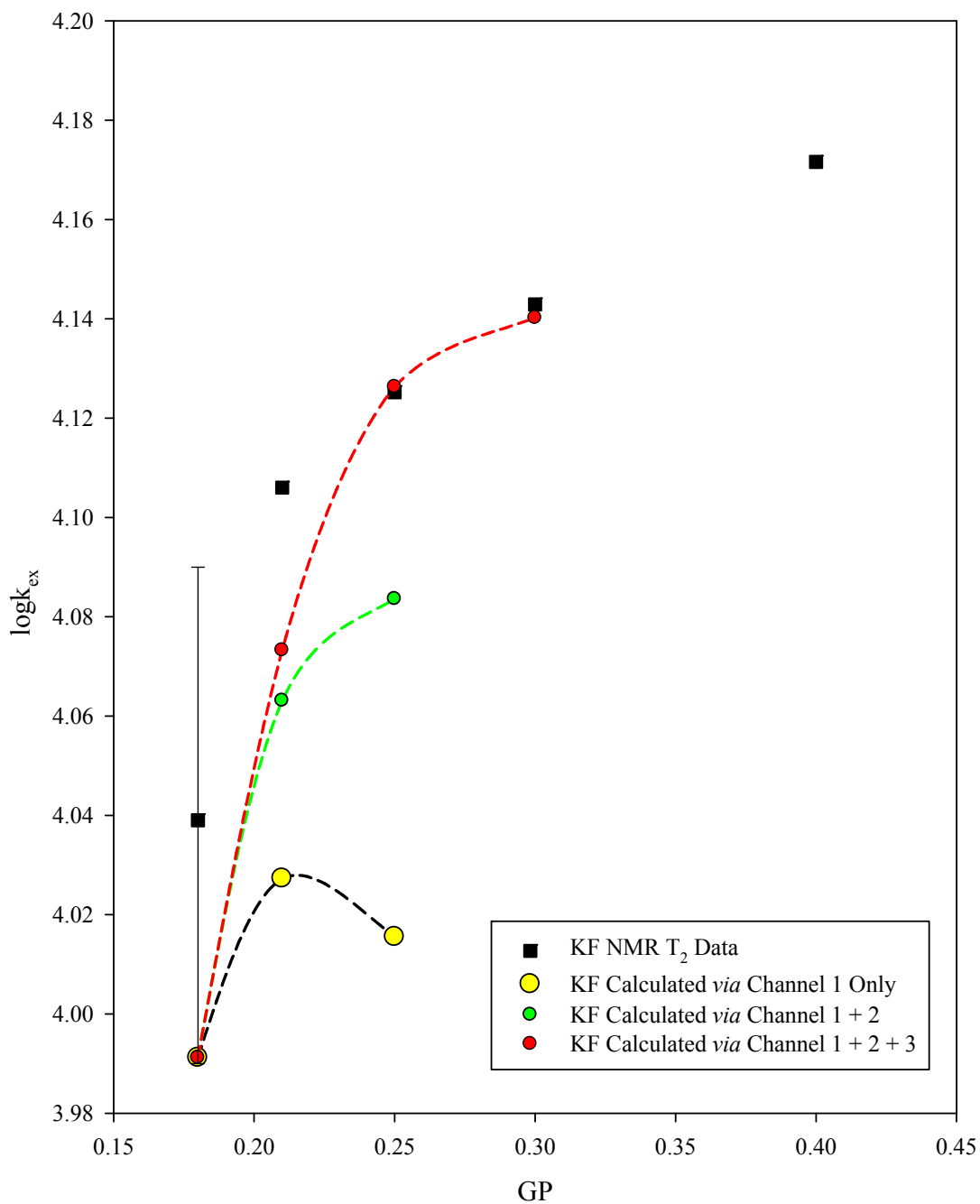


Figure 2.82 Experimental data and kinetic modeling results at 5.00 mM reactants with added KF now using the hydrated F^- radius of 3.89 Å. The T_2 NMR data (black squares) is compared with modeling results using Channel 1 (yellow circles), Channels 1 + 2 (green circles), and Channels 1 + 2 + 3.

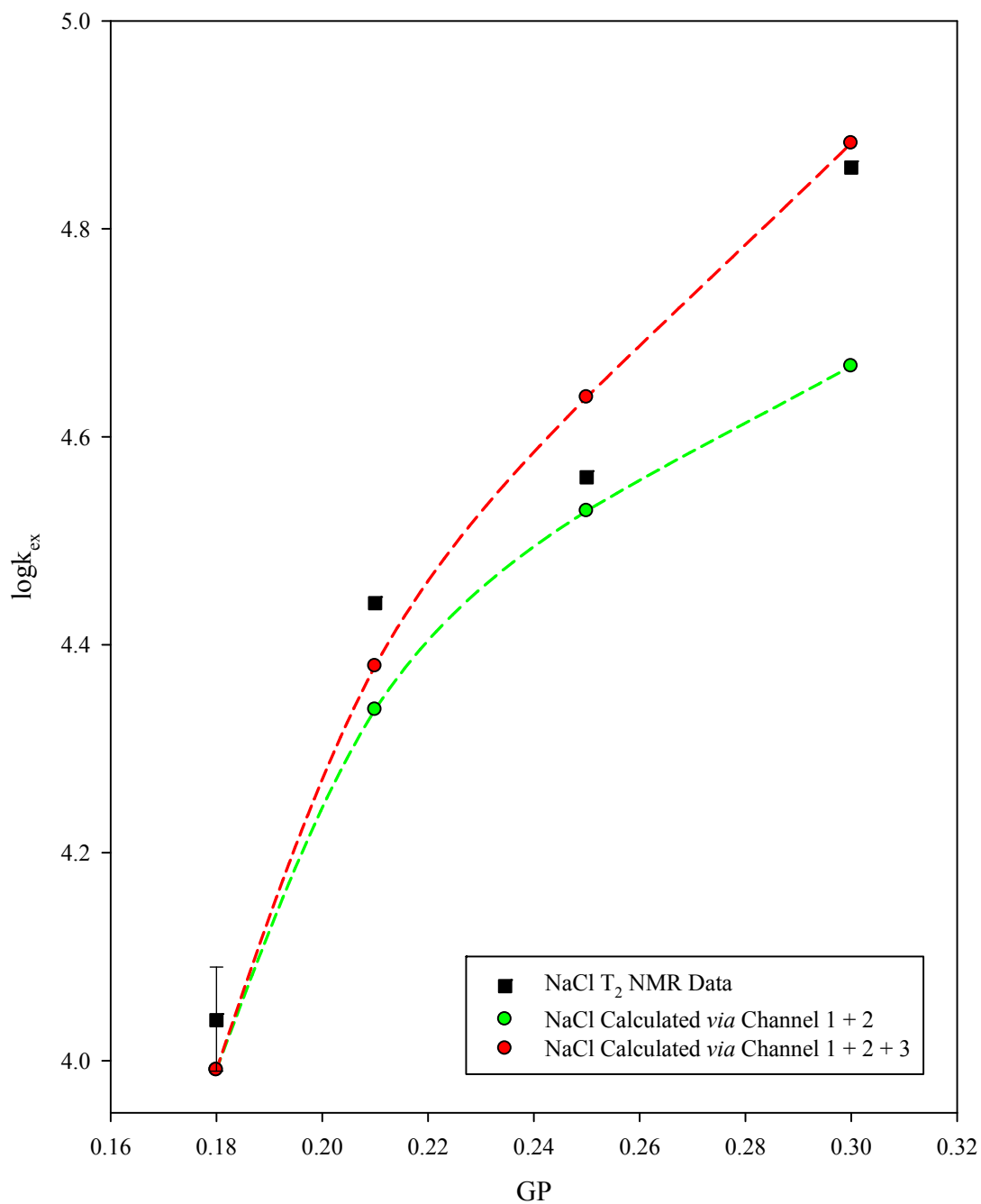


Figure 2.83 Experimental data and kinetic modeling results at 5.00 mM reactants with added NaCl using the crystallographic Cl^- radius of 1.90 Å. The T_2 NMR data (black squares) is compared with modeling results using Channels 1 + 2 (green circles) and Channels 1 + 2 + 3 (red circles).

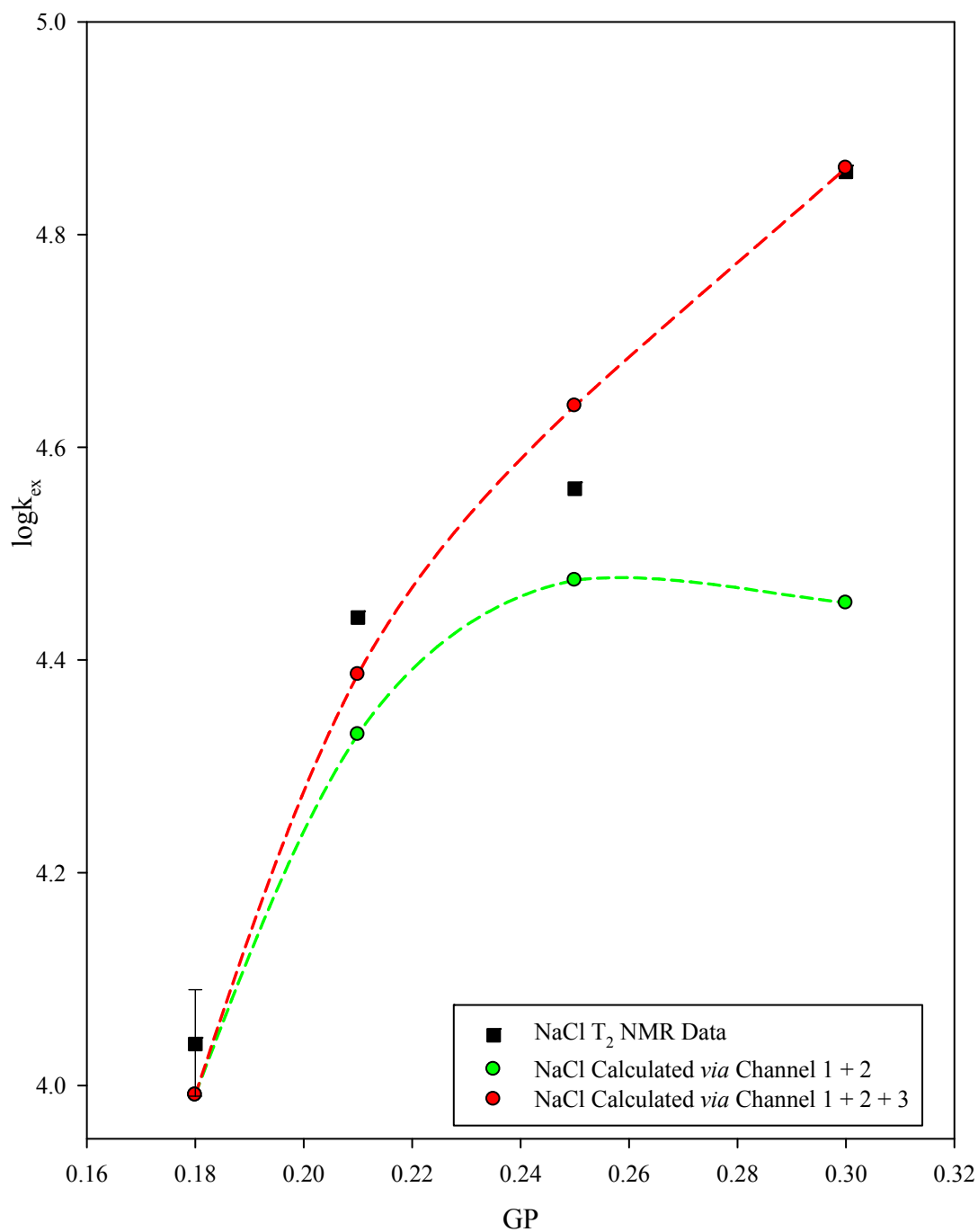


Figure 2.84 Experimental data and kinetic modeling results at 5.00 mM reactants with added NaCl now using the hydrated Cl^- radius of 4.41 Å. The T_2 NMR data (black squares) is compared with modeling results using Channels 1 + 2 (green circles) and Channels 1 + 2 + 3 (red circles).

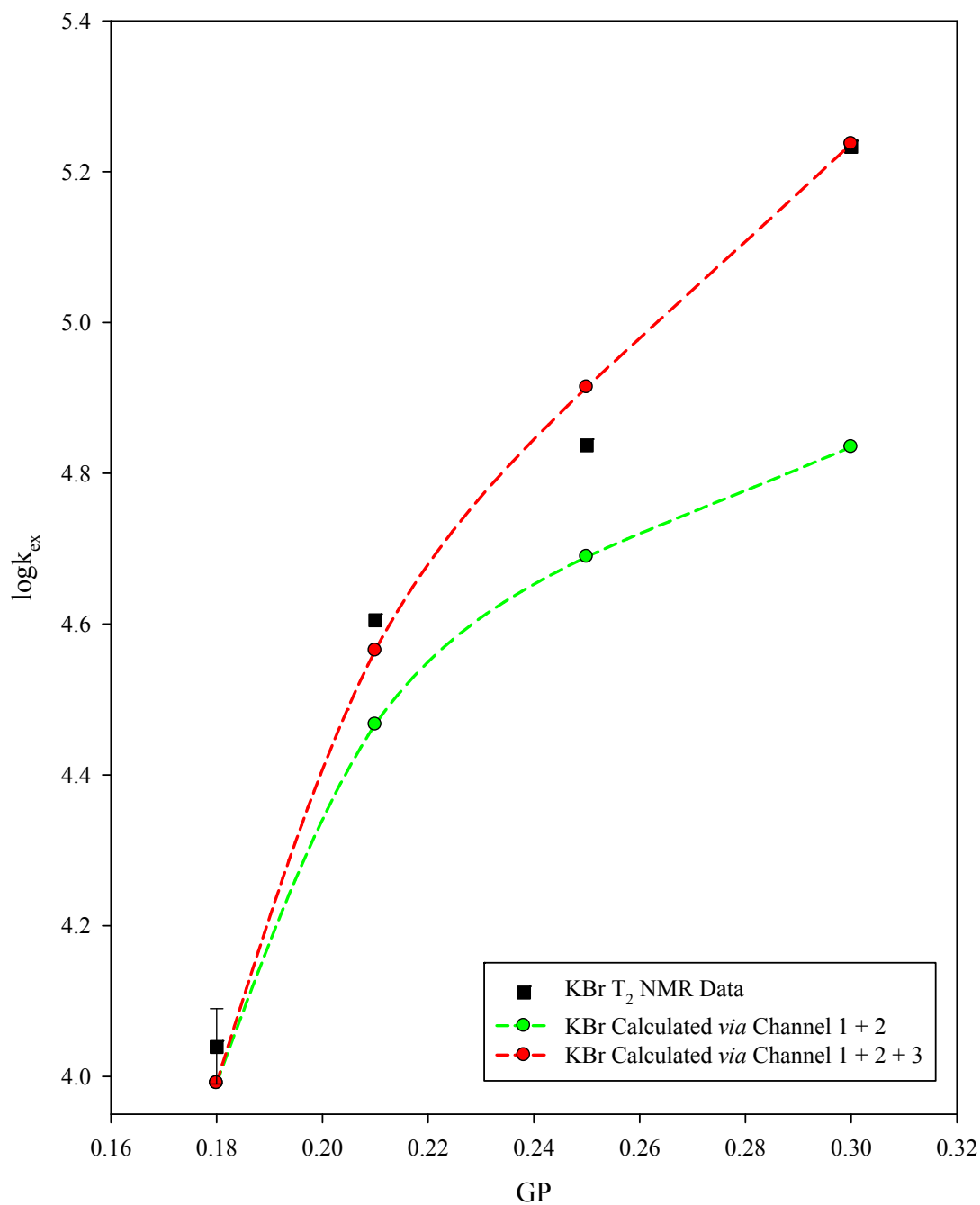


Figure 2.85 Experimental data and kinetic modeling results at 5.00 mM reactants with added KBr using the crystallographic Br⁻ radius of 2.61 Å. The T₂ NMR data (black squares) is compared with modeling results using Channels 1 + 2 (green circles) and Channels 1 + 2 + 3 (red circles).

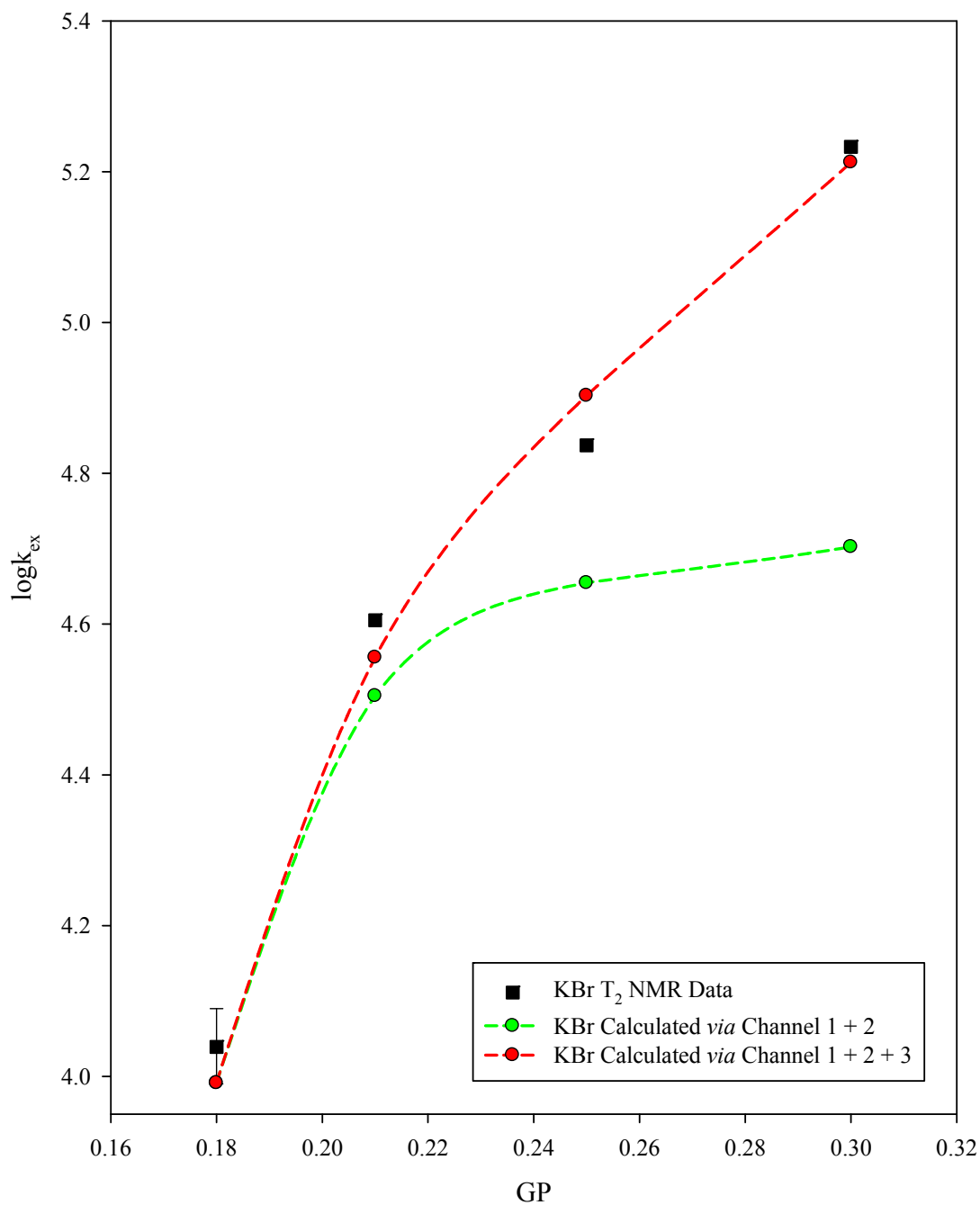


Figure 2.86 Experimental data and kinetic modeling results at 5.00 mM reactants with added KBr now using the hydrated Br^- radius of 4.08 Å. The T_2 NMR data (black squares) is compared with modeling results using Channels 1 + 2 (green circles) and Channels 1 + 2 + 3 (red circles).

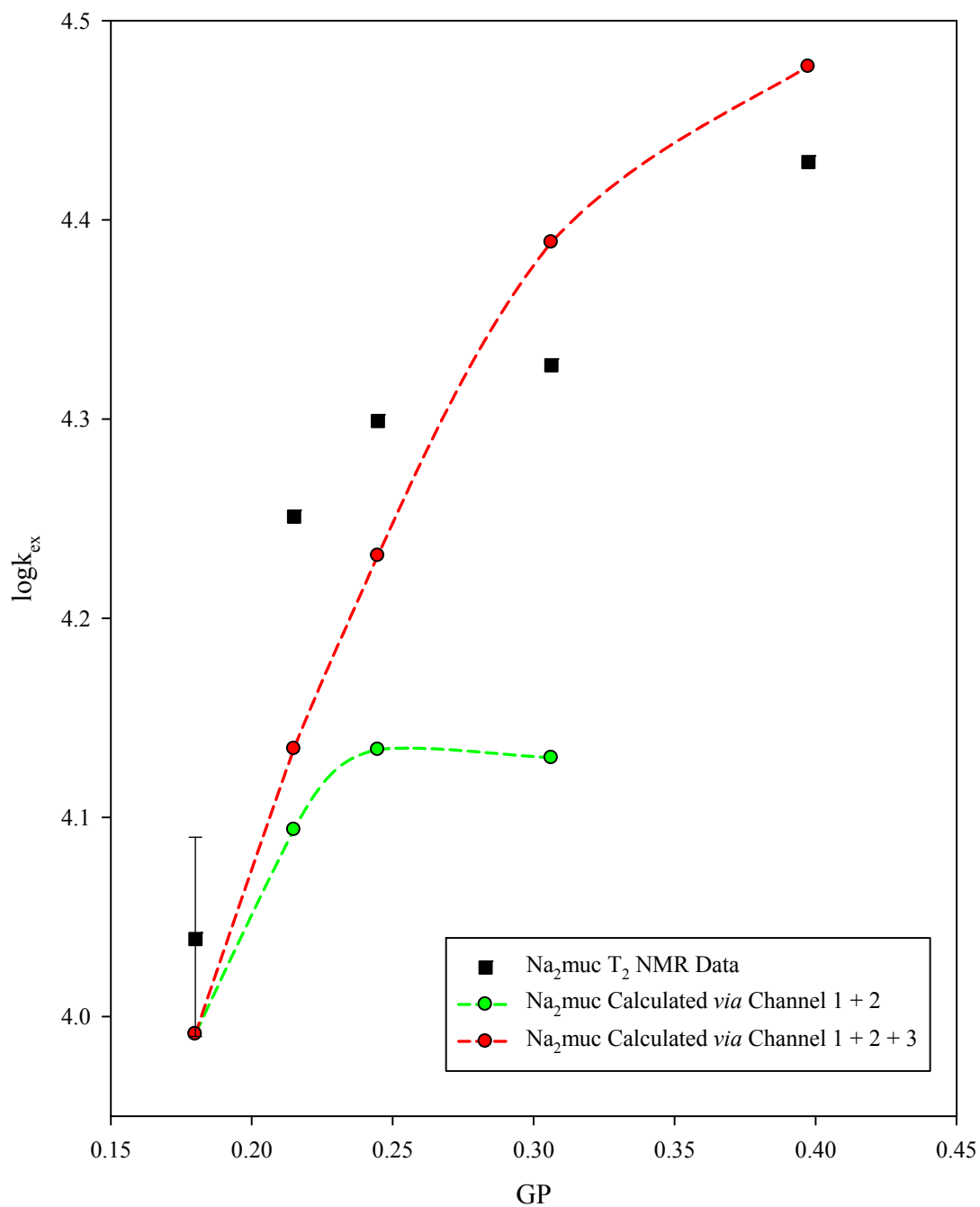


Figure 2.87 Experimental data and kinetic modeling results at 5.00 mM reactants with added Na₂muc using the crystallographic muc²⁻ radius of 3.86 Å. The T₂ NMR data (black squares) is compared with modeling results using Channels 1 + 2 (green circles) and Channels 1 + 2 + 3 (red circles).

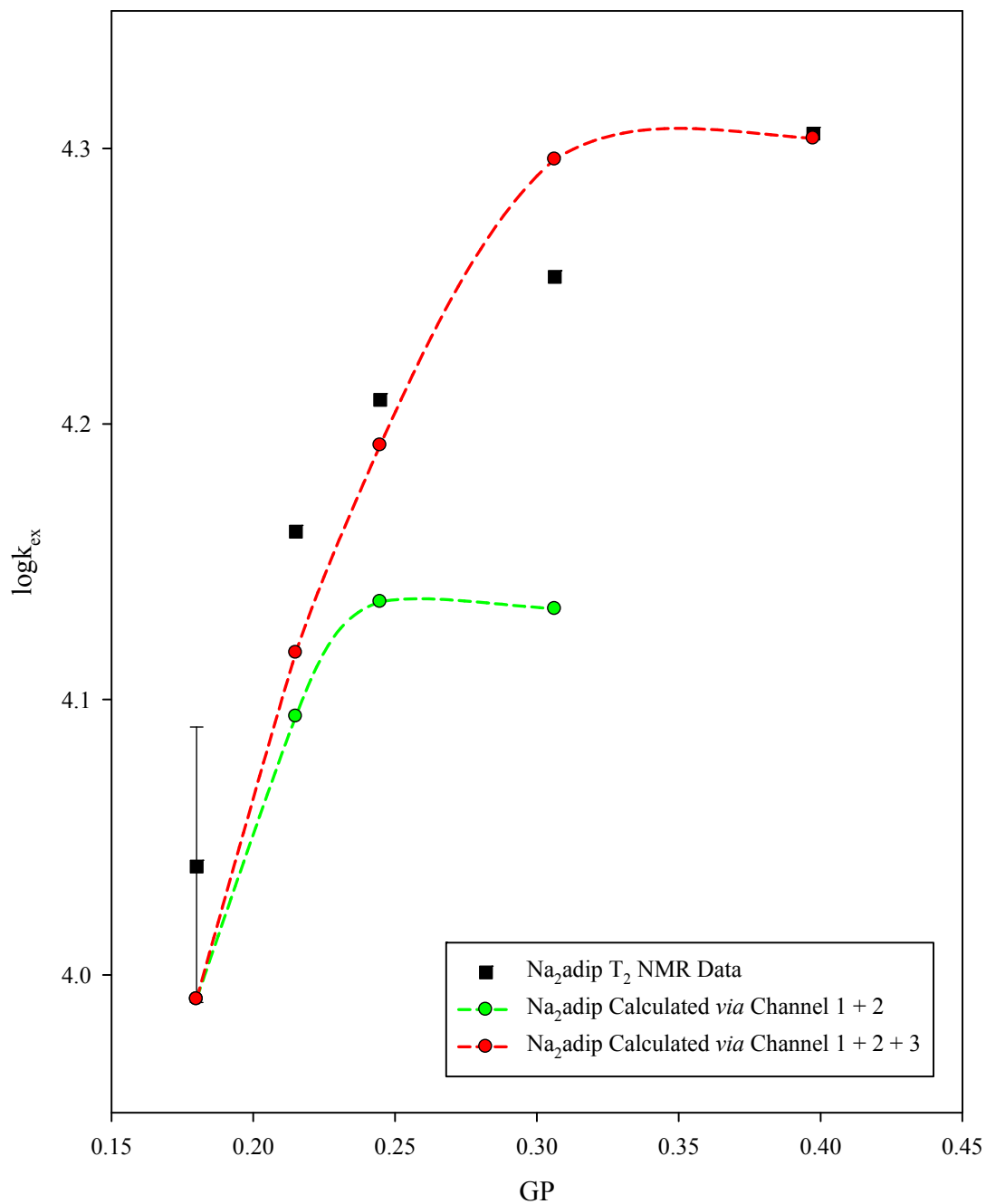


Figure 2.88 Experimental data and kinetic modeling results at 5.00 mM reactants with added Na₂adip using the crystallographic adip²⁻ radius of 3.97 Å. The T₂ NMR data (black squares) is compared with modeling results using Channels 1 + 2 (green circles) and Channels 1 + 2 + 3 (red circles).

Modeling of the 5.00 mM reactants data using the crystallographic halide radii again yield a progressive increase in $k_{\text{ETX}}/k_{\text{ET}}$ with best-fit values of 0.04, 2.3, and 4.7 for F^- , Cl^- , and Br^- , respectively. These results confirm what was previously found by Qin using a channel model to fit experimental kinetic data for reaction (2-2) as well and the previous ratios of $k_{\text{ETX}}/k_{\text{ET}}$ were 0.08 for F^- , 2.0 for Cl^- , and 3.6 for Br^- .⁸ When fitting the F^- data however, only the first few points could be fit due to constraints of our model resulting in our model predicting lower rates at larger added salt concentrations than those predicted at smaller added salt concentrations.

Using the hydrated radii for F^- , Cl^- , and Br^- ions at 5.00 mM reactants, F^- now gave an unchanged $k_{\text{ETX}}/k_{\text{ET}}$ value of 0.04 and we again obtained somewhat lower $k_{\text{ETX}}/k_{\text{ET}}$ ratios for Cl^- at 1.6, and for Br^- at 2.4. Although the ratio of $k_{\text{ETX}}/k_{\text{ET}}$ for the F^- ion is equivalent for both the crystallographic and hydrated radii, a limit was reached for the maximum value of k_{ETX} in order to fit our experimental data.

Our modeling of the kinetic for data fmuc^{2-} and adip^{2-} led us to ratios of $k_{\text{ETX}}/k_{\text{ET}}$ equal to 0.1 for both muc^{2-} and adip^{2-} . This appears to reflect a limit which has been reached for the minimum value of k_{ETX} which can be used in order to fit our experimental data. This is due to a limitation of our model as well as equations (1-41) to (1-44) as will be discussed further on.

2.17.6 Kinetic modeling of added hexacyano's at $[\text{Ru}^{\text{II}}] = [\text{Ru}^{\text{III}}] = 0.10 \text{ mM}$

Kinetic simulations were continued in order to capture and assess the much more extreme ET catalysis of reaction (2-2) at 0.10 mM reactants which was observed upon adding the hexacyano salts: $\text{K}_4\text{Fe}(\text{CN})_6$, $\text{K}_4\text{Ru}(\text{CN})_6$, and $\text{K}_4\text{Os}(\text{CN})_6$. The best-fit k_{ET} , k_{ETX} , and k_{ETXX} values arrived at are listed in Table 2.48. The experimental and best-fit calculated rate constants obtained using equations (2-36) to (2-38) are listed in Table 2.49 and the best-fit curves are illustrated in Figures 2.89 to 2.92.

Table 2.48 Best-fit k_{ET} , k_{ETX} , and k_{ETXX} rate constants for reaction (2-2) corresponding to first-order ET inside the presumed PC, PCX, and PCXX reactive intermediates (based on iterative fitting of the $\log k_{\text{ex}}$ vs. added salt curves measured at $[\text{Ru}^{\text{II}}] = [\text{Ru}^{\text{III}}] = 0.10 \text{ mM}$ for the various hexacyano salts studied). These optimized values lead to the model-calculated rates listed in Table 2.49. The $k_{\text{ETX}}/k_{\text{ET}}$ and $k_{\text{ETXX}}/k_{\text{ETX}}$ ratios are listed in the final two columns.

Ion	$k_{\text{ET}}^{(a)}$	$k_{\text{ETX}}^{(b)}$	$k_{\text{ETXX}}^{(c)}$	$k_{\text{ETX}}/k_{\text{ET}}^{(d)}$	$k_{\text{ETXX}}/k_{\text{ETX}}^{(e)}$
$\text{Fe}(\text{CN})_6^{4-}$ ($r = 4.24 \text{ \AA}$)	8.6×10^4	5.0×10^5	9.0×10^6	5.8	18.0
$\text{Os}(\text{CN})_6^{4-}$ ($r = 4.35 \text{ \AA}$)	8.6×10^4	9.0×10^4	4.3×10^{10}	5.8	4.8×10^5
$\text{Ru}(\text{CN})_6^{4-}$ ($r = 4.38 \text{ \AA}$)	8.6×10^4	5.0×10^4	1.2×10^8	0.6	2400

(a) Estimated uncertainty of $\pm 7\%$, (b) Estimated uncertainty of $\pm 5\text{-}10\%$, (c) estimated uncertainty of $\pm 30\%$, (d) estimated uncertainty of $\pm 8\text{-}12\%$, and (e) estimated uncertainty of $\pm 33\%$.

Table 2.49 Experimental and model-calculated rate constants at 0.10 mM reactants for reaction (2-2) as a function of GP arrived at using the three-channel model summarized in equations (2-36) through (2-38) and best-fit rate constants listed in Table 2.49 (the relevant ionic radii are taken from Tables 2.36 and 2.37). The data and fitted curves are illustrated in Figures 2.89 to 2.91.

K₄Fe(CN)₆

r =4.24 Å	GP	logk_{ex} (expt.)	logk_{ex} (calc.) Channel 1 Only	logk_{ex} (calc.) Channels 1 and 2	logk_{ex} (calc.) Channels 1, 2, and 3
	0.0291262	3.318 ± 0.051	3.318	3.318	3.318
	0.0291268	3.439	3.318	3.368	3.368
	0.0291287	3.547	3.318	3.492	3.492
	0.0291363	3.485	3.318	3.791	3.791
	0.0292516	4.705	3.314	4.725	4.725

K₄Os(CN)₆

r =4.35 Å	GP	logk_{ex} (expt.)	logk_{ex} (calc.) Channel 1 Only	logk_{ex} (calc.) Channels 1 and 2	logk_{ex} (calc.) Channels 1, 2, and 3
	0.0291262	3.318 ± 0.051	3.318	3.318	3.318
	0.0291419	3.399	3.318	3.498	3.534
	0.0291890	3.770	3.316	3.802	4.028
	0.0292516	4.443	3.314	4.025	4.444
	0.0293764	5.010	3.311	4.280	4.943
	0.0296243	5.467	3.303	4.553	5.488

K₄Ru(CN)₆

r =4.38 Å	GP	logk_{ex} (expt.)	logk_{ex} (calc.) Channel 1 Only	logk_{ex} (calc.) Channels 1 and 2	logk_{ex} (calc.) Channels 1, 2, and 3
	0.0291262	3.318 ± 0.051	3.318	3.318	3.318
	0.0291890	3.475	3.316	3.643	3.659
	0.0293764	4.178	3.311	4.053	4.140
	0.0296243	4.463	3.303	4.310	4.481
	0.0301134	4.947	3.288	4.582	4.886
	0.0310664	5.340	3.257	4.859	5.346

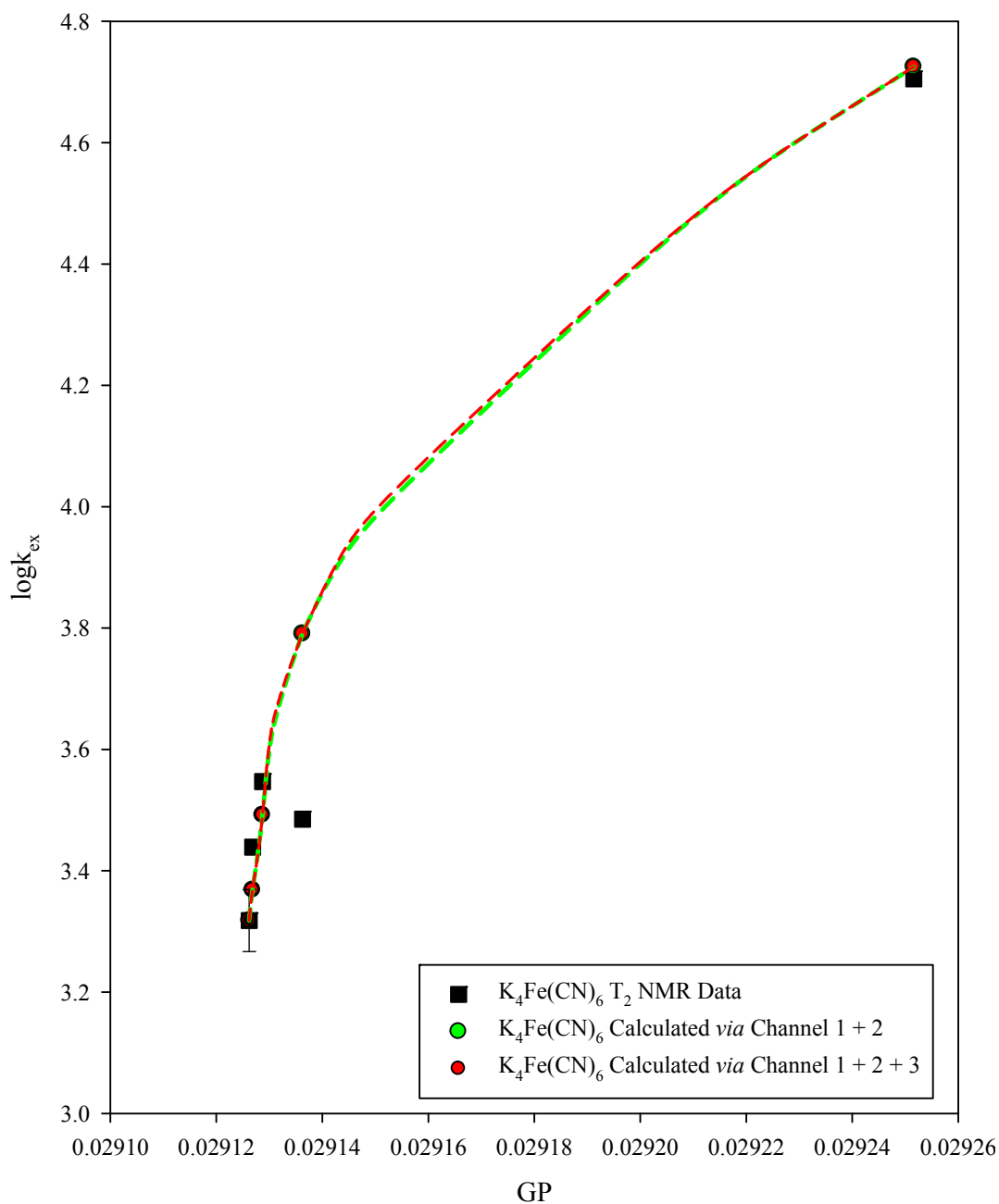


Figure 2.89 Experimental data and kinetic modeling results at 0.10 mM reactants with added K₄Fe(CN)₆ (presumed crystallographic Fe(CN)₆⁴⁻ radius of 4.24 Å). The T₂ NMR data (black squares) is compared with modeling results using Channels 1 + 2 (green circles) and Channels 1 + 2 + 3 (red circles).

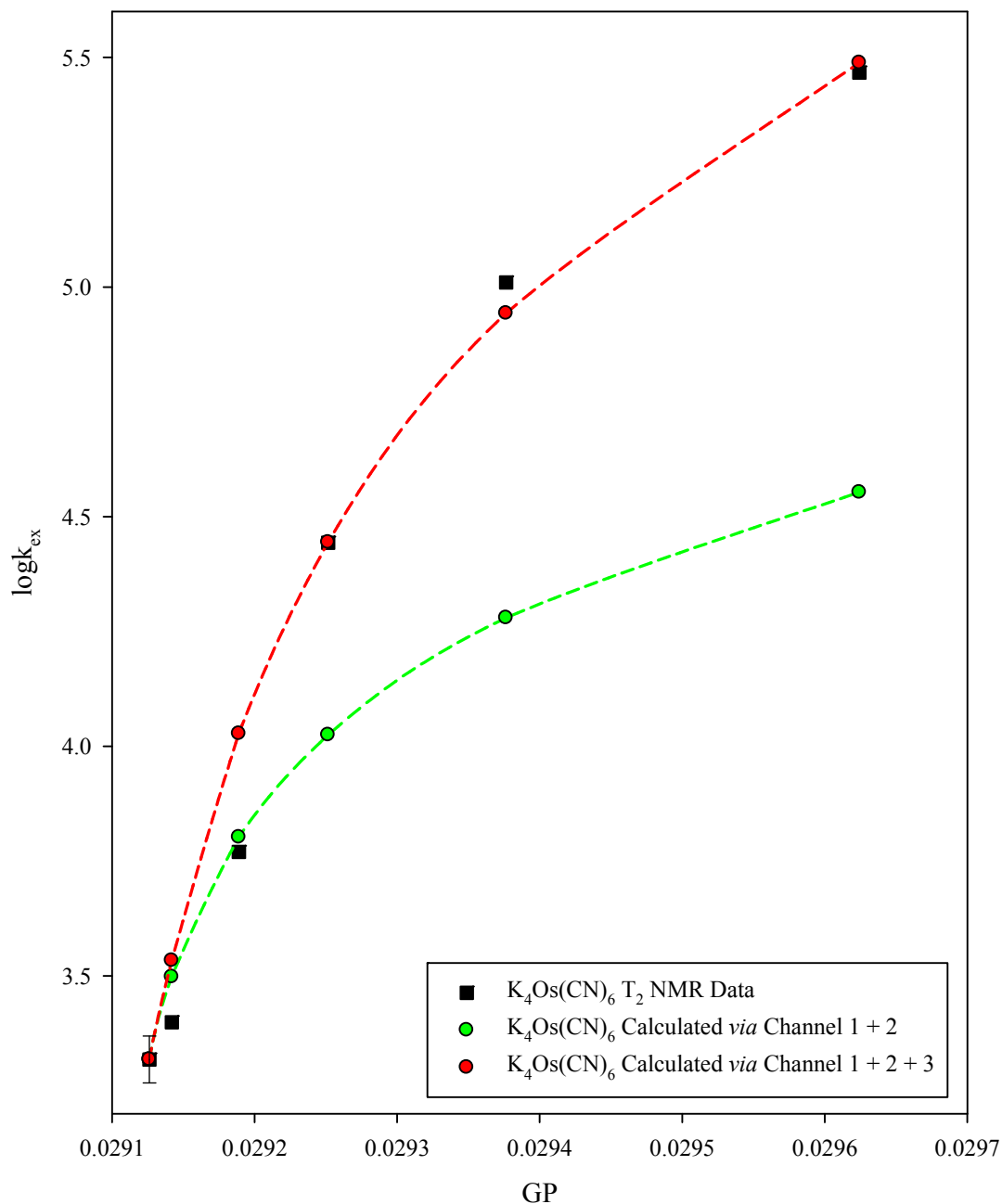


Figure 2.90 Experimental data and kinetic modeling results at 0.10 mM reactants with added $\text{K}_4\text{Os}(\text{CN})_6$ (presumed crystallographic $\text{Os}(\text{CN})_6^{4-}$ radius of 4.35 Å). The T_2 NMR data (black squares) is compared with modeling results using Channels 1 + 2 (green circles) and Channels 1 + 2 + 3 (red circles).

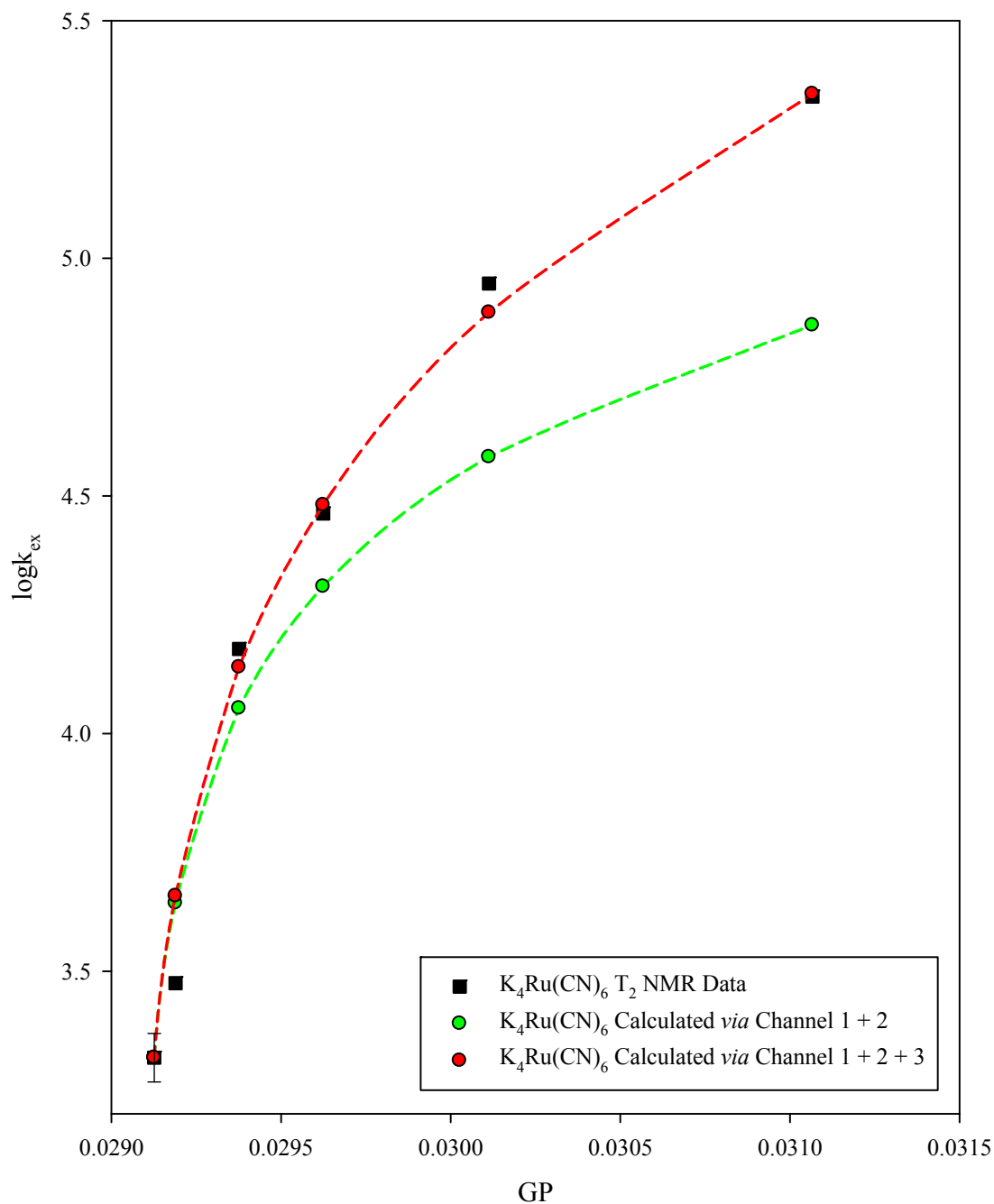


Figure 2.91 Experimental data and kinetic modeling results at 0.10 mM reactants with added $\text{K}_4\text{Ru}(\text{CN})_6$ (presumed crystallographic $\text{Ru}(\text{CN})_6^{4-}$ radius of 4.38 Å). The T_2 NMR data (black squares) is compared with modeling results using Channels 1 + 2 (green circles) and Channels 1 + 2 + 3 (red circles).

Previous kinetic modeling work had been completed on kinetic data obtained *via* stopped-flow⁹ for reaction (2-1) with these same added hexacyano salts using similar crystallographic radii to the ones used here (those data having been modeled using the SpecFit program which simulates and fits stopped-flow absorbance *vs.* time-kinetic data). However, as was previously noted in section 2.15, our rate data obtained using T₂ measurements deviated from the stopped-flow data due to the relatively extended duration of the T₂ experiment and sample decomposition which resulted in an observed decay overtime in the rate of ET. Therefore, the results reported here have a large error (in the downward direction) associated with them. When we compare the ratio of $k_{\text{ETX}}/k_{\text{ET}}$ for the three hexacyano salts with the halides, we find values for 5.8 (Fe^{II}(CN)₆⁴⁻), 5.8 (Os^{II}(CN)₆⁴⁻), and 0.6 (Ru^{II}(CN)₆⁴⁻) – the first two of which resemble values found for Cl⁻ (5.3). However, if we compare the ratio of $k_{\text{ETXX}}/k_{\text{ETX}}$ with those of the halides, we find values of 18.0 (Fe^{II}(CN)₆⁴⁻), 4.7x10⁵ (Os^{II}(CN)₆⁴⁻), and 2400 (Ru^{II}(CN)₆⁴⁻) which are much larger than any of the halides. These results, while inconclusive due to decomposition artifacts, still support the notion of added hexacyano salts facilitating ET *via* quantum super-exchange^{41,60} as was theorized previously by Mehmood.⁹

2.17.7 Kinetic modelling of added hexacyano at [Ru^{II}] = [Ru^{III}] = 5.00 mM

Finally, we applied our model to the kinetic data for reaction (2-2) at 5.00 mM reactants in the presence of small amounts of K₄Fe(CN)₆, K₄Ru(CN)₆, and K₄Os(CN)₆. The best-fit k_{ET} , k_{ETX} , and k_{ETXX} values arrived at are listed in Table 2.50. The experimental and model-calculated rate constants are listed in Table 2.51

and illustrated in Figures 2.92 to 2.94. As noted previously, in order to fit our measured $\log k_{\text{ex}}$ vs. GP plots at these larger reactants concentrations, we split the difference between the implied starting $\log k_{\text{ex}}$ value (no added salt) calculated using equation (2-33) and our experimentally derived $\log k_{\text{ex}}$ value resulting in the addition of +0.09 log units to our calculated $\log k_{\text{ex}}$ values at 5.00 mM reactants ($4.12 - 3.94 = 0.176$, $0.18/2 = +0.09$ log units).

Table 2.50 Best-fit k_{ET} , k_{ETX} , and k_{ETXX} rate constants for reaction (2-2) corresponding to first-order ET inside the presumed PC, PCX, and PCXX reactive intermediates (based on iterative fitting of the $\log k_{\text{ex}}$ vs. added salt curves measured at $[\text{Ru}^{\text{II}}] = [\text{Ru}^{\text{III}}] = 5.00 \text{ mM}$ for the various hexacyano salts studied). These optimized values lead to the model-calculated rates listed in Table 2.51. The $k_{\text{ETX}}/k_{\text{ET}}$ and $k_{\text{ETXX}}/k_{\text{ETX}}$ ratios are listed in the final two columns.

Ion	$k_{\text{ET}}^{(a)}$	$k_{\text{ETX}}^{(b)}$	$k_{\text{ETXX}}^{(c)}$	$k_{\text{ETX}}/k_{\text{ET}}^{(d)}$	$k_{\text{ETXX}}/k_{\text{ETX}}^{(e)}$
$\text{Fe}(\text{CN})_6^{4-}$ ($r = 4.24 \text{ \AA}$)	8.6×10^4	1.0×10^7	7×10^8	116	70
$\text{Os}(\text{CN})_6^{4-}$ ($r = 4.35 \text{ \AA}$)	8.6×10^4	1.0×10^5	2.7×10^7	1.2	270
$\text{Ru}(\text{CN})_6^{4-}$ ($r = 4.38 \text{ \AA}$)	8.6E+04	9.8E+03	9.8E+03	0.1	1.0

(a) Estimated uncertainty of $\pm 7\%$, (b) Estimated uncertainty of $\pm 8\text{-}12\%$, (c) estimated uncertainty of $\pm 30\text{-}35\%$, (d) estimated uncertainty of $\pm 10\text{-}12\%$, and (e) estimated uncertainty of $\pm 17\%$.

Table 2.51 Experimental and model-calculated rate constants at 5.00 mM reactants for reaction (2-2) as a function of GP arrived at using the three-channel model summarized in equations (2-36) through (2-38) and best-fit rate constants listed in Table 2.48 (the relevant ionic radii are taken from Tables 2.36 and 2.37). The data and fitted curves are illustrated in Figures 2.92 to 2.94.

K₄Fe(CN)₆

r =4.24 Å	GP	logk_{ex} (expt.)	logk_{ex} (calc.) Channel 1 Only	logk_{ex} (calc.) Channels 1 and 2	logk_{ex} (calc.) Channels 1, 2, and 3
	0.17501	4.120	4.032	4.032	4.032
	0.17543	-	-	6.149	6.127
	0.17607	-	-	6.540	6.543
	0.18109	7.239	-	7.268	7.435
	0.18319	7.612	-	7.384	7.604

K₄Os(CN)₆

r =4.35 Å	GP	logk_{ex} (expt.)	logk_{ex} (calc.) Channel 1 Only	logk_{ex} (calc.) Channels 1 and 2	logk_{ex} (calc.) Channels 1, 2, and 3
	0.17501	4.120	3.944	4.032	4.032
	0.17543	-	-	4.377	4.385
	0.17669	-	-	4.790	4.834
	0.17915	-	-	5.119	5.230
	0.18112	5.430	-	5.266	5.425

K₄Ru(CN)₆

r =4.38 Å	GP	logk_{ex} (expt.)	logk_{ex} (calc.) Channel 1 Only	logk_{ex} (calc.) Channels 1 and 2	logk_{ex} (calc.) Channels 1, 2, and 3
	0.17501	4.110	4.032	4.032	4.032
	0.17543	-	-	4.076	4.077
	0.17669	-	-	4.183	4.193
	0.17915	-	-	4.329	4.371
	0.18112	4.489	-	4.414	4.485

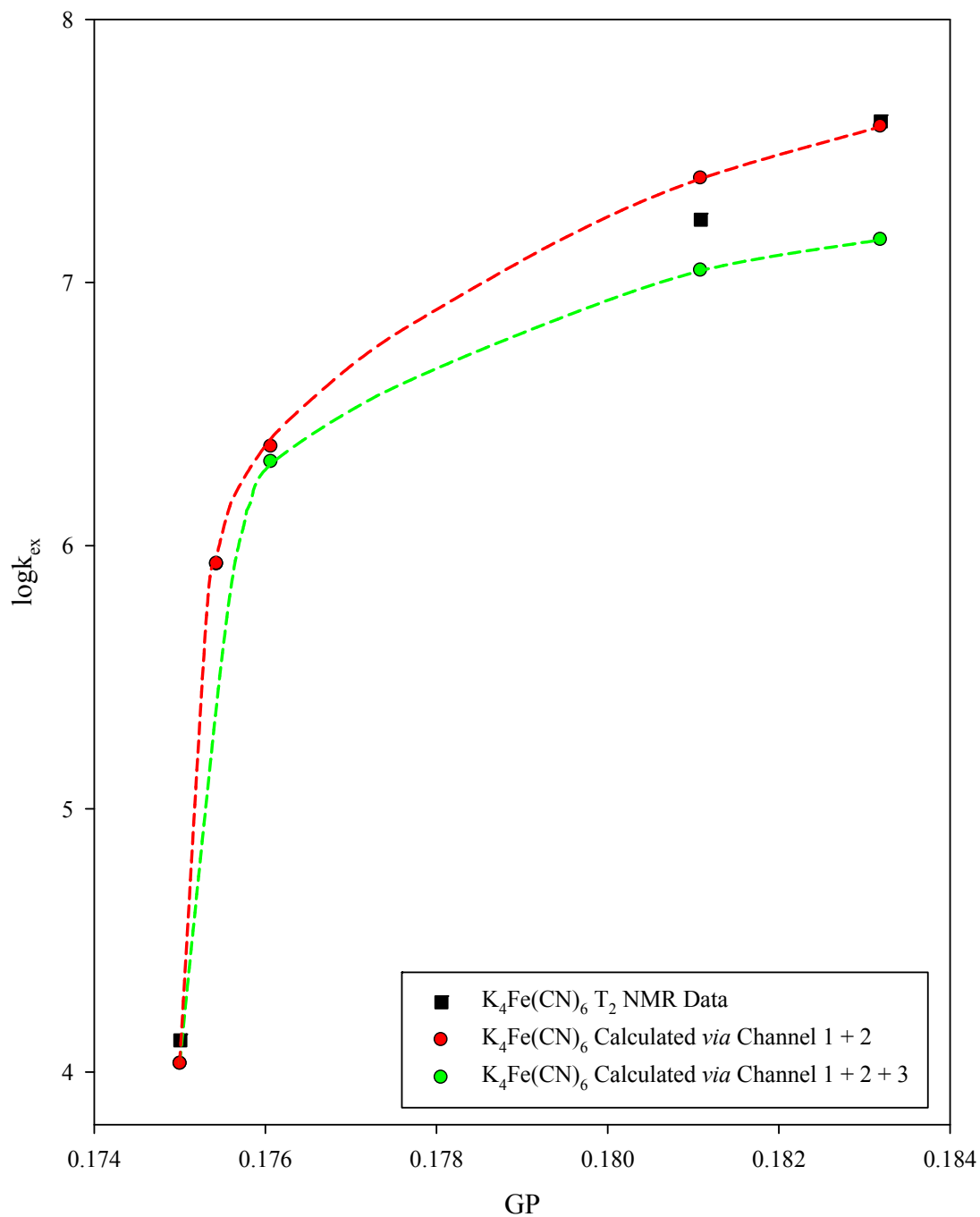


Figure 2.92 Experimental data and kinetic modeling results at 5.00 mM reactants with added $\text{K}_4\text{Fe}(\text{CN})_6$ (presumed crystallographic $\text{Fe}(\text{CN})_6^{4-}$ radius of 4.24 Å). The T_2 NMR data (black squares) is compared with modeling results using Channels 1 + 2 (green circles) and Channels 1 + 2 + 3 (red circles).

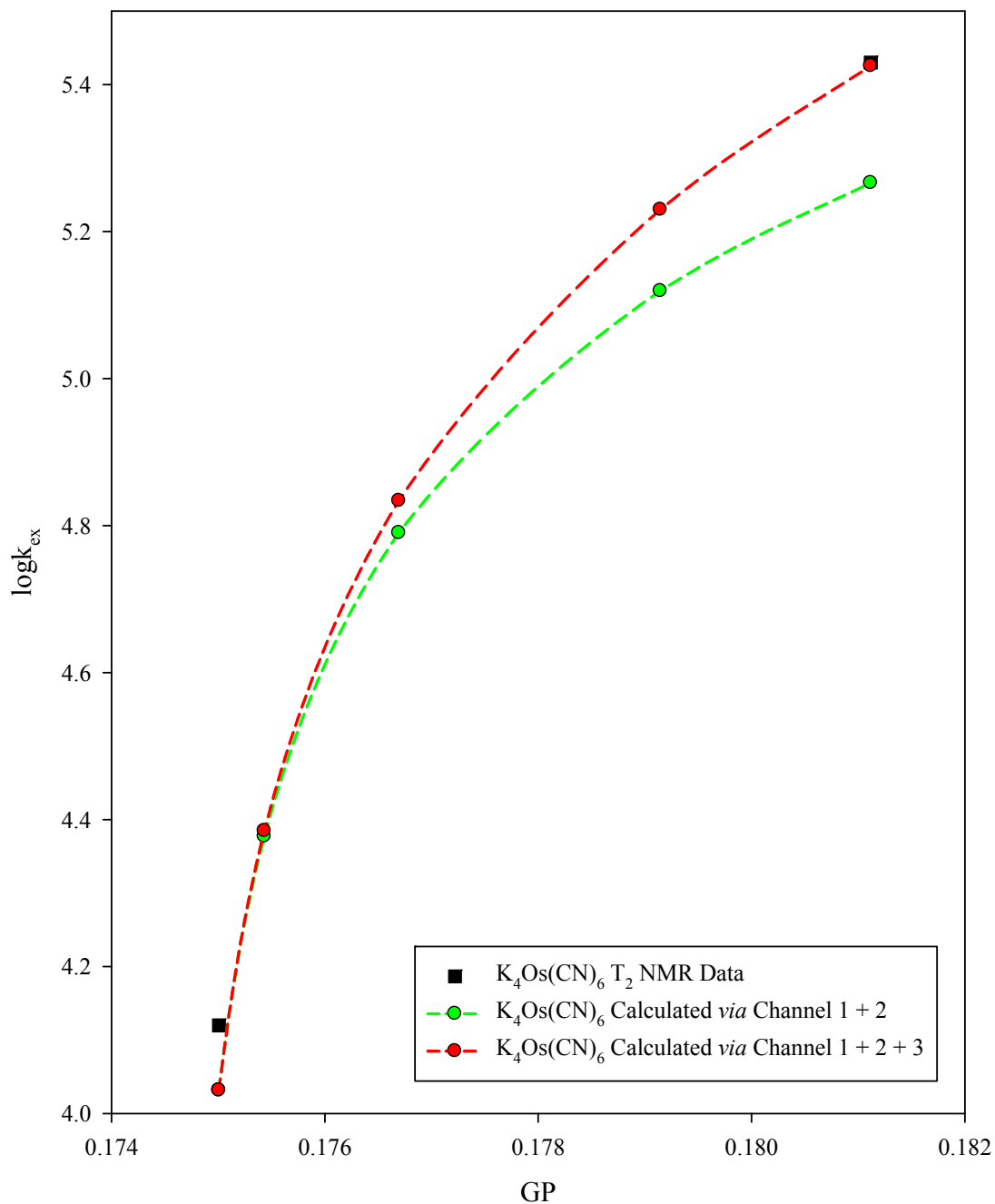


Figure 2.93 Experimental data and kinetic modeling results at 5.00 mM reactants with added $\text{K}_4\text{Os}(\text{CN})_6$ (presumed crystallographic $\text{Os}(\text{CN})_6^{4-}$ radius of 4.35 Å). The T_2 NMR data (black squares) is compared with modeling results using Channels 1 + 2 (green circles) and Channels 1 + 2 + 3 (red circles).

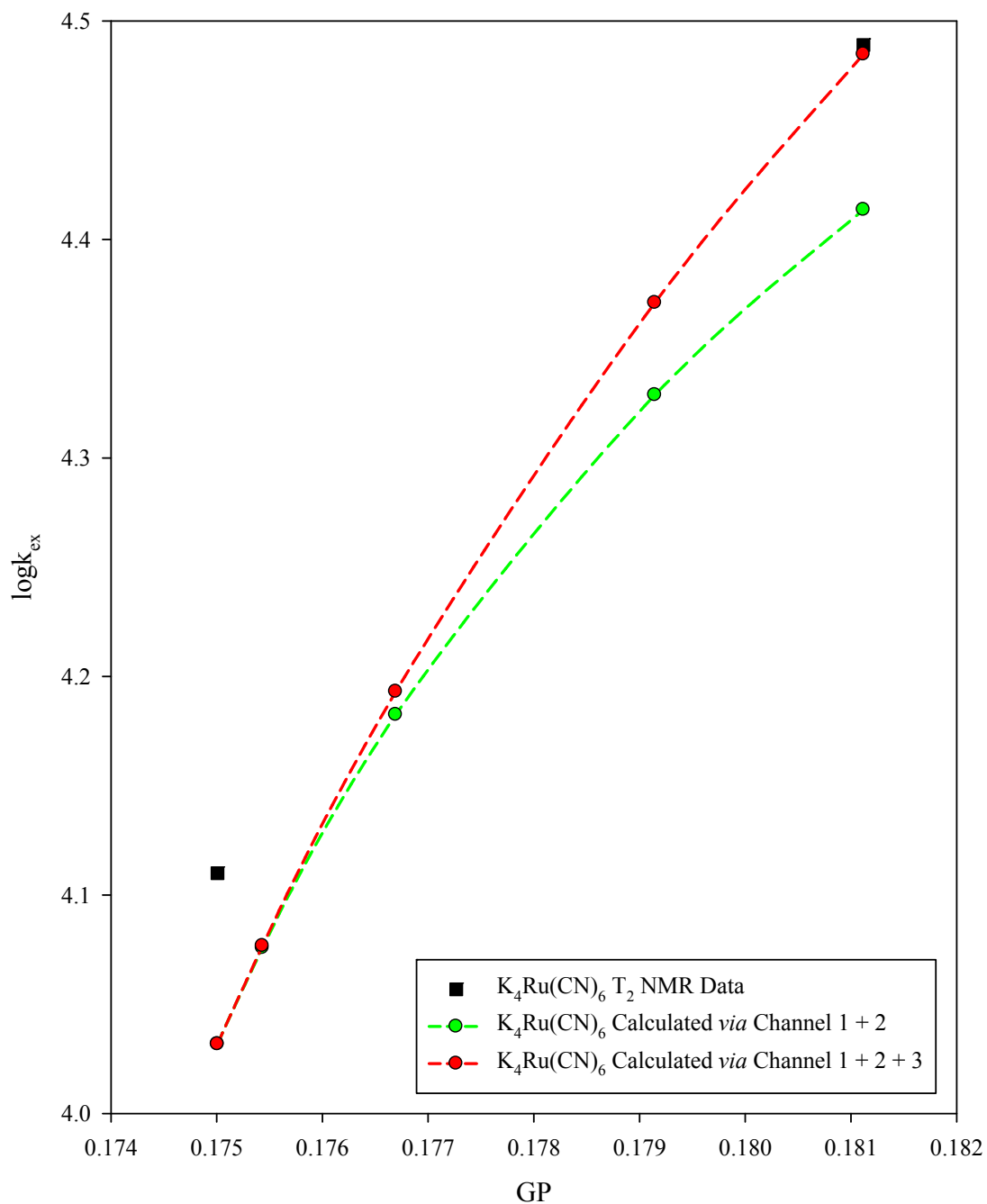


Figure 2.94 Experimental data and kinetic modeling results at 5.00 mM reactants with added $\text{K}_4\text{Ru}(\text{CN})_6$ (presumed crystallographic $\text{Ru}(\text{CN})_6^{4-}$ radius of 4.38 Å). The T_2 NMR data (black squares) is compared with modeling results using Channels 1 + 2 (green circles) and Channels 1 + 2 + 3 (red circles).

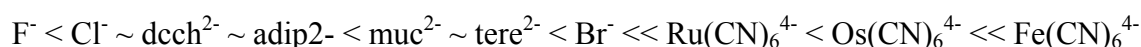
Our modeling of these data was impaired by the fact that we only collected two or three data points on account of the observed decay in rate enhance as was noted previously in section 2.15, therefore all values reported here have a slightly larger error associated with them. Previous kinetic modeling work completed on data obtained under the same conditions by Qin⁸ used similar values for radii as the ones used here (this data was modeled using a 2-Channel model which predicatively models NMR line-broadening data), therefore, the results are directly comparable. The best-fit $k_{\text{ETX}}/k_{\text{ET}}$ ratios found in our work for the hexacyano salts were 116 for $\text{Fe}(\text{CN})_6^{4-}$, 1.2 for $\text{Os}(\text{CN})_6^{4-}$, and 0.1 for $\text{Ru}(\text{CN})_6^{4-}$. These values are in very good agreement with the line-broadening based rates and $k_{\text{ETX}}/k_{\text{ET}}$ ratios obtained by Qin; 126 for $\text{Fe}(\text{CN})_6^{4-}$, 1.5 for $\text{Os}(\text{CN})_6^{4-}$, and 0.5 for $\text{Ru}(\text{CN})_6^{4-}$.

2.18 Discussion

The most basic signal of what we refer to here as “catalysis” of ET reaction (2-2) by added salt is an early, upwards curvature in the experimental $\log k_{\text{ex}}$ vs. GP plot as opposed to the strictly-linear behavior predicted by the DBH equation (1-36) or the slightly “convex” (over the full GP range) behavior predicted by equations (2-36) to (2-38), even in the limit of no specific ion-pairing as given by equation (2-33) (see Figure 2.54).

The simplest approach to describing this observed catalysis was to report the approximate “early” and “late” $\log k_{\text{ex}}$ vs. GP slopes for a given anion and then regard any divergence between them as a sign of catalysis (where the most catalytic anions were those with the largest “early” slopes, see section 2.13). As shown in Table 2.15,

the most ideal-behaving kinetic salt effects were encountered at 0.10 mM reactants with added fluoride. This is the only anion exhibiting “simple” salt behavior and it alone yields the predicted Debye-Huckel-Bronsted slope of 6.1 (this only being true however over the most dilute portion of $[F^-]$ range investigated). After F^- the levels of catalytic efficacy went as:



For the salts investigated as a function of reactants concentration, the shapes of the salt curves show decreased catalysis at all reactants concentration > 0.10 mM. For fluoride, the (still approximately linear) $\log k_{ex}$ vs. GP slope progressively drops all the way to 0.52 ± 0.14 at 5.00 mM (see Figures 2.28, 2.26, 2.30, and 2.31).

The kinetic modeling work was conducted as a way to quantitatively assess the degree of a given anion’s catalytic power under the assumption that the catalysis could be captured as an apparent increase in the intramolecular rate of ET, k_{ETX} , inside the ternary PCX intermediate. This would assume that the total rate of ET is greater than the inferred k_{ET} inside the classical precursor complex PC. According to our model used, only in this way could an added anion increase the overall rate of ET beyond the ionic strength effects on the uncatalyzed rate predicted from the Debye-Smolukowsky and Eigen-Fuoss equations (1-41) to (1-42).

From the foregoing discussions, we see that our model appears to work best at the lowest reactants concentration studied which was $[Ru^{II}] = [Ru^{III}] = 0.10$ mM, but as the reactants concentration increased (even to 0.50 mM), we found that the results obtained using the model to simulate experimental data start to deviate from

predictions based solely on the Debye-Huckel-Bronsted equation (1-36)¹¹ or the Debye-Eigen and Debye-Smoluchowski equations (equations (1-41) and (1-42), respectively)³ in the simple pre-equilibrium kinetic limit, equation (1-5).³⁰ This deviation presented itself as a steady downward trend in the best-fit $k_{\text{ETX}}/k_{\text{ET}}$ ratios (essentially due to a falling k_{ETX}), which were required at the higher reactants concentrations. The model-inferred drop in k_{ETX} necessary to reproduce both the declining “simple salt” effect seen with F^- and the drop in catalytic efficacy of the others at reactants concentrations greater than 0.10 mM is considered to be unlikely given that the intramolecular, first-order ET rate inside the PCX ion-triplet would only be expected to vary weakly with the ionic strength of the medium (via the small ion-atmosphere reorganizational energy identified by Ulstrup).¹

In order to analyze the salt-by-salt magnitude of this artifact in the model we have taken the $k_{\text{ETX}}/k_{\text{ET}}$ ratios listed in Tables 2.40, 2.42, 2.44, and 2.46 and plotted them as a function of reactants concentration in Figure 2.95. The pattern of dropping k_{ETX} with increasing reactants concentration is most pronounced with bromide, followed by the (apparently) ET-obstructing fluoride ion which slows the reaction once reactive flux through PCX becomes important (at reactant concentrations > 0.10 mM).

Figure 2.95 displays the ratios of $k_{\text{ETX}}/k_{\text{ET}}$ arrived at by Sista⁶ at 0.10 mM using SpecFit simulations of his stopped-flow data on reaction (2-1) (note the blue, green, and red squares). Also shown are the ratios resulting from modeling of the NMR line-broadening data obtained by Qin⁸ at 5.00 mM reactants using a 2-Channel

model nearly equivalent to ours (note the blue, green, and red stars). Excellent agreement was found among the ratios in all cases of overlapping experimental conditions. Given that the SpecFit modeling approach and our modeling using equations (2-36) to (2-38) represent very different implementations of a formally-equivalent kinetic scheme, the excellent agreement supports the basic correctness of the execution of each respective model.

One possible origin we have considered for the apparent downward trend in $k_{\text{ETX}}/k_{\text{ET}}$ found by our model centers on the fact that the infinite integration limits typically used in applications of equations (1-36) and (1-44) may no longer work at reactants concentrations significantly above 0.10 mM. As shown in Figure 1.11 (see section 1.8), the center-center interreactant distance varies from 255 Å to 69 Å as we go from 0.10 mM to 5.00 mM in $[\text{Ru}^{\text{II}}]$ and $[\text{Ru}^{\text{III}}]$ (using a cubic statistical “lattice model” the $\text{Ru}^{\text{II}}\text{-Ru}^{\text{III}}$ distance goes from 221 Å to 60 Å as calculated by equation (1-48)). Furthermore, using a common reactant radius of 4.5 Å, we find that the edge-edge inter-reactant distance varies even more drastically from 212 Å to 51 Å. Qualitatively, it is easy to see that since added ionic strength eases association of our 2+ and 3+ charged reactants by decreasing the Coulombic work terms (see equation (1-43)), then the accelerating k_{ai} values in the model would decrease upon explicitly using the more realistic, finite separation values. In addition, in solutions where the concentration of added X^- is greater than the concentration of Ru^{III} , the appropriate maximum distance can be found using equation (1-48). To probe the possible

significance of these refinements, we have recomputed the necessary k_{ai} and k_{di} values and remodeled the data for F^- and Br^- at 0.10 mM and 5.00 mM reactants.

Table 2.52 The ratios of k_{ETX}/k_{ET} arrived at for the F^- and Br^- anions (using the crystallographic radii found in Table 2.36) at 0.10 mM and 5.00 mM reactants using both explicit integration limit values and infinite integration limits (when applying equations (1-41) and (1-42)).

Reactants Concentration	k_{ETX}/k_{ET}			
	$F^- (r = 1.50 \text{ \AA})$		$Br^- (r = 2.61 \text{ \AA})$	
	Explicit int. Limits	Infinite Int. Limits	Explicit int. Limits	Infinite Int. Limits
0.01 <u>mM</u>	0.9	0.9	8.7	8.7
5.00 <u>mM</u>	0.04	0.04	3.3	3.3

Table 2.52 shows the explicit integration limit values for the k_{ET}/k_{ETX} ratios as well as the previous ratios (using infinite integration limits) for comparison. This surprising negative result means that we must look elsewhere for the source of the model's failure.

A second possibility lies in the absolute reliability of the calculated k_{ai} and k_{di} values. For example, we when look at the computed k_{ai} and k_{di} values shown below in Table 2.53 for F^- and Br^- (using crystallographic radii) we find values approaching a so-called “speed-limit” violations as noted by Moore and Percin.⁶¹ They noted that the fastest an ion-pair can associate is on the order of 5.3×10^{10} . The values arrived at here are approaching this unrealistic speed limit which could be the source of our model's failure.

Table 2.53 The computed k_{ai} and k_{di} values for the the F^- and Br^- anions (using the crystallographic radii found in Table 2.36) at 0.10 mM reactants with 0.0005 M added salt.

	$F^- (r = 1.50 \text{ \AA})$	$Br^- (r = 2.61 \text{ \AA})$
k_{a2}	2.92×10^{10}	2.13×10^{10}
k_{a4}	4.36×10^{10}	2.91×10^{10}
k_{d3}	1.26×10^{10}	1.15×10^{10}

Another puzzling result was an apparent offset between the ratios of k_{ETX}/k_{ET} arrived at using the crystallographic and hydrated radii opposite of what we would predict (larger radii giving slower rates of ET through PCX). In Table 2.54 the ratios of k_{ETX}/k_{ET} are compared for the halides and dicarboxylates and these values are illustrated as a function of reactants concentration in Figures 2.95 to 2.97.

Table 2.54 The ratios of $k_{\text{ETX}}/k_{\text{ET}}$ arrived at for the halides (using the radii found in Table 2.36) at the various reactants concentrations studied.

Ion	$k_{\text{ETX}}/k_{\text{ET}}$			
	0.10 mM	0.50 mM	1.00 mM	5.00 mM
F^- ($r = 1.50 \text{ \AA}$)	0.9	0.02	0.2	0.04
F^- ($r = 3.89 \text{ \AA}$)	0.6	0.03	0.1	0.0
Cl^- ($r = 1.90 \text{ \AA}$)	5.3	4.5	2.1	2.1
Cl^- ($r = 4.41 \text{ \AA}$)	2.9	2.3	1.2	1.2
Br^- ($r = 2.61 \text{ \AA}$)	8.7	9.3	6.6	3.3
Br^- ($r = 4.08 \text{ \AA}$)	5.0	6.4	4.4	2.2
muc^{2-} ($r = 3.86 \text{ \AA}$)	0.7	0.5	0.3	0.1
adip^{2-} ($r = 3.97 \text{ \AA}$)	0.5	0.2	-	0.1
tere^{2-} ($r = 4.13 \text{ \AA}$)	0.8	-	-	-
$(1,4\text{-dcch})^{2-}$ ($r = 4.11 \text{ \AA}$)	0.7	-	-	-

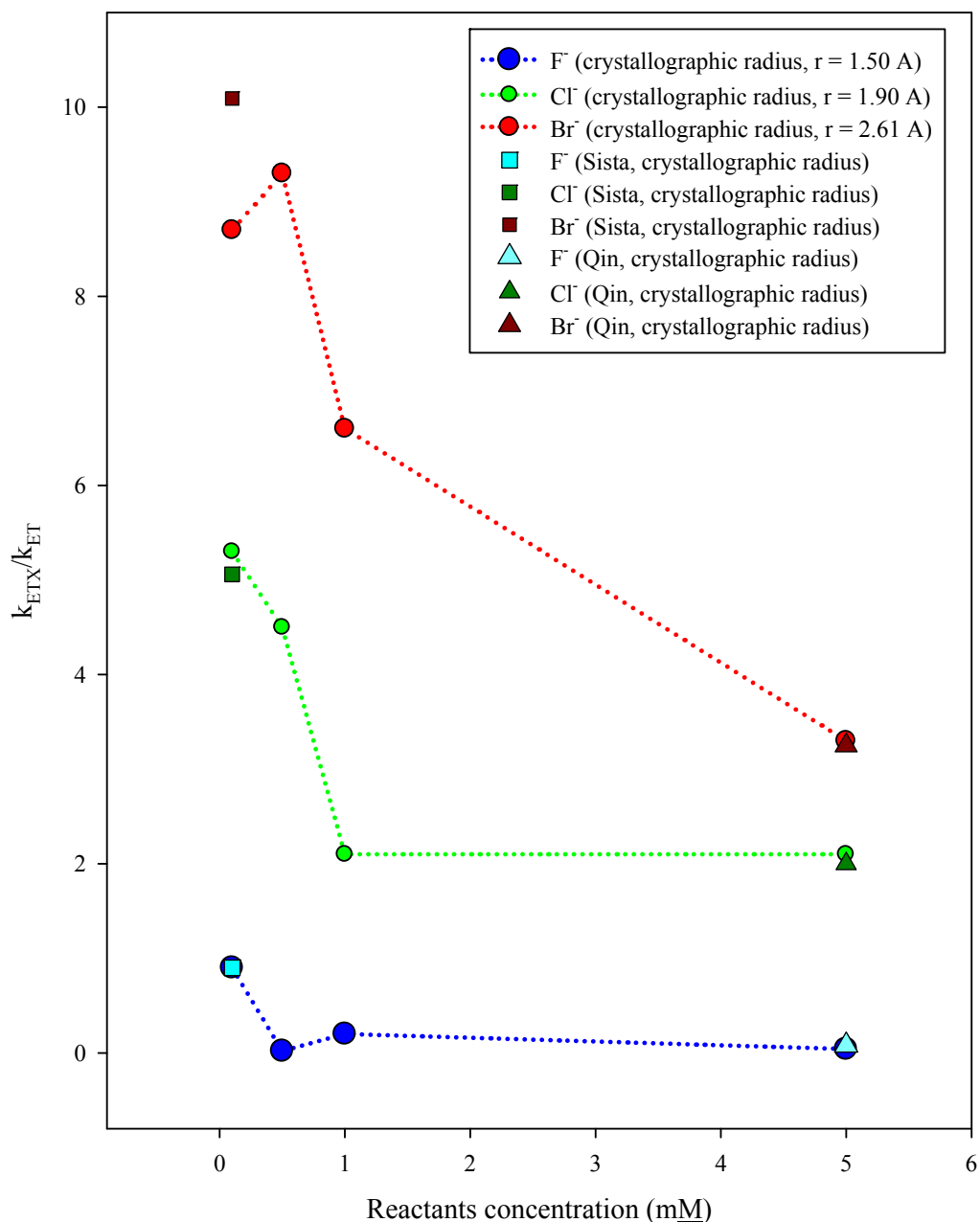


Figure 2.95 The ratios of $k_{\text{ETX}}/k_{\text{ET}}$ arrived at for the halides studied as a function of the reactants concentration (0.10 mM to 5.00 mM reactants). The ratios of $k_{\text{ETX}}/k_{\text{ET}}$ found using crystallographic radii (blue, green, and red circles) as listed in Table 2.36 are compared with those values obtained previously by Sista⁶ (modeling reaction (2-1), 0.10 mM reactants; blue, green, and red squares) and Qin⁸ (modeling reaction (2-2), 5.00 mM reactants; blue, green, and red stars).

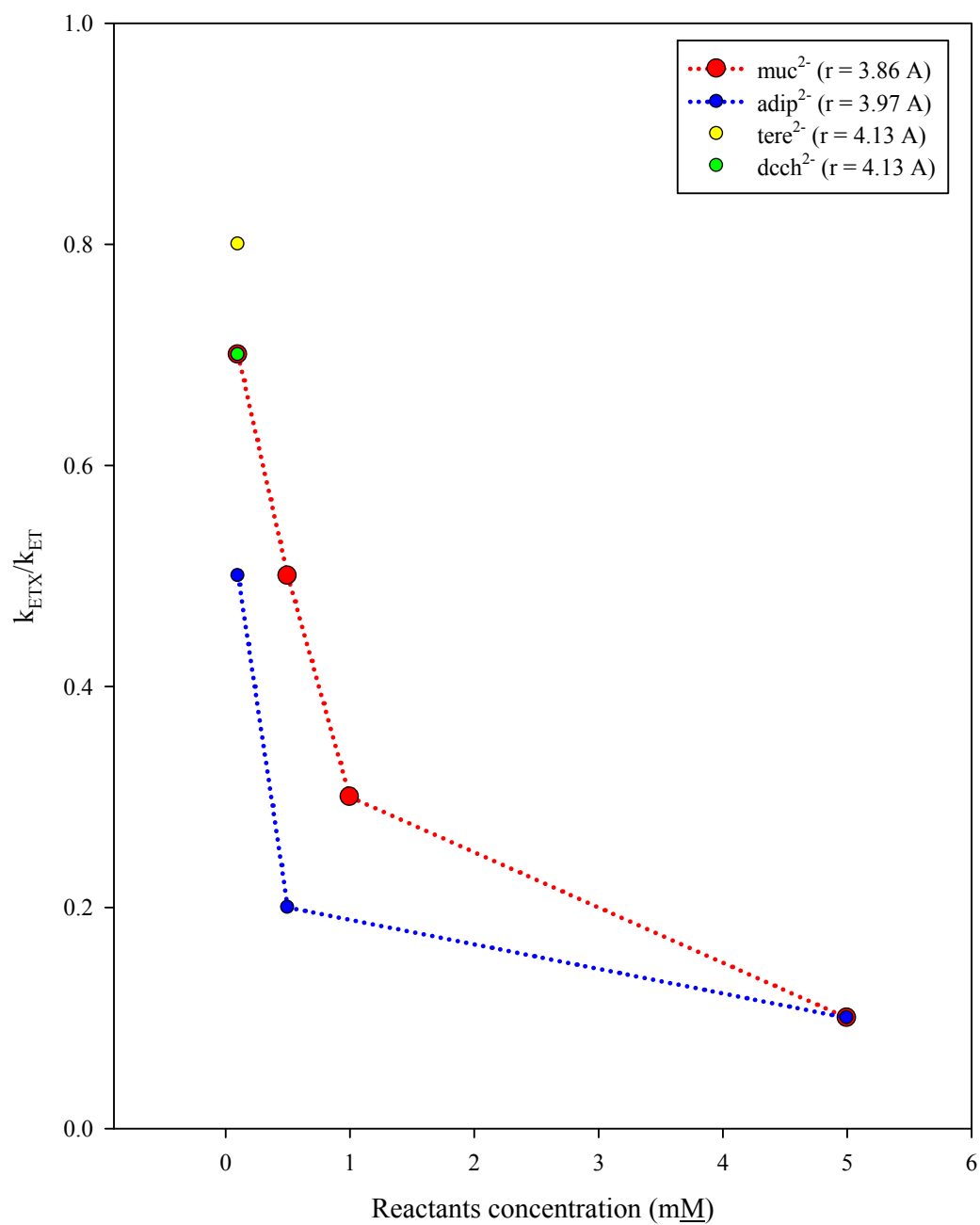


Figure 2.96 The ratios of $k_{\text{ETX}}/k_{\text{ET}}$ arrived at for the dicarboxylate salts studied at as a function of the reactants concentration (the radii used were arrived at using the “volume-tight” keyword in Gaussian 09 geometry optimizations as described in the experimental section, see Table 2.36).

From Table 2.54 and Figure 2.95, we see that increasing the reactants concentration decreases the $k_{\text{ETX}}/k_{\text{ET}}$ ratios for the halides (using the crystallographic radii). The reason for this systematic error is unknown and further investigation is needed. As was found for the halides, the ratio of $k_{\text{ETX}}/k_{\text{ET}}$ also drops for both muc^{2-} and adip^{2-} as the reactants concentration increased. This apparent drop in k_{ETX} could be due to a systematic error in the model's ability to calculate K_{A} for the formation of PCX is essentially not capturing the somewhat rod-like nature of these salts. This effect could also be a real effect due to anisotropic diffusion which would inhibit both dicarboxylate salts to “get in between” these salts at larger concentrations.

From Table 2.40, we see that upon comparing the best-fit k_{ETX} values arrived at for reaction (2-2) in the presence of added dicarboxylate salts at 0.10 mM reactants with those found previously for reaction (2-1) by stopped-flow^{6,9} good agreement was found in every case but muconate. The much lower k_{ETX} value for muc^{2-} upon fitting the NMR kinetic data has been hypothesized to derive from either an inefficiency in its ability to form ion-pairs with the reactants or from the unique impact of the magnetic field on its ability to catalyze the exchange process *via* quantum super-exchange mediation of ET. We speculate that perhaps the strong magnetic field present in the NMR work might be locking muconate along the field axis and therefore impeding its ability to “freely” diffusive through solution.

In Figure 2.97 we have plotted the $k_{\text{ETX}}/k_{\text{ET}}$ ratios for the halides using both the crystallographic and hydrated radii as a function of our equimolar reactants concentration.

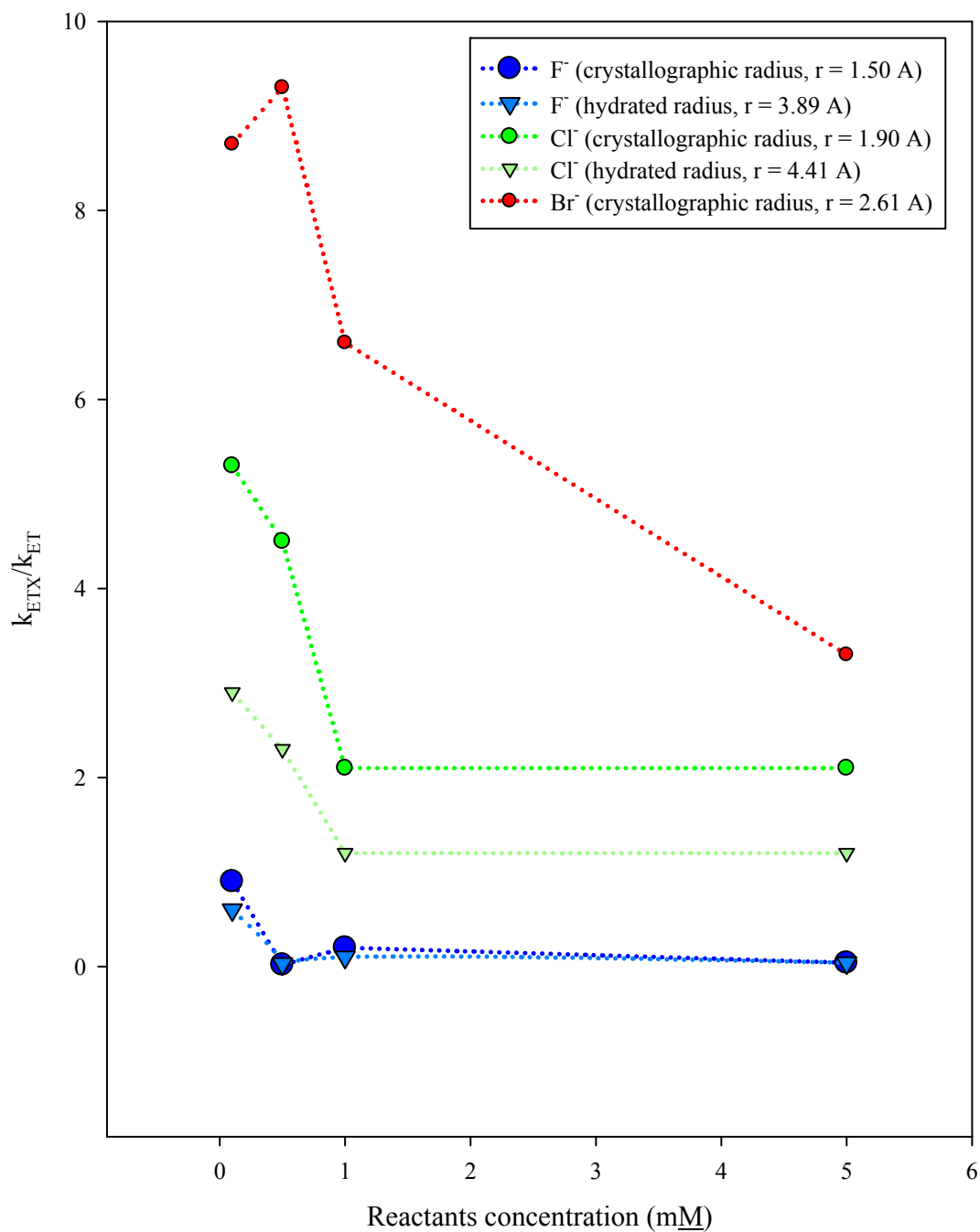


Figure 2.97 The ratios of $k_{\text{ETX}}/k_{\text{ET}}$ arrived at for the halides studied as a function of the reactants concentration (0.10 mM to 5.00 mM reactants). The ratios of $k_{\text{ETX}}/k_{\text{ET}}$ found using crystallographic radii (blue, green, and red circles) are compared with those found using the hydrated radii as listed in Table 2.36.

The ratios of $k_{\text{ETX}}/k_{\text{ET}}$ arrived at using the hydrated halide radii to model our kinetic data, are found to be consistently lower when compared to those using the crystallographic radii to model our kinetic data. When using larger radii one might reasonably expect the association to form $\text{Ru}^{\text{III}} \cdot \text{X}$ ion pairs to occur with less affinity due to lower Coulombic attraction. The slower onset of Channel 2 would then require a higher k_{ETX} value (and therefore higher ratio of $k_{\text{ETX}}/k_{\text{ET}}$). Upon investigating this conundrum we have found that smaller k_{ETX} values inferred from our model when using larger radii (hydrated) to fit the data stems from variations in the excluded volume term (σ^3 , where σ is the sum of the radii, see equation (1-50)) in the equation for k_d . This term makes the values arrived at for K_A to form PCX larger when using the hydrated radii than those found using the crystallographic radii. This non-intuitive enhancement of the PCX pathway therefore requires k_{ETX} to be smaller when using hydrated radii to model kinetic data. In addition, the model-inferred decrease in k_{ETX} values as the concentration of reactants is increased is found in both cases.

Upon applying our kinetic model to our ET reaction as catalyzed by the hexacyano salts, we could only reliably analyze the data obtained at 5.00 mM reactants due to the time-dependent decay of the hexacyano catalysis found at low concentrations of added hexacyano salt observed at 5.00 mM reactants, which was found after the 0.10 mM data was collected. In Table 2.55 we have summarized the ratios of $k_{\text{ETX}}/k_{\text{ET}}$ arrived for these hexacyano salts at 5.00 mM, as well as their corresponding $E_{1/2}$ values, and plotted the log of these ratios *vs.* the $\Delta E_{1/2}$ (*vs.* SCE)

values between the $(\text{NH}_3)_5\text{Ru}^{\text{II/III}}\text{tfmp}$ couple (0.143) and each of the hexacyanos redox potentials values in Figure 2.98.

Table 2.55 The ratios of $k_{\text{ETX}}/k_{\text{ET}}$ found for the various hexacyano salts at 5.00 mM reactants as well as their associated redox potentials (vs. SCE). The ratios in parenthesis are those found by Qin using a 2-Channel model.^{8,43}

Ion	$\text{Fe}(\text{CN})_6^{4-}$ ($r = 4.24 \text{ \AA}$)	$\text{Os}(\text{CN})_6^{4-}$ ($r = 4.35 \text{ \AA}$)	$\text{Ru}(\text{CN})_6^{4-}$ ($r = 4.38 \text{ \AA}$)
$k_{\text{ETX}}/k_{\text{ET}}$	116 (126)	1.2 (1.5)	0.1 (0.45)
$E_{1/2}$	0.2	0.4	0.7
$\Delta E_{1/2}^{(a)}$	0.1	0.3	0.6

(a) $\Delta E_{1/2} = E_{1/2}(\text{M}^{\text{II/III}}(\text{CN})_6) - E_{1/2}(\text{Ru}^{\text{II/III}}(\text{NH}_3)_5\text{tfmp})$ where $E_{1/2}(\text{Ru}^{\text{II/III}}(\text{NH}_3)_5\text{tfmp}) = 0.143$

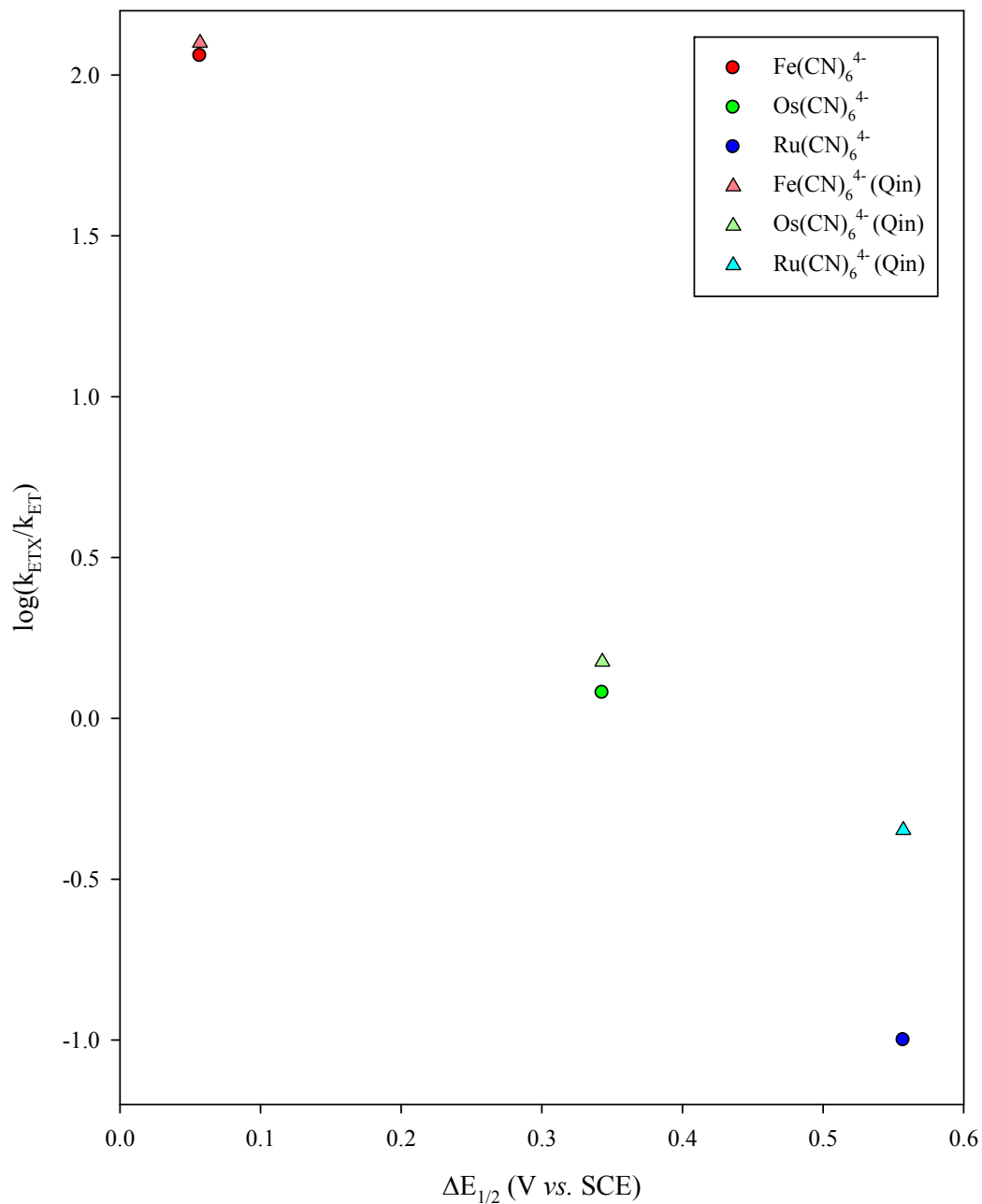


Figure 2.98 The log of the best-fit $k_{\text{ETX}}/k_{\text{ET}}$ ratios arrived at for the various hexacyano salts studied vs. the relevant $\Delta E_{1/2}$ (resulting from the difference of the hexacyanos redox potentials and the $(\text{NH}_3)_5\text{Ru}^{\text{II/III}}/\text{fmp}$ couple, 0.143; red, green, and blue circles) compared with previous results obtained by Qin (red, green, and blue triangles).⁸

To probe the idea of the hexacyano salts catalyzing the ET process *via* “hole-transfer” quantum super-exchange as illustrated in Figure 1.6, we have compared the $k_{\text{ETX}}/k_{\text{ET}}$ ratios with the $\Delta E_{1/2}$ resulting from the difference in the redox potentials of the hexacyanos and the $(\text{NH}_3)_5\text{Ru}^{\text{II/III}}\text{tfmp}$ couple (0.143). When the $\text{M}^{\text{II/III}}(\text{CN})_6^{4-/3-}$ redox potential of a given added salt is closer to that of our reactant species the HOMO of the added salt species will lie closer in energy to that of the “hole” or electron vacancy in the Ru^{III} form of that partner of our ET reacting pair. Therefore, when the ternary association complex is formed, $[\text{A}_5\text{Ru}^{\text{II}}\text{L}, \text{M}^{\text{II}}(\text{CN})_6^{4-}, \text{A}_5\text{Ru}^{\text{III}}\text{L}]^+$, super-exchange is progressively turned on as a function of the energy level of HOMO of our $\text{M}^{\text{II}}(\text{CN})_6^{4-}$ $\text{M} = \text{Ru} \rightarrow \text{Os} \rightarrow \text{Fe}$. Figure 2.98 shows that as the redox potentials of each hexacyano salt studied lie closer to that of our reactant complex, super-exchange mediation is occurring with more ease (as shown by a rise in $k_{\text{ETX}}/k_{\text{ET}}$ ratio).

It is possible that some aspect of this same process may be showing up in the halide data. This would be due to the low lying HOMO's of the halides making it more difficult for the ET process to occur in the ternary association complex $[\text{A}_5\text{Ru}^{\text{II}}\text{L}, \text{X}^- \text{A}_5\text{Ru}^{\text{III}}\text{L}]^{4+}$. When the redox potentials are compared with the associated kinetic salt effects, the redox potential of the F^- anion lies farthest away from our ruthenium complexes and that of Br^- lies the closest therefore making Br^- the most catalytic and F^- the least by the same hole-transfer reasoning.

2.19 Conclusions

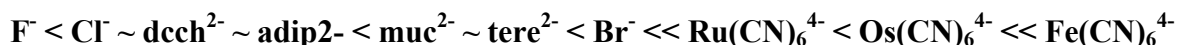
By optimizing the T_2 spin-echo sequence utilizing the ^{19}F nucleus we have measured the kinetics of reaction (2-2) at the reactants concentration range of 0.10 mM used in the earlier stopped-flow work.^{6,7,9} This, combined with line-broadening based work at 5.00 mM reactants⁸, has allowed us to broaden our measurements of kinetic salt effects, as well as self-salting effects, over a very broad reactants concentration range (spanning from 0.10 mM to 5.00 mM). This new adaptation of the very well established CPMG T_2 spin-echo pulse sequence has thus linked the traditional methods for measuring the kinetics of *pseudo*- and *true* self-exchange reactions (stopped-flow at low reactants, and NMR line-broadening at high reactants).

We find that upon increasing the reactant concentrations in our work on reaction (2-2), a non-linear trend in the rate of ET vs. solution GP is obtained. This behavior could be attributed to the excess Cl^- ions in solutions catalyzing our reaction in a way which deviates from the Debye-Hückel-Bronsted equation (and this can be seen by a similar $k_{\text{ET}}/k_{\text{ETX}}$ ratio arrive at for the self-salting modeling data and the added Cl^- modeling data).

At low reactants concentrations (0.10 mM reactants) good agreement was found with previous stopped-flow work^{6,9} on specific kinetic salt effects in *all* cases except that of muconate, therefore validating not only the stopped-flow data but also proving that the *pseudo* self-exchange reactions and this particular *true* self-exchange reaction indeed behave fundamentally the same for this family of complexes (meaning that the assumptions of $\Delta E_{1/2} \ll \lambda_{\text{tot}}$ and $\lambda_{\text{tot}} = \text{constant}$ in the stopped-flow

cases are rigorously valid).¹¹ This agreement was further underscored by comparing temperature dependent stopped-flow and NMR kinetic data. Here we found that essentially-identical salt-induced isokinetic plots for the added halides and dicarboxylates were reproduced for all salts except the unique case of muc^{2-} .

At high reactants concentrations (5.00 mM) *all* kinetic salt curves obtained by T_2 relaxation matched very well with previous NMR line-broadening measurements which solidified our picture of salt effects in the faster exchange region (where the observed salt effects are very different than the classical Debye-Huckel-Bronsted prediction).⁸ At all reactants concentration ranges studied, the catalytic efficacies of the various anions went as noted below:



We have shown that some aspects of this trend lies in the anions abilities to catalyze ET by quantum super-exchange associated with the ionization potentials and $E_{1/2}$ values of the anions.^{6,8} This trend reflects the energetic cost of creating a “hole-transfer” virtual bridge state because the closer the energy levels of the bridge (X) HOMO levels of these added salts are to the t_{2g} e^- vacancy of our $(\text{NH}_3)_5\text{Ru}^{\text{III}}\text{tfpm}$ oxidant complex the more readily ET will occur (with the closest lying HOMO to that of $\text{Fe}(\text{CN})_6^{4-}$ and farthest to that of F^-).

By a careful process of elimination the downward deviation seen here of muconate’s catalytic efficacy as compared to its catalysis of ET measured by stopped-flow has been attributed solely to the presence of the magnetic field in the NMR work. This surprising result requires quenching of the quantum super-exchange

mechanism for muc^{2-} by the field. Another instance of this effect may show up in the work associated with the hexacyano's due to the downward deviations found here relative to the stopped-flow work⁹ at 0.10 mM reactants, but further investigation is needed because of decay effects observed at 5.00 mM reactants with small amounts of hexacyano salts present in solution. The broad outlines of the hexacyano salt curves at 5.00 mM reactants however, confirm that the quantum super-exchange catalysis is indeed occurring *via* the hole-transfer mechanism.

The three-channel kinetic model developed and applied here (see Appendix A) work well at 0.10 mM reactants supporting the notion that reactive flux thru PC, PCX, and presumably PCXX are all necessary to explain the observed kinetic salt effects over the full ranges of [X] studied. This model generally holds over a broad range of $k_{\text{ETX}}/k_{\text{ET}}$ ratios spanning from 0.10 mM reactants to 5.00 mM reactants with slight downward deviations in k_{ETX} and k_{ETXX} . This model can therefore be assumed to be a good predictive tool for how these ET reactions occur in solution, however further investigation is still needed to determine how the underlying equations this model is based on break down at larger reactant concentrations (> 0.10 mM reactants).

References

1. Curtis, J. C.; Inagaki, M.; Chun, S. J.; Eskandari, V.; Luo, X.; Pan, Z. N.; Sankararaman, U.; Pengra, G. E.; Zhou, J.; Hailey, P.; Laurent, J.; Utalan, D. *Chemical Physics* 2006, 326, 43-53.
2. Robinson, R.; Stokes, R. Electrolyte Solutions, 2nd Ed. Dover Publications Inc. Mineola, NY. 2002, 73-86.
3. Kirk, A. D.; Cai, L.-Z.; Kneeland, D. M. *J. Phys. Chem. A*. 1997, 101, 3871.
4. Chiorboli, C.; Indelli, M. T.; Scandola, M. A. R.; Scandola, F. *J. Phys. Chem.* 1988, 92, 156.
5. Fawcett, R. W. Liquids, Solution, and Interfernecees. Oxford University Press. New York, NY. 2004, 96-145.
6. Sista, P. Master's Thesis. University of San Francisco, 2009.
7. Inagaki, M. Master's Thesis. University of San Francisco, 2006.
8. Qin, A. Master's Thesis. University of San Francisco, 2012.
9. Mehmood, F. Master's Thesis. University of San Francisco, 2012.
10. Bertin, I.; Luchinat, C. NMR of Paramagnetic Molecules in Biological Systems. Benjamin/Cummings Publishing Company, Inc. . 1986, 12-101.
11. Brown, G.; Sutin, N. *J. Am. Chem. Soc.* 1979, 101, 883.
12. Eskandari, V. Master's Thesis. University of San Francisco, 2006.
13. Ivlev, B. *Phys. Rev. C*. 2013, 87, 34619.
14. Curtis, J.; Meyer, T. *Inorg. Chem.* 1982, 21, 1562.
15. Sandstom, J. Dynamic NMR Spectroscopy. Academic Press. New York, NY. 1982, 6-80.
16. Ige, J.; Ojo, J.; Olubuyude, O. *Inorg. Chem.* 1981, 20, 1757.

17. Levitt, M. Spin Dynamics: Basics of Nuclear Magnetic Resonance 2nd Ed. John Wiley & Sons Ltd. England. 2009, 260-300.
18. Gardiner, W. C. Rates and Mechanism of Chemical Reactions. W. A. Benjamin Inc. New York, NY. 1969, 35-234.
19. Connors, K. A. Chemical Kinetics: The Study of Reaction Rates in Solution. VCH Publishers. New York, NY. 1990, 166-253.
20. Nielson, R.; Wherland, S. *J. Am. Chem. Soc.* 1985, 107, 1505.
21. Meagher, N. E.; Juntunen, K. L.; Salhi, C. A.; Ochrymowycz, L. A.; Rorabacher, D. B. *J. Am. Chem. Soc.* 1992, 114, 10411.
22. McConnell, H. M.; Berger, S. B. *The Journal of Chemical Physics* 1957, 27, 230.
23. Takeda, M.; Stejskal, E. *J. Am. Chem. Soc.* 1960, 82, 25.
24. Allerhand, A.; Moll, R. *J. Magn. Reson.* 1969, 1, 488.
25. Biller, J.; Eaton, S.; Eaton, G.; Rosen, G. *J. Magn. Reson.* 2011, 212, 370.
26. Keifer, P. *Concepts in Mag. Res.* 1999, 11, 168.
27. Allen, A. D.; Bottomley, F.; Harris, R.; Reinsalu, V. P.; Senoff, C. V. *J. Amer. Chem. Soc.* 1967, 89, 5595.
28. Howe, J. L. *J. Amer. Chem. Soc.* 1896, 18, 981.
29. Magarian, N.; Oda, J.; Curtis, J.; Schweitert, C., (University of San Francisco, 2011).
30. Marcus, R. A. *The Journal of Chemical Physics* 1965, 43, 679.
31. Claridge, T. D. High-Resolution NMR Techniques in Organic Chemistry, Volume 27, Second Edition. Elsevier Ltd. Oxford, UK. 2009,
32. Ernst, R. R. *Adv. Magn. Reson.* 1966, 2, 1-135.
33. Amman, C.; Meier, P.; Merbach, A. *J. Magn. Reson.* 1982, 46, 319.
34. Teng, Q. Structural Biology: Practical NMR Applications. Birkhauser. 2005, 106.

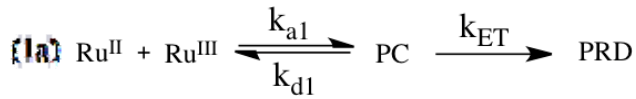
35. Allerhand, A.; Moll, R. *J. Magn. Reson.* 1969, 1, 488.
36. Inagaki, M. University of San Francisco, 2006.
37. Koppenol, W. H. *Biophys. J.* 1980, 29, 493.
38. Pan, Z. University of San Francisco, 2003.
39. Chen, P.-K. University of San Francisco, 2010.
40. Creutz, C. *Progress in Inorganic Chemistry* 1983, 30, 1-73.
41. McConnel, H. M. *Journal of Chemical Physics* 1961, 35, 508.
42. Curtis, J. C.; Mao, W.; Qian, Z.; Yen, H.-J. *J. Am. Chem. Soc.* 1996, 118, 3247.
43. Liu, L.; Guo, Q.-X. *Chemical Reviews* 2001, 101, 673-696.
44. Steinfeld, J.; Francisco, J.; Hase, W. Chemical Kinetics and Dynamics. Prentice-Hall. Englewood Cliffs, NJ. 1989, 14-15, 308-341.
45. Mortimer, R. G. Physical Chemistry (2nd Edition). Academic Press. Burlington, MA. 2000, 233, 949.
46. North, A. The Collision Theory of Chemical Reactions in Liquids. John Wiley & Sons Ltd. New York, NY. 1964, 1-14.
47. Berry, S.; Stuart, A.; Ross, J. Physical Chemistry, 2nd Ed.. Oxford University Press. New York, NY. 2000, 97-99, 911-919.
48. Hill, T. *Proc. Natl. Acad. Sci. USA.* 1976, 79, 679.
49. Lau, K. W.; Hu, A. M.-H.; Yen, M. H.-J.; Fung, E. Y.; Grzybicki, S.; Matamoros, R. *Inorganica Chimica Acta* 1994, 226, 137.
50. Bolton, J. R.; Archer, M. D. *Journal of the American Chemical Society* 1991, 65, 228.
51. Myers, R. *Inorg. Chem.* 1968, 68, 123.
52. Guggenheim, E. A.; Turgeon, J. C. *Trans. Faraday Soc.* 1955, 51, 747-761.

53. Chang, J. P.; Fung, E. Y.; Curtis, J. C. *Inorg. Chem.* 1986, 4233.
54. Sutin, N. *Prog. Inorg. Chem.* 1983, 30, 441.
55. Kielland, J. *J. Am. Chem. Soc.* 1937, 59, 1675.
56. Frisch, M. J.; Trucks, G. W.; Schlegel, H. B.; Scuseria, G. E.; Robb, M. A.; Cheeseman, J. R.; Scalmani, G.; Barone, V.; Mennucci, B.; Petersson, G. A.; Nakatsuji, H.; Caricato, M.; Li, X.; Hratchian, H. P.; Izmaylov, A. F.; Bloino, J.; Zheng, G.; Sonnenberg, J. L.; Hada, M.; Ehara, M.; Toyota, K.; Fukuda, R.; Hasegawa, J.; Ishida, M.; Nakajima, T.; Honda, Y.; Kitao, O.; Nakai, H.; Vreven, T.; Montgomery Jr., J. A.; Peralta, J. E.; Ogliaro, F.; Bearpark, M. J.; Heyd, J.; Brothers, E. N.; Kudin, K. N.; Staroverov, V. N.; Kobayashi, R.; Normand, J.; Raghavachari, K.; Rendell, A. P.; Burant, J. C.; Iyengar, S. S.; Tomasi, J.; Cossi, M.; Rega, N.; Millam, N. J.; Klene, M.; Knox, J. E.; Cross, J. B.; Bakken, V.; Adamo, C.; Jaramillo, J.; Gomperts, R.; Stratmann, R. E.; Yazyev, O.; Austin, A. J.; Cammi, R.; Pomelli, C.; Ochterski, J. W.; Martin, R. L.; Morokuma, K.; Zakrzewski, V. G.; Voth, G. A.; Salvador, P.; Dannenberg, J. J.; Dapprich, S.; Daniels, A. D.; Farkas, Ö.; Foresman, J. B.; Ortiz, J. V.; Cioslowski, J.; Fox, D. J., (Gaussian, Inc., Wallingford, CT, USA, 2009).
57. Meng, S. Master's Thesis. University of San Francisco, 2011.
58. Fawcett, R. W. Liquids, Solutions, and Interfaces. Oxford. 2004, 96.
59. Sutin, G. M. B. N. *Journal of the American Chemical Society* 1978, 101, 883-892.
60. Paulson, B.; Miller, J.; Gan, W.-X.; Closset, G. *J. Am. Chem. Soc.* 2005, 127, 4860.
61. Moore, J.; Pearson, R. Kinetics and Mechanism. Wiley. 1981,

Appendix A

Derivation of the Three-Channel Kinetic Model

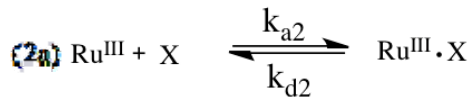
Channel 1 (Flux through the intermediate, PC)



For formation of PC:

$$-\frac{d\text{Ru}_0^{\text{II}}}{dt} = -\frac{d\text{Ru}_0^{\text{III}}}{dt} = k_{a1}[\text{Ru}_0^{\text{II}}][\text{Ru}_0^{\text{III}}] - k_{d1}[\text{PC}] \quad (\text{A-1})$$

The term $[\text{Ru}_0^{\text{III}}]$ does not account for the following:



In order to account for the formation of $\text{Ru}^{\text{III}} \cdot \text{X}$ we must first solve for $[\text{Ru}^{\text{III}} \cdot \text{X}]$ below,

$$-\frac{d\text{Ru}_0^{\text{III}}}{dt} = -\frac{d\text{X}}{dt} = k_{a2}[\text{Ru}_0^{\text{III}}][\text{X}] - k_{d2}[\text{Ru}^{\text{III}} \cdot \text{X}] = 0 \quad (\text{A-2})$$

$$[\text{Ru}^{\text{III}} \cdot \text{X}] = K_{A2}[\text{Ru}_0^{\text{III}}][\text{X}] \quad (\text{A-3})$$

Now, we can rewrite equation (A-1) accounting for the formation of $\text{Ru}^{\text{III}} \cdot \text{X}$,

$$-\frac{d\text{Ru}_0^{\text{II}}}{dt} = -\frac{d\text{Ru}_0^{\text{III}}}{dt} = k_{a1}[\text{Ru}_0^{\text{II}}]([\text{Ru}_0^{\text{III}}] - [\text{Ru}_0^{\text{III}} \cdot \text{X}]) - k_{d1}[\text{PC}] \quad (\text{A-4})$$

When we substitute for $[\text{Ru}^{\text{III}} \cdot \text{X}]$ from equation (A-5) we obtain,

$$-\frac{d\text{Ru}_0^{\text{II}}}{dt} = -\frac{d\text{Ru}_0^{\text{III}}}{dt} = k_{a1}[\text{Ru}_0^{\text{II}}]([\text{Ru}_0^{\text{III}}] - K_{A2}[\text{Ru}_0^{\text{III}}][\text{X}]) - k_{d1}[\text{PC}] \quad (\text{A-5})$$

$$-\frac{dRu_0^{II}}{dt} = -\frac{dRu_0^{III}}{dt} = k_{a1}[Ru_0^{II}][Ru_0^{III}](1 - K_{A2}[X]) - k_{d1}[PC] \quad (A-6)$$

Equation (A-6) accounts for all pathways in Channel 1 for which Ru_0^{II} and Ru_0^{III} can react. We now must apply the steady state approximation to the intermediate precursor complex (PC). In order to simplify this task we can apply equation (A-6) to account for formation of PC from Ru_0^{II} and Ru_0^{III} . We also need to account for the formation of products from PC; therefore the following equation is found,

$$-\frac{dPC}{dt} = k_{a1}[Ru_0^{II}][Ru_0^{III}](1 - K_{A2}[X]) - k_{d1}[PC] - k_{ET}[PC] \quad (A-7)$$

If we then apply the Steady-State approximation (SST) and solve for [PC] we obtain:

$$-\frac{dPC}{dt} = k_{a1}[Ru_0^{II}][Ru_0^{III}](1 - K_{A2}[X]) - k_{d1}[PC] - k_{ET}[PC] = 0 \quad (A-8)$$

$$[PC](k_{d1} + k_{ET}) = k_{a1}[Ru_0^{II}][Ru_0^{III}](1 - K_{A2}[X]) \quad (A-9)$$

$$[PC] = \frac{k_{a1}[Ru_0^{II}][Ru_0^{III}](1 - K_{A2}[X])}{k_{d1} + k_{ET}} \quad (A-10)$$

Now we can solve for the rate of formation of the products, PRD. From this we obtain the following equation,

$$\text{rate} = \frac{dPRD}{dt} = k_{ET}[PC] \quad (A-11)$$

If we plug in values obtained for [PC] in equation (A-10) we obtain,

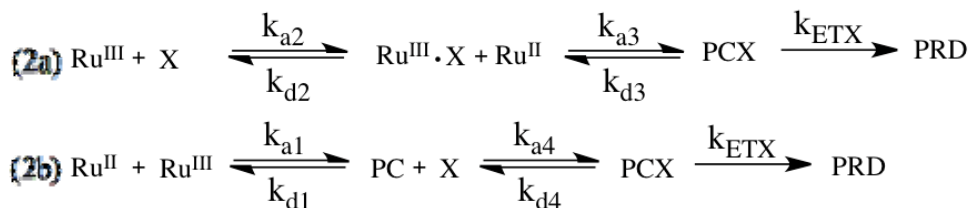
$$\text{rate} = k_{ET} \frac{k_{a1}[Ru_0^{II}][Ru_0^{III}](1 - K_{A2}[X])}{k_{d1} + k_{ET}} \quad (A-12)$$

If $k_{d1} \gg k_{ET}$ as is the case for our reaction, then the following equation is found,

$$\text{rate} = k_{\text{ET}} K_{\text{A1}} [\text{Ru}_0^{\text{II}}][\text{Ru}_0^{\text{III}}](1 - K_{\text{A2}}[\text{X}]) \quad (\text{A-13})$$

Equation (A-13) will be used to calculate the rate associated using Channel 1.

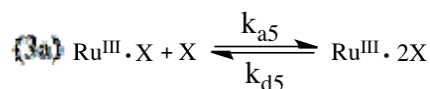
Channel 2 (Flux through the intermediate, PCX)



We will first focus on formation of PCX through Channel (2a). Through applying the same methodology as was done for Channel 1 we find,

$$-\frac{d\text{Ru}_0^{\text{III}} \cdot \text{X}}{dt} = -\frac{d\text{Ru}_0^{\text{II}}}{dt} = k_{\text{a3}}[\text{Ru}_0^{\text{II}}][\text{Ru}_0^{\text{III}} \cdot \text{X}] - k_{\text{d3}}\text{PCX} \quad (\text{A-13})$$

As in Channel 1 for the loss of Ru_0^{III} through Channel (2a), we must account for the formation of $\text{Ru}_0^{\text{III}} \cdot 2\text{X}$ Channel (3a) as illustrated below.



When we solve for formation of $\text{Ru}_0^{\text{III}} \cdot 2\text{X}$ we obtain the following,

$$-\frac{d\text{Ru}_0^{\text{III}} \cdot \text{X}}{dt} = -\frac{d\text{X}}{dt} = K_{\text{A2}} k_{\text{a5}}[\text{Ru}_0^{\text{III}} \cdot \text{X}][\text{X}] - k_{\text{d5}}[\text{Ru}^{\text{III}} \cdot 2\text{X}] = 0 \quad (\text{A-14})$$

$$[\text{Ru}^{\text{III}} \cdot 2\text{X}] = K_{\text{A5}}[\text{Ru}_0^{\text{III}} \cdot \text{X}][\text{X}] \quad (\text{A-15})$$

Substituting for $\text{Ru}_0^{\text{III}} \cdot \text{X}$ from equation (A-3) we obtain,

$$[\text{Ru}^{\text{III}} \cdot 2\text{X}] = K_{\text{A2}} K_{\text{A5}} [\text{Ru}_0^{\text{III}}] [\text{X}]^2 \quad (\text{A-16})$$

Now we can rewrite equation (A-13) accounting for the formation of $\text{Ru}^{\text{III}} \cdot 2\text{X}$,

$$-\frac{d\text{Ru}_0^{\text{III}} \cdot \text{X}}{dt} = -\frac{d\text{Ru}_0^{\text{II}}}{dt} = k_{\text{a3}} [\text{Ru}_0^{\text{II}}] ([\text{Ru}_0^{\text{III}} \cdot \text{X}] - [\text{Ru}_0^{\text{III}} \cdot 2\text{X}]) - k_{\text{d3}} \text{PCX} \quad (\text{A-17})$$

Applying the substitution for $[\text{Ru}_0^{\text{III}} \cdot 2\text{X}]$ as defined by equation (A-16) we obtain,

$$-\frac{d\text{Ru}_0^{\text{III}} \cdot \text{X}}{dt} = -\frac{d\text{Ru}_0^{\text{II}}}{dt} = k_{\text{a3}} [\text{Ru}_0^{\text{II}}] ([\text{Ru}_0^{\text{III}} \cdot \text{X}] - K_{\text{A2}} K_{\text{A5}} [\text{Ru}_0^{\text{III}}] [\text{X}]^2) - k_{\text{d3}} \text{PCX} \quad (\text{A-18})$$

When simplifying equation (A-18) and applying all necessary substitutions the following is found,

$$-\frac{d\text{Ru}_0^{\text{III}} \cdot \text{X}}{dt} = -\frac{d\text{Ru}_0^{\text{II}}}{dt} = k_{\text{a3}} K_{\text{A2}} [\text{Ru}_0^{\text{II}}] [\text{Ru}_0^{\text{III}}] [\text{X}] (1 - K_{\text{A5}} [\text{X}]) - k_{\text{d3}} \text{PCX} \quad (\text{A-19})$$

Now that we have an expression for Channel (2a) we must apply the same methodology to Channel (2b) as follows,

$$-\frac{d\text{PC}}{dt} = -\frac{d\text{X}}{dt} = k_{\text{a4}} [\text{PC}] [\text{X}] - k_{\text{d4}} \text{PCX} \quad (\text{A-20})$$

When we substitute for $[\text{PC}]$ (as was defined in equation (A-10)) and assume $k_{\text{d1}} \gg k_{\text{ET}}$ we obtain,

$$-\frac{d\text{PC}}{dt} = -\frac{d\text{X}}{dt} = k_{\text{a4}} K_{\text{A1}} [\text{Ru}_0^{\text{II}}] [\text{Ru}_0^{\text{III}}] [\text{X}] (1 - K_{\text{A2}} [\text{X}]) - k_{\text{d4}} \text{PCX} \quad (\text{A-21})$$

Now we can apply the SST for PCX as shown below,

$$\begin{aligned} -\frac{d\text{PCX}}{dt} = & k_{\text{a3}} K_{\text{A2}} [\text{Ru}_0^{\text{II}}] [\text{Ru}_0^{\text{III}}] [\text{X}] (1 - K_{\text{A5}} [\text{X}]) - k_{\text{d3}} \text{PCX} + \\ & k_{\text{a4}} K_{\text{A1}} [\text{Ru}_0^{\text{II}}] [\text{Ru}_0^{\text{III}}] [\text{X}] (1 - K_{\text{A2}} [\text{X}]) - k_{\text{d4}} \text{PCX} - k_{\text{ETX}} [\text{PCX}] = 0 \end{aligned} \quad (\text{A-22})$$

$$[\text{PCX}](k_{d3} + k_{d4} + k_{\text{ETX}}) = k_{a3}K_{A2}[\text{Ru}_0^{\text{II}}][\text{Ru}_0^{\text{III}}][\text{X}](1 - K_{A5}[\text{X}]) + k_{a4}K_{A1}[\text{Ru}_0^{\text{II}}][\text{Ru}_0^{\text{III}}][\text{X}](1 - K_{A2}[\text{X}]) \quad (\text{A-23})$$

$$[\text{PCX}] = \frac{k_{a3}K_{A2}[\text{Ru}_0^{\text{II}}][\text{Ru}_0^{\text{III}}][\text{X}](1 - K_{A5}[\text{X}]) + k_{a4}K_{A1}[\text{Ru}_0^{\text{II}}][\text{Ru}_0^{\text{III}}][\text{X}](1 - K_{A2}[\text{X}])}{k_{d3} + k_{d4} + k_{\text{ETX}}} \quad (\text{A-24})$$

If $k_{d3} \gg k_{\text{ETX}}$ and $k_{d4} \gg k_{\text{ETX}}$ then we can neglect k_{ETX} in the denominator in equation (A-24),

$$[\text{PCX}] = [\text{Ru}_0^{\text{II}}][\text{Ru}_0^{\text{III}}][\text{X}] \frac{k_{a3}K_{A2}(1 - K_{A5}[\text{X}]) + k_{a4}K_{A1}(1 - K_{A2}[\text{X}])}{k_{d3} + k_{d4}} \quad (\text{A-25})$$

Now we can solve for the rate of formation for the products, PRD, through Channel 2. From this we obtain the following equation,

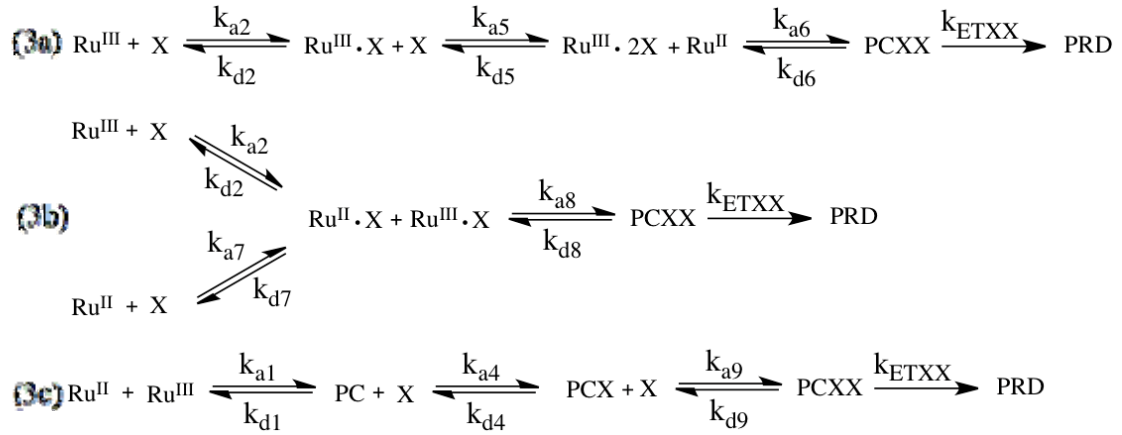
$$\text{rate} = \frac{d\text{PRD}}{dt} = k_{\text{ETX}}[\text{PCX}] \quad (\text{A-26})$$

Substituting in for $[\text{PCX}]$ (as defined in equation (A-25)) we obtain the rate equation associated with Channel 2,

$$\text{rate} = k_{\text{ETX}}[\text{Ru}_0^{\text{II}}][\text{Ru}_0^{\text{III}}][\text{X}] \frac{k_{a3}K_{A2}(1 - K_{A5}[\text{X}]) + k_{a4}K_{A1}(1 - K_{A2}[\text{X}])}{k_{d3} + k_{d4}} \quad (\text{A-27})$$

Equation (A-28) will be used to calculate the rate associated using Channel 2.

Channel 3 (Flux through the intermediate, PCXX)



We will first focus on formation of PCXX through Channel (3a). Through applying the same methodology as was done for Channels 1 and 2 we find,

$$-\frac{d\text{Ru}_0^{\text{III}} \cdot 2\text{X}}{dt} = -\frac{d\text{Ru}_0^{\text{II}}}{dt} = k_{\text{a}6}[\text{Ru}_0^{\text{II}}][\text{Ru}_0^{\text{III}} \cdot 2\text{X}] - k_{\text{d}6}\text{PCXX} \quad (\text{A-28})$$

When we apply the substitution for $[\text{Ru}_0^{\text{III}} \cdot 2\text{X}]$ as was defined in equation (A-16) we obtain,

$$-\frac{d\text{Ru}_0^{\text{III}} \cdot 2\text{X}}{dt} = -\frac{d\text{Ru}_0^{\text{II}}}{dt} = k_{\text{a}6}\text{K}_{\text{A}2}\text{K}_{\text{A}5}[\text{Ru}_0^{\text{II}}][\text{Ru}_0^{\text{III}}][\text{X}]^2 - k_{\text{d}6}\text{PCXX} \quad (\text{A-29})$$

Now that we have an expression for Channel (3a) we must apply the same methodology to Channel (3b) as follows,

$$-\frac{d\text{Ru}_0^{\text{III}} \cdot \text{X}}{dt} = -\frac{d\text{Ru}_0^{\text{II}} \cdot \text{X}}{dt} = k_{\text{a}8}[\text{Ru}_0^{\text{II}} \cdot \text{X}][\text{Ru}_0^{\text{III}} \cdot \text{X}] - k_{\text{d}8}\text{PCXX} \quad (\text{A-30})$$

In order to account for the formation of $[\text{Ru}_0^{\text{II}} \cdot \text{X}]$ we would apply the same methodology as was done when accounting for the formation of $[\text{Ru}_0^{\text{III}} \cdot \text{X}]$ as defined by equation (A-3),

$$-\frac{d\text{Ru}_0^{\text{II}}}{dt} = -\frac{d\text{X}}{dt} = k_{a7}[\text{Ru}_0^{\text{III}}][\text{X}] - k_{d7}[\text{Ru}_0^{\text{II}} \cdot \text{X}] = 0 \quad (\text{A-31})$$

$$[\text{Ru}_0^{\text{II}} \cdot \text{X}] = K_{A7}[\text{Ru}_0^{\text{II}}][\text{X}] \quad (\text{A-32})$$

When equations (A-3) and (A-32) are substituted into equation (A-30) we obtain,

$$-\frac{d\text{Ru}_0^{\text{III}} \cdot \text{X}}{dt} = -\frac{d\text{Ru}_0^{\text{III}} \cdot \text{X}}{dt} = k_{a8}K_{A2}K_{A7}[\text{Ru}_0^{\text{II}}][\text{Ru}_0^{\text{III}}][\text{X}]^2 - k_{d8}\text{PCXX} \quad (\text{A-33})$$

Now that we have expressions for Channels (3a) and (3b) we must apply the same methodology to Channel (3c) as follows,

$$-\frac{d\text{PCX}}{dt} = -\frac{d\text{X}}{dt} = k_{a9}[\text{PCX}][\text{X}] - k_{d9}\text{PCXX} \quad (\text{A-34})$$

When we plug in the values for $[\text{PCX}]$ which is defined by equation (A-25) we obtain,

$$-\frac{d\text{PCX}}{dt} = -\frac{d\text{X}}{dt} = k_{a9}[\text{Ru}_0^{\text{II}}][\text{Ru}_0^{\text{III}}][\text{X}]^2 \frac{k_{a3}K_{A2}(1 - K_{A5}[\text{X}]) + k_{a4}K_{A1}(1 - K_{A2}[\text{X}])}{k_{d3} + k_{d4}} - k_{d9}\text{PCXX} \quad (\text{A-35})$$

Now we can apply the SST for PCXX as follows,

$$-\frac{d\text{PCXX}}{dt} = k_{a9}[\text{Ru}_0^{\text{II}}][\text{Ru}_0^{\text{III}}][\text{X}]^2 W - [\text{PCXX}](k_{d6} - k_{d8} - k_{d9}) - k_{\text{ETXX}}[\text{PCXX}] = 0 \quad (\text{A-36})$$

$$W = k_{a6}K_{A2}K_{A5} + k_{a8}K_{A2}K_{A7} + k_{a9} \left(\frac{k_{a3}K_{A2}(1 - K_{A5}[\text{X}]) + k_{a4}K_{A1}(1 - K_{A2}[\text{X}])}{k_{d3} + k_{d4}} \right) \quad (\text{A-37})$$

When we solve for [PCX] we obtain,

$$[\text{PCXX}] = k_{a9} [\text{Ru}_0^{\text{II}}] [\text{Ru}_0^{\text{III}}] [\text{X}]^2 \text{Y} \quad (\text{A-38})$$

$$\text{Y} = \left(\frac{k_{a6} K_{A2} K_{A5} + k_{a8} K_{A2} K_{A7} + k_{a9} \left(\frac{k_{a3} K_{A2} (1 - K_{A5} [\text{X}]) + k_{a4} K_{A1} (1 - K_{A2} [\text{X}])}{k_{d3} + k_{d4}} \right)}{k_{d6} + k_{d8} + k_{d9} + k_{\text{ETXX}}} \right) \quad (\text{A-39})$$

When $k_{d6} \gg k_{\text{ETXX}}$, $k_{d8} \gg k_{\text{ETXX}}$, and $k_{d9} \gg k_{\text{ETXX}}$ then k_{ETXX} can be neglected in the dominator of equation (A-39). Now we can solve for the formation of products,

$$\text{rate} = -\frac{d\text{PRD}}{dt} = k_{\text{ETXX}} [\text{PCXX}] \quad (\text{A-40})$$

Substituting in the values of [PCXX] defined in equation (A-38) we obtain the rate equation for Channel 3,

$$\text{rate} = -\frac{d\text{PRD}}{dt} = k_{\text{ETXX}} k_{a9} [\text{Ru}_0^{\text{II}}] [\text{Ru}_0^{\text{III}}] [\text{X}]^2 \text{Y} \quad (\text{A-41})$$

$$\text{Y} = \left(\frac{k_{a6} K_{A2} K_{A5} + k_{a8} K_{A2} K_{A7} + k_{a9} \left(\frac{k_{a3} K_{A2} (1 - K_{A5} [\text{X}]) + k_{a4} K_{A1} (1 - K_{A2} [\text{X}])}{k_{d3} + k_{d4}} \right)}{k_{d6} + k_{d8} + k_{d9}} \right) \quad (\text{A-42})$$

When calculating the total rate for our three channel model we must add the rates calculated for each channel defined by equations (A-13), (A-27), and (A-41).